Using Heterogeneous 3D Earth Models To Constrain Interseismic and Postseismic Deformation in Southern California and Nepal

Thesis by
John Christopher Rollins

In Partial Fulfillment of the Requirements for
the degree of
Doctor of Philosophy

CALIFORNIA INSTITUTE OF TECHNOLOGY
Pasadena, California

2018
(Defended November 9, 2017)

John Christopher Rollins
ORCID: 0000-0002-5291-6956

ACKNOWLEDGEMENTS

Nothing in this thesis could have existed without the support of a large cast of characters, many of whom saw me through the last six years and many others who helped to make the last six years possible in the first place. The first person I need to thank is Jean-Philippe Avouac, who has been second to none as an advisor, inspiration and friend throughout the course of my Ph.D. I estimate that I am an order of magnitude more comfortable talking with Jean-Philippe about my research than I am thinking to myself about my research. This is the inverse of how things usually are for a student, and that inverse is a big reason why I got to the end of the road. In all moments when I was anxious, intimidated by factors I could not control, or confused about where to focus my efforts, Jean-Philippe was calm, cool and collected. He advises with an innate sense that the student makes the science and not the other way around, and therefore advises people, not projects; he looks for the best project to match a student's skill set, and how to work that match. This human perspective is coupled with a keen scientific eye for what might make a good project and a powerful sense of what questions to ask, what connections can be made between ideas from widely ranging disciplines, where a certain technique might find its best use, and – perhaps most importantly – what a given project originally sought to find out and what we learn and do not learn from a given result. In summary, if I am ever lucky enough to advise students of my own, my advising routine will essentially be my best impersonation of Jean-Philippe.

I next need to thank the other members of my thesis committee, Nadia Lapusta, Mike Gurnis and Rob Clayton. Nadia has been a great mentor, friend and guide from the very beginning – including sending me the original warm welcome as I was accepted into the Caltech Seismo Lab and letting me crash a Caltech colloquium honoring Jim Rice on the previous day – until the very end of my Ph.D., raising several excellent discussion points and ideas for my projects in the discussion with my committee during my defense. She was particularly a lifesaver as my on-campus advisor and representative during my application to a NASA Earth and Space Science Fellowship in 2015, and she welcomed me into her research group as one of her own during this time. I will always remember these moments when she stepped in and will always owe her for them. Mike Gurnis, my academic advisor, is another person without whom I would not be here today. I think Mike saw a path forward toward progress and good places, a path that at times I was either too confused to see or too disorganized to want to look for. Mike always kept me honest and made sure that I stuck with it rather than drifting, and did so in a friendly and supportive way. The final member of my committee is Rob Clayton, who is something of a father figure to students, particularly us in Seismo (I think there is a reason why he is the other faculty member who goes to the student-faculty lunches with John Grotzinger), and has been a great person to have on my thesis committee, particularly with the knowledge he brought to bear on the Los Angeles basin project.

There are many other GPS faculty I need to thank – Victor Tsai for helping me stay on track in TAing Hydrology and recover whatever problem-solving skills I had left by the side of the road previously, Pablo Ampuero for his collaboration on work involving viscoelastic relaxation and his friendship, Mark Simons for teaching Ge 118 and Ge 167, without which I wouldn't have gotten far, and too many others to list here. I also owe thanks to many other faculty around campus. This includes in particular Dennis Kochmann, who was the final member of my thesis advisory committee and was a great person to ask research questions of. Dennis' answers to emails from students are so thorough that I have no idea how he ever gets anything else done; anyone who was lucky enough to take Continuum Mechanics from him, as I was, can attest to these legendary email responses and more generally to his abilities as a teacher. He is missed on Caltech campus.

I next need to thank another guy I miss seeing on campus: my academic big brother, Sylvain Barbot. Sylvain is the main reason I know how to do anything on the practical side; he spent hours teaching me MATLAB, shell scripting, inverse theory, space geodesy, and topics in postseismic relaxation during my first year at Caltech. In addition to the fact that Sylvain's code RELAX forms the bread and butter of Chapters 2 and 5 of my thesis, many of the MATLAB and shell scripts I used throughout are modified (or in some cases unmodified) versions of Sylvain's codes, and he had a hand in every step of the way on the practical side, for example in testing GAMRA and writing output scripts for it. As essentially a liberal arts student that happens to also be interested in natural disasters and stumbled through an undergraduate geology major completely avoiding courses in computer science, I would have gotten nowhere at Caltech without Sylvain.

There are several other collaborators I need to thank. First is Walter Landry, the architect of GAMRA, who tirelessly helped me with using the code and answered dozens of emails about what value to set what parameter to. Another is Adriano Gualandi, who did all of the nitty-gritty work processing data and extracting the postseismic signal from GPS data in Nepal as used in Chapter 5, and who has become a great friend both at and away from the office. Another is Zach Ross, who spearheaded the project that forms the Appendix of my thesis, has been a buddy for many years, and is an inspirational young scientist in that he knows how to be rigorous without forgetting how to get excited. Finally, there is Donald Argus at JPL, who has helped substantially with the Los Angeles basin project and has been a great supporter and friend over the past two years.

I need to thank several people who have dotted the is and crossed the ts for me and helped things go smoothly over the past six years. Foremost are Heather Steele, Lisa Christiansen, and Carolina Oseguera, who made everything work without a hitch. I will miss having them around. Also a huge help has been Naveed Near-Ansari, who manages the GPS computing cluster and shows every time you talk to him why it is best to have a person doing that. I would be nowhere without Naveed. Edwin Tan Seng Tat is the Naveed of the computing cluster at the Earth Observatory of Singapore, which I used for a brief period in the middle of my Ph.D. I am not sure if Edwin sleeps, as he responded to emails from me 24/7 and always helped me sort out technical issues in a flash. I hope to someday meet Edwin and shake his hand and thank him in person.

The same gratitude is owed to several other support staff that make things run so smoothly that sometimes one doesn't even notice it, like the weather in Pasadena. Kim Baker-Gatchalian and Donna Mireles have been terrific in particular putting up with all of us in the Seismo Lab. Dian Buchness, Liz Boyd and Julie Lee have been fantastic, always a friendly face at the exact moment a student needed one (whoever manages the screening for their position does a hell of a job). I need to thank Tony Diaz, who helped me with all sorts of library inquiries and poster-printing issues (including one at 5 in the morning before an 8 AM poster session), and Rosy Diaz (not related), who punched in my NASA Earth and Space Science Fellowship as Nadia's assistant in 2015. I also need to thank the staff who run Broad Café (in particular Lucy) and Red Door Café for supplying the caffeine that enabled much of this work to ever get done. On a more serious note, I want to very much thank Dr. Lee Coleman and Dr. Jon-Patrik Pedersen for the time they have taken to work with me and for the thoughtfulness with which they have done so.

Outside of Caltech, there are three figures on the science side in particular who are much of the reason I ever made it into and through grad school. The first is Ross Stein, who mentored me as an intern at the U.S. Geological Survey Menlo Park right out of high school and through college. In addition to putting up with my disorganization and laziness with infinite patience, Ross taught me scientific writing and illustration, organization of a project, submission of a paper to a journal, public speaking and elevator pitches, and dislocation modeling, which formed much of the skill set I could bank on from the beginning at Caltech. The second is Tom Jordan, who mentored me on the project at the

Southern California Earthquake Center that become my undergraduate thesis. Tom is a titan in earthquake science but will always take an hour and a half of undivided time with a student regardless of how busy he is. Although I and most of us will never get close to emulating his quantitative chops, this attribute is one I will emulate if I am ever lucky enough to get the chance to teach. The third “science dad” is James Dolan, who has been a fantastic collaborator, supporter and father figure to me both at USC and in Los Angeles during my time at Caltech, in particular in the setup and interpretation of the Los Angeles basin project in Chapter 3. Tom and James got me hooked on the scientific and humanitarian importance of earthquake science in Southern California, and I will never be unhooked due to the example of their passion for it. I hope that Chapters 3 and 4 of this thesis might show that their passion has indeed been infectious, and that I am hooked.

I have been incredibly fortunate to have a set of friends, both at Caltech and outside, without whom I would not be here today. The obvious starting point is Bryan Riel and Tobias Bischoff, my roommates for five of the six years I was at Caltech and my surrogate older brothers. They helped me grow up during graduate school, with an innate sense of when to let me figure it out on my own and when to say “Dude.” They also contributed to the science content of my thesis; several topics and techniques they tossed around during discussions in the living room ended up making it into my work and would not have otherwise. Along with Jean-Philippe and many other faculty members, Tobi and Bryan are much of the reason why, when people ask me how Caltech was, I respond that it was a good learning experience. I need to thank Howard Hui, Stephen Perry and Reed Scharff, also surrogate brothers of mine. They saw me through my Ph.D. including both good times and tough times, and every second they were in my company, they showed that they wiould always be there as the strongest of friends and that we were always going to make it together, wherever it is. The list of surrogate family members at Caltech and in Pasadena extends far beyond these five brothers. In GPS, there is Voon, who would blush if she looked into the future and saw how successful she is going to be; Giuliana and Jen, who were exactly the friends I needed; Natalia and Elle, who raised the bar for how awesome people can be; Men-Andrin, who is the person I want to be at his age; Brent and Miki, who have always been inspirations to me; Daniel, Vish and Jorge, who light up the office in ways I cannot; Frank, Ted and Adam, who are exactly the characters every department and branch of science needs whenever things start to feel monotonic; Scmechah and Asaf, who along with Bryan and Stephen got me through first year and continue to be inspirations; and my officemates over the past few years, Zhongwen, Dongzhou, Dan,

Yingdi, and in particular Rachel, Celeste and Ethan, who have brightened the office over the past year. There are the many members of Jean-Philippe's group, who I am lucky to know as collaborators and as friends, in particular Stacy, who is destined for greatness; Jonny, Sylvain and Vicky, who had better come back stateside down the line; and Kristel, who it seems is unlikely to do so as a result of doing too well in France but whom I consider an academic older sister. These are but a few of a long list of GPS characters that I am unfairly truncating here. Outside GPS, there are my roommates Belinda and Nikola; the latter's mine shift crew including Burali; Rachel, Vipul and Marcello; and an even longer list of friends that saw me through the last few years. This includes my bandmates, Konstantin, Erik and Chris, with whom I have greatly enjoyed playing and spending time.

I was lucky to begin attending research conferences while still an undergrad and to meet a host of people in the seismological community whom I consider family. These are Amir and many others from USC; Harmony, Kayla, Julian, Allie, Jacqui and many other brothers and sisters from UC Riverside (the entirety of which I consider home, in addition to USC and now Caltech); and those from Stanford (in particular Sam and Kali), Colorado, KU, the USGS and too many other places to name. The greatest joy of being a young earthquake scientist is that I get to have you as peers and friends and get to see you one or more times a year, and that is much of the reason that I intend to ride this as long as I can.

There is also a long line of friends around Los Angeles and elsewhere without whom I would not be here today. There is Meharban, whom I will miss greatly; Mike, whom I already do; Trevor, who has continued to be the best of friends and whom I hope to see in Alaska; Maya, who I ran into at exactly the right time; Lesley, who saw me through the earliest and most firehose-like part of grad school with unwavering support; Jenna, whom I also ran into at exactly the right time; James, who I am glad came back to town; Mickey, who I wish had never left; Jes and Brian; the crew from Bowlunch, whom I hope to see again; and very importantly Andy, Calvin, Chow, Dilfer, Kirst and the Goonies, who are family to me and alongside whom it has been a joy and an inspiration to grow up. There are many characters from earlier in my life, including Adam Perl, who taught me to find joy in problem solving and self-improvement. I want to thank in particular Max Hammer, my best friend throughout much of my early life, who passed away this past April. Max is probably much of the reason that almost any of the aforementioned characters wanted to be my friend in the first place: he taught me what was cool in life and how to be a guy, set me on a course to finding the music I listen to today, and was an inspiration on the piano and in life. I love you and miss you, Max.

While I am rewinding to the beginning of the tape, I need to thank my teachers from elementary school and high school and college, who helped to foster a love of learning, a passion for writing, and a sense of purpose. In particular I want to thank Peter Brodie, in whose company I had so much fun being a "nerd" that I didn't care what anyone else thought, and whom I hope to see again. I also very much need to thank my parents, who have seen me through my entire path here with endless support and love and have been the best of role models in how to walk down that path. I love you and promise to give back to you for all you have given to me.

Lastly, I want to thank Jeff Freymueller at the University of Alaska Fairbanks, whom has given me a next step. Let's do this thing.

ABSTRACT

We characterize interseismic strain accumulation across the Los Angeles basin and postseismic deformation following the 2010 Mw=7.2 El Mayor-Cucapah and 2015 Mw=7.8 Nepal earthquakes using geodetic data. These settings are all characterized by strong 3D heterogeneities of elastic structure, ductile properties, fault geometries, and fault slip behavior, and we use constaints from seismology, long-term tectonic modeling, geology, and other sources to construct detailed models of these heterogeneities. Postseismic surface displacements following the 2010 El Mayor-Cucapah earthquake indicate viscoelastic relaxation in the shallow Salton Trough mantle and possibly the lower crust, a process that would have been enhanced by high heat flow induced by crustal extension at the tip of the Gulf of California. We find that a dense and prolonged aftershock sequence in the Yuha Desert may have been driven by aseismic afterslip coupled with fluid flow. Our study of interseismic strain accumulation across the Los Angeles basin shows that the soft sedimentary basin has a first-order effect on the elastostatic Green's functions mapping fault creep and locking at depth to surface deformation, and therefore on the estimation of interseismic fault creep rates and strain accumulation at depth. We infer modest interseismic coupling on the three major thrust faults underlying the Los Angeles basin, corresponding to an annual seismic moment deficit buildup rate (to be presumably released in earthquakes) of 1.7 +1.2/-0.5 x 10^{17} Nm/yr. We estimate the long-term seismicity model needed to balance the rate of moment deficit accumulation assuming a truncated Gutenberg-Richter magnitude-frequency distribution of earthquakes. The long-term catalog is consistent with the instrumental rates of small and moderate earthquakes and tops out at a M~6.9 earthquake every ~430 years. Finally, we characterize the postseismic deformation following the 2015 Nepal earthquake using models of the thermal structure, state of stress, and rheology that are based on the long-term evolution and topography of the Himalaya. The rheological structure based on these models predicts negligible postseismic viscoelastic deformation. Afterslip on the downdip extension of the rupture cannot realistically explain the observed displacements either. We find that the postseismic deformation is well explained by a combination of afterslip on the downdip edge of the coseismic rupture (as well as a narrow zone in between the mainshock and a large aftershock) and, more prominently, transient viscoelastic relaxation in the hot Tibetan crust. These processes contribute to the stress loading of the Main Himalayan Thrust.

PUBLISHED CONTENT AND CONTRIBUTIONS

Chapter 2: “Postseismic Deformation Following the 2010 M=7.2 El Mayor-Cucapah Earthquake: Observations, Kinematic Inversions, and Dynamic Models” by C. Rollins, S.D. Barbot and J.-P. Avouac, Pure and Applied Geophysics, 2015, doi:10.1007/s00024-014-1005-6.

- I carried out the analysis and wrote the manuscript with the assistance of S.D. Barbot and J.-P. Avouac.

Appendix: “Aftershocks Driven by Afterslip and Fluid Pressure Sweeping Through a Fault-Fracture Mesh” by Z.E Ross, C. Rollins, and E.S. Cochran, E. Hauksson, J.-P. Avouac, and Y. Ben-Zion, Geophysical Research Letters, 2017, doi:10.1002/2017GL074634.

- I carried out the analysis of the geodetic data, carried out the kinematic modeling of the afterslip source based on this data in Figures A.1 and A.3a, and contributed to the interpretation and the writing and organization of the paper.

TABLE OF CONTENTS

LIST OF ILLUSTRATIONS

LIST OF TABLES

Chapter 1

INTRODUCTION

An observer looking closely at the Earth for a period of a few years will observe the Earth's lithosphere (its outermost and stiffest layer) accumulating strain due to a variety of causes and releasing that strain in a variety of ways. Chief among these is tectonic deformation: oceanic plates are continuously pulled towards subduction zones and into the mantle by the negative buoyancy of the subducting slabs attached to them, dragging them beneath or beside neighboring plates and inducing a gradual buildup of shear strain near plate boundaries. The relatively cold, brittle upper crust releases this strain on the timescale of seconds in earthquakes and steadily in fault creep, and the hotter, ductile lower crust and mantle release this strain by steady creep and bulk ductile flow [e.g. Burgmann and Dresen, 2008] (Figure 1.1). Superimposed on this suite of behaviors (sometimes called the seismic cycle) is a host of other sources of strain and processes by which it is accommodated. Volcanic magma chambers can inflate and deflate over the course of months [e.g. Liu et al, 2011; Riel et al, 2015]. The weight of water, snow and ice depresses the lithosphere into the underlying mantle, and the removal of this weight allows it to gradually rebound upward over tens of thousands of years (as most spectacularly observed in regions formerly covered by ice caps during the last Ice Age, e.g. Simons and Hager [1997]). The management of aquifers and oil fields by humans, as well as the seasonal heating and cooling of the Earth's surface, induces volumetric expansion and contraction on the timescale of months and years [e.g. Argus et al 2005, Tsai 2011]. Each of these processes contributes uniquely to deformation observed at the surface.

Even given the diversity of these individual processes, the deformation of the Earth's lithosphere one might observe over a year or a lifetime is especially rich, varied and complex for at least two reasons. The first is that these processes happen everywhere: every fault has some variant of a seismic cycle, every active volcano has a magma chamber, every icecap and monsoon depresses the lithosphere, every aquifer affects the surrounding volume, and the entire Earth's crust is heated and cooled seasonally. The second, and central to much of this thesis, is that these processes are physically coupled and therefore every instance of one of these processes dynamically affects, and is dynamically affected by, every instance of every process that is sufficiently close to it in space. This occurs

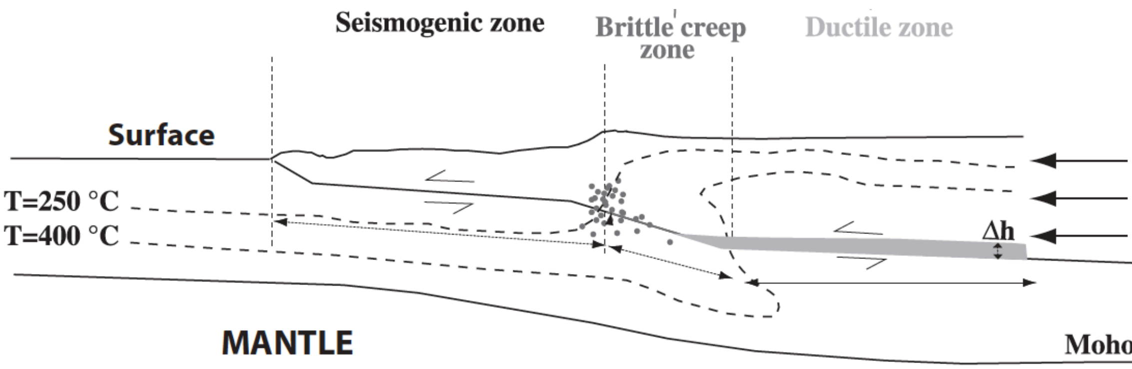

Figure 1.1. Schematic modified from Perfettini and Avouac [2004] showing the coupled roles of seismic and aseismic processes in accommodating tectonic strain.

between different instances of the same process; an example of this seen in Chapter 3 is that a set of overlapping faults can work in parallel to accommodate the contraction across a region, via both earthquakes and steady creep. This dynamic feedback also occurs between different deformation processes: an earthquake can stretch the crust around a nearby volcano and induce an eruption [e.g. Hill et al, 2002], or the hydrological loading force of rain and snow can affect the rates of earthquakes on nearby faults, as observed in the Himalaya [e.g. Chanard et al, 2014]. An example of this seen in Chapters 2 and 5 is postseismic deformation: an earthquake causes sudden warping of the surrounding crust and mantle, momentarily accelerating the steady processes of fault creep and bulk ductile flow; and these relaxation processes also feed back on one another in turn (Figure 1.2).

A key challenge in the study of lithospheric deformation, then, is to accurately represent these kind of complexities while keeping the science as simple as possible. Although it is highly unlikely that they are anything close to benchmarks for doing so, the studies compiled in this thesis attempt to strike this balance. They attempt to do so in two common ways, which might be seen as unifying characteristics of the chapters presented here. The first is that they incorporate data-based models of deformation that vary in all three dimensions in settings where such models have often not yet been incorporated or used for the same purpose. Chapter 2 is a study of postseismic deformation following the 2010 Mw=7.2 El Mayor-Cucapah earthquake that brings in 3D seismology-based models of the Mohorovicic discontinuity (the crust-mantle boundary) and the lithosphere-asthenosphere boundary (the base of the lithosphere), as well as 3D models of fault creep in various geometries, to inform conceptions of how the crust and mantle may have deformed to relax the stress changes induced by the earthquake. Chapters 3 and 4 are a two-part study of strain accumulation in the Los Angeles basin that brings in 3D seismology-based models

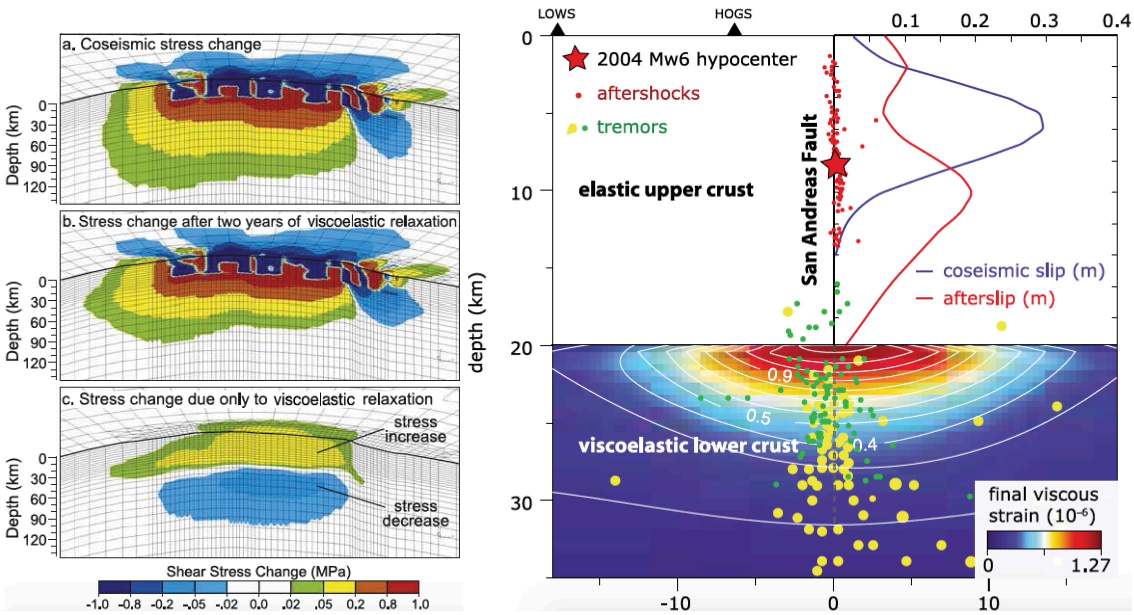

Figure 1.2. Figures from Freed et al [2006] (left) and Bruhat et al [2011] (right) showing how gradual deformation processes at depth are accelerated by coseismic stress changes.

of fault geometry and elastic structure, in particular the soft sediments of the basin, to improve the estimation of how quickly strain is accumulating on faults that underlie the basin. Chapter 5 is a study of postseismic deformation following the 2015 Mw=7.8 Nepal earthquake that brings in 2D and 3D models of the thermal structure, state of stress, fault geometry and rheology of the Himalaya to characterize the mechanisms contributing to the deformation observed.

The second way in which the studies here attempt to more accurately characterize complex settings is by incorporating models of various deformation processes feeding back on one another. Chapter 2 features dynamic models in which afterslip, viscoelastic relaxation in the lower crust, and viscoelastic relaxation in the mantle all work in concert to relax the stress changes imparted by the 2010 El Mayor-Cucapah earthquake. Chapter 3 studies the ways that three faults beneath the Los Angeles basin may trade off and work in concert to accommodate north-south shortening across the region (Figure 1.3) and discusses ways in which time-dependent deformation such as viscoelastic relaxation following the 1857 Fort Tejon earthquake could be affecting the inferred shortening rate. Chapter 5 presents a model of coupled afterslip and viscoelastic relaxation working in parallel to relax the stress changes imparted by the 2015 Gorkha earthquake.

The complexity of each of the settings studied here means that any study of subsurface processes will involve both a large number of parameters and a large number of

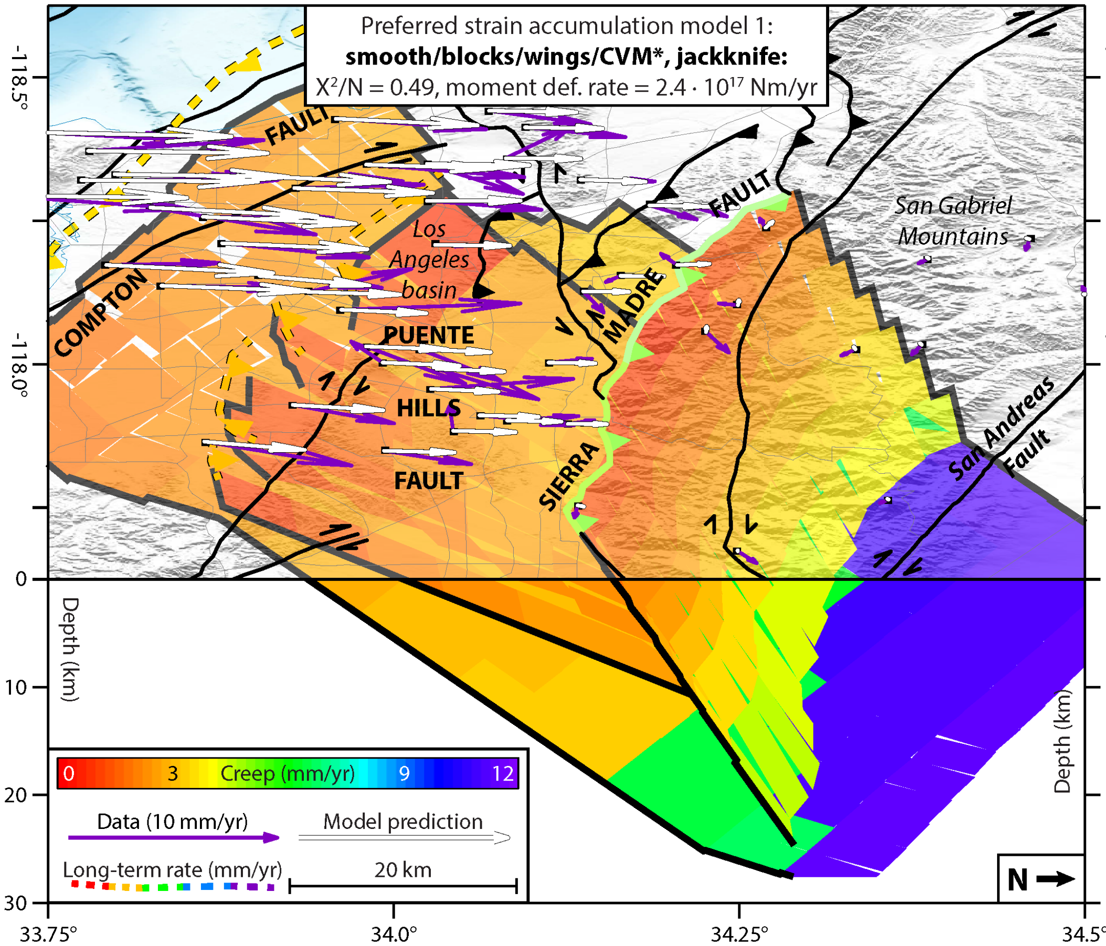

Figure 1.3. Creep rates on a system of thrust faults beneath Los Angeles as inferred from geodetic shortening at the surface (Chapter 3).

assumptions that may be difficult to express as parameters, as particularly seen in Chapters 3 and 4. Continuing advances in computing mean that future students may be able to examine the various factors that go into each problem all at once – ideally in a Bayesian setting that weights their possibilities of contribution and reflects their tradeoffs – rather than one by one, as often done here (except in the aforementioned coupled deformation models). The author hopes nevertheless that some of the considerations touched on in these studies might be useful to future workers.

Chapter 2

POSTSEISMIC DEFORMATION FOLLOWING THE 2010 MW=7.2 EL MAYOR-CUCAPAH EARTHQUAKE: OBSERVATIONS, KINEMATIC INVERSIONS AND DYNAMIC MODELS

(Published as “Postseismic Deformation Following the 2010 M=7.2 El Mayor-Cucapah Earthquake: Observations, Kinematic Inversions, and Dynamic Models” by C. Rollins, S.D. Barbot and J.-P. Avouac, Pure and Applied Geophysics, 2015)

ABSTRACT

Due to its location on a transtensional section of the Pacific-North American plate boundary, the Salton Trough is a region featuring large strike-slip earthquakes within a regime of shallow asthenosphere, high heat flow and complex faulting, and so postseismic deformation there may feature enhanced viscoelastic relaxation and afterslip that is particularly visible at the surface. The 2010 Mw=7.2 El Mayor-Cucapah earthquake was the largest shock in the Salton Trough since 1892 and occurred close to the U.S.-Mexico border, and so the postseismic deformation recorded by the continuous GPS network of southern California provides an opportunity to study the rheology of this region. Three-year postseismic transients extracted from GPS displacement timeseries show four key features: 1) 1-2 cm of cumulative uplift in the Imperial Valley and ~1 cm of subsidence in the Peninsular Ranges, 2) relatively large cumulative horizontal displacements >150 km from the rupture in the Peninsular Ranges, 3) rapidly decaying horizontal displacement rates in the first few months after the earthquake in the Imperial Valley, and 4) sustained horizontal velocities, following the rapid early motions, that were still visibly ongoing three years after the earthquake. Kinematic inversions show that the cumulative three-year postseismic displacement field can be well fit by afterslip on and below the coseismic rupture, though these solutions require afterslip with a total moment equivalent to at least a Mw=7.2 earthquake and higher slip magnitudes than those predicted by coseismic stress changes. Forward modeling shows that stress-driven afterslip and viscoelastic relaxation in various configurations within the lithosphere can reproduce the early and later horizontal velocities in the Imperial Valley, while Newtonian viscoelastic relaxation in the asthenosphere can reproduce the uplift in the Imperial Valley and the subsidence and large westward displacements in the Peninsular Ranges. We present two forward models of dynamically coupled deformation mechanisms that fit the postseismic transient well: a model combining afterslip in the lower crust, Newtonian viscoelastic relaxation in a localized zone in the lower crust beneath areas of high heat flow and geothermal activity, and Newtonian viscoelastic relaxation in the asthenosphere; and a second model that replaces the afterslip in the first model with viscoelastic relaxation with a stress-dependent viscosity in the mantle. The rheology of this high-heat-flow, high-strain-rate region may incorporate elements of both these models and may well be more complex than either of them.

2.1. Introduction

In addition to earthquakes, the earth's lithosphere accommodates tectonic strain through aseismic processes such as slow slip on faults, bulk ductile flow, and elastic deformation coupled with pore fluid motion. A large earthquake imparts stress changes to the crust and mantle that can accelerate these processes: segments of faults surrounding the coseismic rupture may be driven to slip aseismically [e.g., Marone et al, 1991; Hearn et al, 2002; Perfettini and Avouac, 2002; Freed, 2007]; sections of the crust and mantle may behave viscoelastically, relaxing coseismic elastic stress changes through ductile flow [e.g., Nur and Mavko, 1974; Deng et al, 1998; Pollitz et al, 2003]; and pore fluids may move away from areas of increased pressure [e.g., Peltzer et al, 1998; Jonsson et al, 2003, Fialko 2004]. These processes may cause observable transient displacement at the surface, and the measurement of this transient with geodetic methods can in principle be used to identify the associated processes, thereby shedding light on the rheology of the crust and mantle.

The Salton Trough is a region where surface displacements due to these processes may be particularly detectable. Located on a transtensional section of the Pacific-North American plate boundary in southernmost California and northwestern Mexico, this region represents a transition between the transform tectonics of southern California to the northwest and the extensional regime of the East Pacific Rise to the southeast. The extensional component of relative plate motion has thinned the lithosphere, bringing the low-viscosity asthenosphere up to within ~45 km of the surface (compared to a regional average of ~80 km) [Lekic et al, 2011] (Figure 2.1), and the very high heat flow and geothermal activity in this region [e.g., Lachenbruch et al, 1985] imply that viscosities are also reduced in the crust [e.g., Williams et al, 2012]. Meanwhile, the transform component of relative plate motion is accommodated by large strike-slip earthquakes that impart large stress changes to this structure, as well as a complex array of faults that may slip aseismically [e.g., Rymer et al, 2011]. The 2010 Mw=7.2 El Mayor-Cucapah earthquake was the largest shock in the Salton Trough since at least 1892 [Hauksson et al, 2011] and may have induced significant viscoelastic relaxation, afterslip and poroelastic rebound, and so the surface deformation following this earthquake may yield unique insights into the rheology of this region. This earthquake also provides a unique opportunity to determine whether a rheological structure inferred by seismic methods – the Lekic et al [2011] lithosphere-asthenosphere boundary – is also visible in geodetic deformation. A previous study of deformation following this earthquake [Pollitz et al, 2012] found that the postseismic velocity field did indeed suggest a laterally heterogeneous rheological structure

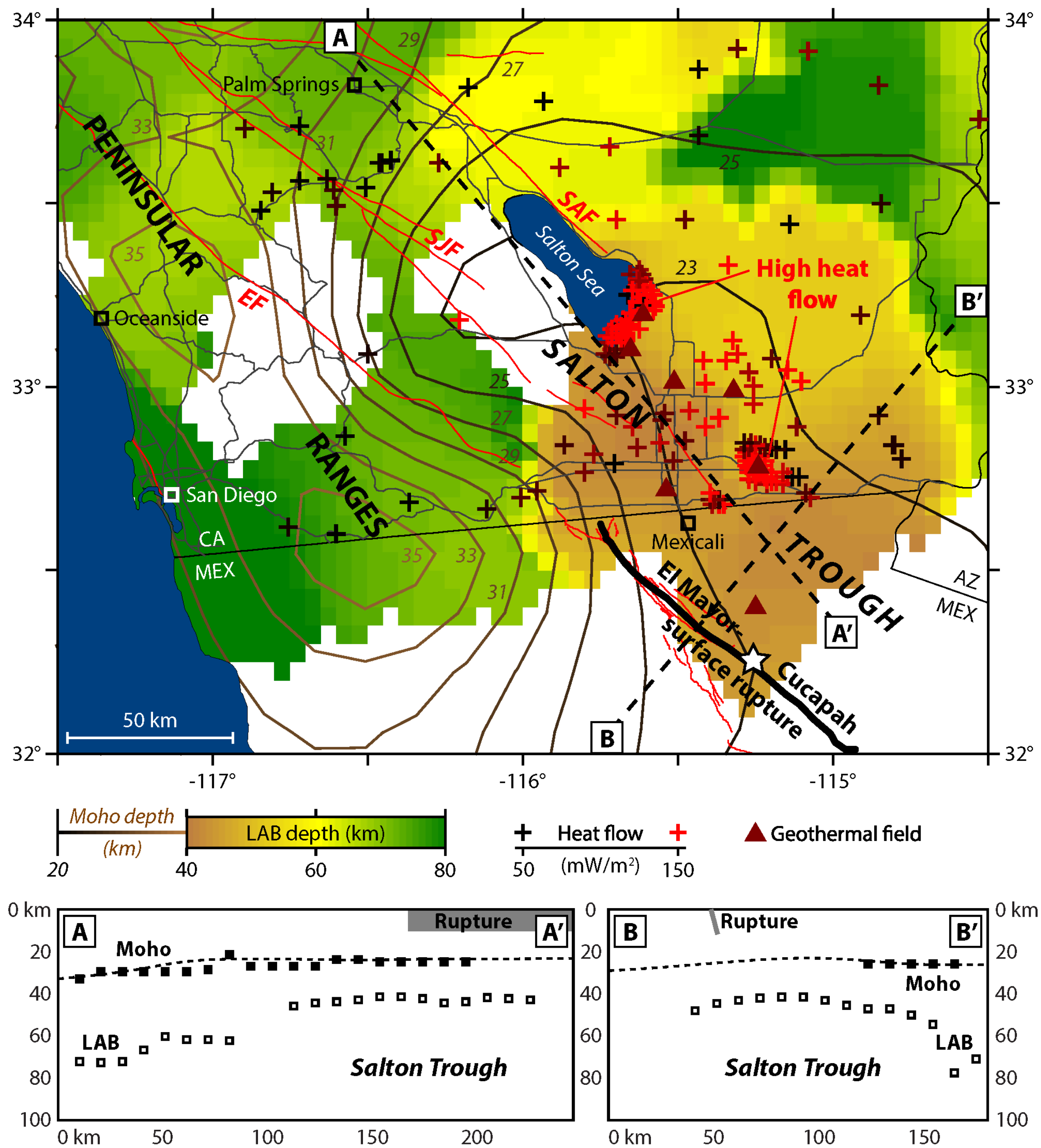

Figure 2.1. a) The El Mayor-Cucapah earthquake occurred in the Salton Trough, a region featuring a shallow lithosphere-asthenosphere boundary (colored surface; data from Lekic et al [2011], shallow Moho (brown contours; data from Tape et al [2012]), high heat flow (red crosses; data from USGS California Heat Flow Data Map), and geothermal activity (red triangles). **b)** Cross sections through the Salton Trough, respectively adapted from cross sections FF' and EE' in Lekic et al [2011], show that the earthquake occurred above shallow lithosphere-asthenosphere boundary and Moho.

in the upper mantle beneath the Salton Trough. A more recent study [Gonzalez-Ortega et al, 2014] found that early near-field GPS and InSAR displacements in Mexico could be fit to afterslip on the coseismic rupture but that geodetic displacements farther from the rupture required a longer-wavelength mechanism, for which they suggested distributed viscoelastic relaxation.

2.2. Coseismic deformation and implications for postseismic relaxation

The El Mayor-Cucapah earthquake ruptured ~110 km of a series of northwest-striking faults within the Sierra Cucapah and Sierra El Mayor ranges on the west side of the Mexicali Valley, just south of the US/Mexico border [Hauksson et al, 2011]. Wei et al [2011] used a joint inversion of seismic, geodetic and remote sensing data to produce a best-fitting rupture model for the earthquake. Although the surface rupture followed a roughly linear trace, the dominant slip surface at depth swung over from a southwest-dipping plane to a northeast-dipping plane over the length of the rupture. The earthquake featured approximately a 2:1 ratio of right-lateral to normal slip. We model the coseismic displacement and strain fields produced by the Wei et al [2011] slip model in an elastic halfspace using Coulomb 3.3 [Toda et al, 2005; Lin and Stein, 2004]. Both elastic modeling and coseismic vertical displacements at UNAVCO GPS stations (discussed in the next section) indicate that the Imperial Valley underwent uplift during the mainshock (Figure 2.2a), a perhaps surprising finding given that the region north of a northwest-striking right-lateral earthquake should be an extensional quadrant in seismological terms, where the first recorded motion should be downward. Cross sections of the coseismic displacement and strain fields (Figure 2.2b, c) reveal that the crust and mantle in the Imperial Valley were pulled upwards and southeast towards the rupture during the mainshock, uplifting the surface there. The vertical extension ε_{zz} under the Imperial Valley was positive at >50 km depth, beneath the Lekic et al [2011] lithosphere-asthenosphere boundary, but negative at 20-30 km depth in the lower crust and mantle lithosphere. This distribution of coseismic uplift, subsidence and strain at depth may be characteristic of surface-rupturing strike-slip earthquakes (Figure 2.S1). The normal component of coseismic slip imparted a similar vertical strain distribution beneath the rupture, with vertical extension at >50 km depth but vertical compression at 20-30 km depth (Figure 2.2c). As we will show, this strain field has important implications for the simulated viscoelastic responses of the asthenosphere, lower crust and mantle lithosphere.

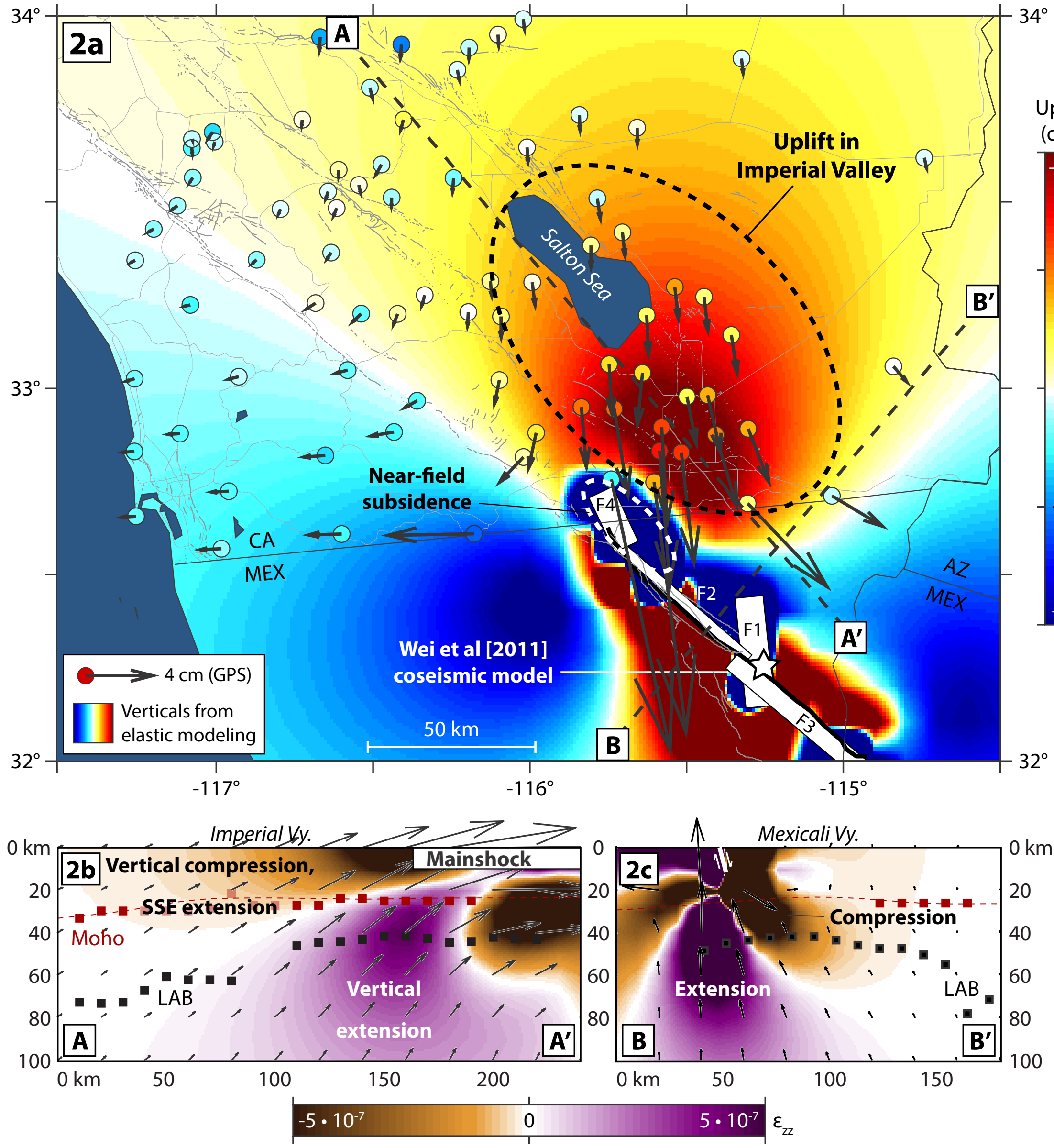

Figure 2.2. a) Coseismic displacements at UNAVCO GPS stations (arrows are horizontal displacements; colored circles are vertical displacements) and in elastic modeling using the Wei et al [2011] slip model for the El Mayor-Cucapah earthquake (colored surface represents modeled vertical displacements) indicate coseismic uplift in the Imperial Valley, a seismological extensional quadrant. **b, c)** Cross sections of coseismic displacement and vertical extension ε_{zz} in elastic modeling show that material beneath the Imperial Valley was pulled upward and towards the rupture, uplifting the surface there and causing vertical extension below ~40 km depth and compression above that. The normal component of slip also pulled material upward beneath the rupture.

2.3. GPS data and extraction of postseismic displacement timeseries

The UNAVCO Plate Boundary Observatory's network of continuous GPS stations provided coverage of surface deformation north of the U.S.-Mexico border before, during and after the El Mayor-Cucapah earthquake. The Scripps Orbit Processing and Array Center (SOPAC; sopac.ucsd.edu) uses the GAMIT/GLOBK processing software to produce daily three-component position timeseries for each UNAVCO station. These timeseries contain a linear trend due to continuous plate motions; annual and semiannual oscillations; instantaneous offsets from earthquakes, station maintenance and changes in processing methods; the offsets associated with the El Mayor-Cucapah mainshock; and finally the decaying transient signal of postseismic deformation (Figure 2.3). We use nonlinear least-squares to fit the timeseries to

$$x(t) = C_1 + C_2\, t + C_3 \sin(2\pi t) + C_4 \cos(2\pi t) + C_5 \sin(2\pi t) + C_6 \cos(2\pi t) + C_7\, H(t) \\ + C_8 \log(1 + t/C_9) + C_{10}\, (1\text{-}\exp(\text{-}t/C_{11})) + D_i\, H(t - t_i), \qquad (2.1)$$

where C_1 is a constant offset, C_2 is the secular velocity, C_3 and C_4 are coefficients of the annual oscillation, C_5 and C_6 are coefficients of the semiannual oscillation, C_7 is the magnitude of the coseismic offset, C_8 is the magnitude of a logarithmic decay function with characteristic time C_9, C_{10} is the magnitude of an exponential decay with characteristic time C_{11}, and D_i are the magnitudes of instantaneous offsets at times t_i represented by the Heaviside step functions $H(t - t_i)$. In this scheme the postseismic transient is fit to the combination of the logarithmic and exponential functions. Due in part to noise in the data, nonlinear least-squares has the potential to become caught in local minima and potentially miss the best-fitting decay parameters. To reduce the effect of this, we run nonlinear least-squares on the timeseries ten times using ten different pairs of initial values for C_9 and C_{11} randomized in log space between 0.1 and 10, then use the average of the ten best-fit decays as the comprehensive best-fit transient. To estimate the uncertainty in the fit due to noise and uncertainty in the data, we generate four supplementary timeseries consisting of the data plus a vector of Gaussian noise multiplied by the SOPAC daily formal position errors, run the process ten times on each supplementary timeseries (with initial relaxation times randomized as before) to generate 40 alternative decays, and estimate the daily uncertainty in each component of position as the daily root-mean-squared difference between the 40 alternatives and the comprehensive best-fit decay. This method produces estimates of coseismic and cumulative postseismic displacements that are generally quite similar to

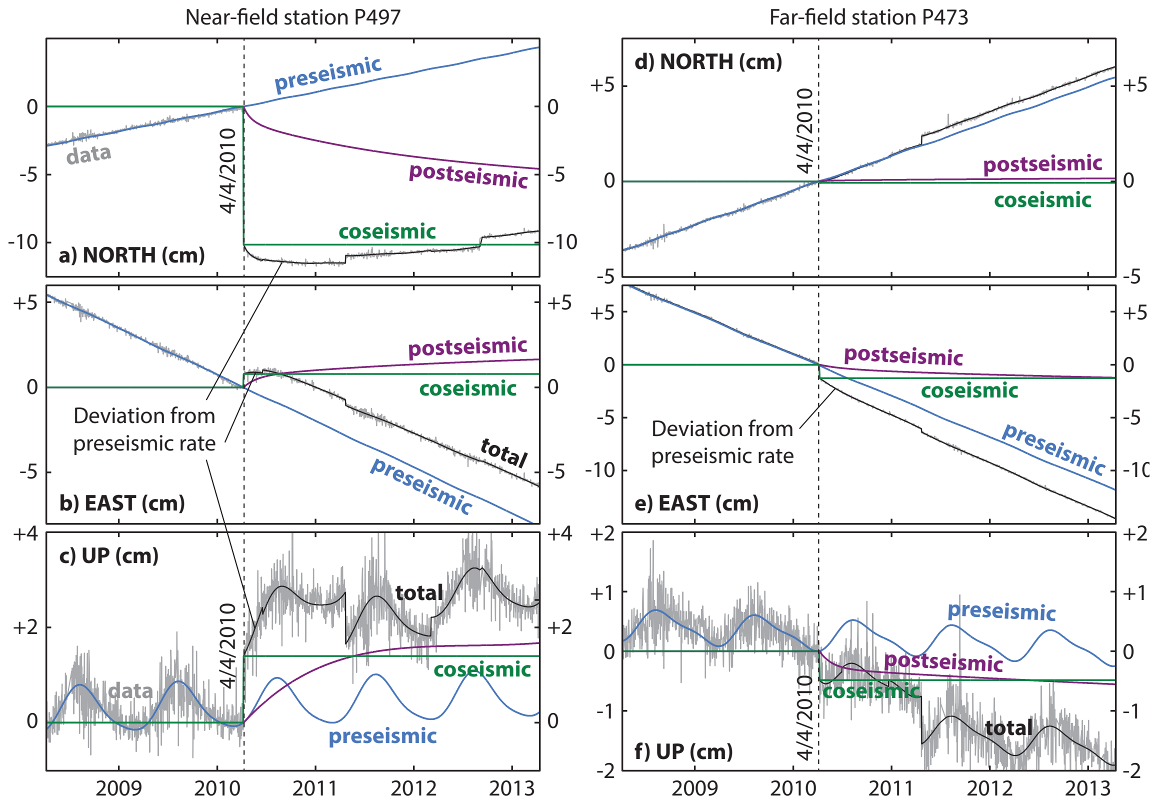

Figure 2.3. We extract coseismic and postseismic displacement signals from daily three-component position timeseries at UNAVCO GPS stations. **a-c)** Timeseries at near-field station P497 show clear southward, eastward and upward deviations from background rates following the mainshock. **d-f)** Postseismic signals are more subtle at far-field station P473 but a westward postseismic transient is visible.

those estimated by SOPAC (Figure 2.S2, Figure 2.S3). As a result of using a single decay function, the SOPAC methodology incorrectly ascribes some of the very early horizontal displacements in the Imperial Valley to coseismic displacement (Figure 2.S2b), while our method correctly separates the two (Figure 2.3a).

Following the earthquake, UNAVCO installed a set of continuous GPS stations near the rupture in Mexico to image postseismic deformation there. These stations did not record the first segment of postseismic deformation, making estimates of total postseismic displacements difficult, and they do not contain preseismic timeseries from which linear motion rates and periodic oscillations could be reliably extracted. However, Plattner et al [2007] calculated linear motion rates at sites near these stations using a previously installed campaign GPS network, and Pollitz et al [2012] estimated velocities of postseismic deformation at these stations by subtracting off the linear motion rate from the nearest

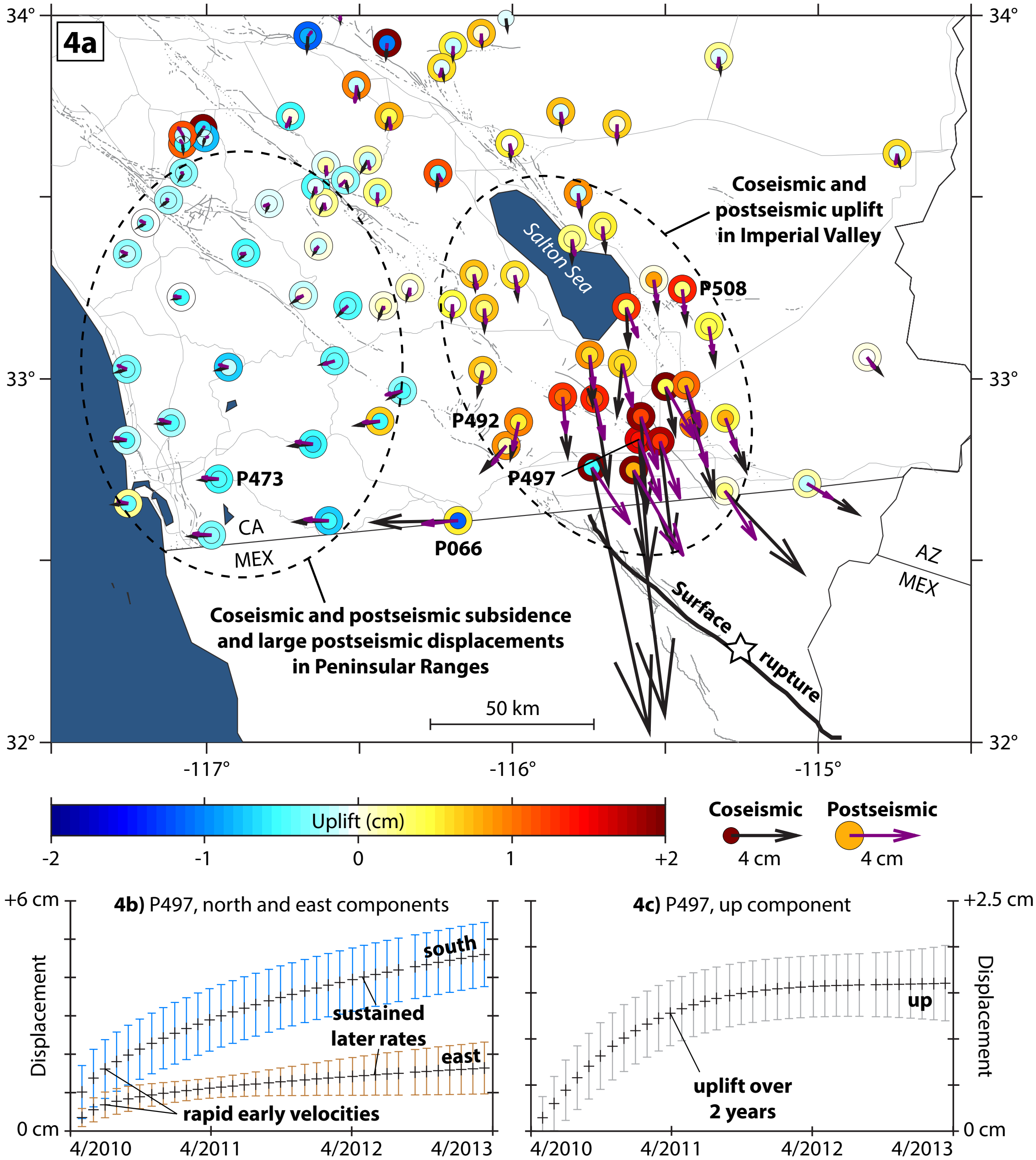

Figure 2.4. a) Comparison of coseismic displacements (black arrows and small shaded circles) and cumulative 3-year extracted postseismic displacements (purple arrows and large shaded circles) shows that the postseismic deformation, like the coseismic, includes uplift in the Imperial Valley and subsidence in the Peninsular Ranges, and that horizontal postseismic displacements are approximately half the magnitude of coseismic horizontals in the near-field but equal in the far-field. **b, c)** Extracted timeseries at station P497 show rapidly decaying horizontal motion rates in the first postseismic year followed by sustained horizontal motion that was still ongoing three years after the mainshock. Gray bars here and in subsequent timeseries figures are noise-based estimates of daily uncertainties in extracted postseismic decays.

Plattner et al [2007] site to each station. We follow the same practice as Pollitz et al [2012] to obtain partial estimated timeseries of horizontal deformation at those stations.

2.4. Extracted postseismic displacements

Extracted postseismic transients in the first three years after the mainshock feature four key characteristics (Figure 2.4). First, cumulative three-year displacements include 1-2 cm of uplift in the Imperial Valley and ~1 cm of subsidence in the Peninsular Ranges relative to background rates (Figure 2.4a). The uplift in the Imperial Valley can be robustly linked to postseismic processes because of its sign, magnitude and duration. GPS stations there were observed to be subsiding at ~0-4 mm/yr prior to the earthquake, as expected for a region undergoing extension [Crowell et al, 2013], meaning that the extracted postseismic uplift is both too large and of the wrong sign to be explainable by steady-state tectonic processes. It is also unlikely to result from seasonal surface processes; it appears to occur steadily over 18 months (Figure 2.4c), and the dominant surface signal following an earthquake in April should be subsidence, not uplift, due to lowering of the water table during the dry summer. Second, cumulative horizontal postseismic displacements are approximately half the magnitude of horizontal coseismic displacements in the Imperial Valley but of approximately equal magnitude to them >150 km west of the rupture in the Peninsular Ranges (Figure 2.4a), suggesting that a deep, long-wavelength deformation process featured in postseismic deformation. Third, displacement timeseries at stations in both the Imperial Valley and Peninsular Ranges feature rapidly decaying horizontal velocities in the first few months after the mainshock (Figure 2.4b). Fourth, these rapid early motions decay to sustained horizontal velocities that were still visibly ongoing three years after the mainshock (Figure 2.4b).

2.5. Kinematic inversions for afterslip

Fault zones may extend down into the lower crust and perhaps the mantle as discrete interfaces that may slip aseismically in response to coseismic stress changes [e.g. Hearn et al, 2002; Perfettini and Avouac, 2004; Burgmann and Dresen, 2008]. To determine whether the entire postseismic displacement pattern can be explained by afterslip, we invert cumulative three-year postseismic displacements (purple arrows in Figure 2.4a, black arrows in Figure 2.5d and all subsequent figures showing surface displacements) for slip on the principal rupture planes of the Wei et al [2011] coseismic slip model and/or modeled downward extensions of those planes into the lower crust and

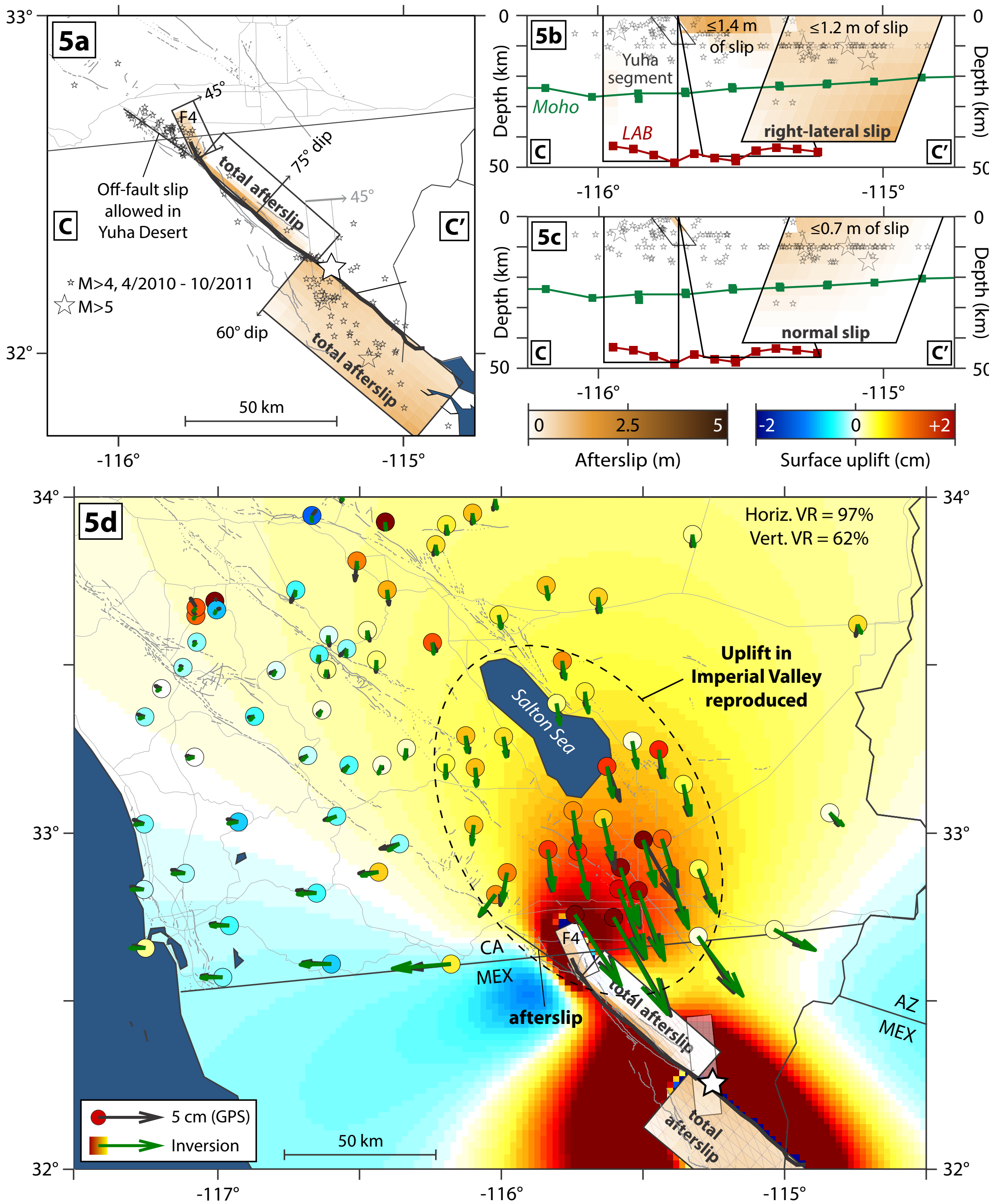

Figure 2.5. Inversion of 3-year cumulative postseismic GPS displacements for afterslip on the main coseismic rupture planes, on modeled downward extensions of the coseismic rupture planes into the lower crust and mantle lithosphere, and in the Yuha Desert. **a)** Slip is allowed on planes F2, F3 and F4 of the Wei et al [2011] model for the mainshock (between 0 and 12 km down dip from their top edges) and on downward extensions of F2 and F3 to the lithosphere-asthenosphere boundary (between 12 and 48 km down dip). Slip

is also allowed on a 30-km-long segment extending northwest into the Yuha Desert to fit the aftershocks and surface creep there to first order and any possible creep at greater depth; this segment has a vertical dip and extends to 48 km depth. **b, c)** The inversion assigns up to 1.4 m of right-lateral slip on plane F2 and up to 1.2 m of right-lateral slip and 0.7 m of normal slip on the downward extension of plane F3, equivalent in total moment to a M=7.2 earthquake. **d)** The inversion produces variance reductions of 97% and 62% in horizontal and vertical displacements, respectively.

mantle lithosphere, in various combinations. We run inversions for slip in five different depth ranges: 1) on the coseismic rupture, between 0 and 12 km down dip from the top edges of planes F2, F3 and F4 of the Wei et al [2011] coseismic model (Figure 2.S4); 2) on modeled downward extensions of planes F2 and F3 into the lower crust, between 12 and 24 km down dip from the top edges of those planes (extending approximately down to the Tape et al [2012] Moho) (Figure 2.S5); 3) on both the coseismic rupture and the modeled lower crustal extensions (Figure 2.S6); 4) on the downward extensions of planes F2 and F3 into the lower crust and mantle lithosphere, between 12 and 48 km down dip from the top edges of those planes (extending approximately down to the Lekic et al [2011] lithosphere-asthenosphere boundary) (Figure 2.S7); and 5) on both the coseismic rupture and the modeled downward extensions into the lower crust and mantle lithosphere (Figure 2.5). Slip plane F2, comprising most of the northwest half of the rupture, dips 75° to the northeast, while slip plane F3, comprising the southeast half, dips 60° to the southwest. In the geometries allowing slip on the downward extensions of these planes, we experiment with geometries in which 1) the downward extensions have the same dips as the coseismic planes; 2) the downward extensions dip 15° more shallowly than the planes do on the coseismic rupture; and 3) the downward extensions are vertical. We also allow slip on a 30-km-long segment extending northwest from the northwest end of plane F2 into the Yuha Desert, the site of distributed surface creep following the earthquake [Rymer et al, 2011] and a rich aftershock sequence [Kroll et al, 2013] including a M=5.7 aftershock in June 2010. (For reference, Pollitz et al [2012] found that this deformation was well fit by slip on a similar 45-km-long dislocation extending northwest from the rupture.) This slip plane is assigned a vertical dip and in each inversion, it extends to the same depth that the main slip planes do. For consistency with coseismic slip, we enforce that the rake of the slip is between 180° (pure right-lateral) and -90° (pure normal). We subdivide the slip into square patches 6 km on a side and regularize the inversions using the $S^{-1/2}T$ methodology of Ortega [Ph.D. thesis, 2013], where S is the matrix describing the data's sensitivity to slip on each

Inversion setup			Variance reduction (%)	
Slip on coseismic rupture	Between rupture and Moho	Between Moho and LAB	Horizontal	Vertical
Yes	No	No	97	63
Yes	Coseismic dips	No	97	63
Yes	Vertical dips	No	97	62
Yes	Dips 15° shallower	No	97	63
No	Coseismic dips	No	94	49
No	Vertical dips	No	94	36
No	Dips 15° shallower	No	95	50
No	Coseismic dips	Coseismic dips	94	47
No	Vertical dips	Vertical dips	94	31
No	Dips 15° shallower	Dips 15° shallower	95	47
Yes	Coseismic dips	Coseismic dips	97	62
Yes	Vertical dips	Vertical dips	97	62
Yes	Dips 15° shallower	Dips 15° shallower	98	63

Table 2.1. Variance reductions of cumulative 3-year horizontal and vertical postseismic displacements in the kinematic inversions.

patch (calculated as the diagonal of G^TG, where G is the Green's function matrix) and T is the Laplacian operator. As described in Ortega [2013], the matrix $S^{-½}T$ must be multiplied by a prefactor ε to be of suitable magnitude as a smoothing matrix. We find that the highest value in S – the sensitivity of the data to normal slip on the northwesternmost, shallowest patch on plane F4, approximately 4.1 x 10^{-4} – is a suitable value for ε, yielding a scheme that visibly heavily smoothes patches far into Mexico and at depth while allowing for visible spatial heterogeneity in slip on the segments closest to the southern California GPS network (e.g. Figure 2.S4). Other details of the inversion technique are given in Barbot et al [2013].

The inversion for afterslip on the coseismic rupture fits most of the three-year cumulative displacement field, achieving a variance reduction of 97% in horizontal displacements and 63% in vertical displacements (Figure 2.S4). Due to the first-order similarities between the coseismic and postseismic displacement fields, particularly in vertical displacements (Figure 2.4), it is not surprising that further slip on the coseismic rupture can fit most of the postseismic displacement field. In terms of the verticals, uniform slip between 0 and 10 km depth on a northwest-striking fault should produce uplift north of the rupture (Figure 2.S1a), and thus the inversions that allow for slip to the surface should have no problem reproducing the uplift in the Imperial Valley barring other factors. However, the inversion assigns up to 1.7 m of right-lateral slip on plane F2 and up to 3.3 m of right-lateral slip and 1.4 m of normal slip on plane F3, equivalent in total moment to a M=7.2 earthquake, the same magnitude as the mainshock (Figure 2.S4). Allowing slip at greater depth does not reduce the total moment of slip required but does smear the slip over a greater area and reduces the maximum slip required: the inversion that allows for slip on the downward lower crustal extensions of planes F2 and F3 as well as on the coseismic rupture (Figure 2.S6) assigns up to 2.2 m right-lateral slip and 1.1 m normal slip on plane F3, and the inversion that allows for slip into the mantle lithosphere as well as on the coseismic rupture (Figure 2.5) assigns only up to 1.4 m right-lateral slip on plane F2 and and 1.2 m right-lateral slip and 0.7 m normal slip on plane F3. Making the dips of the downward extensions 15° shallower than on the coseismic rupture has little effect on the fit to the displacement field, though making the downward extensions vertical significantly reduces the fit to vertical displacements (Table 2.1).

As discussed previously, postseismic horizontal displacements were approximately half the magnitude of coseismic displacements in the near-field but of similar magnitude in the far-field, suggesting that postseismic deformation may have involved a deeper, longer-wavelength mechanism than a simple continuation of coseismic slip, and the contributions of slip in the lower crust and mantle in the inversions that allow for it are consistent with this. However, the inversions that disallow afterslip in the seismogenic zone have significantly more trouble fitting the pattern of vertical displacements. Uniform slip below the seismogenic depth range on a northwest-striking fault should produce subsidence north of the rupture (Figure 2.S1c), and so inversions that only allow for slip below the seismogenic depth range will struggle to reproduce the postseismic uplift in the Imperial Valley. The inversion that allows for slip on the downward lower crustal extensions of planes F2 and F3 without allowing slip on the coseismic rupture above them (Figure 2.S5) requires several meters of both right-lateral and normal slip on the lower crustal extension of plane F3 – equivalent in total moment to a M=7.3 earthquake, greater than the mainshock – and achieves only a 49% variance reduction in the vertical displacement field, visibly fitting the uplift in the Imperial Valley and the subsidence in the Peninsular Ranges less well. As before, allowing for slip into the mantle helps reduce the maximum slip required (Figure 2.S7) but does not help fit the vertical displacements, achieving only a 49% variance reduction in the verticals and still requiring slip equivalent to a M=7.3 earthquake.

The observation that slip on the coseismic rupture alone can fit the three-year cumulative horizontal and vertical displacement field well, and that allowing slip at greater depth reduces the maximum slip required, suggests that much of the spatio-temporal postseismic transient in southern California may be explainable by some combination of shallow and deep afterslip. However, the requirement of a total moment of slip equivalent to at least a M=7.2 earthquake may make these solutions physically implausible. We thus turn to forward modeling to determine whether simulated afterslip driven by coseismic stress changes can achieve the magnitudes of slip required by the kinematic inversions and can reproduce the time evolution of displacements observed at GPS stations.

2.6. Forward modeling methodology

We use Relax (geodynamics.org/cig/software/relax) to simulate the coseismic stress changes imparted by the Wei et al [2011] coseismic slip model for the El Mayor-Cucapah earthquake to the surrounding medium, the relaxation of those mechanisms by hypothesized postseismic processes, and the spatio-temporal evolution of surface deformation that would result from each process. At each timestep, Relax simulates all postseismic mechanisms as equivalent body forces in a generalized viscoelastoplastic halfspace, allowing for the simulation of multiple dynamically coupled mechanisms relaxing coseismic stress changes in concert [Barbot and Fialko 2010a, 2010b]. The use of an elastic halfspace (here with a uniform shear modulus of μ=30 GPa) is required by the Fourier-domain Green's function used in Relax and may cause biases in estimated coseismic stress changes and in the response of postseismic deformation mechanisms, particularly in the mantle [Hearn and Burgmann, 2005]. Consequently, the forward models presented in the following sections are best viewed as simple endmember models.

2.7. Forward modeling of stress-driven afterslip

We use Relax to model time-dependent afterslip on the modeled downward extensions of coseismic rupture planes F2 and F3 and on the previously described vertical plane extending northwest into the Yuha Desert. Afterslip in Relax is driven by coseismic shear stress transfer and governed by a constitutive rate-dependent friction law,

$$v = 2v_0 \sinh(\Delta\tau/((a-b)\sigma)), \qquad [2.2]$$

where v is the slip rate on the segment, v_0 is a reference velocity, a and b are frictional parameters, $\Delta\tau$ is the coseismic shear stress change on the fault, and σ is the normal stress on the fault, assumed constant in time [Barbot et al, 2009]. This is a regularized, steady-state version of the laboratory-derived rate-and-state friction law [e.g. Marone, 1998] that has been shown appropriate to model afterslip in a number of settings [e.g. Marone et al,

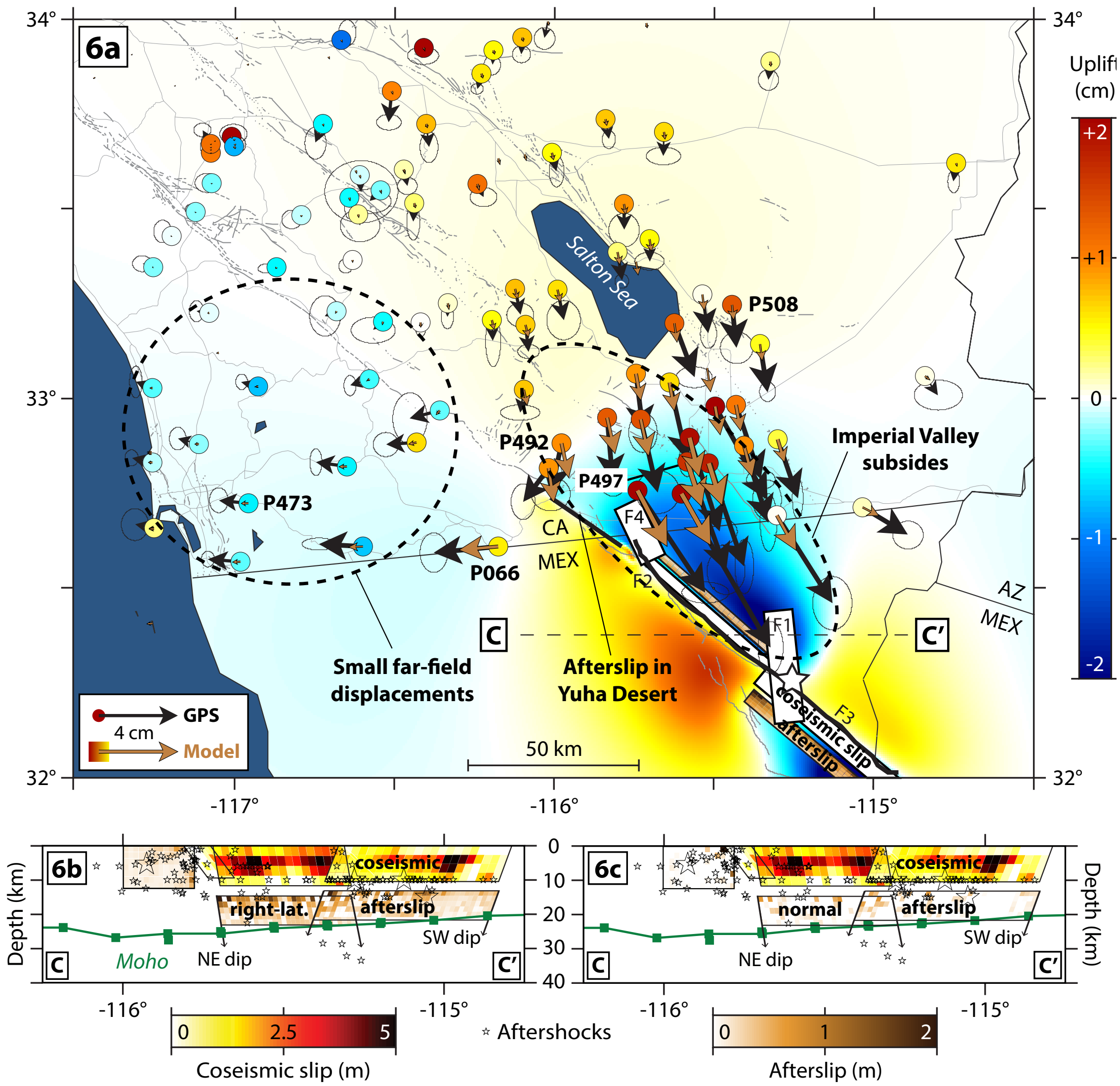

Figure 2.6. Forward modeling of stress-driven afterslip on modeled downward extensions of coseismic slip planes F2 and F3 in the Wei et al [2011] coseismic model into the lower crust. The afterslip is allowed between 15 and 24 km down dip from the top edges of these planes, is driven by coseismic shear stress changes and is governed by a rate-strengthening friction law with (a-b)σ = 1 MPa. Slip is also allowed on a 30-km-long segment extending northwest into the Yuha Desert to fit the aftershocks and surface creep there to first order; this segment has a vertical dip and extends to 12 km depth. **a)** This afterslip model produces horizontal surface displacements with the correct azimuth but the wrong pattern of uplift and subsidence. **b, c)** Slip decreases away from the coseismic rupture, as expected for a stress-driven mechanism.

1991; Hearn et al, 2002; Miyazaki et al, 2004; Perfettini and Avouac, 2004; Barbot et al, 2012]. We explore a range of values for both v_0 and (a-b)σ; appropriate values for the latter estimated from previous studies of afterslip on continental faults are typically on the order of 1 MPa [e.g. Perfettini and Avouac, 2004; Perfettini and Avouac, 2007].

We model afterslip in nine different geometries: 1) on lower crustal extensions of planes F2 and F3 of the Wei et al [2011] coseismic model (between 15 and 24 km down dip from the top edges of those planes) with the same dips as on the coseismic rupture; 2) on lower crustal extensions of F2 and F3 with dips 15° shallower than on the coseismic rupture; 3) on lower crustal extensions of F2 and F3 with vertical dips; 4) on extensions of F2 and F3 down to the lithosphere-asthenosphere boundary (between 15 and 48 km down dip from the top edges of those planes), with the same dips as on the coseismic rupture; 5) on the segment extending into the Yuha Desert, with vertical dip and extending down to 12 km depth; 6) on the Yuha segment extending down to 24 km depth; on the Yuha segment extending down to 48 km depth; 7) on both the lower crustal extensions of F2 and F3, with the same dips as the coseismic rupture, and the Yuha segment extending down to 12 km depth; 8) on the same extensions of F2 and F3 plus the Yuha segment extending down to 24 km depth; and 9) on the extensions of F2 and F3 down to the lithosphere-asthenosphere boundary plus the Yuha segment extending down to 48 km depth. The coseismic shear stress change that drives the afterslip is infinite at the edges of the coseismic slip patches, so for computational stability, we add 3 km of spacing between the bottom of coseismic slip (at ~12 km depth) and the top of the downward extensions of F2 and F3 (at ~15 km depth), and 6 km of spacing between the northwest end of F2 and the segment extending into the Yuha Desert (Figure 2.6). The rake of the afterslip is unconstrained. Models that simulate afterslip on the coseismic rupture itself produce little afterslip there because the coseismic shear stress change for right-lateral slip is strongly negative on most of the rupture (due to the coseismic stress drop), and so we cannot estimate how afterslip on the coseismic rupture could have contributed to the postseismic transient in a time-dependent sense. This does not preclude the possibility that afterslip did occur on the coseismic rupture, however, especially if the real slip distribution was more spatially heterogeneous at fine scales than that of Wei et al [2011].

We find that afterslip on the downward extensions of the rupture and in the Yuha Desert produces subsidence in the Imperial Valley rather than the uplift observed here (Figure 2.6a; Figure 2.S8a), consistent with the observation that a northwest-striking dislocation below seismogenic depth should produce subsidence to the north (Figure 2.S1d). We find that afterslip on the lower crustal extensions of planes F2 and F3, and in the Yuha Desert extending down to 12 or 24 km depth, with $(a-b)\sigma = 1$ MPa, can reproduce

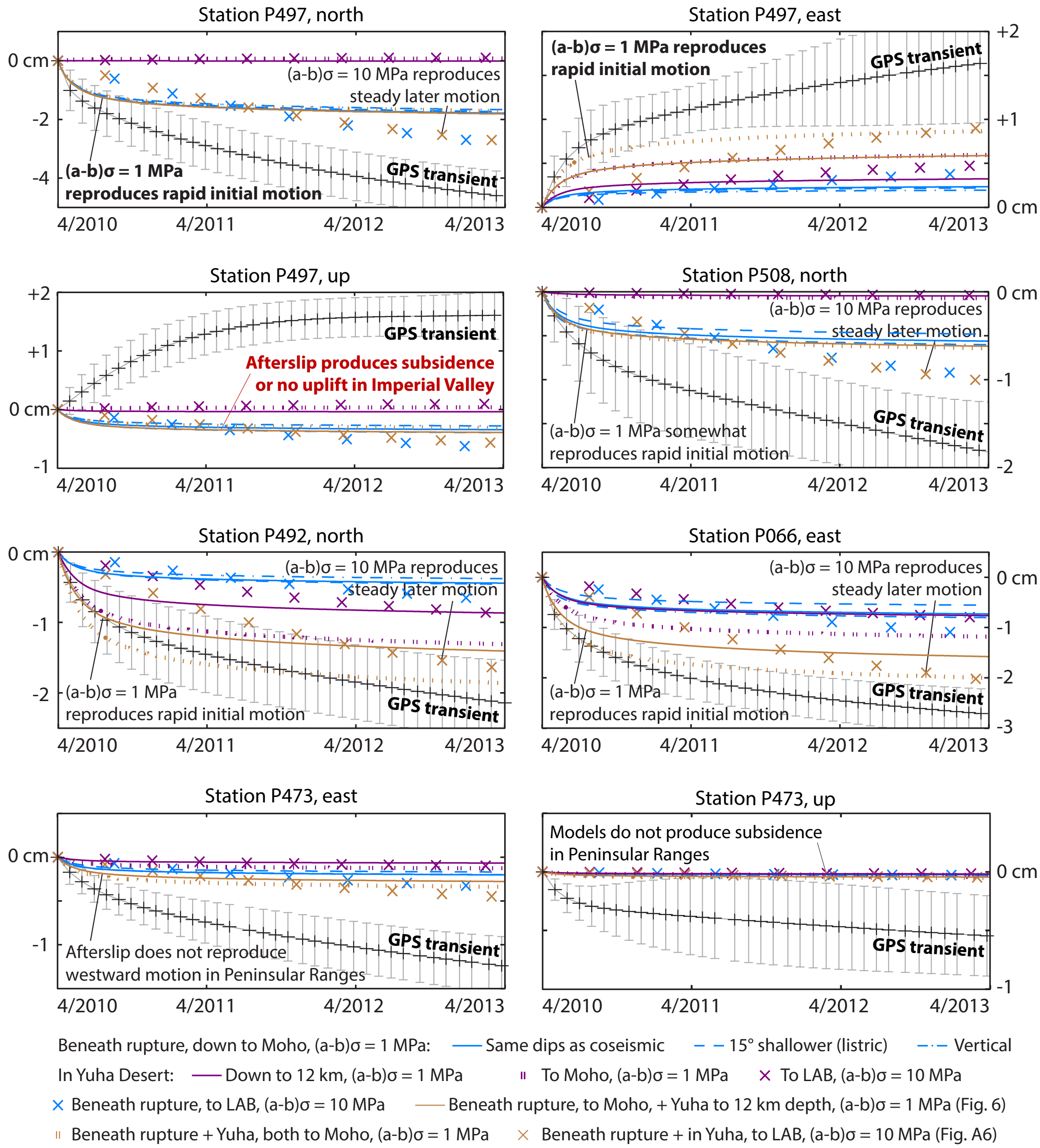

Figure 2.7. Comparison of extracted GPS timeseries at several GPS stations (locations indicated in Figure 2.6) with synthetic timeseries of surface displacement generated by modeled stress-driven afterslip. While lower crustal afterslip with (a-b)σ = 1 MPa reproduces the rapid early displacement rates in the Imperial Valley, afterslip extending into the mantle lithosphere with (a-b)σ = 10 MPa reproduces the sustained later displacement rates in the Imperial Valley.

the rapidly decaying early horizontal motions in the Imperial Valley well (Figure 2.7), and afterslip on planes extending down to the lithosphere-asthenosphere boundary with (a-b)σ

= 10 MPa can reproduce the later, sustained horizontal motions in the Imperial Valley. (Although 10 MPa is an order of magnitude higher than values for (a-b)σ estimated from previous studies of afterslip in the crust, it may not be inappropriate for slip in the mantle as σ should increase with depth.) Models featuring slip into the mantle with (a-b)σ = 1 MPa overshoot the rapid initial displacements in the Imperial Valley, and models featuring slip only into the crust with (a-b)σ = 10 MPa do not produce significant surface displacements. Although we are not able to simulate afterslip with spatially variable frictional parameters, the success of each model at reproducing a key aspect of displacement timeseries in the Imperial Valley suggests that much of the horizontal motion there could be fit to an afterslip mechanism that incorporates elements of both these models. However, none of the afterslip models reproduce the large displacements or the subsidence in the Peninsular Ranges (Figure 2.7). Cumulative three-year displacements on the afterslip planes in these forward models are considerably less than the displacements that were assigned to fit the far-field displacements in the kinematic inversions that allowed for slip into the mantle. Geometrically, the (a-b)σ = 10 MPa model is equivalent to the kinematic inversion that allows slip on downward extensions of planes F2 and F3 into the mantle but not on the coseismic rupture (Figure 2.S7). Whereas that inversion assigned well over a meter of right-lateral and normal slip on most of the slip planes, including beneath the Moho, the total stress-driven afterslip in the (a-b)σ = 10 MPa model after three-years is well under a meter across most of the planes (Figure 2.S8). Even the kinematic inversion that allowed for slip on the coseismic rupture as well as into the mantle (Figure 2.5) still assigned close to a meter of right-lateral and normal slip on much of the planes to fit the far-field displacements. Thus it can be said that at least in this configuration, featuring a rate-strengthening friction law with (a-b)σ = 10 MPa, the cumulative afterslip at depth predicted after three years is not enough to fit three-year surface displacements in the far-field. This motivates us to assess whether distributed viscoelastic relaxation could also have been responsible for some components of the observed postseismic transient.

2.8. Forward modeling of viscoelastic relaxation in the lower crust

The very high heat flow in the Salton Trough [Lachenbruch et al, 1985] suggests that the lower crust there there may have reduced viscosity [Williams et al, 2012] and thus might have produced a visible signal of viscoelastic relaxation following the El Mayor-Cucapah earthquake. However, the Moho shallows to ~22 km in the Salton Trough from >30 km in much of southernmost California [Tape et al, 2012] (Figure 2.8), and so one

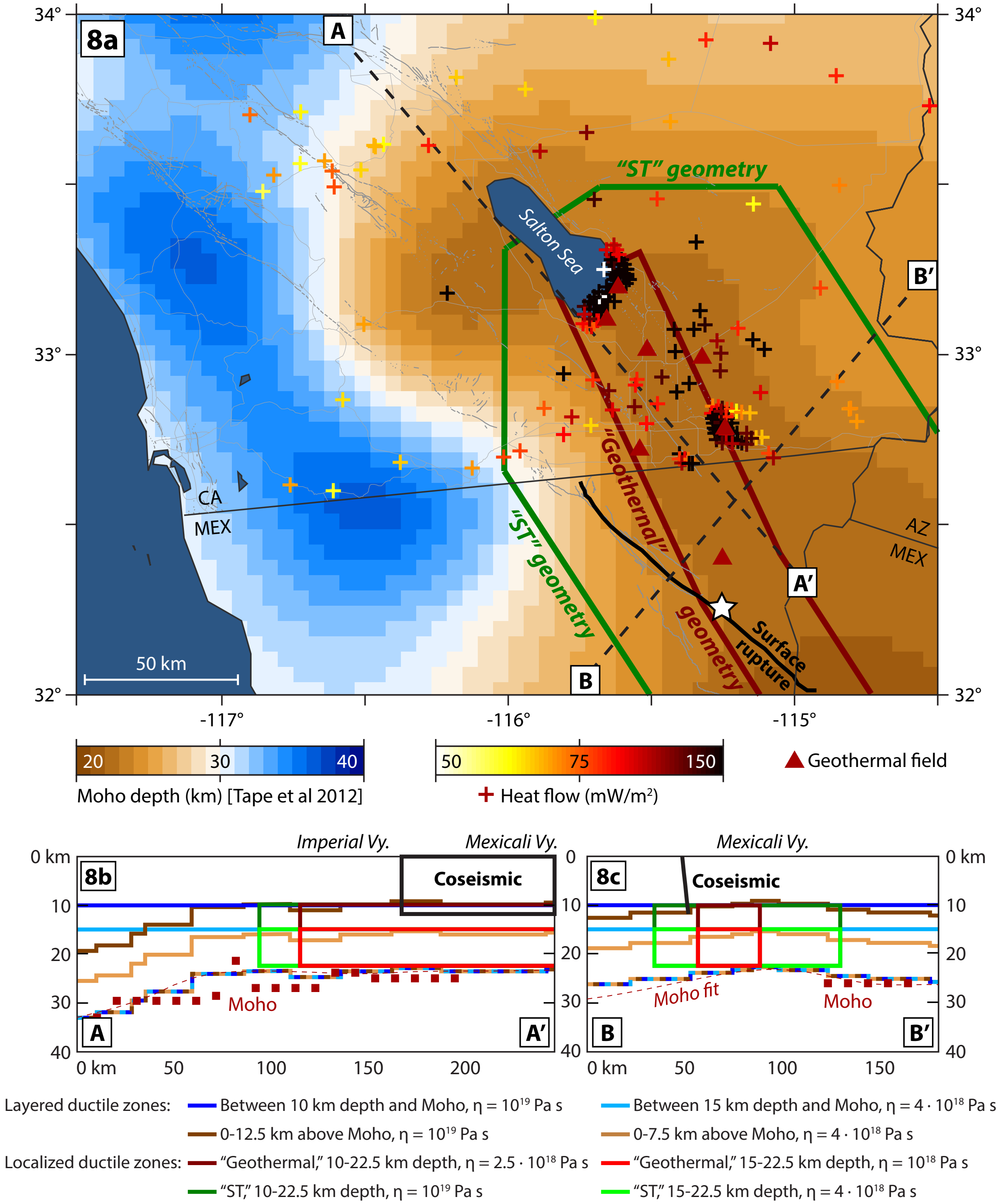

Figure 2.8. We simulate viscoelastic relaxation in eight postulated geometries for low-viscosity zones in the lower crust: 1) a ductile zone between 10 km depth and the Tape et al [2012] Moho surface at all locations; 2) the same geometry but with a top depth of 15 km; 3) a ductile zone 0-12.5 km above the Moho surface at all locations; 4) a ductile zone 0-7.5 km above the Moho surface; 5) a ductile zone from 10-22.5 km depth in the "geothermal" geometry, a narrow zone in the Salton Trough beneath locations of high heat flow and geothermal activity; 6) from 15-22.5 km depth in the "geothermal" geometry; 7) a ductile

zone at 10-22.5 km depth in the “ST” geometry, above the zone of shallow Lekic et al [2011] lithosphere-asthenosphere boundary in the Salton Trough; and 8) from 15-22.5 km depth in the “ST” geometry. a) Mapview of Moho depth, heat flow, geothermal areas and geometries of modeled localized ductile zones. b, c) Cross sections of Moho depth and geometries of modeled ductile zones.

might alternatively suppose that the lower crust of the surrounding regions, with a greater thickness of potentially low-viscosity material, might have featured more heavily in postseismic deformation than the Salton Trough lower crust. To test these hypotheses, we use Relax to model viscoelastic relaxation in eight different postulated geometries of ductile zones in the lower crust: 1) a layered ductile zone between a depth of 10 km and the Tape et al [2012] Moho surface at all locations; 2) a similar layered zone between a depth of 15 km and the Moho surface; 3) a layered ductile zone 0-12.5 km above the Moho surface at all locations; 4) a similar layered zone 0-7.5 km above the Moho surface; 5) a localized ductile zone from 10-22.5 km depth in the “geothermal” geometry, a narrow zone in the Salton Trough beneath locations of high heat flow and geothermal activity; 6) a localized zone from from 15-22.5 km depth in the “geothermal” geometry; 7) a localized ductile zone at 10-22.5 km depth in the “ST” geometry, above the zone of shallow Lekic et al [2011] lithosphere-asthenosphere boundary in the Salton Trough; and 8) a localized zone from 15-22.5 km depth in the “ST” geometry (Figure 2.8). Viscoelastic relaxation in Relax is driven by coseismic changes in deviatoric stress and can be governed either by a Newtonian rheology,

$$d\gamma/dt = \tau/\eta, \qquad [3]$$

where $d\gamma/dt$ is the viscous strain rate, τ is the deviatoric stress and η is the Newtonian viscosity, or by a stress-dependent viscosity

$$d\gamma/dt = C\tau^n, \qquad [3]$$

where C is a coefficient dependent on factors such as grain size, water content and temperature [e.g. Freed and Burgmann, 2004] and n is an exponent. Within each of the geometries, we model three alternative rheologies: 1) a Newtonian rheology, 2) a stress-dependent viscosity with n=2.5, consistent to first order with laboratory observations of dry quartzite and some of wet quartzite, and a stress-dependent viscosity with n=4, consistent with other laboratory studies of wet quartzite [Freed and Burgmann, 2004].

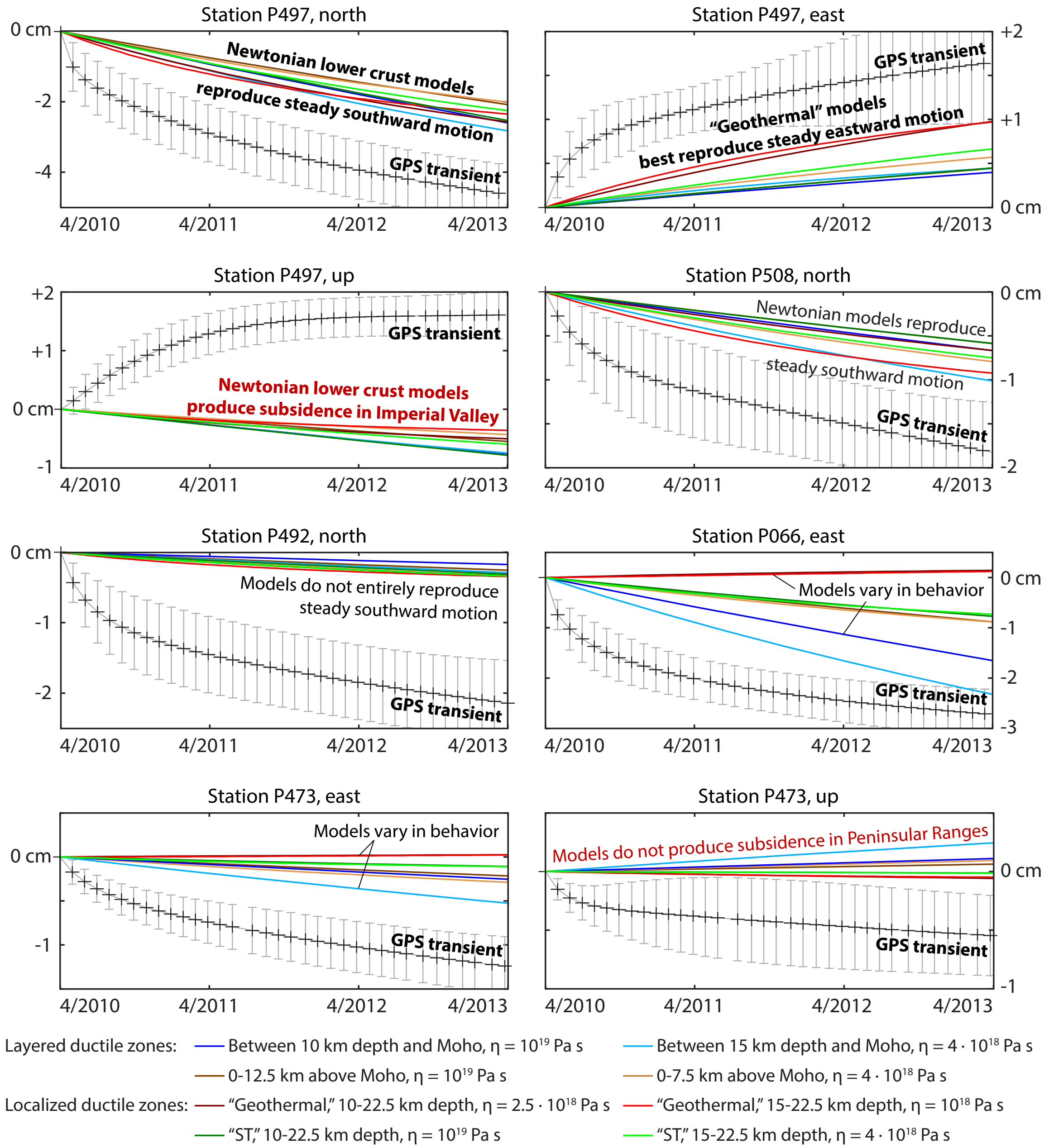

Figure 2.9. Comparison of extracted GPS timeseries at several GPS stations (locations indicated in Figure 2.4a) with synthetic timeseries of surface displacement generated by Newtonian viscoelastic relaxation in the modeled lower crustal ductile zones.

The mainshock likely imparted vertical compression at 22.5 km depth (Moho depth) beneath the northern Imperial Valley and beneath and just northeast of the rupture (Figure 2.S9). Viscoelastic relaxation of this compression should have featured material flowing out of those regions at depth, causing subsidence at the surface, and indeed we find that simulated viscoelastic relaxation in the lower crust produces subsidence in the Imperial Valley regardless of the geometry or rheology prescribed (Figure 2.S10, Figure 2.S11, Figure 2.S13), meaning that it alone cannot explain the observed postseismic transient. However, we find that Newtonian viscoelastic relaxation in the modeled lower crustal ductile zones with $\eta=10^{18}$-10^{19} Pa-s can reproduce the sustained horizontal velocities that followed the rapidly decaying early motions at GPS stations in the Imperial Valley (Figure 2.9). In particular, Newtonian viscoelastic relaxation in the "geothermal" geometry with $\eta=2.5 \times 10^{18}$ Pa-s (with a top depth of 10 km) or 10^{18} Pa-s (with a top depth of 15 km) matches the azimuth of the sustained horizontal velocities in the Imperial Valley well, producing the highest ratio of eastward to southward velocities at station P497 of all geometries modeled (Figure 2.9). A stress-dependent viscosity with n=2.5 concentrates higher rates of displacement closer to the mainshock in both space and time and produces surface displacements that can match both the rapidly decaying early motion and the later sustained velocities at some stations, again with relaxation in the "geothermal" geometries producing the most eastwardly motions at station P497 (Figure 2.S12). A stress-dependent viscosity with n=4 concentrates high displacement rates even closer to the mainshock in time and cannot fit the sustained horizontal displacements well but can fit some of the rapid initial velocities (Figure 2.S14).

2.9. Forward modeling of viscoelastic relaxation in the mantle lithosphere

The models of viscoelastic relaxation in the lower crust assume a relatively weak crust over a relatively strong mantle. Alternative conceptions of lithospheric strength feature a relatively strong crust over a relatively weak mantle lithosphere, or both a weak lower crust and weak mantle lithosphere [e.g. Burgmann and Dresen 2008], and so it is useful to assess whether viscoelastic relaxation in the mantle lithosphere could also explain aspects of the observed postseismic deformation. We simulate viscoelastic relaxation with Newtonian and stress-dependent rheologies in three postulated geometries for low-viscosity zones in the mantle lithosphere (Figure 2.10): the "ML" geometry, a ductile zone between the Tape et al [2012] Moho surface and a simple geometric approximation to the Lekic et al [2011] lithosphere-asthenosphere boundary at all locations; the "ST" geometry, a ductile zone at 22.5-45 km depth above the zone of shallow Lekic et al [2011] lithosphere-asthenosphere boundary in the Salton Trough, and the "geothermal" geometry, a ductile zone at 22.5-45 km depth in a narrow zone in the Salton Trough beneath locations of high heat flow and geothermal activity. Within these three geometries, we model two alternate

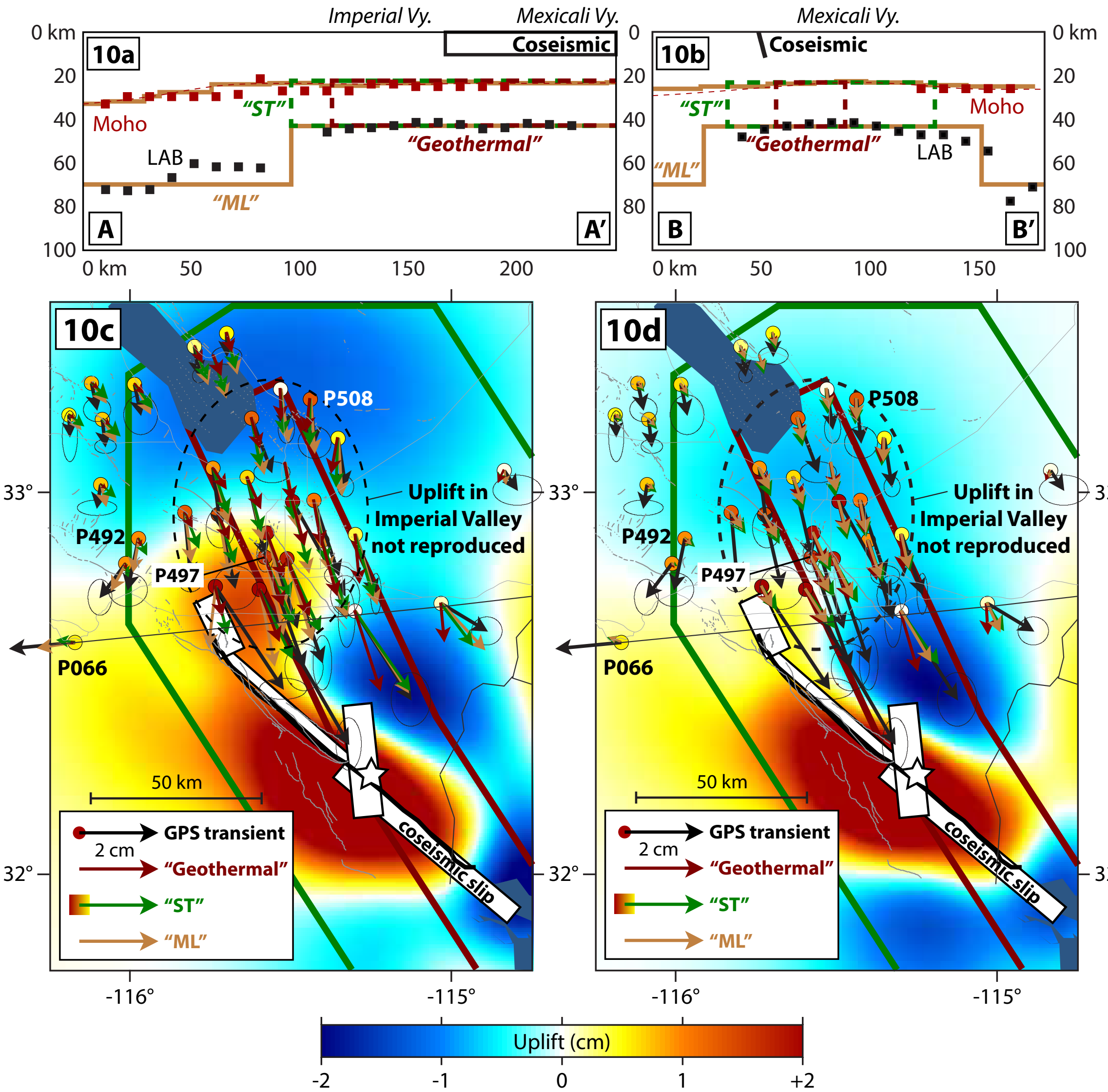

Figure 2.10. We simulate viscoelastic relaxation in three postulated geometries for low-viscosity zones in the mantle lithosphere: the "ML" geometry, a ductile zone between the Tape et al [2012] Moho surface and the geometrically approximated Lekic et al [2011] lithosphere-asthenosphere boundary at all locations; the "ST" geometry, from 22.5-45 km depth above the zone of shallow Lekic et al [2011] lithosphere-asthenosphere boundary in the Salton Trough, and the "geothermal" geometry, from 22.5-45 km depth in a narrow zone in the Salton Trough beneath locations of high heat flow and geothermal activity. **a, b)** Cross sections of the modeled geometries; the locations of the cross sections are depicted in Figure 2.8. **c)** Synthetic three-year surface displacements at GPS stations generated by Newtonian viscoelastic relaxation in the modeled lower crustal ductile zones. The vertical displacement field is from the "ST" model. **d)** Synthetic three-year surface displacements at GPS stations generated by viscoelastic relaxation with a stress-dependent viscosity (n=3.5) in the modeled mantle lithosphere geometries. The vertical displacement field is from the "ST" model.

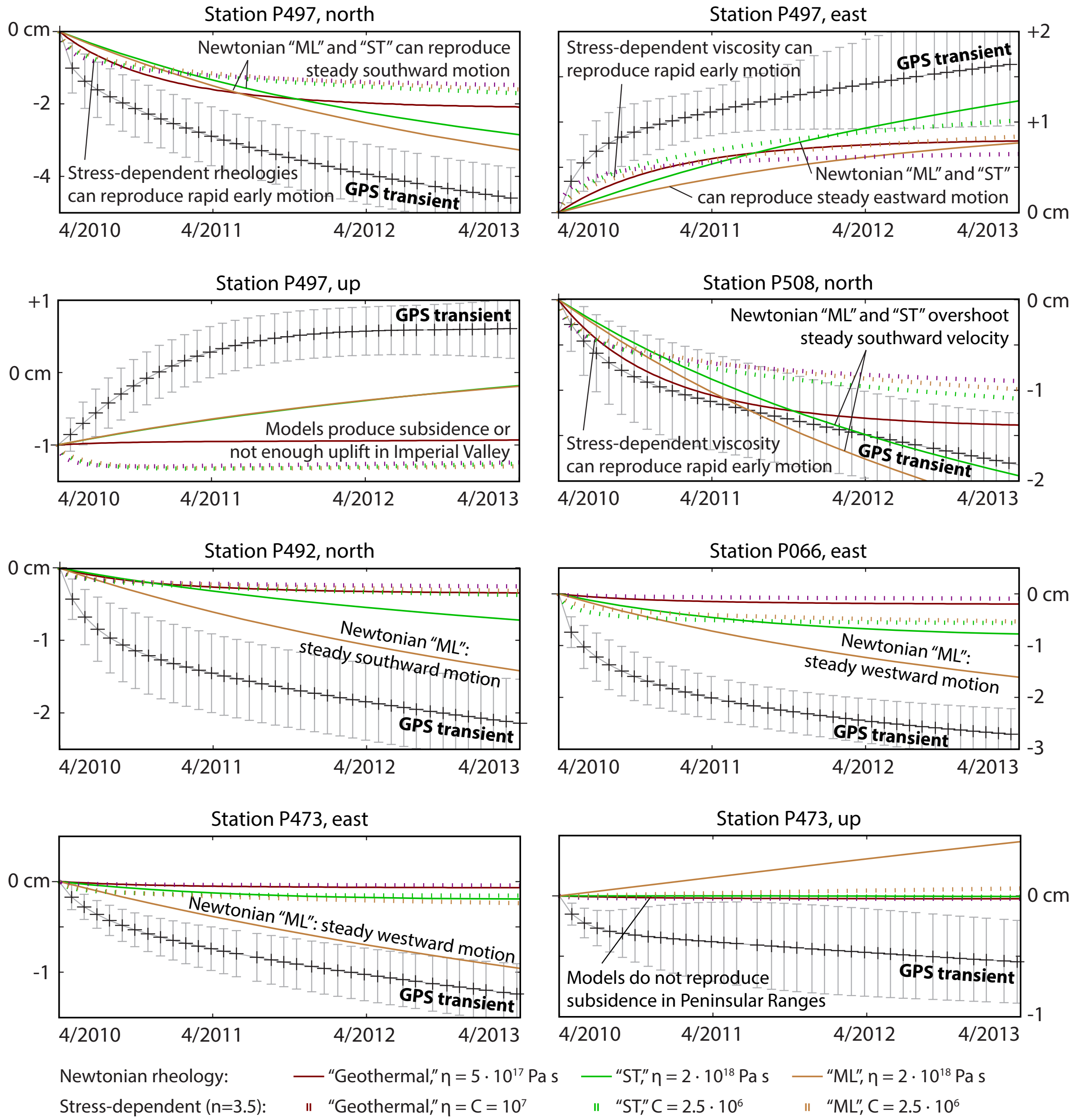

Figure 2.11. Comparison of extracted GPS timeseries at several GPS stations (locations indicated in Figure 2.4a and 2.10) with synthetic timeseries of surface displacement generated by viscoelastic relaxation with Newtonian and stress-dependent (n=3.5) rheologies in the modeled ductile zones in the mantle lithosphere.

rheologies: a linear Newtonian rheology and a stress-dependent viscosity with n=3.5, consistent with laboratory observations of dislocation creep in dry and wet olivine and thought to be perhaps the dominant rheology in the upper mantle [e.g. Kirby, 1983; Hirth and Kohlstedt 2003, Freed and Burgmann 2004, Karato 2008].

We find that Newtonian viscoelastic relaxation with $\eta=2 \times 10^{18}$ Pa-s in the "ML" and "ST" geometries produces steady horizontal motion that resembles that observed in the Imperial Valley to first order (Figure 2.10). However, this mechanism cannot reproduce the magnitude of the steady horizontal velocities at station P497 (at least with the geometries used here) without overshooting the inferred velocities at station P508, further from the rupture on the northeast side of the Imperial Valley (Figure 2.11), whereas Newtonian viscoelastic relaxation in the lower crust had no problem reproducing the steady velocities at both stations (Figure 2.9). This can be thought of as reflecting the fact that the mantle lithosphere is deeper than the lower crust and relaxation there will produce a broader deformation pattern at the surface, with slower velocities closer to the rupture and faster velocities farther from the rupture. Viscoelastic relaxation with a stress-dependent viscosity (n=3.5) in the mantle lithosphere can to some extent reproduce the rapidly decaying early horizontals in the Imperial Valley (Figure 2.11). Though Newtonian viscoelastic relaxation in the mantle lithosphere produces some uplift around the rupture and just northeast of it (Figure 2.10), probably reflecting the coseismic vertical extension at 22.5-45 km depth there (Figure 2.S9), neither a Newtonian nor a stress-dependent viscosity can reproduce the systematic uplift observed at GPS stations in the Imperial Valley (Figure 2.10). This suggests that viscoelastic relaxation can produce uplift there only if it occurs below ~45 km depth, the depth of the Lekic et al [2011] lithosphere-asthenosphere boundary. Newtonian viscoelastic relaxation in the "ML" geometry can reproduce the steady westward velocities at station in P473 in the Peninsular Ranges but produces steady uplift there; none of the models can reproduce the subsidence observed there (Figure 2.11).

2.10. Forward modeling of viscoelastic relaxation in the asthenosphere

Lekic et al [2011] imaged the lithosphere-asthenosphere boundary in southern California with receiver functions and found that the asthenosphere shallowed to a depth of ~45 km in the Salton Trough, compared to regional average of ~70 km. Thus, viscoelastic relaxation in the asthenosphere could have contributed to the observed postseismic transient, and if so, the lateral heterogeneity in its geometry imaged by seismic methods might also be visible using this method, which samples deformation over timescales many orders of magnitude longer. We model viscoelastic relaxation in four postulated geometries for the effective ductile asthenosphere: model "1D45", in which viscoelastic relaxation is allowed between 45 km depth and the base of the model (~300 km depth); model "1D70", a 1D model allowing relaxation below 70 km depth; model "ST+", a 3D

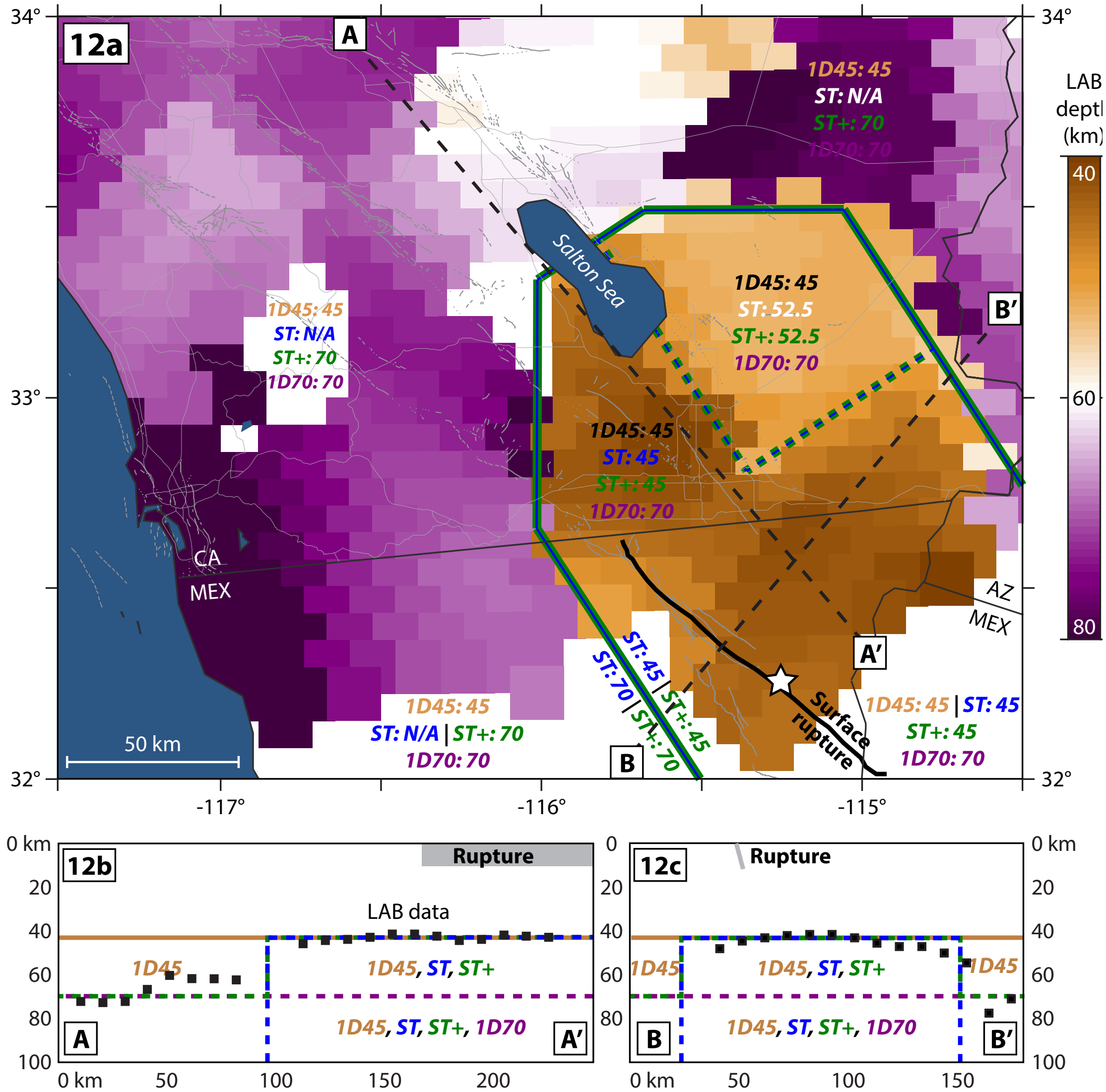

Figure 2.12. We simulate viscoelastic relaxation in four alternate postulated geometries for the asthenosphere: model 1D45 (gold), a 1D model in which viscoelastic relaxation is allowed below 45 km depth; model 1D70 (purple), in which viscoelastic relaxation is allowed below 70 km depth; model ST+ (green), in which the top of the viscoelastic zone approximates the geometry of the regional lithosphere-asthenosphere boundary inferred by Lekic et al [2011], and model ST (blue or white), which approximates the Lekic et al [2011] lithosphere-asthenosphere boundary in the Salton Trough and forbids viscoelastic relaxation outside of it. **a)** Mapview of Lekic et al [2011] lithosphere-asthenosphere boundary depth and geometries of modeled ductile zones. Sets of numbers prefaced by model names are the top depths of each model at the specified locations. **b, c)** Cross sections of Lekic et al [2011] lithosphere-asthenosphere boundary depth and geometries of modeled ductile zones.

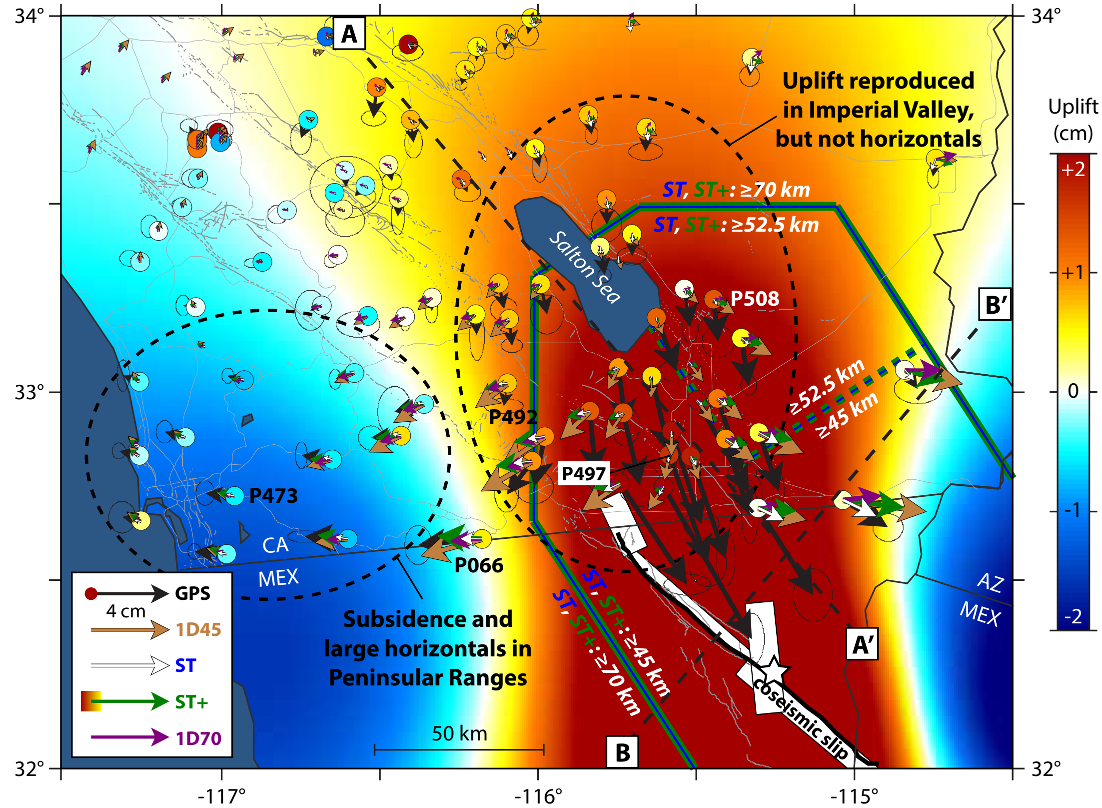

Figure 2.13. Three-year cumulative surface displacements produced by Newtonian viscoelastic relaxation $\eta=5 \times 10^{17}$ Pa-s) in the four geometries for the asthenosphere. Viscoelastic relaxation in the asthenosphere reproduces the uplift observed in the Imperial Valley and the subsidence and westward displacements in the Peninsular Ranges. Predicted verticals are from model "ST+."

geometry approximating that of the Lekic et al [2011] lithosphere-asthenosphere boundary; and model "ST", a 3D geometry that follows the Lekic et al [2011] lithosphere-asthenosphere boundary within the Salton Trough and disallows viscoelastic relaxation outside of it (Figure 2.12). Within these four geometries, we model two alternate rheologies: a linear Newtonian rheology and a stress-dependent viscosity with n=3.5.

The mainshock imparted vertical extension at 70 km depth beneath the Imperial Valley and beneath the central part of the rupture (Figure 2.S15). Viscoelastic relaxation should feature asthenospheric material rising from beneath the extended zones, causing recompression of material at the top of the asthenosphere and uplift at the surface. We find that Newtonian viscoelastic relaxation in the 1D45, ST+ and 1D70 models, the three geometries that allow for viscoelastic relaxation outside of the Salton Trough, can qualitatively reproduce the uplift in the Imperial Valley and the subsidence and sustained

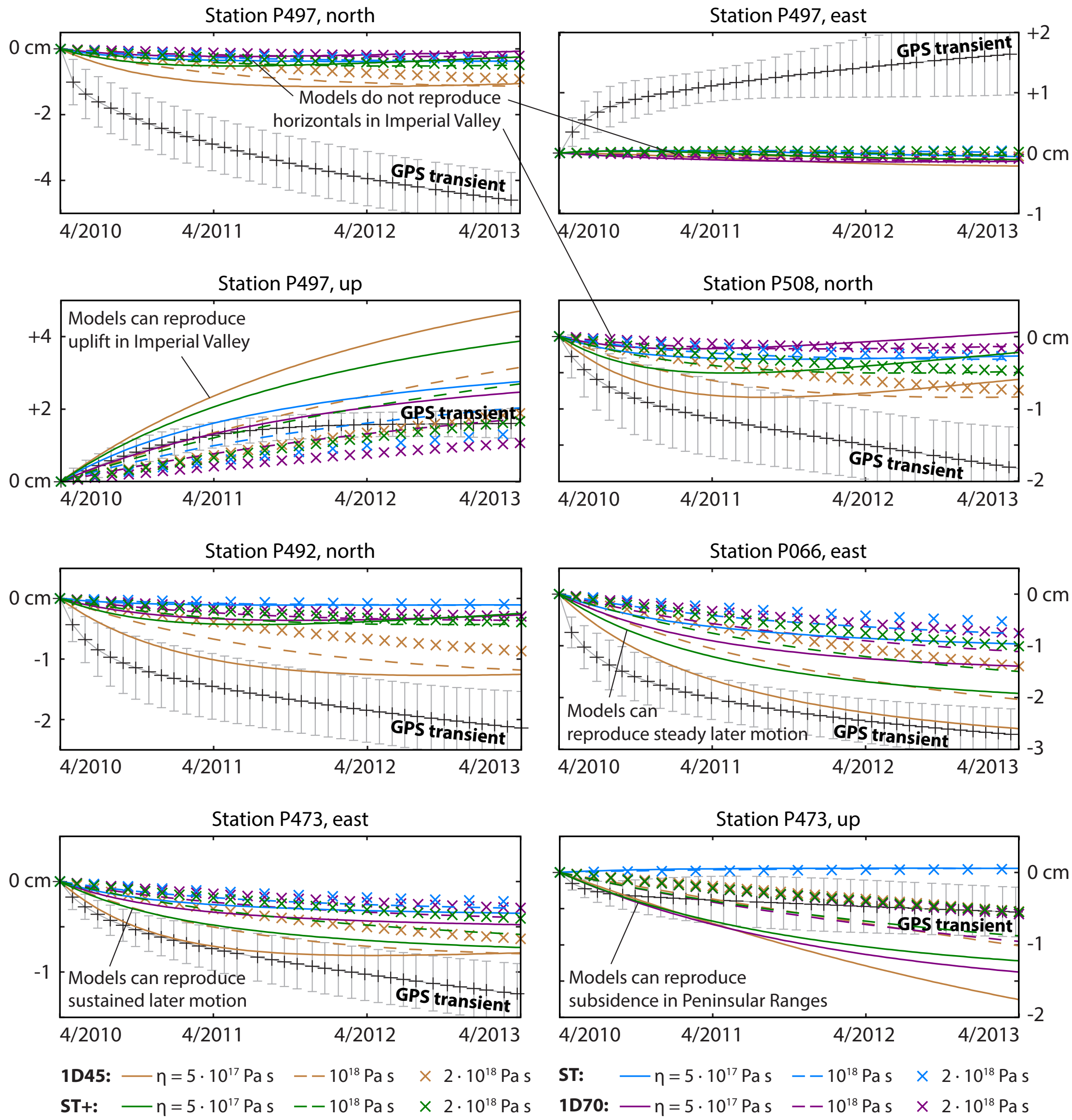

Figure 2.14. Comparison of extracted GPS timeseries at several GPS stations (locations indicated in Figure 2.13) with synthetic timeseries of surface displacement generated by Newtonian viscoelastic relaxation in the modeled geometries for the asthenosphere. Viscoelastic relaxation in the "1D45", "ST+" and "1D70" geometries can qualitatively reproduce the uplift at station P497, the sustained westward velocities observed at stations P066 and P473, and the subsidence observed at station P473.

westward velocities in the Peninsular Ranges (Figure 2.13). Tradeoffs between Newtonian viscosity and geometry make identification of a best-fitting geometry difficult; for example, the sustained westward velocities at stations P066 and P473 can be qualitatively reproduced by Newtonian viscoelastic relaxation with η=1-2 x 10^{18} Pa-s in the 1D45 geometry, with η=5 x 10^{17}-10^{18} Pa-s in the ST+ geometry, or η=5 x 10^{17} Pa-s in the 1D70 geometry (Figure 2.14). Newtonian viscoelastic relaxation in the ST geometry, confined to the Salton Trough, requires viscosities well below η=5 x 10^{17} Pa-s (the minimum tested) to fit the horizontal velocities in the Peninsular Ranges and does not reproduce the subsidence observed there. Cross sections of cumulative inelastic (viscous) strain after three years of viscoelastic relaxation (Figure 2.S16) show that although the major viscoelastic relaxation occurs close to the mainshock, some relaxation does occur outside of the Salton Trough in the 1D45, ST+ and 1D70 geometries, and the failure of the ST geometry to reproduce the far-field horizontals or verticals suggests that this relaxation outside the Salton Trough is important. Beyond this, however, the tradeoffs between viscosity and geometry suggest that surface displacements are relatively insensitive to the geometry of the modeled asthenosphere. Models featuring a stress-dependent viscosity with n=3.5 concentrate the viscoelastic relaxation closer to the rupture and reproduce neither the far-field displacements nor the full distribution of vertical displacements (Figure 2.S17, Figure 2.S18). Neither a Newtonian nor a stress-dependent viscosity can reproduce the observed horizontal displacements in the Imperial Valley; the process is relatively deep and its surface displacements are broad, featuring small displacements close to the rupture and larger displacements far from the rupture. Nonetheless, Newtonian viscoelastic relaxation in the asthenosphere appears to be best candidate mechanism of those modeled to reproduce the subsidence, steady westward velocities and large cumulative displacements in the Peninsular Ranges, suggesting that this mechanism may well have played a role in postseismic deformation.

2.11. Multiple-mechanism models

No single deformation mechanism (as modeled here) reproduces the entire transient of postseismic displacement observed in GPS timeseries, suggesting that the observed transient resulted from multiple processes acting in concert. Here we present two endmember models of multiple mechanisms acting in concert that offer relatively good fits to the observed transient. These models operate on the assumption that each of the four key aspects of postseismic deformation – uplift in the Imperial Valley, large westward displacements in the Peninsular Ranges, the rapid initial offset in near-field timeseries, and the sustained displacement signal that followed it – was essentially produced by a single deformation mechanism. As shown previously, the uplift in the Imperial Valley and the subsidence and relatively large westward displacements in the Peninsular Ranges can be

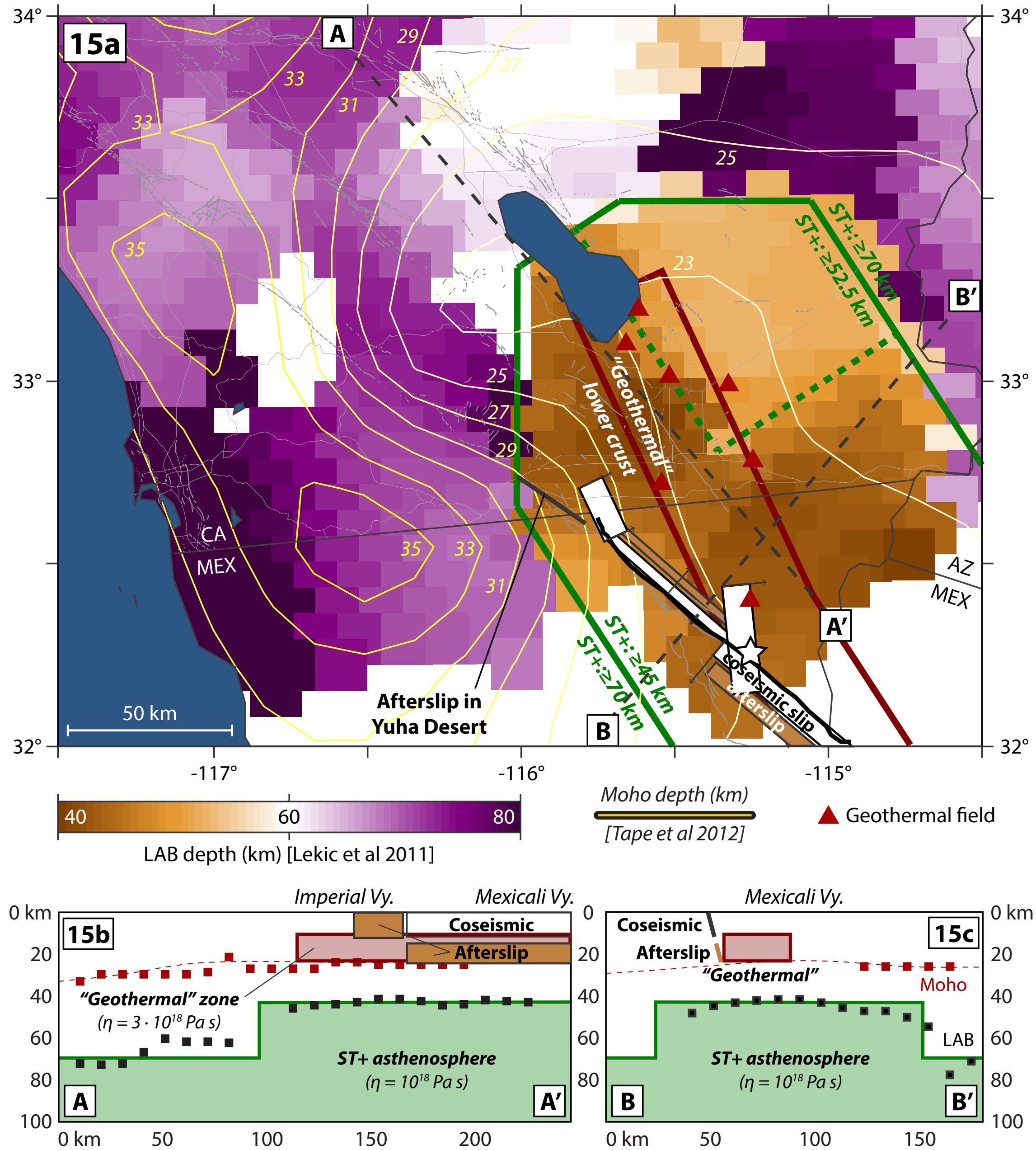

Figure 2.15. Setup of the first coupled multiple-mechanism model, featuring afterslip on the downward extensions of the coseismic rupture down to the Moho and on a segment extending northwest into the Yuha Desert that extends down to 12 km depth, Newtonian viscoelastic relaxation from 10-22.5 km depth in the "geothermal" lower crust geometry η=3 x 10^{18} Pa-s), and Newtonian viscoelastic relaxation in the "ST+" asthenosphere (η= 10^{18} Pa-s). **a)** Mapview of Lekic et al [2011] lithosphere-asthenosphere boundary depth, Tape et al [2012] Moho depth, geothermal areas, and model setup. **b, c)** Cross sections of Lekic et al [2011] lithosphere-asthenosphere boundary depth and Moho depth and model setup.

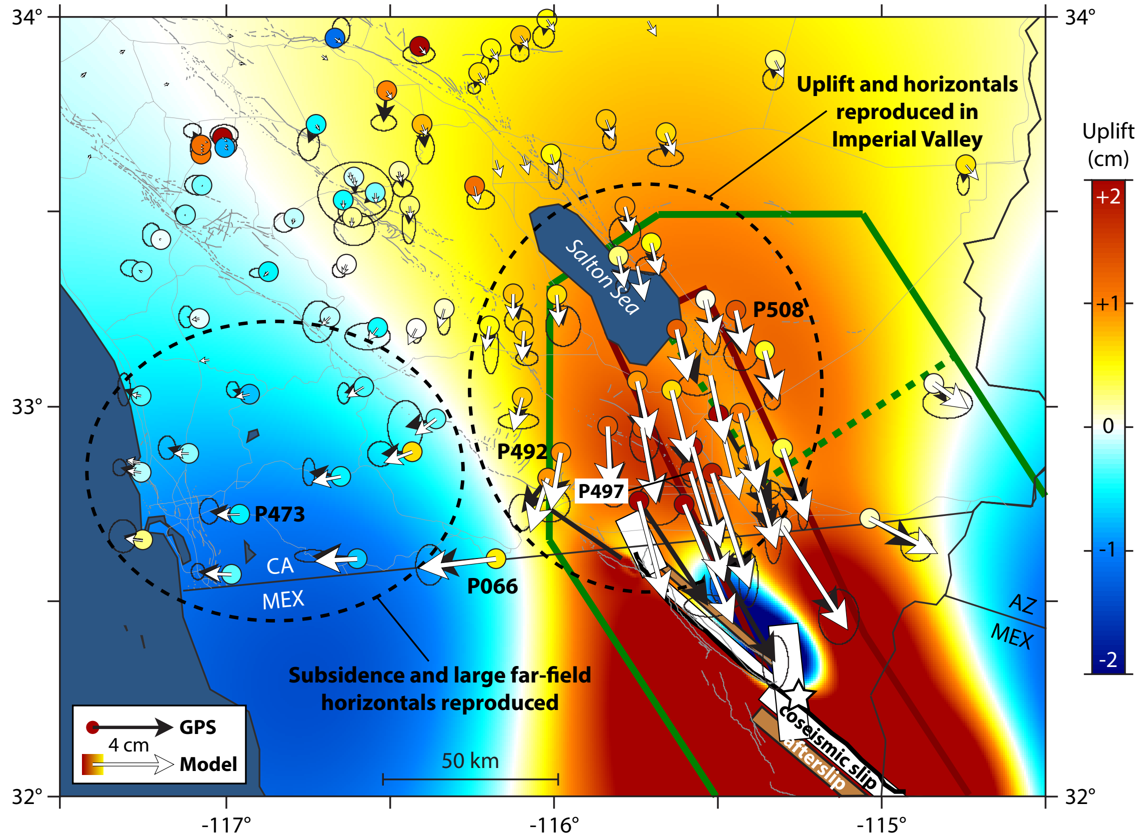

Figure 2.16. Comparison of three-year cumulative horizontal and vertical postseismic displacements at GPS stations with cumulative synthetic displacements generated by the first coupled model.

reproduced by Newtonian viscoelastic relaxation in the asthenosphere; the sustained horizontal motions in the Imperial Valley can be reproduced by Newtonian viscoelastic relaxation in the lower crust and/or mantle lithosphere (and in particular, Newtonian viscoelastic relaxation in the localized "geothermal" lower crustal ductile zone fits the azimuth of the sustained velocity at station P497 without overshooting the velocity at station P508); and the rapidly decaying early horizontal motions in the Imperial Valley and Peninsular Ranges can be reproduced by afterslip on the downward extensions of the rupture and in the Yuha Desert with (a-b)σ ~ 1 MPa or by viscoelastic relaxation with a stress-dependent viscosity in the lower crust and/or mantle. The two multiple-mechanism models presented here differ only in the mechanism they use to reproduce the rapidly decaying early motion. The first coupled model reproduces this signal with afterslip on downward extensions of coseismic rupture planes F2 and F3 extending down to the Moho and on a segment extending northwest into the Yuha Desert that extends down to 12 km

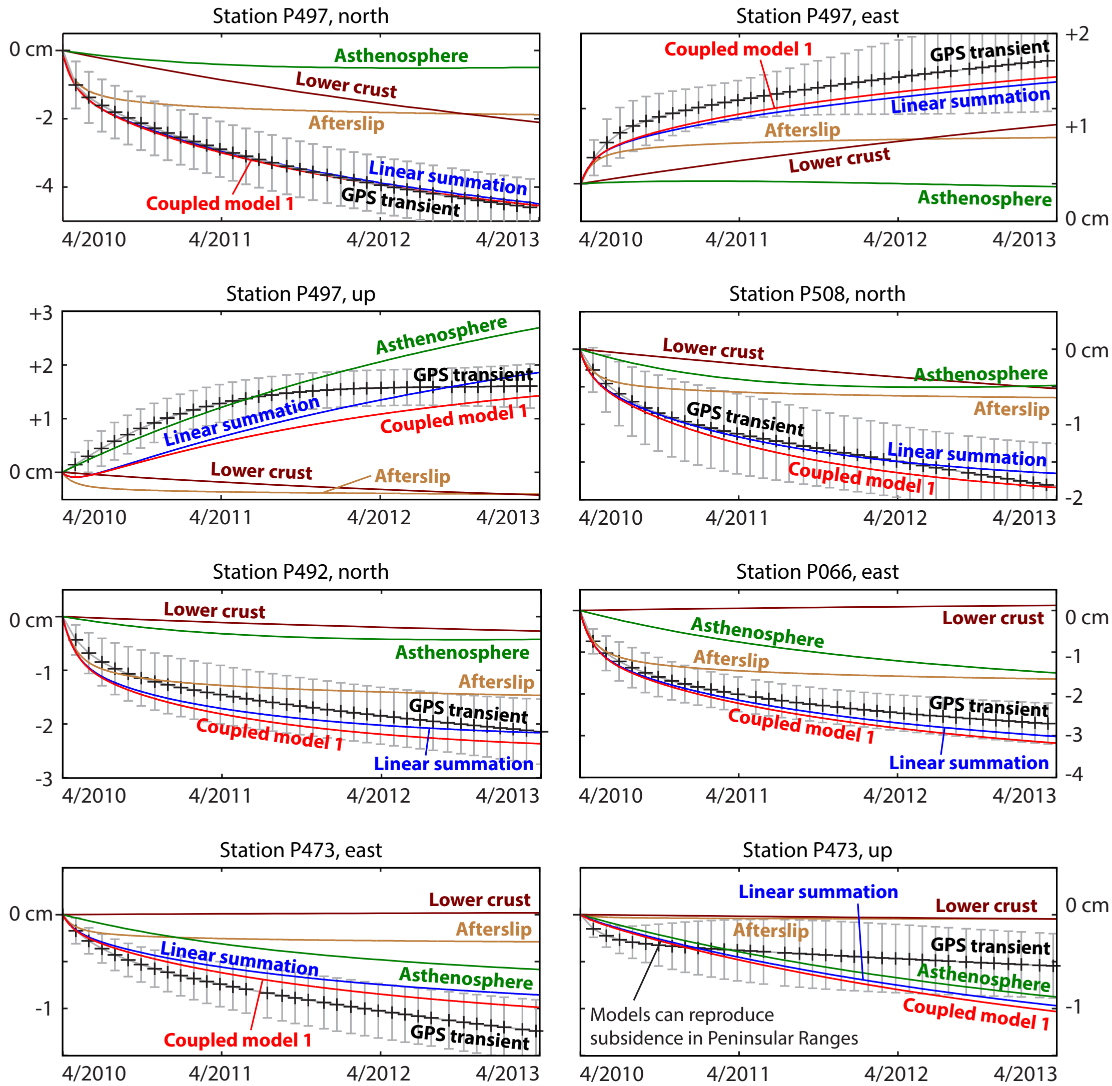

Figure 2.17. Comparison of extracted GPS timeseries at several GPS stations (locations indicated in Figure 2.16) with synthetic timeseries of surface displacement generated by the first coupled model.

depth (the approximate maximum depth of postseismic seismicity there from Kroll et al [2013]). This mechanism operates in concert with Newtonian viscoelastic relaxation with $\eta=3 \times 10^{18}$ Pa-s in the “geothermal” lower crustal ductile zone extending from 10-22.5 km depth and Newtonian viscoelastic relaxation with $\eta=10^{18}$ Pa-s in the “ST+” model for the asthenosphere (Figure 2.15). As such, this model can be viewed as an exploration of how well the postseismic transient can be fit without stress-dependent rheologies. The model reproduces the horizontal and vertical displacement field well, with variance reductions of 93% in cumulative three-year horizontal displacements, 92% in time-dependent fits to

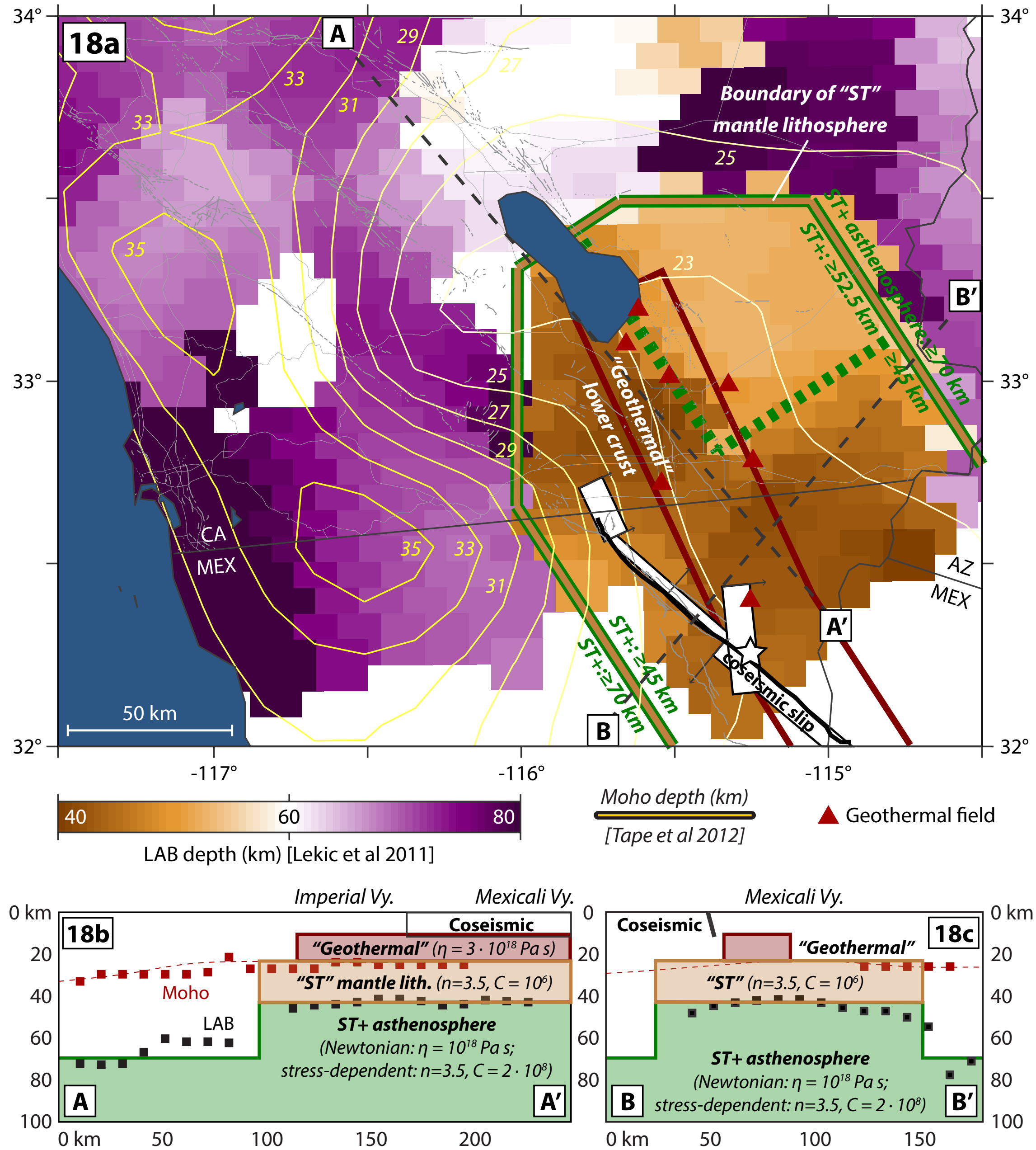

Figure 2.18. Setup of the second coupled model, featuring Newtonian viscoelastic relaxation in the "geothermal" lower crust geometry η=3 x 10^{18} Pa-s), viscoelastic relaxation with a stress-dependent viscosity (n=3.5, C = 10^6) in the "ST" geometry for the mantle lithosphere, and both a Newtonian η=10^{18} Pa-s) and stress-dependent (n=3.5, C = 2 x 10^8) rheology in the "ST+" asthenosphere. **a)** Mapview of Lekic et al [2011] lithosphere-asthenosphere boundary depth, Tape et al [2012] Moho depth, geothermal areas, and model setup. **b, c)** Cross sections of Lekic et al [2011] lithosphere-asthenosphere boundary depth and Moho depth and model setup.

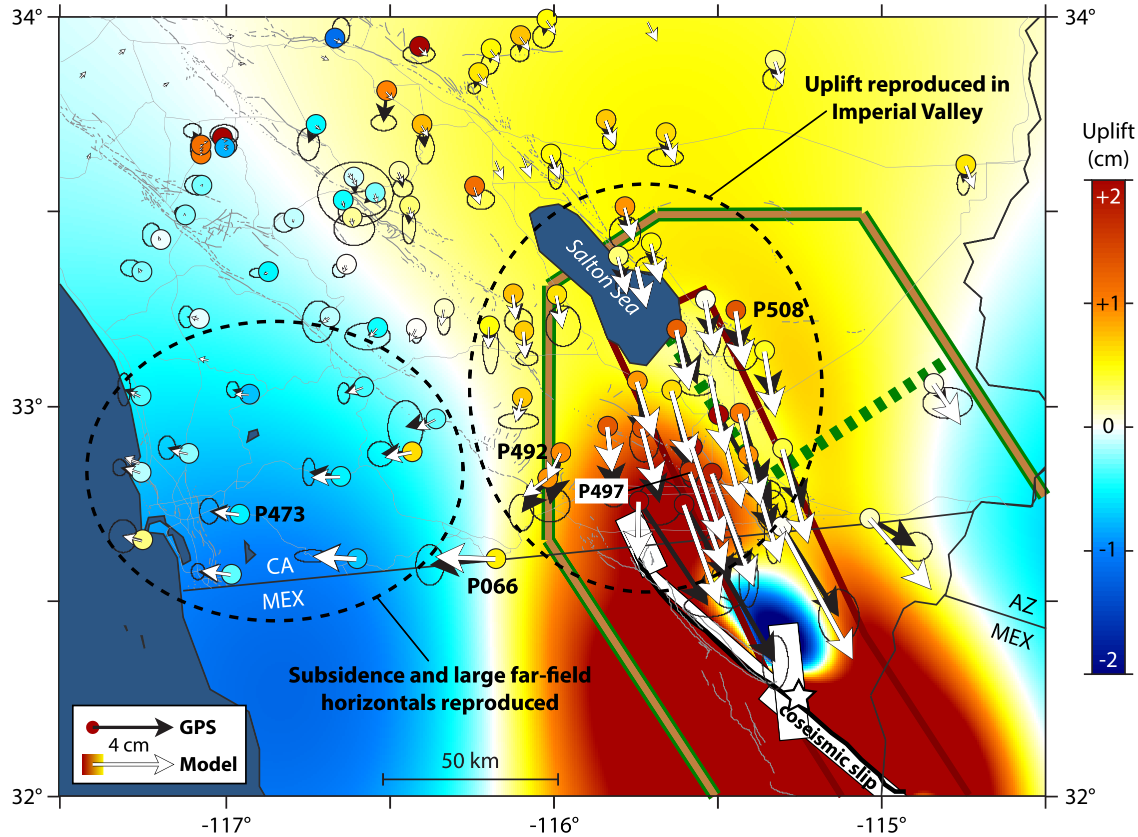

Figure 2.19. Comparison of three-year cumulative horizontal and vertical postseismic displacements at GPS stations with cumulative synthetic displacements generated by the second coupled model.

horizontal displacement timeseries, 49% in cumulative three-year vertical displacements and 48% in time-dependent fits to vertical displacement timeseries (Figure 2.16). The model reproduces timeseries of horizontal displacement within uncertainties at stations at a variety of azimuths from the rupture (Figure 2.17). Although we cannot estimate variance reductions of cumulative displacements or in timeseries at stations in Mexico due to the incomplete temporal coverage there, this model also fits the estimated postseismic velocities there well to first order (Figure 2.S19). To assess the extent to which the different mechanisms in the model feed back on one another in a nonlinear way, we also plot the summations of displacement timeseries of the individual mechanisms (Figure 2.17). Surface displacement timeseries from the coupled model are markedly similar to these summed timeseries, suggesting a low degree of feedback between the mechanisms.

The second multiple-mechanism model retains the Newtonian viscoelastic relaxation with $\eta = 3 \times 10^{18}$ Pa-s from 10-22.5 km depth in the "geothermal" lower crustal

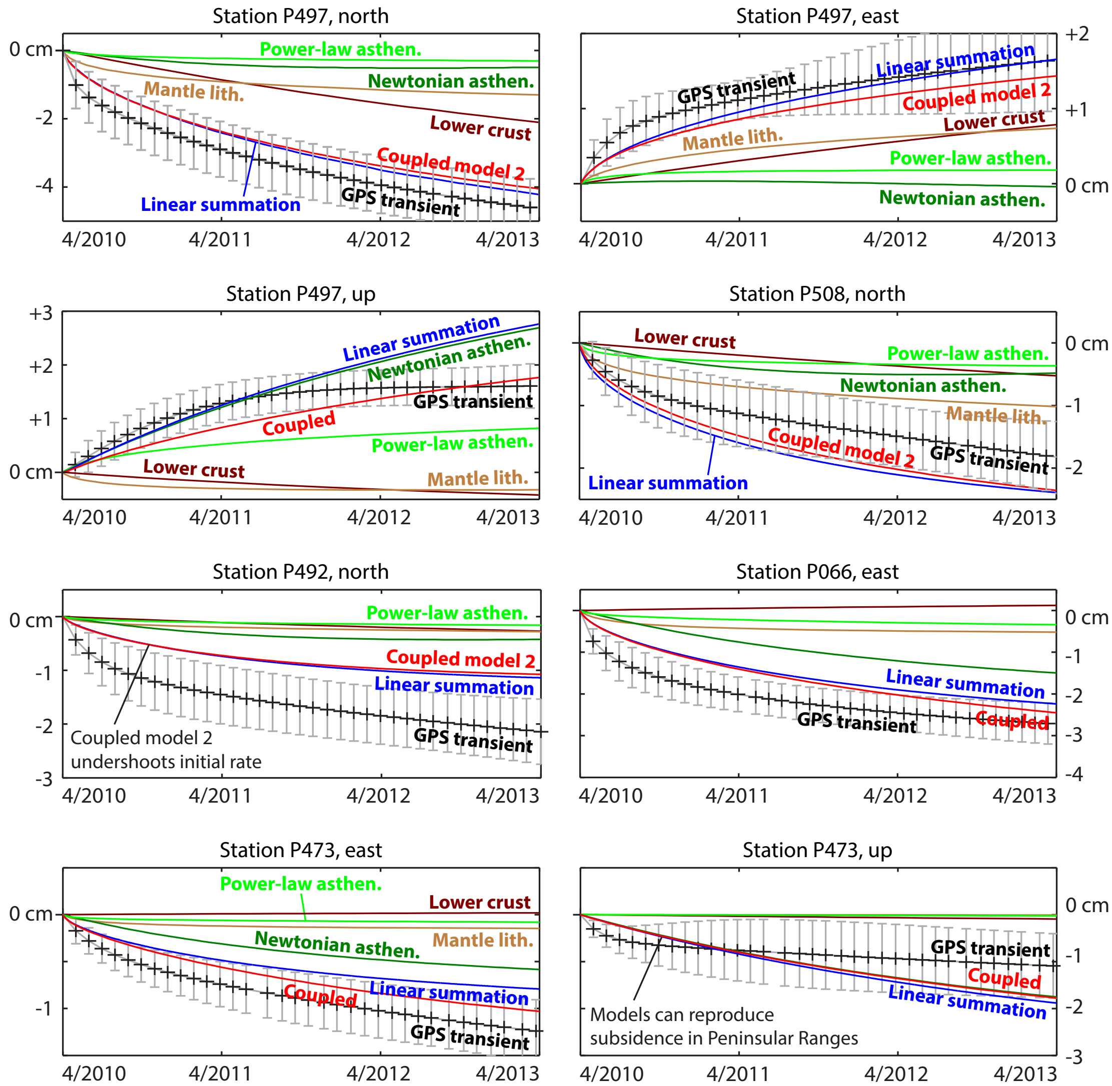

Figure 2.20. Comparison of extracted GPS timeseries at several GPS stations (locations indicated in Figure 2.19) with synthetic timeseries of surface displacement generated by the second coupled model.

ductile zone and Newtonian viscoelastic relaxation with $\eta=10^{18}$ Pa-s in the "ST+" model for the asthenosphere, but replaces the afterslip in the first model with viscoelastic relaxation with a stress-dependent viscosity (n=3.5) in the mantle lithosphere and "ST+" asthenosphere, with coefficients $C = 10^6$ in the mantle lithosphere and $C = 2 \times 10^8$ in the asthenosphere (Figure 2.18). This model can be viewed as an exploration of how well the postseismic transient can be fit by a purely viscoelastic model. The model achieves variance reductions of 85% both in cumulative three-year horizontal displacements and in time-dependent fits to horizontal displacement timeseries, and achieves a better fit to the verticals than the first coupled model, with a variance reduction of 59% in cumulative three-year vertical displacements and 56% in time-dependent fits to vertical displacement timeseries (Figure 2.19). The model reproduces the horizontal and vertical transients at station P497 relatively well (Figure 2.20); it overshoots southward displacements in the eastern Imperial Valley (Figure 2.19) but reproduces the general character of the southward displacement timeseries at station P508 (Figure 2.20). The model undershoots the rapidly decaying early southward velocity at station P492 and the rapidly decaying early westward velocity at station P066 (Figure 2.20), two of the closest stations to the Yuha Desert, suggesting that those displacements were related to a more localized process than viscoelastic relaxation in the upper mantle. In Mexico, the model reproduces the approximate northward postseismic velocity at station PLPX and the eastward velocity at station PLTX less well than the first coupled model (Figure 2.S20), although high uncertainties in the approximate velocities at those stations make quantitative comparison impractical. As with the first coupled model, timeseries of surface displacement from the second model differ only subtly from summed timeseries of surface displacement from the individual participating mechanisms (Figure 2.20). We note that both preferred models predict strong subsidence in a localized region in the Mexicali Valley (Figure 2.16, 2.19); upon examination this subsidence appears to be related to the lower crustal component of viscoelastic relaxation, and specifically to result from an edge effect where the "geothermal" geometry governing it passes close to the rupture (compare Figure 2.S10a and 2.S10b). The geometry of the effectively low-viscosity region in the lower crust is poorly constrained in Mexico and so this component of the model prediction is not robust.

2.12. Discussion

Many of the endmember mechanisms modeled here can reproduce key aspects of the observed postseismic transient (Table 2.2), consistent with well-known tradeoffs between mechanisms of postseismic deformation [e.g., Burgmann and Dresen 2008]. Kinematic inversions show that the cumulative three-year postseismic displacement field in southern California can be well fit to afterslip on the coseismic rupture and possibly the downward extensions of the main rupture planes (Figure 2.5, Figure 2.S24), hinting at the possibility that some combination of shallow and deep afterslip could explain much of the postseismic transient in space and time. Forward modeling shows that stress-driven afterslip in the lower crust and Yuha Desert with $(a-b)\sigma \sim 1$ MPa can reproduce the rapidly decaying early horizontal velocities in the Imperial Valley, and afterslip extending into the

Key aspect of postseismic transient	Modeled mechanisms that can reproduce aspect
Uplift in Imperial Valley and subsidence in Peninsular Ranges	Afterslip on coseismic rupture (kinematic inversion)
	Newtonian viscoelastic relaxation in asthenosphere
Relatively large westward displacements in Peninsular Ranges	Newtonian viscoelastic relaxation in "ML" mantle lithosphere
	Newtonian viscoelastic relaxation in asthenosphere
Rapidly decaying early horizontal velocities Imperial Valley	Afterslip with $(a-b)\sigma \sim 1$ MPa
	Viscoelastic relaxation with stress-dependent viscosity ($n = 2.5$) in lower crust
	Viscoelastic relaxation with stress-dependent viscosity ($n = 4$) in lower crust
	Viscoelastic relaxation with stress-dependent viscosity ($n = 3.5$) in mantle lithosphere
Sustained horizontal velocities in Imperial Valley following rapid early motions	Afterslip with $(a-b)\sigma \sim 10$ MPa
	Newtonian viscoelastic relaxation in lower crust
	Viscoelastic relaxation with stress-dependent viscosity ($n = 2.5$) in lower crust (?)
	Newtonian viscoelastic relaxation in mantle lithosphere

Table 2.2. Key aspects of the observed postseismic transient and the modeled deformation mechanisms that can reproduce them.

upper mantle with (a-b)σ ~ 10 MPa can reproduce the sustained horizontal velocities following them. Although this combination of lower crustal and upper mantle afterslip does produce subsidence in the Imperial Valley rather than the uplift observed there, afterslip on the coseismic rupture could have produced uplift in the Imperial Valley as the coseismic rupture did (Figure 2.3) and as expected for a northwest-striking dislocation that comes to the surface (Figure 2.S1a). And although these forward afterslip models fail to reproduce the subsidence or large displacements in the Peninsular Ranges due to the lower slip predicted at depth than required in the kinematic inversions, it is possible that afterslip obeying a different constitutive law than simple rate-strengthening friction, or even a different spatial variability of a similar friction law, may be able to produce more slip at depth than modeled here and may be able to fit the far-field displacements more successfully, possibly in conjunction with afterslip on the coseismic rupture. Another possibility is that either of the near-field signals could result from flow in a very weak ductile shear zone in the lithosphere, activated by coseismic slip and/or afterslip above it [Montesi and Hirth 2003]. Although dynamically activated shear zones may generally be unlikely to produce significant postseismic surface deformation [Takeuchi and Fialko 2013], the high heat flow in the Salton Trough could conceivably result in a very low-viscosity shear zone that does so here. Therefore it is possible that much of the postseismic transient could be the result of afterslip or localized shear deformation.

Nevertheless, the best candidate mechanism to fit the subsidence and relatively large cumulative westward displacements in the Peninsular Ranges, as well as the uplift in the Imperial Valley, appears to be viscoelastic relaxation in the asthenosphere (Figure 2.14). This is consistent with the findings of Gonzalez-Ortega et al [2014], who found that neither afterslip on the coseismic rupture nor poroelastic rebound in the crust could reproduce displacements at GPS stations in southernmost California even in the first six months following the rupture and inferred that viscoelastic relaxation played a role in the postseismic transient (though that study did not consider afterslip below the coseismic rupture). Although we find that a Newtonian rheology in the asthenosphere can reproduce those aspects of the data well, a setting featuring a stress-dependent viscosity in the upper mantle and a background stress state of much greater magnitude than the coseismic stress changes could result in a quasi-linear viscoelastic behavior. Thus, we cannot unequivocally conclude that the asthenosphere beneath the Salton Trough has a dominantly Newtonian rheology – only that a Newtonian-esque response to coseismic stress changes fits these aspects of the postseismic transient well. Newtonian viscoelastic relaxation in the "ST" geometry for the asthenosphere, confining the ductile region to the Salton Trough, requires a viscosity well below η=5 x 10^{17} Pa-s to fit the westward velocities in the Peninsular Ranges and may not reproduce the subsidence observed there. Newtonian viscoelastic relaxation in the other three geometries can qualitatively reproduce the sustained westward velocities and subsidence in the Peninsular Ranges and the uplift in the Imperial Valley with viscosities of η=5 x 10^{17} Pa-s - η=2 x 10^{18} Pa-s, with tradeoffs between geometry and Newtonian viscosity (Figure 2.14). The actual rheological structure of the upper mantle is undoubtedly more complex than modeled here, in particular due to the inverse exponential dependence of viscosity on temperature [e.g. Karato 2008], and thus the asthenosphere models used here are very much first-order approximations. Nevertheless, we can conclude that deep viscoelastic relaxation obeying a Newtonian rheology with an isotropic background stress state can reproduce several key aspects of the postseismic transient.

The inferred Newtonian viscosity of η~10^{18} Pa-s in the asthenosphere is consistent with a viscosity of η=5 x 10^{17} Pa-s - 10^{18} Pa-s inferred for the upper mantle under the Gulf of California from postseismic relaxation following a M=6.9 earthquake in 2009 [Malservisi et al, 2012] and with values in the range of of 10^{18} Pa-s inferred for the upper mantle beneath the Basin and Range, another extensional regime [Kaufmann and Amelung 2000, Bills 2007]. Luttrell et al [2007] inferred an upper mantle viscosity of 10^{19} Pa-s for the Salton Trough region, an order of magnitude higher than our estimates, from periodic surface loading associated with filling of prehistoric Lake Cahuilla. That value was obtained assuming an elastic thickness of 35 km, and figure 5a of Luttrell et al [2007] suggests that the data could also be fit with a viscosity an order of magnitude lower and an elastic layer 40-50 km thick, closer to the inferred lithospheric thickness in the Salton Sea region [Lekic et al 2011]. At the same time, the viscosity inferred here for the asthenosphere is a factor of 10^3-10^4 lower than estimates derived from postglacial rebound studies [e.g., Burov 2007]. Although this may to some extent reflect the extensional environment of the Salton Trough, it echoes longstanding discrepancies between mantle viscosity values inferred in postseismic deformation studies and those implied by longer-timescale processes. More locally, Fay and Humphreys [2005] found that the distribution of slip rates across the San Andreas, San Jacinto and Elsinore faults required a strong lower crust with long-term viscosity of at least 5 x 10^{19} Pa-s. One possibility is that inferred viscosities on the timescale of postseismic deformation could simply reflect the transient behavior of a biviscous or multiviscous upper mantle in which the effective steady-state viscosity could be one or more orders of magnitude higher [Meade et al, 2013]. The higher asthenospheric viscosity inferred by Luttrell et al [2013], for example, could result from the longer relevant timescale of the process examined in that study.

Pollitz et al [2012] found that postseismic GPS displacements following the El Mayor-Cucapah earthquake were well fit by a model of viscoelastic relaxation in two regimes: a Newtonian lower crust with viscosity 3.2 x 10^{19} Pa-s and an upper mantle with a biviscous rheology featuring a transient phase of relaxation followed by a steady-state phase. The best-fitting upper mantle featured a laterally heterogeneous rheological structure with transient and steady-state viscosities of 1.2 x 10^{17} Pa-s and 3.2 x 10^{18} Pa-s (respectively) beneath the Salton Trough and transient and steady-state viscosities of 3.4 x 10^{18} Pa-s and 9.2 x 10^{19} Pa-s (respectively) beneath the Peninsular Ranges to the west and the Southern California River Desert to the east. Despite the different rheologies used here, our second multiple-mechanism model (Figures 2.18-2.20) is similar in principle to the best-fitting structure of Pollitz et al [2012], ascribing the rapid early velocities in the Salton Trough to nonlinear viscoelastic relaxation in a laterally heterogeneous upper mantle. Our first multiple-mechanism model (Figures 2.15-2.17) shows that the rapid early velocities can also be reproduced by afterslip in the crust, with the remaining aspects of the transient reproduced solely by Newtonian viscoelastic relaxation. The upper mantle may be more likely dominated by stress-dependent creep than a Newtonian rheology [e.g., Hirth and Kohlstedt 2003; Karato 2008], and the success of our first master model in reproducing much of the postseismic transient does not mean that stress-dependent rheologies are negligible in this region: as discussed previously, the deformation we fit to Newtonian viscoelasticity may actually result from relaxation in an upper mantle with a stress-dependent viscosity and a high background deviatoric stress state. Nonetheless, both of our coupled models can be useful in understanding the basic time behaviors of these processes as well as the tradeoffs between afterslip and viscoelastic relaxation. In general, the high heat flow in the Salton Trough region and the high shear strain rates associated with the Pacific-North American plate boundary mean that the postseismic deformation following the El Mayor-Cucapah earthquake may have featured aspects of both these models and may have been much more complex than either of them.

2.13. Conclusions

Three-year cumulative postseismic surface displacements following the El Mayor-Cucapah earthquake can be fit intriguingly well by slip on the coseismic rupture and below, and forward models of afterslip in the lower crust and mantle can reproduce multiple key aspects of postseismic displacement timeseries in the Imperial Valley, making it conceivable that afterslip could possibly explain much of the observed transient in southern California. The key aspects of the transient can also be reproduced by viscoelastic relaxation in the crust and mantle, and in particular, viscoelastic relaxation in the asthenosphere may be the best candidate mechanism to explain the pattern of postseismic uplift and subsidence and relatively large westward displacements observed far from the rupture in the Peninsular Ranges. We present two endmember models of multiple coupled mechanisms that reproduce much of the postseismic transient in space and time: one combining afterslip and Newtonian viscoelastic relaxation in the lower crust and asthenosphere, and one combining Newtonian and stress-dependent rheologies in the lower crust, mantle lithosphere and asthenosphere. The tradeoffs between these two models are consistent with well-known tradeoffs between afterslip and viscoelastic relaxation.

2.A. Supporting Information

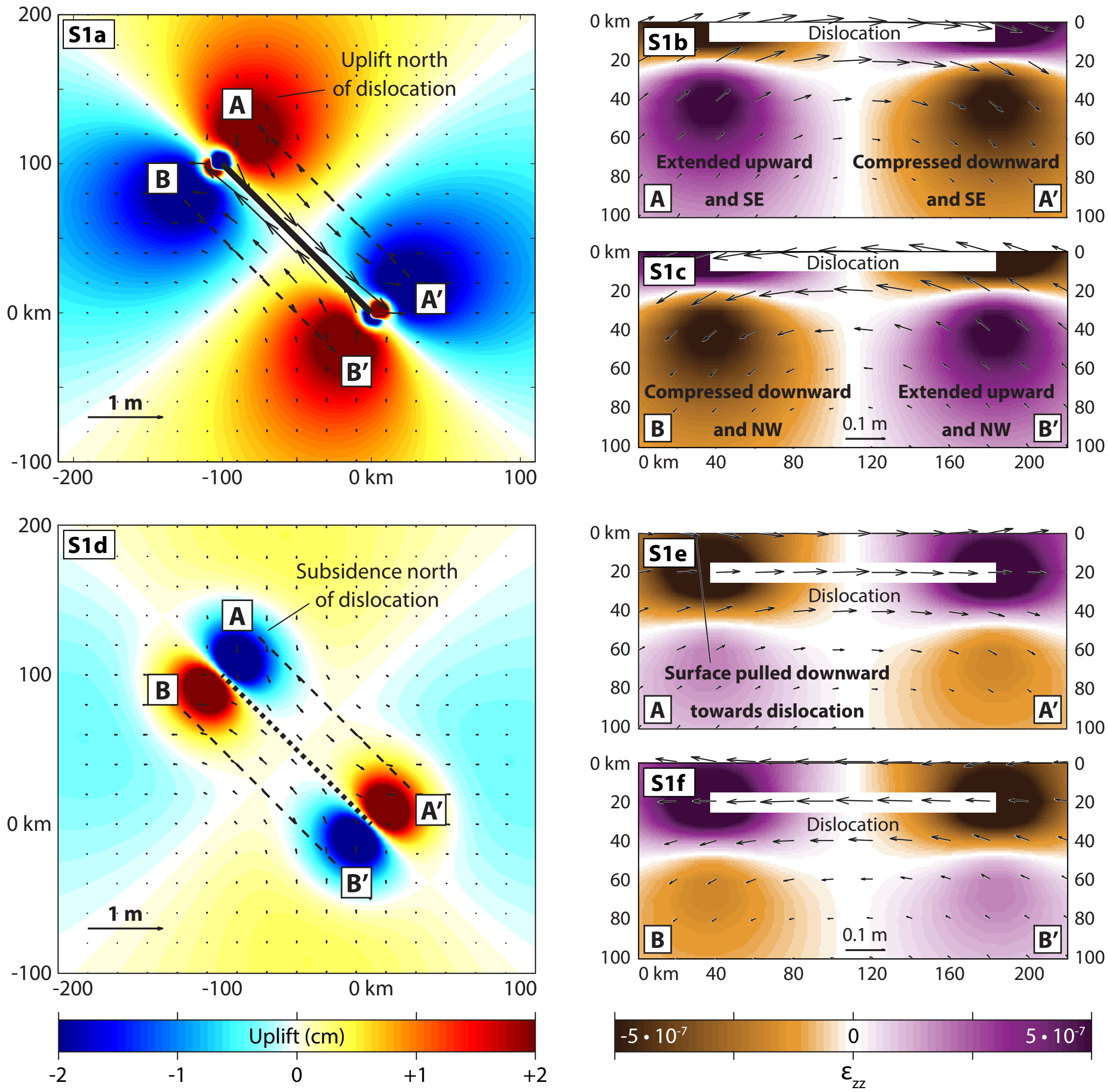

Figure 2.S1. a) 2 m of right-lateral slip on a vertical northwest-striking fault from 0-10 km depth produces surface uplift in extensional quadrants and subsidence in compressional quadrants. **b, c)** Cross sections of coseismic displacement parallel to the dislocation show that material in extensional quadrants is extended upward as well as towards the dislocation, and material in compressional quadrants is compressed downward and away from the dislocation. Material on the left half of cross section A-A' corresponds to the Imperial Valley in the El Mayor-Cucapah earthquake. **d)** 2 m of right-lateral slip on a vertical northwest-striking fault from 15-25 km depth produces near-field subsidence in extensional quadrants and near-field uplift in compressional quadrants. **e, f)** Material at the surface just north of the northwest end is pulled downward towards the dislocation.

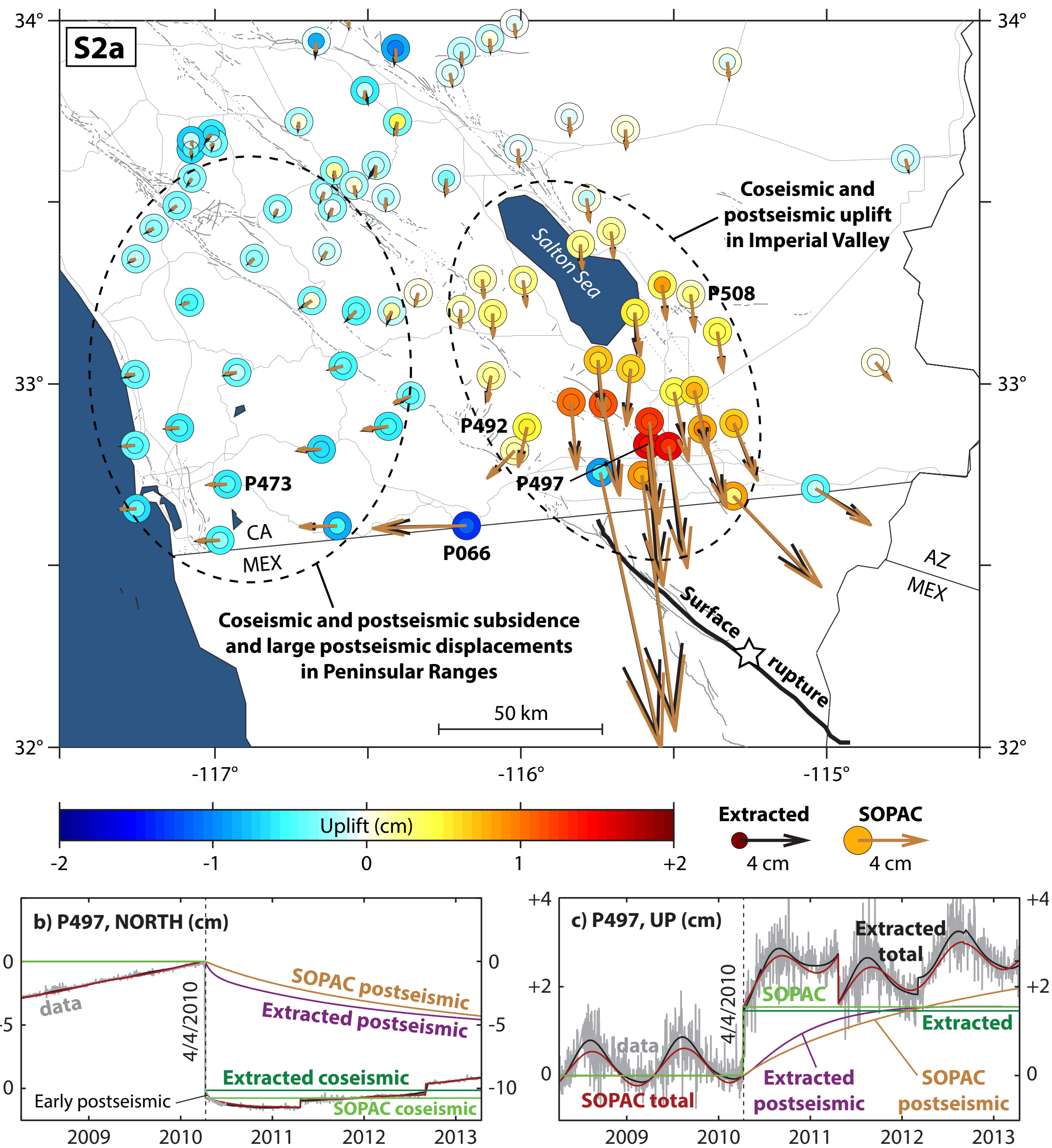

Figure 2.S2. Comparison of extracted coseismic displacements at GPS stations with coseismic displacements estimated by SOPAC. **a)** Horizontal and vertical coseismic displacements are generally similar between the two estimates. **b)** Timeseries estimated by SOPAC use only a single decay term and incorrectly ascribe some of the very early horizontal postseismic displacement in the Imperial Valley to coseismic displacement. **c)** Comparison of vertical displacement timeseries at station P497 in the Imperial Valley.

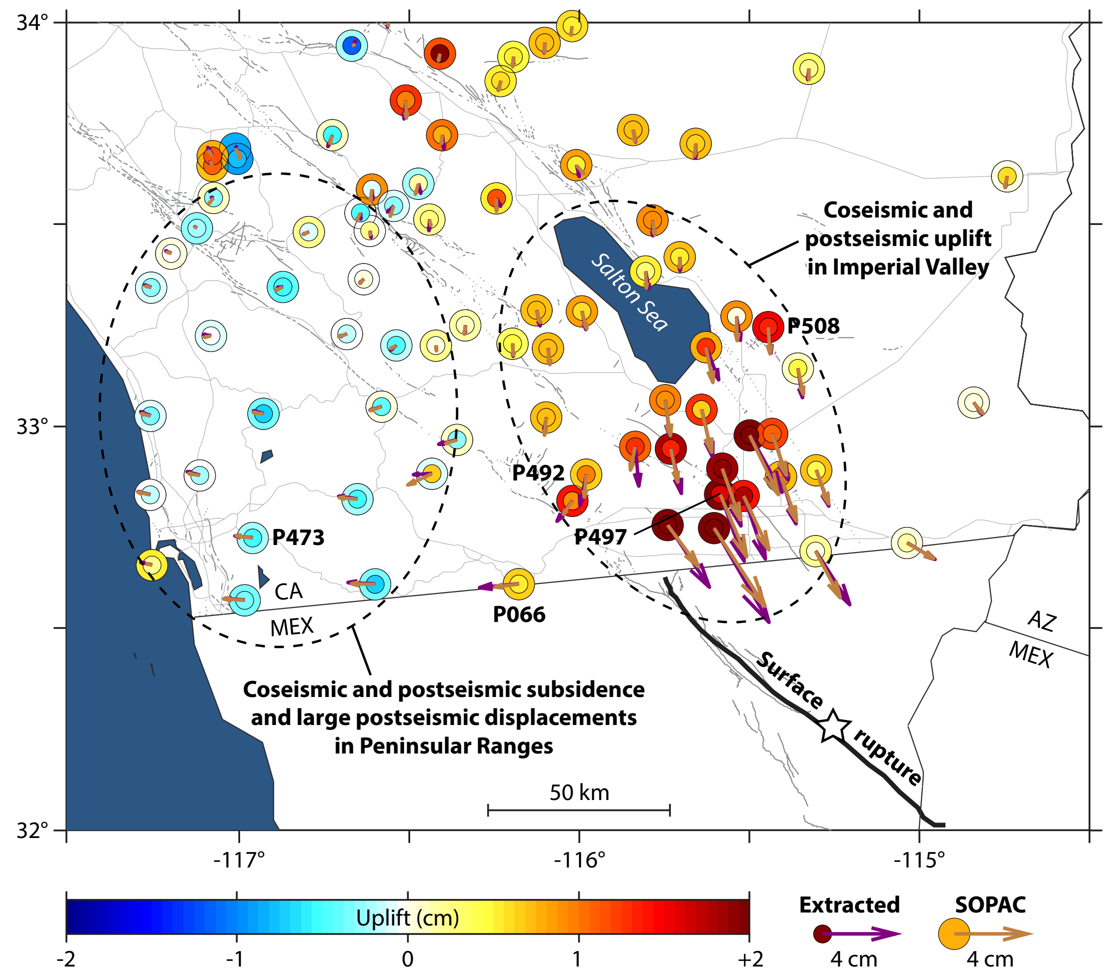

Figure 2.S3. Comparison of cumulative extracted three-year postseismic displacements at GPS stations with cumulative three-year postseismic displacements estimated by SOPAC.

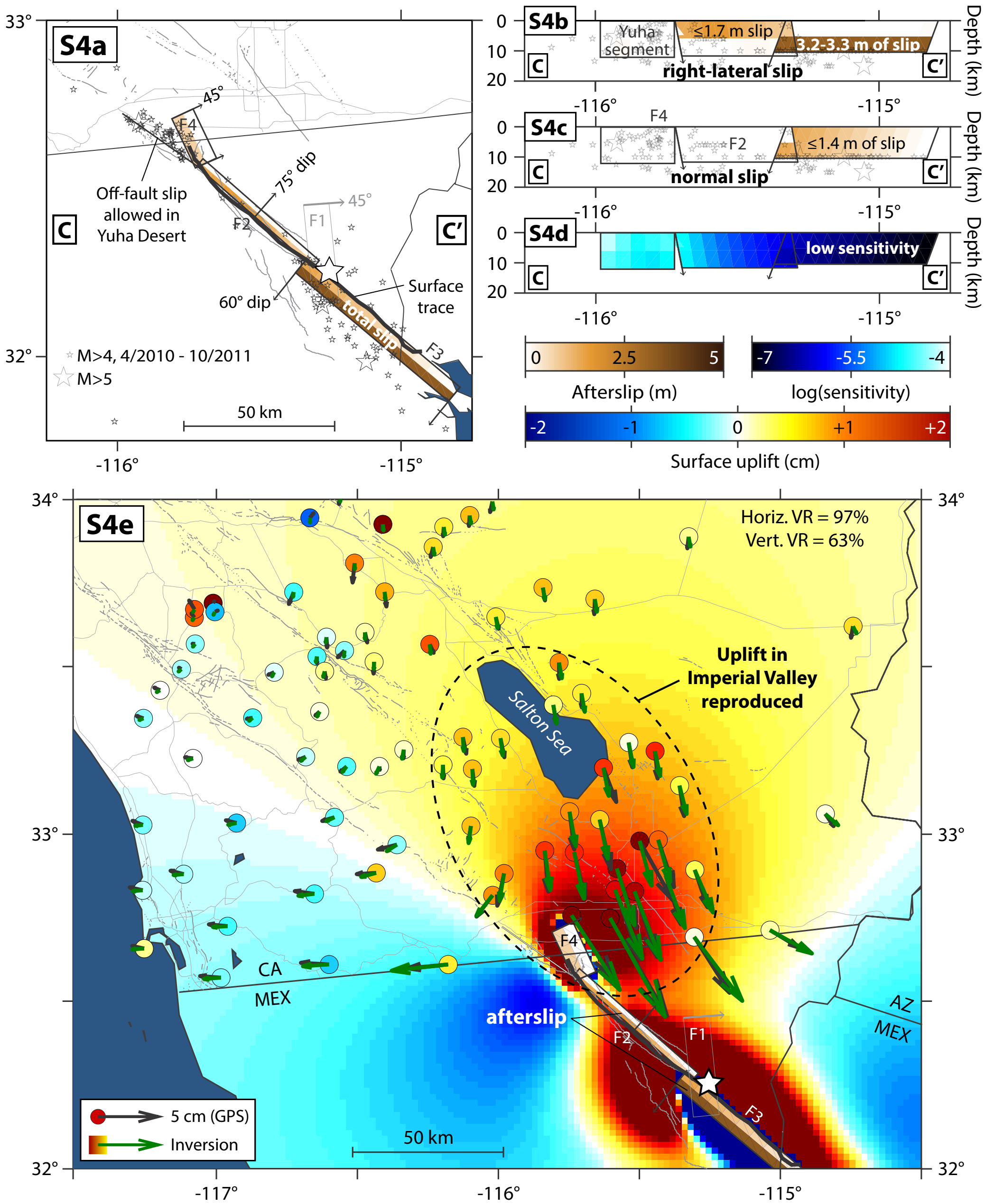

Figure 2.S4. Inversion of 3-year cumulative postseismic GPS displacements for afterslip on the main coseismic rupture planes and in the Yuha Desert. **a)** Slip is allowed on planes F2, F3 and F4 of the Wei et al [2011] model for the mainshock between 0 and 12 km down dip from their top edges (~0-12 km depth). Slip is also allowed on a 30-km-long segment extending northwest into the Yuha Desert to fit the aftershocks and surface creep there to first order; this segment has a vertical dip and extends to 12 km depth. **b-d)** The inversion assigns up to 1.7 m of right-lateral slip on plane F2 and up to 3.3 m of right-lateral slip and 0-1.4 m of normal slip on plane F3, equivalent in total moment to a M=7.2 earthquake. **e)** The inversion produces 97% and 63% variance reductions in horizontal and vertical displacements, respectively.

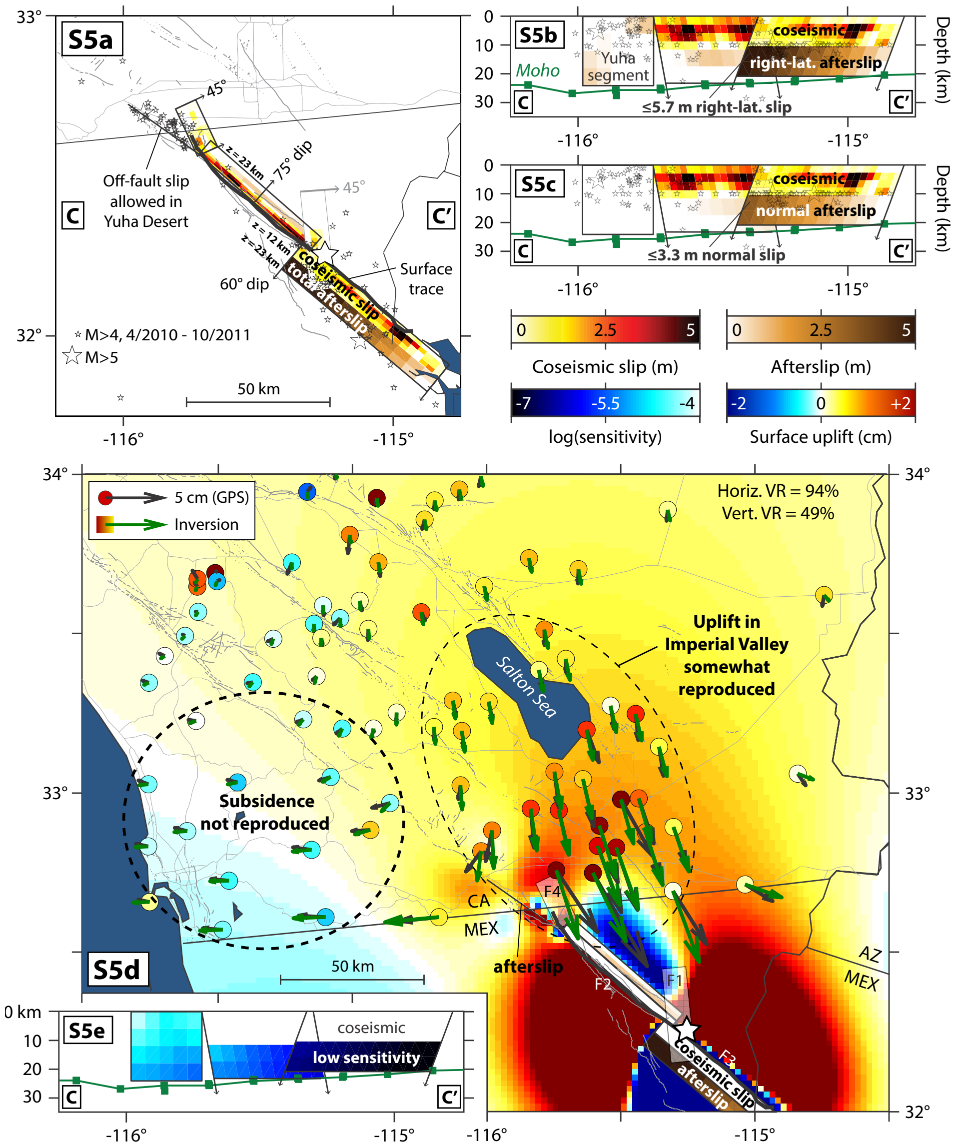

Figure 2.S5. Inversion of 3-year cumulative postseismic GPS displacements for afterslip in the lower crust and Yuha Desert. **a)** Slip is allowed on the extensions of slip planes F2 and F3 from the Wei et al [2011] coseismic model into the lower crust, between 12 and 24 km down dip from the top edges of those segments (~12-24 km depth; 24 km is the approximate Moho depth). Slip is also allowed on a 30-km-long segment extending northwest into the Yuha Desert to fit the aftershocks and surface creep there to first order and any possible slip at greater depth; this segment has a vertical dip and extends to 24 km depth. **b-c, e)** The inversion assigns up to 5.7 m of right-lateral slip and 3.3 m of normal slip on the lower crustal extension of plane F3, equivalent in total moment to a M=7.3 earthquake. **d)** The inversion produces variance reductions of 94% and 49% in horizontal and vertical displacements, respectively; the observed pattern of uplift and subsidence is visibly less well fit here than in models that allow for slip on the coseismic rupture.

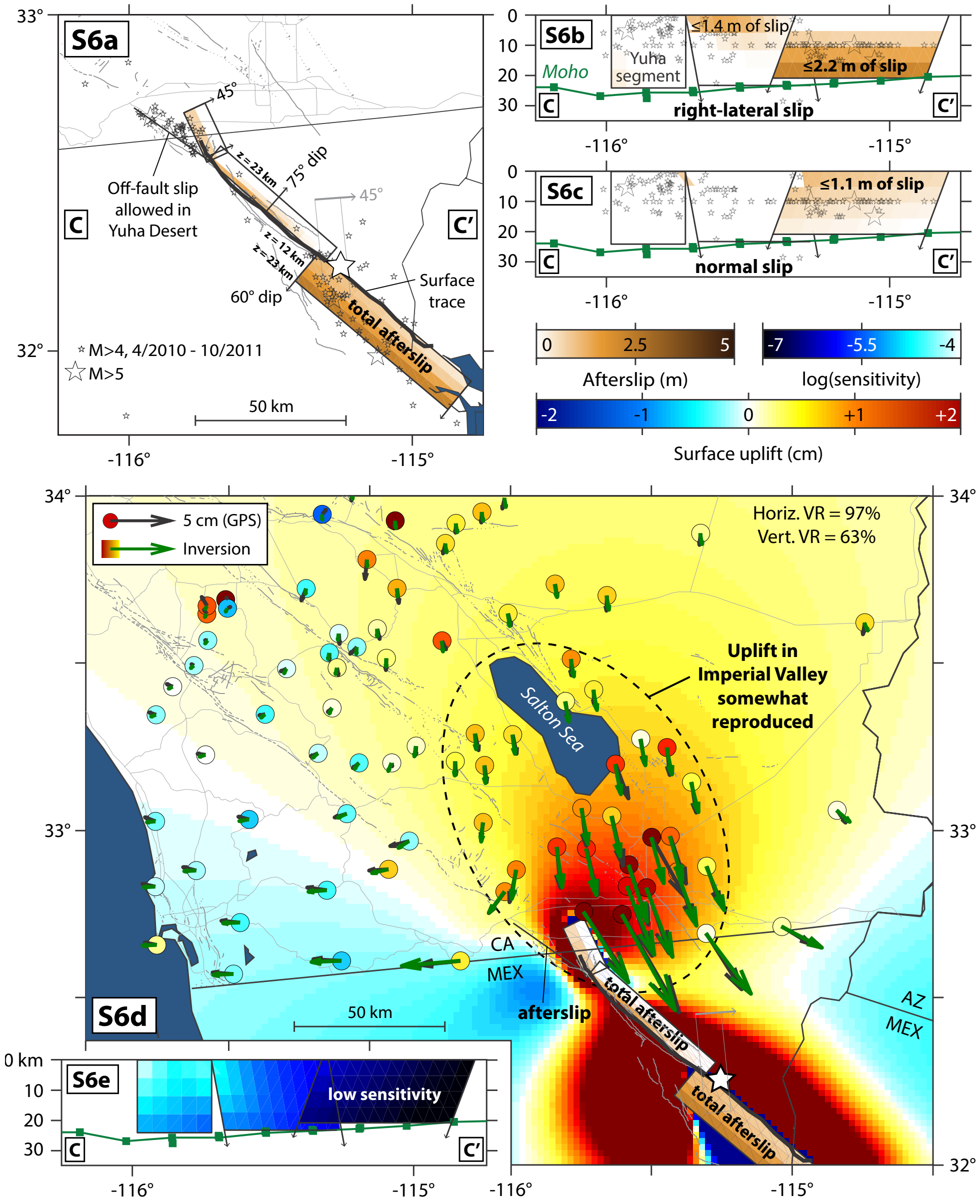

Figure 2.S6. Inversion of 3-year cumulative postseismic GPS displacements for afterslip on the main coseismic rupture planes, on modeled downward extensions of the coseismic rupture planes, and in the Yuha Desert. **a)** Slip is allowed on planes F2, F3 and F4 of the Wei et al [2011] model for the mainshock (between 0 and 12 km down dip from their top edges) and on extensions of F2 and F3 into the lower crust (between 12 and 24 km down dip). Slip is also allowed on a 30-km-long segment extending northwest into the Yuha Desert to fit the aftershocks and surface creep there to first order and any possible slip at greater depth; this segment has a vertical dip and extends to 24 km depth. **b-c, e)** The inversion assigns up to 2.2 m of right-lateral slip and 1.1 m of normal slip on plane F3 and its lower crustal extension, equivalent in total moment to a M=7.2 earthquake. **d)** The inversion produces 97% and 63% variance reductions in horizontal and vertical displacements, respectively.

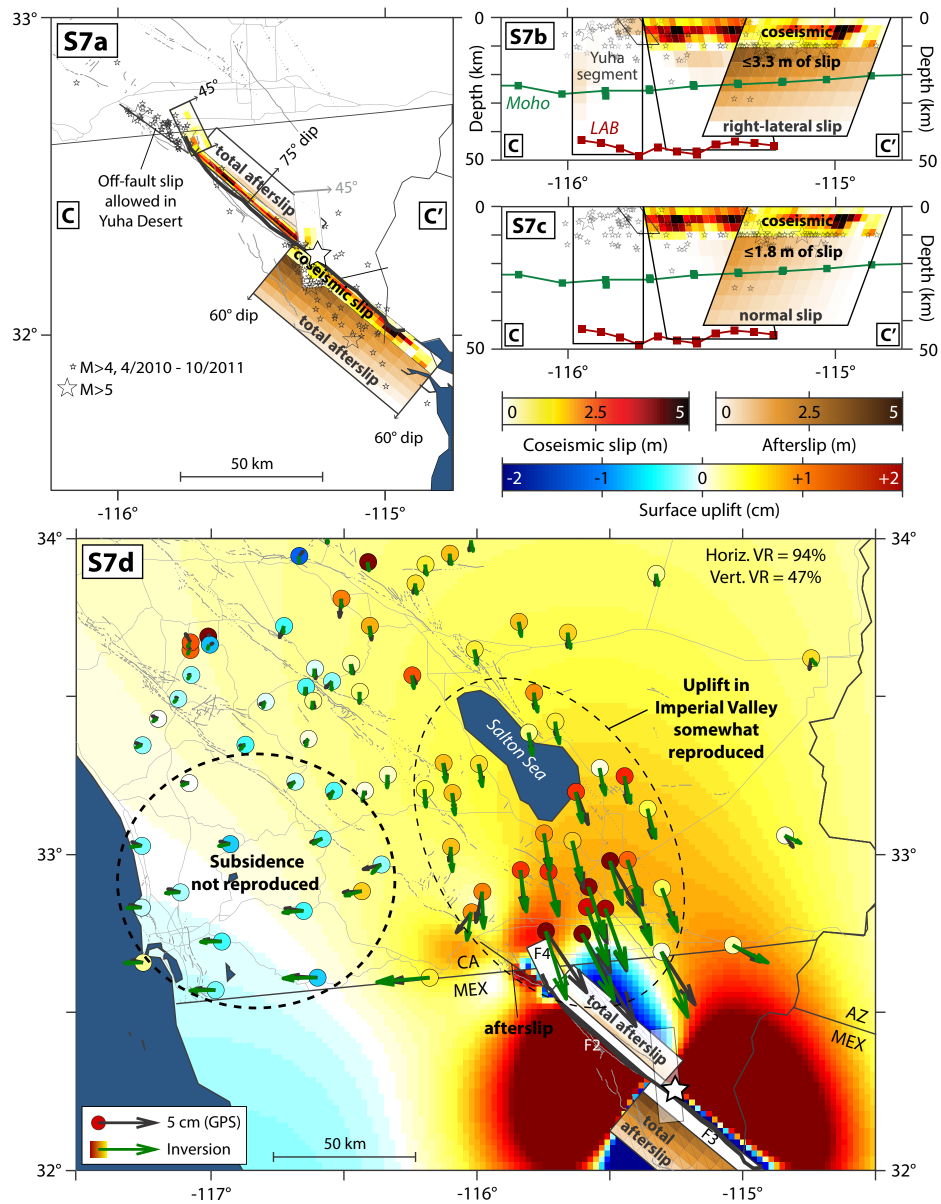

Figure 2.S7. Inversion of 3-year cumulative postseismic GPS displacements for afterslip in the lower crust, mantle lithosphere and Yuha Desert. **a)** Slip is allowed on the extensions of slip planes F2 and F3 from the Wei et al [2011] coseismic model into the lower crust and mantle lithosphere, at distances between 12 and 48 km down dip from the top edges of those segments. Slip is also allowed on a 30-km-long segment extending northwest into the Yuha Desert to fit the aftershocks and surface creep there to first order and any possible slip at greater depth; this extension has a vertical dip and extends to 48 km depth. **b, c)** The inversion assigns up to 3.3 m of right-lateral slip and 1.8 m of normal slip on the deep extension of plane F3, equivalent in total moment to a M=7.3 earthquake. **d)** The inversion produces variance reductions of 94% and 47% in horizontal and vertical displacements, respectively; the distribution of uplift and subsidence is visibly less well fit here than in models that allow for slip on the coseismic rupture.

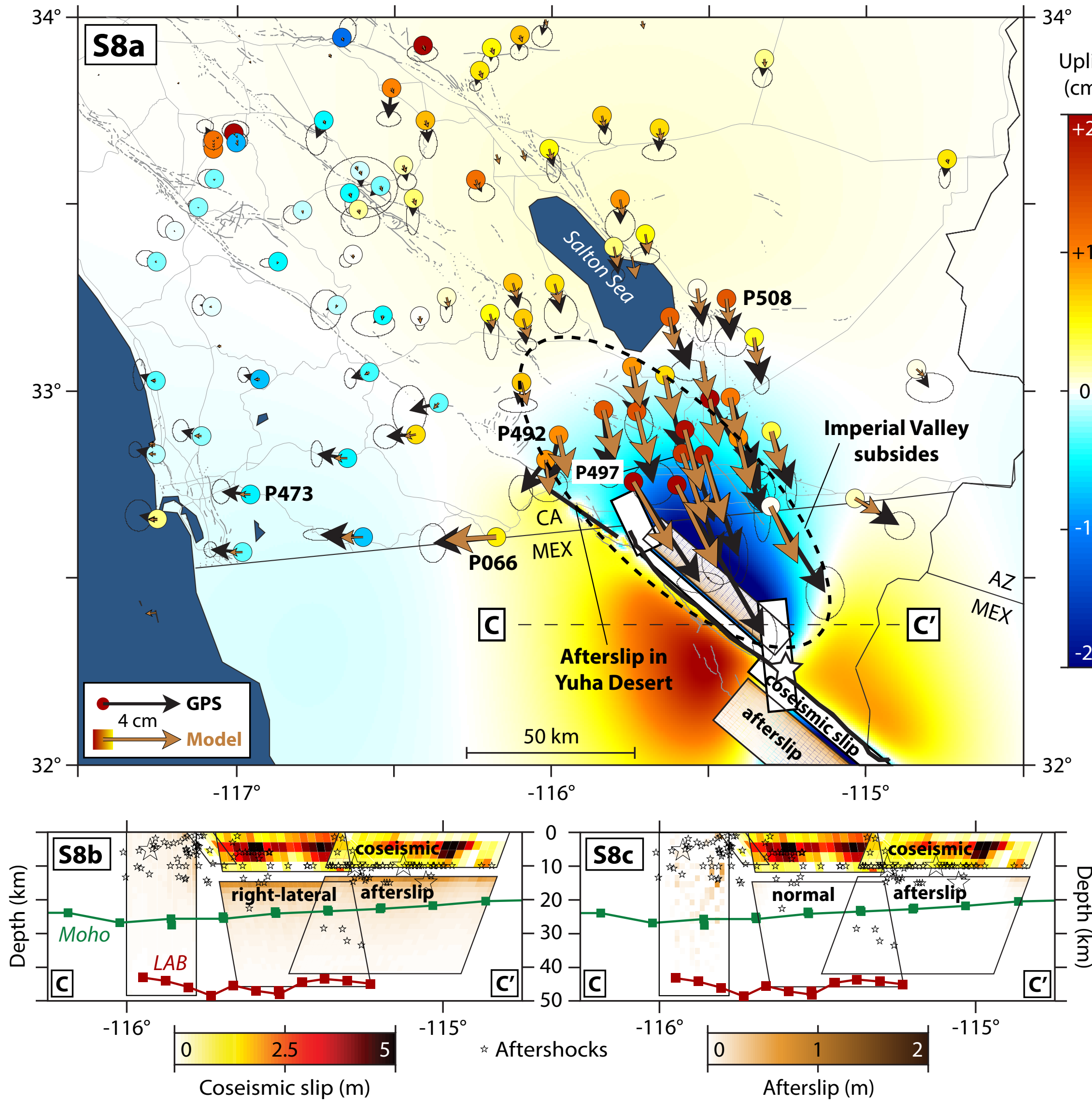

Figure 2.S8. Forward modeling of stress-driven afterslip on modeled downward extensions of coseismic slip planes F2 and F3 in the Wei et al [2011] coseismic model into the lower crust and mantle lithosphere. The afterslip is allowed between 15 and 48 km down dip from the top edges of these planes, is driven by coseismic shear stress changes and is governed by a rate-strengthening friction law with (a-b)σ = 10 MPa. Slip is also allowed on a 30-km-long segment extending northwest into the Yuha Desert; this segment has a vertical dip and extends to 48 km depth. **a)** This afterslip model produces horizontal surface displacements with the correct azimuth but the wrong pattern of uplift and subsidence. **b, c)** Slip decreases away from the coseismic rupture, as expected for a stress-driven mechanism.

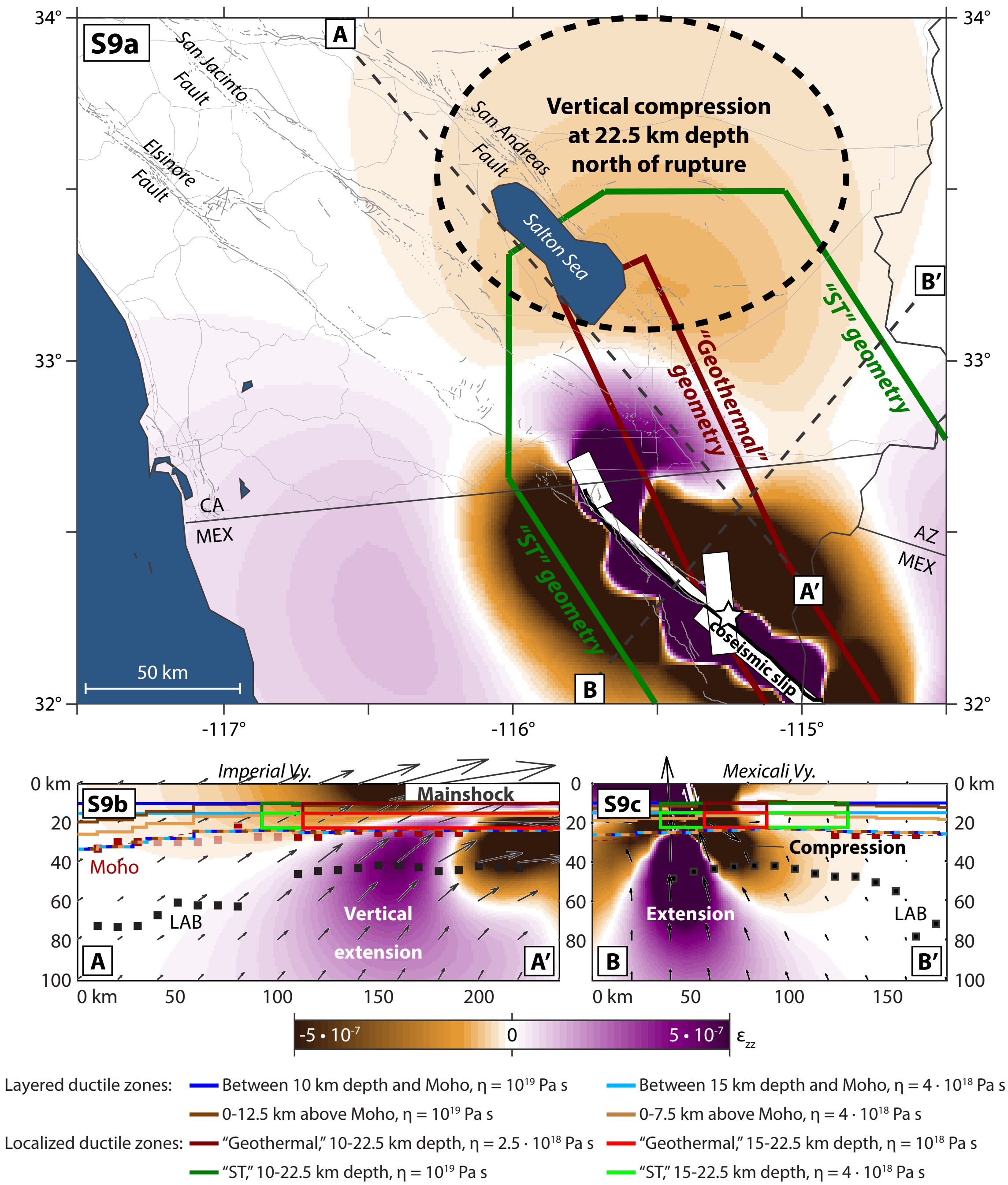

Figure 2.S9. a) Mapview and **b, c)** cross sections of vertical extension ε_{zz} imparted by the mainshock at 22.5 km depth (Moho depth in the Salton Trough). The lower crust and mantle lithosphere beneath the northern Imperial Valley and beneath the rupture underwent vertical compression during the mainshock.

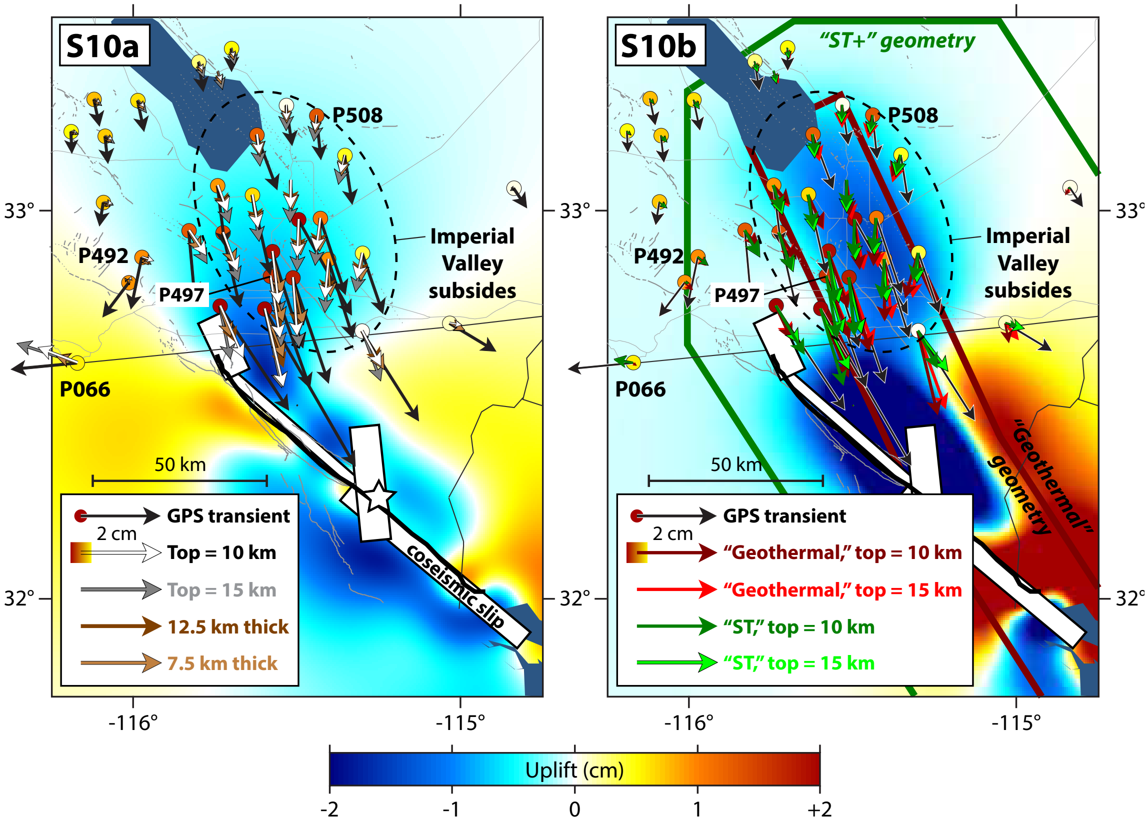

Figure 2.S10. Synthetic three-year surface displacements at GPS stations (locations shown in Figure 2.4a) generated by Newtonian viscoelastic relaxation in the modeled lower crustal ductile zones. All eight models produce subsidence in the Imperial Valley (Figure 2.9). **a)** Horizontal displacements from the four models with geometries that are not confined to the Salton Trough. Vertical displacements from the model prescribing viscoelastic relaxation between 10 km depth and the Moho. **b)** Horizontal displacements from the four models with geometries localized within the Salton Trough. Vertical displacements from the model prescribing viscoelastic relaxation in the "geothermal" geometry below 10 km depth.

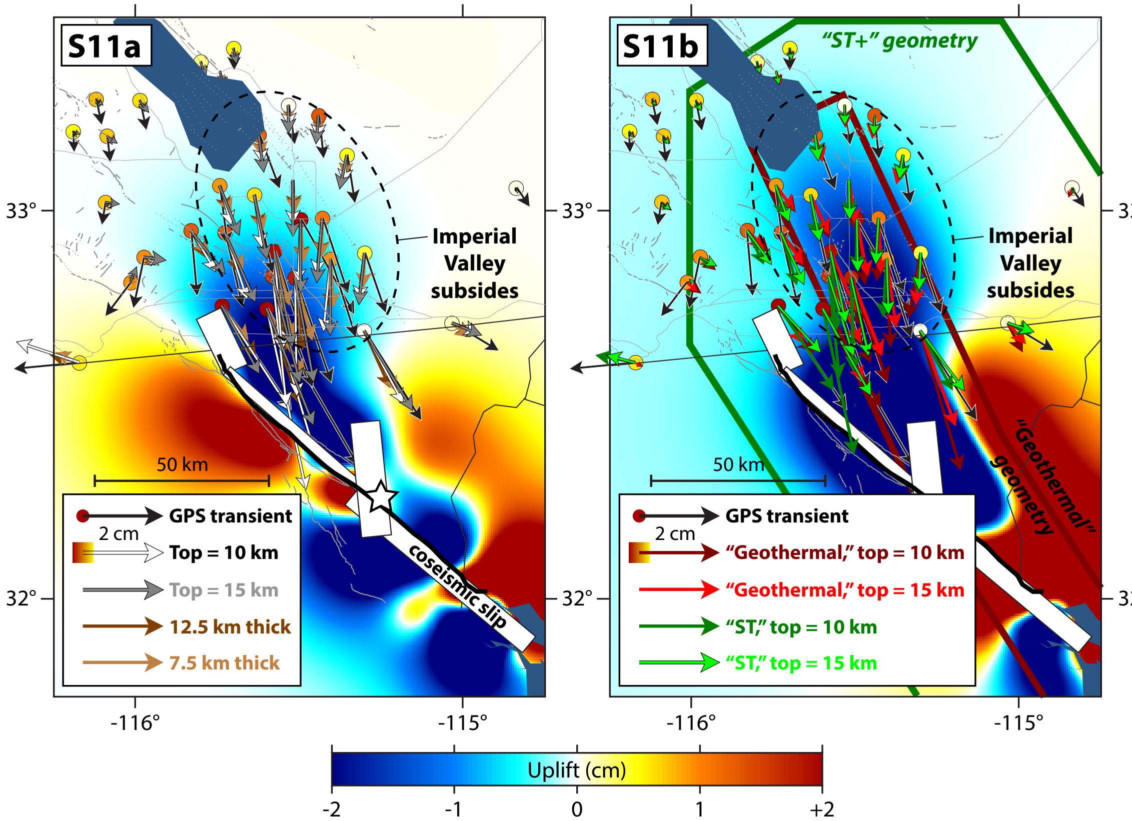

Figure 2.S11. Synthetic three-year surface displacements at GPS stations generated by viscoelastic relaxation with a stress-dependent viscosity (n=2.5) in the modeled lower crustal ductile zones. All eight models produce subsidence in the Imperial Valley (Figure 2.S12). **a)** Horizontal displacements from the four models with geometries that are not confined to the Salton Trough. Vertical displacements from the model prescribing viscoelastic relaxation between 10 km depth and the Moho. **b)** Horizontal displacements from the four models with geometries localized within the Salton Trough. Vertical displacements from the model prescribing viscoelastic relaxation in the "geothermal" geometry below 10 km depth.

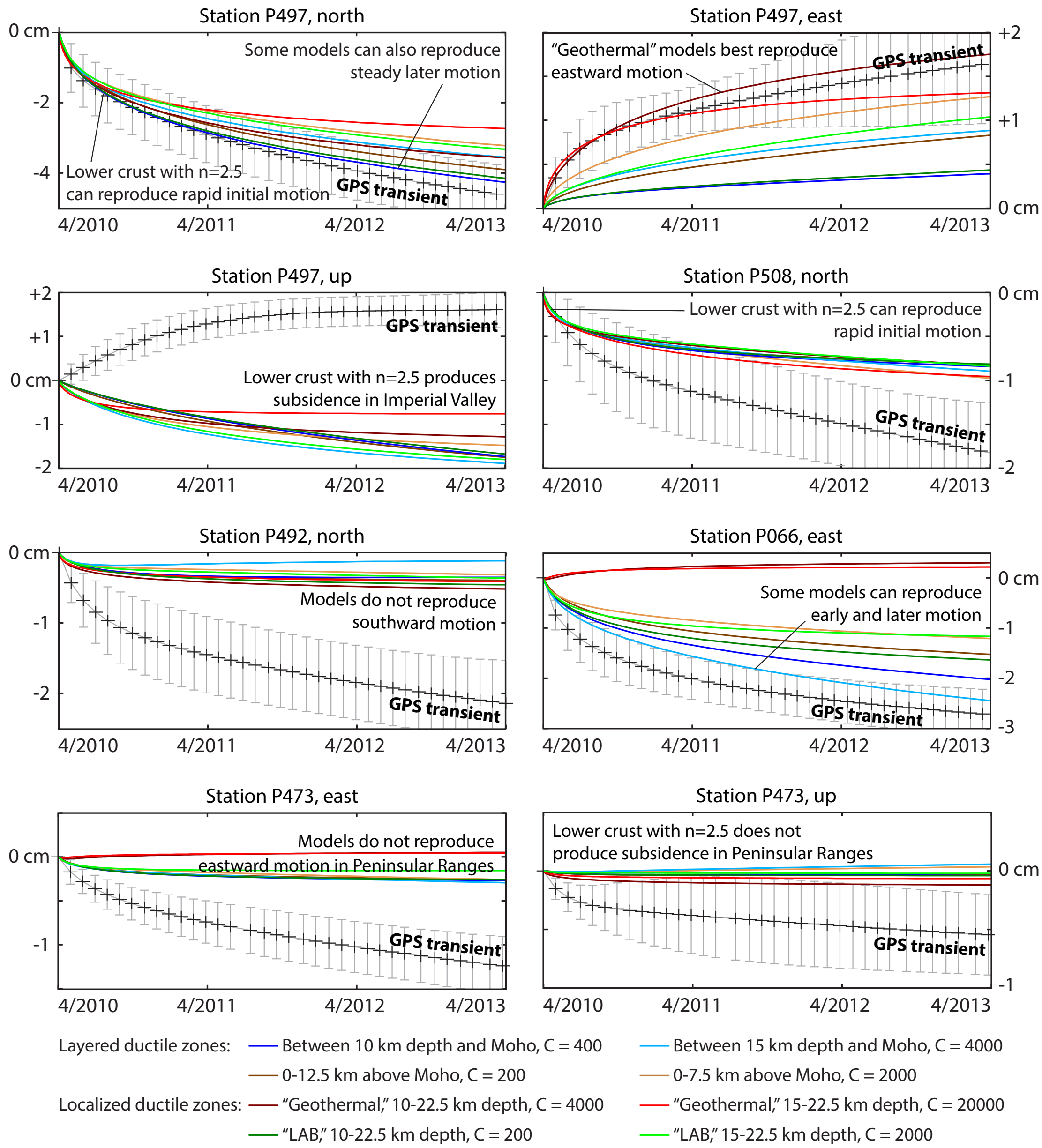

Figure 2.S12. Synthetic timeseries of surface displacement at several GPS stations (locations indicated in Figure 2.4a and 2.S10) generated by viscoelastic relaxation with a stress-dependent viscosity (n=2.5) in the modeled lower crustal ductile zones.

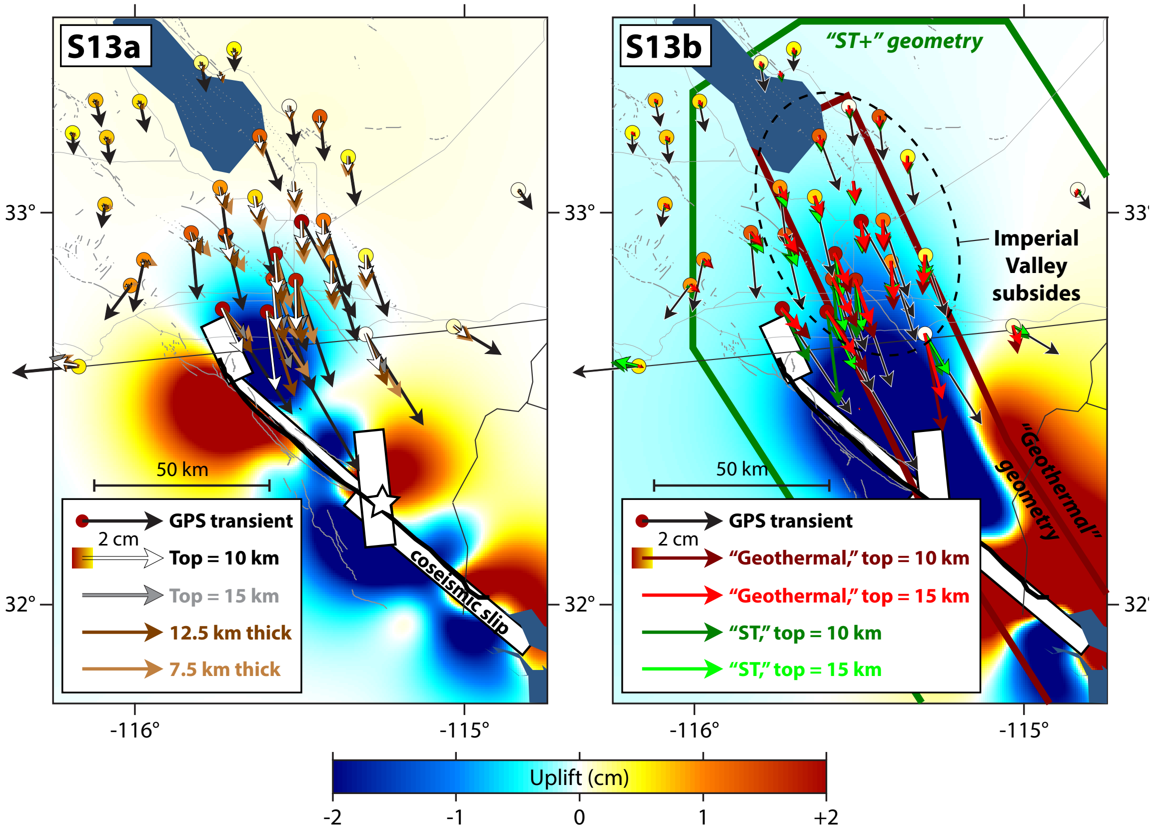

Figure 2.S13. Synthetic three-year surface displacements at GPS stations generated by viscoelastic relaxation with a stress-dependent viscosity (n=4) in the modeled lower crustal ductile zones. All eight models produce subsidence in the Imperial Valley (Figure 2.S14). **a)** Horizontal displacements from the four models with geometries that are not confined to the Salton Trough. Vertical displacements from the model prescribing viscoelastic relaxation between 10 km depth and the Moho. **b)** Horizontal displacements from the four models with geometries localized within the Salton Trough. Vertical displacements from the model prescribing viscoelastic relaxation in the "geothermal" geometry below 10 km depth.

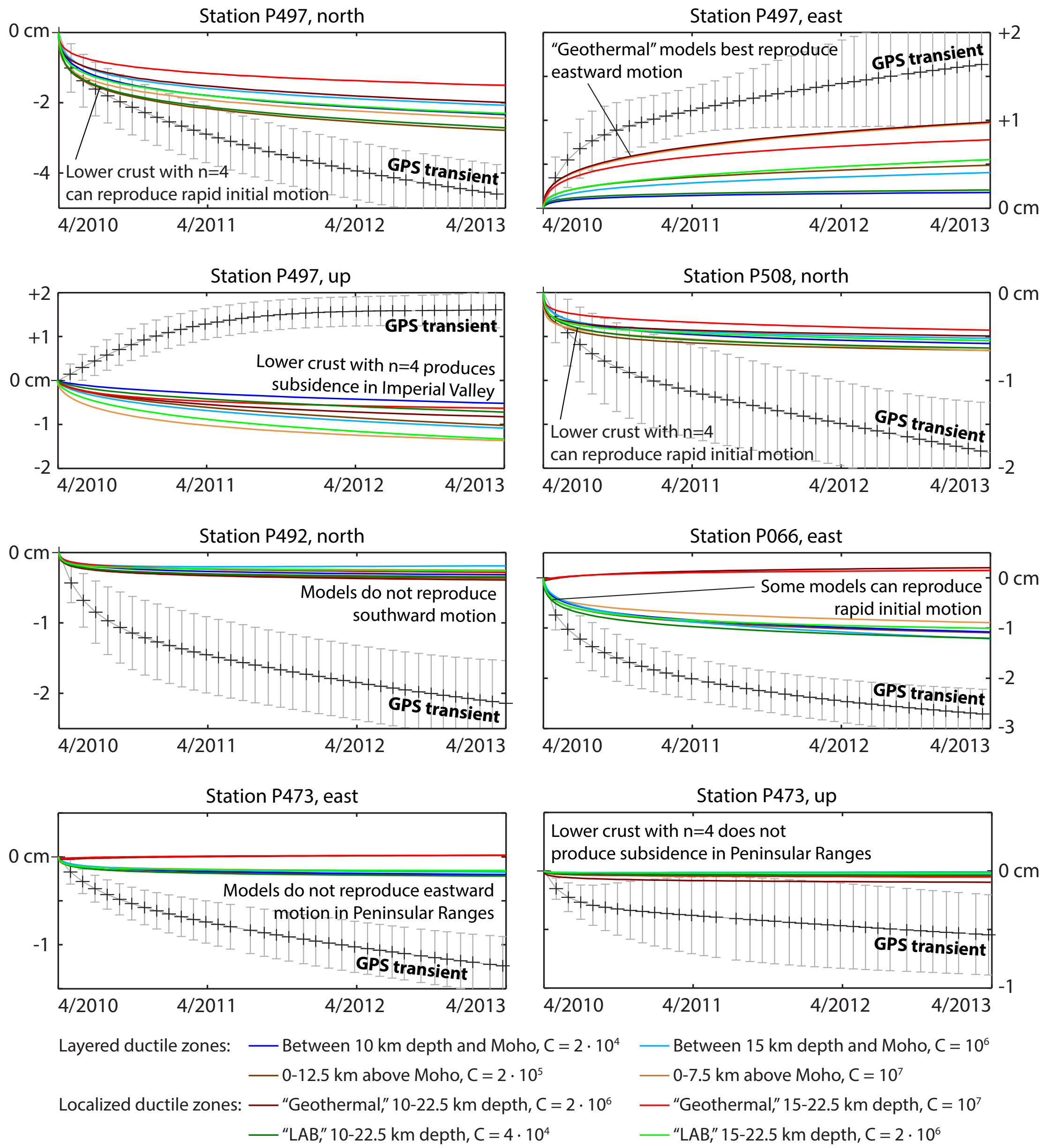

Figure 2.S14. Synthetic timeseries of surface displacement at several GPS stations (locations indicated in Figure 2.4a and 2.S10) generated by viscoelastic relaxation with a stress-dependent viscosity (n=4) in the modeled lower crustal ductile zones.

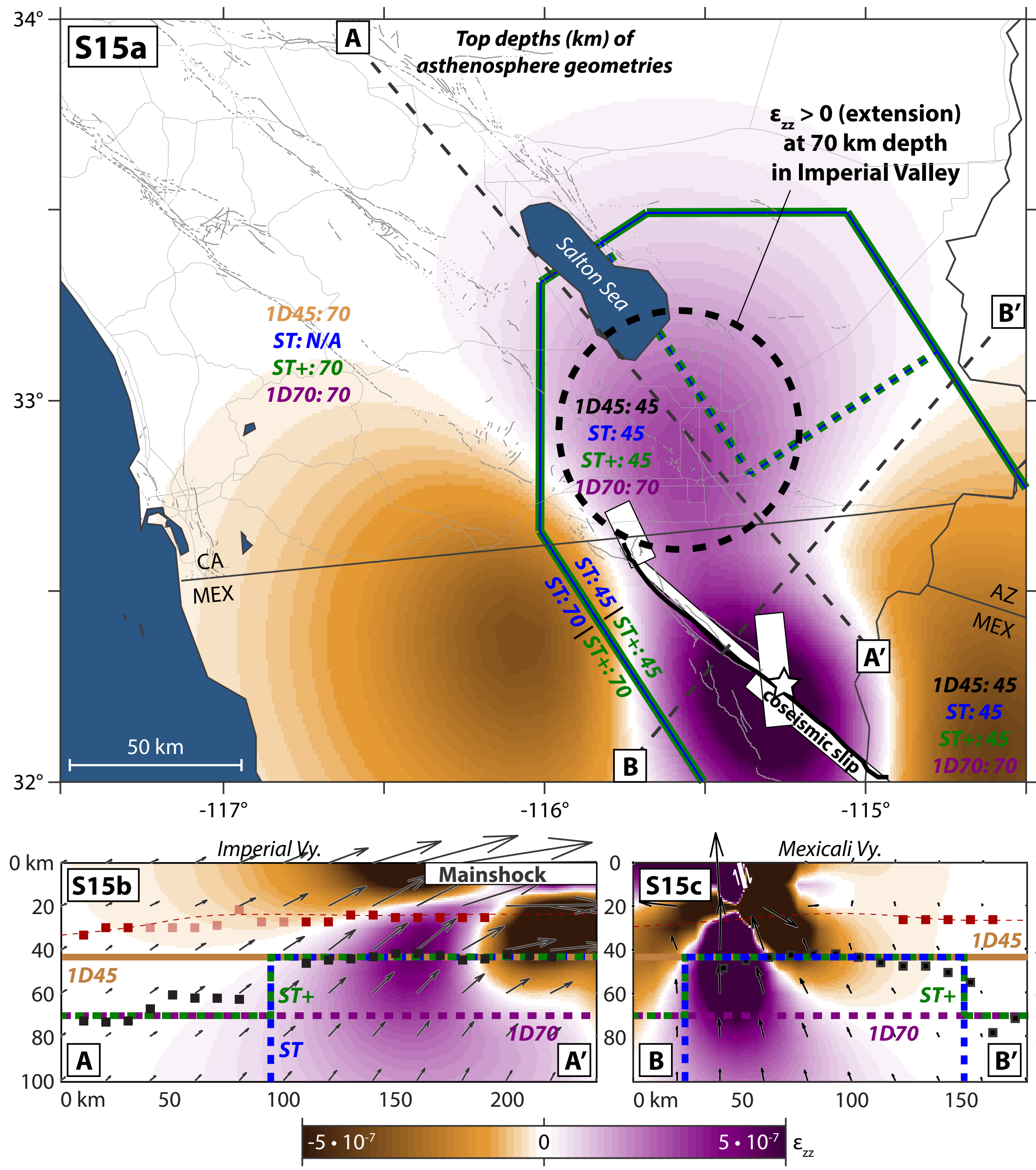

Figure 2.S15. Mapview and cross sections of vertical extension ε_{zz} imparted by the mainshock at 70 km depth, which is within the asthenosphere in all three model geometries we use. The mainshock imparted vertical extension at 70 km depth beneath the Imperial Valley and beneath the central part of the rupture.

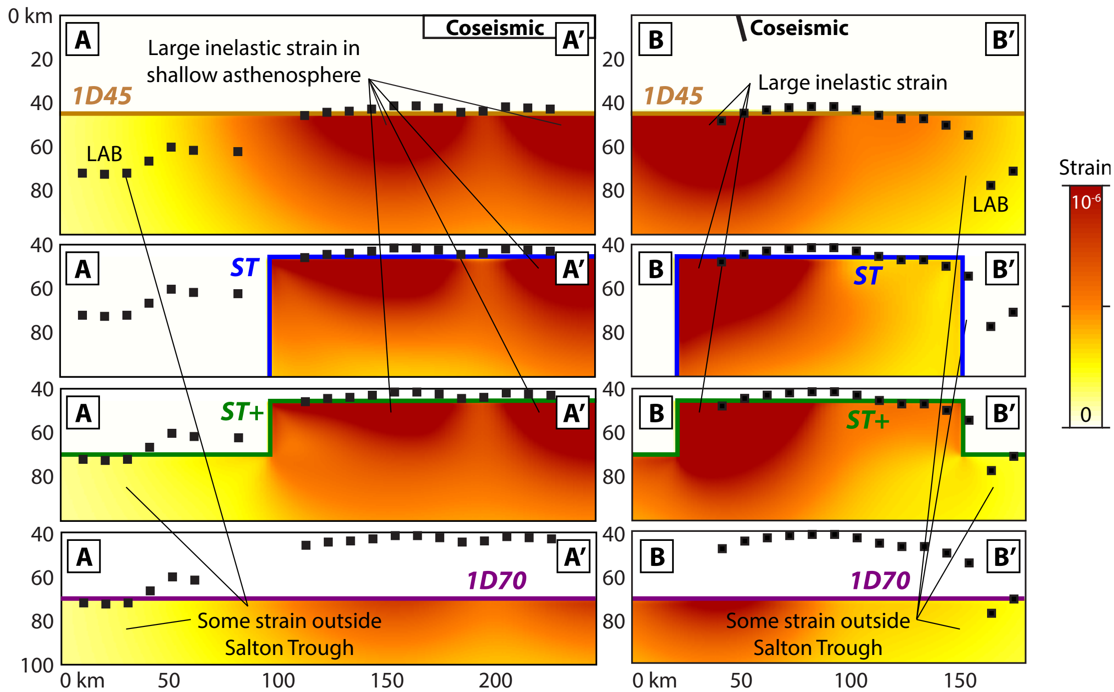

Figure 2.S16. Cross sections of cumulative inelastic (viscous) strain after three years of Newtonian viscoelastic relaxation in the four geometries for the asthenosphere show that although the major viscoelastic relaxation is concentrated close to the rupture, some inelastic strain does occur outside of the Salton Trough.

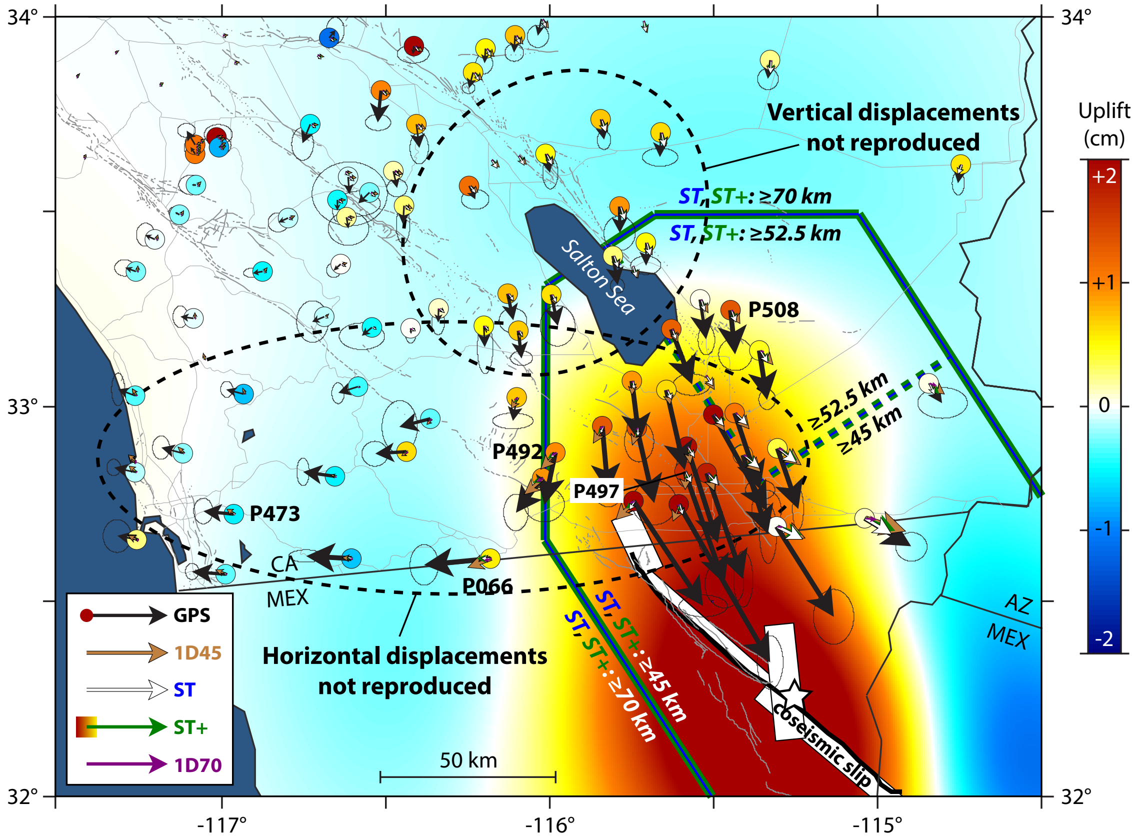

Figure 2.S17. Three-year cumulative surface displacements from viscoelastic relaxation with a stress-dependent viscosity (n=3.5) in the four modeled geometries for the asthenosphere. This mechanism can to some extent reproduce the uplift in the Imperial Valley but does not reproduce the amplitude of subsidence observed in the Peninsular Ranges or the horizontal displacements observed anywhere in southern California.

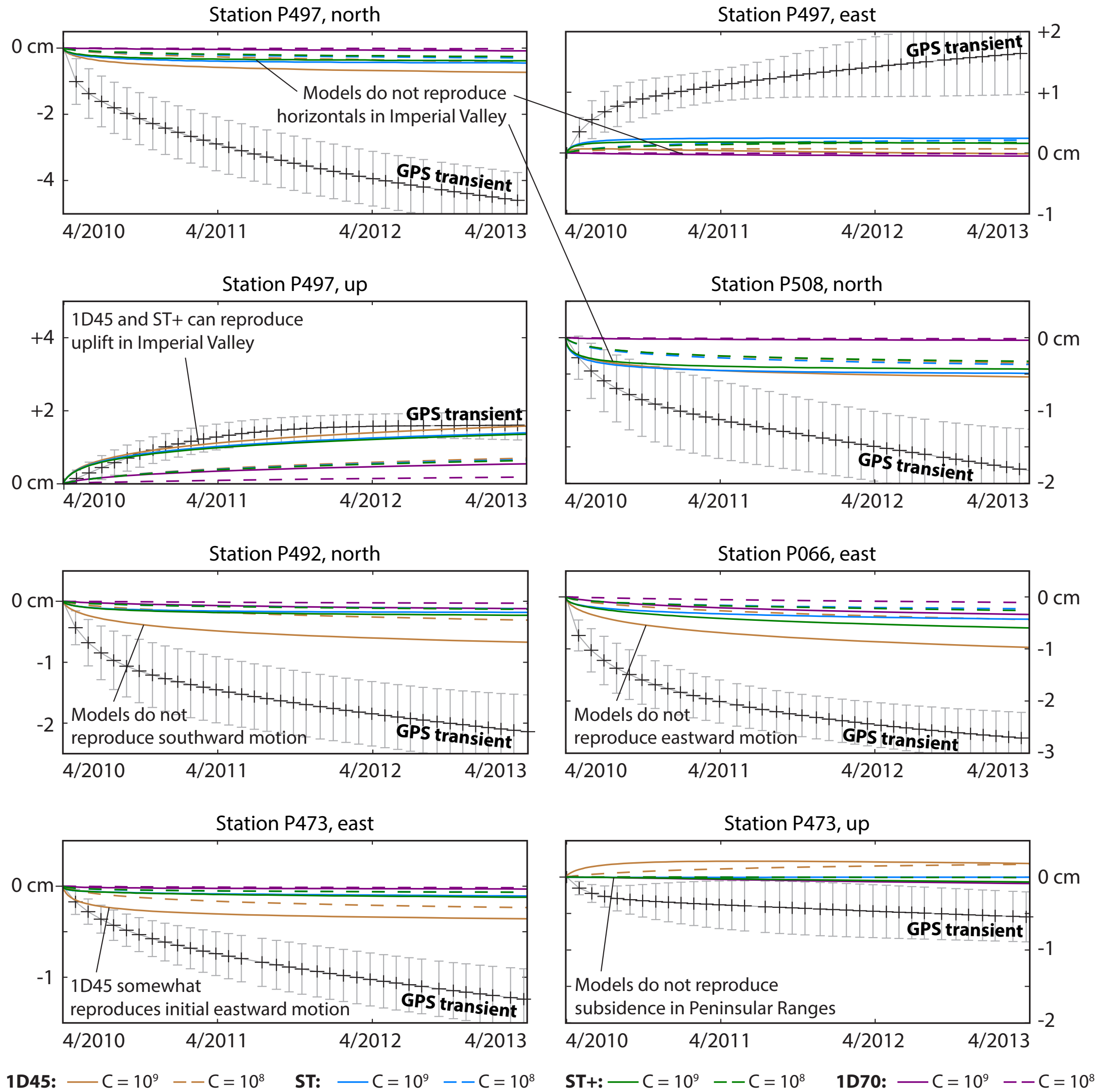

Figure 2.S18. Synthetic timeseries of surface displacement at several GPS stations (locations indicated in Figure 2.S17) generated by stress-dependent viscoelastic relaxation (n=3.5) in the modeled geometries for the asthenosphere. This mechanism can reproduce the uplift at station P497 in the Imperial Valley and possibly the rapid early eastward motion at station P473 but no other aspect of the transient.

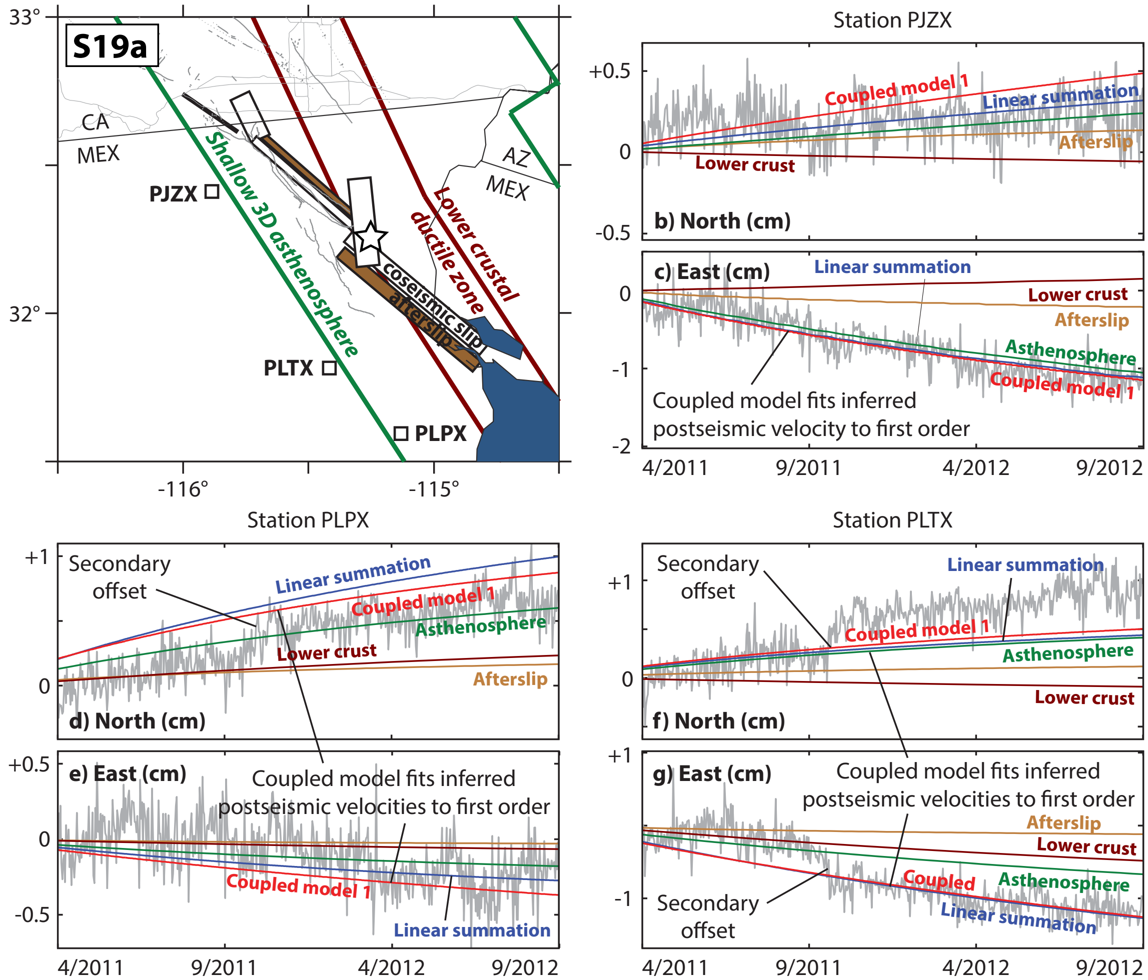

Figure 2.S19. a) Locations of stations PJZX, PLPX and PLTX in Mexico compared to the geometry of the first coupled model. **b-g)** Comparison of best-fit GPS timeseries at stations PJZX, PLPX and PLTX in Mexico with synthetic timeseries of surface displacement generated by the first coupled model.

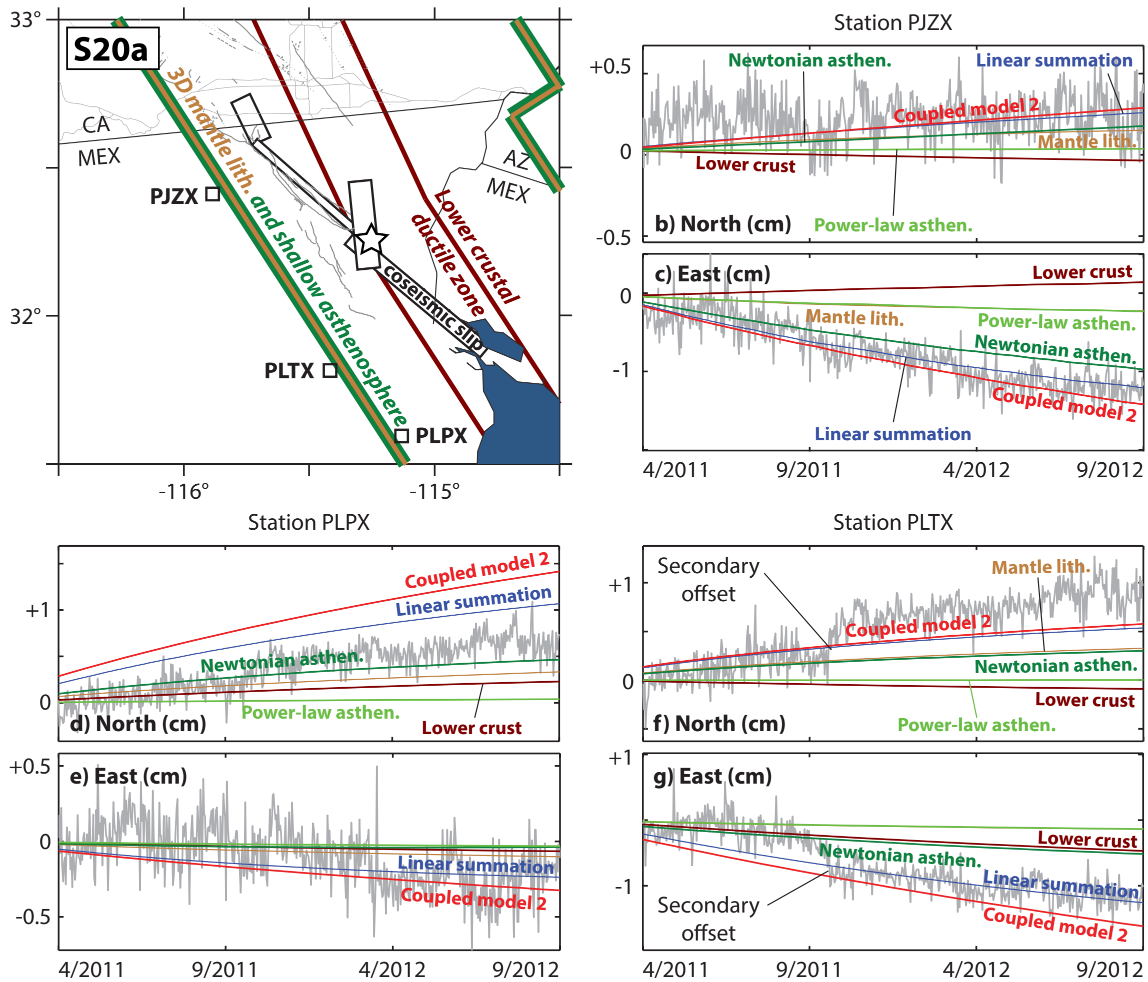

Figure 2.S20. a) Locations of stations PJZX, PLPX and PLTX in Mexico compared to the geometry of the second coupled model. **b-g)** Comparison of best-fit GPS timeseries at stations PJZX, PLPX and PLTX in Mexico with synthetic timeseries of surface displacement generated by the second coupled model.

Chapter 3

STRAIN ACCUMULATION ON FAULTS BENEATH LOS ANGELES

ABSTRACT

Geodetic data show that the Los Angeles area is contracting in the north-south direction at ~8.5 mm/yr. To characterize the seismic hazard due to this shortening, we assess how it is being accommodated by subsurface faults using detailed 3D models of fault geometry and heterogeneous elastic structure based on seismologic and geologic data. The sedimentary basin beneath Los Angeles has a substantial effect on the elastostatic Green's functions that map subsurface fault slip rates to surface motions and therefore on the estimation problem. We find that strain accumulation on major strike-slip faults beneath Los Angeles likely accounts for no more than ~2 mm/yr of north-south shortening across the Los Angeles area. Exploring a wide range of model assumptions, we formally invert the GPS data for the slip rates and distribution of strain accumulation on the three major thrust faults beneath the city, the Sierra Madre, Puente Hills and Compton thrust faults, as well as a north-dipping decollement. Preferred models feature the three faults each slipping at ~3-4 mm/yr over the long term and currently accruing interseismic strain mostly on their upper sections, with seismic moment deficit (which is presumably released in earthquakes) currently accruing at a total rate of 1.7 +1.2/-0.5 x 10^{17} Nm/yr. The estimated depth distribution of seismic moment deficit accumulation matches the depth distribution of seismicity in the LA basin to first order. Although coupling is inferred to decrease with depth on the faults, the models also correctly predict that seismicity rates should decrease upward in the upper few km because the Puente Hills and Compton faults are modeled as blind, with deformation updip of their tips (which would add 50% to the inferred moment deficit accumulation rate if counted) assumed to be a separate process.

3.1. Introduction

In California, the Pacific plate moves northwest at ~50 mm/yr relative to the North American plate [e.g. DeMets et al, 2010], generating horizontal shear strain across the plate boundary. The majority of this strain is accommodated by right-lateral slip on the San Andreas Fault and other northwest-striking faults [e.g. Ellsworth et al, 1990; Lisowski et al, 1991]. Near Los Angeles, however, the San Andreas makes a large leftward bend and is misaligned by ~20° with the relative plate motion direction for ~200 km (Figure 3.1, inset), resulting in an oblique plate collision with a component of north-south shortening at a high angle to the fault. Much of this shortening is accommodated by reverse slip on the north- and south-dipping thrust faults of the Transverse Ranges [e.g. Morton and Yerkes 1987; Donnellan et al, 1993; Marshall et al, 2013], including several that underlie the Los Angeles metropolitan area (Figure 3.1a) [e.g. Shaw et al, 2015]. Geodetic and geologic data suggest that Los Angeles proper is undergoing ~5-6 mm/yr of contraction in the north-south direction, ~8 mm/yr including islands offshore [e.g. Davis et al, 1989; Feigl et al, 1993; Shen et al, 1996; Walls et al, 1998; Argus et al, 1999; 2005], and geologic, seismologic and strain data confirm that this north-south shortening is the principal strain in the crust beneath the city [Zoback et al, 1987; Davis et al, 1989; Hauksson et al, 1990; Li et al, 1996; Yang and Hauksson, 2011, 2013]. The fastest contraction – and therefore perhaps the greatest seismic hazard – is ~50 km from the San Andreas in the northern Los Angeles basin, rather than in the San Gabriel Mountains despite their >3-km relief [Lisowski et al, 1991; Argus et al 1999, 2005] (Figure 3.1a, colored contours; Figure 3.2). This shortening produced the damaging 1971 M~6.7 San Fernando, 1987 M~5.9 Whittier Narrows and 1994 M~6.7 Northridge shocks (Figure 3.1) and poses a continued hazard to Los Angeles [e.g. Dolan et al, 1995; Field et al, 2005], and so it is essential to determine where, and how quickly, it is being accommodated by strain accumulation on subsurface faults.

Paleoseismologic studies suggest that this north-south shortening has produced large Holocene earthquakes on three north-dipping thrust faults beneath Los Angeles, the Sierra Madre, Puente Hills and Compton faults (from north to south). The Sierra Madre may have ruptured in two earthquakes since 15 Ka with magnitudes as high as M~7.5 [Rubin et al, 1998], the Puente Hills may have ruptured in three earthquakes since 8.1 Ka with magnitudes as high as M~7.2-7.4 [Dolan et al, 2003; Leon et al, 2007], and the Compton may have ruptured in six earthquakes since 14 Ka with magnitudes as high as M~7.0-7.4 [Leon et al, 2009]. Seismic reflection data, earthquake hypocenters and geologic constraints also suggest the presence of a decollement at depth beneath the San Gabriel

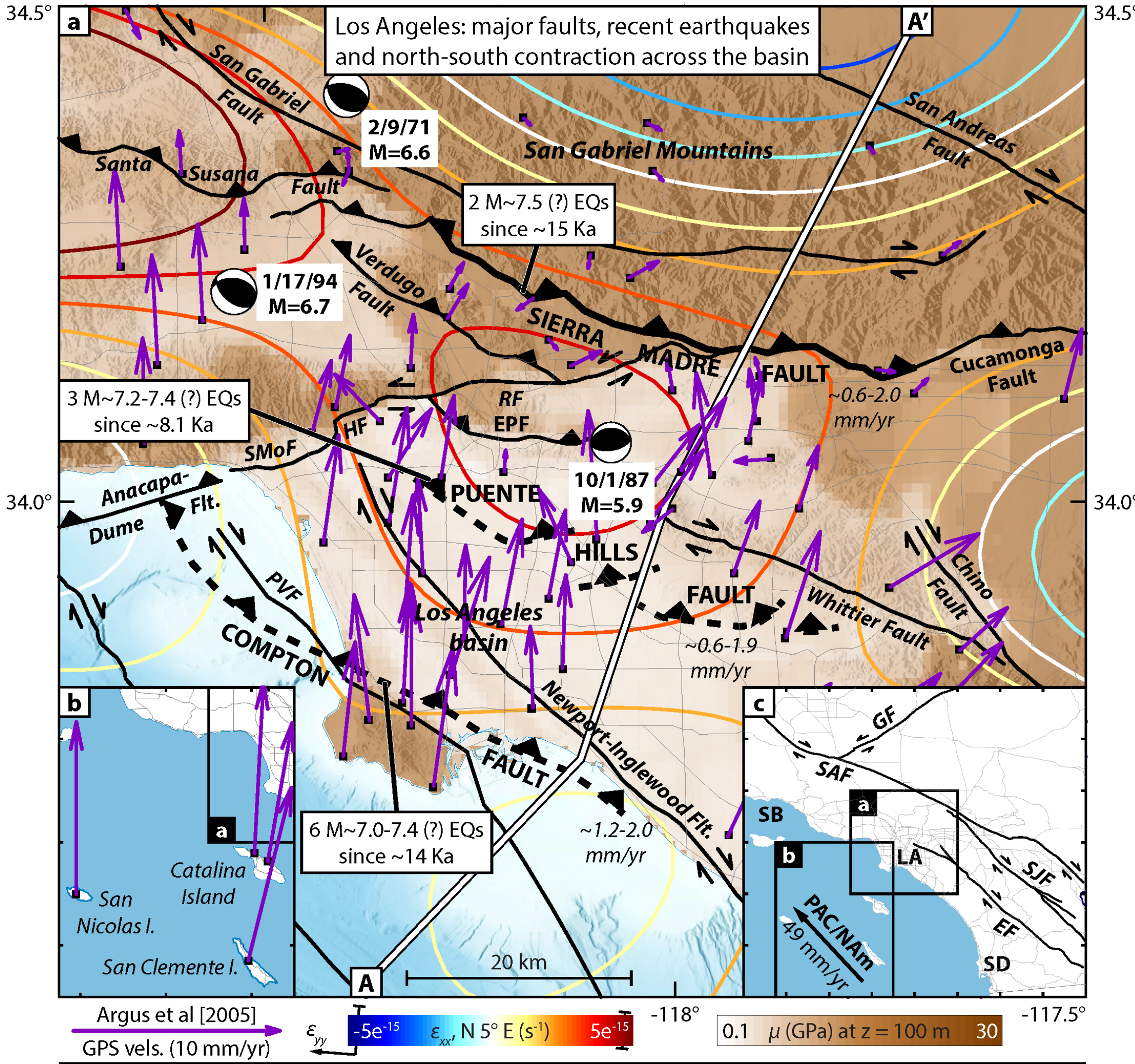

Figure 3.1. a) Major tectonic and geodetic features of the Los Angeles basin. Purple arrows are shortening-related GPS velocities relative to the San Gabriel Mountains [Argus et al, 2005]. Colored contours are uniaxial strain in the N ~5° E direction estimated from the GPS using the spherical-wavelet method of Tape et al [2009]. Background shading is the shear modulus μ at 100 m depth in the CVM* (described in the text). Thicker and thinner black lines are upper edges of thrust and strike-slip faults, respectively, dashed for blind faults. Epicenters of the 1971, 1987 and 1994 earthquakes are from SCEDC; focal mechanisms are from Heaton [1982] for 1971 and Global CMT Catalog for 1987 and 1994. Profile A-A' follows LARSE line 1 [Fuis et al, 2001] onshore and line M-M' of Sorlien et al [2013] offshore. Gray lines are highways. SMoF: Santa Monica Fault. HF: Hollywood Fault. RF: Raymond Fault. EPF: Elysian Park Fault. Estimated paleoearthquakes are from Rubin et al [1998], Leon et al [2007] and Leon et al [2009]. **b)** GPS velocities on islands. **c)** Regional tectonics. Black lines and pairs of half-arrows, respectively, are major faults and their slip directions. Black arrow is velocity of Pacific plate relative to North American plate from Kreemer et al [2014], courtesy of UNAVCO Plate Motion Calculator.

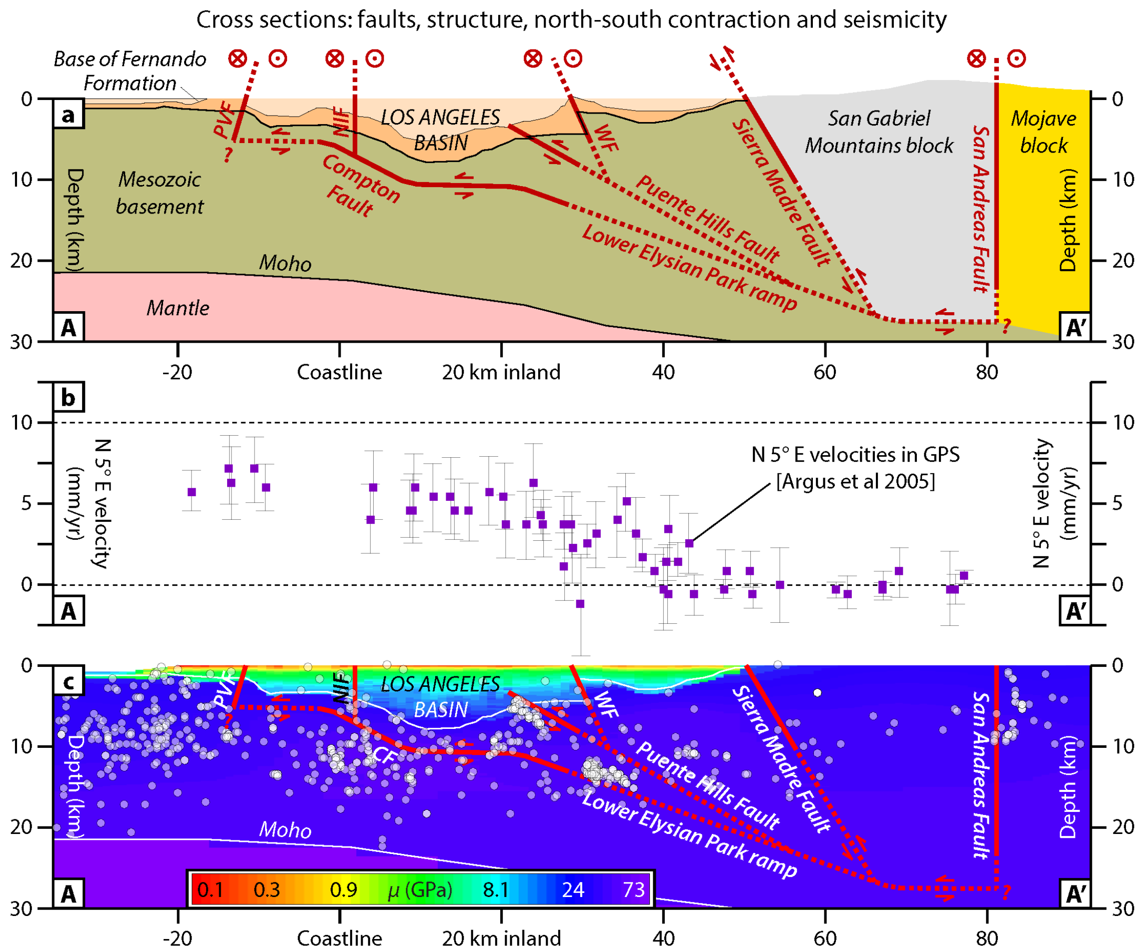

Figure 3.2. a) Cross sections of faults, structure, north-south contraction and seismicity along profile A-A'. Red lines are fault surfaces as meshed here (Figure 3.5), dashed where uncertain [Shaw and Suppe, 1996; Shaw and Shearer, 1999; Fuis et al, 2012]. Geometries of basin, basement and mantle are from Shaw et al [2015]; geometry of base of Fernando Formation is interpolated from Sorlien et al [2013] (offshore), Wright [1991] (coastline to Whittier Fault) and Yeats [2004] (Whittier Fault to Sierra Madre Fault); topography is from Fuis et al [2012]. **b)** Projections of Argus et al [2005] GPS velocities (relative to San Gabriel Mountains) onto the direction N 5° E and 1σ uncertainties. **c)** Seismotectonic features. Distribution of shear modulus is from the CVM*. Translucent white circles are relocated 1981-2016 M≥2 earthquakes whose epicenters lie within the mesh area of the three thrust faults and decollement [Hauksson et al, 2012 and updated].

Mountains, into which the Sierra Madre and Puente Hills faults may root [Hadley and Kanamori, 1978; Ryberg and Fuis, 1998; Fuis et al, 2001; Meigs et al, 2003; Myers et al, 2003]. This decollement may extend further southward [e.g. Davis et al, 1989; Humphreys and Hager, 1990; Wright, 1991; Sorlien et al, 2013] and connect to the Compton Fault via a ramp-flat-ramp geometry [Shaw and Suppe, 1996]. This would make the three faults a typical fold-and-thrust belt (Figure 3.2).

Several previous studies have used the geodetically observed shortening to build models of interseismic strain accumulation on these faults. Two discrepancies have emerged from this line of work. The first is that the slip rates on these faults inferred from structural geology and paleoseismology are generally around ~1-1.5 mm/yr [Walls et al, 1998; Tucker and Dolan, 2000; Shaw et al, 2002; Leon et al, 2007; Bergen et al, 2017; Shaw and Suppe, 1996; Leon et al, 2009], and it is difficult to reconcile ~8 mm/yr of total shortening with these comparably low slip rates. For example, Argus et al [2005] fit the geodetic shortening to a model of a north-dipping edge dislocation accumulating strain at 9 ± 2 mm/yr above 6 ± 2 km depth beneath northern Los Angeles, a slip rate nearly an order of magnitude faster than any geologic rates. Meade and Hager [2005] split the shortening between two north-dipping faults slipping at ~4 mm/yr each, still substantially higher than the geologic rates. Walls et al [1998] postulated that as much as half of the shortening could be taking place via escape tectonics on strike-slip faults near Los Angeles, chief among them the right-lateral Palos Verdes, Newport-Inglewood and Whittier faults [McNeilan and Rockwell, 1996; Hauksson, 1987; Gath et al, 1992] and the left-lateral Raymond-Hollywood-Santa Monica fault system [Weaver and Dolan, 2000; Dolan et al, 2000]. Argus et al [1999], however, found that this model far overpredicted the relative east-west surface velocities in Los Angeles. Although Hager et al [1999] invoked time-dependent postseismic relaxation to explain a similar (but opposite) rate discrepancy in the Ventura basin, Glasscoe et al [2004] showed that it was unlikely to explain the discrepancy in Los Angeles. More recently, Marshall et al [2009] and Daout et al [2016] fit the geodetic shortening to models of strain accumulation on thrust and strike-slip faults that featured slip rates within range of the geologic rates. The former model predicts a somewhat gentler contractional gradient than the GPS (and actually fits an unknown portion of it to the modeled truncation of the creeping Lower Elysian Park Fault beneath north-central Los Angeles), and the latter model fits only the northern portion of the shortening projected onto the San Andreas-perpendicular direction rather than the north-south direction. Nevertheless, these models suggest that the total shortening rate and geologic slip rates may be reconcilable by invoking moderately detailed pictures of strain accumulation.

The second discrepancy, however, is that the fault locking depths (above which the faults are modeled as fully locked and below which they are freely slipping) are respectively 6 ± 2, 8 and 3 km in the Argus et al [2005], Marshall et al [2009] and Daout et al [2016] models. If the creeping-to-locked transition indicates a change in fault rheology (e.g. that ductile processes take over below it), one would expect no seismicity below the locking depth; however, the 95th-percentile depth of seismicity in the Los Angeles basin in the Hauksson et al [2012] relocated catalog is 15.47 km. The source of this discrepancy may lie in the elastic structure: although most published studies of strain accumulation in Los Angeles model the earth as an elastic halfspace, Los Angeles sits atop a deep sedimentary basin [e.g. Shaw et al, 2015] that may significantly affect the relationship between subsurface strain accumulation and surface deformation. In particular, previous studies have shown that if a fault lies below a low-stiffness near-surface layer, an analysis using a uniform elastic model will erroneously infer the fault as being shallower than it actually is [Arnadottir and Segall, 1991; Bernard et al, 1997; Cattin et al, 1999].

In this study, we use high-quality geodetic data at the surface, detailed 3D models of faults and subsurface structure, and a suite of kinematic inversion techniques to characterize strain accumulation on major faults underlying Los Angeles. We examine how the rapid north-south contraction rate might be reconciled with the low inferred geologic slip rates, whether the modeling of the sedimentary basin may partially reconcile the inferred locking depths with the distribution of seismicity, and whether the strike-slip faults may contribute to the observed shortening.

3.2. The geodetic shortening

The gradual motion at the surface in Los Angeles results not only from local tectonic shortening but also from 1) deformation due to management of aquifers and oil fields [e.g. Bawden et al, 2001] and 2) strain accumulation on the San Andreas system [e.g. Argus et al, 1999]. Argus et al [2005] prepared a field of GPS velocities relative to the San Gabriel Mountains in which they corrected for these effects by modeling each of them and subtracting the model-predicted velocities from an uncorrected field. This dataset is thus appropriate for estimating the pattern of local strain accumulation and we use it here (Figure 3.1, purple arrows), as previously done by Argus et al [2005] and by Marshall et al [2009].

Strain accumulation on the San Andreas system is the dominant geodetic signal in Southern California [e.g. Meade and Hager 2005], and so it might be thought that the inferred velocity field in Los Angeles may depend on the way that the San Andreas is modeled. Dislocation modeling, however, shows that the two are largely independent (Figure 3.3): the basin is outside the reach of most of the velocity perturbation from strain

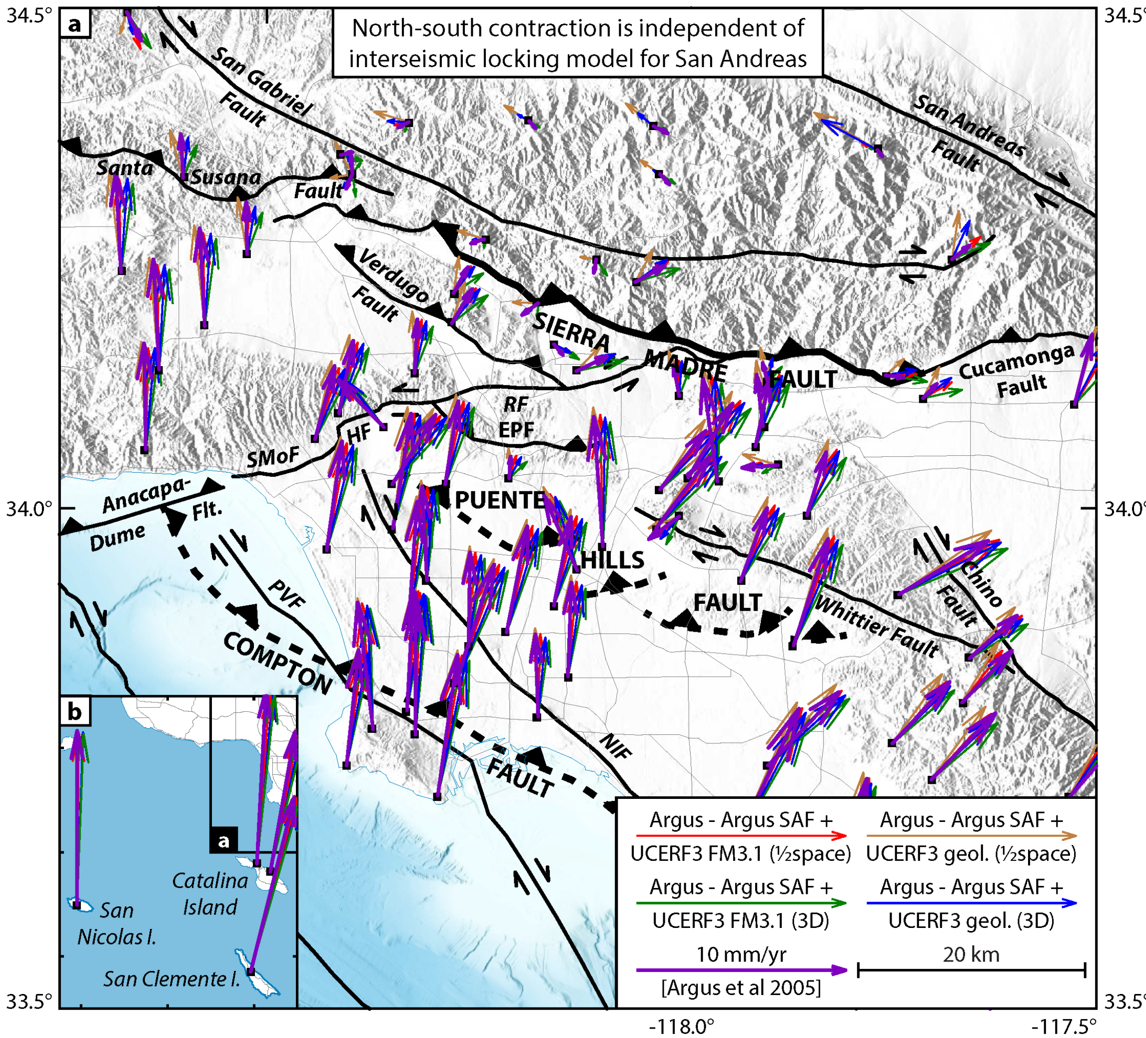

Figure 3.3. The inferred shortening across the Los Angeles basin depends only weakly on the assumed interseismic locking model for the San Andreas Fault. Purple arrows are Argus et al [2005] velocities. The four other sets of arrows are Argus et al [2005] velocities, minus velocities calculated from the Argus et al [2005] model of interseismic locking on the San Andreas (which used an elastic halfspace model), plus velocities calculated from four alternate models of backslip (interseismic locking) prescribed down to the UCERF3 locking depths [Field et al, 2014]. Red arrows use the UCERF3 "FM3.1" slip rates for the San Andreas system in an elastic halfspace model. Tan arrows use the UCERF3 consensus "geologic" rates in an elastic halfspace model. Green arrows use the "FM3.1" slip rates in the heterogeneous material model described in the text. Blue arrows use the "geologic" rates in the heterogeneous material model. The inferred shortening rate is minimally dependent on the model used and the inferred azimuth varies by only a few degrees between models. Note that the use of the "geologic" rates implies shear of several mm/yr across the San Gabriel Mountains, while Argus et al infer no such shear, consistent with inferred inactivity of the San Gabriel Fault in this region [e.g. Powell, 1993].

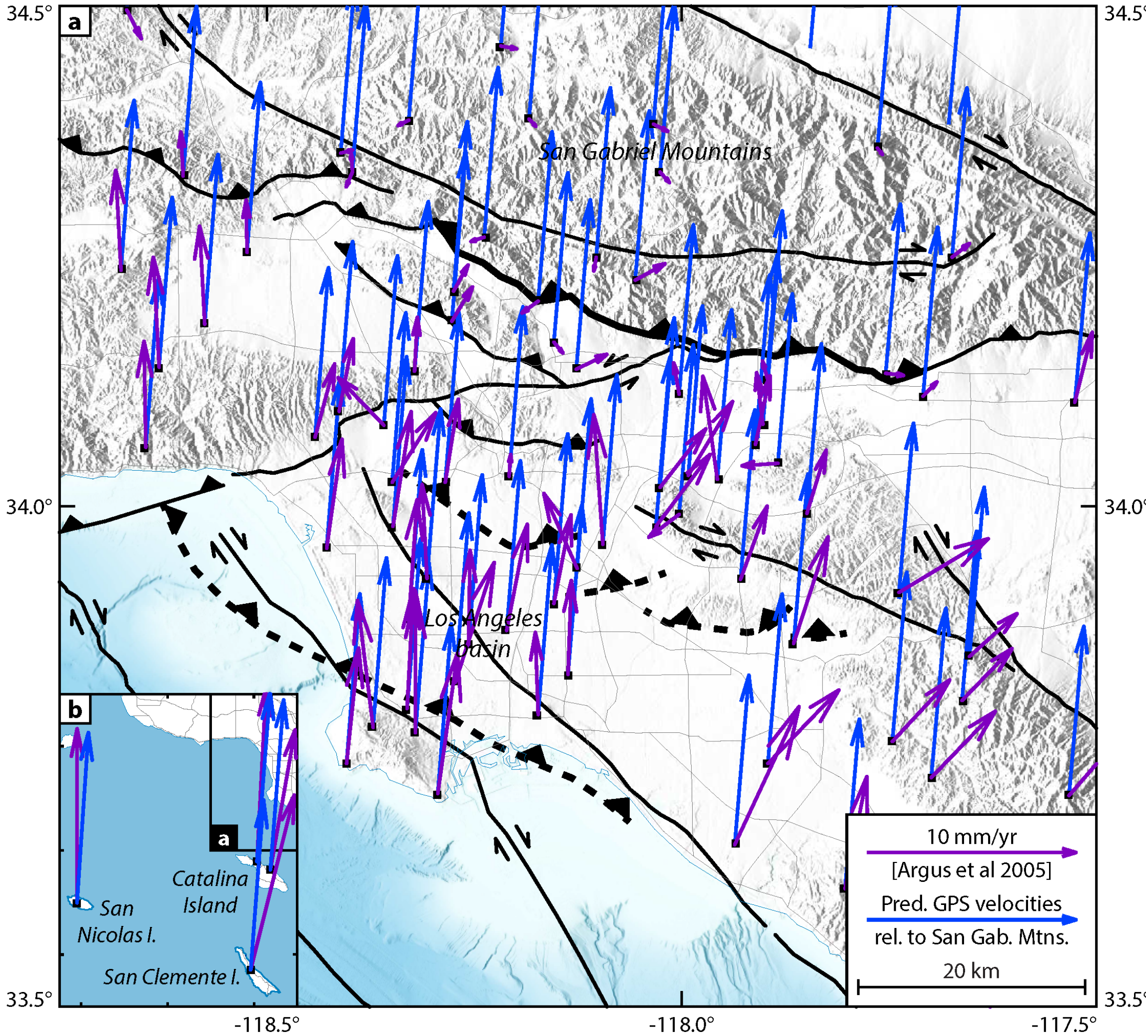

Figure 3.4. Kinematic model of long-term convergence across the Los Angeles basin as rotation about an Euler pole describing the motion of Catalina, San Nicolas and San Clemente Islands relative to the San Gabriel Mountains. **a)** Mapview of predicted velocities at on-land GPS stations. This velocity field dictates the slip directions on faults and is used to determine their long-term slip rates. **b)** Observed GPS velocities on islands used to calculate the Euler pole.

accumulation on the fault, and the inferred shortening is thus likely robust. This is consistent with the aforementioned studies that suggest that north-south contraction is the principal strain in Los Angeles, and not merely a minor component of a more complex stress field. Other details of data preparation can be found in Appendix 3.1.

The shortening can be approximated as the sum of plate-scale convergence plus local-scale strain accumulation that resists that convergence. (The actual plate-scale relative motion in Los Angeles is oblique right-lateral convergence, but as the preceding discussion suggests, the convergence component is locally both more important than and mostly independent of the right-lateral component.) We characterize the plate-scale convergence with respect to the San Gabriel Mountains by fitting Argus et al [2005] GPS velocities on offshore islands to a model of global rotation about an Euler pole in a least-squares sense. The pole is located at 1.42° S, 141.36° E, and the predicted plate-scale term in Los Angeles is a steady velocity field at N 4.74 +/- 0.23° E at 8.5 mm/yr (Figure 3.4), consistent with the shortening rates and azimuths inferred from geodesy, seismology and other sources [e.g. Zoback et al, 1987; Li et al, 1996; Argus et al, 1999, 2005]. The Argus et al [2005] velocity field (Figure 3.1a) shows that as one moves northward across Los Angeles, the convergence velocity relative to the San Gabriel Mountains gradually decreases from the plate-scale rate to zero due to subsurface strain accumulation. In the subsequent inversions for strain accumulation, we enforce that slip on the faults occurs in the plate-scale convergence direction.

In addition, the method of Kostrov [1974] can be used to estimate the rate of accumulation of seismic moment deficit across Los Angeles without accounting for fault geometry, subsurface structure or details of the shortening pattern. As recounted by Meade and Hager [2005], the total moment accumulation rate in this method is estimated as $2\mu\alpha H\varepsilon$, where μ is the shear modulus, α is the deforming area, H is the seismogenic thickness and ε is the regional strain rate. The inferred shortening rate is ~8.5 mm/yr between offshore islands and the San Gabriel Mountains ~100 km away, corresponding to an estimated shortening-related strain rate of 85 nanostrain/yr. Assuming that the relevant deforming area is 50 km in width, using the 95th-percentile depth of seismicity in the Los Angeles basin in the Hauksson et al [2012] catalog (15.47 km) as the seismogenic thickness and assuming a shear modulus of 30 GPa, we calculate a moment accumulation rate of 3.9 x 10^{17} Nm/yr. We refine this estimate in the following sections to incorporate the complex fault geometries, the elastic heterogeneity of the subsurface, and the possibility that a fraction of the strain is anelastic.

3.3. Faults and elastic structure, elastostatic Green's functions, and some inferences

3.3.1. Models of faults and elastic structure

Details of fault geometry can affect estimation problems using geodetic data [e.g. Marshall and Morris, 2012], and so it is important to use the most accurate fault representations possible in this setting. The Community Fault Model, version 5 (CFM5), a component of the Unified Structural Representation [Shaw et al 2015], provides detailed

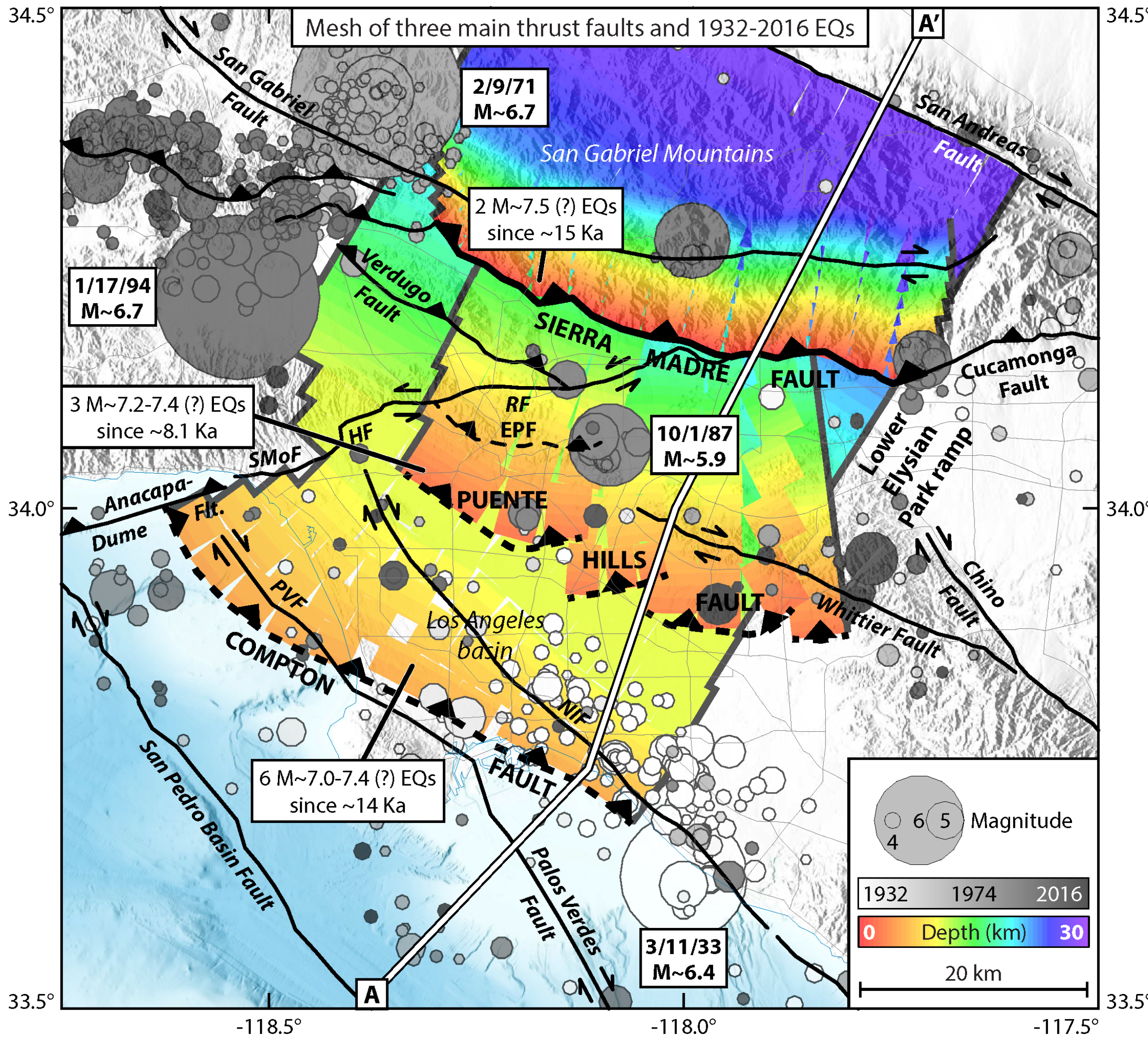

Figure 3.5. Meshed geometries of the three main thrust faults beneath the Los Angeles basin, colored by depth, and relocated M≥3.5 earthquakes, 1932-2016, scaled by magnitude and shaded grayscale by year. 1932-1980 locations are from SCEDC catalog; 1971 San Fernando earthquake hypocentral depth and magnitude are from Heaton [1982]); 1981-2016 locations are from Hauksson et al [2012 and updated].

3D geometries for dozens of faults in the Los Angeles region. Marshall et al [2009] remeshed a previous version of the CFM for use in dislocation modeling and have updated their mesh to reflect the CFM5 [S. Marshall, personal communication, 2016] (Figure 3.S1). Working from the updated Marshall mesh and in some cases the raw CFM5, we build a detailed 3D mesh in which the Sierra Madre, Puente Hills and Compton faults root into a decollement structure that is based on the Lower Elysian Park ramp (Figure 3.2), thus forming a fully connected fold-and-thrust belt as suggested by Davis et al [1989]. While the Sierra Madre Fault breaks the surface at the southern edge of the San Gabriel Mountains,

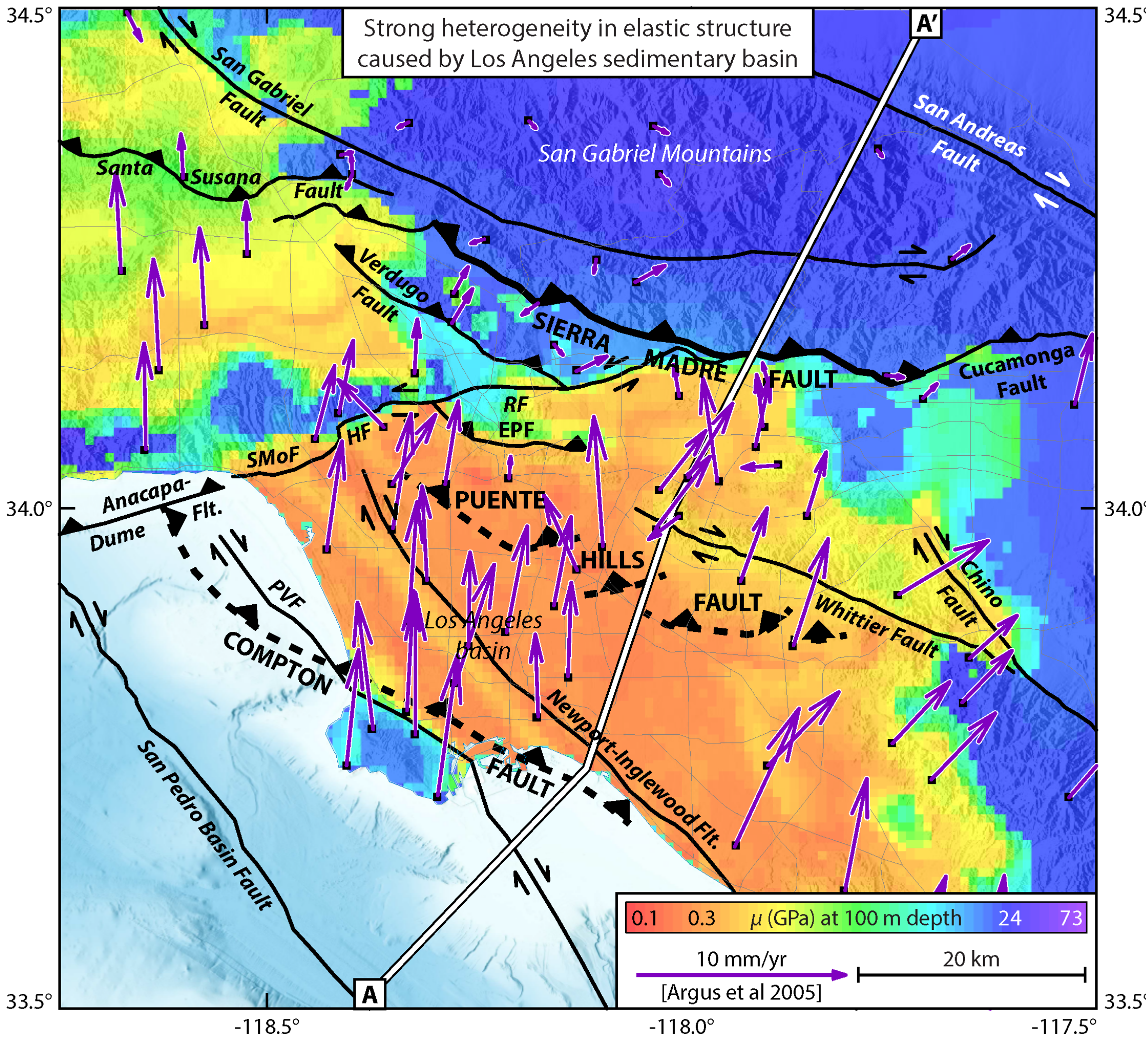

Figure 3.6. Lateral distribution of μ at 100 m depth in the CVM* (logarithmic color scale).

the Puente Hills and Compton are blind thrust faults, with top edges respectively at ~3 and ~5 km depth (Figure 3.5); this requires some additional modeling considerations as described in Appendix 3.4. We also mesh the major strike-slip faults in the Los Angeles area and use them subsequently in separate models. Details of the meshing are provided in Appendix 3.2.

The CFM5 is accompanied in the Unified Structural Representation by the Community Velocity Model-Harvard 15.1 (CVM-H15.1), a detailed model of subsurface structure of Southern California that includes sedimentary basins and other material contrasts such as the Moho and ocean floor. The CVM-H15.1 provides estimates of compressional wave speed V_p, shear wave speed V_s, and density ρ at 100 m resolution in the vertical direction and 1 km resolution in the horizontal direction in the top 15 km of the southern California crust, and at 1 km vertical and 10 km horizontal resolution between 15 and 200 km depth (Figure 3.S2). For the computation of elastostatic Green's functions, we convert the V_p, V_s, and ρ provided by the CVM-H15.1 to the Lame parameters λ and μ using the classical seismic wave equations, $V_p = ((\lambda + 2\mu)/\rho)^{1/2}$ and $V_s = (\mu/\rho)^{1/2}$, yielding a detailed model of elastic heterogeneity that we hereafter call the CVM* (Figure 3.1a, shaded background, and Figure 3.6). (Although the material properties of the subsurface are controlled by a wide range of factors, previous studies have shown that the effect of elastic heterogeneity on elastostatic Green's functions is dominantly a function of variations in the shear modulus [Masterlark, 2003]; therefore this λ-μ representation is likely adequate for our purposes.) The contrast in V_s between the Los Angeles basin and the surrounding crust is roughly an order of magnitude at the surface (Figure 3.S2), translating into a contrast of two orders of magnitude in μ (Figure 3.6). Details of the CVM* are provided in Appendix 3.3.

We use GAMRA, an adaptive-meshing finite-difference dislocation modeling method [Landry and Barbot, 2016], to compute elastostatic Green's functions that map displacements on the patches of the quadrilateral fault mesh through the material heterogeneity of the CVM* to displacements at GPS stations at the surface. The computation requires some minor modifications to the CVM* that are described in Appendix 3.3. The adaptive-meshing nature of GAMRA allows us to compute elastostatic Green's functions at 100 m vertical resolution in the basins, the same resolution as the information provided by the CVM-H15.1, without requiring this resolution elsewhere in the computations.

3.3.2. Elastostatic Green's functions incorporating the sedimentary basin

Comparison of slip models run in an elastic halfspace model with those run in the CVM* reveals that the Los Angeles basin amplifies surface displacements from slip on faults underlying it by up to 50% (Figure 3.7, 3.S7, 3.S8c). The effect is the opposite for slip on a fault that lies within the basin rather than underlies it: the basin cannot sustain the displacement field as effectively as crustal rock and so the displacement field falls off closer to the fault (Figure 3.S5, 3.S8a, 3.S9-S13). We note also, as discussed by Marshall et al [2009], that slip on the Sierra Madre Fault produces far larger horizontal displacements in the footwall than in the hanging wall due to the fault's steep (~55°) dip (Figure 3.S6 and 3.S8b), suggesting that the fast contraction observed in geodetic data between the Puente Hills and Sierra Madre faults could be interpreted as resulting from strain accumulation on

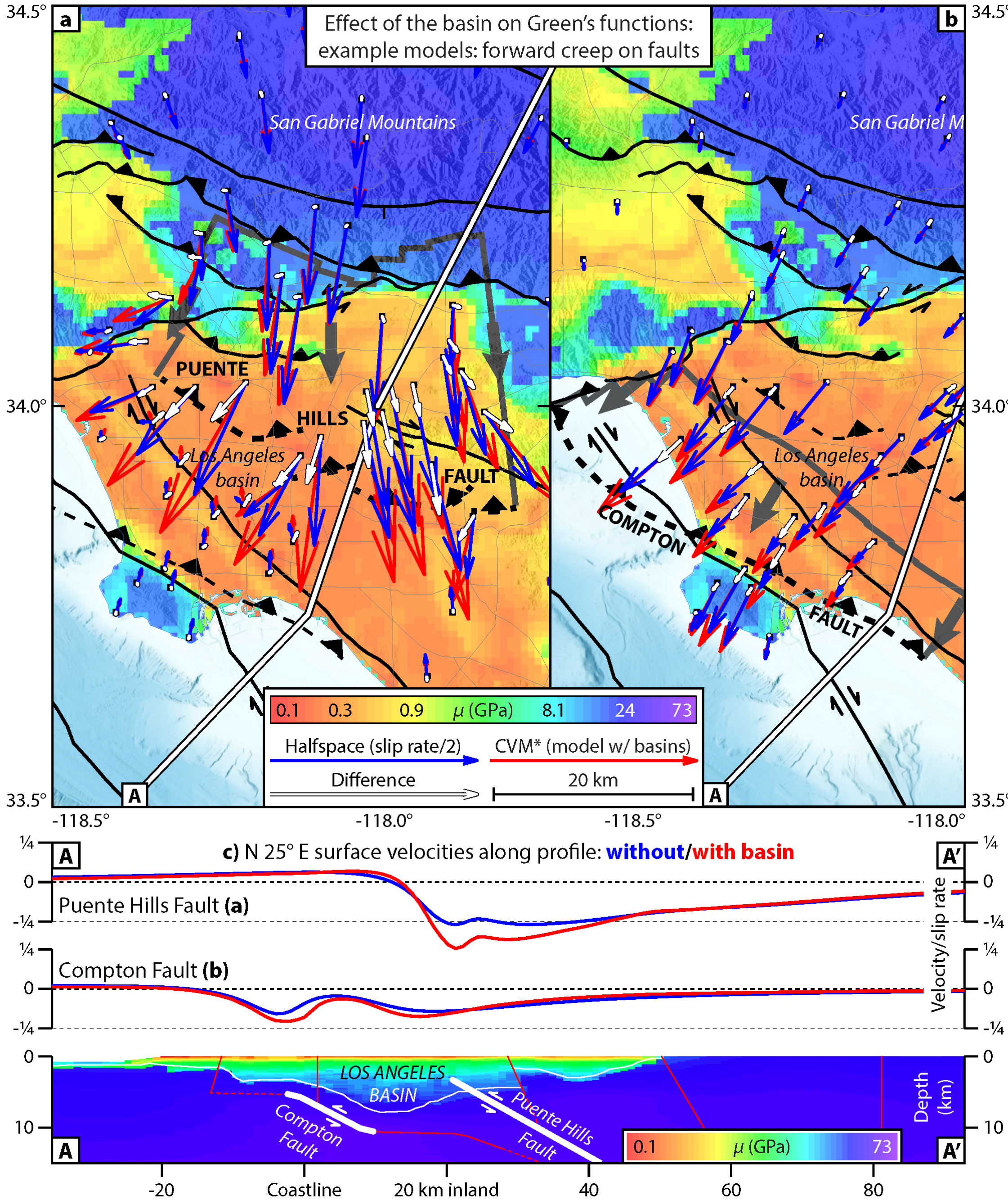

Figure 3.7. The Los Angeles basin amplifies surface displacements for slip on the Puente Hills **(a)** and Compton **(b)** faults, as shown here with forward models of uniform slip on each fault. Blue arrows are resulting surface velocities at Argus et al [2005] GPS stations calculated in an elastic halfspace model. Red arrows are surface velocities calculated using the CVM*. White arrows are the difference between the two sets of synthetic velocities. Background colormap is the distribution of μ at 100 m depth in the CVM*. Fault meshes are outlined in gray. **c)** Synthetic velocities projected into the N 25° E direction along profile A-A', colored as above.

either fault or on both. Slip on the Elysian Park Fault imparts only a small elastostatic perturbation at the surface (basin or no basin) due to its small size and shallow position (Figure 3.S9). We infer that the larger Compton, Puente Hills and Sierra Madre faults are therefore more likely to contribute to the observed shortening across Los Angeles.

3.3.3. Potential contribution of strike-slip faults to north-south contraction

We also compute elastostatic Green's functions for slip on the major strike-slip faults in and around the Los Angeles basin (Figures 3.S10-13) in order to assess how much the interseismic velocity field could be affected by strain accumulation on them. To place an upper bound on this effect, we generate a "liberal" model in which all of the strike-slip faults are prescribed to slip at their UCERF3 consensus "geologic" slip rates between locking depths of ~5 km (the shallowest depth that we can model here without having them creep at the surface, owing to the ~5-km fault patch size) and a maximum depth of 75 km (the approximate depth to the lithosphere-asthenosphere boundary in Los Angeles [Lekic et al, 2011]). This model produces a ~1.8 mm/yr north-south contractional gradient across the Los Angeles basin with comparatively low velocities in the east-west direction, as the east-west components of the various faults' displacement fields sum to near zero in the basin (Figure 3.S14). Models in which the faults are creeping all the way to the surface or extend to infinite depth produce 2.1 mm/yr of shortening. Thus, as proposed by Walls et al [1998], Bawden et al [2001] and Marshall et al [2009], we find that a portion of the north-south contractional gradient observed in GPS may be related to strike-slip faulting. However, 1) the total contraction, even in this liberal model, is less than a quarter of the ~8.5 mm/yr observed; and 2) the fastest contraction is around the Palos Verdes fault rather than in the northern Los Angeles basin, which is inconsistent with the GPS data (Figure 3.1a). We thus turn to the thrust faults, which may accommodate a larger portion of the contractional gradient.

3.4. Kinematic inversions for strain accumulation on thrust faults

3.4.1. Overall scheme and misfit statistic

We invert the Argus et al [2005] velocities at 54 stations overlying the Sierra Madre, Puente Hills and Compton faults for the pattern of strain accumulation on these thrust faults using the backslip framework [Savage 1983]. This framework expresses the pattern of interseismic creep on a thrust fault as the sum of uniform reverse creep at the fault's long-term slip rate plus backward creep (normal slip, or backslip) on the sections accumulating strain, with the rate of backward creep expressing how rapidly they are doing so. We extend this to the three thrust faults, with the model parameters being the three long-term slip rates and the pattern of backslip throughout the system. Generally, we seek to find the model **m*** that minimizes the quantity $||(\mathbf{d} - \mathbf{Gm})/\boldsymbol{\sigma}||_2$ subject to some regularization [e.g. Aster, 2012]. Here **d** is the vector of the east and north components of GPS velocities and **σ** is the vector of their one-sigma uncertainties, whose computation is described in Appendix 1. The matrix **G** consists of the three "steady-state" forward terms from the backslip method (one for each fault); the elastostatic Green's functions for backslip (normal slip) on the subdivided patches of the fault mesh (computed within the CVM*); and finally a vector of each station's predicted velocity from the plate-scale motion term (Figure 3.4), which allows for rigid-body motion of the entire network about the previously computed Euler pole. In all inversions, we enforce that slip on the faults is in the N ~5° E convergence direction, so the columns of **G** are the Green's functions from a mixture of dip slip and strike slip depending on the orientations of the patches forming the fault mesh. Note that this means that the output slip rates on the faults are also slip rates in the convergence direction.

We quantify each model's fit to the data using the weighted root-mean square error,

$$X^2/N = ((\mathbf{d} - \mathbf{Gm})/\boldsymbol{\sigma})^2/N, \qquad [3.1]$$

where N is the length of the data vector. This quantity is similar to the reduced chi-squared but does not subtract the number of model parameters from N as this number is meaningless for regularized models [Chlieh et al, 2011]. (Note that the X^2/N values of many of the subsequent inversions are smaller than 1, showing that on average the models match the observations within uncertainties. A X^2/N value of ~0.5, as we obtain with our best models, corresponds to a mean misfit of about 0.8 mm/yr on each velocity component at each station overlying the mesh.) The Argus et al [2005] uncertainties may be conservatively large as they include each station's absolute velocity uncertainty in a global reference frame.)

The output backslip rates on the fault patches can be used to derive two other quantities that are of use. The first is the interseismic coupling, defined as a patch's backslip rate divided by the fault's long-term slip rate and describing the extent to which the patch is creeping (coupling = 0) or stuck at present day (coupling = 1). Secondly, we can derive the rate of accumulation of seismic moment deficit on each fault patch. This is taken to be the backslip rate multiplied by the patch's area and by the interpolated value of the shear modulus μ at the patch center from the CVM* (Figure 3.S3). The total rate of seismic moment deficit accumulation in a given strain accumulation model is then the sum of these rates on the patches.

3.4.2. The "blocks" formulation, the modeling of blind faults, and the "wings" vs. "no-wings" boundary condition

There are two additional factors to consider that affect the composition of **G**. The first is whether the steady-state forward term for each fault, which is a guess of how the fault offsets material over geologic time, should describe 1) block motion between a rigid hanging wall and rigid footwall or 2) uniform forward creep along the fault. We refer to these respectively as the "blocks" and "sheets" formulations. We begin with the "blocks" formulation, which assumes that the faults offset rigid blocks that, relative to the San Gabriel Mountains, are all rotating about the Euler pole used to model the plate-scale convergence term and are doing so at fractions of the plate-scale convergence velocity. The forward term in **G** for each fault is then a spatial Heaviside function in the predicted plate-scale convergence velocity field (Figure 3.4) representing the long-term velocity discontinuity at the fault's surface break [e.g. Matsuura et al 1986, Ader et al, 2012] due to the long-term block motion across it. This can be translated into the fault's inferred long-term slip rate.

Modeling the long-term motion as steps in the convergence rate across the faults' surface breaks encounters complications on the Puente Hills and Compton faults as they do not break the surface. The deformation between the upper edges of these faults and their projected surface breaks must be explicitly modeled in the "blocks" formulation (otherwise it is implicitly modeled as free slip). As described in Appendix 3.4, we model this deformation as complete coupling (backslip at the fault's long-term slip rate) on the updip projections of these faults (done by adding the Green's functions from slip on these updip projections to the step function at the surface break) and then do not count this coupling in the estimates of strain accumulation. This implicitly assumes that the deformation updip of the upper edges is completely elastic. In reality, these parts of the subsurface deform anelastically over geologic time due to fault-tip folding [e.g. Allmendinger and Shaw 2000]. However, this folding may predominantly occur during earthquakes rather than interseismically, as is assumed in paleoseismologic studies of these faults [e.g. Dolan et al 2003; Leon et al 2009], and therefore it may be justifiable to treat the interseismic deformation of these updip regions as elastic (and essentially as minimal, driven only by external sources of strain, as done here).

The second factor that affects the elements of **G** is whether the model should account for strain accumulation on faults east and west of the Los Angeles basin. If the interseismic velocity field in Los Angeles resulted only from strain accumulation on the Sierra Madre, Puente Hills and Compton faults, one might expect it to show toroidal motion on the sides of the basin, as seen in the models of uniform forward slip on the faults (Figure 3.7, Figure 3.S7). Instead, the Argus et al [2005] velocities on the edges of the basin do not deviate greatly from the N ~5° E convergence direction, suggesting that faults to the east and west may influence those velocities. We therefore use two alternate formulations of strain accumulation east and west of the faults that are essentially boundary conditions. In the "wings" formulation, as referred to hereafter, we model the faults as extending semi-infinitely in both directions away from Los Angeles perpendicular to the N ~5° E convergence direction (Figure 3.S15-S16). In the "no-wings" formulation, no strain accumulation is allowed west and east of the basin. Details of these formulations are given in Appendix 3.4.

3.4.3. The "smooth" inversion method

The first inversion scheme we use, hereafter called the "smooth" scheme, is a bounded least-squares scheme with spatial smoothing, two inequalities and one equality,

$$\mathbf{m}_{est} = \mathrm{argmin}(\|(\mathbf{d} - \mathbf{Gm})/\boldsymbol{\sigma}\|_2 + \lambda\|\mathbf{S}^{-1/2}\Delta^2\mathbf{m}_{backslip}\|_2), \quad [3.2.1]$$

$$\mathbf{Am} \leq 0, \quad [3.2.2]$$

$$\mathbf{m}_{backslip} \geq 0, \quad [3.2.3]$$

$$\mathbf{m}_{backslip}(z = z_{max}) = 0. \quad [3.2.4]$$

Spatial smoothing is commonly used in models of interseismic strain accumulation [e.g. Chlieh et al, 2008, 2011; Liu et al, 2010; Ader et al, 2012] and could be interpreted as a guess that fault rheology varies gradually in space; it is also justifiable in that it penalizes abrupt variations in creep rates, which if real would cause singularities in strain rate and strain buildup. We impose this regularization by penalizing the discrete Laplacian of the portion of the model vector describing the backslip distribution, $\nabla^2\mathbf{m}_{backslip}$ (the Laplacian takes into account the variable patch sizes as per the method included in the PCAIM software [Kositsky and Avouac, 2010]), modulated by $\mathbf{S}^{-1/2}$, where $\mathbf{S} = \mathrm{diag}(\mathbf{G}^T\mathbf{G})$ is the sensitivity, large for well-resolved patches and small for poorly resolved patches (Figure 3.S17), following Ortega [2013]. This modulates the relative weight of smoothing; the overall weight of smoothing λ is chosen as the point of maximum positive curvature of a modified version of the "L-curve" [e.g. Aster et al, 2012] as described in Appendix 3.5. We also enforce that the backslip on each patch of a fault cannot exceed the long-term slip rate inferred for that fault. For full self-consistency, this must be enforced dynamically while the long-term slip rates are solved for in the inversion. We enforce this with the matrix operation $\mathbf{Am} \leq 0$, where each (nonzero) row of the matrix **A** operates on a given patch and contains a 1 that multiplies the entry in the model vector corresponding to that patch's backslip rate (near the diagonal of **A**) and a -1 that multiplies the entry corresponding to for the fault's step function in surface velocity divided by the cosine of the fault's average dip. In addition, we enforce that the entire model vector must be nonnegative, $\mathbf{m}_{\text{backslip}} \geq 0$, except for the entries corresponding to the northernmost, deepest patches on the flat at the base of the decollement, where we enforce zero backslip, $\mathbf{m}_{\text{backslip}}(z = z_{\max}) = 0$, as commonly done [e.g. Burgmann et al 2005, Ader et al 2012]. Finally, for added robustness, we use this least-squares inversion in a delete-half jackknife scheme [e.g. Tichelaar and Ruff 1989], in which it is performed on 1,000 sets of velocities using half of the 58 GPS stations (all sets are ensured to have at least one station offshore). The results discussed subsequently for the "smooth" method are then the weighted means and weighted 16$^{\text{th}}$ and 84$^{\text{th}}$ percentiles of the sets of 1,000 models, where each individual model's assigned weight is the inverse exponential of its X^2/N value.

Many of the models subsequently discussed use the "smooth" inversion method, the "blocks" variant of the backslip framework, the "wings" formulation, and elastostatic Green's functions computed with the CVM*. We call this scheme the smooth/blocks/wings/CVM* method and label the models as such; alternate schemes are described using similar four-term nomenclature. Appendices 3.6 and 3.7 describes several performance tests of the smooth/blocks/wings/CVM* scheme.

3.4.4. Inversions for strain accumulation on the Puente Hills Fault; the effect of the sedimentary basin

Before inverting the GPS for strain accumulation on the three thrust faults, we follow Argus et al [2005, 2015] and invert the GPS velocities at stations overlying the mesh for strain accumulation in a model that features the Puente Hills Fault ramping into a localized decollement (Figure 3.8), using the smooth/blocks/wings/CVM* framework.

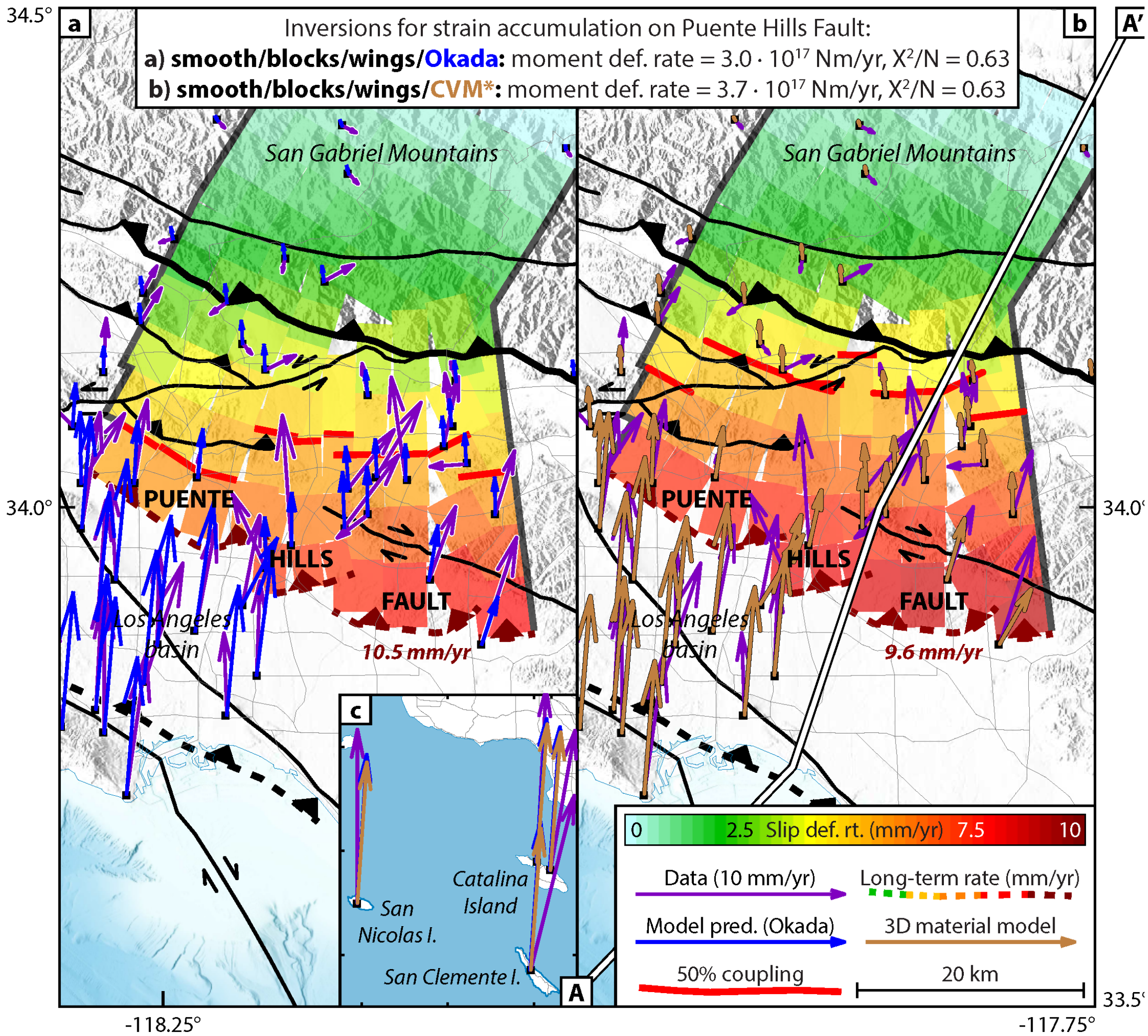

Figure 3.8. Inversions of the GPS velocity field for strain accumulation on the Puente Hills Fault and a narrow decollement in a) an elastic halfspace model and b) the CVM*, using the smooth/blocks/wings scheme. **a-b)** Mapviews of backslip (colored patches), long-term slip rates (colored dashed lines and shallow colored patches), and observed (purple) and predicted (blue or tan) velocities at GPS stations. More strain accumulation is inferred on the fault when the CVM* is used. **c)** Comparison of observed GPS velocities on islands with velocities predicted by the two models.

We then run a complementary inversion in which the regularization is identical but the elastostatic Green's functions are computed in an elastic halfspace model [Okada, 1985] and the output moment accumulation rate on each patch is computed assuming a uniform shear modulus μ = 30 GPa. The first-order finding, consistent with Argus et al [2015], is that deeper strain accumulation is required to fit the contractional gradient with the basin (Figure 3.8b) than without (Figure 3.8a), as inferred in other contexts featuring elastic heterogeneity [e.g. Arnadottir and Segall 1991, Bernard et al 1997]. The moment deficit accumulation rate of the weighted mean CVM* model is 20-25% larger than that of the halfspace model, a number which arises again in the models subsequently described. As a measure of the portion of the fault that could be described as more locked or more freely creeping, we compute the depth to the first patch on which the interseismic coupling is less than 50%. This 50% coupling depth (compare red lines in Figure 3.8a and 3.8b) steps down by ~3 km when the CVM* Green's functions are used. The halfspace and CVM* models fit the data approximately equally well, with a X^2/N of 0.63 each. The observation that adding elastic heterogeneity to the model does not greatly affect the quality of fit is also seen in subsequent models.

3.4.5. Other single-fault models

Next, we use the smooth/blocks/wings/CVM* scheme to invert the GPS for strain accumulation in a model that features the Sierra Madre Fault ramping into the northernmost section of the decollement (Figure 3.S19). The weighted mean model fits the data less well than the Puente Hills model, with a X^2/N of 0.85. Although the fastest north-south contraction in the model does occur in the Sierra Madre Fault's footwall, as predicted by the forward slip model (Figure 3.S6, 3.S8b), it does not extend far south enough from the fault to match the shortening observed in northern Los Angeles in the GPS (Figure 3.9, green line). Setting the overall weight of smoothing artificially lower than that chosen automatically in the inversion scheme (to essentially allow the model to overfit the data as an experiment) does not solve this issue. This implies that the shortening observed in the GPS cannot be explained by strain accumulation on the Sierra Madre alone, and points to the need of including a source of strain beneath the basin itself.

We then invert the GPS for strain accumulation in a model featuring the Compton Fault and Lower Elysian Park decollement (Figure 3.S20). The weighted mean model fits the data approximately as well as the Puente Hills model that uses the CVM*, with a X^2/N of 0.62; this is not surprising as the fault system is laterally extensive and the north-south shortening in the GPS can be fit somewhat adequately with a decrease in velocities midway down it (Figure 3.9, gray). This model has a moment deficit accumulation rate of 5.7×10^{17} Nm/yr – far larger than the rate inferred in the Puente Hills or Compton single-fault models or any of the the subsequent three-fault models – as there is simply a large area of the decollement accumulating strain at a high rate. Nevertheless, one takeaway from this model is that the observed shortening, which as seen previously is fastest in the basin, implies a

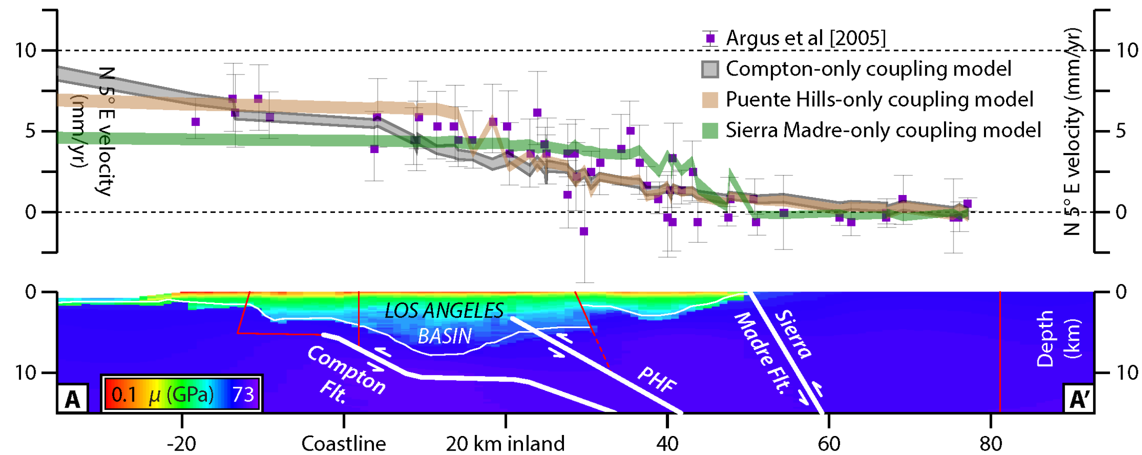

Figure 3.9. Comparison, along profile A-A', of observed GPS velocities with those predicted by models of strain accumulation on the Compton (gray; Figure 3.S20), Puente Hills (tan; Figure 3.8b and Sierra Madre (green; Figure 3.S19) faults. Velocities and uncertainties are projected onto the direction N 5° E. All models use the smooth/blocks/wings/CVM* scheme.

decollement that is dominantly creeping north of the basin rather than locked there.

The caveat for all three of the single-fault models, as with the models of Argus et al [2005], is that the inferred slip rates are 9-10 mm/yr, many times higher than any of the geologic slip rates in the Los Angeles area. These models nevertheless are useful as evaluations of endmember hypotheses about how the shortening is being accumulated, and it could be argued that the high slip rates invoked here favor hypotheses in which multiple faults are building up strain, as will be examined next. A comparison of the data in profile A-A' with the model-predicted velocities from each of the single-fault models (Figure 3.9) suggests that the relatively fast shortening observed in the northern Los Angeles basin may imply sources of strain both at the front of the San Gabriel Mountains (e.g. the Sierra Madre Fault) and beneath the basin itself (e.g. the Puente Hills and/or Compton faults).

3.4.6. Three-fault strain accumulation models: Model 1 (smooth/blocks/wings/CVM*)

We then invert the GPS for strain accumulation on a mesh featuring the Sierra Madre, Puente Hills, and Compton faults and decollement with the smooth/blocks/wings/CVM* scheme (Figure 3.10). The model, subsequently referred to as Model 1, features the Sierra Madre, Puente Hills and Compton faults respectively slipping at 4.6 +1.1/-1.3, 3.1 +0.8/-0.8 and 3.6 +1.0/-1.1 mm/yr over the long term, with high interseismic coupling inferred on the upper Sierra Madre and Puente Hills faults, moderate coupling on the upper Compton, and low coupling on the underlying decollement (Figure

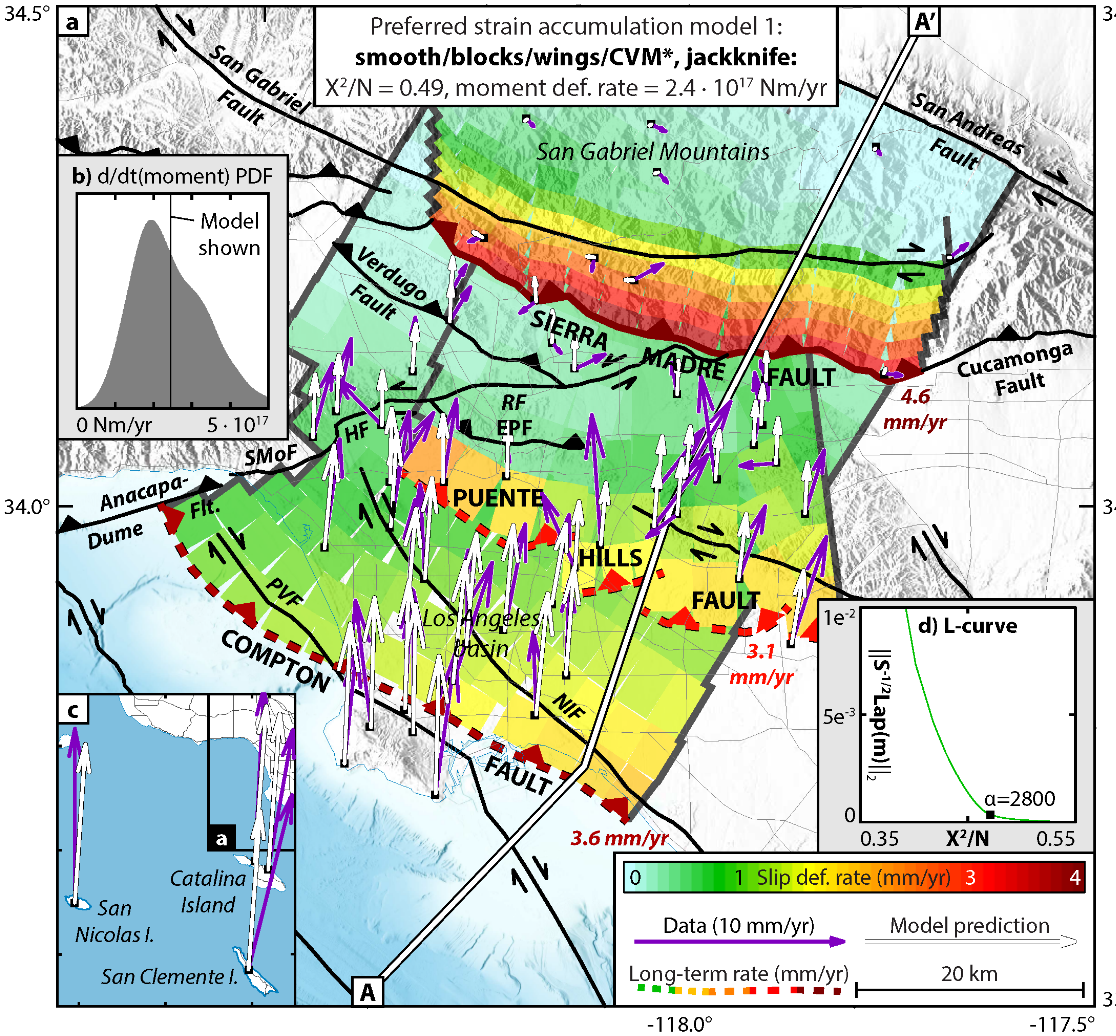

Figure 3.10. Model 1 of strain accumulation on the Compton, Puente Hills and Sierra Madre faults, using the smooth/blocks/wings/CVM* scheme. **a)** Mapview of backslip rates (colored patches), long-term slip rates (colors of the solid and dashed fault traces, also noted next to the faults), and observed (purple) and predicted (white) velocities at GPS stations. **b)** Weighted PDF of the moment buildup rates in the 1,000 delete-half jackknife models of which the model plotted here is the weighted average. **c)** Comparison of observed and predicted velocities on islands. **d)** L-curve used to choose the weight of sensitivity-modulated Laplacian smoothing in the inversion.

3.10). The decollement is implied to be creeping at 11.3 +0.9/-0.9 mm/yr at the base of the model (Figure 3.S21). The uncertainty in the decollement's slip rate is less than the Euclidean norm of the uncertainties in the three faults' slip rates because the three faults trade off in partitioning the slip rate in different models, echoing other cases where covarying slip rates in a multiple-fault setting sum to a comparatively well-constrained total rate [e.g. Freymueller et al, 1999]. The 1,000 delete-half jackknife samples make for 1,000

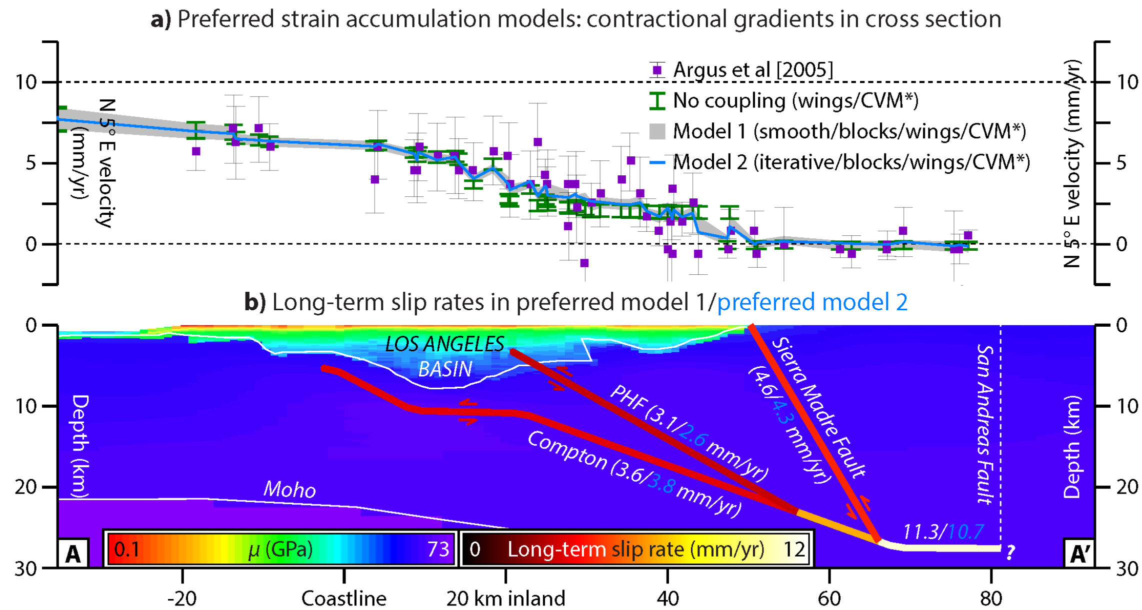

Figure 3.11. a) Comparison, along profile A-A', of observed GPS velocities with those predicted by models 1 and 2 and the "null" (green; Figure 3.S24) model of strain accumulation. **b)** Long-term slip rates in preferred model 1 (colored segments).

measurements of the cumulative rate of seismic moment deficit accumulation; the PDF of this quantity peaks at 2.0 x 10^{17} Nm/yr and its one-sigma range is 1.5-3.4 x 10^{17} Nm/yr (Figure 3.10b). The weighted mean of the 1,000 strain accumulation models (Figure 3.10a) produces a seismic moment deficit accumulation rate of 2.4 x 10^{17} Nm/yr, which is also the weighted mean of the 1,000 samples of moment deficit accumulation rate. The weighted-mean strain accumulation model fits the data well, with $X^2/N = 0.49$, but visibly does not overfit the data as a result of the smoothing and the enforcement that slip is in the N ~5* E convergence direction (Figure 3.10a; Figure 3.11a). Although the fastest backslip is on the upper sections of the faults, the fastest moment accumulation rate is at greater depth (Figure 3.S22) due to the increase of shear modulus with depth in the CVM* (Figure 3.S3); this will become important in the subsequent comparison with the depth distribution of seismicity. The output from a single model fit to all of the GPS velocities overlying the mesh is similar to the weighted mean model from the jackknife, with a moment deficit accumulation rate of 2.5 x 10^{17} Nm/yr and X^2/N of 0.47 (Figure 3.S23).

3.4.7. A "null model" and sensitivity to noise in the data

It is instructive to assess the contribution that the inferred strain accumulation from partial coupling on the Sierra Madre, Puente Hills and Compton faults makes to the model's fit. To do so, we invert the Argus et al [2005] velocities for a reference model in which the three faults are entirely creeping at their long-term slip rates, accruing no moment deficit in the interseismic period. This is computed by taking the smooth/blocks/wings/CVM* estimation procedure and removing both the Green's functions corresponding to backslip and the regularization of backslip, leaving

$$\mathbf{m}_{est} = \mathrm{argmin}(\|(\mathbf{d} - \mathbf{G}_{\mathbf{steps}}\mathbf{m})/\boldsymbol{\sigma}\|_2), \quad [3.3]$$

where $\mathbf{G}_{steps}$ consists of the Green's functions from the steps in the convergence rate over each fault plus the rigid-body rotation about the global Euler pole. Note that this **G** accounts for the blind nature of the Puente Hills and Compton faults and therefore still incorporates Green's functions that use the CVM*, as described in Appendix 3.4. This inversion also uses the "blocks" and "wings" formulations. The weighted mean output model fits the data well with $X^2/N = 0.57$, although not as well as Model 1 ($X^2/N = 0.49$). It yields slip rates of 3.7, 3.6 and 2.9 on the Sierra Madre, Puente Hills and Compton faults, respectively (Figure 3.S24). In profile, the surface velocities predicted by this model take the form of three steps over the faults that are broad in the case of the Puente Hills and Compton faults because those faults are blind (Figure 3.11). Model 1 visibly provides a somewhat better fit to the rapid contraction in the northern Los Angeles basin than does the null model; however, the contribution of the strain accumulation to the overall model fit can be concluded to be rather subtle. A no-strain-accumulation model with the "no-wings" formulation performs less well, with a X^2/N of 0.77.

We thus run several tests to evaluate the possibility that the strain accumulation inferred in the first preferred model could in fact be the result of fitting noise in the data. This is particularly important as Marshall et al [2009] inferred that the Argus et al [2005] anthropogenic velocities may have been overestimated at several stations in the basin and found that most of their forward models' misfit to the Argus et al [2005] velocities occurred at these stations (although they did nonetheless infer nonzero strain accumulation on the faults). In the first test, we generate synthetic surface velocities from a model in which the three faults are freely slipping at 4 mm/yr each and add Gaussian noise scaled by half the data uncertainties. This produces visible scatter in the synthetic velocity field (Figure 3.S25a, white arrows) and should also be a particularly rigorous test at the stations with large inferred anthropogenic motions, as the Argus et al [2005] velocity uncertainties at those stations include uncertainties in the inferred anthropogenic motions that are themselves scaled by the amplitudes of the inferred anthropogenic motions. We then reinvert the noisy velocity field for strain accumulation on the three faults using the smooth/blocks/wings/CVM* formulation. As with the smooth/blocks/wings/CVM* inversion of the real data, we compute an overall weight of smoothing λ as dictated by an L-curve, run the smoothed scheme in 1,000 delete-half jackknife iterations, and use the misfit-weighted mean of the models as the preferred output model. The inferred moment deficit accumulation rate in this model is 1.0×10^{16} Nm/yr, less than 5% of that inferred in Model 1 (Figure 3.S25b). In the second test, we take the Argus et al [2005] velocities and add Gaussian noise scaled by half the data uncertainties at each station, again producing visible scatter in the velocity field (Figure 3.S26a), then reinvert the noisy velocity field as above. Two iterations of this second test yield estimates of strain accumulation that are virtually indistinguishable from Model 1, with weighted mean moment deficit accumulation rates that are only marginally smaller at 2.2 and 1.9×10^{17} Nm/yr, respectively (Figure 3.S26a and 3.S26b). Together, these results suggest that models with zero strain accumulation and models with some strain accumulation are indeed distinguishable above random noise and other factors.

Following this, we subject the smooth/blocks/wings/CVM* method to a set of tests in which we model the Sierra Madre, Puente Hills and Compton faults as slipping at 4 mm/yr over the long-term, completely locked above a specified locking depth, and freely slipping below that. We generate synthetic surface velocities from these slip models within the CVM*, then reinvert the synthetics for the inferred distribution of strain accumulation and the long-term slip rates. We perform this test for a variety of input locking depths. The inferred long-term slip rates track the input slip rates well over the range of locking depths (Figure 3.S27c) except for very deep locking depths (for which case the model is poorly resolved and is also dragged towards zero by the combination of the smoothing and the zero-backslip restriction at the base). The imposition of spatial smoothing and the limited resolving power of the inversion does result in visible "smearing" [e.g. Evans and Meade, 2012] of the distribution of strain accumulation for many of the models (Figure 3.S27a-b), and the inferred moment rate somewhat exceeds the input for models with shallow locking depths (Figure 3.S27d). For example, an input model locked down to 10.5 km depth, corresponding to a moment deficit accumulation rate of 2.53×10^{17} Nm/yr, the test infers a weighted mean rate of 3.44×10^{17} Nm/yr, 36% higher than the input (Figure 3.S27a-b). This finding ultimately motivates us to use both Model 1 and a second, sparser strain accumulation model that will be introduced subsequently.

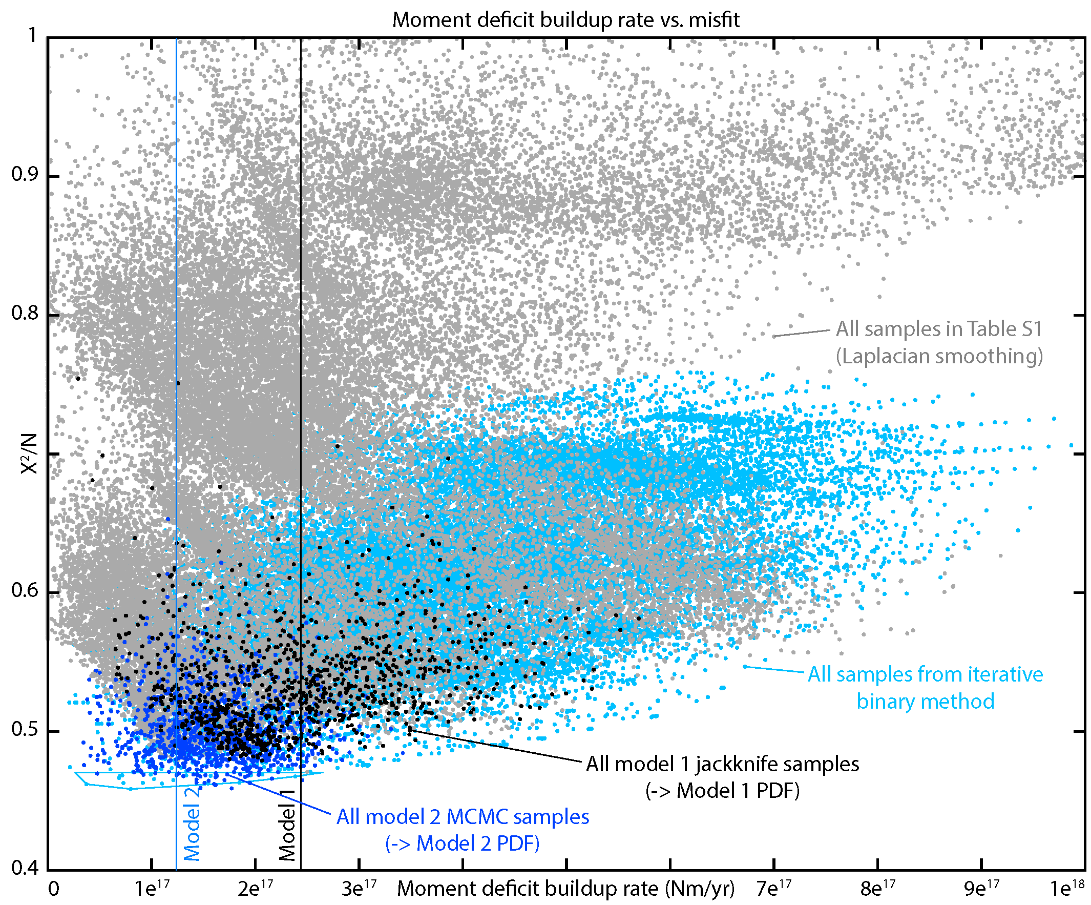

Figure 3.12. Distribution of moment deficit buildup rate vs. misfit in the ensemble of "smooth" models in Table 3.S1 (gray), the 1,000 jackknife models from Model 1 (black), the binary models of strain accumulation (light blue), and the MCMC samples comprising the PDF of Model 2 (dark blue). The moment deficit buildup rates of Models 1 and 2 are shown with the vertical black lines.

Next, we carry out further tests to evaluate whether a range of models with widely varying moment accumulation rates can fit the observed shortening relatively well. We run a suite of models in which the Sierra Madre, Puente Hills and Compton faults are variously parametrized as freely slipping, accruing strain, or nonexistent (Table 3.S1). The models are formulated within the "blocks" framework; we test both "wings" and "no-wings" formulations; all models use Green's functions computed from the CVM*; and all inversions use the "smooth" scheme, with the weight of smoothing chosen from a separate L-curve for each model. We then plot the misfits and moment rates of all of the 1,000 jackknife estimations from all of the models in the suite (Figure 3.12, gray dots). This representation shows that models with modest strain accumulation perform better than models with no strain accumulation or comparably rapid strain accumulation, with a broad global minimum around 1-2.5 x 10^{17} Nm/yr. The overall misfit function is markedly similar in shape to Figure 6 of Marshall et al [2009], which plots the misfits of that study's physics-driven forward models to the Argus et al [2005] dataset against the locking depths imposed in the models (which can with some caution be used as a proxy for moment accumulation rate). The 1,000 jackknife samples from Model 1 (Figure 3.12, black dots) sit near the global minimum and appear to sample the good-fitting region well, suggesting that the PDF of moment deficit accumulation rate derived from these samples (Figure 3.10b) may be a suitable representation of the range of moment deficit accumulation rates that fit the shortening pattern in Los Angeles relatively well.

Finally, to assess the sensitivity of the smooth/blocks/wings/CVM* inversion method to certain aspects of the GPS velocity field, we perform tests in which we alternately 1) exclude the GPS velocities on offshore islands, which reduces the total convergence rate to ~6 mm/yr; 2) add stations in the Mojave Desert (with velocities prepared as discussed in Appendix 3.1); 3) take the starting GPS velocity field and subtract off the synthetic velocity field derived from the forward model of strike-slip faults (Figure 3.S14), then invert; 4) subtract off the strike-slip field and also exclude islands. We find that the total seismic moment accumulation rate in all of these inversions is little changed from that in Model 1 (Appendix 3.7; Figures 3.S28-2.S30). This suggests that the inversion scheme and estimated moment buildup rate may be relatively robust against perturbations (Appendix 3.7). We thus proceed with cautious optimism that Model 1 may be a useful characterization of subsurface strain accumulation.

3.4.8. Three-fault strain accumulation models: perturbations to preferred model 1

To test the effect that the elastic structure has on the estimation of strain accumulation, we perform the same three-fault inversion used to generate Model 1 (with identical smoothing and parametrization) but with elastostatic Green's functions from an elastic halfspace model. Like the Puente Hills case, the weighted mean model infers less strain accumulation at depth (Figure 3.S31), a higher slip rate on the Puente Hills Fault, an equally good fit to the data ($X^2/N = 0.49$), and a moment accumulation rate (computed assuming $\mu = 30$ GPa) approximately 25% less than the CVM* model at 2.0 x 10^{17} Nm/yr. We then perform the three-fault inversion with Green's functions from the CVM* but under the "no-wings" parametrization, confining strain accumulation to the basin. As might be expected from the models of uniform reverse slip on the faults (Figure 3.7), this model predicts toroidal motion with relatively fast east-west velocities on the sides of the fault system, and as this toroidal motion is not seen in the GPS velocities, the “no-wings” model struggles to fit the data, with $X^2/N = 0.71$ (Figure 3.S32). The fit to the velocities on islands is particularly poor (Figure 3.S32b) compared to that of Model 1 (Figure 3.10c). One might expect faster strain accumulation to be inferred on the faults in the no-wings parametrization, as the wings are not absorbing any of the shortening and the faults have to take up more of the slack. Counterintuitively, however, the weighted mean moment deficit accumulation rate in the smooth/blocks/no-wings/CVM* model is 2.0×10^{17} Nm/yr, slightly less than the 2.4×10^{17} in Model 1. This appears to be because the no-wings model does a poor job at fitting the overall shortening rate. We conclude that the inclusion of the wings is key to accurately constraining the strain accumulation on the faults, and thus favor the smooth/blocks/wings/CVM* scheme used in Model 1.

3.4.9. The “sheets” formulation of long-term motion

The “blocks” formulation, in which the long-term motions on the faults are described kinematically as step functions in velocity at the surface (modified for the blind Puente Hills and Compton faults), is founded on the assumption that the long-term deformation across the faults can be described as rigid-body motion. The accuracy of this assumption is somewhat ambiguous for the faults studied here. Following Savage [1983], the long-term motion on a reverse fault might instead be described as uniform reverse slip on the entire fault; this only produces a step function in velocity at the surface if the fault is planar, which is not the case for the Sierra Madre, Puente Hills and Compton faults and the decollement modeled here. The internal inconsistency of applying the rigid-body motion assumption to deformation along nonplanar subduction zones has been highlighted by Chlieh et al [2004] and Kanda and Simons [2010]. The alternate hypothesis that the long-term motion can be described by uniform forward creep on the fault, it is worth noting, is itself perhaps most applicable to such subduction zones (as noted by Savage [1983]) and other plate-scale cases where the fault may be mature enough to be a driver of local tectonics. Whether this is true for the thrust faults underlying Los Angeles is ambiguous. Nevertheless, it is instrumental to assess how sensitive the inferred strain accumulation is to the assumption that the long-term motion is rigid-body motion. To assess this, we try out the assumption that it is uniform forward creep.

The underlying interpretation, regardless of the specific assumed long-term motion, is that over the long term the prescribed forward motion will move one entire side of the study area past the other, with the backslip only describing interseismic strain accumulation that is released in earthquakes. While the step functions in the "blocks" formulation inherently describe this, models of the long-term deformation as uniform reverse creep must explicitly account for the large-scale motions in a way that does not throw off the estimation problem. This is often done in 2D by extending the slipping fault semi-infinitely away from the study area [e.g. Savage and Burford 1973, Jolivet et al 2015, Daout et al 2016]. Here we extend this to 3D by modeling a large-scale regional decollement extending north, west and east beneath the Mojave Desert from the north end of the Lower Elysian Park decollement (Figure 3.S33), on which we enforce reverse slip in the N ~5° E convergence direction (with the top side of the decollement moving S ~5° W and the bottom side moving N ~5° E). The long-term motion on the Sierra Madre Fault, for example, is then modeled as uniform reverse creep on 1) the fault, 2) the section of the Lower Elysian Park decollement below its intersection with the fault, and 3) the regional decollement. The other two faults are modeled in the same way, and slip on the decollement is included in each fault's long-term motion as it is assumed to be feeding that motion, as in Daout et al [2016]. The column of **G** corresponding to each fault's long-term motion is then the vector of Green's functions from the forward slip on that fault and the decollement computed in the CVM*. The implication is then that the volumes separating the faults are thrust sheets, with the long-term displacement producing a component of tilting; as such, we call this alternate parametrization of the backslip framework the "sheets" formulation. The "no-wings" assumption is easily modeled within this framework by simply not including the wings anywhere in the models; the "wings" assumption is modeled by adding uniform reverse slip on each faults' wings to the corresponding forward term in **G**, with backslip on the wings and its smoothing then modeled the same way as in the "blocks" formulation. We then couch this formulation in the "smooth" inversion scheme, with the same "L-curve" and jackknife method; the inversion is then identical to those in previous models except for the three columns of **G** corresponding to the forward terms.

3.4.10. The "sheets" formulation: effect on the inferred strain accumulation

We invert the GPS data overlying the mesh for strain accumulation on the three faults in a scheme that combines the "smooth" inversion method and the "sheets" assumption with the "wings" formulation and the Green's functions computed within the CVM*, which we refer to as the smooth/sheets/wings/CVM* scheme. The inferred strain accumulation is not dissimilar to Model 1, with the highest backslip rates on the upper Sierra Madre and Puente Hills faults and $X^2/N = 0.52$ (Figure 3.S34). The main difference in this model is that the strain accumulation and slip rate on the Puente Hills are faster and those on the Compton are slower than those in the first preferred model. The slip rate on the Sierra Madre Fault is also faster, at 5.7 mm/yr, although the pattern of strain accumulation on it is similar to that in the first preferred model. We find that the smooth/sheets/wings/CVM* scheme is generally more prone than the smooth/blocks/wings/CVM* scheme to inferring high slip rates on the Sierra Madre Fault. This likely occurs because the slip rate on the regional decollement beneath the Mojave is not especially well constrained (as all of the data is south of it) and this then factors most heavily into the slip rate on the Sierra Madre Fault, as there are fewer stations overlying the Sierra Madre-decollement pairing – and thus fitting the corresponding forward term in **G** – than overlying the Puente Hills-decollement pairing or especially the Compton-decollement pairing. This drawback is somewhat addressed by adding the corrected velocities at the stations in the Mojave Desert (Appendix 3.1) to the data; doing so reduces the Sierra Madre's inferred slip rate to 5.2 mm/yr (Figure 3.S35). The key overall finding, however, is that despite these differences in long-term slip rates and strain accumulation, the weighted mean cumulative moment deficit accumulation rate is 2.2×10^{17} Nm/yr without the Mojave stations or 2.1×10^{17} Nm/yr with them – quite similar to the rate in Model 1. This suggests that this range of moment deficit accumulation rate may be in the right ballpark.

As with the "blocks" formulation, substituting in elastostatic Green's functions computed in an elastic halfspace for the CVM* Green's functions in the "sheets" formulation results in 1) lower inferred backslip rates on the faults, 2) a cumulative moment deficit accumulation rate that is 20-25% lower, 3) a similar model misfit ($X^2/N = 0.50$), and 4) a higher slip rate on the Puente Hills Fault (Figure 3.S36). This suggests that these effects, seen in the Puente Hills example and in the first preferred model, may also be independent of the specific formulation of long-term deformation and may be reliable takeaways. We also model the "no-wings" formulation in conjunction with the "sheets" framework (Figure 3.S37). Although this model does not fit the data better than the smooth/blocks/no-wings/CVM* model, with a chi-squared of 0.70, it infers much higher backslip rates on the three faults and a total moment deficit accumulation rate of 4.1×10^{17} Nm/yr, more than double that inferred in the smooth/blocks/no-wings/CVM* setup. This is more in line with the intuitive hypothesis that strain accumulation should be inferred higher on the faults if the wings are assuming to not be taking up any of the slack.

We note also that in the "sheets" formulation, a model featuring the three faults slipping freely yields a X^2/N value of 0.65, higher than the value of 0.57 obtained in the corresponding no-strain-accumulation model in the "blocks" formulation, and less similar to the value of 0.52 in the "sheets" model where the three faults are building up strain. This also tentatively suggests that the strain accumulation on the faults is indeed detectable.

3.4.11. Iteratively testing binary models of strain accumulation; Model 2

Finally, it is instructive to assess whether the imposition of spatial smoothing in the "smooth" inversion procedure could be affecting the estimates of strain accumulation, as some previous tests of the smooth/blocks/wings/CVM* method reveal that this method may somewhat overestimate the moment accumulation rate for shallow locking depths (Figure 3.S27c). We therefore devise an alternate estimation scheme. In this scheme, the GPS data is fit to a suite of models in which strain accumulation is prescribed as having a binary behavior with depth: each fault is enforced to be accumulating strain at its full long-term slip rate over a prescribed depth range, uniformly along strike, and to be freely slipping at all other depths (Figure 3.S38). Each of the three faults is then represented by a single column of **G** that consists of the long-term deformation plus the summed Green's functions from backslip over the prescribed depth range. The only parameters to solve for in the inversion are then the three long-term slip rates as well as the fourth term describing uniform background motion about the global Euler pole; this is essentially a simplification of the formulation of Meade and Hager [2005] with the location of the Euler rotation poles imposed. As in Model 1, these models use the "blocks" formulation of long-term slip rates, the "wings" formulation of off-fault deformation, and Green's functions computed with the CVM*. We then iterate over every possible combination of upper and lower locking depths on the three faults and compute the slip rates and the misfit for each model, yielding a large ensemble of estimations of the locked portions and slip rates.

Several conclusions can be gleamed from plots of all model misfits against the upper and lower locking depths on each fault in each binary model (Figure 3.13) and against the slip rates on each fault (Figure 3.S39). All of the best-fitting models feature the Sierra Madre Fault's upper locking depth at the surface (light green Xs) and its lower locking depth below the surface (dark green dots) – i.e. a coupled upper Sierra Madre Fault. The fit gradually deteriorates with increasing lower locking depth on the Sierra Madre. All of the very best-fitting models also feature the top 3 km of the Puente Hills locked (brown Xs and dots). This feature's impact on the fit is less than for the Sierra Madre, and the

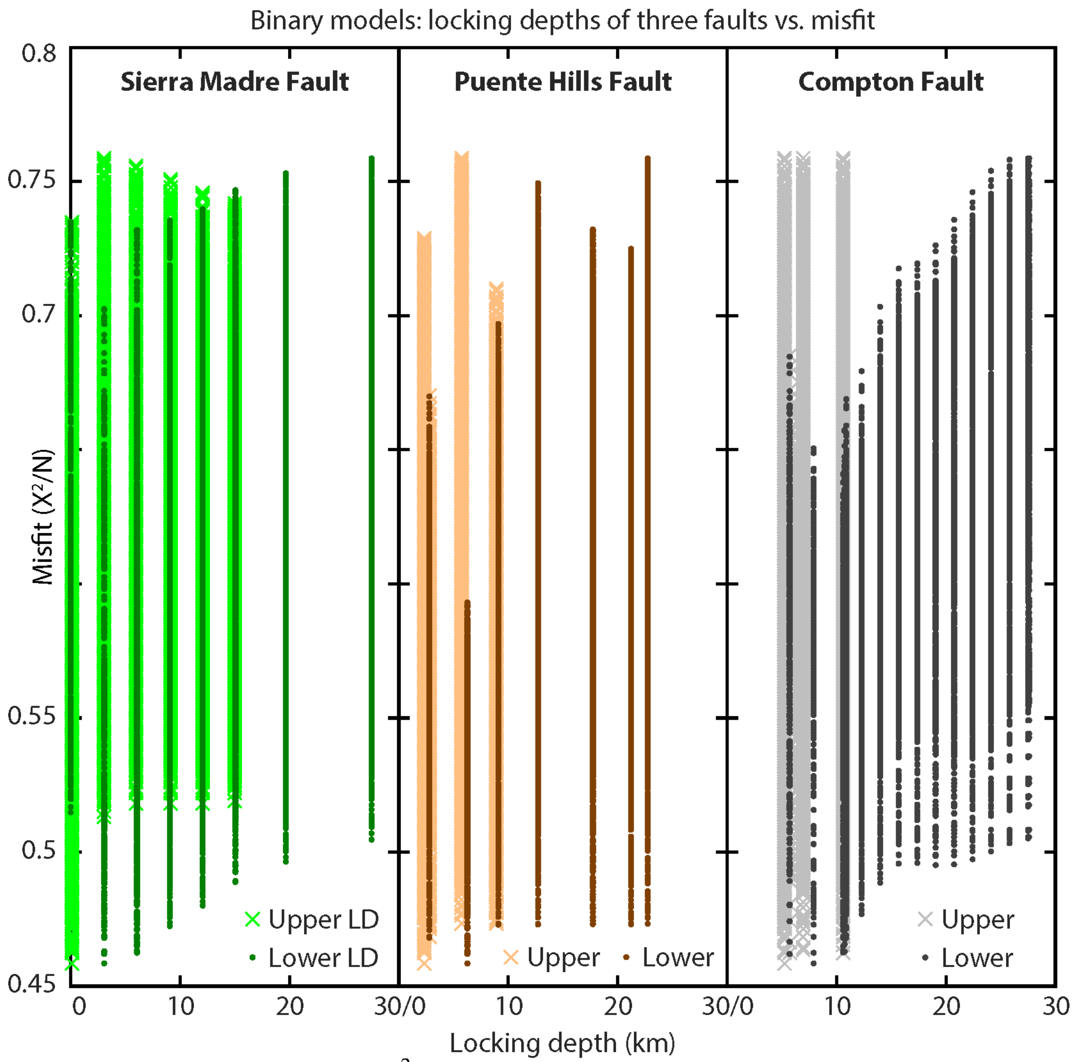

Figure 3.13. Distribution of X^2/N values of the binary models as a function of the upper and lower locking depths on the Sierra Madre, Puente Hills and Compton faults.

gentle decrease in fit with increasing lower locking depth is not seen for the Puente Hills, likely because the Puente Hills is a smaller fault. The choice of upper and lower lockingdepth on the Compton-decollement system has a more ambiguous effect on the data (gray Xs and dots), but as on the Sierra Madre, the misfit worsens with increasing lower locking depth on the Compton-decollement system – suggesting that the decollement is indeed likely creeping beneath the northern Los Angeles basin, as observed in the smoothed inversion for slip on the Compton-decollement system alone (Figure 3.S20). All of the best-fitting models also feature slip rates of 4-5 mm/yr on the Sierra Madre, 2-3 mm/yr on the Puente Hills, and ~4 mm/yr on the Compton (Figure 3.S39), consistent with Model 1.

Plotted in misfit vs. moment deficit accumulation rate space, the individual binary models define a similar overall locus as the smoothed jackknife models in Table 3.S1, with the best models accruing seismic moment deficit at a modest rate and the fit gradually worsening with increasing moment deficit accumulation rate (Figure 3.12, light blue samples). Although the curve is rather broad, the very best binary models have moment deficit accumulation rates of ~1 x 10^{17} Nm/yr, lower than the ~2 x 10^{17} for the best jackknife samples for Model 1. This echoes the possible upward bias in moment deficit accumulation rate inferred by the smooth/blocks/wings/CVM* scheme and suggests that it may be warranted to use the best binary models to form an alternative picture of strain accumulation beneath Los Angeles. To do so, following Elliott et al [2016], we select the binary models with normalized log-likelihoods of 0.96 or greater, of which there are 19 (Figure 3.14b). The cutoff value of 0.96 was chosen by inspection of models above and below it (Elliott et al use 0.95); we subsequently describe a method of estimating a unified model automatically, which we find yields a similar result. As with the jackknife samples in the "smooth" method, we then compute the misfit-weighted mean backslip distribution, long-term slip rates, and moment accumulation rate of the selected models to yield a single estimate of each.

The resulting model (Figure 3.14a), hereafter referred to as Model 2, shares some similarities to Model 1, with respective slip rates of 4.3, 2.6 and 3.8 mm/yr on the Sierra Madre, Puente Hills and Compton faults, relatively fast strain accumulation on the upper Sierra Madre and Puente Hills faults, and nearly identical model-predicted velocities in profile. The inferred backslip distribution, however, is markedly more sparse, containing no strain accumulation on the deeper sections of the faults and yielding a total moment deficit accumulation rate of 1.2 x 10^{17} Nm/yr, only 50% as fast as Model 1. The difference may result from a combination of two factors. The first is the aforementioned possible upward bias in moment deficit accumulation rate inferred by the smooth/blocks/wings/CVM* scheme. The second, somewhat a converse to the first, is that this iterative method does not test models in which the strain accumulation decreases steadily with depth; the only model featuring nonzero strain accumulation on the Puente Hills Fault between 3 and 15 km depth, for example, is a model in which the strain accumulation is uniform over that depth range. Argus et al [2005] shows that binary models of creep and locking can produce surface velocity distributions with secondary features that are not observed in the data, and this may increase the misfit in all but the sparsest models. In light of these tradeoffs and the fact that the fit of Model 2 is indeed slightly better than that of Model 1 ($X^2/N = 0.46$), it is

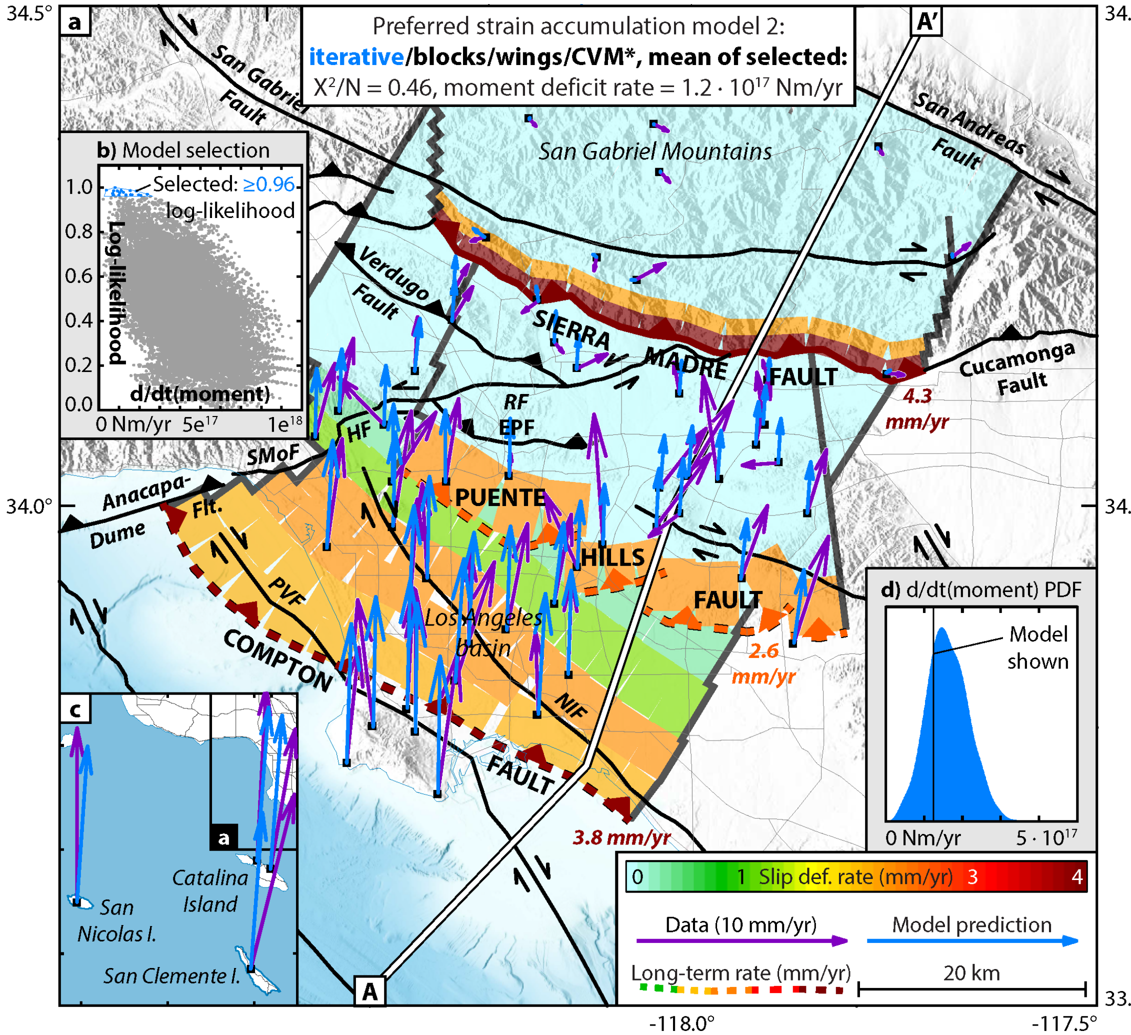

Figure 3.14. Model 2 of strain accumulation on the Compton, Puente Hills and Sierra Madre faults, the weighted average of the iterative binary models (which use the CVM* and the "blocks" and "wings" formulations) with normalized log-likelihood ≥0.96. **a)** Mapview of backslip rates (colored patches), long-term slip rates (colors of the solid and dashed fault traces, also noted next to the faults), and observed (purple) and predicted (blue) velocities at GPS stations. **b)** Distribution of moment rate vs. normalized log-likelihood in the suite of "binary" models and of the models chosen here. **c)** Comparison of observed and predicted velocities on islands. **d)** Corresponding PDF of moment deficit accumulation rate.

probably worthwhile to consider both representations of strain accumulation at depth. We thus use both models in the subsequent analysis.

We also devise a method to automatically produce a unified model of strain accumulation from a suite of binary models without manual model class selection. In all of the previous estimates, we combined multiple models into a single model by computing the misfit-weighted mean of the various models, with each model's weight being the inverse exponential of its chi-squared value. The approach of the automatic method is to simply introduce an extra denominator within the inverse exponential, changing the relative weighting of the models with respect to their misfits (a very small denominator, for example, will only use the lowest-misfit model; a very large denominator will weight all models approximately equally), and iterate over a range of values for the denominator and evaluate the misfit of the corresponding weighted model. We find that a value of 0.0525 for the denominator produces a weighted model with a minimal misfit of $X^2/N = 0.457$ (Figure 3.S40b). The model is similar to Model 2 in most aspects, with the only differences being that less strain accumulation is inferred on the Compton and Sierra Madre Faults below their upper sections (Figure 3.S40a); the total seismic moment deficit accumulation rate is 1.1×10^{17} Nm/yr, similar to that of Model 2.

To accompany these unified estimations of strain accumulation, we wish to derive a PDF of moment deficit accumulation rate corresponding to Model 2 as a counterpart to the PDF corresponding to Model 1 (Figure 3.10b), so that the two might be combined into a single probabilistic estimate of moment deficit accumulation rate. As the iterative binary method is a rather nonuniform exploration of the model space, we instead generate this PDF using a Monte Carlo Markov Chain approach that is inspired by Model 2. We use slice sampling [Neal, 2003] (as implemented in MATLAB) to produce 100,000 samples of the posterior PDF corresponding to the log-likelihood function

$$\mathbf{p} = -\tfrac{1}{2}(\mathbf{d} - \mathbf{Gm})^2/\boldsymbol{\sigma}^2 - \tfrac{1}{2}(\mathbf{m}(\mathbf{m}<0))^2/(\boldsymbol{\sigma}')^2 - \tfrac{1}{2}(\mathbf{Am}(\mathbf{Am}>0))^2/(\boldsymbol{\sigma}')^2$$
$$- \tfrac{1}{2}(\mathrm{sum}(\mathbf{m}_{\mathrm{steps}}) - 0.0085)^2/(\boldsymbol{\sigma}')^2, \qquad [3.4]$$

where as before, $\mathbf{d}$ and $\boldsymbol{\sigma}$ are the vectors of east and north velocities at all stations overlying the fault mesh. The matrix $\mathbf{G}$ is an 11-parameter model consisting of the background rotation rate about the Euler pole, the three long-term fault slip rates (assuming the "blocks" formulation of long-term motion), and seven backslip parameters corresponding to the seven total depth ranges at the tops of the three faults that have nonzero backslip rates in Model 2 (Figure 3.14). Each of the seven corresponding columns of $\mathbf{G}$ consists of the summed Green's functions from uniform backslip on all the fault patches in one of the seven depth ranges, similar to the binary models; here, however, the backslip rate in each depth range is a free parameter rather than being enforced to be complete locking. This restricts strain accumulation to the upper sections of the three faults as dictated by Model 2, so as to specifically explore the model space around this model. From the previous least-squares schemes, we import priors that backslip on each fault must be nonnegative and must not exceed the corresponding fault slip rate (enforced by a reduced version of the same matrix **A**). To enforce these priors with hard bounds may prevent the chain from exploring models with near-zero slip on a given patch [Minson et al, 2013] or here near-complete coupling on a given patch, so instead we devise soft bounds defined by "half-Gaussians." In these, any negative backslip worsens the misfit function proportional to its amplitude below zero, and any backslip that exceeds its fault's long-term slip rate worsens the misfit function proportional to how much it exceeds the slip rate, with both proportions scaled by a factor σ' and expressed within a Gaussian misfit function (3.4). This is a guess that within an uncertainty σ', no backslip should be negative and no backslip should exceed its fault's long-term slip rate. Because the GPS velocities and backslip rates are both on the order of mm/yr, a plausible candidate for **σ**' is simply mean(σ), the mean one-sigma uncertainty in the GPS velocities, about 1.7 mm/yr. We find through trial and error that a better value for **σ**' is one-third the mean GPS uncertainty; this helps keep the models from having negative cumulative moment deficit accumulation rates (only two samples of 100,000 have negative cumulative rates using **σ**' = σ/3, compared to 36 samples for σ' = σ/2). This then represents a prior belief that no backslip should be more negative than the data uncertainty or exceed its fault's long-term slip rate by more than the data uncertainty at the 3σ confidence level. Finally, we also enforce that the three steps in the long-term convergence rate over each of the three faults must approximately sum to 8.5 mm/yr, enforced by a Gaussian prior with the same scaling **σ**'; this prior was motivated by the results of some stability tests using an elastic halfspace model (Figure 3.S44) and has little effect on the chain that uses the elastostatic Green's functions computed with the CVM*.

The output models from the resulting chain (thinned to one of every 100 models to reduce serial correlation) produce a PDF of moment deficit accumulation rate that peaks at 1.46×10^{17} Nm/yr (Figure 3.14d), slightly higher than the weighted-mean rate of Model 2. This is not surprising as 1) the 19 models used to form Model 2 represent only the very minimum of the moment deficit accumulation rate vs. misfit surface, whereas the MCMC method is sensitive to the broader nature of the general surface; and 2) as discussed previously, the iterative method used to form Model 2 does not test models with depth-variable coupling and as such may be biased towards sparse solutions. Model 2 might therefore be described as a finding that the north-south contraction can be fit with strain accumulation only on the upper sections of the faults, and the corresponding PDF as an exploration of what that might mean for the moment deficit accumulation rate. The MCMC samples reside firmly in the general lowest-misfit region of the distribution of moment deficit accumulation rates vs. misfit (Figure 3.12, dark blue dots), covering both the region near ~2 x 10^{17} Nm/yr preferred by the jackknife models comprising Model 1 and the region of somewhat lower moment deficit accumulation rate suggested by the very lowest-misfit binary models. We are thus optimistic that these samples may provide a good counterpart to the 1,000 jackknife samples in forming a unified PDF of the moment deficit accumulation rate.

As a stability test, we also explore models where we remove the synthetic velocities from the forward strike-slip model (Figure 3.S14) from the GPS and then invert the remainder for strain accumulation on the thrust faults using the iterative/blocks/wings/CVM* scheme, then produce a unified estimation of strain accumulation from the mean of the models with normalized log-likelihood ≥0.96. As with the "smooth" scheme and consistent with intuition, the main effect is to reduce the inferred slip rate on the Compton to ~2 mm/yr, and the inferred strain accumulation pattern does not change dramatically (Figure 3.S41). This suggests that the models derived from the "iterative" method are also relatively robust on their own terms.

Finally, as done for the smooth/blocks/wings scheme, we test the iterative/blocks/wings scheme with Green's functions computed in an elastic halfspace model. We first plot the misfits of the individual resulting models against the locking depths (Figure 3.S42) and slip rates (Figure 3.S43) on the three faults. Whereas the very best-fitting models from the iterative/blocks/wings/CVM* scheme featured an upper and lower locking depth of 3 and 6 km on the Puente Hills Fault (Figure 3.13), no such preference is visible in the models using an elastic halfspace assumption (Figure 3.S42). The very best-fitting of the elastic halfspace models also feature slightly higher slip rates on the Puente Hills and Compton faults (Figure 3.S43) than did the very best iterative/blocks/wings/CVM* models (Figure 3.S39). We then combine the models with normalized log-likelihood ≥0.96 into a unified estimate of strain accumulation and use the aforementioned MCMC procedure to sample the PDF of the total moment deficit accumulation rate, as done for the iterative/blocks/wings/CVM* scheme. The unified model features more strain accumulation on the Compton Fault and less strain accumulation on the Puente Hills than Model 2, resulting in a slightly higher overall moment deficit accumulation rate in both the unified model and the PDF than in Model 2 (Figure 3.S44). This is in fact the reverse of what was observed with the smooth/blocks/wings scheme, where models using an elastic halfspace model (Figure 3.S33) had somewhat lower total moment deficit accumulation rates than models using the CVM*. The iterative/blocks/wings method appears to generally favor a picture of faster strain accumulation on the Compton Fault than the smooth/blocks/wings method does (compare Figures 3.10 and 3.14), and this difference appears in both the backslip rates and the long-term slip rate on the Compton when an elastic halfspace assumption is used (Figure 3.S44). The latter observation is in fact what motivated the aforementioned extra prior in the MCMC method that bounds the sum of the steps in the long-term convergence rate to be near 8.5 mm/yr. This behavior appears to be limited to the elastic halfspace model and to not affect models that use the CVM*; in fact the slip rate on the Compton is nearly the same in Models 1 and 2.

Finally, as was done for the "smooth" scheme, we test the iterative scheme with the "no-wings" boundary condition, restricting strain accumulation to the three thrust faults beneath the Los Angeles basin, and then combine the models with normalized log-likelihood $\geq$0.96 into a unified estimate of strain accumulation (Figure 3.S45). As was observed for the "smooth" scheme, the GPS data is fit markedly less well under this assumption than under the "wings" boundary-condition, with a X^2/N of 0.66 compared to the value of 0.46 in Model 2. The overall moment deficit accumulation rate is actually the same as that in Model 2, at 1.2 x 10^{17} Nm/yr, a behavior also observed when using the "no-wings" boundary condition with the "smooth" scheme (compare Figure 3.S34 and 3.10). This again appears to be a product of the relatively poor fit to the data; the unified model, as with the smooth/blocks/no-wings/CVM* model (Figure 3.S34), implies toroidal motion on the sides of the basin that is not seen in the GPS (Figure 3.S45). The "wings" boundary condition thus appears to be the better assumption.

3.5. Implications of the strain accumulation models

3.5.1. Depth distributions of moment accumulation, moment release and seismicity

One way to evaluate the predictive power of a model of strain accumulation is to assess how well it predicts the local depth distribution of earthquake behavior. Although many rheological factors influence the latter, one intuitive hypothesis is that an abundance of earthquakes over a given depth range might indicate a general rheological tendency towards stick-slip behavior and an absence of earthquakes might indicate general stable-sliding behavior. To the extent to which this is accurate, interseismic coupling models should predict comparatively high strain accumulation at depths where earthquakes occur frequently and low strain accumulation where they are sparse. One of the principal motivations for this study was the disparity between the distribution of seismicity in Los Angeles – the 95th-percentile depth of earthquakes whose epicenters overlie the mesh of the three thrust faults and decollement is 15.47 km – and the lower locking depths of 6 ± 2, ~8 and ~3 km in the strain accumulation models of Argus et al [2005], Marshall et al [2009] and Daout et al [2016], which imply that earthquakes should not occur below those depths (all other factors being equal). The high-quality seismic catalogs available for the Los Angeles basin afford us the opportunity to evaluate our models in the same way. The Southern California Earthquake Data Center provides locations and magnitudes for earthquakes throughout Southern California from 1932 to present day. Hauksson et al [2012] relocated this catalog for the period 1981-2011 and have since updated their relocated catalog to include earthquakes through mid-2016 (http://scedc.caltech.edu/research-tools/alt-2011-dd-hauksson-yang-shearer.html). Here we use the earthquakes in the relocated Hauksson et al catalog, which we refer to as HYS16, whose epicenters lie within the boundary of the mesh of the three thrust faults and decollement.

We compare the depth distribution of seismic moment deficit accumulation in the two preferred strain accumulation models with two measures of the depth distribution of seismicity. The first is the depth distribution of seismic moment release in the selected earthquakes in the HYS16 catalog (Figure 3.15a). The immediate conclusion is that the latter is governed by the largest few earthquakes in the HYS16 catalog (Figure 3.15a, purple polygon), in particular the 1987 M~5.9 Whittier Narrows and 1991 M~5.8 Sierra Madre earthquakes, and is thus subject to statistics of small numbers. As such, a quantitative comparison of strain accumulation and release by depth is not tenable. However, one useful conclusion can be gleamed from the comparison visually: Model 2, which has the slightly lower misfit of the two, predicts no strain accumulation below ~10 km and thus predicts that the 1987 Whittier Narrows earthquake, the largest in Los Angeles in the last 45 years, should never happen. Model 1 might thus be said to be more consistent with the deeper seismicity beneath Los Angeles.

Figure 3.15b then compares the depth distribution of moment deficit accumulation rate in the strain accumulation models against the number of earthquakes per km depth in the mesh area. (If earthquakes are assumed to follow the same magnitude-frequency statistics at all depths and are assumed to be point sources, the distribution of the rate of earthquakes should in fact mirror the distribution of moment release in a sufficiently

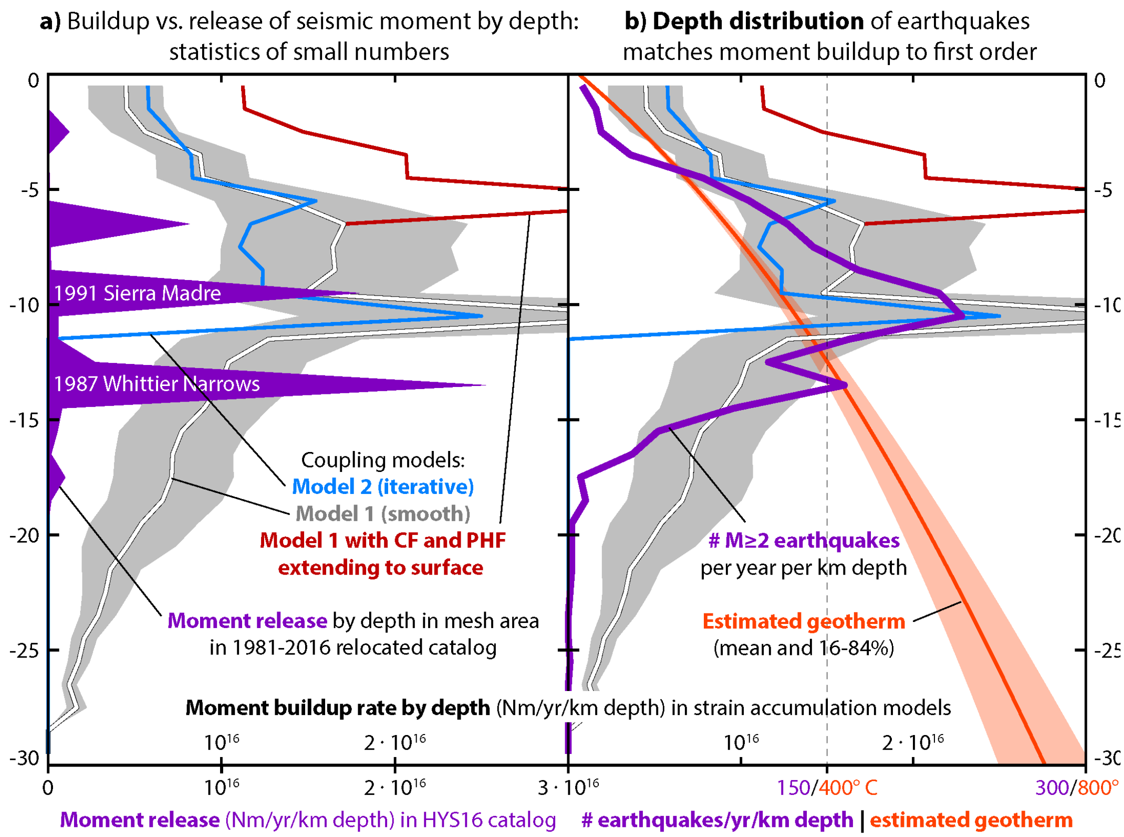

Figure 3.15. Depth distributions of moment deficit accumulation rate in the coupling models compared with **a)** the depth distribution of moment release rate in earthquakes in the Hauksson et al [2012 and updated] relocated catalog whose epicenters lie within in the mesh area of the thrust faults and decollement and **b)** the depth distribution of the rate of the same earthquakes. The red curves denote the depth distribution of moment deficit accumulation in a modified version of preferred model 1 where all three faults extend to the surface. The orange PDF by depth is an estimated geotherm assuming exponential decay of heat production with depth (Appendix 8). **a)** The moment release rate in earthquakes in the mesh area (purple polygon) is dominated by a few large events; preferred model 2 predicts no strain accumulation at the depth of the Whittier Narrows earthquake. **b)** The (scaled) depth distribution of earthquake occurrence (purple line) matches the depth distribution of moment deficit accumulation rate in the coupling models to first order. Preferred model 1 overestimates the relative rate of earthquakes at the deep end of the range; preferred model 2 underestimates it. The surface-breaking version of model 1 (red line) predicts proportionally high strain accumulation in the upper 6 km.

populated catalog. This assumption may therefore be somewhat valid for small earthquakes in particular). The strain accumulation models predict the general shape of depth distribution of earthquakes to first order, with low rates near the surface, a peak at ~10 km depth, and a decrease below that depth (Figure 3.15b). Although the strain accumulation rate in our models decreases with depth from the tops of faults, the seismic moment accumulation rate increases with depth in the upper 10 km for two reasons. The first is that the Puente Hills and Compton faults are blind, and as such only begin adding to the picture at ~3 and ~5 km depth, respectively. Secondly, the shear modulus in the CVM* interpolated onto the fault patches, which is multiplied with the backslip rate (and the fault area) to yield the moment deficit accumulation rate, increases with depth (Figure 3.S3); therefore the moment accumulation rate on even the surface-breaking Sierra Madre Fault, for example, peaks at ~6-9 km depth in the first preferred model (Figure 3.S22). For comparison, we construct a supplementary strain accumulation model in which we take Model 1 and count the strain accumulation on the artificial upper projections of these faults (Appendix 3.4), which was not counted in the main model. This model predicts an increase in moment deficit accumulation rate toward the surface that, unlike the two preferred models, does not track the depth distribution of seismicity (Figure 3.15b, red line). We thus conclude that, all other factors being equal, the depth distribution of earthquake rates in Los Angeles appear to be consistent with a system featuring strain accumulation on blind thrust faults and mostly anelastic deformation updip of their tips.

Below the peak at ~10 km depth, the depth distribution of earthquakes in the mesh area decays to zero at ~19 km depth (Figure 3.15b), with a small secondary peak at ~13 km that upon comparison with the left panel appears to be the 1987 Whittier Narrows sequence. Model 1 predicts that earthquake rates should be nonzero down to the base of the decollement at 27.5 km depth (as the backslip gently decays with depth); this proportionally overpredicts the rates of earthquakes below ~15 km depth. Model 2, as previously discussed, predicts no earthquakes below ~10 km depth. If the depth distribution of earthquake rates is indeed a proxy for the rate of seismic moment accumulation on faults, it predicts that the true strain accumulation pattern may lie in between the predictions of the two preferred models. The two models may thus constitute conservative lower and upper bounds on the true behavior at depth.

3.5.2. Spatial distribution and PDF of seismic moment deficit accumulation rate

We combine models 1 and 2 into a map of the spatial distribution of moment deficit accumulation rate per area in Los Angeles (Figure 3.16a). The moment deficit accumulation rate at each point on the map sums the moment deficit accumulation rate on all of the portions of fault that underlie that point, averaged between the two strain accumulation models. The highest values are found around the Sierra Madre Fault, a result

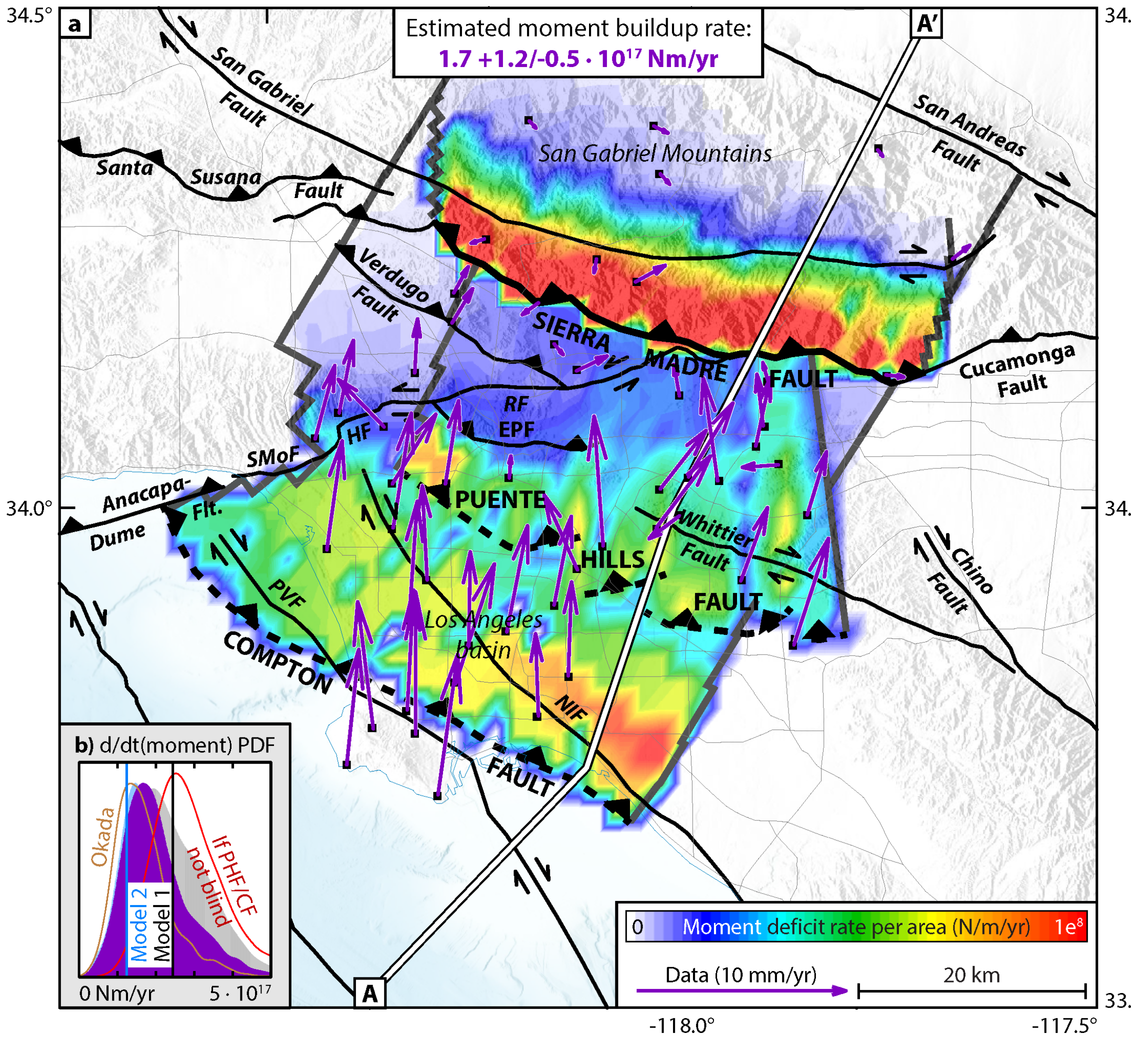

Figure 3.16. Spatial distribution and PDF of moment deficit buildup rate in Los Angeles as inferred from Models 1 and 2. **a)** Spatial distribution of moment deficit buildup rate per area. The highest values are found near the Sierra Madre Fault, with more moderate rates near the Puente Hills and Compton faults. **b)** Unified PDF of moment deficit accumulation rate (purple object) formed by combining the PDFs from Model 1 (gray) and Model 2 (blue). Red line denotes the PDF if strain accumulation on the updip extensions of the Puente Hills and Compton faults were counted.

of two factors. The first is that both strain accumulation models infer this fault to have the highest long-term slip rate of the three and infer its upper section to be mostly or completely locked. The second is that the fault's steep northward dip means that a given distance in the north-south direction will correspond to a larger down-dip distance on the Sierra Madre, and therefore a larger moment deficit accumulation rate (as moment takes into account the length and width of a given region), than the other two faults. The moment deficit accumulation rate per area is comparably moderate over the Puente Hills and Compton faults. Note that the use of the "wings" boundary condition in both models 1 and 2 implies that the moment deficit accumulation rate per area would in fact project eastward and westward from its values on the faults (e.g. Figure 3.S16); we do not plot that feature here as we do not intend to make a quantitative estimate of the moment deficit accumulation rate outside the Los Angeles basin.

We then combine the two PDFs of moment deficit accumulation rate corresponding to the two models into a single unified PDF, using the 1,000 jackknife samples from Model 1 and 1,000 samples from the thinned chain in Model 2. The unified PDF peaks at 1.67 x 10^{17} (Figure 3.16b, purple object) and its 16^{th}- and 84^{th}- percentile values are respectively 1.23 and 2.90 x 10^{17} Nm/yr. The longer tail on the upper end is consistent with the shape of the moment deficit accumulation rate vs. misfit function (Figure 3.12), in which the misfit decreases quickly between 0 and ~1-2 x 10^{17} Nm/yr and then increases gradually with increasing moment deficit accumulation rate. For reference, a rate of 1.67 x 10^{17} Nm/yr is equivalent to a Mw=7.0 earthquake every ~240 years, but it will be seen in the following chapter that this estimate is erroneous as it does not take into account the fact that this moment accumulation should be released by earthquakes at a variety of magnitudes. We also construct the PDF of moment deficit accumulation rate that would result if strain accumulation on the surface projections of the Puente Hills and Compton faults were counted; this PDF peaks at 2.53 x 10^{17} Nm/yr (Figure 3.16b, red line), a rate 50% faster than the main PDF (with 16^{th}- and 84^{th}- percentile values 1.98 and 3.75 x 10^{17} Nm/yr, respectively). This suggests, consistent with the comparison with seismicity rates by depth, that the blind nature of the Puente Hills and Compton faults has a first-order effect on the picture of strain accumulation beneath Los Angeles and its implications. Finally, we compute the PDF of moment deficit accumulation rate assuming an elastic halfspace model, combining the PDFs from Figure 3.S31 and Figure 3.S44. This PDF peaks at 1.34 x 10^{17} Nm/yr, with 16^{th}- and 84^{th}-percentile values 1.02 and 2.33 x 10^{17} Nm/yr (Figure 3.16b, tan line), a notably slower rate than with the basin model. This shows that the basin has a first-order effect on the ultimate estimation of strain accumulation at depth.

3.6. Discussion

3.6.1. Effect of the sedimentary basin on the estimation problem

We find that the Los Angeles basin amplifies elastostatic Green's functions from slip on faults underlying it by up to 50% (Figure 3.7), consistent with the effects of near-surface material heterogeneity inferred in previous studies. In particular, Cattin et al [1999, their Figure 5] computed elastostatic Green's functions from slip on a dislocation in a substrate overlain by a weak near-surface layer and found that the amplification by the layer approaches 50% when the layer is around two orders of magnitude less stiff than the substrate, approximately the contrast in shear modulus between the Los Angeles basin and surrounding crust at the surface (Figure 3.6). The finding that the basin dampens the elastostatic Green's functions for slip on faults within it, causing them to decay towards zero closer to the slip source (Figures 3.S5, 3.S8a; 3.S9-3.S13), is also consistent with previous studies [e.g. Zhao and Muller, 2004; Segall, 2010]. We find that the specific model of the basin used has almost no effect on the computed Green's functions (Figure 3.S4; Appendix 3.3), which stands in contrast to the finding from simulations of seismic shaking that the details of the near-surface structure have a strong effect on ground motions [e.g. Taborda and Bielak, 2014]. The low sensitivity to this in the elastostatic Green's functions, however, is consistent with previous elastostatic studies; in particular, Cattin et al [1999, their fig. 5] found, in models of a low-stiffness near-surface layer overlying an elastic substrate, that the amplification depends little on whether the layer is 1% or 5% as stiff as the substrate, as the amplification by the near-surface layer approaches ~50% asymptotically as its stiffness is decreased.

We find that incorporating the CVM* into inversions for strain accumulation increases the inferred strain accumulation on the faults at depth and thus their effective inferred locking depths. In our inversions for strain accumulation on the Puente Hills Fault (Figure 3.8), for example, incorporating the CVM* pushes the depth at which 50% coupling occurs down by ~3 km. This echoes previous studies that have shown that incorporating elastic heterogeneity into models often results in deeper inferred slip [e.g. Arnadottir and Segall, 1991; Kyriakopoulos et al, 2013].

3.6.2. Contribution of the strike-slip faults to the north-south shortening

Walls et al [1998] proposed that around 50% of the inferred north-south shortening across Los Angeles could be the product of east-west escape tectonics on the various strike-slip faults in the city. Argus et al [1999] found, however, that this model significantly overpredicted the east-west surface velocities in northern Los Angeles as compared to GPS data. Both studies modeled long-term displacements across the faults rather than interseismic strain accumulation on them. Bawden et al [2001] modeled interseismic strain accumulation on the strike-slip faults at their consensus geologic slip rates and found that they could be contributing ~0.7 mm/yr of the north-south contraction; they found that accounting for the strike-slip faults also changed the inferred azimuth of the shortening by ~20°. We note that Bawden et al modeled interseismic strain accumulation on the strike-slip faults using backslip down to ~10 km depth on the fault geometries. The other modeling elements we find are required in the "blocks" formulation of the backslip method, such as the steps over the faults and the infinite extensions of faults along strike, suggest that modeling strike-slip strain accumulation with localized backslip sources may not be entirely self-consistent (although it may be approximately correct on the scale of the basin). Our model of the strike-slip faults follows the Savage and Burford [1973] deep-slip scheme, which is more physically self-consistent for finite faults and also produces nonzero surface velocities far from the faults. This is most similar to the physical forward-slip models of Marshall et al [2009] and Daout et al [2016], although it also incorporates the CVM* Green's functions. We find that interseismic strain accumulation on the strike-slip faults could be contributing up to ~2 mm/yr of north-south contraction, about 50% of the value postulated by Walls et al [1998], higher than that inferred by Bawden et al [2001] and qualitatively consistent with the Marshall et al [2009] picture of thrust and strike-slip faults accommodating the north-south contraction in concert. The key finding here is that interseismic strain accumulation on the strike-slip faults could contribute to the north-south contraction while producing very little east-west motion in the basin (Figure 3.S14). This contrasts with the findings of Argus et al [1999], which modeled the long-term motions rather than interseismic strain accumulation, and Bawden et al [2001], which as mentioned modeled the interseismic strain accumulation in a different way.

It is worth noting, however, that our model of strike-slip deformation is quite "liberal" in two ways. The first is that the faults are modeled as being locked down to only ~5 km depth, exactly the sort of shallow locking depth whose mismatch with the local 95th-percentile depth of seismicity partially motivated this study. We note that a model where the faults are locked down to ~10 km depth (as modeled by Bawden et al), and creeping forward at their long-term rates between that depth and 75 km, produces ~1.6 mm/yr of north-south contraction compared to the ~1.8 mm/yr with a 5-km locking depth; therefore the shallow locking depth may not be of great importance to the overall finding. The second way in which this model is rather liberal, however, is that all of the faults are modeled as extending down to 75 km depth (the approximate depth to the lithosphere-asthenosphere boundary in Los Angeles as imaged by Lekic et al [2011]) as discrete interfaces and slipping at their UCERF3 "geologic" rates down to that depth. This is highly speculative. Localized seismicity has been inferred to extend to >20 km depth along the Newport-Inglewood Fault, suggesting that the fault may extend into the mantle as a discrete interface [Inbal et al, 2016]. However, the Palos Verdes Fault, the fastest-slipping of the strike-slip faults at ~3 mm/yr [McNeilan and Rockwell, 1996], has been proposed as being a backthrust (with a proportionally large strike-slip component of slip) that extends only a few km deep and roots into the upper Compton Fault [Shaw and Suppe, 1996]. The Whittier Fault also likely intersects the Puente Hills Fault at depth, complicating the mechanics of slip on it even if it does continue deeper into the crust [Griffith and Cooke, 2004]. Therefore, our model of the strike-slip faults is intentionally designed to provide an upper bound on how much they may contribute to the north-south contraction observed in the GPS data. These deep fault extensions may nevertheless serve as a proxy for distributed right-lateral shear in the mantle beneath these faults [e.g. Wright, 1991]. We conclude that the strike-slip faults may be contributing a fraction of the north-south shortening, though likely not as large a fraction as the thrust faults. Therefore, although our models assume that all contraction across Los Angeles is due to thrust faults, this approximation likely has little effect on the estimate of the rate of moment deficit accumulation, particularly as the overall inferred strain budget still counts the strain that might be associated with strike-slip faulting.

3.6.3. Some inferences from the strain accumulation models

The Argus et al [2005] GPS velocities relative to the San Gabriel Mountains (Figure 3.1a) do not display the toroidal motion on the edges of the Los Angeles basin seen in models of uniform slip on the thrust faults beneath the basin (Figure 3.7, Figure 3.S7), suggesting that faults east and west of the basin also influence the velocities in the basin. The “wings” formulation allows for strain accumulation east and west of the basin to help fit the contraction across the basin, and as such does a demonstrably better job at doing so than the “no-wings” formulation, which enforces that strain accumulation is confined to the Sierra Madre, Puente Hills and Compton faults. These alternate formulations may be applicable to studies of interseismic strain accumulation in other settings where the faults are not effectively semi-infinite with respect to the estimation problem.

The unified estimate of the moment deficit accumulation rate, 1.7 +1.2/-0.5 x 10^{17} Nm/yr, assumes implicitly that strain updip of the fault tips is accommodated anelastically and does not need to be counted in the budget of seismic moment accumulation and release. If this strain accumulation is counted, the moment deficit accumulation rate would be 2.5 +1.3/-0.5 Nm/yr, approximately 50% faster. This is still substantially lower than the estimate of 3.9 x 10^{17} Nm/yr estimated using the method of Kostrov [1974], which does not take into account the specific pattern of shortening, the faults that accommodate it, the elastic structure, or the portion of the strain accumulation that might be accommodated anelastically. Our estimates of cumulative moment accumulation rate are also lower than that of Meade and Hager [2005], which estimated that tectonic strain is accumulating on two faults underlying northern metropolitan Los Angeles that are accruing strain equivalent to a Mw~7.0 earthquake every 200 years each, or a Mw~7.2 earthquake in total, corresponding to a moment deficit accumulation rate of ~4 x 10^{17} Nm/yr. The latter is a regional-scale study with many more faults, and thus necessarily had to prescribe a locking depth of 15 km on most faults and to assume that they extend to the surface. Our results suggest that the picture of interseismic strain accumulation in Los Angeles is substantially more subtle than can be fit to models with prescribed locking depths and becomes yet more subtle when the fact that the Puente Hills and Compton faults are blind is taken into account. Nevertheless, we are able to detect a smaller, but nonzero, strain accumulation rate on the thrust faults, in agreement with the result of Marshall et al [2009]. This suggests that the details of fault geometry and elastic structure are important to consider in estimates of strain accumulation at the local level and therefore at the regional level, as the former figures into the latter.

3.6.4. Comparison with the depth distribution of seismicity

The depth distribution of seismic moment accumulation in the preferred strain accumulation models reproduces the overall shape of the depth distribution of earthquake rates in Los Angeles, particularly in the upper ~10 km (Figure 3.15b). It should be noted that this is not an unequivocal validation of our strain accumulation models; in particular, by counting all earthquakes in the HYS16 catalog that occur within the mesh area, we are comparing strain accumulation on three faults to earthquakes in the volume around the three faults, which may not be entirely rigorous. This comparison can nevertheless be viewed as a “sanity check”; for example, the strain accumulation models would be questionable if they predicted that moment deficit accumulation should be fastest at 20 km depth, or at the surface. The strain accumulation models do not visibly fail this “sanity check”; as such, we keep both on hand for combined use in the assessment of implications for earthquake behavior in the following chapter.

The observation of relatively low earthquake rates in the upper few km of the crust appears to support the assumption that deformation updip of the tips of the Puente Hills and Compton faults may be dominantly anelastic. As shown by the red curve in Figure 3.15b, counting the strain accumulation updip of the tips of the Puente Hills and Compton faults in Model 1 produces a depth distribution of moment deficit accumulation rate that is not consistent with the upward decrease of seismicity towards the surface in the upper few km. It is worth noting that even though these updip extensions run through low-stiffness basin sediments, which might be expected to dampen the seismic moment computed on them, they still overshoot the depth distribution of seismicity. Therefore, at least judging by this model, it seems that the upward decrease in seismicity towards the surface cannot be explained away by near-surface elastic properties – one also needs the Puente Hills and Compton faults to be blind to generate this feature. The depth distribution of earthquake rates, then, seems to point to strain accumulation on a network of faults that are either blind or accruing negligible seismic strain towards the surface.

The two preferred models of strain accumulation predict starkly different depth distributions of moment accumulation below the peak at ~10 km depth: the "smooth" model predicts a smoothly decaying moment accumulation rate distribution down past 20 km depth, while the "iterative" model predicts no strain accumulation below 10 km depth, including none at the depth of the 1987 M=5.9 Whittier Narrows earthquake (Figure 3.15a). The characteristics of strain accumulation below ~10 km depth are likely poorly constrained by the geodetic data. This may not be surprising as 1) model resolution decreases with depth and 2) the faults in Los Angeles, in particular, begin to overlap and merge at depth. Higher-resolution geodetic data is therefore needed to elucidate the nature of strain accumulation at depth in this region. Worth noting, however, is that the Whittier Narrows earthquake occurred on the central Puente Hills Fault at a depth (~13 km) where Model 1 infers low, but nonzero, strain accumulation on the fault (Figure 3.10), and only 2 km above the 95th-percentile depth of seismicity (Figure 3.15b). This is reminiscent of the inferred location of the 2015 M~7.9 Gorkha earthquake at the lower edge of the locked portion of the Main Himalayan Thrust [e.g. Avouac et al, 2015] and the hypothesis that moderate to large earthquakes may nucleate near the base of the seismogenic zone [e.g. Yang and Hauksson, 2013].

The depth distribution of seismicity and interseismic coupling is commonly thought to depend primarily on temperature [e.g. Avouac, 2015]. To evaluate this possibility for Los Angeles, we estimate a geotherm for the Los Angeles area (Figure 3.15b, orange curve) using five measurements of temperature and heat flow in the eastern Los Angeles basin provided by the SMU Heat Flow Database and assuming that heat production decays exponentially with depth [e.g. Tanaka and Ishikawa, 2002]. This is done in a Bayesian framework; details are provided in Appendix 8. The peak of the depth distribution of seismicity, and of seismic moment accumulation rate in the two coupling models, corresponds to a temperature of ~350° C in the estimated geotherm; this is consistent with laboratory measurements on quartzo-feldspathic rocks that show a transition from rate-weakening (stick-slip) to rate-strengthening (creeping) behavior in the temperature range ~300-450° C [e.g. Blanpied et al, 1991]. The two strain accumulation models might thus be seen as respectively consistent with hypotheses that the brittle-ductile transition should occur gradually (model 1) or abruptly (model 2). While the geotherm does not indicate that one model is preferable over the other, it serves as another "sanity check" that suggests that the overall characteristics of the strain accumulation models may be plausible. In any case, it is plausible that increasing temperature is the main reason for the inferred aseismic creep on the deeper extensions of the faults beneath the basin. The resulting distribution of creep and locking contrasts with the example of the Main Himalayan Thrust beneath the Kathmandu basin, for example, on which temperatures are likely <350* C and full interseismic locking is inferred [Ader et al, 2012].

3.6.5. Inferred long-term slip rates as compared to geologic and paleoseismologic rates of slip and uplift

The inferred slip rates on the Sierra Madre, Puente Hills and Compton faults are 4.6, 3.1 and 3.6 mm/yr in Model 1 and 4.3, 2.8 and 3.7 mm/yr in Model 2, respectively. These rates are substantially higher than most estimates from geologic and paleoseismologic studies. On the Sierra Madre, Walls et al [1998] estimated a slip rate of 1-2 mm/yr on the western section of the fault, Tucker and Dolan [2001] estimated a slip rate of 0.6-0.9 mm/yr on the central section, and Rubin et al [1998] inferred ~11 m of total displacement in two paleoearthquakes since ~15 Ka, translating into an average slip rate of ~0.6 mm/yr [Glasscoe et al, 2004]. Meigs et al [2003] estimated a slip rate of 3.5-5.5 mm/yr on the western Sierra Madre based on offset geologic horizons, an estimate we will return to. On the Puente Hills, Bergen et al [2017] inferred a recent slip rate of 1.33 +0.4/-0.2 mm/yr on the western Los Angeles segment; Leon et al [2009] and Myers et al [2003] inferred slip rates of 1.1-1.6 mm/yr (1.4-2.4 mm/yr in an alternate estimate) and 1.5 mm/yr on the Santa Fe Springs segment, respectively; and Shaw et al [2002] and Myers et al

[2003] inferred slip rates of 1.28 mm/yr and 1.5 mm/yr on the Coyote Hills segment, respectively. On the Compton, Shaw and Suppe inferred a slip rate of 1.2 mm/yr from structural constraints and Leon et al [2009] inferred a slip rate of 1.4 mm/yr from paleoseismologic constraints, although the latter study speculated that the true slip rate could be as high as ~2 mm/yr. These slip rates are generally substantially lower than the rates in our models and do not sum to the geodetic contraction rate of 8.5 mm/yr across the basin.

The mystery seems to deepen when one considers uplift and subsidence rates inferred from geodesy: although these are heavily influenced by anthropogenic motions at most sites in the basin [Bawden et al, 2001; Argus et al, 2005] and thus were not usable in the estimation problem here, they are generally close to zero, even at sites in the San Gabriel Mountains that should be minimally contaminated by anthropogenic signals [Hu et al, 2016, fig. 4a]. Exhumation rates in the San Gabriel Mountains are also inferred to be ~1 mm/yr [Blythe et al, 2000]. Meanwhile, our model, by virtue of accommodating ~8.5 mm/yr of contraction via three dipping faults that root into a decollement, predicts several mm/yr of uplift. Although the "blocks" formulation cannot realistically be used to predict vertical motions [e.g. Kanda et al, 2010], the "sheets" formulation can, as it predicts a tilting behavior of fault-separated blocks that may not be irreconcilable with geologic constraints [e.g. Meigs et al, 2003]. The "sheets" model that uses the Mojave stations, predicting a slip rate of 5.2 mm/yr on the Sierra Madre Fault (Figure 3.S35), predicts 5.6 mm/yr of uplift in the San Gabriel Mountains even with the fault accumulating strain. This is much faster than the geodetic uplift rates inferred by Hu et al [2016] and is risible on its face as it predicts that the mountains should achieve an elevation of 5.6 km in one million years. To append this to the question posed by Walls et al [1998], the question is then how one can accommodate ~8 mm/yr of north-south contraction 1) with thrust faults whose geologic slip rates do not sum to that and 2) without generating almost any uplift.

We first address the uplift discrepancy. This can actually be somewhat resolved by considering the forces at play that dislocation theory does not model (in the spirit of the "unspecified asthenospheric motions" postulated by Savage [1983]). Specifically, as the Los Angeles crust overlies a mantle that likely flows on interseismic timescales, isostatic balance dictates that the thrusting of one mass over another via fault slip should be followed by the sinking of the entire body. As argued by Donnellan et al [2001] and Glasscoe et al [2004], over 80% of the crustal shortening and thickening accommodated by the faults in northern Los Angeles should go into the construction of a crustal root beneath the San Gabriel Mountains; less than 20% should be detectable as surface uplift. The ~1 mm/yr exhumation rate inferred by Blythe et al [2000] therefore translates to a crustal thickening rate of ~5.5 mm/yr, which in turn implies a slip rate of ~5.5 mm/yr on the faults accommodating the shortening and thicknening [Donnellan et al, 2001]. Gravity data indicate that the San Gabriel Mountains are isostatically compensated [Hauksson, 2011], perhaps supporting this hypothesis. This is in agreement with the Meigs et al [2003] estimate of 3.5-5.5 mm/yr slip on the Sierra Madre Fault from offset geologic horizons (as argued in that paper), and seismic reflection data indeed support the existence of a crustal root underlying the San Gabriel Mountains whose dimensions imply a shortening and thickening rate as high as ~7 mm/yr [Godfrey et al, 2002]. The uplift rates observed in geodesy might then lag behind even the ~1 mm/yr exhumation rate because the latter rate is partially the result of seismic uplift; the geodetic rates might more likely sample isostatic re-equilibration (sinking) in the interseismic period (perhaps in addition to deep fault creep), consistent with their near-zero values. Seismic studies have also imaged a prominent downwelling in the mantle beneath the San Gabriel Mountains [Humphreys and Hager, 1990; Kohler, 1999], and geodynamic models suggest that this downwelling could exert a ~10 MPa downward suction force on the base of the crust [Fay et al, 2008] that could pull the entire crust down, further decreasing the geodetic uplift rates at the surface. This factor, however, would require that the crust and mantle were not completely decoupled beneath the mountains [Humphreys and Hager, 1990], which is in conflict with the very low coupling we infer on the deep decollement. At any rate, the low uplift rates inferred from geology and geodesy may not be irreconcilable with slip rates of several mm/yr on the thrust faults. This, however, does not explain why slip rates on the Sierra Madre estimated from paleoseismologic studies are ~0.6-2 mm/yr, much lower than the slip rates in our preferred models or invoked by any of the aforementioned arguments. Some hypotheses regarding this discrepancy shall be discussed momentarily, as they may apply to the entire Los Angeles setting.

The slip rate of ~3.6-3.7 mm/yr on the Compton Fault in our strain accumulation models might also be individually reconcilable with the ~1-2 mm/yr slip rate inferred from geologic and paleoseismologic studies through a combination of two factors. First, the Palos Verdes Fault, slipping at 3 mm/yr [McNeilan and Rockwell 1996], might take up some of the shortening that we ascribe to the Compton: the strike-slip faults' potential contribution to the north-south shortening may be at maximum around the Palos Verdes Fault (Figure 3.S14), and removing this "liberal" strike-slip displacement field from the

Argus et al [2005] velocity field before inverting for strain accumulation on thrust faults results in a slip rate of only 2.2 mm/yr on the Compton (Figure 3.S29), closer to the geologic and paleoseismologic rates. Second, the convergence rate relative to the San Gabriel Mountains decreases from ~8.5 mm/yr on offshore islands to ~6 mm/yr in Palos Verdes, and our strain accumulation models essentially assign the Compton to take up all of this shortening. Some portion of this shortening might in reality be taken up by offshore faults; although the aforementioned strike-slip model includes the offshore San Pedro Basin Fault, unmodeled thrust systems might also accommodate it [e.g. Sorlien et al, 2013]. Running the smooth/blocks/wings/CVM* scheme on a dataset that does not include the velocities on islands reduces the Compton slip rate to 2.0 mm/yr (Figure 3.S28), and removing the "liberal" strike-slip displacement field from the no-islands dataset before inverting pushes the Compton slip rate down further to 1.7 mm/yr (Figure 3.S30). These tests suggest that the Compton slip rate may in fact be reconcilable with the geologic and paleoseismologic rates.

Nevertheless, our model-preferred slip rates still sit at or above the top end of estimated values from geologic and paleoseismologic studies on the thrust faults, and in the case of the Sierra Madre they are multiple times larger than paleoseismologic rates. It is worth discussing several factors that could lead to this discrepancy, as they may indeed apply both in Los Angeles and in other settings. The first is that some of the shortening could be accommodated by structures not modeled here. The Sierra Madre Fault may have multiple strands: the Clamshell-Sawpit strand produced the 1991 Sierra Madre earthquake [Hauksson, 1994] and the 1971 San Fernando earthquake may have ruptured two parallel north-dipping strands [Heaton, 1982]. This also includes more localized faults such as the Elysian Park, Verdugo, San Vicente, Walnut Creek, East Montebello Hills, Workman Hill and Peralta Hills Faults [e.g. Marshall et al, 2009] and structures such as a backthrust inferred in the hanging wall of the Puente Hills Fault by Shaw et al [2002] and a multiple-layer thrust system inferred above the Compton Fault in Palos Verdes by Sorlien et al [2013]. Adding any of these structures to the models would likely decrease the long-term slip rates on nearby faults, as the shortening would be more evenly partitioned, but it would be unlikely to change the total moment deficit accumulation rate dramatically, as it would presumably just shift some of the inferred strain accumulation from one fault to another. Denser geodetic coverage of the Los Angeles basin, complete with updated corrections for anthropogenic motions in the geodetic data, will open the door for more complex strain accumulation models than those used here in the future.

Second, fault slip rates could have increased or decreased over time. On the Puente Hills Fault, Myers et al [2003] inferred that a long-term slip rate of ~3 mm/yr on the Santa Fe Springs segment had decreased to 1.3 mm/yr in the Pleistocene, and Bergen et al [2017] inferred that the slip rate on the Los Angeles segment had increased from 0.2 to 1.3 mm/yr. Structural geology arguments also imply that the effective long-term slip rate at a given point on a growing thrust fault may increase with time as the fault propagates through the surrounding medium [S. Barbot, in prep, 2017]. However, these considerations would not help to reconcile the discrepancy between slip rates inferred from geodesy and those inferred from paleoseismology, as the latter should effectively image geologically current slip rates. These arguments also may not apply greatly to the Compton Fault in particular, as the geologic and paleoseismologic rates on it are similar. It should nevertheless be noted that our models, by virtue of imaging interseismic strain accumulation over the period of GPS coverage in Los Angeles, are time-independent. If slip rates have decreased or increased over time on a fault, as suggested by the aforementioned Puente Hills examples, it would therefore not be rigorous to compare our models to an observation such as the total offset on a fault over geologic time.

Third, anelastic deformation of the medium could accommodate the observed north-south shortening, particularly in the soft Los Angeles basin, to a greater extent than that assumed implicitly in our coupling models (in which it is presumed to occur updip of the Puente Hills and Compton faults at their long-term slip rates). Deubendorfer et al [1998], for example, found abundant evidence that off-fault pressure solution creep had participated in the accommodation of tectonic shortening in the Ventura Basin. The fact that sedimentary structures overlying the Compton Fault are cleanly discernable in reflection profiles [Shaw and Suppe, 1996] would seem to favor a system in which deformation is predominantly on-fault. Nevertheless, anelastic deformation may contribute somewhat to the accommodation of north-south shortening.

Fourth, postseismic deformation from past earthquakes could be affecting the interseismic velocity field on the timescale of decades to centuries. The problem with this hypothesis is that postseismic deformation following the Northridge earthquake affected surface velocities for only a few years [Donnellan et al, 1998], and Glasscoe et al [2004] showed that this was the maximum timescale over which postseismic deformation could realistically affect surface velocities in Los Angeles. The last earthquake that could have caused a regional-scale disturbance to geodetic velocities was the 1857 M=7.9 Fort Tejon earthquake; indeed, as shown in theory by Hetland and Hager [2006] and specifically for the 1857 case by Hearn et al [2013], geodetic velocities late in an earthquake cycle should trail the long-term geologic rates, not substantially exceed them as they appear to do in Los Angeles. A simple dislocation model shows that even an ongoing afterslip event featuring 10 mm/yr of slip beneath the 1857 rupture would only produce <1 mm/yr of north-south deformation in Los Angeles (Figure 3.S42). Therefore it is unlikely that postseismic deformation produces shortening across Los Angeles.

Fifth, the paleoearthquakes on the three thrust faults or other past earthquakes on nearby structures, including the 1857 Fort Tejon earthquake, could have triggered long-lasting accelerations or decelerations in long-term slip rates or strain accumulation rates. These stress changes can occur between adjacent sections of the same fault [e.g. Lindsey et al, 2017] or between faults [e.g. Sammis and Smith, 2013]. Although the most recent large earthquake on the Sierra Madre Fault likely predated 8000-10000 BCE [Rubin et al, 1998; Tucker and Dolan, 2001], the most recent event on the Puente Hills Fault could have occurred as recently as 200 years ago [Leon et al, 2007] and either of the most recent two earthquakes on the Compton could have occurred as recently as 700 years ago [Leon et al, 2009]. These earthquakes, along with recent events on neighboring systems, could have potentially affected the picture of strain accumulation imaged here. The exact nature of this effect must remain speculative as it depends heavily on the rupture distributions of the paleoearthquakes, which are themselves speculative.

Finally, some of the observed north-south shortening could be accommodated by shortening beneath the decollement modeled here, for example on undiscovered blind thrust faults such as the source fault of the 1994 Northridge earthquake [e.g. Davis and Namson, 1994] or on a second, deeper decollement [Davis et al, 1989]. Such structures are firmly in the nullspace in our models and are likely to remain so for future geodetic studies of this area.

In closing, it should also be noted that our models assume that the long-term slip rates on the faults are essentially uniform along strike, as the intervening blocks are modeled as rotating about a global Euler pole and the velocity and azimuth of this rotation is nearly constant on the scale of Los Angeles (Figure 3.4). In reality, inferred long-term slip rates have been inferred to vary from west to east along at least the Puente Hills and Sierra Madre faults [e.g. Shaw et al, 2002; Tucker and Dolan, 2001]. Denser geodetic coverage of the north-south shortening, corrected for anthropogenic motions, will open the door for more intricate models of the long-term block motion and strain accumulation. These studies may also expand the picture of strain accumulation beyond the Los Angeles basin to include fault systems and geodetic data in the western Transverse Ranges [e.g. Marshall et al, 2013] and ideally the San Andreas system as a whole. The considerations touched on here may nonetheless prove useful in these future studies.

3.7. Conclusion

We characterize the ways in which the ~8.5 mm/yr of north-south shortening inferred across Los Angeles may be being accommodated by strain accumulation on subsurface faults. We find that the elastic heterogeneity due to the sedimentary fill of the Los Angeles basin has a first-order effect on the estimation problem, and our models for strain accumulation on the Sierra Madre, Puente Hills and Compton faults incorporate techniques and examine assumptions that may be of interest in other studies of interseismic strain accumulation. Based on the wide range of models tested here, we estimate that seismic moment is accumulating on the Sierra Madre, Puente Hills and Compton faults at a rate of 1.7 +1.2/-0.5 x 10^{17} Nm/yr.

3.A. Supporting Information

Appendix 3.1. Details of data preparation

Argus et al [2005] express uncertainties in the GPS velocities as rotated ellipses denoting the 95% confidence regions. For use in the modeling, we approximate the uncertainties in the north and east directions by computing the north/east-axes-aligned bounding boxes of each ellipse (procedure defined in the first posted response on https://stackoverflow.com/questions/87734/how-do-you-calculate-the-axis-aligned-bounding-box-of-an-ellipse). The approximate two-sigma north and east uncertainties are then half the corresponding dimensions of each bounding box (the distances from the center of the box to the edges), so the approximate one-sigma uncertainties, which we use, are then a quarter of these respective dimensions. Most of the error ellipses are nearly circular, so the estimated north and east uncertainties are similar. For the projections of velocities into the N 5° E direction, as shown in several of the figures, uncertainties are half the projections of the ellipses in that direction.

The Argus et al dataset includes velocities at 19 stations in the west Mojave Desert, north of the San Andreas Fault, which could be useful in constraining strain accumulation in Los Angeles as essentially a far-field term on the north side of the problem, provided that the San Andreas can be accounted for. Argus et al subtract their model of strain accumulation on the San Andreas from these stations' velocities but add modeled block motion along the San Andreas (equivalent to the displacement at the modeled slip rates but prescribed from the surface to infinite depth) to their velocities so that they appear to be moving rapidly to the southeast relative to Los Angeles. For limited use in the inversions, we compute the synthetic velocities from the modeled San Andreas block motion and express relative to the San Gabriel Mountains by subtracting the mean synthetic velocity of the stations that are described by Argus et al [2005] as being in the San Gabriel Mountains block (specified in their Table 3) from the total synthetic velocity field. We then subtract these San Gabriel-relative synthetic block motions from the Argus et al velocities at the Mojave stations, yielding approximate velocities relative to the San Gabriel Mountains at these stations without the motion from the San Andreas. As these stations are across the San Andreas and its displacement field from the rest of the problem, their uncertainties then need to include those of the block model. The slip rate on the Mojave section of the San Andreas is 20 ± 4 mm/yr at the 95% confidence level; the approximate one-sigma uncertainties in the synthetic east and north velocities in this model are then 2 sin 295° and 2 cos 295°, respectively, where 295° is the approximate strike of the Mojave section of the

San Andreas. We thus incorporate these estimates into the uncertainties at the Mojave stations.

Appendix 3.2. Details of fault meshing

We base our fault mesh mostly on a remeshing of the CFM5 [Shaw et al, 2015] that is optimized for dislocation modeling [S. Marshall, personal communication, 2016] (Figure 3.S1). In two cases, we use the original CFM5 geometries rather than the Marshall remeshings. First, whereas the CFM5 uses a ~27° dip for the Los Angeles segment of the Puente Hills Fault based on seismic reflection studies [Shaw et al, 2002], the Marshall et al mesh uses a steeper 60° dip as this was found to enable dislocation models (in an elastic halfspace model) to more closely reproduce geologic uplift rates along this segment [Meigs et al, 2008]. We find the seismological evidence for the shallower dip more convincing and thus work from the original CFM5 geometry for this segment. Second, the Marshall et al mesh does not include the offshore San Pedro Basin Fault, so we use the CFM5 mesh for it. We work from the Marshall et al mesh for all other thrust and strike-slip fault segments. While the CFM5 and Marshall et al meshes use triangular fault elements, the solver with which we subsequently compute elastostatic Green's functions requires quadrilateral dislocation sources obeying the Aki-Richards convention (dip direction perpendicular to strike direction), and so we resample the Marshall et al and CFM5 meshes into quadrilateral patches with length and widths of approximately 4.9 km, the median station spacing in the Argus et al [2005] velocity field. (The actual patch lengths and widths vary about this target value as required by the fault geometries).

The CFM5 includes the Lower Elysian Park Fault, a ramp dipping north-northeast beneath the northern Los Angeles basin inferred by Shaw and Suppe [1996], which in the model extends from 10 to ~16 km depth. The CFM5 does not extend this structure northward beneath the San Gabriel Mountains or otherwise include a representation of the decollement inferred there by Fuis et al [2001]. Importantly, the Marshall et al remeshing extends several of the deeper-reaching faults in the CFM5 to 27.5 km depth to simulate deformation in the lower crust, a modification originating in Cooke and Marshall [2006]. The Lower Elysian Park ramp is extended further northeast and downward to 27.5 km depth beneath the San Gabriel Mountains, and the Sierra Madre Fault and part of the Puente Hills Fault are extended downward to ramp off of it. Seismic reflection data suggest that the dip of the inferred decollement shallows as it extends northward beneath the mountains, reaching a bottom depth of ~23 km [Ryberg and Fuis, 1998] or ~20 km [Fuis et al, 2001] near the San Andreas. However, the inversions for strain accumulation are not sensitive to slip on the deepest part of the decollement (Figure 3.S17), and so we work from the geometrically self-consistent realization of the decollement and lower Sierra Madre and Puente Hills faults in the Marshall et al remeshing. This mesh thus forms a nearly continuous model of a fold-and-thrust belt.

Appendix 3.3. Preparation and use of the CVM*

We use GAMRA to compute Green's functions from the CVM* in a volume extending 192 km west, east, north and south from 118° W, 34° N and from the surface to 128 km depth. This conservatively large grid is necessitated by the use of zero-displacement boundary conditions at the edges of the model; benchmarks of dislocations in homogeneous elastic models computed in GAMRA show that Green's functions computed on this grid are within 5% of the Okada [1985] analytic formulation for a variety of fault and station orientations, whereas the use of a smaller grid causes the boundary conditions to bring the displacement solution toward zero too close to the region of data coverage.

The CVM-H15.1 includes a small "high-resolution" volume, encompassing the Los Angeles region down to 15 km depth, which provides V_p, V_s and ρ at 100 m vertical and 250 m horizontal resolution and overprints the "low-resolution" representation in this region. The transition between the high-resolution and low-resolution models on the edges of this region contains artificial steps in the values of the parameters [Shaw et al 2015, fig. 8, lower left panel] because the method of smoothing between the two models is a topic of ongoing development; as such, we remove the high-resolution volume by artificially moving it outside the model [A. Plesch, personal communication, 2016]. The distributions of V_p, V_s, and ρ in the Los Angeles basin do not differ greatly between the high-resolution and low-resolution model, and we find that Green's functions computed with models the high-resolution region are nearly identical to those without (Figure 3.S4). The CVM-H15.1 also includes a "V_{s30}" layer in the upper 350 m (principally for use in near-surface geophysical studies) that can be superimposed on the model in the user interface. We find that the addition of the V_{s30} layer also has almost no effect on computed Green's functions (Figure 3.S4). These findings are in contrast with those from simulations of seismic shaking, which find that the variant of the CVM used has a strong effect on the simulated ground motion [e.g. Taborda and Bielak, 2014]. Cattin et al [1999, their fig. 5] found that, in models of a low-stiffness near-surface layer overlying an elastic substrate, the amplification is not heavily different whether the layer is 1% or 5% as stiff as the substrate, as the amplification by the near-surface layer approaches ~50% asymptotically. The low dependence of the Green's functions on details of the CVM is consistent with this. The elastic model we develop here uses neither the high-resolution nor the V_{s30} component.

The CVM-H15.1 includes water, whose very small shear modulus causes problems in elastostatic modeling because contrasts between the shear moduli of land and water become very large. We thus set the material at all points labeled as water in the CVM-H15.1 to be a soft material whose elastic parameters λ and μ are respectively 2.93e+10 and 2.1e+10, the median λ and μ of all elements labeled "basin" in the CVM-H15.1. This modification should not have much effect on the computed Green's functions because 1) the water is relatively shallow in the offshore region compared to the depth of faults and the vertical dimension of the grid and 2) there is no data in the water.

We found in addition that a few very large contrasts in elastic parameters over small distances on the edge of the basin (the largest a factor-of-580 drop in shear modulus over 1 km in West Hollywood) caused numerical difficulties in the computation of Green's functions, necessitating the creation of a smoothing function that we applied to the material model. The smoothing function finds all horizontal and vertical contrasts in shear modulus between adjacent cells that exceed a prescribed threshold value and changes the two values μ_1^{old} and μ_2^{old} comprising each contrast to two values μ_1^{new} and μ_2^{new} by

$$\mu_1^{new} = (\mu_1^{old})^{99/100} (\mu_2^{old})^{1/100} \text{ and} \quad [3.A1.1]$$
$$\mu_2^{new} = (\mu_1^{old})^{1/100} (\mu_2^{old})^{99/100}, \quad [3.A1.2]$$

essentially an extremely gentle version of geometric mean smoothing (which we deemed more appropriate than arithmetic mean smoothing for the order-of-magnitude contrasts in elastic parameters featured here). Both Lame parameters are smoothed in this way across a given contrast for self-consistency. This 1D procedure is applied simultaneously to all contrasts in the vertical direction in the material model that exceed the threshold value (which are generally most of them), then all such contrasts in the north direction (which are most of the others, mainly a few large contrasts between shoreline sediments and Transverse Ranges crust along the east-west coastline of the Santa Monica Mountains) and then the east direction; the procedure is then repeated iteratively (applied to all remaining contrasts in each iteration) until no contrasts in μ exceed the threshold value. The gentleness of the smoothing operator (for which the aforementioned material contrast in West Hollywood required dozens of iterations) ensures that its 1D nature and the order of directions are not important. To ensure that the smoother had the minimal possible effect on the CVM*, we determined the threshold value (25) by running an extreme model where the Compton, Puente Hills, and Sierra Madre faults and the decollement are all slipping at once and then finding the highest threshold value for which the computation of the Green's function (barely) converged to a solution. Only approximately 1,000 contrasts in shear modulus exceed the threshold value of 25 out of approximately 23,000,000 grid points, and so we are confident that the smoother has a negligible effect on the Green's functions apart from assisting with computational stability.

Appendix 3.4. Additions to the fault mesh required by the backslip method

Steady-state motion on a (planar) fault only produces a step function in velocity at the surface if the fault 1) breaks the surface; 2) extends continuously down dip from the surface to infinite depth (practically, into the model nullspace) and 3) extends along strike in both directions semi-infinitely (practically, into the model nullspace on each side). Therefore, to characterize the long-term motion across each fault with a step function in the plate-scale convergence velocity, as done in the "blocks" variant of the backslip framework, technically requires that the Sierra Madre, Puente Hills and Compton faults all have these characteristics, which they do not. To ensure that the models are as physically self-consistent as possible within this framework, we make three sets of additions to the fault mesh and then carefully handle the way these additions slip in the models.

First, the Puente Hills and Compton faults are blind. Here, we make use of the fact that a fault with a completely locked upper section produces the same instantaneous surface displacement field as a fault with a nonexistent upper section. Therefore, a blind thrust fault can be modeled within the "blocks" variant by artificially projecting the fault to the surface and enforcing that the surface projection is slipping backwards (undergoing normal slip) in the plate-scale convergence direction at a certain slip rate that exactly cancels out the horizontal step in the convergence velocity at the projection's surface break. This slip rate is the step in the convergence rate divided by the cosine of the fault projection's dip, split into dip slip and strike slip on the projection as per its obliquity to the convergence direction. The backslip on the surface projection is then not included in the subsequent estimate of strain accumulation. We thus project the blind Puente Hills and Compton faults to the surface, creating an artificial upper section on each fault (Figure 3.S15, 3.S16). The surface projection of the Puente Hills Fault is a geometrical continuation of the mesh for the main fault in the up-dip direction. The updip projection of the Compton Fault may not be imaginary: Broderick et al [2008] inferred a large shallowly dipping thrust fault beneath Santa Monica Bay, Sorlien et al [2013] inferred a system-level detachment system further to the south based on geologically inferred tilting of the Palos Verdes Peninsula, and Shaw and Suppe [1996] proposed that the Palos Verdes Fault may be a roof thrust that roots into a flat detachment at ~5 km depth. We model the surface projection of the Compton Fault as an upward continuation of the dipping fault in Santa Monica Bay that transitions to a ramp-flat-ramp structure further south with the flat at ~5 km depth, roughly consistent with all three models from the literature. The columns of **G** corresponding to the long-term slip rates on the Puente Hills and Compton faults are then the Heaviside step functions over the fault traces plus the elastostatic Green's functions for normal slip on the upper projections, with the latter scaled by the slip rates enforced on the projections.

The second addition concerns the continuity of the fault mesh in the down-dip direction. First, the Compton Fault and Lower Elysian Park ramp are not connected in the CFM5 or Marshall meshes; the Compton-Lower Elysian Park system is essentially modeled as a ramp-flat-ramp system with the flat missing. We add this flat to the model to connect the two at ~10.5 km depth (Figure 3.5, center), as inferred by Shaw and Suppe [1996]. We also add a flat at 27.5 km depth at the base of the Lower Elysian Park ramp that extends to the surface trace of the San Andreas Fault (Figure 3.5, top), consistent with the interpretation of Fuis et al [2001] that the decollement extends to the San Andreas. Finally, the CFM5 Los Angeles segment of the Puente Hills Fault is not connected to the Lower Elysian Park Fault beneath it, so we add a small connection between the two at ~15-20 km depth; this is unlikely to have much impact on the inversions.

The final addition concerns the along-strike dimensions of the faults. To fit geodetic data to backslip on a confined fault plus a step in convergence velocity across the fault's surface break, blind or not, is to erroneously model the fault as infinite along strike and freely slipping except on the section where backslip is prescribed. The "blocks" variant therefore requires that we model the faults as having "wings," semi-infinite continuations extending perpendicular to the N 5° E convergence direction in both directions away from Los Angeles (Figure 3.S15, 3.S16). We use these wings in two alternate formulations of strain accumulation, as hinted at in the main text. In the "no-wings" formulation, strain accumulation is assumed to be confined to the faults beneath Los Angeles; the wings are therefore enforced to have normal slip at a rate equal to the step in the convergence velocity divided by the cosine of the wings' dips, so as to cancel out the step function at the imaginary surface break west and east of Los Angeles (Figure 3.S15). As with the artificial projections of the Puente Hills and Compton faults, the Green's functions from this normal slip (computed within the CVM*) are then scaled and added to the columns in **G** that describe the step functions. In the "wings" formulation, we allow strain to accumulate on the wings: the Green's functions from backslip on them are included as additional columns in **G** and they enforced to slip backwards at rates that are consistent with the nearest edges of the real faults (Figure 3.S15). The strain accumulation on the wings is then not counted in the analysis, as 1) it is technically infinite and 2) we are principally interested in the faults underlying Los Angeles, and the wings are simply a device to potentially improve the characterization of strain accumulation on them.

Appendix 3.5. Regularizations in the "smooth" inversion method

We enforce spatially variable smoothing in the "smooth" inversion method as per the method of Ortega [2013]. The overall weight of this spatially variable smoothing is chosen as the point of maximum positive curvature of a modified version of the "L-curve." As described by Aster [2012], the "L-curve" for second-order Tikhonov regularization generally pits the misfit norm $||(\mathbf{d} - \mathbf{Gm})/\boldsymbol{\sigma}||_2$ on the x-axis against the norm of the model roughness $||\Delta^2\mathbf{m}_{\text{backslip}}||_2$ on the y-axis in log-log space. (Note that some authors do not take the square root of either [e.g. Segall and Harris 1987], but this is identical in a log-log plot as it is equivalent to multiplying the x and y values both by 2.) Due to the inequality constraints also used in the inversions, we cannot get close to a perfect fit to the data, and so the misfit norm does not span several orders of magnitude. We therefore use a modified L-curve where the abscissa is not the absolute misfit norm but rather the misfit norm minus that of a model with zero smoothing, which in practice allows the abscissa to span multiple orders of magnitude, more closely approaching the purpose of the L-curve. The model roughness norm in our L-curve, $||\mathbf{S}^{-1/2}\Delta^2\mathbf{m}_{\text{backslip}}||$, also includes the sensitivity modulation. These two modifications allow the L-curve to more closely reflect the true importance of the smoothing in the inversions.

In the inversions where we substitute in Green's functions computed in an elastic halfspace for those computed in the CVM*, we keep the regularization identical to that used in the inversions with the CVM*; the **G** used in the sensitivity $\mathbf{G}^{\mathrm{T}}\mathbf{G}$ is the **G** computed with the CVM* and the overall weight of smoothing is carried over from the corresponding inversion that uses the CVM*.

Appendix 3.6. Resolving power of the smooth/blocks/wings/CVM* inversion method

The workhorse inversion scheme in much of this study uses the “smooth” inversion method and features Green’s functions from the “blocks” variant of the backslip framework and the “wings” formulation, both computed within the CVM*. We assess the resolving power of this method in several ways. First, we compute two pairs of data and model resolution matrices (Figure 3.S18). In usage here, $\mathbf{G}_{\mathrm{steps}}$ is the portion of $\mathbf{G}$ featuring the Green’s functions corresponding to the rigid-body rotation term and the three steps in the convergence velocity, one over each fault; $\mathbf{G}_{\mathrm{backslip}}$ is the portion of $\mathbf{G}$ featuring the Green’s functions from backslip on the patches of the faults and wings. The first pair of resolution matrices expresses the stations’ resolving power of the steps and the ability of the steps to be resolved by the data, which following Aster [2012] are respectively $\mathbf{N}_{\mathrm{steps}} = \mathbf{G}_{\mathrm{steps}}\, \mathbf{G}^{\#}_{\mathrm{steps}}$ and $\mathbf{R}_{\mathrm{steps}} = \mathbf{G}^{\#}_{\mathrm{steps}}\, \mathbf{G}_{\mathrm{steps}}$, where

$$\mathbf{G}^{\#}_{\mathrm{steps}} = (\mathbf{G}_{\mathrm{steps}}^{\mathrm{T}}\, \mathbf{C}_{\mathbf{d}}^{\mathbf{-1}}\, \mathbf{G}_{\mathrm{steps}})^{-1}\, \mathbf{G}_{\mathrm{steps}}^{\mathrm{T}}. \qquad [3.A2]$$

Here $\mathbf{C}_{\mathbf{d}}$ is the diagonal matrix containing the squared uncertainties on the Argus et al [2005] velocities at the stations overlying the mesh as computed in Appendix 1. The second pair expresses the stations’ resolving power of the backslip rates on the faults and the ability of the backslip rates to be resolved by the data, respectively $\mathbf{N}_{\mathrm{backslip}} = \mathbf{G}_{\mathrm{backslip}}\, \mathbf{G}^{\#}_{\mathrm{backslip}}$ and $\mathbf{R}_{\mathrm{backslip}} = \mathbf{G}^{\#}_{\mathrm{backslip}}\, \mathbf{G}_{\mathrm{backslip}}$, where

$$\mathbf{G}^{\#}_{\mathrm{backslip}} = (\mathbf{G}_{\mathrm{backslip}}^{\mathrm{T}}\, \mathbf{C}_{\mathbf{d}}^{\mathbf{-1}}\, \mathbf{G}_{\mathrm{backslip}} + \lambda \mathbf{S}^{-1/2}\Delta^{2})^{-1}\, \mathbf{G}_{\mathrm{backslip}}^{\mathrm{T}}. \qquad [3.A3]$$

Here λ is the overall weight of smoothing that is used in the main smooth/blocks/wings/CVM* inversion. These formulations of the resolution do not take into account the enforcement that the backslip rates cannot exceed the long-term slip rates, or the enforcement of nonnegativity or of zero backslip at the base of the model; as such, they understate the actual resolving power of the inversion scheme (making it seem more ambiguous than it is with those constraints). Nevertheless, they are worth using to gain a sense of the relative resolving power of different components of the technique. Figure 3.S18 shows the diagonal entries of these four matrices. As might be expected, the steps in the convergence rate and the uppermost patches are the best-resolved parts of the model, the steps in the convergence rate are best resolved by stations close to overlying them, and the backslip is only well resolved by onshore stations.

Appendix 7. Tests of the sensitivity of Model 1 to certain aspects of the data

It is instrumental to assess the sensitivity of the inversions to certain portions of the GPS velocity field, in particular the effect of including the velocities on offshore islands, which add ~2 mm/yr to the total convergence rate. We therefore invert for strain accumulation in the smooth/blocks/wings/CVM* model using only onshore stations. There is less overall shortening across the Compton Fault in this dataset, and as might be expected, the main effect is that the weighted mean inferred long-term slip rate on the Compton drops to ~2.2 mm/yr from ~3.6 mm/yr in Model 1 (Figure 3.S28). The geologically and paleoseismologically inferred slip rates on the Compton are respectively 1.2-1.4 mm/yr [Shaw and Suppe, 1996; Leon et al, 2009], although the latter study discussed the possibility of a rate as high as 2 mm/yr [Leon et al, 2009]. The slip rate inferred in this no-islands inversion is comparable to this, and it appears that the higher slip rate in our first preferred model is a product of fitting the faster offshore velocities. Notably, however, the inferred strain accumulation in the no-islands model is nearly identical to Model 1, with moderate coupling inferred on the upper Compton, similar slip rates and strain accumulation patterns on the other faults, and a weighted mean moment deficit accumulation rate of 2.3 x 10^{17} Nm/yr, very similar to the 2.4 x 10^{17} Nm/yr in Model 1 (Figure 3.S28).

Another important consideration is whether the strain accumulation model is compatible with interseismic velocities to the north of the problem in the Mojave Desert. The inclusion of the offshore stations affects the inferred slip rate on the Compton, the closest fault to those offshore stations; the inclusion of stations to the north might analogously be expected to affect the inferred slip rate on the Sierra Madre Fault in particular, and perhaps with it the overall model of strain accumulation. The Argus et al [2005] velocities at the Mojave stations include long-term motion on the San Andreas [their fig. 1]; we estimate and remove this long-term motion to express their velocities relative to the San Gabriel Mountains like the rest of the dataset (Appendix 1). We append the corrected velocities at eight stations overlying the northward projection of the decollement to the 58 stations used in the preferred model, then perform the smooth/blocks/wings/CVM* inversion on the enhanced dataset. We find that including the Mojave stations in the inversion has almost no effect on the inferred model of strain accumulation, with a weighted mean moment deficit accumulation rate of 2.3 x 10^{17} Nm/yr (figure not shown). The weighted mean long-term slip rate on the Sierra Madre Fault changes only from 4.6 mm/yr in Model 1 to 4.7 mm/yr and the slip rates on the Puente Hills and Compton are identical to those in Model 1.

Another factor to consider is the effect of the strike-slip faults: the previous modeling showed that they could contribute up to ~2 mm/yr of the north-south convergence across Los Angeles (Figure 3.S14), and it stands to reason that accounting for them might change the inferred pattern of strain accumulation on the thrust faults. To assess this, we take the Argus et al [2005] velocities at the regular 58 stations overlying the mesh and on islands and subtract the synthetic displacement field from the previously discussed model where the strike-slip faults creep at their UCERF3 “geologic” slip rates between ~5 and 75 km depth (Figure 3.S14), then run the smooth/blocks/wings/CVM* inversion on this modified dataset. We find that accounting for the strike-slip faults has only a minimal effect on the inferred strain accumulation, with a weighted mean moment deficit accumulation rate of 2.3 x 10^{17} Nm/yr (Figure 3.S29). Similar to not using the data from the islands, the principal effect of removing the modeled strike-slip displacement field is to lower the weighted mean inferred long-term slip rate on the Compton Fault to 2.0 mm/yr, closer to the paleoseismologically inferred rate. The largest perturbation to the velocity field in the strike-slip model is associated with the Palos Verdes Fault (Figure 3.S14), as it has the fastest inferred geologic slip rate of any of the strike-slip faults at 3 mm/yr [McNeilan and Rockwell, 1996]. The effect of accounting for the strike-slip faults is therefore mostly to subtract some of the north-south shortening in the southern part of Los Angeles, which is otherwise taken up by the Compton Fault in the models. It is therefore perhaps not surprising that the largest effect is to decrease the Compton Fault’s slip rate and that the effect on the inferred strain accumulation on the Puente Hills and Sierra Madre Faults is limited (Figure 3.S29).

We also run a model in which we both subtract the strike-slip displacement field from the data a priori and also exclude the data on islands. This might be expected to decrease the slip rate on the Compton further, and this is indeed the result, with the weighted mean long-term slip rate dropping to 1.7 mm/yr (Figure 3.S30), within range of the geologic and paleoseismologic rates. Even with both of these perturbations simultaneously, the strain accumulation pattern is virtually unchanged from the first preferred model, with a weighted mean moment deficit accumulation rate of 2.6 x 10^{17} Nm/yr. (The slight increase over the preferred model occurs because the overall weight of smoothing in this model is lower, as each model is fit to a different overall weight of smoothing from its own L-curve. This nonlinearity, then, makes the apparent insensitivity of the strain accumulation to the various perturbations modeled all the more encouraging.) The smooth/blocks/wings/CVM* scheme and the first preferred model thus appear to be insensitive to various perturbations and factors to account for.

Appendix 8. Estimation of a geotherm for Los Angeles

The SMU Heat Flow Database (http://geothermal.smu.edu/gtda/) provides four borehole measurements of temperature from the eastern Los Angeles basin at depths ranging from 1.2 to 2.7 km, as well as one borehole measurement of heat flow (73 ± 2) and thermal conductivity (2.09 ± 0.07) at 3.223 km depth. Assuming that heat flow decays exponentially with depth [e.g. Tanaka and Ishikawa, 2002], the measurement of heat flow at 3.223 km depth can be extrapolated to an estimate of surface heat flow as

$$q_s = (q(z = 3.223 \text{ km}) - q_m)/(\exp(-3.223/h)) + q_m, \qquad [3.A4]$$

where q_m is a background heat flow rate and h is the characteristic length scale of the heat production's exponential decay with depth. Then the output surface heat flow value, in concert with the same q_m and h, can be used to compute the temperature at any depth,

$$T(z) = T_s + q_m z/k + (q_s - q_m)/k*h*(1 - \exp(-z/h)), \qquad [3.A5]$$

where T_s is the surface temperature (provided at the first four boreholes) and k is the thermal conductivity. Assuming Gaussian uncertainties on the heat flow and thermal conductivity, varying q_m uniformly from 20 to 40, and varying h uniformly from 5 to 15 km, we compute a large suite of geotherms. We then compute each geotherm's normalized chi-squared misfit (X^2/N) to the four borehole measurements of temperature between 1.2 and 2.7 km depth and weight each geotherm by the inverse exponential of its chi-squared misfit, as done with the jackknife models in the "smooth" inversion method for strain accumulation. We then use these weighted geotherms to estimate the weighted mean and 16^{th} and 84^{th} percentile temperatures at each depth, yielding the geotherm in Figure 3.15b.

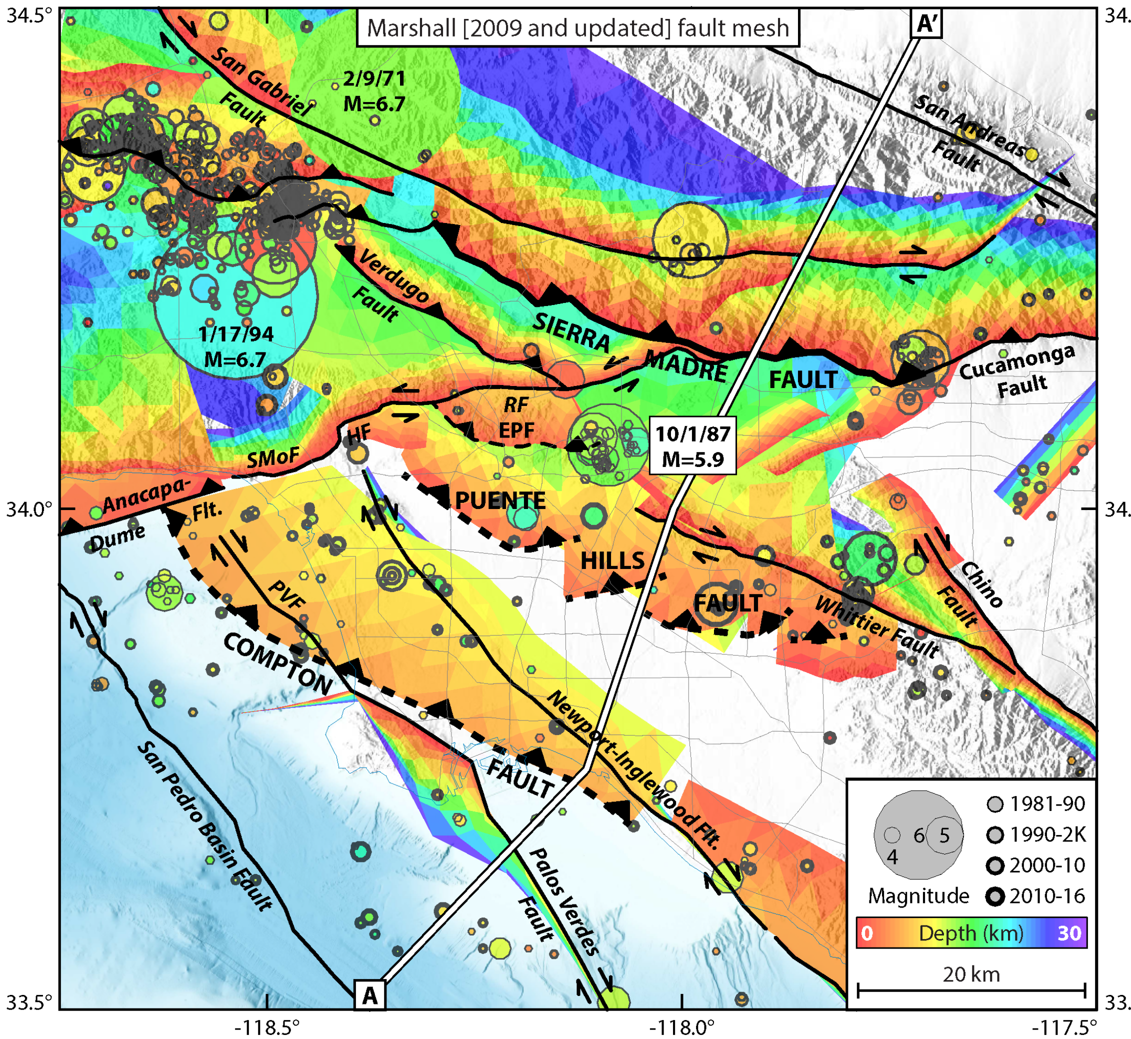

Figure 3.S1. Marshall et al [2009 and updated] triangular mesh of fault geometries (the main basis for the quadrilateral meshes of thrust fault geometries used in this study), colored by depth, and relocated M≥3.5 earthquakes, 1932-2016, scaled by magnitude and shaded grayscale by year. 1932-1980 locations are from SCEDC catalog; 1971 San Fernando earthquake hypocentral depth and magnitude are from Heaton [1982]); 1981-2016 locations are from Hauksson et al [2012 and updated].

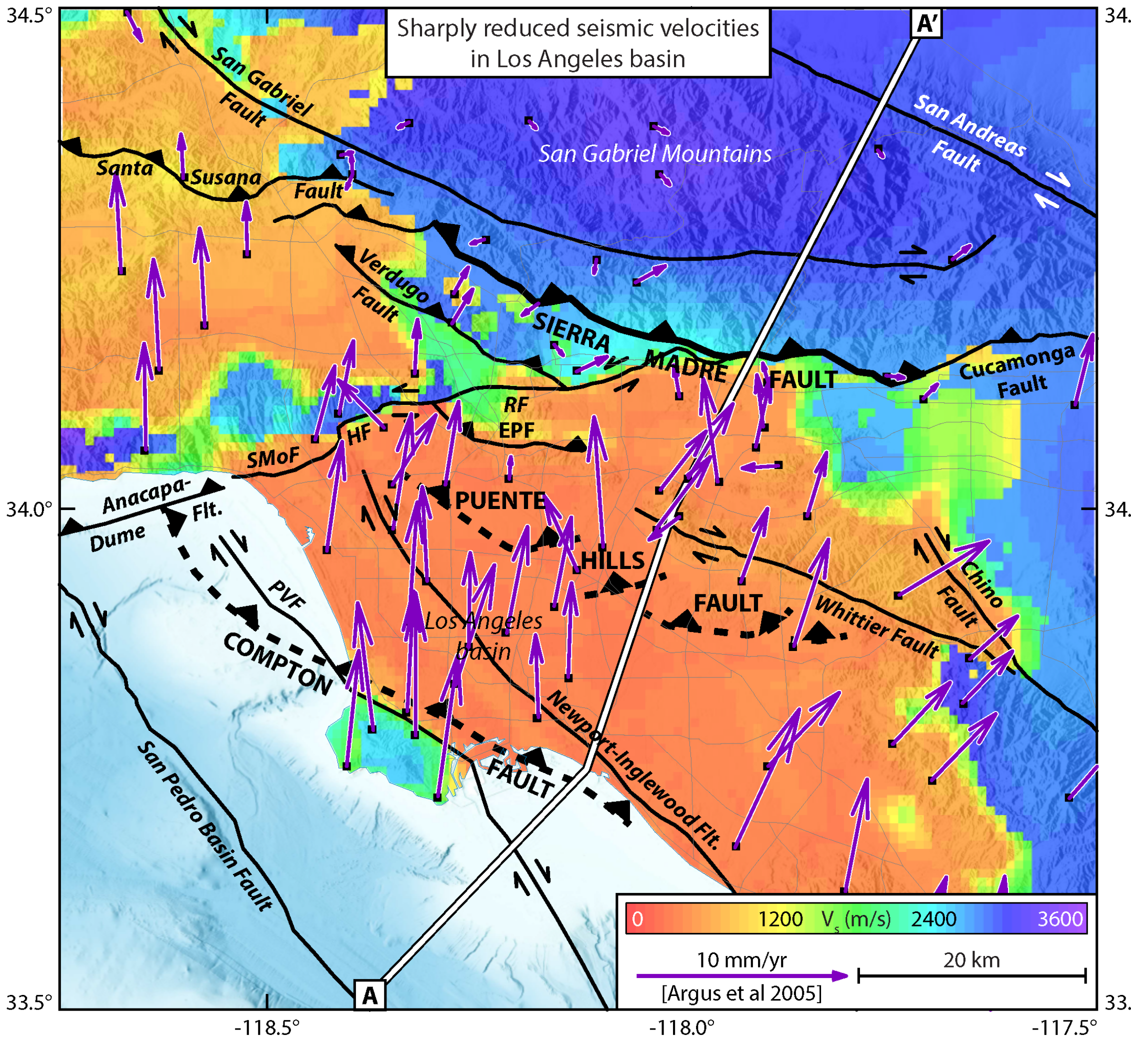

Figure 3.S2. Lateral distribution of the shear-wave velocity V_s at 100 m depth in the SCEC Community Velocity Model, Harvard 15.1 [Shaw et al 2015].

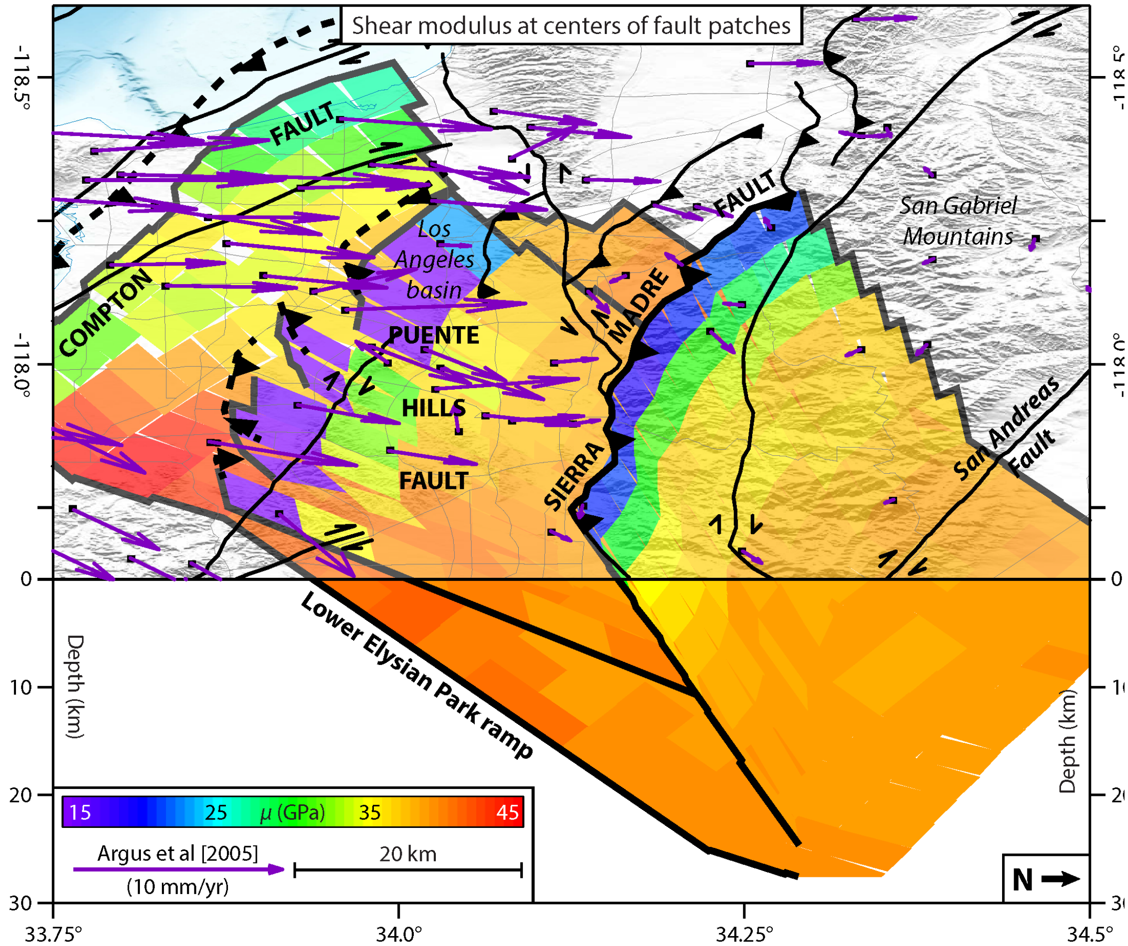

Figure 3.S3. Interpolated value of the shear modulus μ in the CVM* at the center of each patch in the mesh of the three major thrust faults.

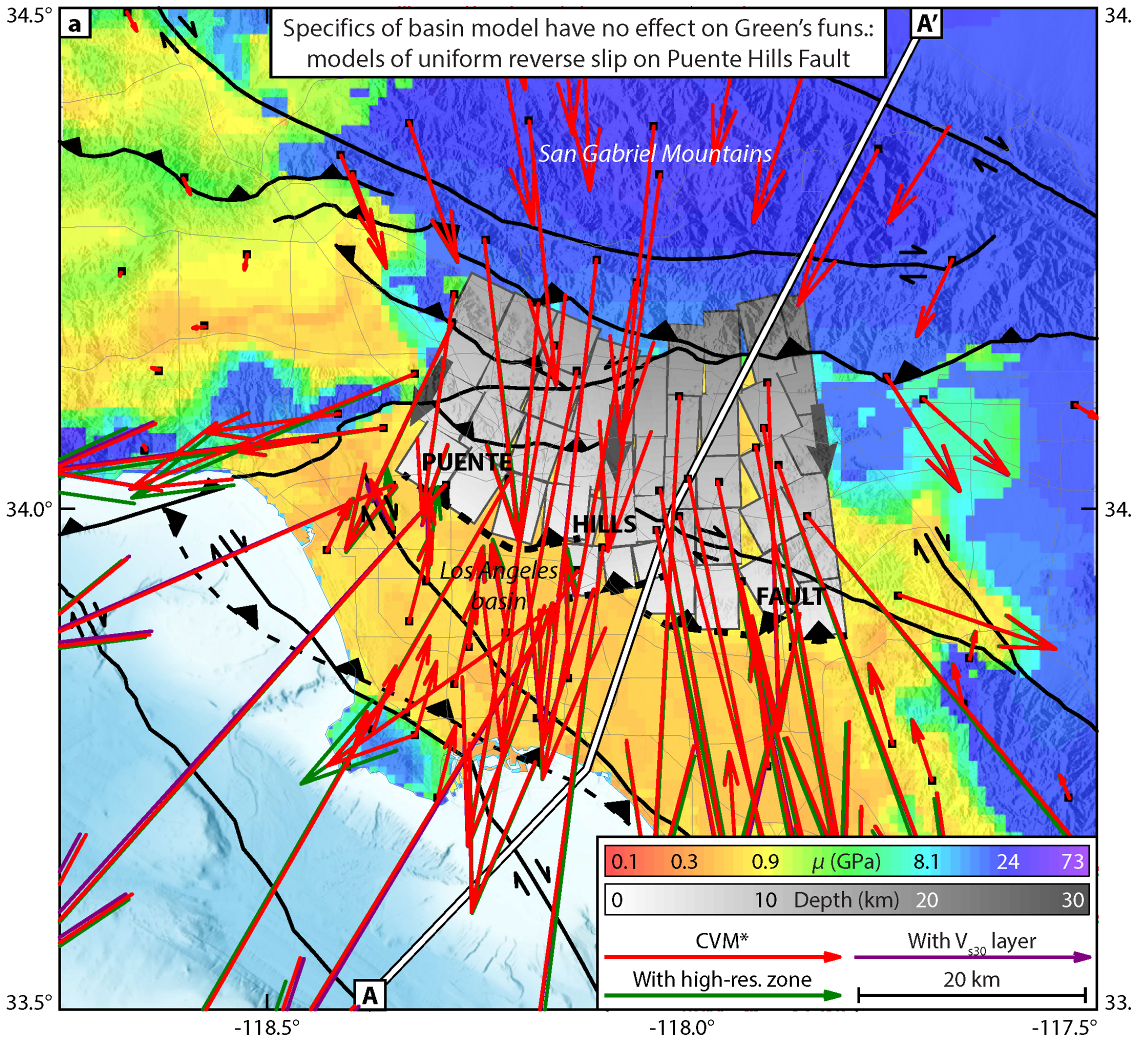

Figure 3.S4. Details of the sedimentary basin model do not affect the elastostatic Green's functions, as demonstrated here with models of uniform reverse slip on the Puente Hills Fault in three alternate basin models provided in Shaw et al [2015]. Red arrows are surface velocities at GPS stations computed with the CVM*; they are the red arrows in Figure 3.7 with larger scaling. Purple arrows are surface velocities at GPS stations in a basin model featuring a "V_{s30}" layer in the upper 350 m. Colored surface is the distribution of the shear modulus μ at 100 m depth in this model; note the higher values of μ in the basin than in the model used in this study (Figure 3.6). Green arrows are surface velocities in a basin model that features a high-resolution ("HR") region in the basin (material model not plotted here). The edges of the HR region, where the model transitions to low-resolution ("LR") coverage, feature artificial transitions in V_p, V_s and ρ because the method of smoothing between the HR and LR regions is a topic of ongoing development; as such, we do not use the HR region in this study. The three alternate basin models produce nearly indistinguishable Green's functions. Fault mesh is shaded grayscale by depth.

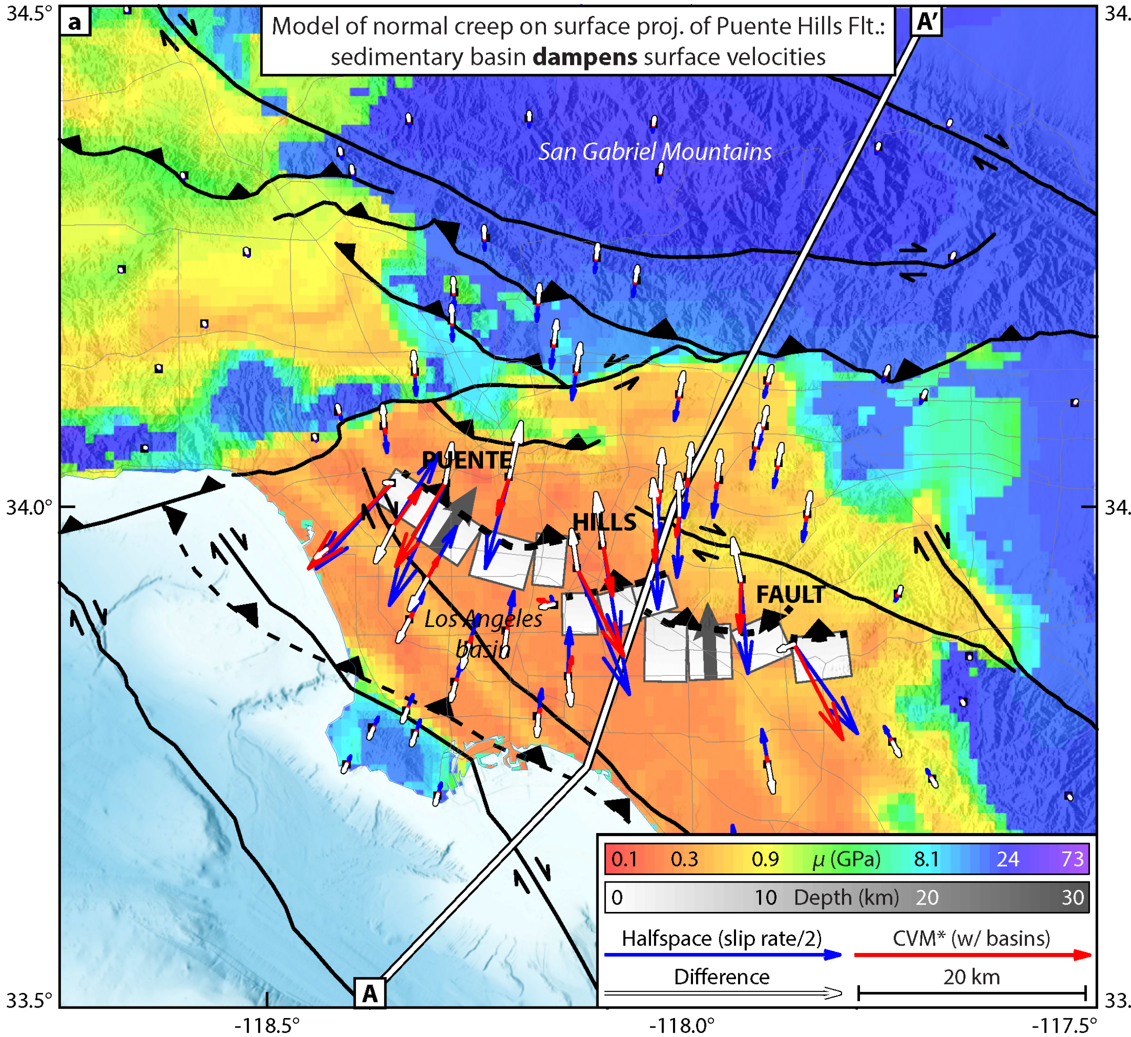

Figure 3.S5. The Los Angeles basin dampens elastostatic Green's functions for slip on faults within the basin, as shown here with a model of uniform normal slip (backslip) on the surface projection of the blind Puente Hills Fault (a modeling element required by the backslip method as explained in Appendix 3.4). Blue arrows are resulting surface velocities at Argus et al [2005] GPS stations assuming an elastic halfspace. Red arrows are surface velocities using the CVM*. White arrows are the difference between the two sets of synthetic velocities. Background colormap is the distribution of the shear modulus μ at 100 m depth in the CVM*. Fault mesh is shaded grayscale by depth.

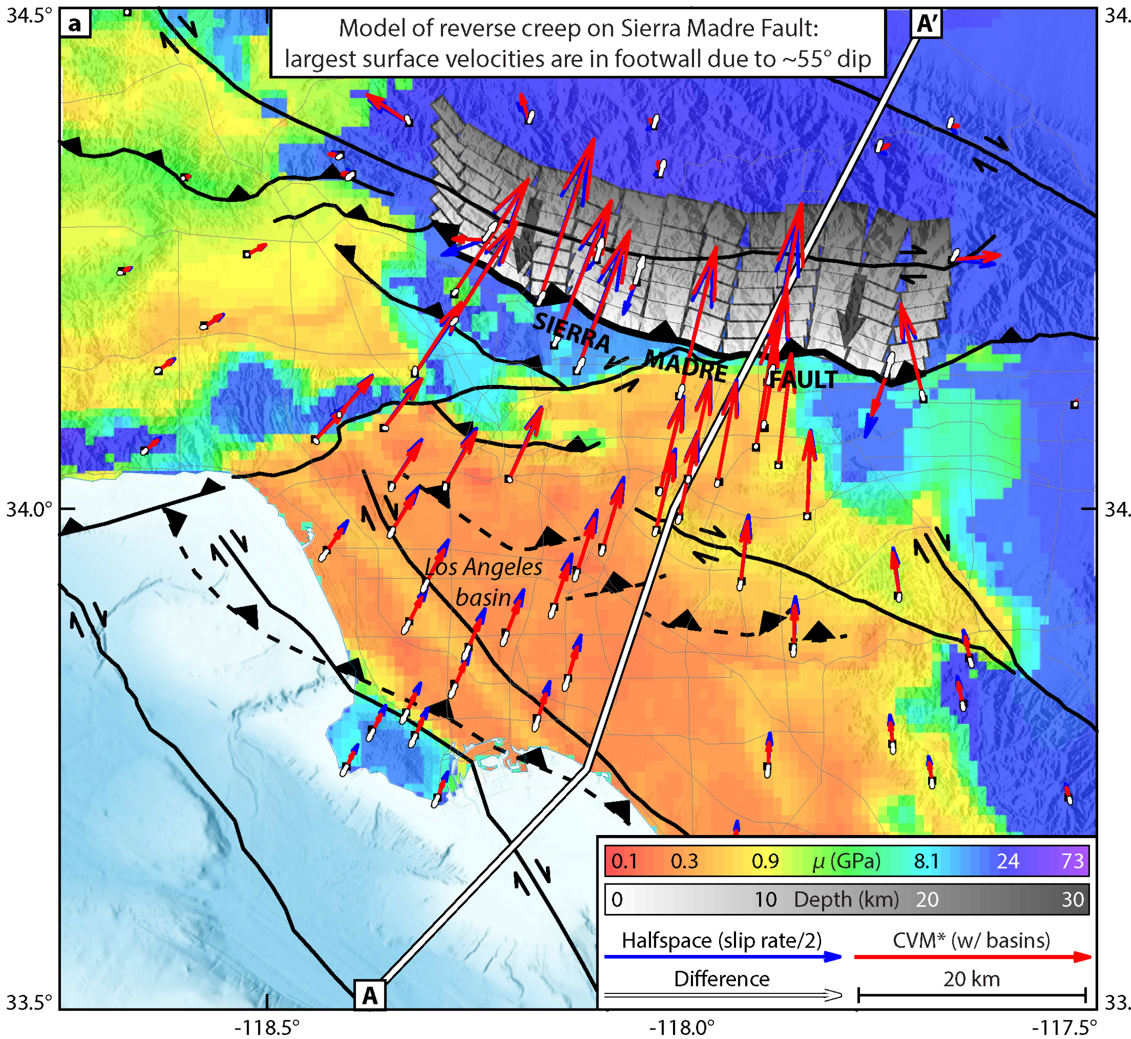

Figure 3.S6. Due to the steep (~55*) inferred dip of the Sierra Madre fault, surface displacements resulting from slip on the fault are concentrated in the footwall rather than the hanging wall, as demonstrated here with a model of uniform reverse slip on the fault. The basin's effect on the Green's functions is limited. Background colormap is the distribution of the shear modulus μ at 100 m depth in the CVM*. Fault mesh is shaded grayscale by depth.

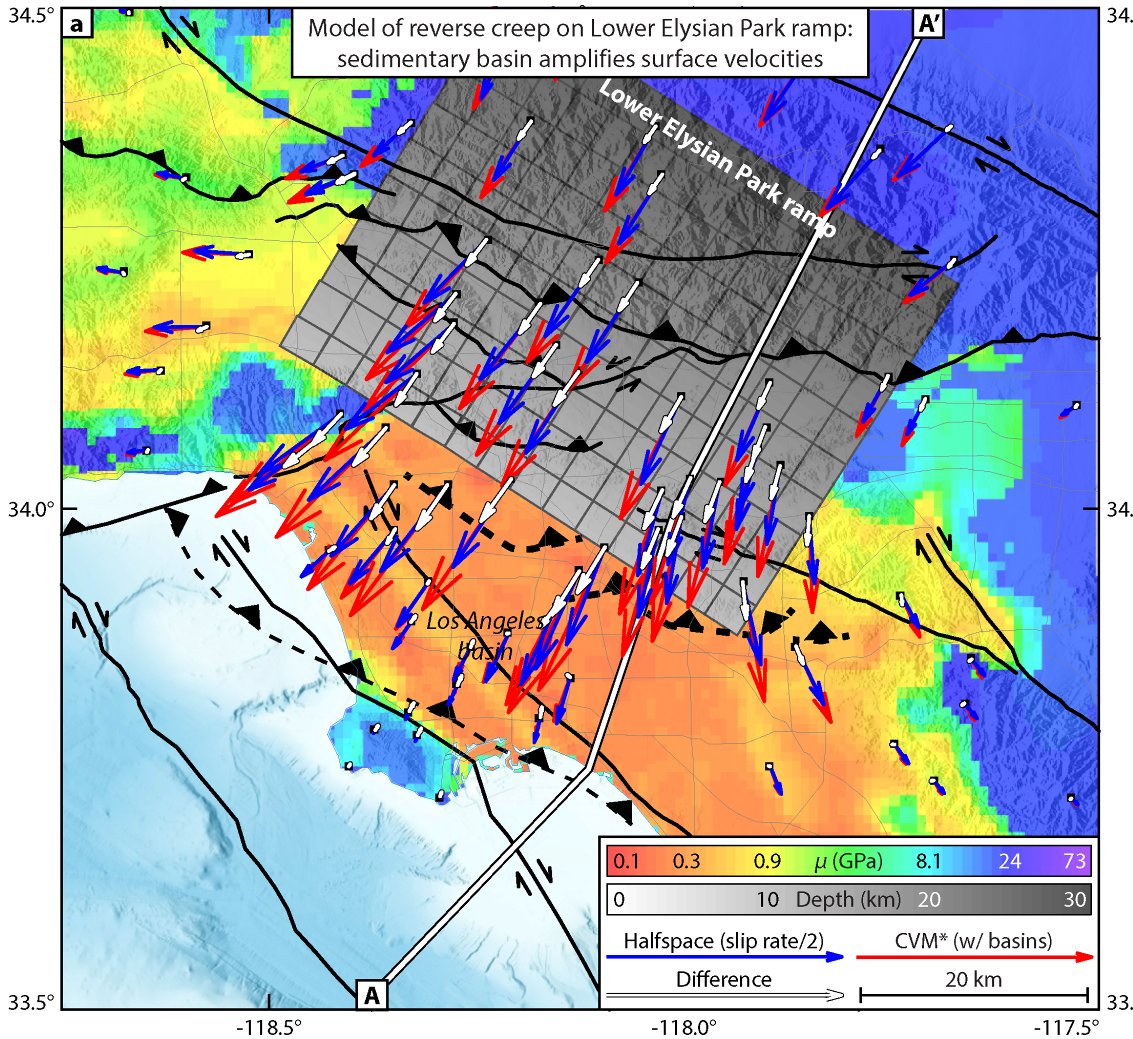

Figure 3.S7. The sedimentary basin amplifies elastostatic Green's functions for slip on the Lower Elysian Park ramp, as demonstrated here with a model of uniform reverse slip on the fault. Background colormap is the distribution of the shear modulus μ at 100 m depth in the CVM*. Fault mesh is shaded grayscale by depth.

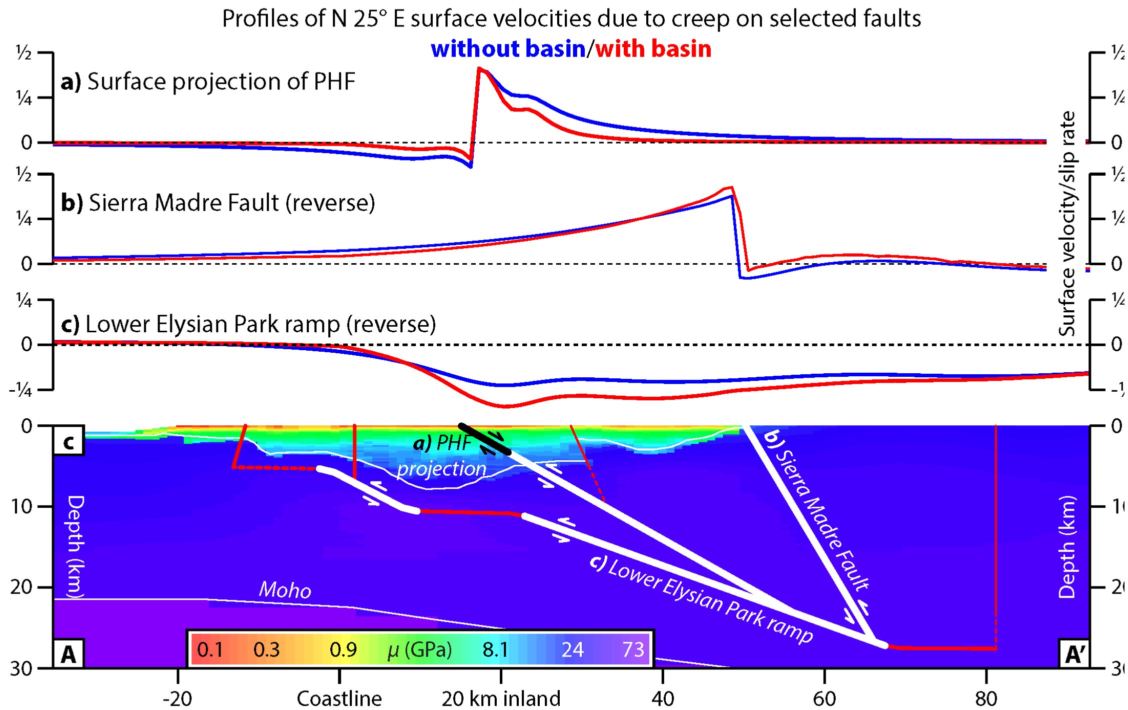

Figure 3.S8. Effect of the Los Angeles basin on elastostatic Green's functions for slip on the surface projection of the Puente Hills Fault, the Sierra Madre Fault, and the Lower Elysian ramp (Supplementary Figures 3.5-3.7). Blue and red lines are the synthetic surface velocities from models of uniform slip on each fault projected into the N 25° E direction along profile A-A', computed in an elastic halfspace model (blue) and the CVM* (red).

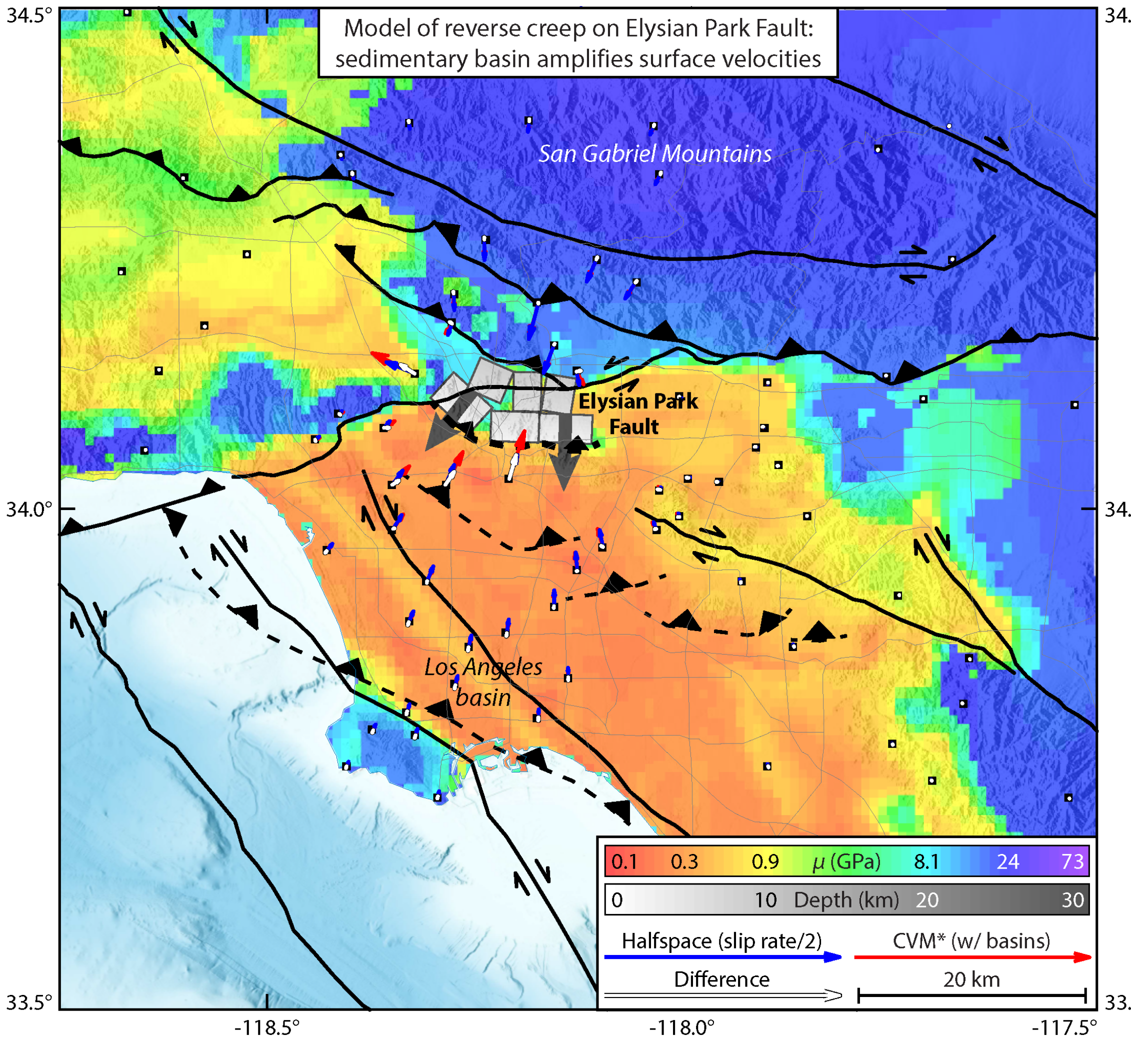

Figure 3.S9. The sedimentary basin amplifies elastostatic Green's functions for slip on the Elysian Park Fault, demonstrated here with a model of uniform reverse slip on the fault. The small size and relatively shallow position of the fault limits its likely effect on surface velocities. Background colormap is the distribution of the shear modulus μ at 100 m depth in the CVM*. Fault mesh is shaded grayscale by depth.

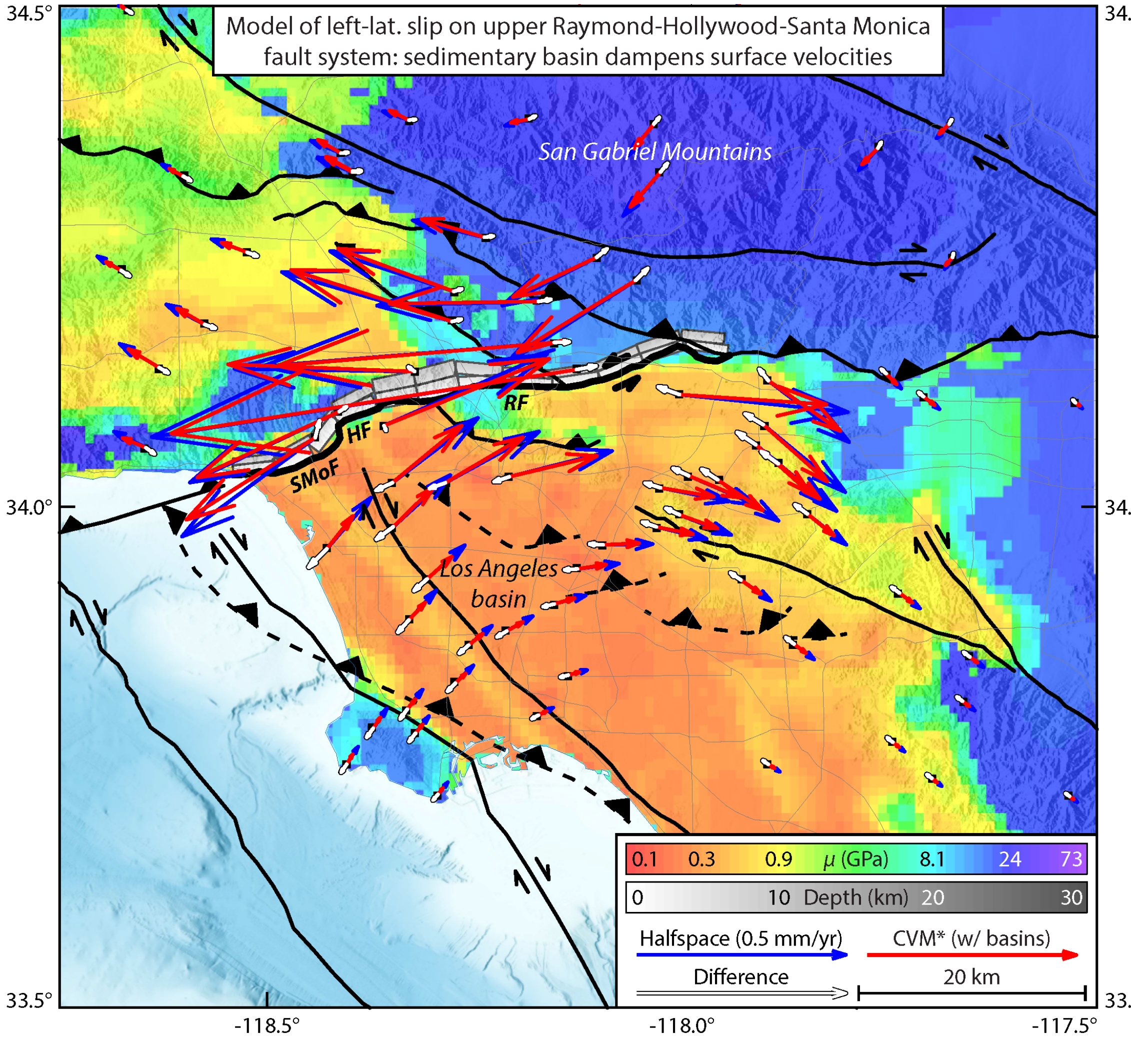

Figure 3.S10. Model of backslip between 0 and ~10 km depth on the left-lateral Raymond-Hollywood-Santa Monica fault system, with backslip at the UCERF3 "geologic" slip rates for each fault, equivalent to interseismic locking over this depth range and creep below it at the geologic rates. The backslip is prescribed to be left-lateral here for intuition's sake; the effect of interseismic locking on the surface velocity field if this model were reality would in fact be the negative of the velocities shown here. The sedimentary basin dampens the effect of interseismic locking on surface velocities. Background colormap is the distribution of the shear modulus μ at 100 m depth in the CVM*. Fault mesh is shaded grayscale by depth.

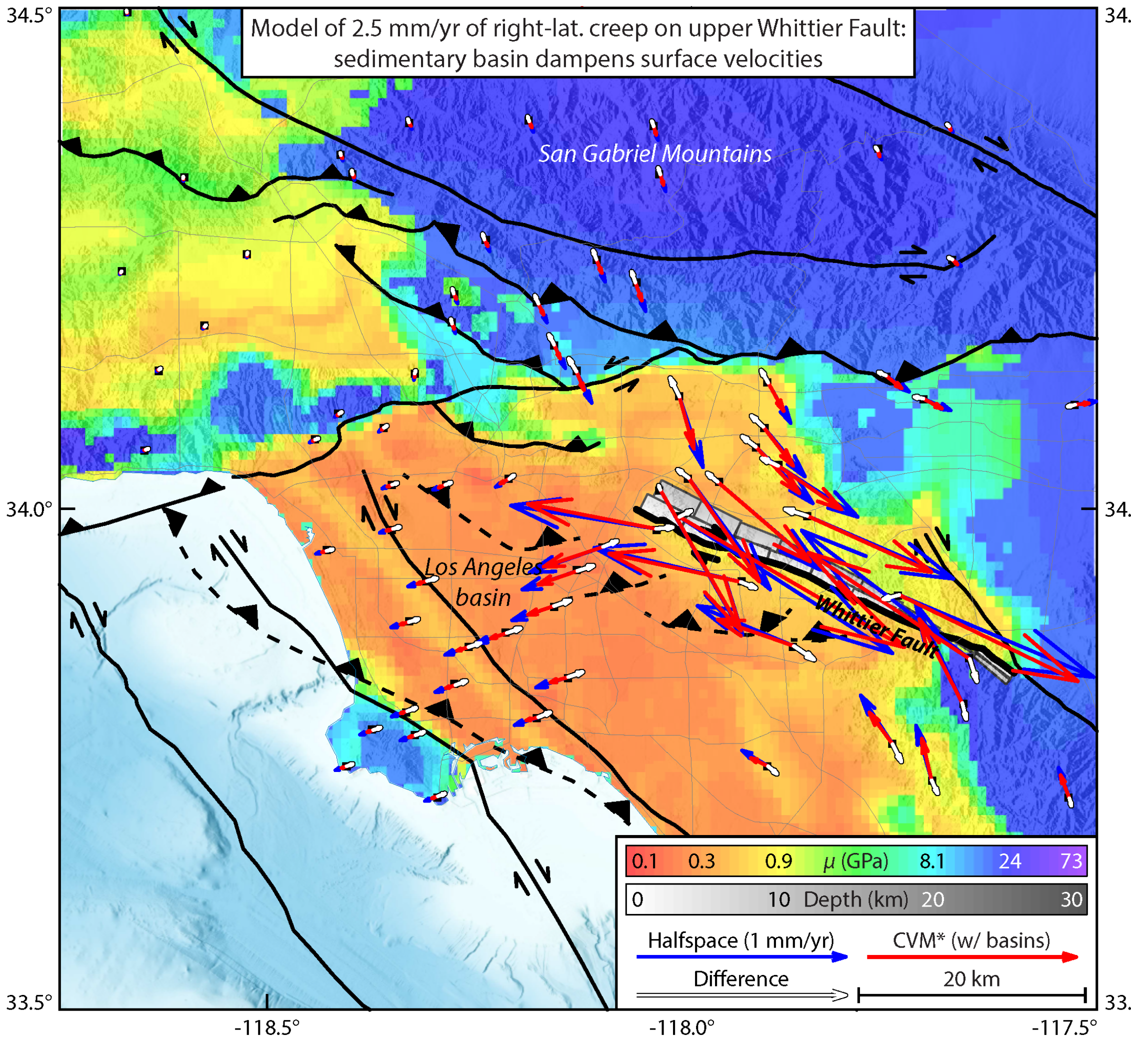

Figure 3.S11. Model of backslip between 0 and ~10 km depth on the right-lateral Whittier Fault, with backslip at the UCERF3 "geologic" slip rate (2.5 mm/yr), equivalent to interseismic locking over this depth range and creep below it at the geologic rates. The backslip is prescribed to be right-lateral here for intuition's sake; the effect of interseismic locking on the surface velocity field if this model were reality would in fact be the negative of the velocities shown here. The sedimentary basin dampens the effect of interseismic locking on surface velocities. Background colormap is the distribution of the shear modulus μ at 100 m depth in the CVM*. Fault mesh is shaded grayscale by depth.

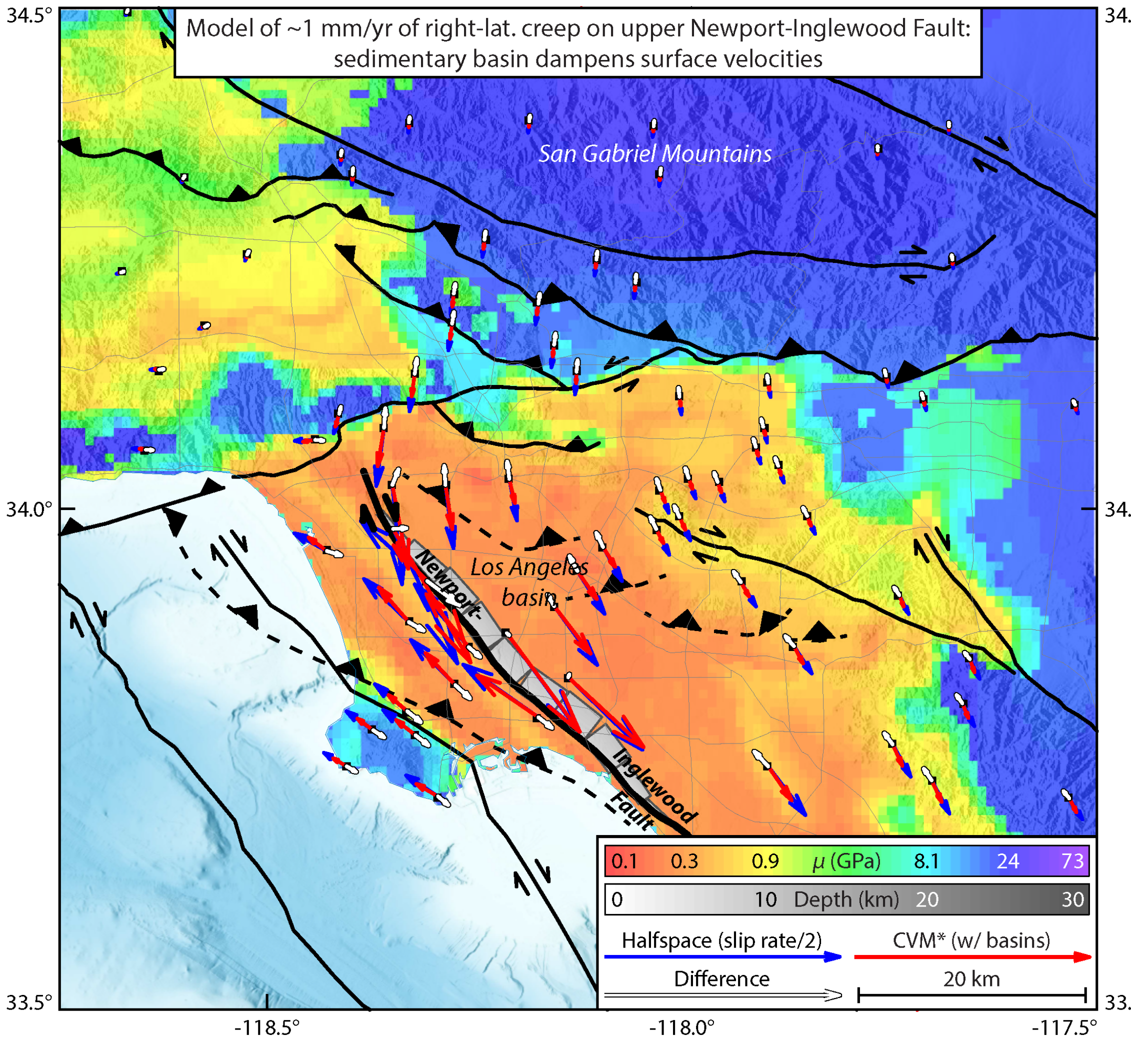

Figure 3.S12. Model of backslip between 0 and ~10 km depth on the right-lateral Newport-Inglewood Fault, with backslip at the UCERF3 "geologic" slip rate (0.6 mm/yr in the northwest and 1.2 mm/yr in the southeast), equivalent to interseismic locking over this depth range and creep below it at the geologic rates. The backslip is prescribed to be right-lateral here for intuition's sake; the effect of interseismic locking on the surface velocity field if this model were reality would in fact be the negative of the velocities shown here. The sedimentary basin dampens the effect of interseismic locking on surface velocities. Background colormap is the distribution of the shear modulus μ at 100 m depth in the CVM*. Fault mesh is shaded grayscale by depth.

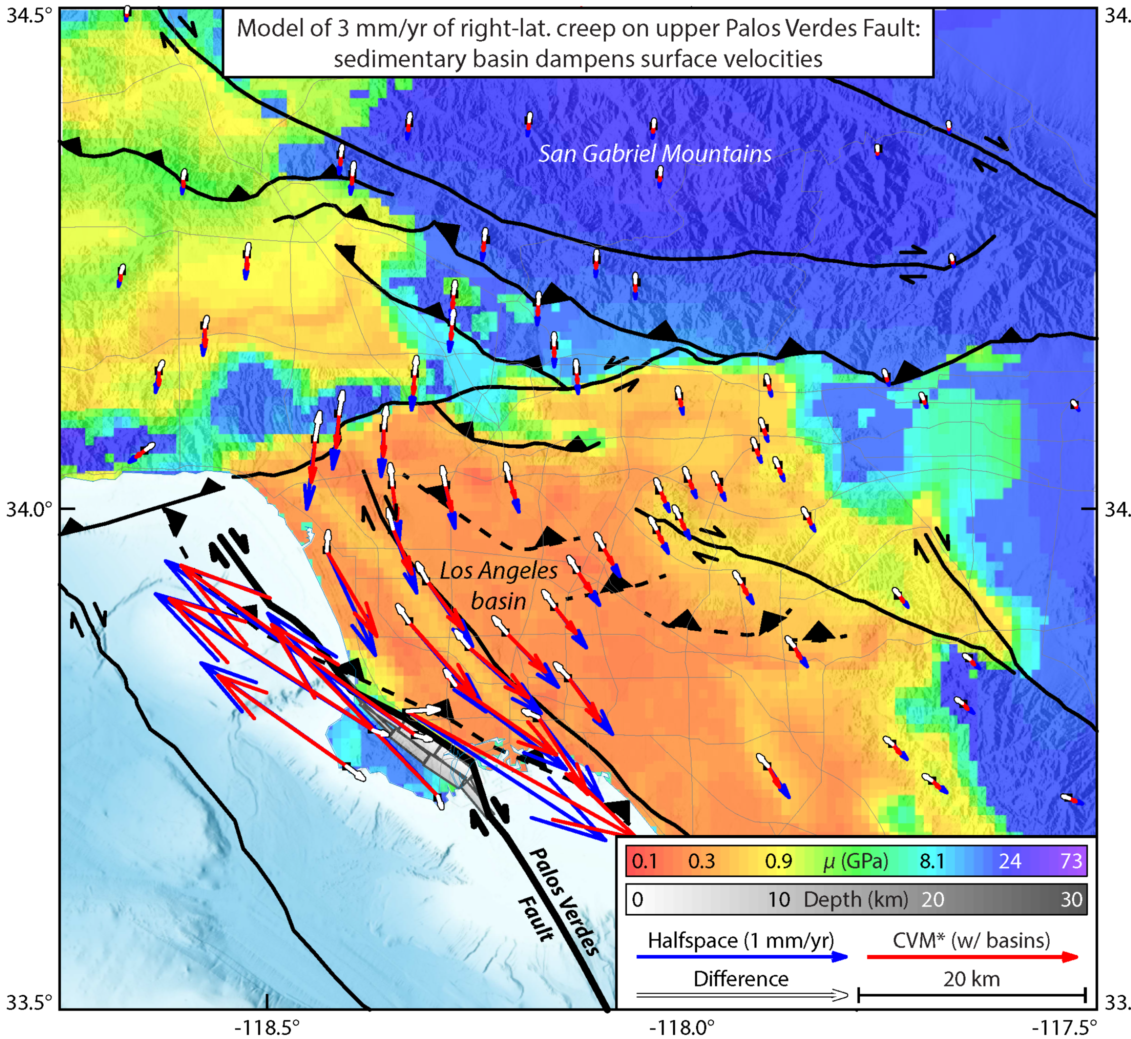

Figure 3.S13. Model of backslip between 0 and ~10 km depth on the right-lateral Palos Verdes Fault, with backslip at the UCERF3 "geologic" slip rate (3.0 mm/yr), equivalent to interseismic locking over this depth range and creep below it at the geologic rates. The backslip is prescribed to be right-lateral here for intuition's sake; the effect of interseismic locking on the surface velocity field if this model were reality would in fact be the negative of the velocities shown here. The sedimentary basin dampens the effect of interseismic locking on surface velocities. Background colormap is the distribution of the shear modulus μ at 100 m depth in the CVM*. Fault mesh is shaded grayscale by depth.

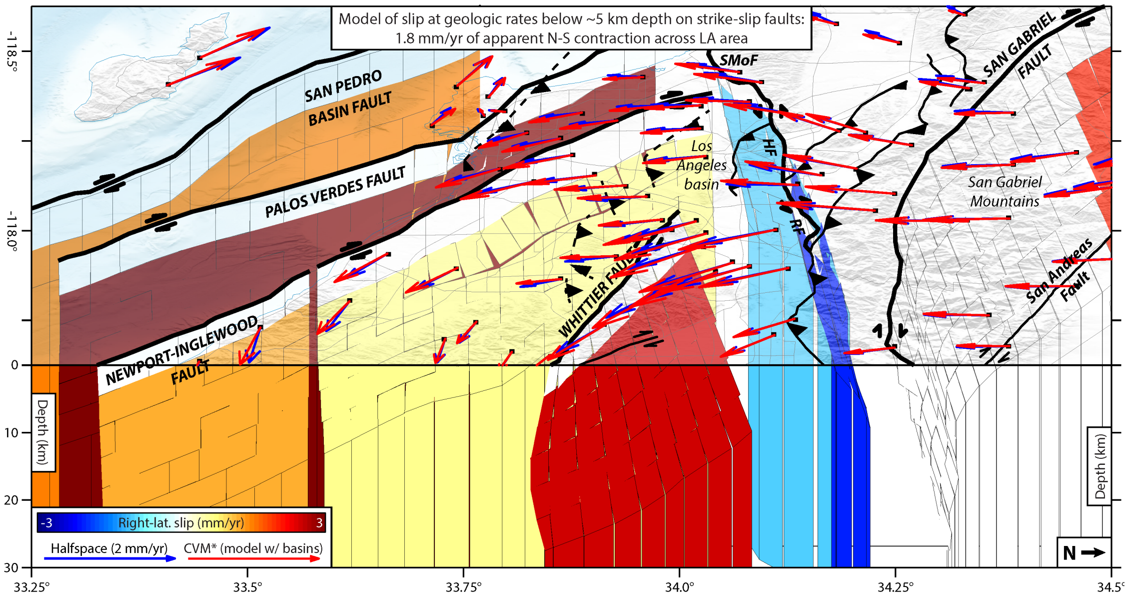

Figure 3.S14. Interseismic locking on strike-slip faults around Los Angeles can produce an apparent north-south contractional gradient of up to ~1.8 mm/yr, as demonstrated here with a model in which the strike-slip faults slip at their UCERF3 "geologic" slip rates between ~5 and 75 km depth. The fault meshes are extended vertically downward from the base of the mesh (~30 km) to 75 km. Blue and red arrows are the surface velocity fields from this configuration calculated in an elastic halfspace model and in the laterally heterogeneous material model, respectively.

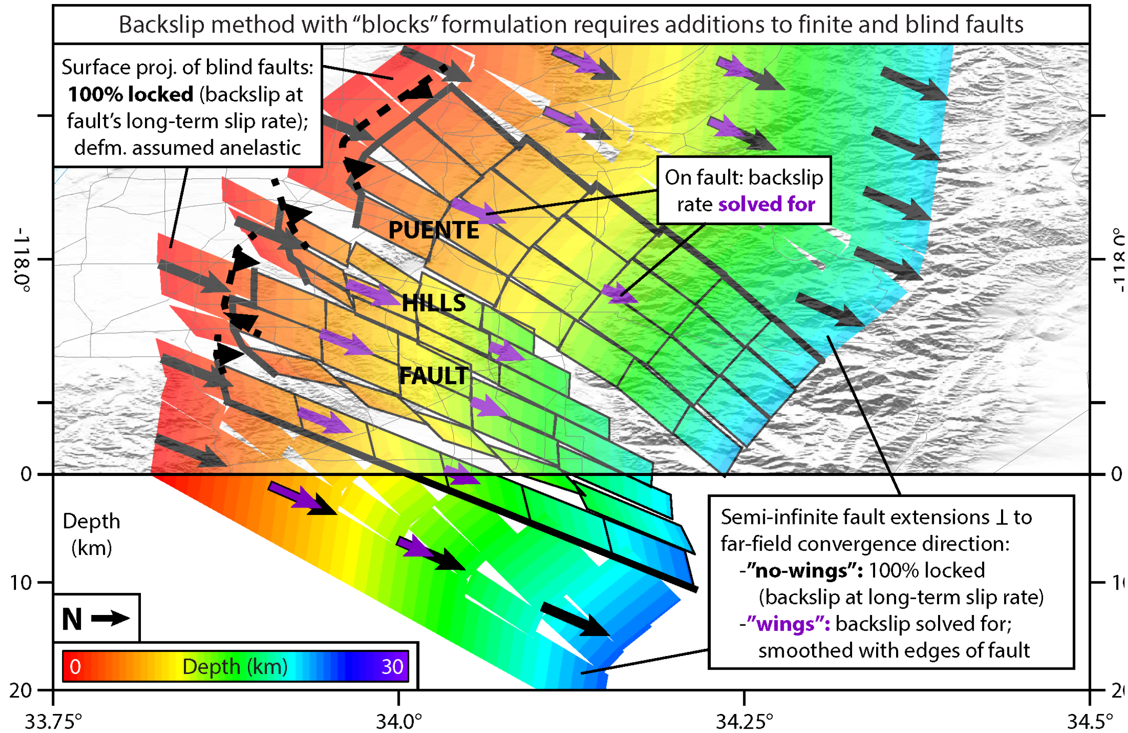

Figure 3.S15. Features added to the fault models for use within the backslip method in the kinematic inversions, as described in the text and Appendix 3.4; example here is the Puente Hills Fault.

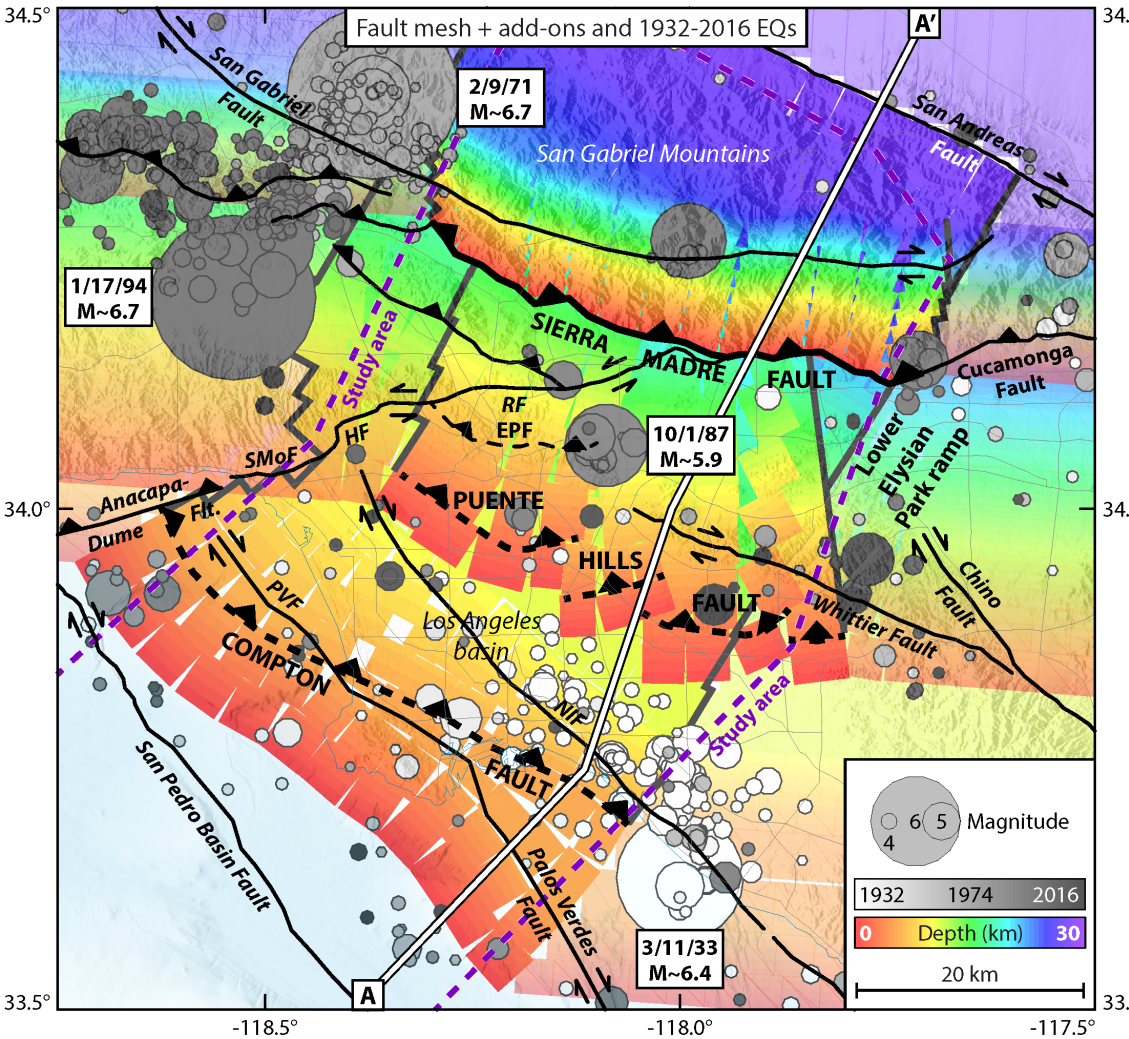

Figure 3.S16. Features added to the fault models for use within the backslip method in the kinematic inversions, as described in the text and Appendix 3.4. The dashed purple line outlines the boundary of the area covered by the GPS stations used.

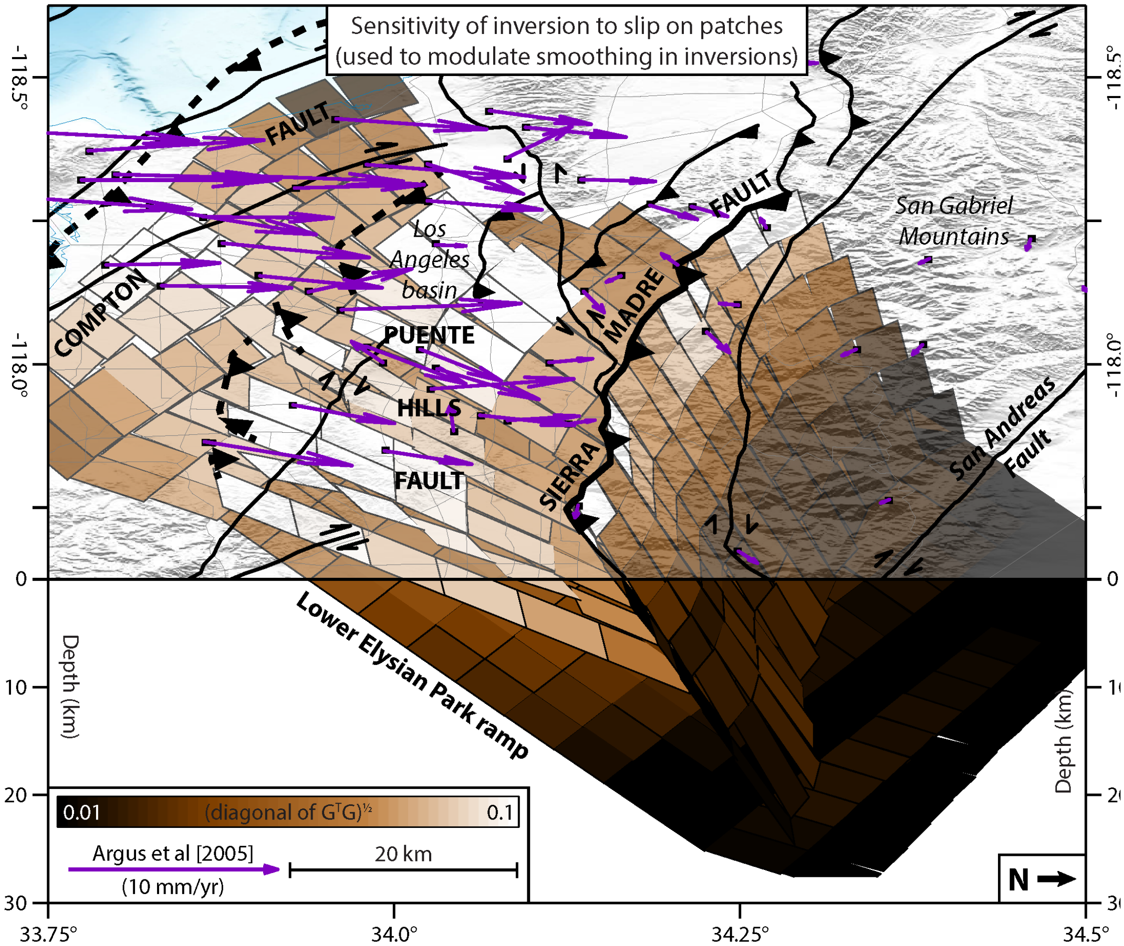

Figure 3.S17. Sensitivity of the inversions to slip on each patch, computed with the method of Ortega [2013] and used to modulate the weight of Laplacian smoothing in the inversions.

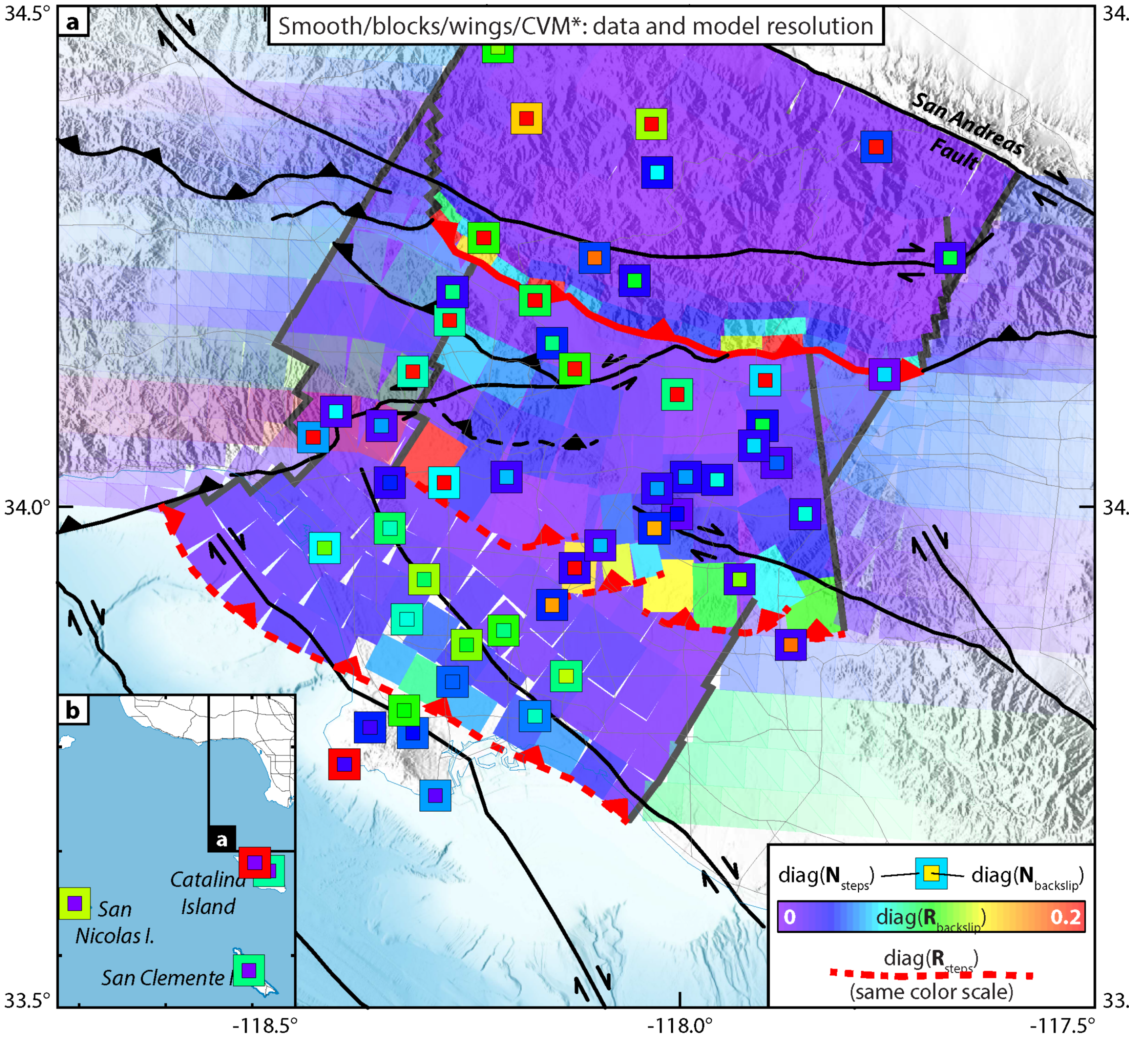

Figure 3.S18. Data and model resolution in the inversions. Both are computed with the formulation of Aster [2012] that incorporates regularization, modified to incorporate the modulation of the Laplacian smoothing by the sensitivity (Figure 3.S17) as in Ortega [2013]. **a)** On-land. Inner and outer colored squares are each station's data resolution to the backslip and to the steps in the convergence velocity, respectively. Colored patches are the model resolution of the faults. **b)** On islands; same color scale.

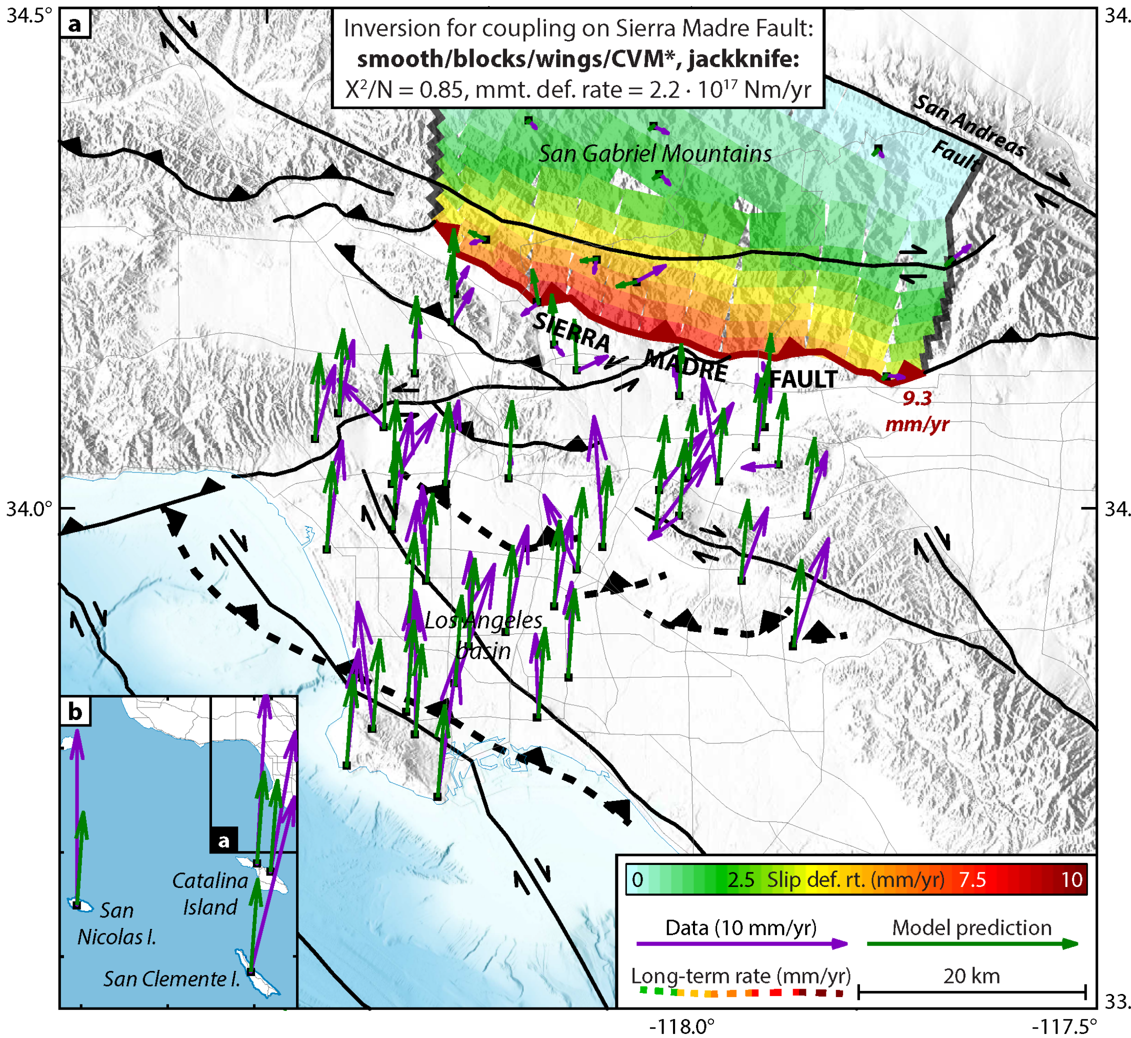

Figure 3.S19. a) Inversion of the GPS velocity field for strain accumulation on the Sierra Madre Fault using the smooth/blocks/wings/CVM* scheme. **b)** Comparison of observed and predicted velocities on islands.

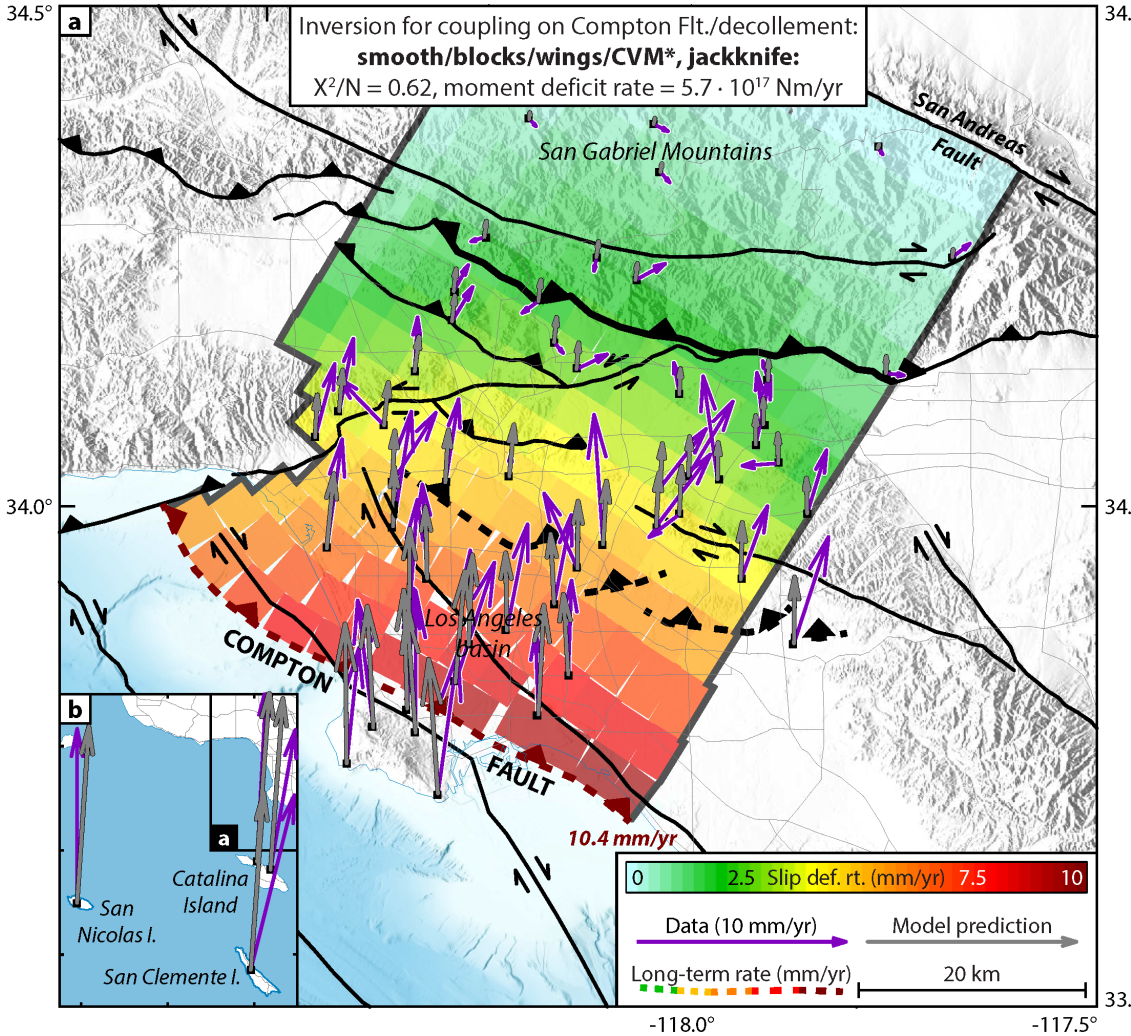

Figure 3.S20. a) Inversion of the GPS velocity field for strain accumulation on the Compton Fault using the smooth/blocks/wings/CVM* scheme. **b)** Comparison of observed and predicted velocities on islands.

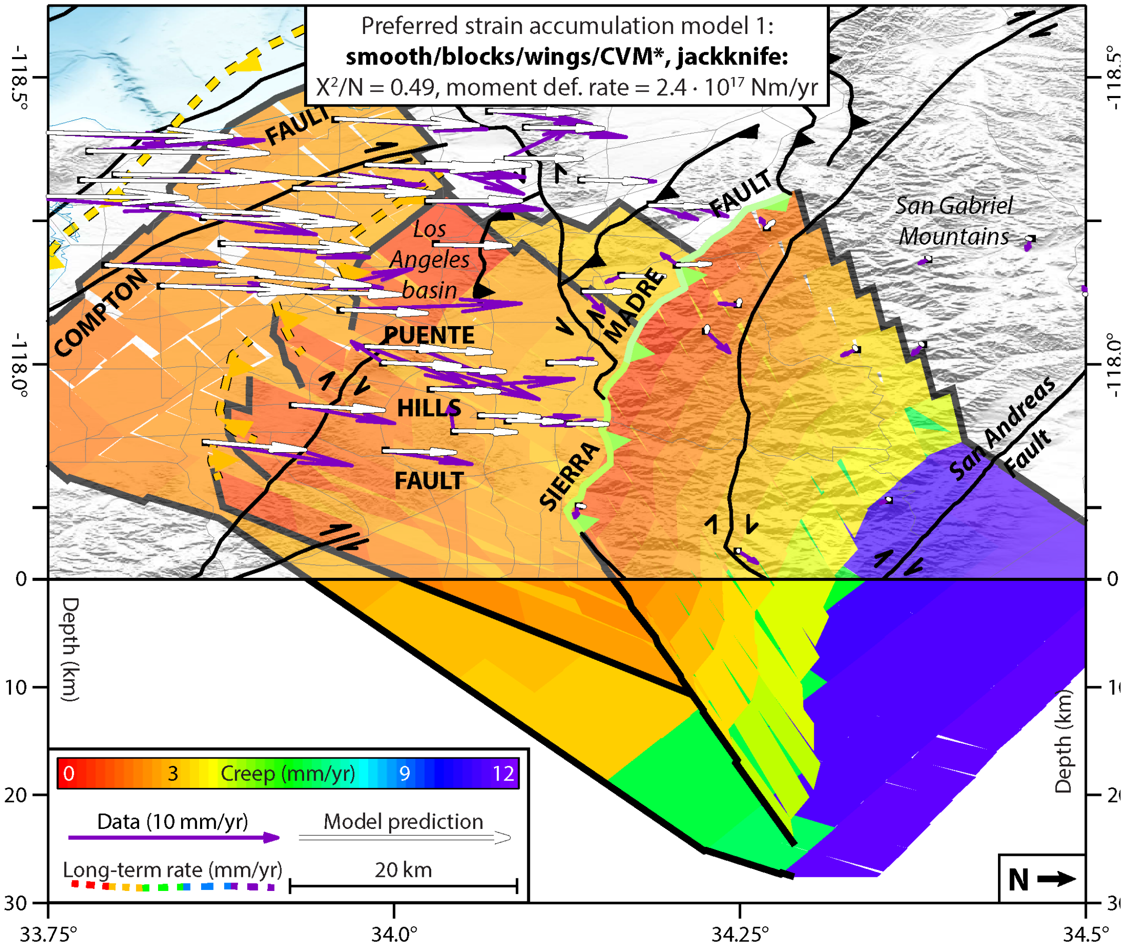

Figure 3.S21. 3D west-facing view of the distribution of the weighted mean creep rate (colored patches) in Model 1 (Figure 3.10).

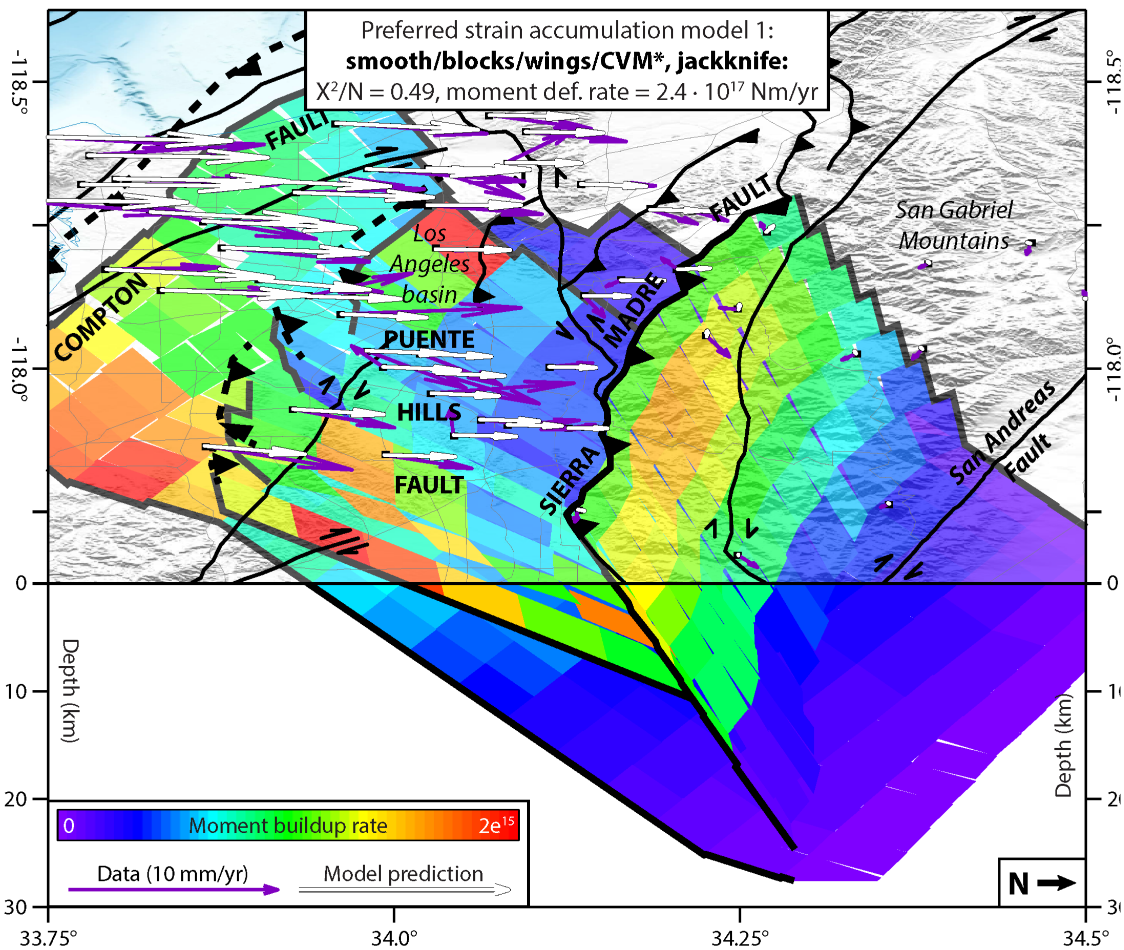

Figure 3.S22. 3D west-facing view of the distribution of the weighted mean moment deficit accumulation rate (colored patches) in Model 1 (Figure 3.10).

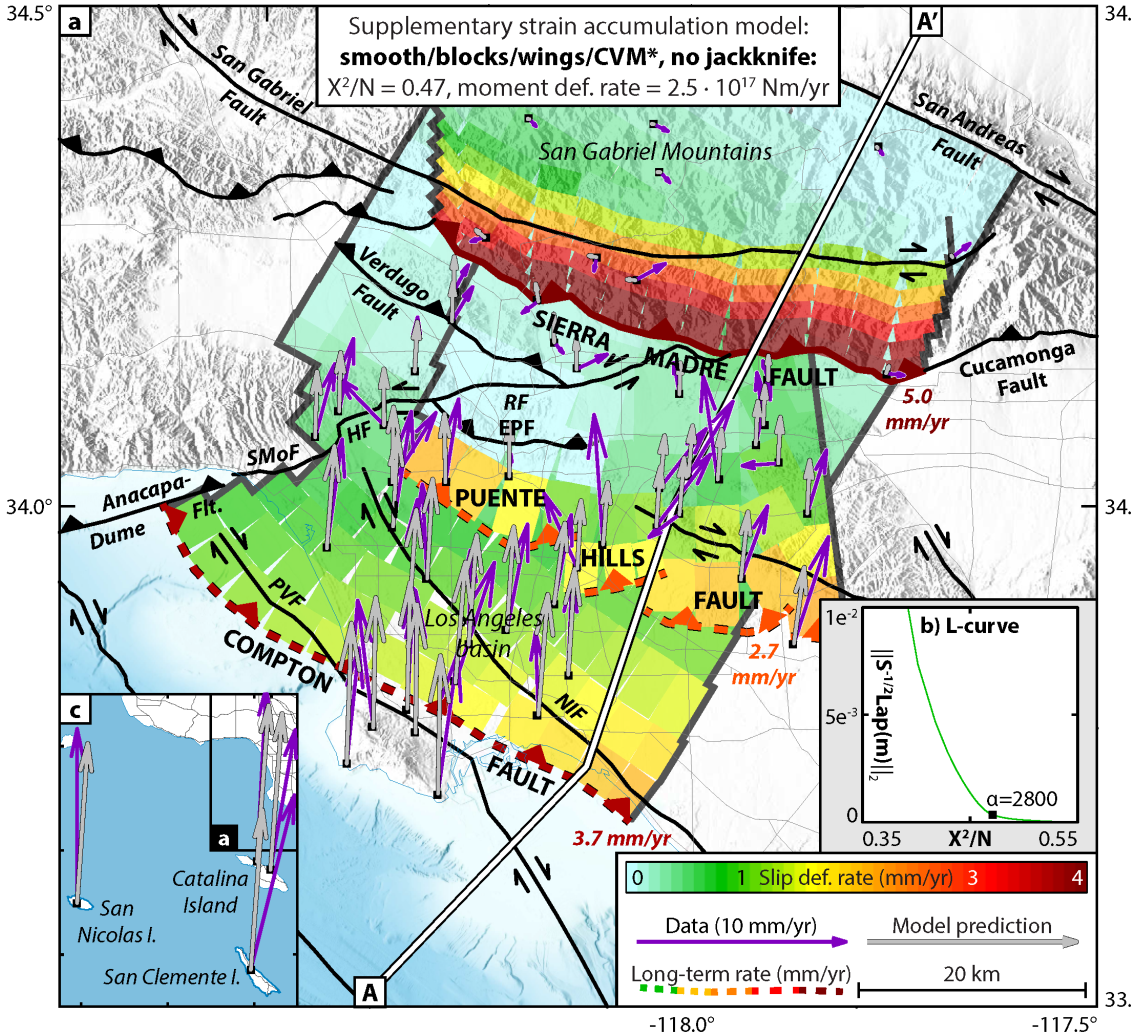

Figure 3.S23. A single inversion using the smooth/blocks/wings/CVM* scheme fit to all of the data (same as model 1 except without the delete-half jackknife scheme.) **a)** Inferred strain accumulation and slip rates are similar to Model 1 (Figure 3.10). **b)** L-curve used to choose the weight of sensitivity-modulated Laplacian smoothing in the inversion. **c)** Comparison of observed and predicted velocities on islands.

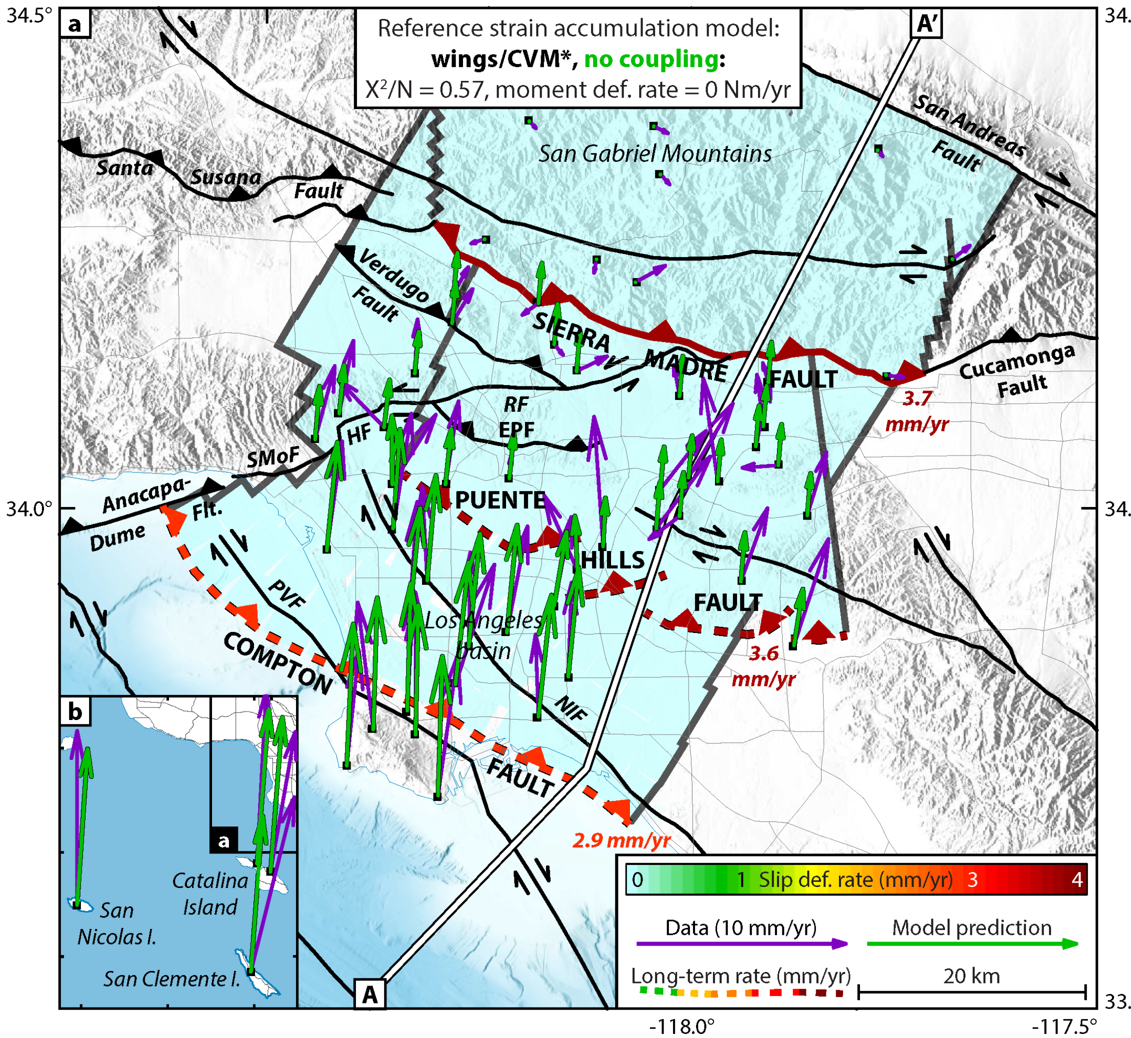

Figure 3.S24. Reference "null" geodetic model: Inversion of GPS velocity field for strain accumulation on the three faults in a model where they accumulate no strain, using the smooth/blocks/wings/CVM* scheme. **a)** Mapview of backslip rates (colored patches, here zero), long-term slip rates (colors of the solid and dashed fault traces, also noted next to the faults), and observed (purple) and predicted (green) velocities at GPS stations. **b)** Comparison of observed and predicted velocities on islands.

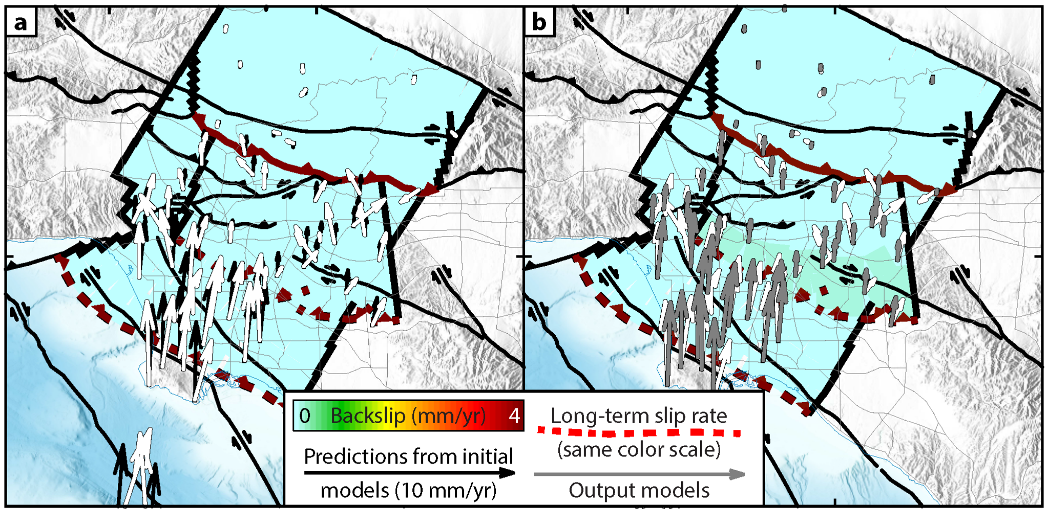

Figure 3.S25. Tests of inversion performance featuring a zero-backslip model with noise. **a)** We generate synthetic surface velocities (black arrows) from a model where the Sierra Madre, Puente Hills and Compton faults have long-term slip rates of 4 mm/yr (colored solid and dashed lines) and have zero backslip (colored patches), run within the CVM* with the "blocks" and "wings" formulations. The synthetic dataset used in the checkerboard test (white arrows) is this predicted velocity field plus Gaussian noise scaled by half the Argus et al [2005] velocity uncertainty of each component at each station. **b)** Inversion of the synthetic surface velocities for the slip rates and backslip distributions on the faults following the smooth/blocks/wings/CVM* scheme. The inversion reproduces the zero model well.

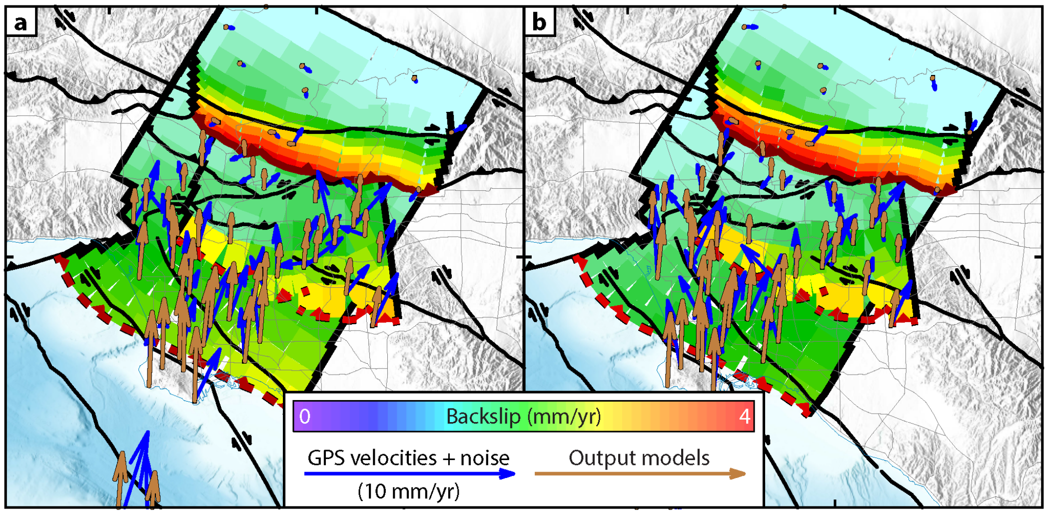

Figure 3.S26. Tests of inversion performance in which the synthetic data is the Argus et al [2005] GPS velocity field plus Gaussian noise scaled by half the Argus et al [2005] velocity uncertainty of each component at each station (two iterations shown). We invert this for the slip rates and backslip distributions on the faults following the smooth/blocks/wings/CVM* scheme. The weighted mean output models are nearly indistinguishable from Model 1 (Figure 3.10).

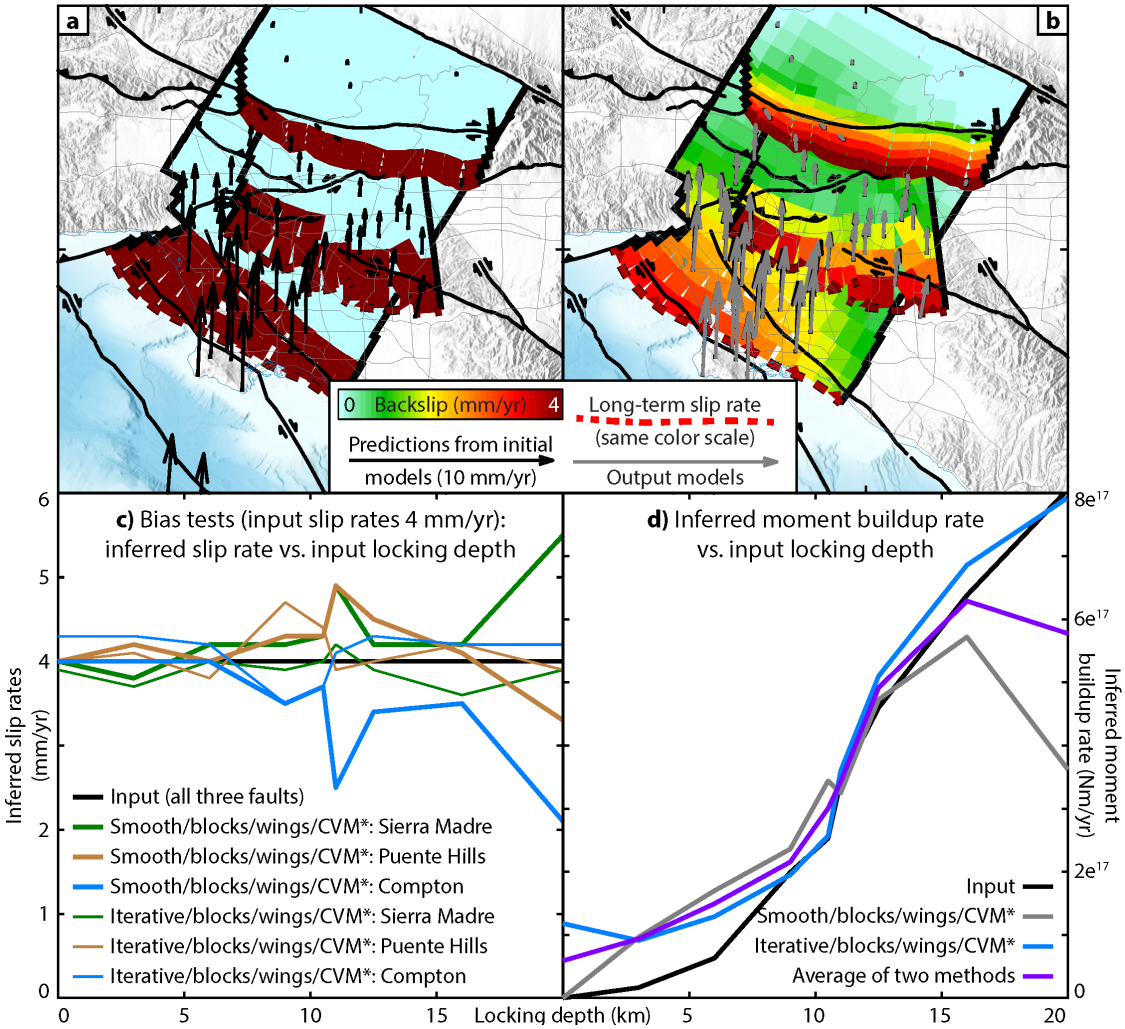

Figure 3.S27. Tests of inversion performance as described in Appendix 6. **a)** We compute synthetic surface velocities (black arrows) from a model where the Sierra Madre, Puente Hills and Compton faults have long-term slip rates of 4 mm/yr (colored solid and dashed lines) and are locked down to ~10 km (colored patches), run within the CVM* using the "wings" and "blocks" formulations. **b)** Inversion of the synthetic surface velocities for the slip rates and backslip distributions on the faults using the smooth/blocks/wings/CVM* scheme. **c-d)** Tests for a range of prescribed locking depths, for both the smooth/blocks/wings/CVM* and iterative/blocks/wings/CVM* inversion schemes. As with Model 2 (Figure 3.14), the estimates from the "iterative" method are the weighted averages of the models that have a normalized log-probability of >0.96. **c)** The methods reproduce the input slip rates well across a range of locking depths. **d)** Both methods somewhat overestimate the moment buildup rate for shallow locking depths (for this configuration of slip rates), while the smooth/blocks/wings/CVM* scheme underestimates the rate for very deep locking depths. Note that the 0.96 log-likelihood cutoff in the iterative method was selected in the real case due to characteristics of models above and below that cutoff. A cutoff of 0.99, for example, would here result in a near-perfect reproduction of the input parameters because the input model is a single binary model.

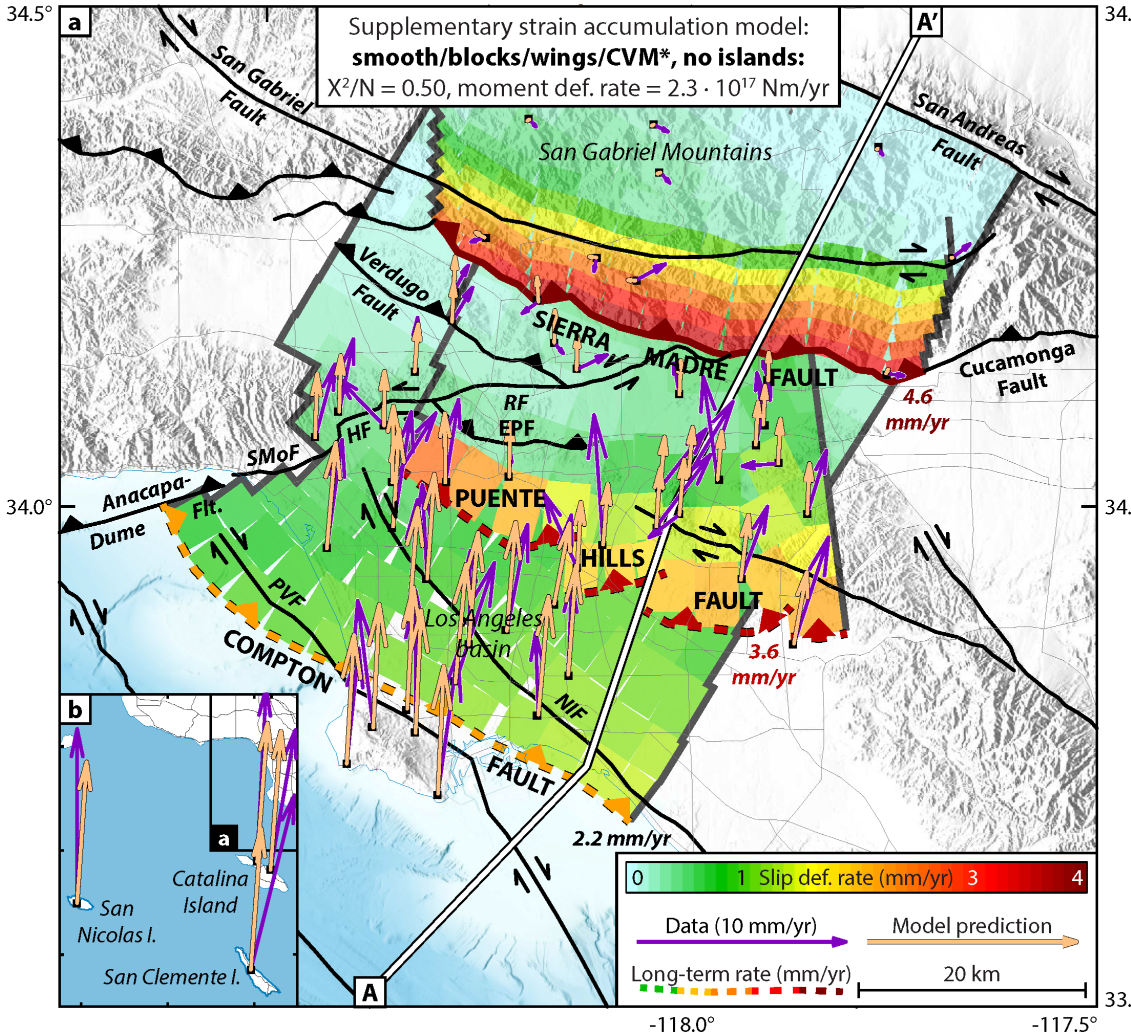

Figure 3.S28. The same three-fault inversion as Model 1 (Figure 3.10) except that the velocities on offshore islands are not used in the inversion. **a)** The slip rate inferred on the Compton Fault is lower than in Model 1. **b)** Comparison of observed and predicted velocities on islands; the model visibly undershoots the data.

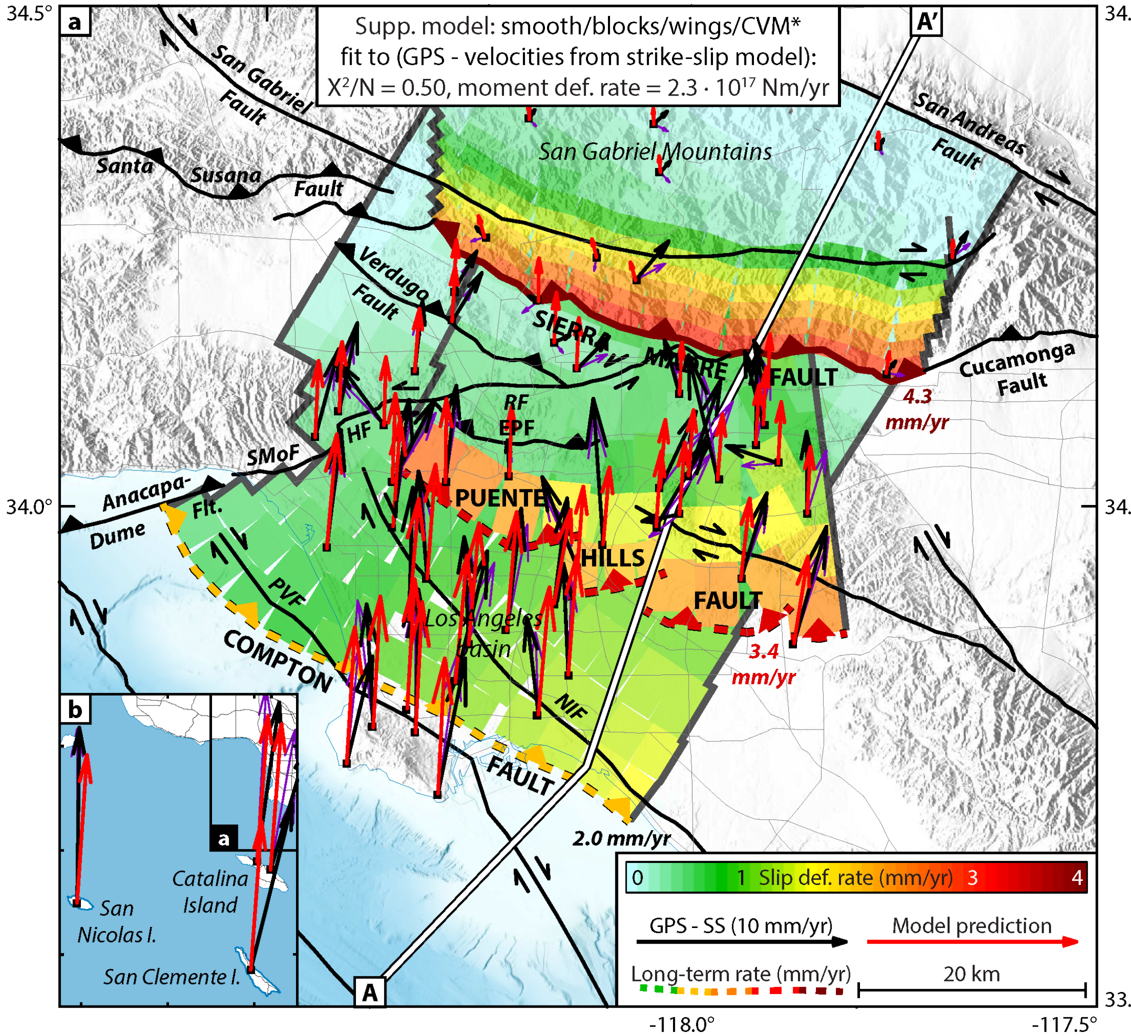

Figure 3.S29. The same three-fault inversion as Model 1 (Figure 3.10) except that the synthetic velocity field from a forward model of strike-slip faults (Figure 3.S14) is removed from the data before inversion. **a)** The slip rate inferred on the Compton Fault is lower than in Model 1. **b)** Comparison of observed and predicted velocities on islands.

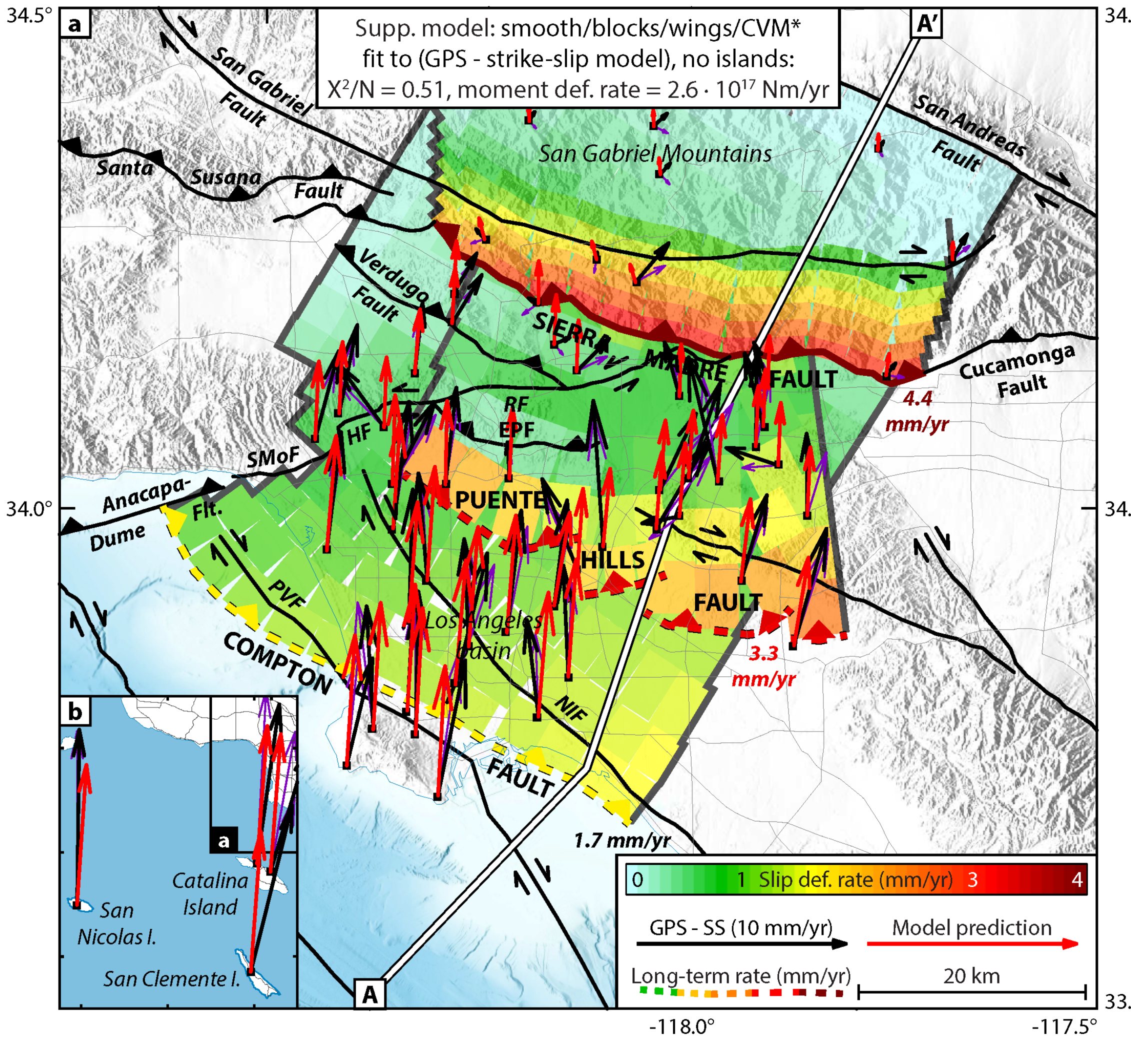

Figure 3.S30. The same three-fault inversion as Model 1 (Figure 3.10) except that the synthetic velocity field from a forward model of strike-slip faults (Figure 3.S14) is removed from the data before inversion and velocities on offshore islands are not counted in the inversion. **a)** The slip rate inferred on the Compton Fault is lower than in preferred model 1. **b)** Comparison of observed and predicted velocities on islands.

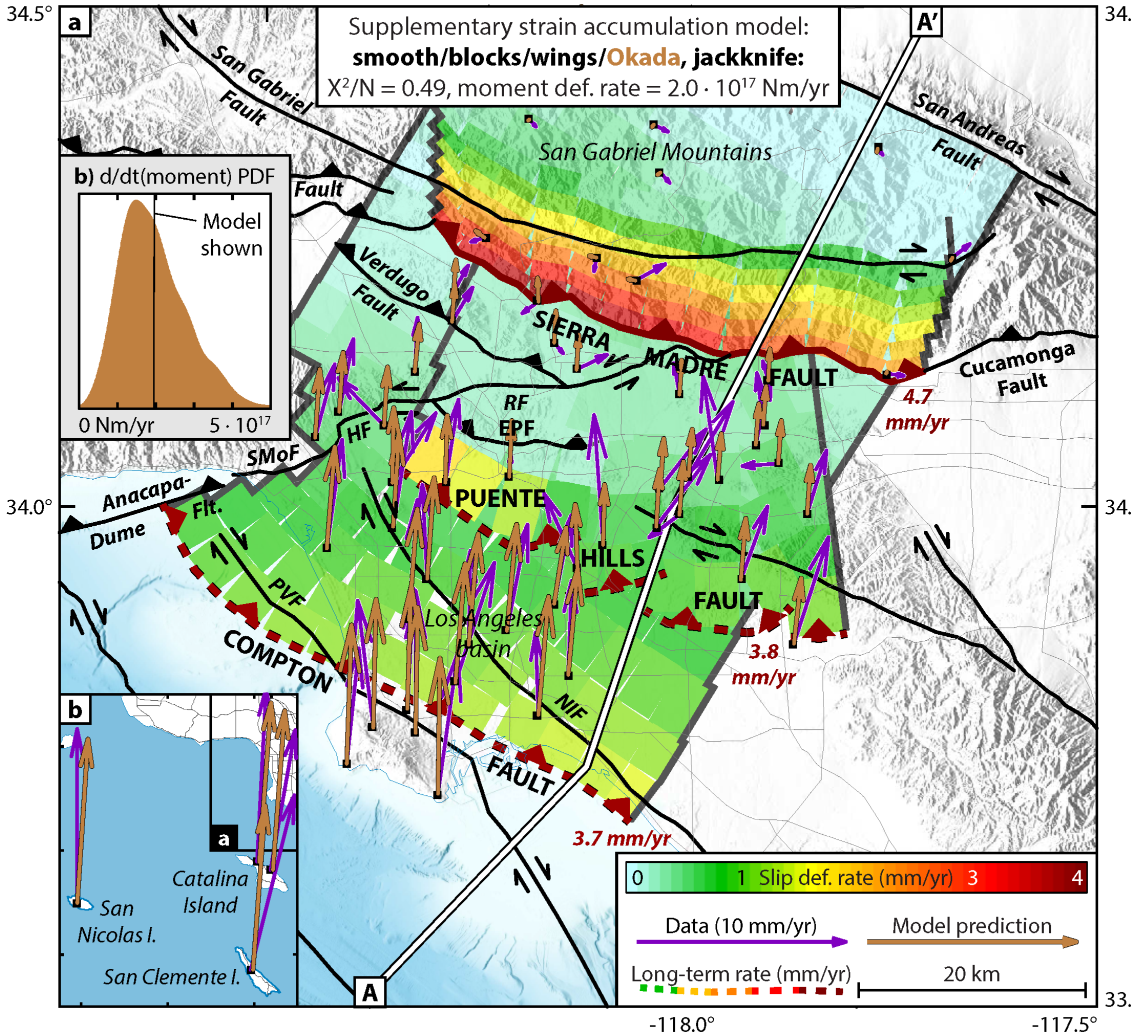

Figure 3.S31. The same three-fault inversion as Model 1 (Figure 3.10) except with an elastic halfspace model. **a)** Inferred strain accumulation is lower than with the CVM*, as in the single-fault case in Figure 3.8. **b)** PDF of total moment deficit accumulation rate. **c)** Comparison of observed and predicted velocities on islands.

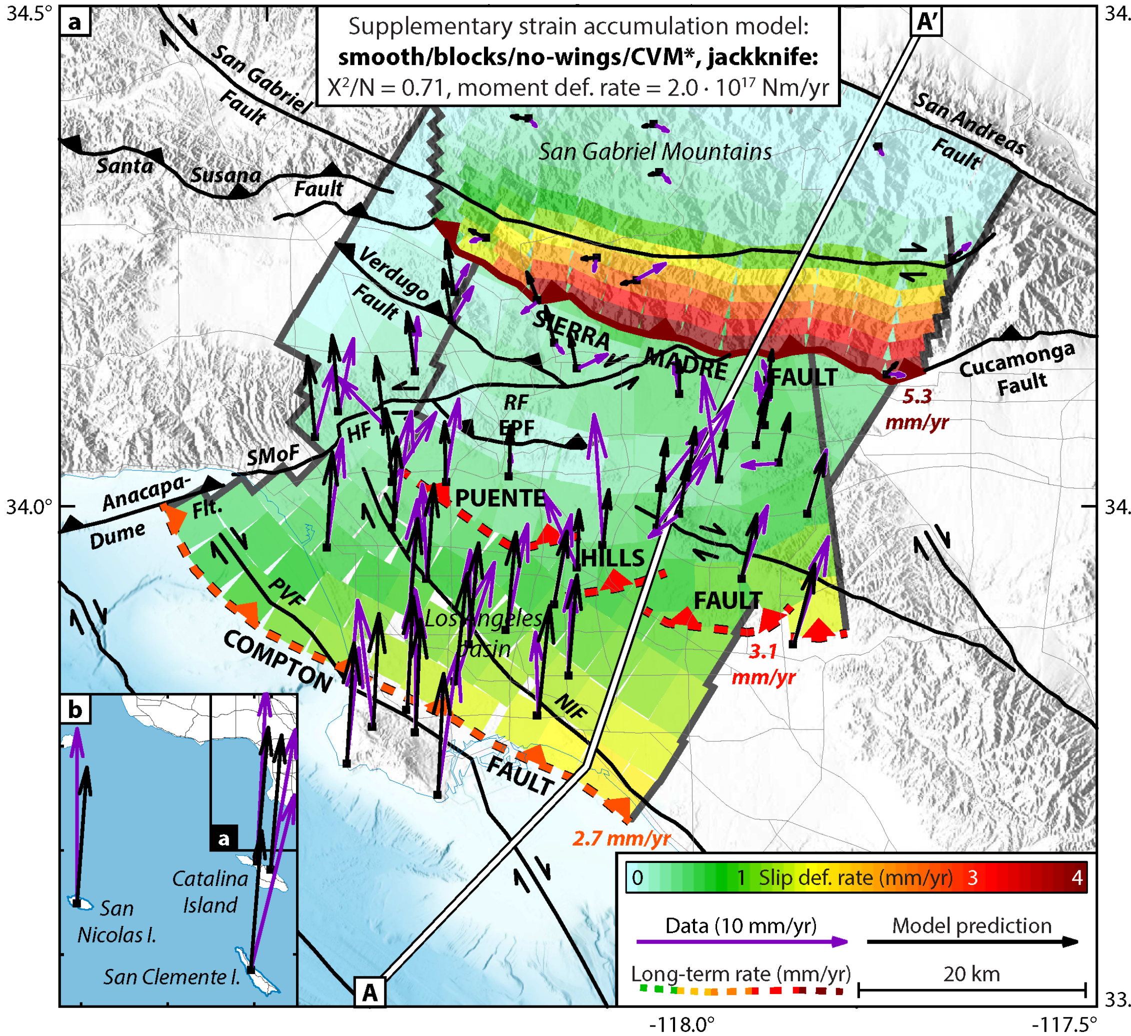

Figure 3.S32. The same three-fault inversion as Model 1 (Figure 3.10) except with the "no-wings" formulation of strain accumulation east and west of the basin. **a)** Mapview of backslip rates (colored patches), long-term slip rates (colors of the solid and dashed fault traces, also noted next to the faults), and observed (purple) and predicted (black) velocities at GPS stations. **b)** Comparison of observed and predicted velocities on islands.

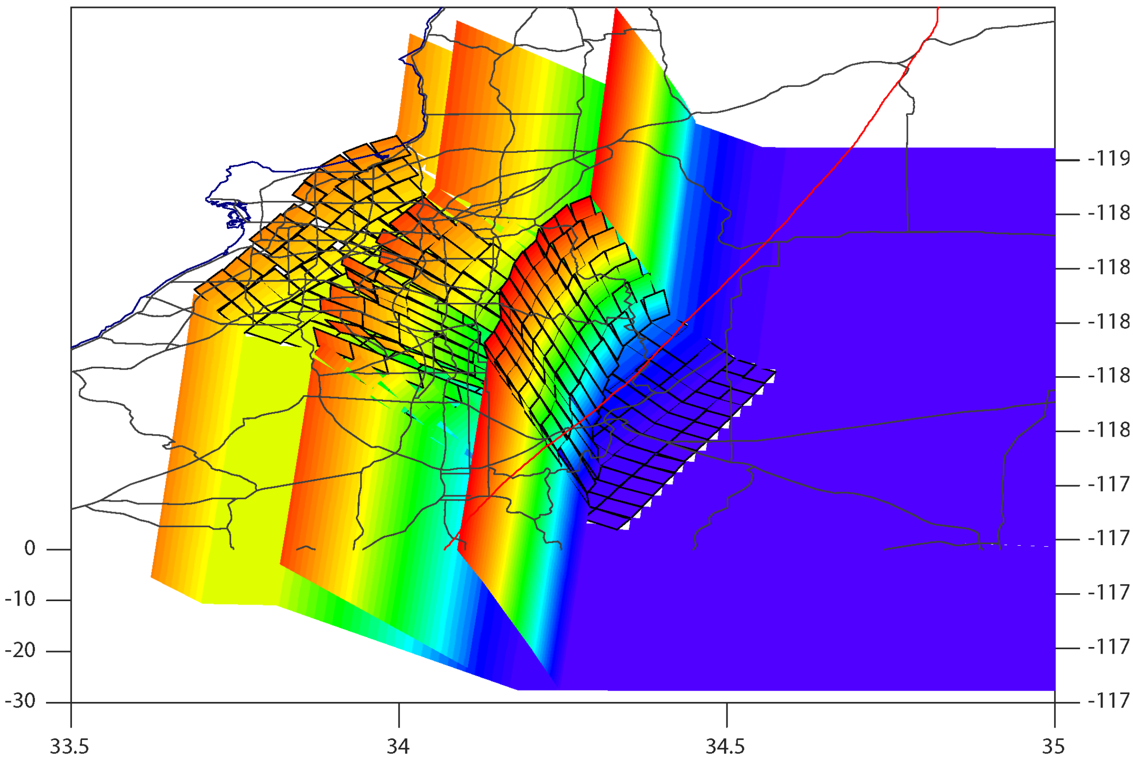

Figure 3.S33. Geometry of the modeled large decollement beneath the Mojave region (27.5 km depth), on which reverse creep is imposed at the sum of the faults' long-term slip rates in the "sheets" formulation of long-term motion.

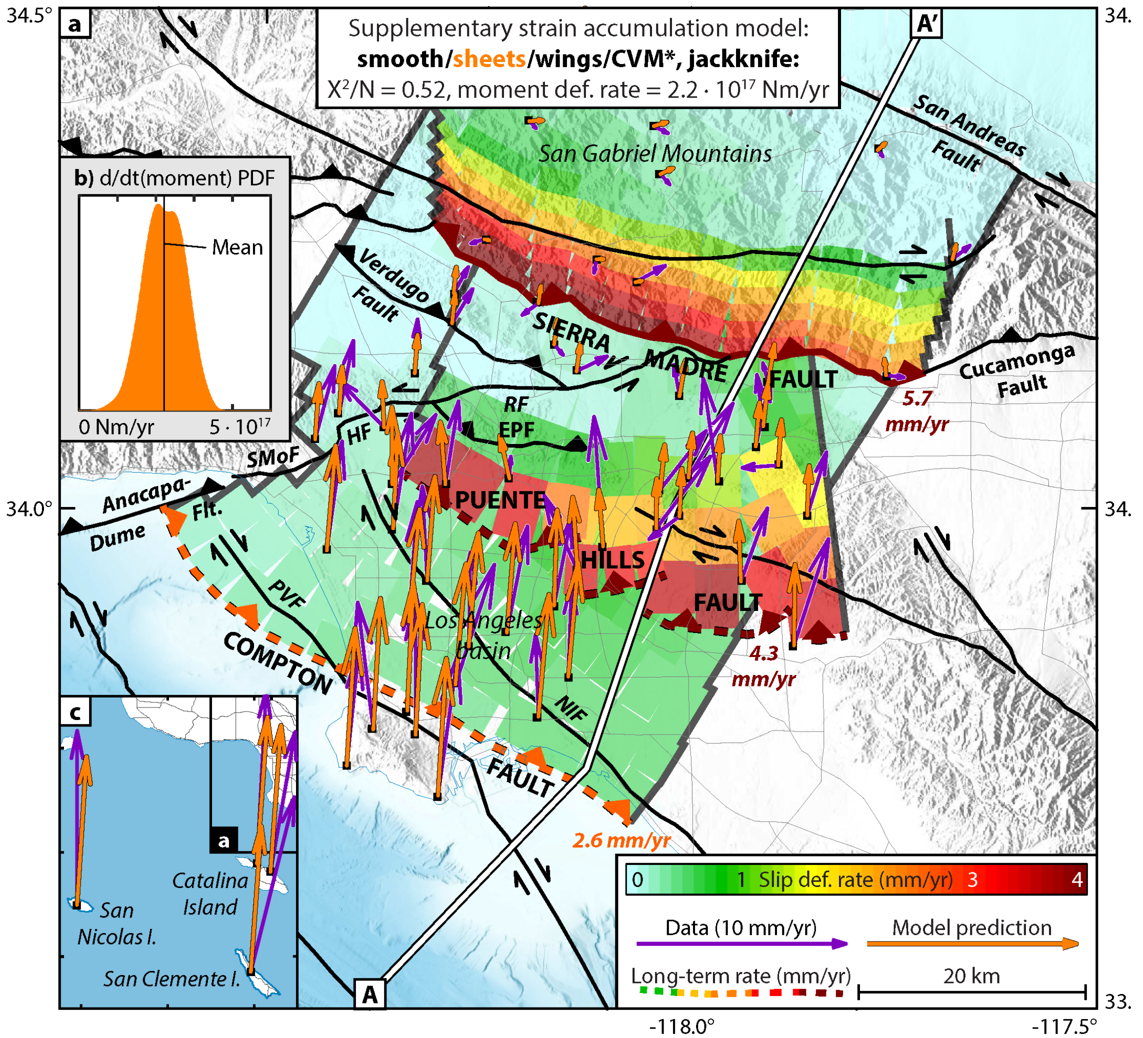

Figure 3.S34. The same three-fault inversion as Model 1 (Figure 3.10) except with the “sheets” formulation of long-term motion. **a)** Inferred strain accumulation is higher on the upper Sierra Madre and Puente Hills faults and lower on the upper Compton Fault than in Model 1, but the moment buildup rate is similar. **b)** Comparison of observed and predicted velocities on islands.

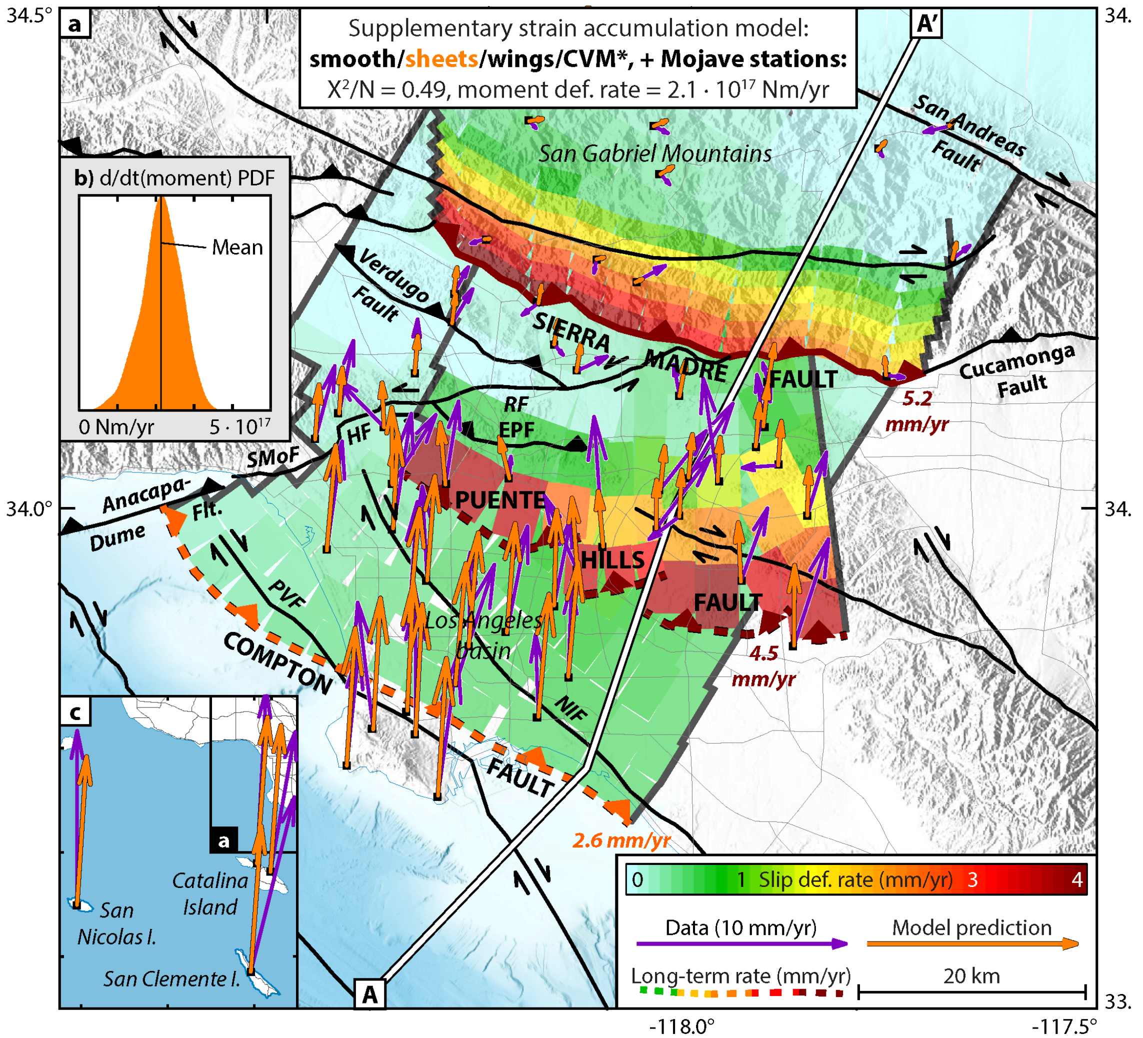

Figure 3.S35. The same three-fault inversion as Model 1 (Figure 3.10) except that the "sheets" formulation is used and velocities at eight stations in the Mojave Desert are included, as described in Appendix 3.1. **a)** Inferred strain accumulation is higher on the upper Sierra Madre and Puente Hills faults and lower on the upper Compton Fault than in Model 1, but the moment buildup rate is similar. **b)** Comparison of observed and predicted velocities on islands.

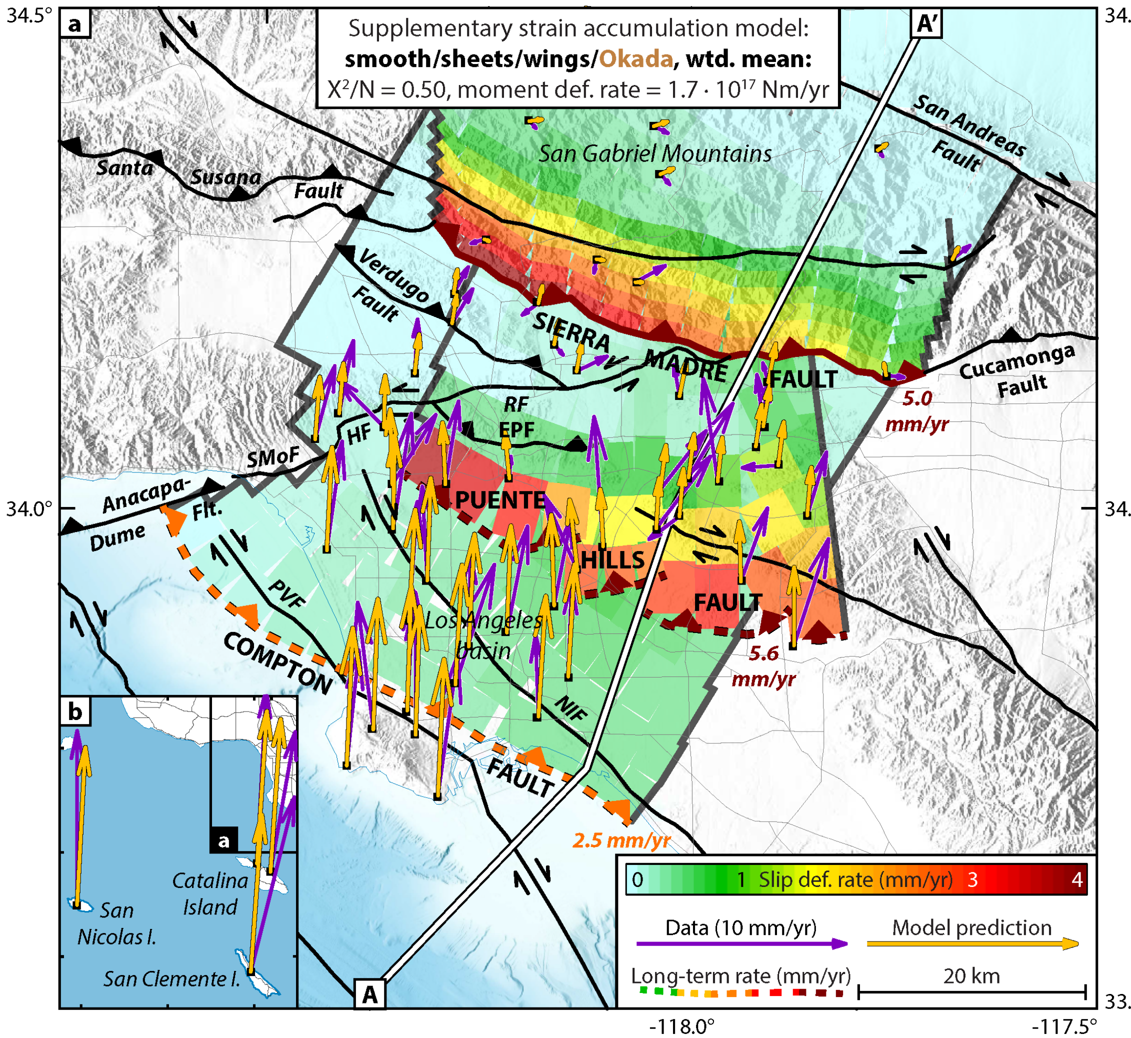

Figure 3.S36. The same three-fault inversion as Model 1 (Figure 3.10) except that the "sheets" formulation is used and an elastic halfspace model is used. **a)** As with the case of modeling the steady-state terms kinematically, less strain accumulation is inferred when using the elastic halfspace model than the CVM* (compare Figure 3.S31 and Figure 3.10). **b)** Comparison of observed and predicted velocities on islands.

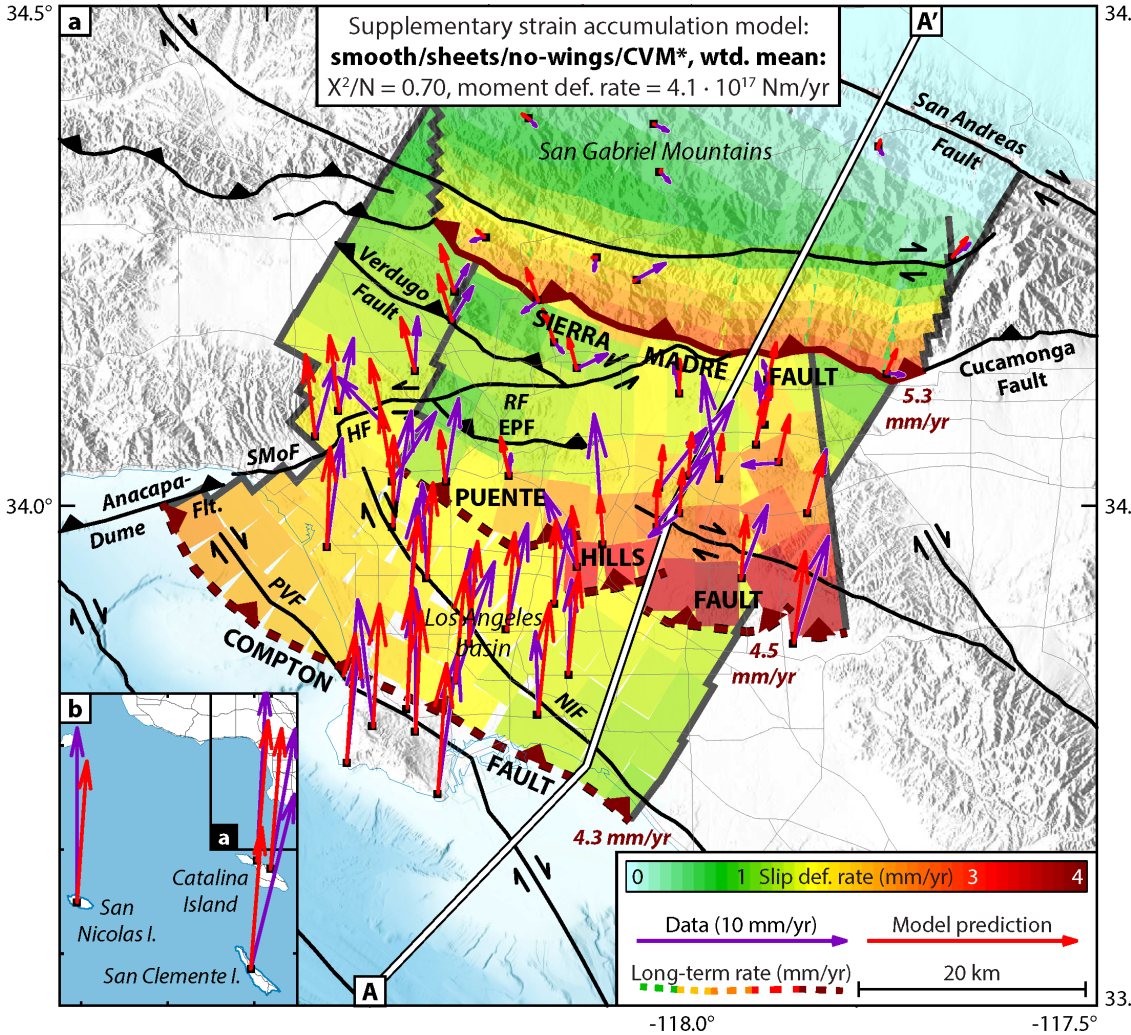

Figure 3.S37. The same three-fault inversion as Model 1 (Figure 3.10) except that the "sheets" and "no-wings" formulations are used. **a)** Faster strain accumulation is inferred on the faults than with the "sheets" and "wings" formulations, as expected (compare with Figure 3.S34); here the "wings" do not contribute to the regional contraction and so the faults must do more work. This effect was not visible with the kinematic steady-state terms (compare Figure 3.S32 and Figure 3.10). **b)** Comparison of observed and predicted velocities on islands.

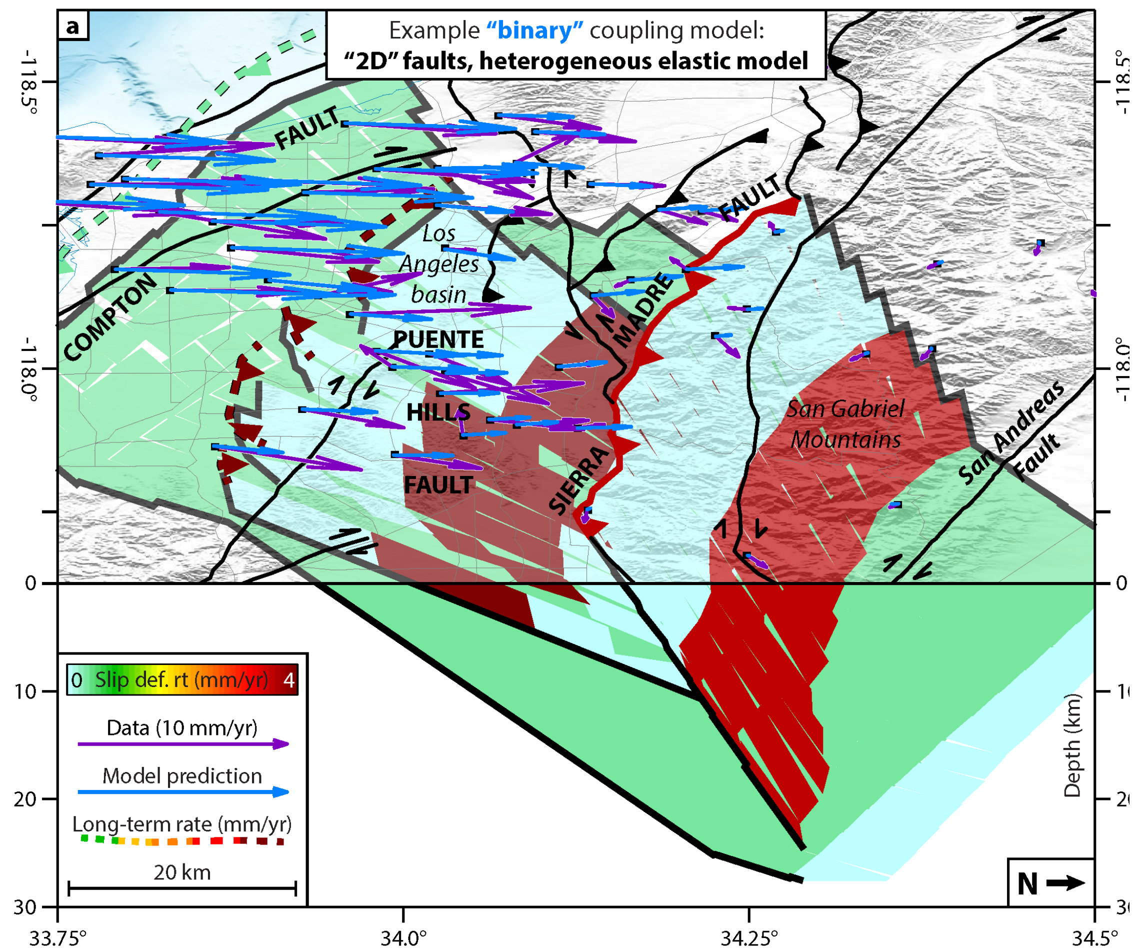

Figure 3.S38. 3D west-facing view of an example "binary" model: the GPS is fit to a creep model in which the Sierra Madre Fault is locked below ~12 km, the Puente Hills is locked between ~9 and ~15 km, and the Compton is locked over its entire depth distribution, using the "blocks" and "wings" formulations and the CVM*. The long-term slip rates and misfit are then computed. As previously, backslip rates are colored patches, long-term slip rates are colors of the solid and dashed fault traces, also noted next to the faults, and observed velocities at GPS stations are purple arrows; predicted are light blue arrows.

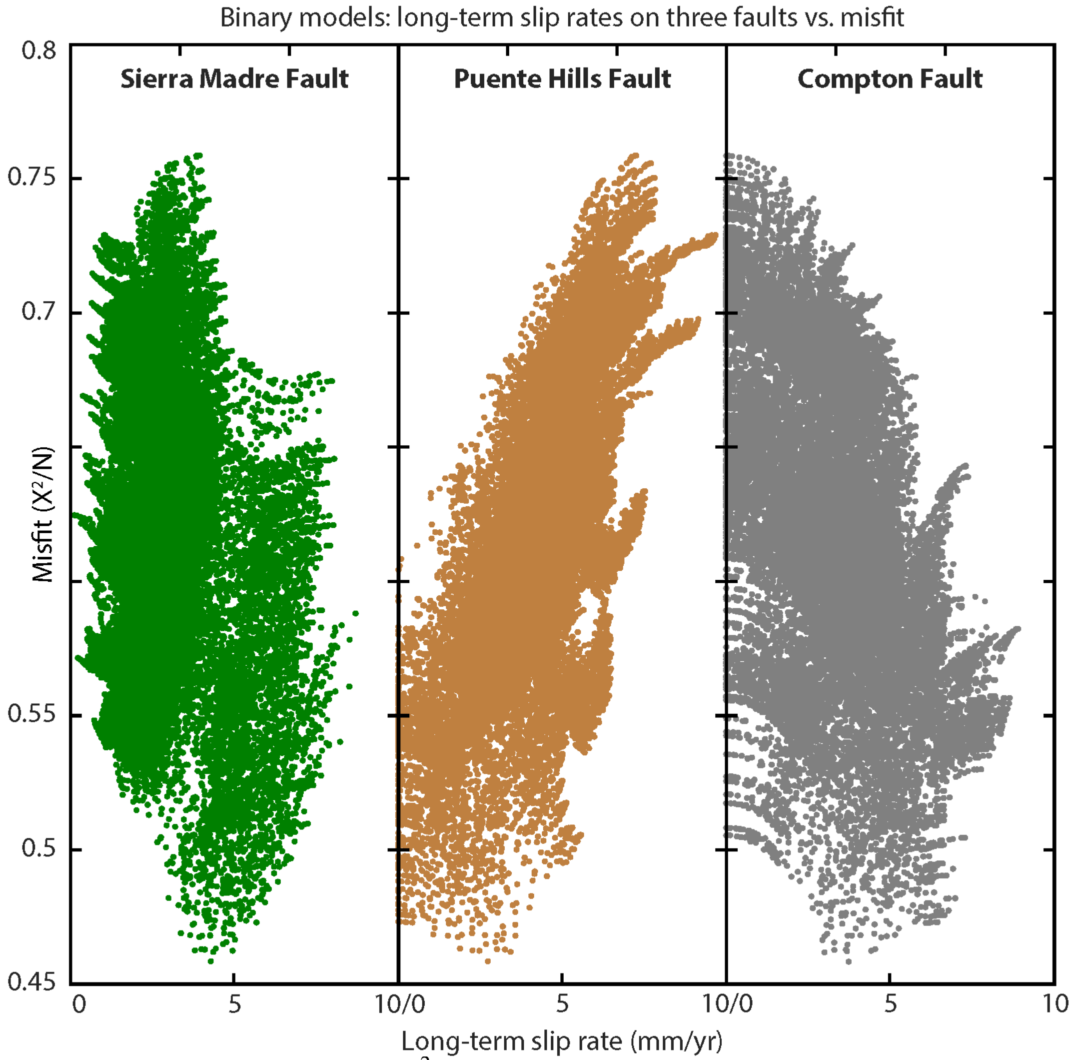

Figure 3.S39. Distribution of X^2/N values of the binary models as a function of the slip rates on the Sierra Madre, Puente Hills and Compton faults.

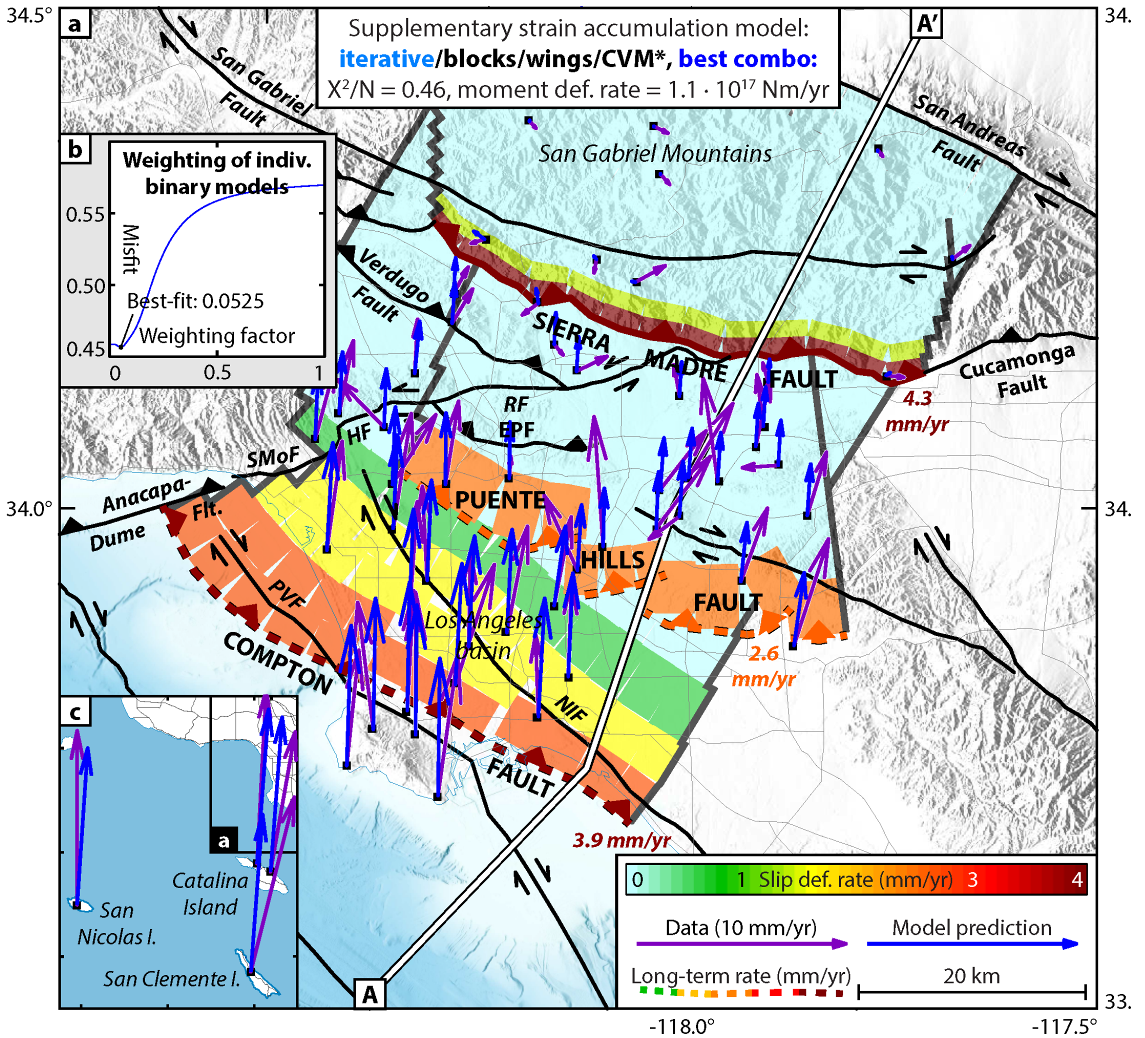

Figure 3.S40. Alternate "iterative" model of strain accumulation on the Compton, Puente Hills and Sierra Madre faults, the weighted average of the binary models (which use the CVM* and the "blocks" and "wings" formulations) in which the weighting is optimized to produce the lowest-misfit combination, as described in the text. **a)** Mapview of backslip rates (colored patches), long-term slip rates (colors of the solid and dashed fault traces, also noted next to the faults), and observed (purple) and predicted (dark blue) velocities at GPS stations. **b)** Distribution of the denominators of the Gaussian weighting function vs. the misfit of the weighted model; the model shown here corresponds to the minimum. **c)** Comparison of observed and predicted velocities on islands.

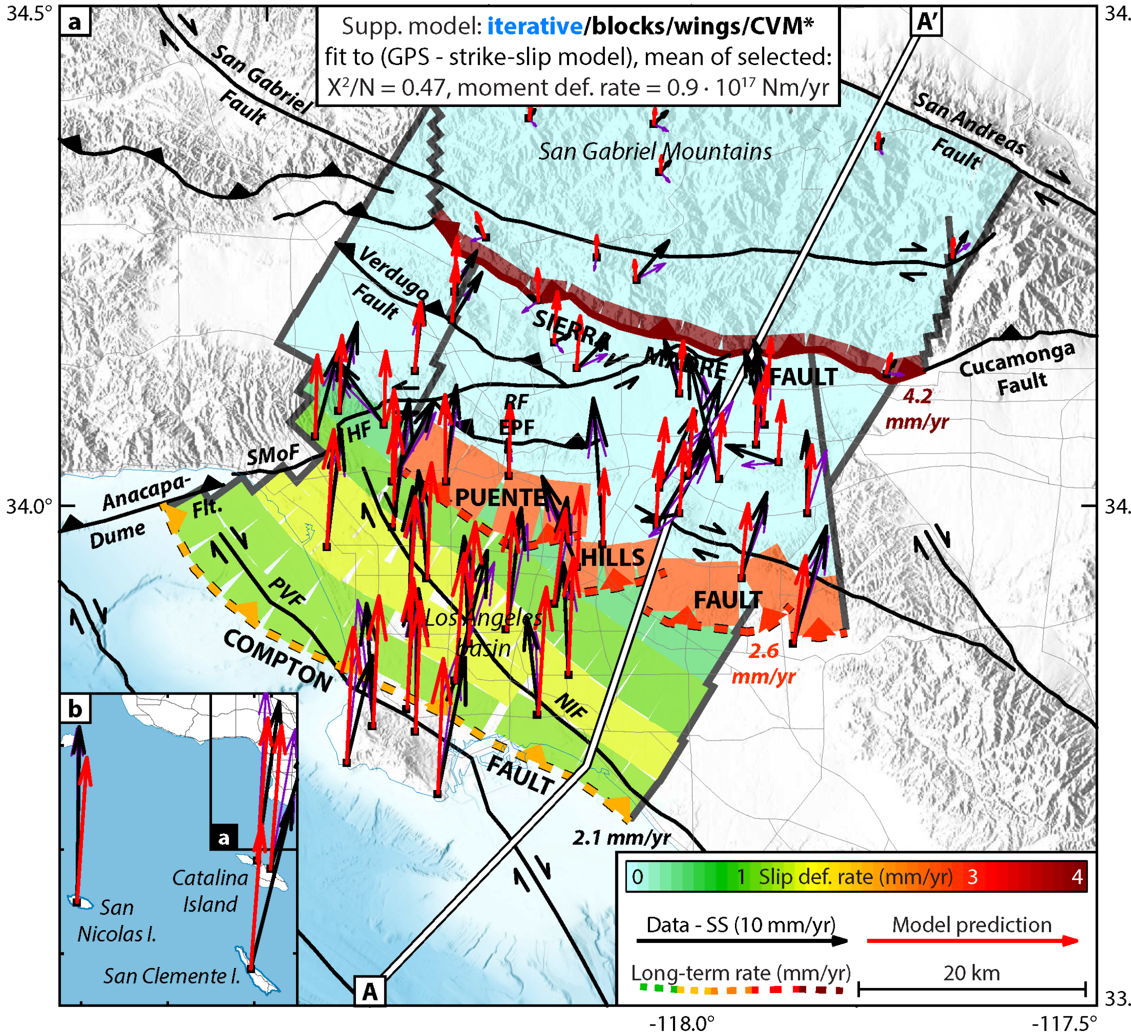

Figure 3.S41. The same three-fault inversion as Model 2 (Figure 3.14) except that the synthetic velocity field from a forward model of strike-slip faults (Figure 3.S14) is removed from the data before inversion. **a)** The slip rate inferred on the Compton Fault is lower than in Model 2. **b)** Comparison of observed and predicted velocities on islands.

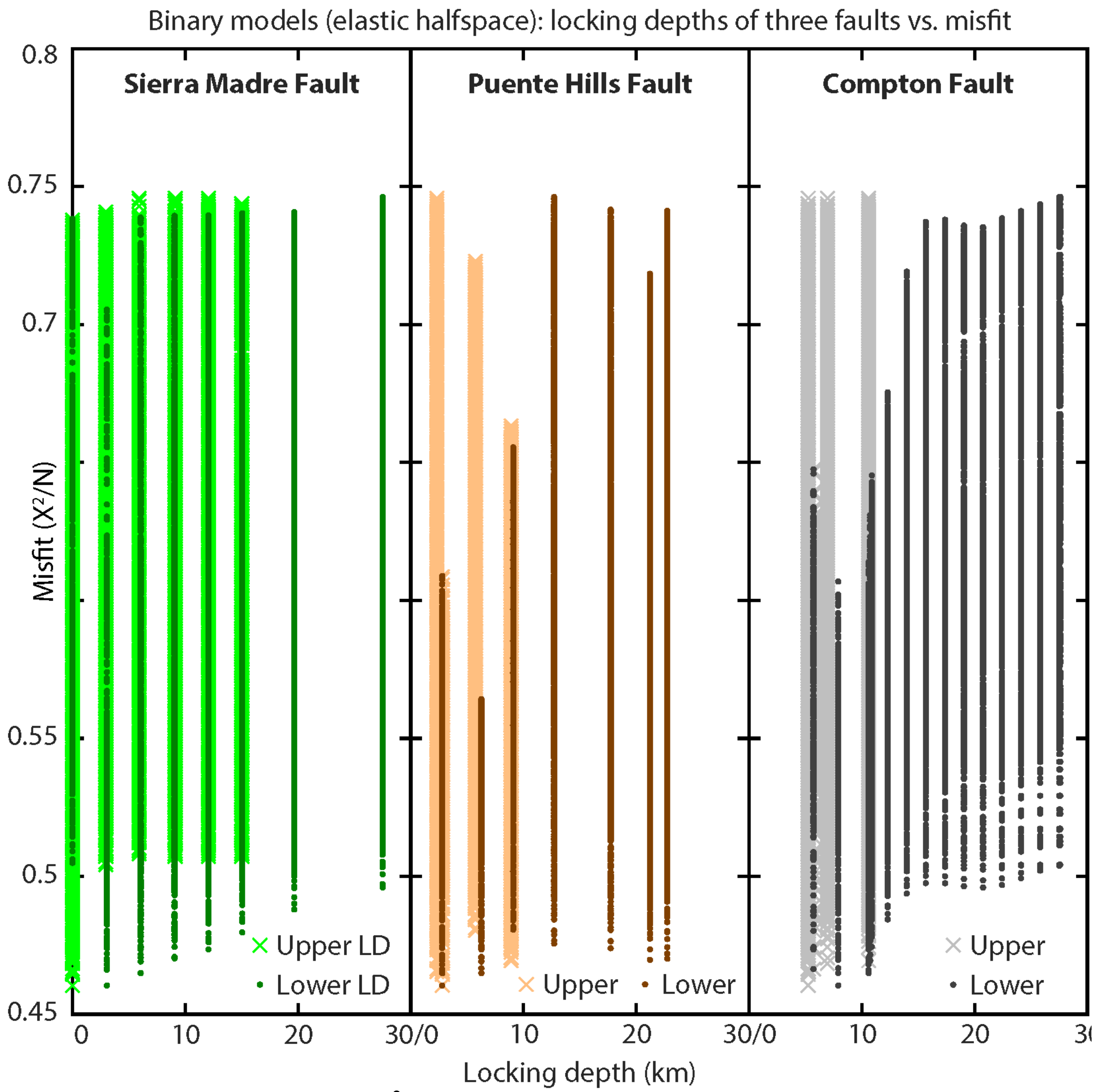

Figure 3.S42. Distribution of X^2/N values of the binary models as a function of the locking depths on the Sierra Madre, Puente Hills and Compton faults if an elastic halfspace model is used.

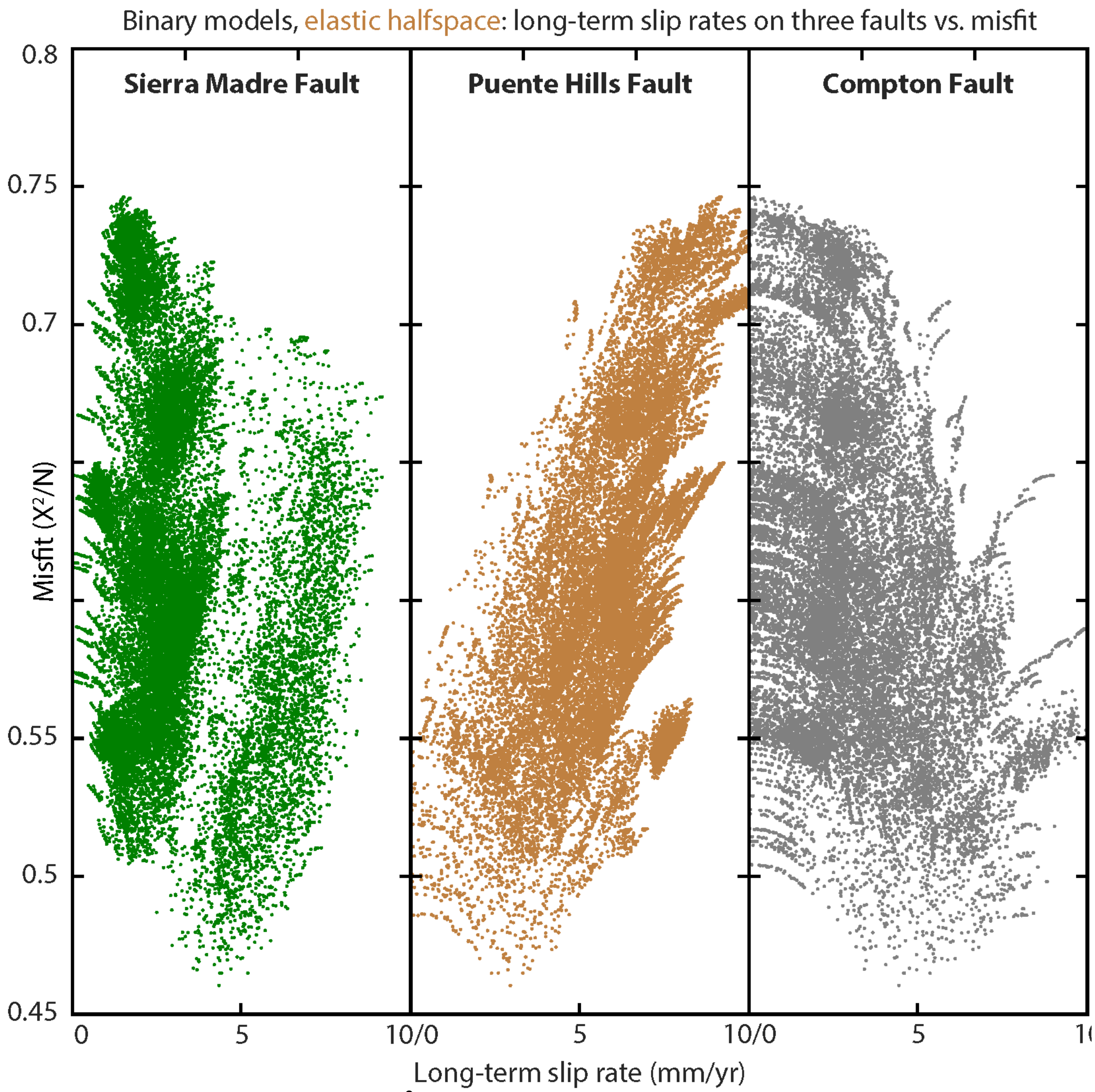

Figure 3.S43. Distribution of X^2/N values of the binary models as a function of the slip rates on the Sierra Madre, Puente Hills and Compton faults if an elastic halfspace model is used.

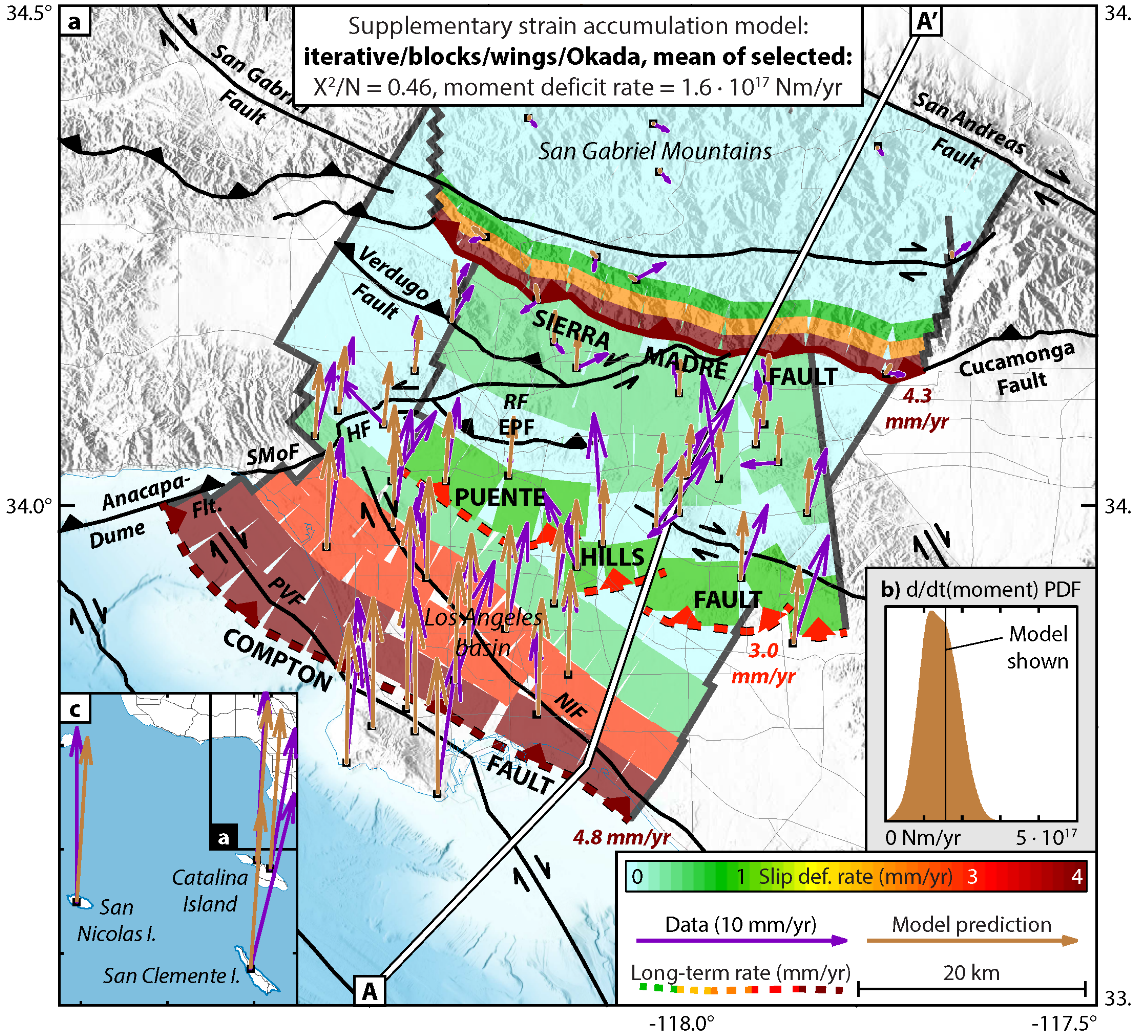

Figure 3.S44. The same three-fault inversion as Model 2 (Figure 3.14) except with an elastic halfspace model. **a)** The model infers more strain accumulation on the Compton Fault and less strain accumulation on the Puente Hills than Model 2, resulting in **b)** a slightly higher moment deficit buildup rate. **c)** Comparison of observed and predicted velocities on islands.

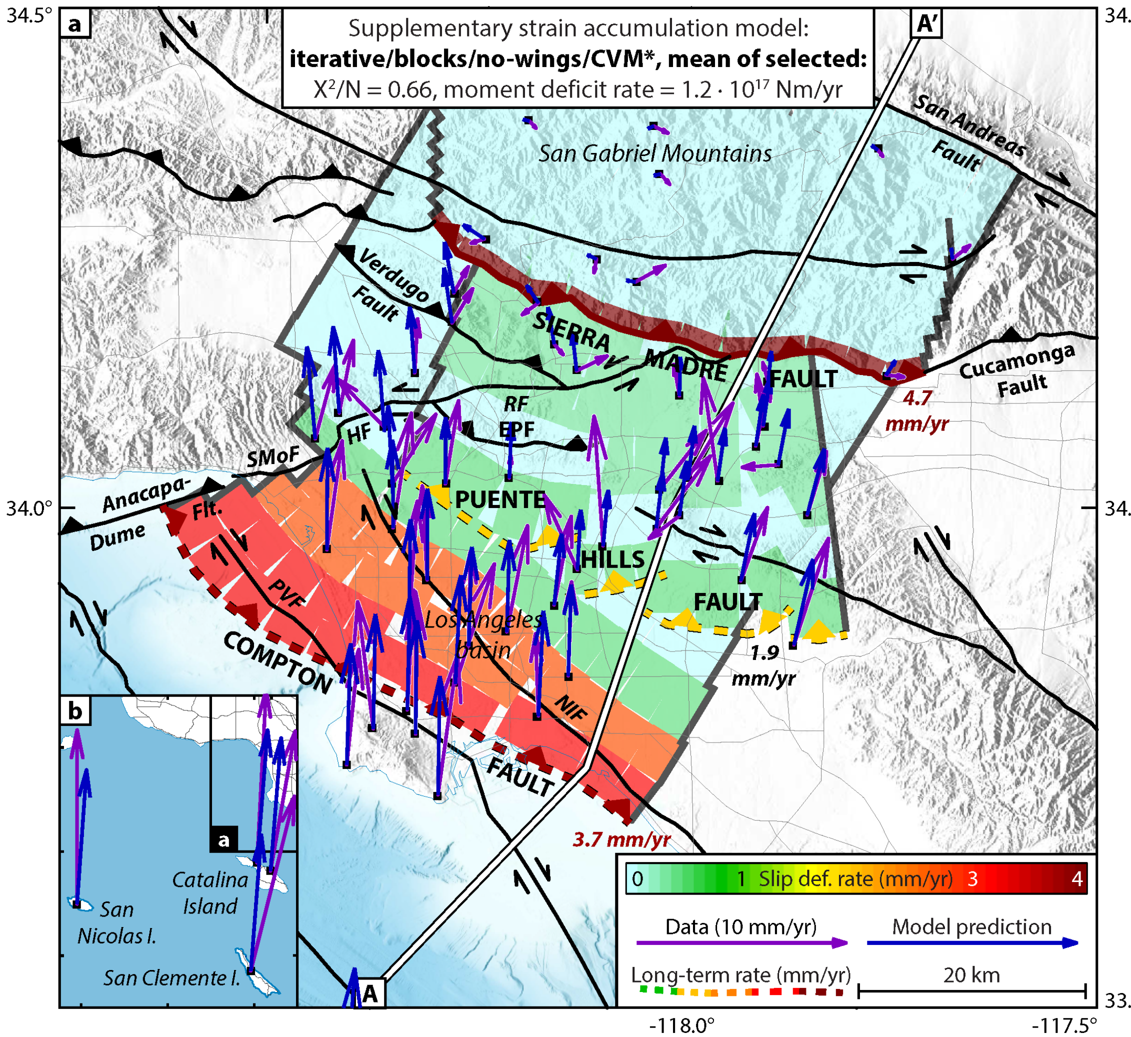

Figure 3.S45. The same three-fault inversion as Model 2 (Figure 3.14) except with the "no-wings" formulation of strain accumulation east and west of the basin. **a)** The model fits the data substantially less well than Model 2, as was the case for the "smooth" scheme (compare Figures 3.S32 and 3.10). **b)** Comparison of observed and predicted velocities on islands.

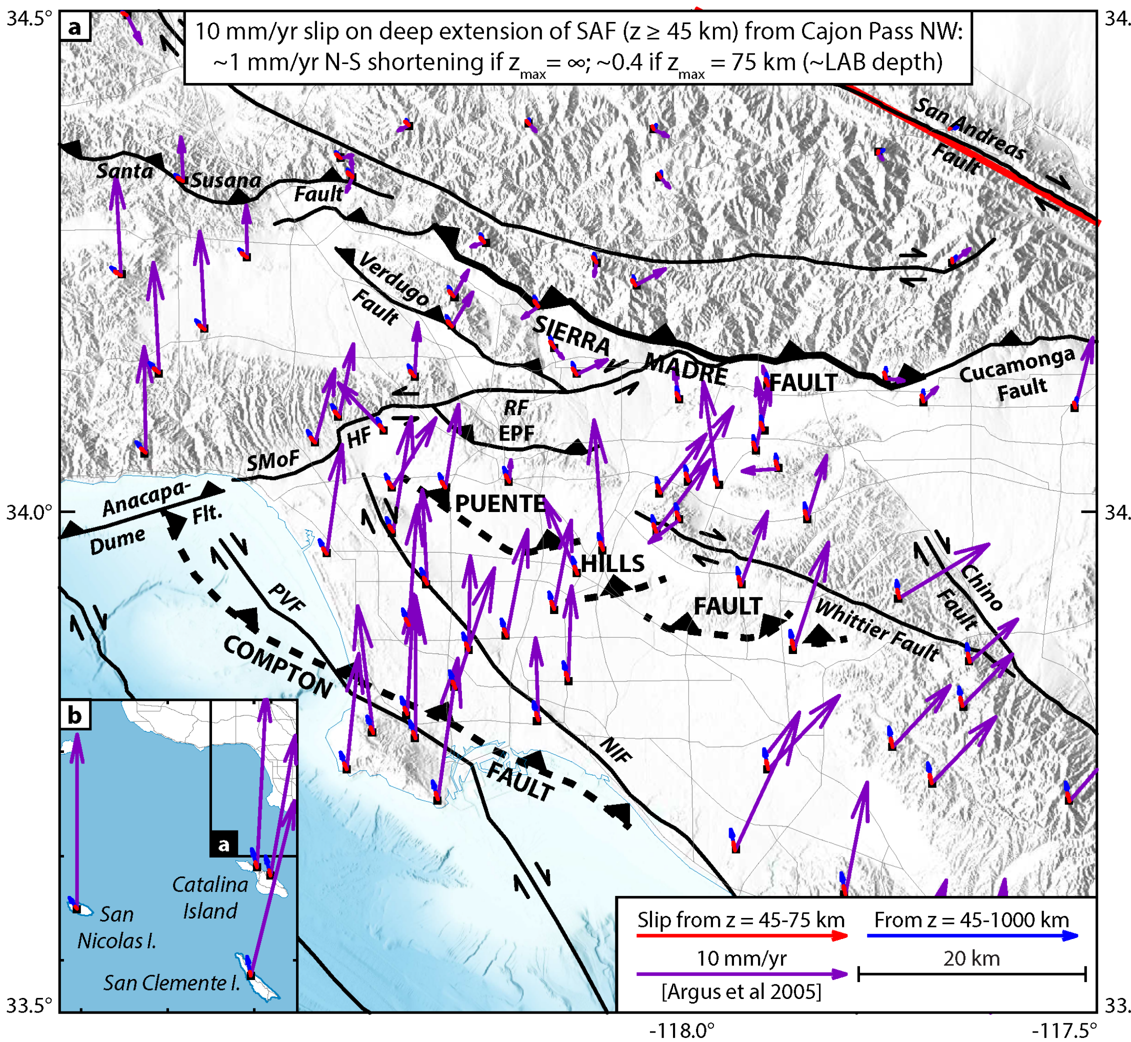

Figure 3.S46. Synthetic velocities computed from a model of 10 mm/yr of forward slip on the San Andreas Fault beneath the 1857 Fort Tejon earthquake's rupture, representing an extreme hypothesis of a continuing afterslip event triggered by the earthquake. The slip produces <1 mm/yr of shortening across Los Angeles.

MODEL SETUP				FIT		Long-term slip rates (mm/yr)			d/dt(moment)
Geometry	SMF	PHF	Compton	VR (%)	X^2/N	SMF	PHF	Compton	(x 10^{17} Nm/yr)
"2D"	-	-	-	37.7	2.57	-	-	-	0.0
			Creeping	70.6	1.15	-	-	9.5 +0.8/-0.7	0.0
			Coupled	84.5	0.62	-	-	10.4 +0.7/-0.7	5.7 +0.8/-0.8
		Creeping	-	78.0	0.87	-	7.2 +0.6/-0.6	-	0.0
			Creeping	79.4	0.84	-	5.8 +0.7/-0.7	2.4 +1.0/-1.2	0.0
			Coupled	85.7	0.59	-	2.2 +0.8/-0.8	7.9 +1.3/-1.3	5.2 +1.1/-1.0
		Coupled	-	84.1	0.63	-	9.6 +0.9/-0.9	-	3.7 +0.9/-0.7
			Creeping	83.2	0.67	-	7.5 +0.8/-0.9	2.1 +1.0/-1.1	2.5 +0.6/-0.5
			Coupled	83.6	0.64	-	6.5 +0.5/-0.6	2.5 +0.8/-0.8	1.4 +0.3/-0.3
	Creeping	-	-	68.1	1.27	6.7 +0.9/-0.9	-	-	0.0
			Creeping	82.7	0.67	4.5 +0.9/-0.8	-	6.8 +0.8/-0.7	0.0
			Coupled	85.9	0.57	2.4 +1.0/-1.0	-	8.7 +1.1/-1.0	4.3 +1.5/-1.6
		Creeping	-	83.9	0.61	3.6 +0.9/-0.8	5.3 +0.7/-0.6	-	0.0
			Creeping	85.6	0.57	3.7 +0.8/-0.9	3.6 +0.7/-0.7	2.9 +0.9/-1.1	0.0
			Coupled	87.0	0.53	2.2 +1.0/-1.1	2.3 +1.0/-1.0	6.3 +2.1/-2.2	4.0 +2.2/-2.5
		Coupled	-	84.5	0.59	2.9 +0.9/-0.9	6.5 +1.0/-1.0	-	1.2 +0.8/-0.7
			Creeping	85.9	0.56	3.1 +0.9/-0.9	4.7 +1.0/-1.1	2.7 +1.0/-1.0	1.0 +0.7/-0.6
			Coupled	87.2	0.52	1.9 +1.1/-0.9	4.1 +0.9/-1.0	4.6 +1.3/-1.4	3.3 +1.6/-1.7
	Coupled	-	-	77.4	0.85	9.3 +0.9/-0.8	-	-	2.2 +0.4/-0.3
			Creeping	85.0	0.56	5.8 +0.6/-0.6	-	6.0 +0.6/-0.7	1.0 +0.3/-0.3
			Coupled	86.4	0.52	6.1 +0.9/-0.9	-	6.2 +0.8/-0.9	2.8 +0.7/-0.7
		Creeping	-	85.0	0.55	4.7 +0.7/-0.6	4.7 +0.6/-0.5	-	0.8 +0.3/-0.3
			Creeping	86.7	0.51	4.8 +0.7/-0.6	2.9 +0.6/-0.5	2.9 +1.0/-1.0	0.8 +0.3/-0.3
			Coupled	87.3	0.49	5.2 +1.1/-1.1	2.1 +0.6/-0.6	4.1 +1.3/-1.2	2.4 +1.0/-0.9
		Coupled	-	85.5	0.54	5.1 +0.9/-0.9	5.1 +0.9/-0.9	-	1.9 +0.7/-0.6
			Creeping	87.0	0.50	5.4 +0.9/-0.9	3.2 +0.8/-0.8	2.9 +0.9/-1.1	1.7 +0.6/-0.5
			Coupled	**87.5**	**0.49**	**4.6 +1.1/-1.3**	**3.1 +0.8/-0.8**	**3.6 +1.0/-1.1**	**2.4 +1.0/-0.9**
	Coupled (Okada)	Coupled (Okada)	Coupled (Okada)	87.3	0.49	4.7 +1.2/-1.3	3.8 +1.0/-0.9	3.7 +1.0/-1.2	2.0 +0.8/-0.9

MODEL SETUP				FIT		Long-term slip rates (mm/yr)			d/dt(moment)
Geometry	SMF	PHF	Compton	VR (%)	X^2/N	SMF	PHF	Compton	(x 10^{17} Nm/yr)
"3D"	-	-	Creeping	68.2	1.39	-	-	9.0 +0.7/-0.6	0.0
			Coupled	82.3	0.89	-	-	10.5 +1.1/-1.0	8.4 +1.4/-1.4
		Creeping	-	74.5	1.09	-	7.4 +0.7/-0.6	-	0.0
			Creeping	77.3	1.04	-	5.7 +0.9/-0.8	2.9 +1.4/-1.6	0.0
			Coupled	82.5	0.86	-	3.1 +0.9/-0.9	6.8 +1.5/-1.5	5.5 +1.4/-1.5
		Coupled	-	79.3	1.00	-	9.2 +0.9/-0.9	-	3.1 +1.0/-1.0
			Creeping	81.9	0.86	-	8.1 +0.8/-0.8	1.9 +1.3/-1.7	3.3 +0.8/-0.8
			Coupled	83.0	0.85	-	6.0 +0.6/-0.6	4.0 +1.3/-1.2	4.8 +1.4/-1.3
	Creeping	-	-	67.8	1.34	7.0 +1.0/-1.0	-	-	0.0
			Creeping	79.4	0.93	4.9 +1.1/-1.0	-	6.0 +1.1/-1.1	0.0
			Coupled	83.7	0.81	2.7 +1.4/-1.5	-	8.2 +1.8/-1.6	4.6 +2.3/-2.3
		Creeping	-	81.8	0.80	4.2 +0.9/-1.0	5.3 +0.9/-0.7	-	0.0
			Creeping	83.6	0.77	4.0 +1.0/-0.9	4.1 +0.7/-0.8	2.2 +1.3/-1.6	0.0
			Coupled	84.7	0.75	2.9 +1.2/-1.2	2.7 +1.1/-1.0	4.9 +2.4/-2.3	2.8 +2.2/-1.9
		Coupled	-	82.4	0.78	3.5 +1.0/-1.0	6.2 +1.1/-0.9	-	1.1 +0.5/-0.6
			Creeping	84.0	0.75	3.1 +1.1/-1.1	5.9 +1.1/-1.2	1.9 +1.3/-1.7	1.8 +1.0/-1.0
			Coupled	85.1	0.72	2.6 +1.2/-1.1	4.2 +0.9/-0.9	3.8 +1.5/-1.6	3.2 +1.6/-1.5
	Coupled	-	-	79.5	0.90	10.8 +1.1/-1.1	-	-	3.5 +0.7/-0.6
			Creeping	82.9	0.75	7.1 +0.7/-0.8	-	4.6 +1.0/-1.2	2.2 +0.4/-0.5
			Coupled	84.7	0.74	5.9 +1.2/-1.2	-	5.7 +1.3/-1.4	3.3 +1.3/-1.1
		Creeping	-	83.7	0.70	6.2 +0.7/-0.8	4.2 +0.6/-0.7	-	1.9 +0.5/-0.6
			Creeping	84.9	0.69	5.7 +0.7/-0.8	3.3 +0.6/-0.6	2.0 +1.3/-1.6	1.6 +0.5/-0.6
			Coupled	85.1	0.71	5.4 +1.2/-1.2	2.6 +0.8/-0.9	3.2 +1.6/-1.8	2.1 +1.2/-1.2
		Coupled	-	84.1	0.70	5.9 +1.1/-1.2	4.9 +1.0/-0.9	-	2.9 +1.0/-0.9
			Creeping	85.0	0.71	5.7 +1.1/-1.0	3.6 +0.8/-0.8	2.0 +1.3/-1.6	2.0 +0.9/-0.8
			Coupled	85.1	0.71	5.3 +1.1/-1.1	3.1 +0.9/-0.8	2.7 +1.4/-1.7	2.0 +1.0/-0.9
	Coupled (Okada)	Coupled (Okada)	Coupled (Okada)	84.8	0.71	5.6 +1.2/-1.3	4.7 +0.9/-1.0	2.2 +1.6/-1.8	1.5 +0.8/-0.9

Table 3.S1. Setups, long-term slip rates, moment deficit accumulation rates, and misfits of each of the models in the suite described in section 3.4.8 (gray dots in Figure 3.12).

Chapter 4

GEODETIC CONSTRAINTS ON THE MAGNITUDE AND FREQUENCY OF LARGE EARTHQUAKES IN LOS ANGELES

ABSTRACT

North-south tectonic shortening across the Los Angeles metropolitan area produces damaging thrust earthquakes such as the 1971 Mw~6.7 San Fernando, 1987 Mw~5.9 Whittier Narrows and 1994 Mw~6.7 Northridge shocks. The return period of such events is poorly constrained, and paleoseismologic studies suggest this shortening may produce thrust earthquakes as large as Mw~7.5. Here we build a Bayesian model of long-term average earthquake behavior in Los Angeles using three tools: 1) a probabilistic estimate of the rate at which seismic moment deficit is accumulating on major thrust faults beneath the Los Angeles basin (accounting for fault geometries and subsurface material heterogeneities), 2) the principle that over the long term this rate of accumulation should be balanced by the release of seismic moment in earthquakes, and 3) the hypothesis that these earthquakes should obey a truncated Gutenberg-Richter magnitude-frequency distribution that tops out at a maximum-magnitude earthquake, with events larger than this magnitude being comparatively rare over the long term. The resulting model matches the rates of small and moderate earthquakes in Los Angeles and tops out at a Mw~6.9 earthquake with an average return period of 430 +270/-150 years. The large suite of estimated long-term earthquake catalogs that go into this estimate also allow one to estimate the probability of observing an earthquake of or exceeding a given magnitude over a given timespan, which can be used in probabilistic seismic hazard assessment.

4.1. Introduction

Geodetic data show that the Los Angeles area is contracting in the north-south direction at ~8.5 mm/yr (Figure 4.1a). This distributed shortening is accommodated by the gradual accumulation of strain on thrust faults such as the Sierra Madre, Puente Hills and Compton faults and the sudden release of (the elastic component of) that strain in damaging earthquakes such as the 1971 Mw=6.7 San Fernando, 1987 Mw=5.9 Whittier Narrows and 1994 Mw=6.7 Northridge shocks. In addition to these recent earthquakes, paleoseismologic studies suggest that the Sierra Madre Fault may have ruptured in two earthquakes since 15 Ka with magnitudes as high as Mw~7.5 [Rubin et al, 1998], the Puente Hills Fault may have ruptured in three earthquakes since 8.1 Ka with magnitudes as high as Mw~7.2-7.4 [Dolan et al, 2003; Leon et al, 2007], and the Compton thrust fault may have produced six earthquakes since 14 Ka with magnitudes as high as Mw~7.0-7.4 [Leon et al, 2009]. An earthquake like these would be devastating not only because of these faults' proximity to the Los Angeles metropolitan area but also because the sedimentary fill of the Los Angeles basin amplifies shaking in earthquakes [e.g. Bowden and Tsai, 2017]. It is therefore crucial to make an assessment of the seismic hazard associated with this north-south shortening.

Rollins et al [Chapter 3] show that the shortening may be principally accommodated by strain accumulation and release on the Sierra Madre, Puente Hills and Compton faults (Figure 4.2a) and that seismic moment deficit accumulates on these systems at a total annual rate of 1.7 +1.2/-0.5 x 10^{17} Nm/yr (Figure 4.2b, purple PDF). This estimate incorporates the heterogeneous material properties of the Los Angeles basin; if those were not taken into account, the estimate would be 1.3 +1.0/-0.3 x 10^{17} Nm/yr (Figure 4.2b, tan line). These rates are relatively modest compared to previous estimates (e.g. 43% of the rate estimated by Meade and Hager [2005]), and one factor in this is the consideration that the Puente Hills and Compton faults are blind, with their upper fault tips respectively at ~3 and ~5 km depth. Rollins et al [Chapter 3] assumed that deformation updip of the upper tips of these faults is anelastic and does not contribute to seismic hazard. If it were alternatively assumed that strain does accumulate updip of these faults (at a rate consistent with the modeling) and factors into earthquake production, the rate of moment deficit accumulation would be 2.5 +1.3/-0.5 x 10^{17} Nm/yr (Figure 4.2b, red line).

In this study, we translate this into a model of long-term earthquake likelihood [e.g. Shen et al, 2007; Rong et al, 2014; Bird et al, 2014; Hsu et al, 2016] using two additional tools. The first is the principle that over the long term, the rate of moment deficit accumulation should be balanced by the rate of moment release in earthquakes [Brune

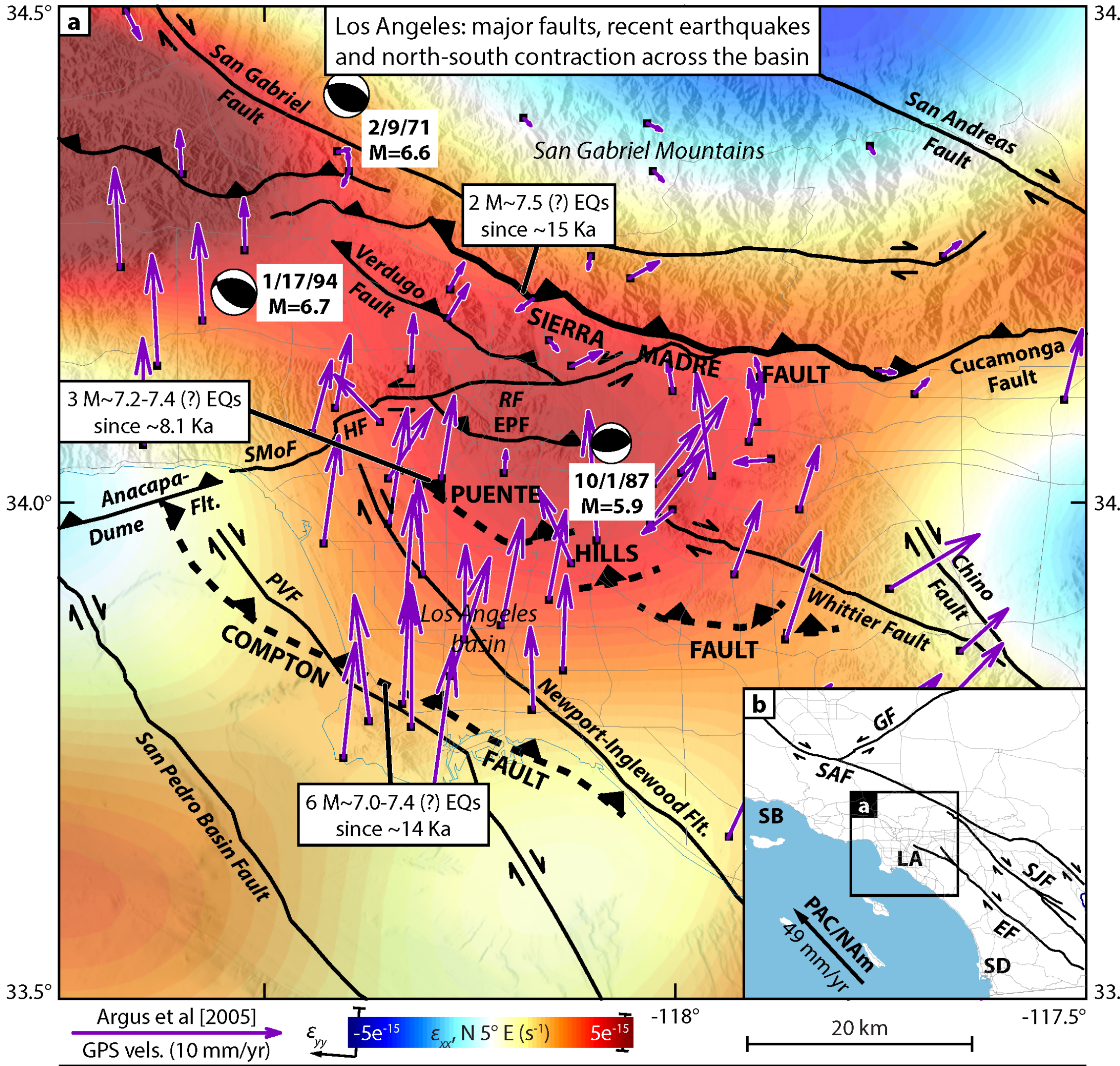

Figure 4.1. a) North-south shortening, active faults and large earthquakes in the Los Angeles basin. Purple arrows are shortening-related GPS velocities relative to the San Gabriel Mountains [Argus et al, 2005]. Shading is uniaxial strain in the N ~5° E direction estimated from the GPS using the spherical-wavelet method of Tape et al [2009]. Thicker and thinner black lines are upper edges of thrust and strike-slip faults, respectively, dashed for blind faults. Epicenters of the 1971, 1987 and 1994 earthquakes are from SCEDC; focal mechanisms are from Heaton [1982] for 1971 and Global CMT Catalog for 1987 and 1994. Gray lines are highways. SMoF: Santa Monica Fault. HF: Hollywood Fault. RF: Raymond Fault. EPF: Elysian Park Fault. **b)** Regional tectonics. Black lines and pairs of half-arrows, respectively, are major faults and their slip directions. Black arrow is velocity of Pacific plate relative to North American plate from Kreemer et al [2014], courtesy of UNAVCO Plate Motion Calculator.

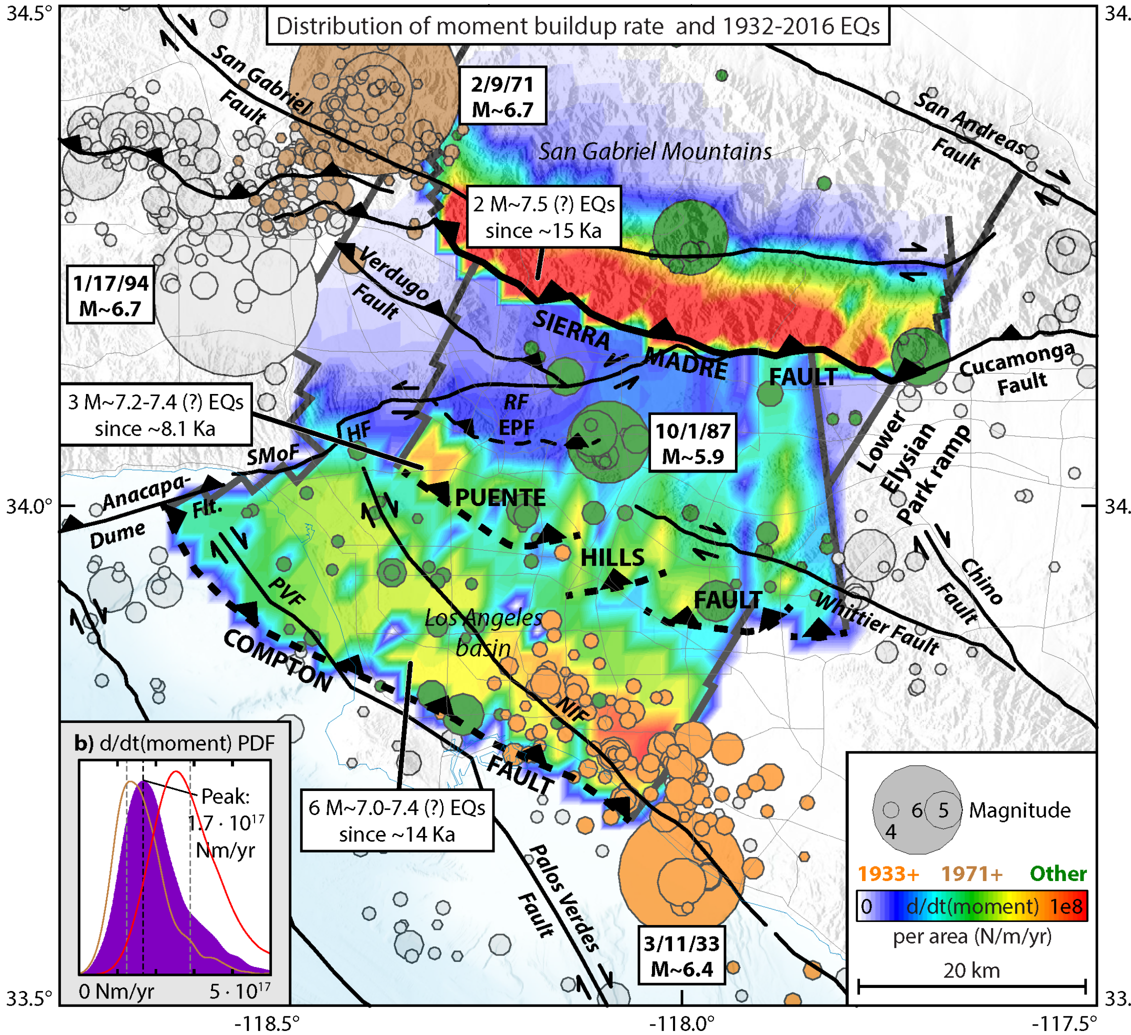

Figure 4.2. a) Spatial distribution of moment deficit buildup rate in Los Angeles from Rollins et al (Chapter 3) and color-coded earthquake "subcatalogs" that differ on whether the 1933 M=6.4 Long Beach and the 1971 M=6.7 San Fernando earthquakes and their aftershocks are counted. **b)** PDF of moment deficit accumulation rate. Red line denotes the PDF if strain accumulation on the updip surface extensions of the blind Puente Hills and Compton faults is counted.

1968, Molnar 1979]. The second is the high-quality seismic catalog in Los Angeles (Figure 4.2a), which provides constraints on the relative occurrence rates of small, moderate and large earthquakes and therefore on the relative contribution they make to balancing the budget of moment accumulation. The Southern California Earthquake Data Center provides locations and magnitudes for earthquakes throughout Southern California from 1932 to present [Hutton et al, 2010]. Hauksson et al [2012] relocated this catalog for the period 1981-2011 and have since updated their relocated catalog to include earthquakes

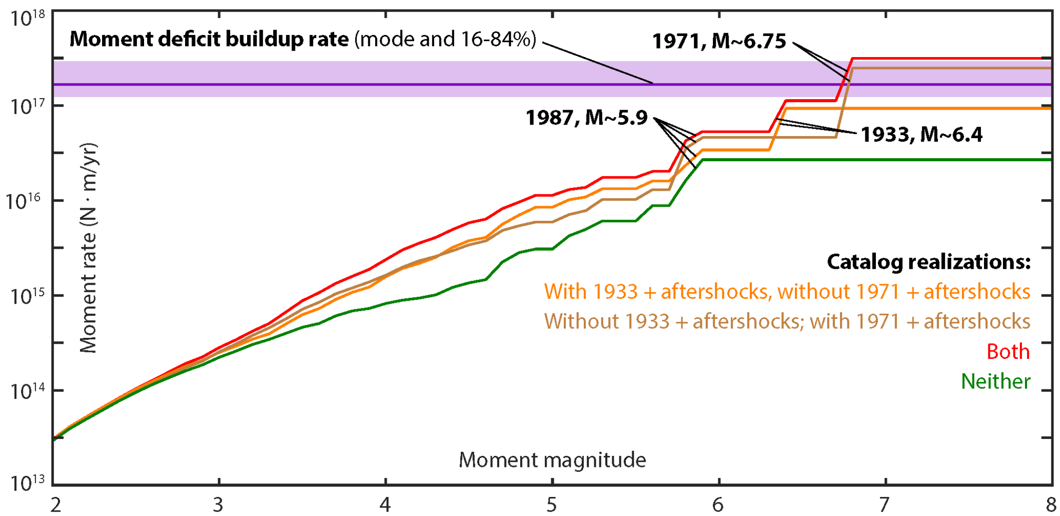

Figure 4.3. Visual estimate of the magnitude of earthquakes needed so that the rate of moment release in earthquakes would balance the geodetically inferred moment deficit accumulation rate (purple PDF). The colored lines denote, at each magnitude, the cumulative moment release per year by earthquakes up to that magnitude in each of the four subcatalogs as indicated.

through mid-2016 (http://scedc.caltech.edu/research-tools/alt-2011-dd-hauksson-yang-shearer.html). We therefore use the SCEDC catalog for the period 1932-1980 and the updated Hauksson et al catalog, which we henceforth refer to as HYS16, for the period 1981-2016. The earthquakes we consider are those that lie within the area of the mesh of the Sierra Madre, Puente Hills and Compton faults and the north-dipping decollement in Chapter 3. We use these tools to determine a long-term model of seismicity in Los Angeles that balances the geodetically inferred rate of moment deficit accumulation and is consistent with the instrumental catalog at small and moderate magnitudes. We focus in particular on the 2D probability distribution of the magnitude and recurrence interval of the largest earthquake in the model.

4.2. Qualitative comparison of strain accumulation vs. release in earthquakes

As a first pass, one can simply compare the total moment release in the 84-year instrumental catalog to the total moment that should have accumulated in that period according to the geodesy-based model. More illustrative is to make this comparison at a variety of cutoff magnitudes; one can then visually estimate how large earthquakes need to become in order to balance the moment budget [Stevens and Avouac, 2016, fig. 1]. Figure 4.3 shows this comparison using the PDF of moment deficit accumulation rate and four "subcatalogs," alternate versions of the combined SCEDC and HYS16 catalogs that differ on whether the 1933 Mw~6.4 Long Beach and 1971 Mw~6.7 San Fernando earthquakes (and their aftershocks), which lie on the periphery of the study area, are included or not (Appendix 4.1, Figure 4.2). Whether the moment budget has been balanced over the last 84 years, in this approach, visibly depends entirely on whether the 1933 and 1971 earthquakes are counted. This method provides no way of knowing whether it is correct to do so – whether it is statistically likely that a Mw=6.4 or a Mw=6.7 earthquake should have shown up in the 84-year instrumental catalog. This comparison also ignores the moment released by earthquakes that are small enough to go undetected by seismic networks, which could contribute nontrivially to the overall moment release rate.

4.3. Quantitative assessment of the implications for earthquake behavior: method

To correct for these limitations, we assume that over the long term seismicity obeys a Gutenberg-Richter relation, which enables us to estimate the frequencies of large (and small, undetected) earthquakes by extrapolating the statistics of small and moderate earthquakes. The Gutenberg-Richter relation expresses the observation that in sufficiently populated catalogs, the frequency $N(M \geq M_w)$ of earthquakes with moment magnitude equal to or exceeding a given M_w often obeys a log-linear relation,

$$\log_{10} N(\geq M_w) = a - bM_w, \quad [4.1]$$

with the parameters a and b describing the intercept and slope of the log-linear relation. If this is assumed to hold for all magnitudes up to the maximum-magnitude earthquake, we can use the statistics of small earthquakes in Los Angeles to estimate those of large earthquakes over time. Building on the formulation of Molnar [1979], Stevens and Avouac [2017] have devised an iterative method to estimate the maximum-magnitude earthquake and the long-term seismic catalog based on 1) a moment deficit accumulation rate, 2) an earthquake catalog, 3) a magnitude of completeness characterizing the catalog, and 4) the parameter b describing the relative rates of earthquakes over the range of magnitudes (Appendix 4.2). All four pieces are constrained in Los Angeles. Rollins et al [Chapter 3] have determined the probability density function (PDF) of the moment deficit accumulation rate. For the seismic catalog, we use each of the four previously described "subcatalogs" that differ on whether they count the 1933 and 1971 earthquakes and their aftershocks. As described in Appendix 4.3, we choose M_c=3.5-4.0, and we determine a PDF for the appropriate b-value using 1,050 samples from the with-1933/with-1971 subcatalog (Figure 4.S1). Finally, some of the moment deficit that accumulates in the interseismic period may be released aseismically, for example in afterslip following earthquakes. We assume that 25% of deformation occurs aseismically based on observations following the Northridge earthquake [Donnellan et al, 1998]; we assess the effect of this assumption subsequently.

4.4. Quantitative assessment of the implications for earthquake behavior: results

Our preferred long-term earthquake model combines the full PDF of the moment deficit accumulation rate (Figure 4.2b), all samples of the b-value, and all four subcatalogs of the long-term earthquake catalog. The estimated long-term earthquake catalog lies in the middle of the four subcatalogs at small and moderate magnitudes (Figure 4.4). The 2D probability density function of the magnitude and frequency of the maximum-magnitude earthquake peaks at a Mw=6.87 earthquake with a return period of ~430 +280/-170 years (16^{th} and 84^{th} percentiles); the one-dimensional one-sigma uncertainties on the magnitude are +1.23/-0.37. Based on the paleoseismologic studies and their uncertainties, the aggregate mean magnitude and recurrence interval of paleoearthquakes on the three thrust faults are respectively Mw=7.31 ± 0.24 and 920 +100/-80 years (Figure 4.4, black rectangle). Although the 2D PDF of the maximum earthquake needed to balance the moment budget peaks at a smaller and more frequent event, the PDF is long-tailed on the high-magnitude/high-recurrence-interval end, and the likelihood of the maximum earthquake's magnitude exceeding Mw=7.31 is 41%; the one-dimensional median Mmax and recurrence interval are respectively Mw=7.18 and 1210 years.

We can also use the 8.4 million estimates of the long-term earthquake catalog that go into this preferred model to assess the long-term likelihoods of earthquakes of all magnitudes in Los Angeles. To do so, we assume that individual earthquakes follow a Poisson process, wherein the likelihood of observing exactly k earthquakes of or exceeding a given magnitude over a given timespan τ is

$$\exp(-\lambda\tau)(\lambda\tau)^k/k!, \qquad [4.2]$$

where λ is the frequency of earthquakes of or exceeding that magnitude, provided by each of the long-term earthquake catalogs [e.g. Stevens and Avouac, 2016; Michel et al, 2017]. In each catalog, this probability is zero for all magnitudes exceeding the catalog's M_{max} as the Gutenberg-Richter distribution is truncated there. The probability of observing at least one earthquake of or exceeding a given magnitude is then one minus the probability of

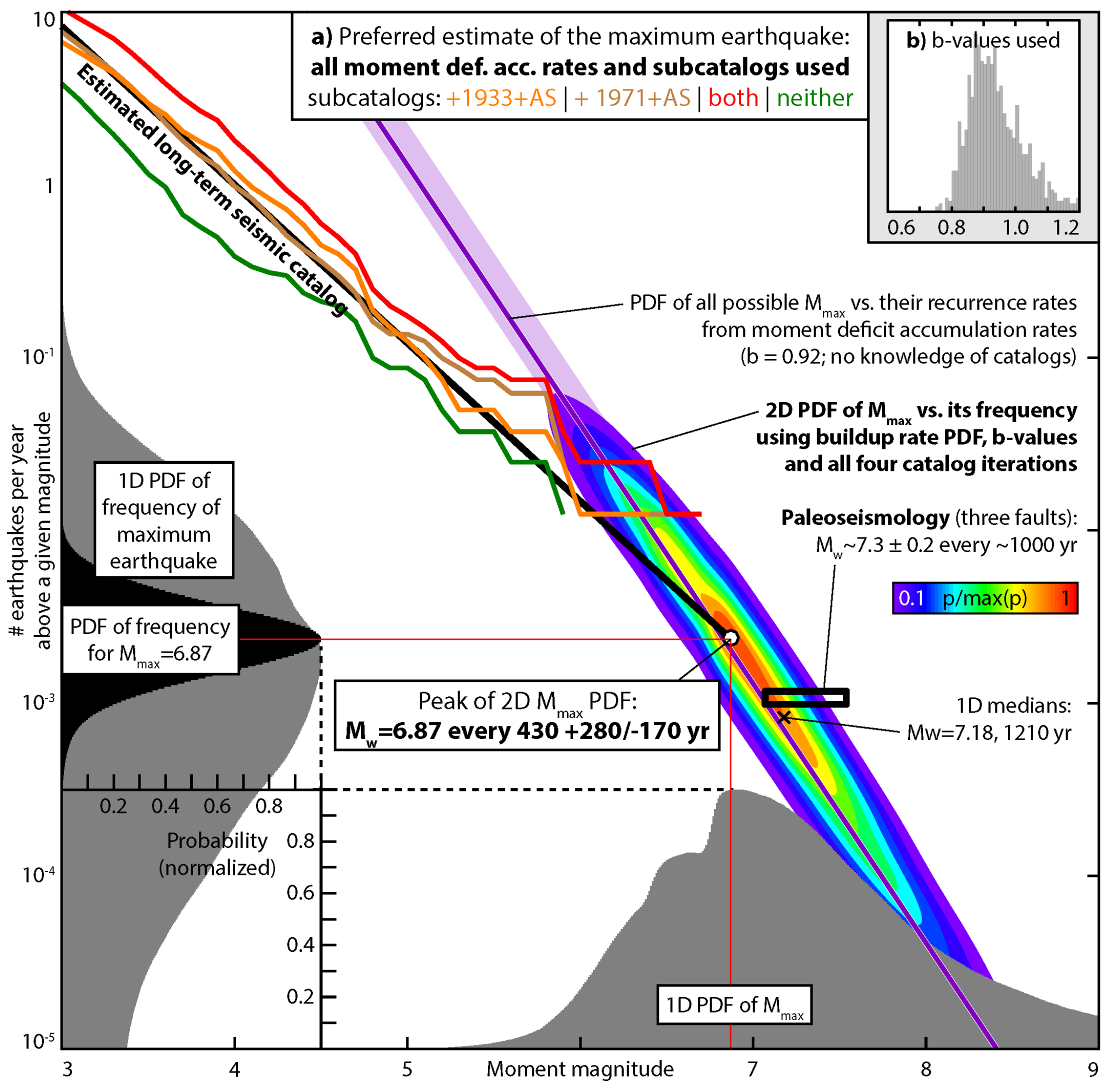

Figure 4.4. a) Preferred quantitative estimate of the long-term seismic catalog and the maximum earthquake based on the instrumental catalog and the strain accumulation models. Red, orange, tan and green lines are subcatalogs; this model combines the estimates using each. Purple object is the PDF of possibilities for the maximum earthquake's magnitude and return period using the geodetically inferred moment accumulation rate and assuming b=0.92 (slope -3b/2 as per Molnar et al [1979]). Colored contours are the 2D PDF of the estimated maximum earthquake's magnitude and return period; thick black line is the estimated long-term seismic catalog. Black box denotes the aggregate return period and magnitudes of earthquakes inferred on the three faults from paleoseismology. **b)** Histogram of b-values.

observing no such earthquakes, 1 - exp(-$\lambda\tau$), where exp(-$\lambda\tau$) is the k = 0 case of the Poisson process. We assess these probabilities for each of the long-term earthquake catalogs and then use the mean of all the catalogs (as the catalogs are assumed to sample the space of

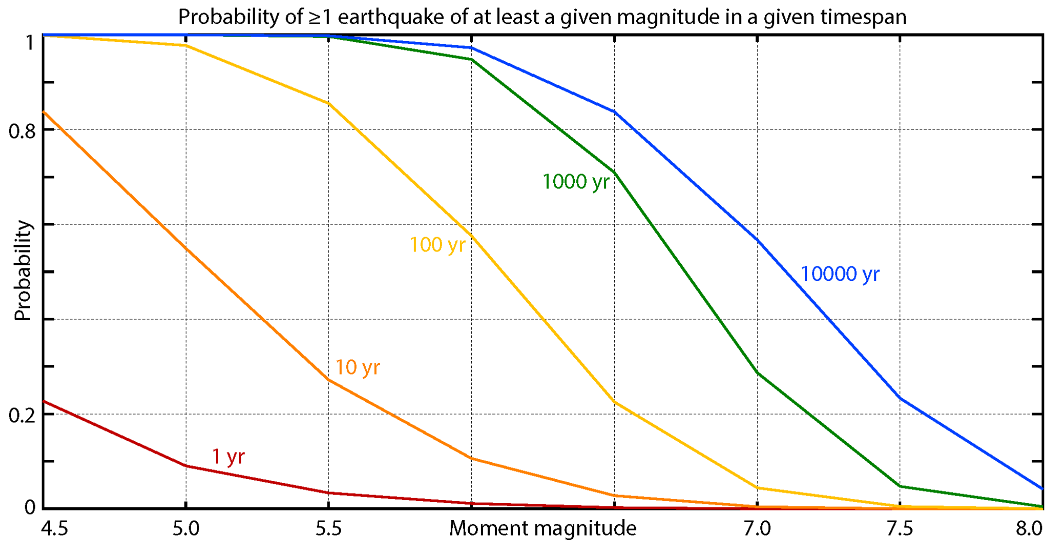

Figure 4.5. Mean probabilities of observing at least one earthquake of or exceeding a given magnitude in the study area over a variety of timespans, as derived from the models that make up Figure 4.4.

possible catalogs proportional to the probability distribution). The probability of observing at least one Mw≥6.0 earthquake in Los Angeles, for example, is 97% over 10,000 years, 95% over 1,000 years, 58% over 100 years, and 11% over 10 years (Figure 4.5); for a Mw≥6.5 shock, the probabilities are 84% over 10,000 years, 71% over 1,000 years, 23% over 100 years, and 2.8% over 10 years (Figure 4.5). The probability of observing three or more Mw≥6.0 earthquakes in the 84-year timespan of the instrumental catalog, which is one minus the summed probabilities of observing zero, one or two such events, is 11.6%, implying that it is statistically unlikely that three earthquakes such as the 1971 M~6.7 San Fernando, 1933 M~6.4 Long Beach and 1987 M~5.9 Whittier Narrows shocks would occur in Los Angeles over 84 years. This can also be seen visually from Figure 4.4, which shows that the rates of earthquakes of or exceeding those magnitudes are several times lower in the inferred long-term catalog than they are in the subcatalogs. The probability of observing at least one Mw≥7.0 earthquake in Los Angeles is 57% over 10,000 years, 29% over 1,000 years, 4.5% over 100 years, and 0.4% over 10 years (Figure 4.5). This implies that it may actually be rather unlikely to observe a paleoseismologic record featuring Mw≥7 earthquakes about every 1,000 years; speculations as to the cause of this discrepancy are provided in the Discussion.

We assess the sensitivity of this result to the various strain accumulation models, catalogs and assumptions. To begin, we use each of the four subcatalogs individually. When we use only the subcatalog that includes both the 1933 and 1971 earthquakes and their aftershocks, the estimated long-term catalog is more populous at small and moderate magnitudes and the PDF of the maximum-magnitude earthquake peaks at a Mw=6.46 earthquake every 100 +60/-40 years (Figure 4.S2), a much smaller and more frequent earthquake than the preferred estimate. This model implies that the 1971 Mw~6.7 earthquake, which is included in the subcatalog that builds it, is statistically unlikely. When we use only the subcatalog that includes the 1933 earthquake and its aftershocks but not the 1971 sequence (Figure 4.S3), the estimated long-term catalog follows the magnitude-frequency distribution of the subcatalog and the PDF of the maximum-magnitude event peaks at a Mw=6.74 earthquake every 270 +180/-90 years. When we use the subcatalog that includes the 1971 sequence but not the 1933 sequence, the PDF of the maximum-magnitude event peaks at a Mw=6.88 earthquake every 430 +280/-160 years (Figure 4.S4). Finally, when we use the subcatalog that includes neither the 1933 nor the 1971 sequence, the estimated long-term catalog is far less populous at small and moderate magnitudes and the PDF of the maximum-magnitude earthquake peaks at a Mw=7.36 shock every 2290 +1600/-810 years, a much larger and rarer maximum-magnitude earthquake (Figure 4.S5). Although this magnitude is similar to those of the earthquakes inferred from paleoseismology, the recurrence interval is more than twice the aggregate of the paleoearthquakes.

If we assume that slip is 100% seismic, rather than 80% seismic as all of the previous estimates have done, the long-term catalog is nearly identical to that in the preferred model at small and moderate magnitudes – not surprising as the same four subcatalogs are used – but the effective moment accumulation rate is larger and the PDF of the maximum-magnitude earthquake peaks at a Mw=7.00 event every 540 +330/-210 years, closer to the inferred magnitude-frequency behavior of the paleoearthquakes (Figure 4.S6). We can alternatively relax the assumption that the deformation above the Puente Hills and Compton faults is anelastic by using the PDF of moment deficit accumulation rate that includes strain accumulation in those updip projections, which peaks at 2.5 x 10^{17} Nm/yr (Figure 4.2b, red line). One then needs to include the earthquakes that occur in the areas bounded by those updip projections, which includes several moderate earthquakes offshore (Figure 4.2b); hence the estimated long-term catalog is more populous at small and moderate magnitudes than in the preferred model. The PDF of the maximum-magnitude earthquake nevertheless peaks at a Mw=6.92 event every 340 +180/-110 years (Figure 4.S7), larger and more frequent than in the model where the faults are blind, as might be expected due to the higher moment deficit accumulation rate. Finally, we can explore the effect of the Los Angeles basin on the estimate of the long-term earthquake catalog by using the PDF of moment deficit accumulation that assumes an elastic halfspace model (Figure 4.2b, tan line). The PDF of the maximum-magnitude earthquake in this case peaks at a Mw=6.85 event every 460 +320/-160 years (Figure 4.S8), only slightly different from the preferred estimate incorporating the basin structure. The overall PDF of the maximum-magnitude earthquake, however, is visibly shifted towards smaller magnitudes compared to the preferred model; the 1D median magnitude and recurrence interval at Mw=7.05 and 960 years, respectively, and the probability of M_{max} exceeding 7.31 is 35% rather than 41% in the preferred model. This is expected, as the moment deficit accumulation rate is somewhat lower with the elastic halfspace assumption.

4.5. Discussion

Our preferred model shows that the elastic strain accumulation in the interseismic period can be accommodated by a Gutenberg-Richter frequency-magnitude distribution of earthquakes that is consistent with the rates of small and moderate earthquakes in the instrumental catalog. The PDF of the maximum-magnitude earthquake's magnitude and recurrence interval peaks at a magnitude 6.87 earthquake every 430 years (Figure 4.4). Our method allows for quantifying the uncertainties on the magnitude and recurrence interval in terms of a 2D probability density function; although the peak is smaller and more frequent than the inferred paleoearthquakes on the Sierra Madre, Puente Hills and Compton faults, the 2D PDF is long-tailed on the upper end and the probability of the maximum-magnitude earthquake exceeding the average paleoearthquake magnitude is 41%. However, the long-term earthquake catalogs suggest that the probability of observing at least one Mw≥7.0 earthquake in 1,000 years is only 29%, suggesting that it may be statistically unlikely to observe Mw≥7 paleoearthquakes at the aggregate recurrence interval of ~920 years. This discrepancy may be due to several causes. The first may be that we report on the mean of the probabilities of observing such an event in all of the long-term catalogs; as the catalogs are truncated at M_{max} and the preferred M_{max} is 6.87, the probability of ever observing a Mw≥7.0 earthquake is in fact zero in many of the catalogs, leading to a long-tailed distribution with zero mode and median but nonzero mean. Another statistic may better represent the range; for example, the 16^{th}- and 84^{th}- percentile probabilities of observing at least one Mw≥7.0 earthquake over 1,000 years are respectively 0% and 65%. The magnitudes of paleoearthquakes on the thrust faults may also be overestimated: these were computed from estimates of slip in the earthquakes using empirical slip-magnitude scaling relations from Wells and Coppersmith [1994] that were based on statistics from both strike-slip and thrust earthquakes, and Leon et al [2009] noted that if one projected slip to estimated magnitude using empirical relations based only on thrust earthquakes, the estimated paleomagnitudes could in fact be ~0.5 lower. This would place them well within the range of our maximum-magnitude estimate. In parallel, the aggregate paleoseismological recurrence interval of ~900 years we estimate here is based only on earthquakes on the Sierra Madre, Puente Hills and Compton faults and would go down if one added paleoearthquakes on other faults within our study area, such as three large-magnitude Holocene earthquakes recently inferred on the Newport-Inglewood Fault [Leeper et al, 2017]. Self-consistency, however, would require that the estimate of total moment deficit accumulation rate then include the accumulation rate on those faults, and the latter is difficult to estimate with geodetic data as Rollins et al [Chapter 3] found that those faults are unlikely to contribute much to the north-south shortening.

It is also worth noting that our model is a long-term average and even if the 2D PDF for the maximum earthquake were a 2D delta function at Mw=6.87 and 430 years, this would not imply that larger earthquakes should never occur, only that they would overshoot the moment budget given the rest of our model and should on average be balanced by proportional quiescence in the catalog. The timescale over which this balance may exist is unknown, as large earthquakes may cluster in time over thousands of years [McCalpin et al 1996, Rockwell et al 2000, Dolan et al 2007, Benedetti et al 2013]. Therefore the M>7 events inferred from paleoseismology may simply constitute the behavior of a system of which our models are an asymptotic long-term average.

Two assumptions involved in our approach are also worth noting. First, as with the comparison of moment deficit accumulation rate and earthquake statistics by depth in Chapter 3, we assume that it is valid to count all earthquakes whose epicenters lie within the area covered by the mesh of the Sierra Madre, Puente Hills and Compton faults – that is, all earthquakes within the volume around the faults. Ideally, it would be more self-consistent to only count earthquakes that demonstrably occurred on one of the three faults (using some distance metric). However, our models of strain accumulation on the thrust faults are themselves characterizations of strain accumulation within the surrounding volume, and as discussed in Chapter 3, it is unlikely that adding more faults to the models of strain accumulation would vastly change the overall moment deficit accumulation rate. Therefore our strain accumulation models may be an adequate proxy for the general strain accumulation that drives seismicity within the volume. Second, we are also assuming that seismicity in the Los Angeles area can be described with a single b-value, whereas the b-value of seismicity may in reality vary between faults and between earthquake sequences (Appendix 4.1). Denser geodetic coverage of the shortening in the Los Angeles area will open the door for comparison of strain accumulation and release on a single-fault basis. In our view, the variability introduced by whether the 1933 and 1971 earthquakes and their aftershocks are counted may be an adequate proxy for the kind of variability that may be encountered in more complex or more localized studies.

Our long-term catalog implies that Mw≥6.4 earthquakes should occur once every ~155 years and therefore that on average an 84-year earthquake catalog in Los Angeles should not include two of them as the 1932-2016 catalog does; in other words, the seismicity over the last 84 years exceeds the estimated long-term earthquake behavior in terms of total moment release. The earthquake history of Los Angeles may be closer to our long-term model if a longer timespan is considered: the Toppozada [2002] historical catalog includes only two Mw≥6 earthquakes in Los Angeles proper between 1769 and 1932, and one of them (the June 28, 1769 earthquake felt by the Portola expedition) has alternatively been hypothesized as having occurred on the San Joaquin Hills Fault in Orange County [Grant et al, 2002], leaving only a M~6 earthquake in 1855 that Yerkes et al [1985] hypothesized as having occurred on the Raymond Fault. This along with the Long Beach, Whittier Narrows and San Fernando earthquakes would tentatively bring the total to four Mw≥5.9, three Mw≥6.0, two Mw≥6.4 and one Mw≥6.7 earthquake in the past 248 years, over which our long-term catalog predicts there should on average be 4.6, 3.7, 1.6 and 0.8, respectively. The earthquake history from 1769 to present may perhaps then be more representative of the long-term behavior predicted by our model.

All the same, a Mw=6.9 earthquake has approximately twice the moment as the 1994 M~6.7 Northridge earthquake. Such an event would therefore pose considerable hazard to Los Angeles considering these faults' proximity to the metropolitan area. It is important to emphasize that this event is only the largest of a population of earthquakes of various magnitudes in our long-term earthquake model. For example, the model predicts that about every 500 years, averaged over the long term, the north-south shortening should be accommodated by slip in three Mw≥6.4 earthquakes, two of which would be Mw≥6.6 and one of which would be Mw~6.9. Any of these earthquakes could be highly damaging due to these faults' proximity to the metropolitan area and the amplifying effect of the Los Angeles basin sediments. Our seismicity model can be used to derive probabilistic seismic hazard models in the Los Angeles basin that account for these site effects.

4.A. Supporting Information

Appendix 4.1. Four "subcatalogs" combining the SCEDC and HYS16 catalogs

As we do not count strain accumulation west and east of the Sierra Madre, Puente Hills and Compton faults in our estimate of moment accumulation, self-consistency dictates that we should only count earthquakes from the SCEDC and HYS16 catalogs that occurred in the two-dimensional area covered by the mesh of the three faults and underlying decollement. This turns out to cause ambiguities in the use of the SCEDC catalog because the 1933 M~6.4 Long Beach earthquake and the 1971 M~6.7 San Fernando earthquake, the largest two earthquakes near Los Angeles in the catalog, are both located as having occurred just off the fault mesh and their aftershock sequences onlap the mesh edges (Figure 4.2). These two sequences comprise most of the seismicity in the mesh area between 1932 and 1980, and the choice of how to account for them may therefore have substantial implications for the inferred balance of moment accumulation and release. Although we are assessing strain accumulation on thrust faults, strain accumulation on the Newport-Inglewood Fault (on which the 1933 earthquake occurred) might contribute to the observed north-south shortening; and though the 1971 earthquake likely occurred on one or more western extensions of the Sierra Madre Fault [e.g. Heaton, 1982], strain accumulation on this branch may contribute to the shortening that we inferred as occurring on the Sierra Madre Fault. The choice of whether to count these earthquakes is therefore ambiguous. We handle this ambiguity by creating four alternate versions of the 1932-1980 SCEDC catalog for Los Angeles: one including both earthquakes and their aftershock sequences; one including the 1933 earthquake and its aftershocks but not the 1971 earthquake or its aftershocks; one including the 1971 sequence but not the 1933 sequence; and one including neither sequence (Figure 4.2). We characterize the aftershocks of the 1971 earthquake as all earthquakes that occurred within 20 km of the epicenter in space and within one year of the mainshock. Tests with various radii and timespans indicate that the specific choice of radius and timespan does not have a strong influence on the population inferred. Aftershocks of the 1933 Long Beach earthquake are likely less well located as the network coverage was more sparser at the time [e.g. Hutton et al, 2010]; we thus characterize aftershocks of the 1933 event as earthquakes that occurred within 35 km of the epicenter in space and within one year of the mainshock. We find again that the choice of radius and timespan again does not have a strong influence on the population inferred. The HYS16 catalog contains no such ambiguities; we exclude the Northridge earthquake and its aftershocks, as those occurred almost entirely off the mesh (Figure 4.2) and are definitively associated with a fault system that is not included in the estimates of moment accumulation rate. The four subcatalogs we use are thus the four interpretations of the 1932-1980 catalog plus the HYS16 catalog in the mesh area.

Appendix 4.2. Method to assess the long-term seismic catalog

The Gutenberg-Richter relation expresses the observation that in sufficiently populated catalogs, the frequency $N(M \geq M_w)$ of earthquakes with moment magnitude equal to or exceeding a given M_w often obeys a log-linear relation (4.1), with the parameters a and b describing the intercept and slope of the log-linear relation. Molnar [1979] combined this relation with the definition of moment magnitude and derived a method to estimate the frequency of earthquakes of or exceeding any given moment magnitude using 1) a moment accumulation rate (e.g. from geodesy), 2) the parameter b and 3) a value for the moment magnitude of the largest earthquake, M_{max}. This can be estimated for a variety of values of M_{max}; each estimate produces a line with slope -b describing the rates of all earthquakes up to the estimated M_{max}. The endpoints of the lines form a locus with slope -3b/2 that describes the frequency of the maximum earthquake as a function of its assumed magnitude [Avouac, 2015, fig. 2b]. A given seismic catalog can then be plotted in the same cumulative magnitude-frequency space; its best-fitting a and b can be determined at its magnitude of completeness [e.g. Hutton et al, 2010], and in fact the b-value inferred from the catalog should be the one used in the application of the Molnar [1979] procedure. If it is assumed that the seismic catalog, over the long term, should obey the inferred Gutenberg-Richter statistics at all magnitudes up to the maximum earthquake, the catalog can simply be approximated by the line of slope –b and intercept a. The intersection point between this line and the M_{max} line is then the estimated magnitude and frequency of the largest earthquake needed to close the slip budget [e.g. Stevens and Avouac, 2016].

The one internal inconsistency in this approach lies in the assumption that the earthquakes that will eventually even the seismic catalog out to resemble the Gutenberg-Richter line in magnitude-frequency space (as assumed) will occur in isolation – that, for example, the M=6.6 earthquakes implied by the statistics of smaller earthquakes in Los Angeles, but missing from the 84-year instrumental catalog, will eventually occur at the rates governed by the inferred a and b value and will simply drop into the catalog when they do, with no effect on the rates of smaller earthquakes. This assumption ignores the fact that earthquakes have aftershocks. In reality, the earthquakes missing from the catalog in Los Angeles may contribute aftershocks that raise or lower the rates of smaller earthquakes, and the long-term a-value may turn out to be higher or lower than that currently inferred from the instrumental catalog. Stevens and Avouac [2017] devised an iterative method to estimate a long-term catalog using the magnitude-frequency statistics of an instrumental catalog in a way that accounts for the missing earthquakes and their aftershocks. In this method, 1) an instrumental catalog is described by a best-fit a and b value; 2) at a given magnitude, earthquakes that are missing from the catalog are added to it; 3) the aftershocks of those earthquakes are added to the catalog (they are assumed to obey the same b-value as well as Bath's law, with a gap in magnitude of ~1.2 between the mainshock and largest aftershock; and 4) the a-value is recomputed using the modified catalog. If the catalog sits above the G-R line at a given magnitude rather than below it, earthquakes are subtracted rather than added, as are their aftershocks. This procedure is then repeated at the next highest magnitude increment. This method also incorporates the estimated magnitude-frequency line for M_{max} as dictated by a given interseismic moment accumulation rate: the Gutenberg-Richter distribution described by a and b is assumed to be truncated at the M_{max} line, with no earthquakes larger than that. The synthetic earthquakes and their aftershocks are then added or subtracted in descending order from M_{max} down to the inferred magnitude of completeness as per the above method; when the magnitude of completeness is reached, the magnitude and frequency of the maximum earthquake are re-estimated as the intersection point between the new G-R line and the maximum-earthquake line. The procedure is then repeated downwards from the new M_{max}, usually converging to a stable estimation of M_{max} within a few iterations [Stevens and Avouac, 2017]. This allows for a quantitative estimate of the maximum-magnitude earthquake in a way that takes into account the implications of the Gutenberg-Richter interpretation self-consistently.

Appendix 4.3. Selection of the magnitude of completeness and the b-value

Although the magnitude of completeness in Los Angeles is estimated to have been below M=3.0 for much of the instrumental period [Hutton et al, 2010, fig. 5a], aftershocks of the 1971 earthquake have a magnitude of completeness around M~3.5 (Hutton et al [2010], fig. 5b); the incompleteness below this magnitude likely results from a temporary increase in the detection threshold due to saturation from the aftershock sequence [Hutton et al, 2010]. Therefore Mc≥3.5 seems a good choice. For added stability and robustness in the Stevens and Avouac [2017] procedure, we add synthetic earthquakes in the procedure from the evolving M_{max} down to Mw=3.5 but, at each iteration, estimate the evolving synthetic catalog's a-value at every 0.05 magnitude value between 3.5 and 4.0 and then use the mean of these estimates as the a-value that determines the evolving G-R line.

We generally estimate the b-value for Los Angeles at a given reference magnitude using the maximum-likelihood method of Aki [1965], but the specific choice of catalog and reference magnitude is also nontrivial. While the b-value for all of Southern California (as estimated from the Aki method) is close to 1.0 at a wide range of reference magnitudes (Hutton 2010 and Figure 4.S1c), the estimated b-value in the mesh area varies strongly with reference magnitude, even above M=3.5 (Figure 4.S1b). This is apparently not due to incomplete coverage or selection issues related to the mesh area: the aftershock sequences of the 1987 Whittier Narrows and 1991 Sierra Madre earthquakes had extremely low b-values of 0.67 and 0.6, respectively [Hauksson and Jones, 1989; Hauksson, 1994], and the HYS16 catalog in the mesh area reflects this, dipping to a b-value of ~0.6 at M~4.0 (Figure 4.S1b). The version of the catalog that includes the 1933 and 1971 earthquakes and their aftershocks, the other 1932-1980 earthquakes in the mesh area, and the HYS16 earthquakes in the mesh area, is visibly more stable above M=3.5 in terms of Aki b-value than the other subcatalogs (Figure 4.S1b, red line), likely because it includes the most earthquakes. We therefore compute b-values from this subcatalog. At every 0.05 magnitude value between 3.5 and 4.0 (Figure 4.S1b, black squares), we compute 50 estimates of the b-value from delete-half jackknife iterations of this subcatalog using the Aki [1965] method (which average out to the same b-value as that determined from the entire catalog), for a total of 1,050 estimates of the b-value for Los Angeles. These b-values display a wide spread (Figure 4.4b) and have a median value of ~0.92. This is essentially a compromise set, motivated equally by the b~1 nature of southern California as an entirety (Figure 4.S1c), the compellingly low b-values of the recent earthquakes in the Los Angeles basin, and the statement by Hutton et al [2010, p. 20] that "A b-value of ~0.9 would be much more consistent with the observed number of M>6 earthquakes [in southern California]." Hutton et al [2010] note that aftershocks of the 1933 Long Beach earthquake may have had a magnitude of completeness as high as 3.9 and use a conservatively high Mc of 4.2 to determine the b-value. We find that selecting b-values from the with-1933/with-1971 subcatalog between M=4.0 and M=4.5, which produces a distribution with median ~0.98, and using M=4.0-4.5 as the range of M_C in the iterative method for self-consistency, produces an ultimate M_{max} estimate that is only 0.01 different than the estimate derived with this set and M_C range. Therefore the final results do not seem to be sensitive to small changes in the b-value or catalog. We therefore run the Stevens and Avouac [2017] method on 1,000 estimates of moment accumulation rate from each of the two preferred strain accumulation models combined with 1,050 b-values and using each of the four iterations of the combined SCEDC/HYS16 catalog.

Supplementary Figures

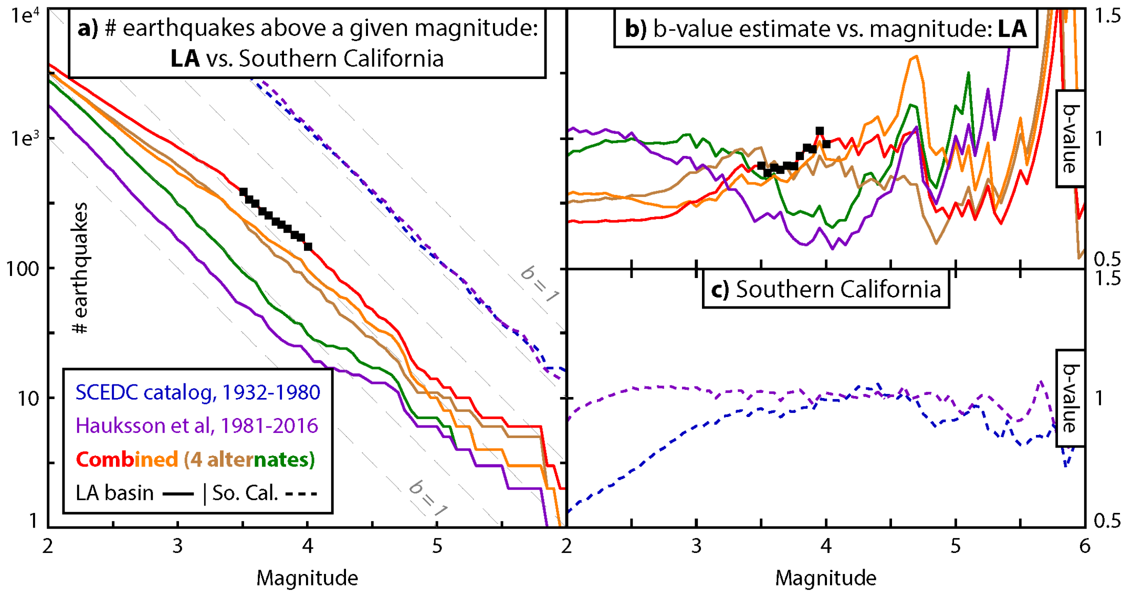

Figure 4.S1. Estimate of the b-value of seismicity in the Los Angeles basin. **a)** Cumulative number of earthquakes above each magnitude for the LA subcatalogs (solid) and for all of Southern California (dashed). Dashed gray lines indicate a Gutenberg-Richter distribution with b = 1 at a variety of a-values. **b)** Estimate of the b-value for seismicity in the Los Angeles basin for a variety of reference magnitudes as per the method of Aki [1965], for the four subcatalogs and the Hauksson et al [2012] relocated catalog (purple), shown for reference. We use 1,000 b-values computed using the Aki method on resamples of the red catalog (with-1933/with-1971) at magnitudes 3.5-4.0 (black squares). **c)** b-values vs. reference magnitude for all of Southern California, for the 1932-1980 SCEDC (blue) and 1981-2016 relocated (purple) catalogs.

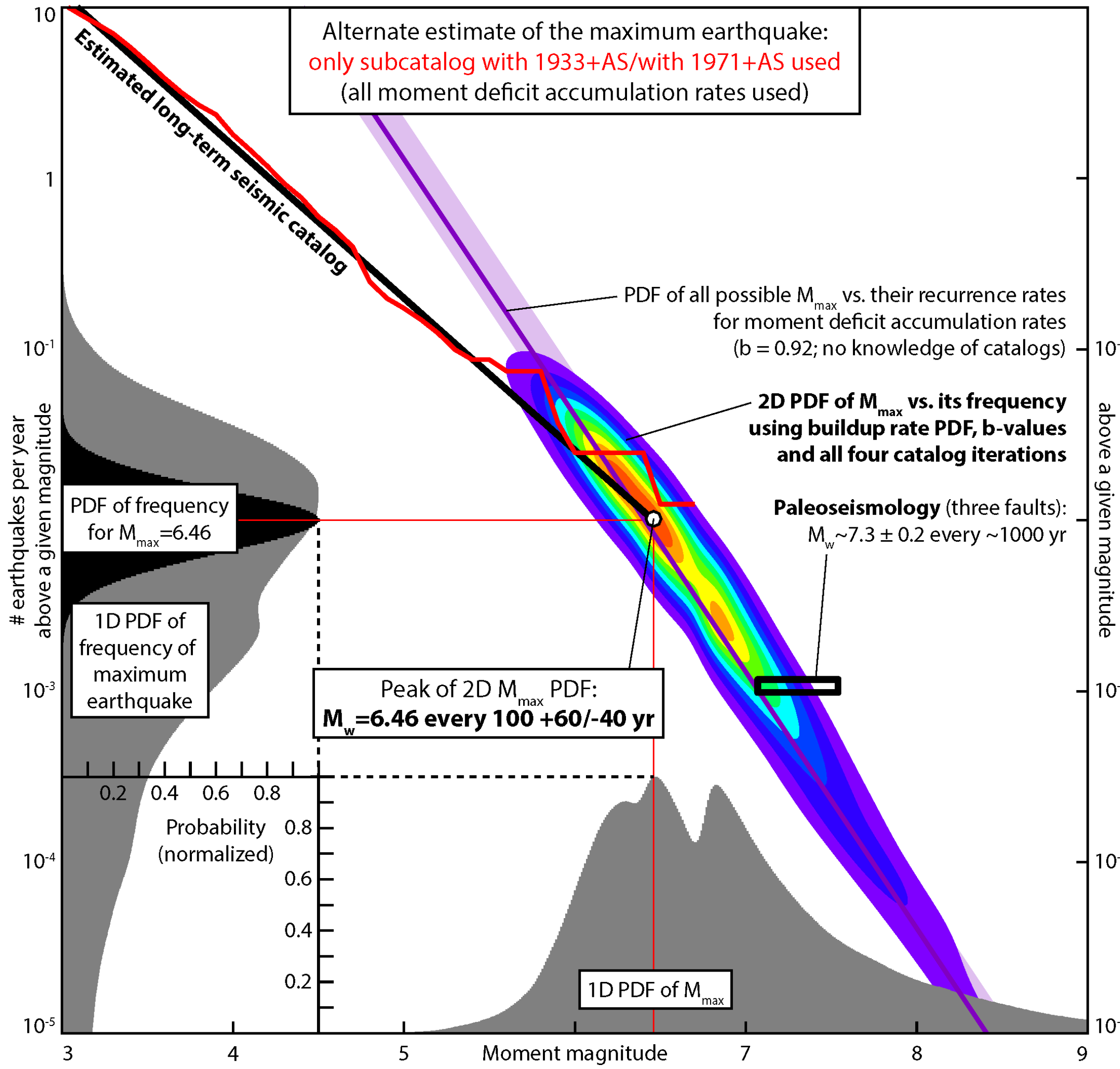

Figure 4.S2. Same as Figure 4.4 except that the only subcatalog used includes the 1933 and 1971 earthquakes and their aftershocks (red line), resulting in a smaller and more frequent maximum-magnitude earthquake.

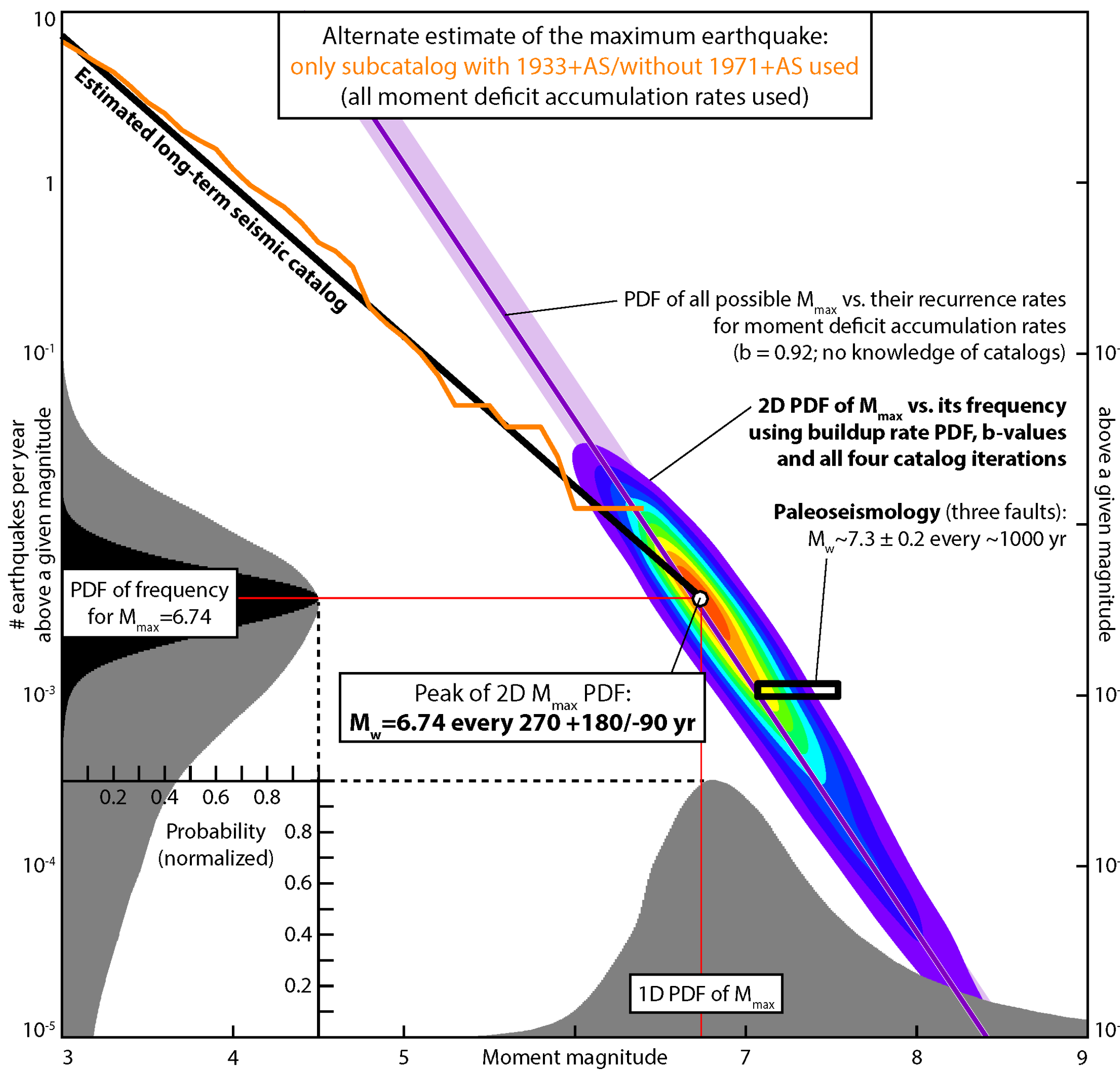

Figure 4.S3. Same as Figure 4.4 except that the only subcatalog used includes the 1933 earthquake and its aftershocks, but does not include the 1971 earthquake or its aftershocks (orange line).

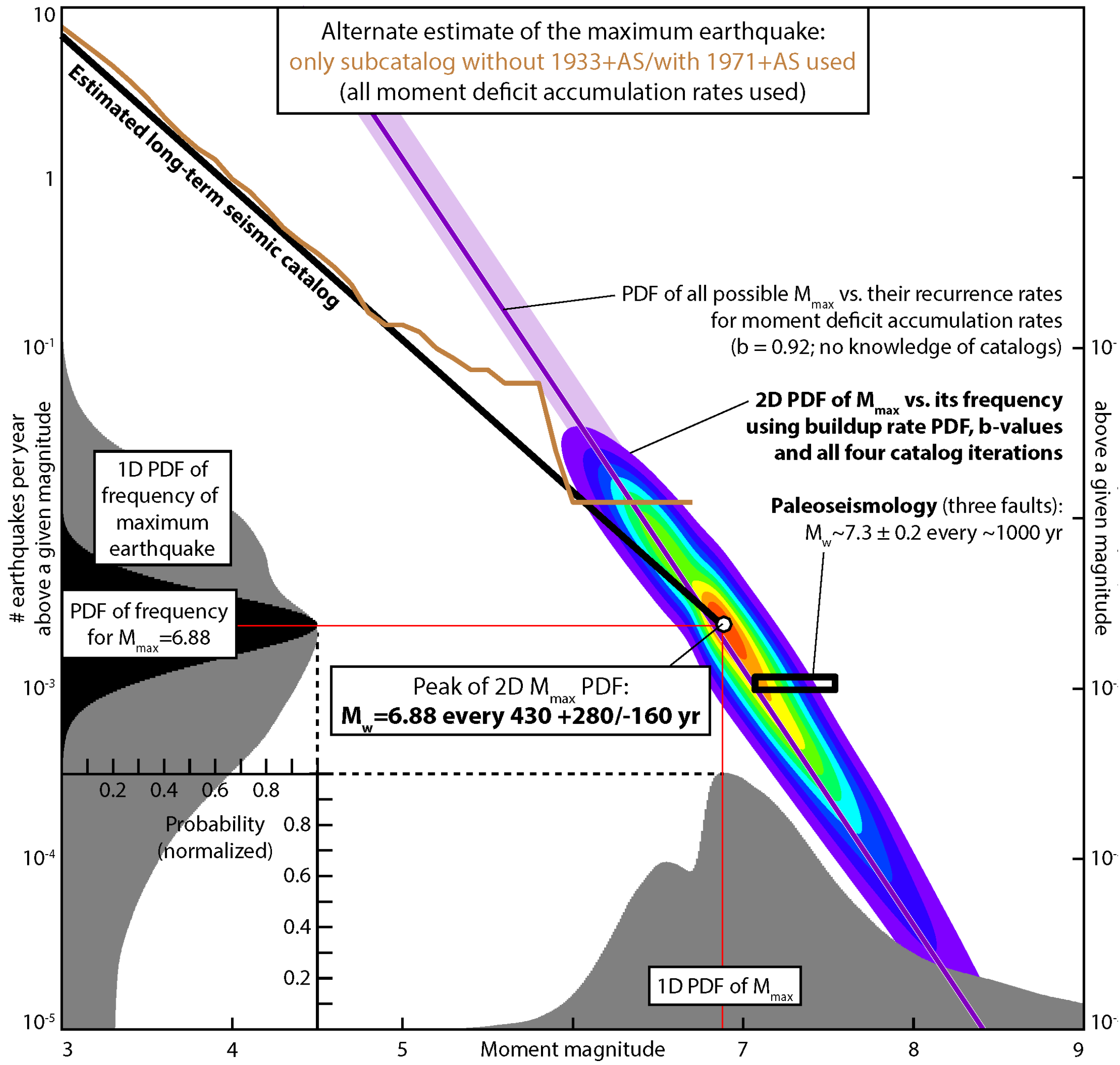

Figure 4.S4. Same as Figure 4.4 except that the only subcatalog used does not include the 1933 earthquake or its aftershocks, but does include the 1971 earthquake and its aftershocks (tan line).

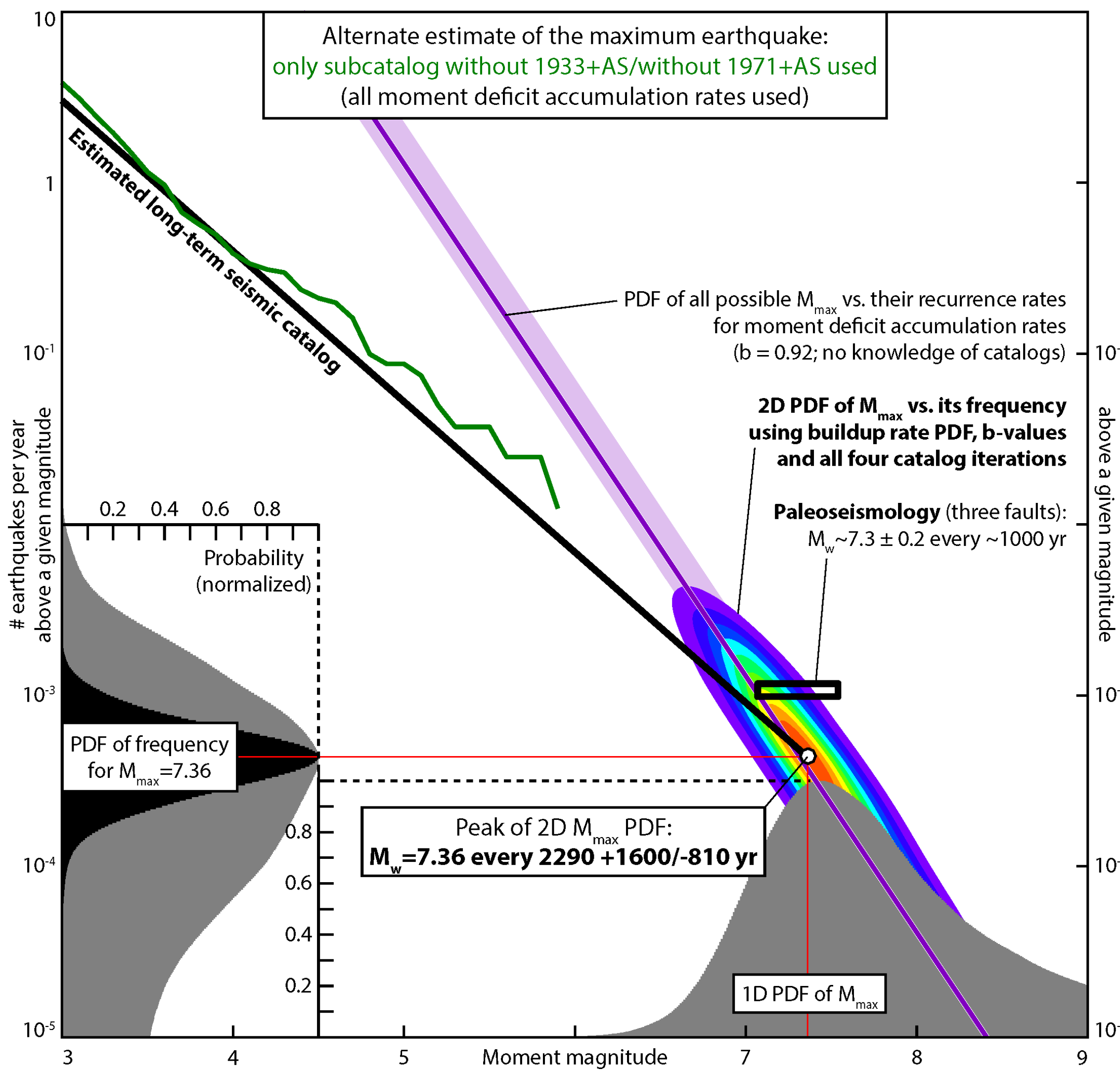

Figure 4.S5. Same as Figure 4.4 except that the only subcatalog used does not include the 1933 or 1971 earthquakes or their aftershocks (green line), resulting in a larger and rarer maximum-magnitude earthquake.

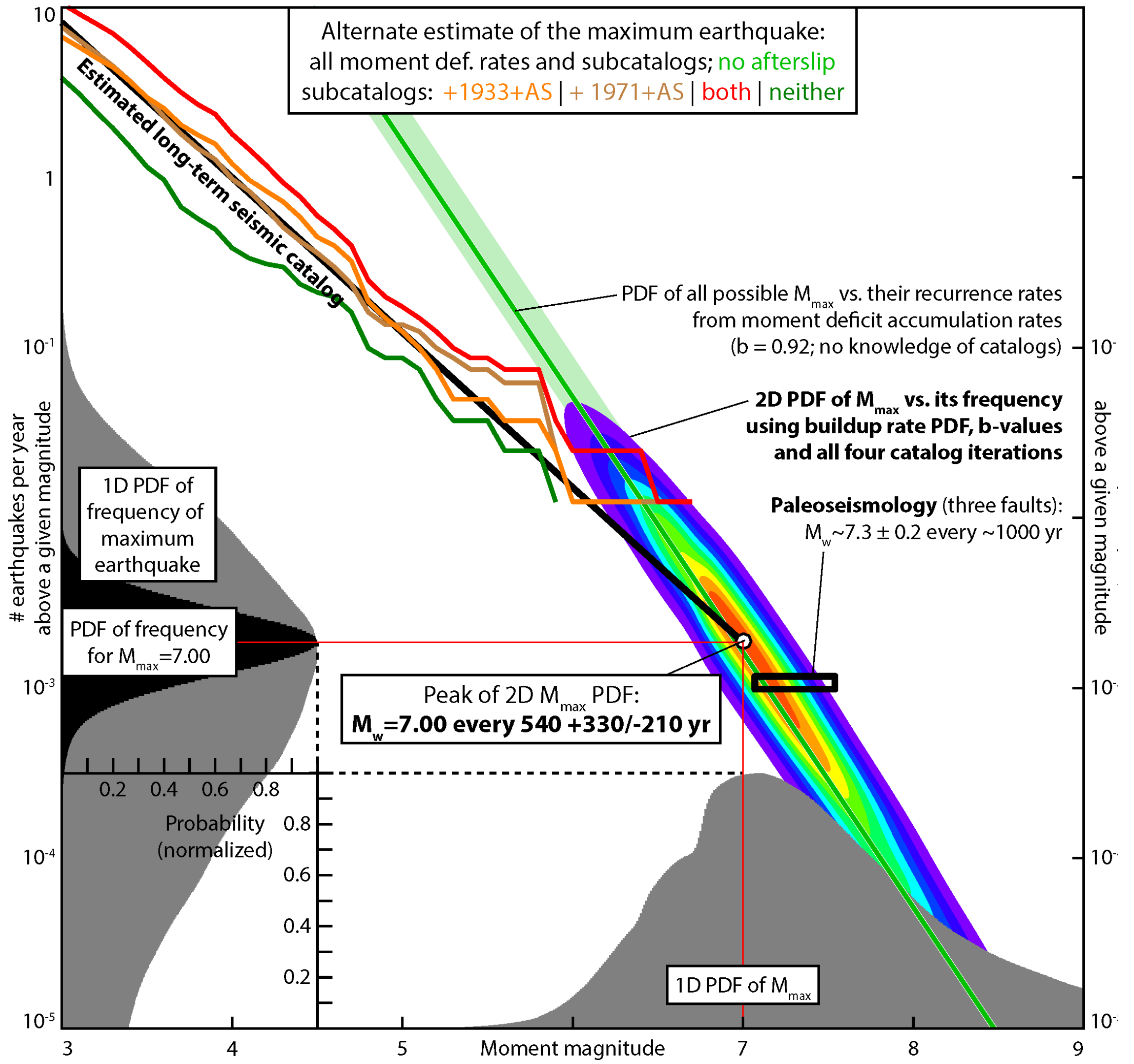

Figure 4.S6. Same as Figure 4.4 except earthquakes are assumed to have no afterslip, resulting in a larger maximum-magnitude earthquake.

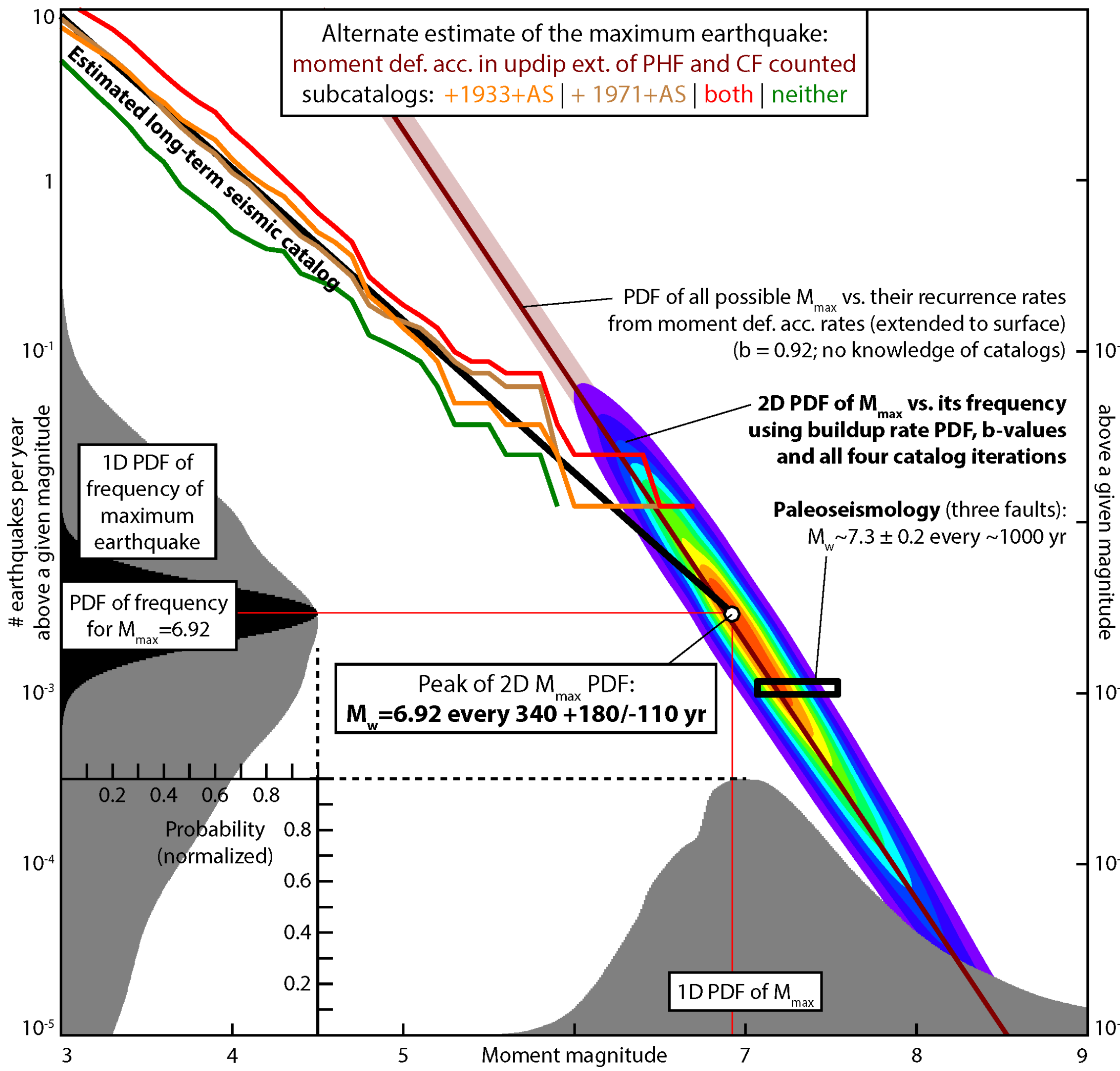

Figure 4.S7. Same as Figure 4.4 except that the PDF of moment rate accumulation counts the strain in the updip extensions of the Puente Hills and Compton faults (Figure 4.2b, red line).

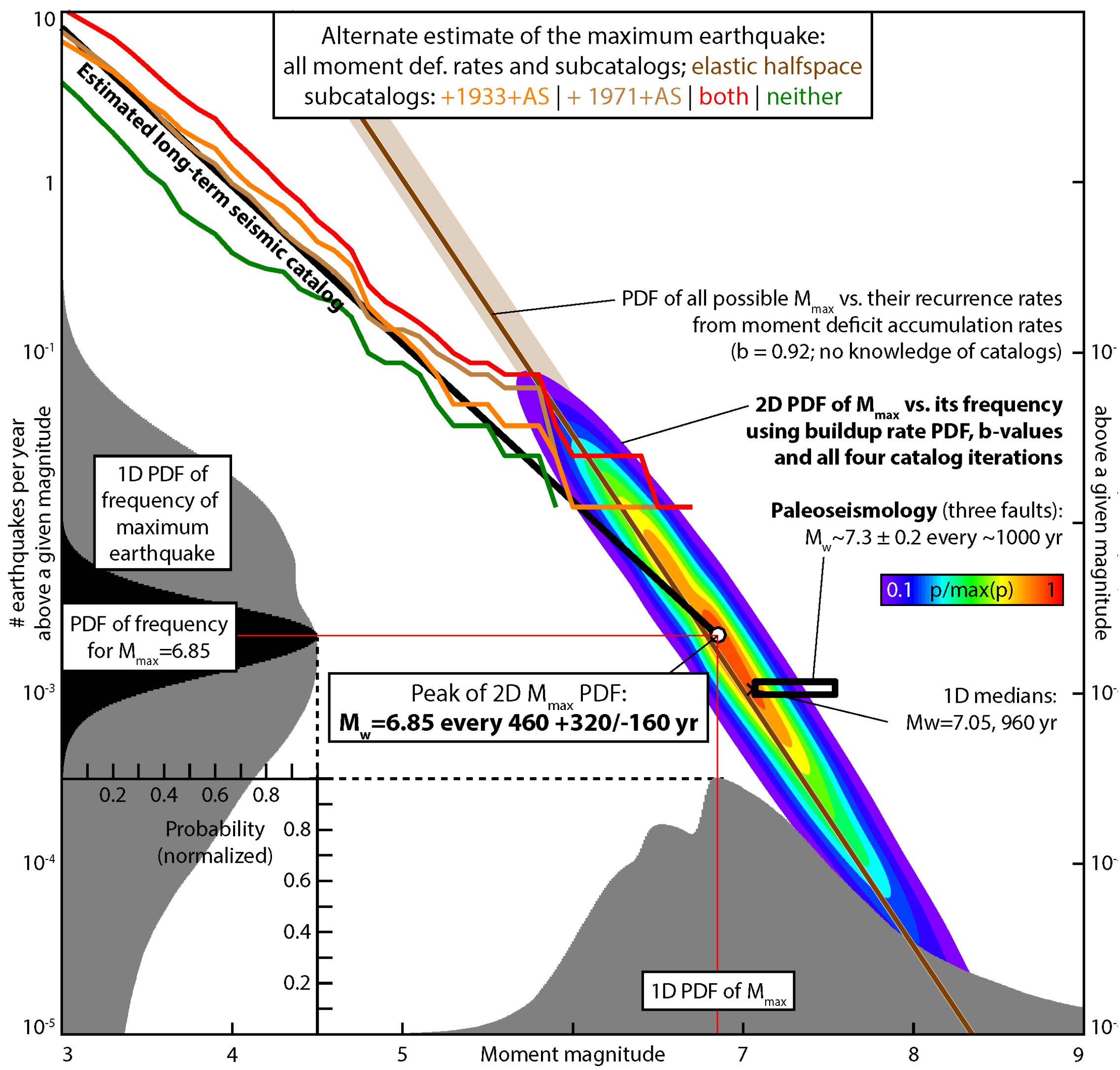

Figure 4.S8. Same as Figure 4.4 except that the PDF of moment rate accumulation assumes an elastic halfspace model (Figure 4.2b, tan line).

Chapter 5

POSTSEISMIC DEFORMATION FOLLOWING THE 2015 MW=7.8 GORKHA EARTHQUAKE: IMPLICATIONS FOR THE RHEOLOGY OF THE TIBETAN CRUST

ABSTRACT

The 2015 Mw=7.8 Gorkha, Nepal earthquake ruptured the lower edge of the interseismically locked portion of the Main Himalayan Thrust (MHT) and was followed by distributed postseismic deformation in the Himalaya and southern Tibet. We use continuous GPS measurements of this deformation to investigate the causative processes at depth. Although cumulative 1.12-year postseismic displacements can be fit to afterslip downdip of the rupture in a kinematic inversion, the afterslip distribution invoked extends >100 km downdip from the coseismic rupture with nearly uniform slip, a behavior that we find is not predicted by stress-driven forward models. We infer that the deformation beneath southern Tibet is more likely due to viscoelasticity enhanced by the high (>600° C) midcrustal temperatures there, and develop models of ductile flow that account for the thermal structure, prestress, rheology and fault geometries. The crustal rheology inferred from these constraints, however, predicts virtually no postseismic viscoelastic relaxation, and viscoelastic flow in the subducting Indian mantle would have produced displacements that are opposite to those observed in both horizontal and vertical motion. Our preferred hypothesis is that postseismic deformation resulted from transient (non-steady-state) viscoelastic relaxation in the Tibetan upper crust plus localized afterslip along the downdip edge of the mainshock and on a narrow segment between the mainshock and a Mw=7.3 aftershock. Although the kinematic inversion would suggest that postseismic deformation released 16% as much seismic moment as the mainshock in the first 1.12 years, afterslip in our preferred dynamic model contributes only 2.3% of the mainshock's moment release, with viscoelastic relaxation playing a larger role. We estimate that the first 1.12 years of postseismic deformation re-increased the shear stress by ≥0.05 MPa over ~40% of the portion of the MHT that ruptured in the Gorkha earthquake.

5.1. Introduction

Strain at plate boundaries is accommodated both suddenly in earthquakes and gradually by steady deformation processes such as creep and ductile flow. The way these processes work together to accommodate strain governs the nature of plate boundaries and affects the likelihood of earthquakes along them. Earthquakes induce a sudden perturbation to the surrounding stress field and thus can accelerate or decelerate these processes, leading to accelerated surface deformation measurable with geodetic methods (postseismic deformation). This accelerated deformation can provide clues about how these processes operate over longer timescales [e.g. Pollitz et al 2000, 2003, 2015; Deng et al 1998; Freed et al 2010, 2012; Ryder et al 2011; Bruhat et al 2011].

The India-Eurasia collision zone is a region where constraining these processes, and their interaction with the earthquake cycle, is of particular importance. The societal importance of studying the controlling factors behind the earthquake cycle there is paramount, as the Himalayan arc is home to 400 million people and may host millenary earthquakes as large as Mw=9 or greater [Stevens and Avouac 2016]. The scientific importance is also great, as it is the one example where a collision between two plates occurs on land and can therefore be studied in detail from both sides (by geodetic, geologic and other methods). The April 25, 2015 Mw=7.8 Gorkha, Nepal earthquake imparted a stress perturbation to the surrounding crust and mantle, and Global Positioning System (GPS) stations in Nepal and southern Tibet detected a broad signal of accelerated postseismic deformation in the year following the earthquake (Figure 5.1). The study of this deformation provides an opportunity to probe the mechanical properties of this populous plate boundary.

A number of studies have documented and analyzed the postseismic deformation following the Gorkha earthquake [e.g. Gualandi et al 2016] and have disagreed on the causative processes, with some inferring that the deformation was due to afterslip downdip of the coseismic rupture [Kang and Fialko, in press] and others inferring viscoelastic relaxation as the dominant process [Zhao et al 2017]. Here we expand on these studies by using GPS data in southern Tibet and by developing more sophisticated dynamic models consistent with the thermal structure, prestress conditions, rheology and fault geometries of the Himalaya. This study builds on previous work constraining the subsurface structure of the Himalaya, including geological structure and the geometry of faults [e.g. Pandey et al 1995, Hauck et al 1998, Schulte-Pelkum et al 2005, Nabelek et al 2009, Elliott et al 2016], long-term slip rates on those faults [e.g. Lave and Avouac 2000, Herman et al 2010],

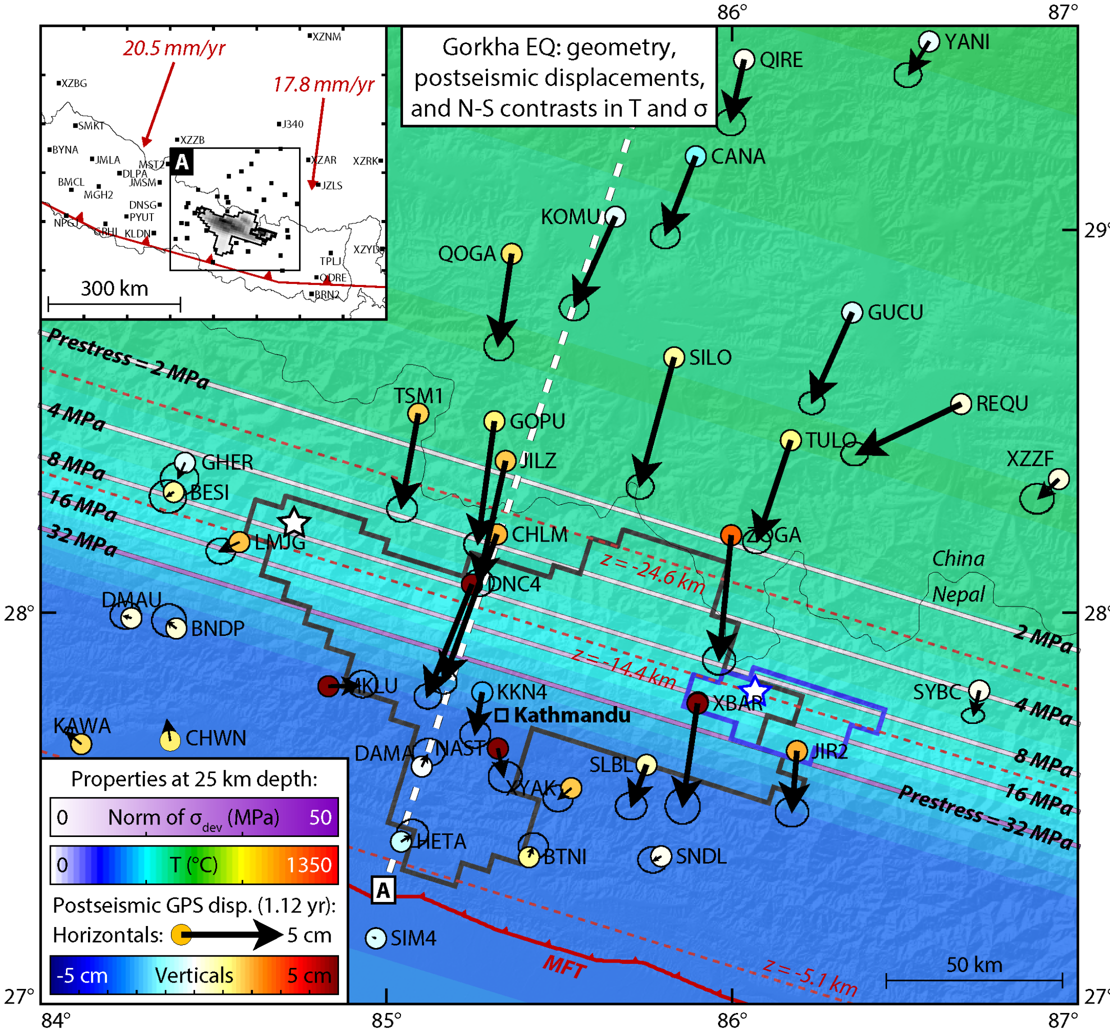

Figure 5.1. Setting of the Gorkha earthquake and cumulative postseismic displacements at GPS stations 1.12 years after the mainshock (filled circles and black arrows). Color shading: temperature at 25 km depth from Henry et al [1997]. Purple contours: second invariant of deviatoric stress tensor at 25 km depth from Godard et al [2004]. Red solid and dashed lines: surface trace and depth contours on Main Himalayan Thrust (MHT) in Elliott et al [2016] ramp-flat-ramp-flat geometry. Thick black and blue lines: outlines of mainshock and 5/12/2015 Mw=7.3 aftershock (>0.25-m slip contours) from Elliott et al [2016] slip models. Black and blue stars: epicenters of mainshock and aftershock. Dashed white line: profile for cross sections (extends 300 km N 18° E from surface trace of MFT). Inset: tectonic setting and large-scale geodetic network.

models of temperature based on erosion rates and theoretical and petrological constraints [e.g. Royden, 1993; Henry et al, 1997; Herman et al, 2010], dynamic models of long-term deformation and stress based on erosion and temperature [e.g. Cattin and Avouac 2000, Godard et al 2004], and geodetic constraints on interseismic coupling and strain accumulation [e.g. Ader et al 2012; Stevens and Avouac 2015]. Our findings can be compared with those of previous studies of the rheology of neighboring regions using postseismic deformation [e.g. Ryder et al 2011, Jouanne et al 2011, Wang and Fialko 2014, Huang et al 2014] or other approaches [e.g. Unworth et al 2005, Hilley et al 2005, England et al 2013, Doin et al 2015].

A variety of studies collectively indicate that the India-Asia collision is predominantly accommodated by thrusting along a master fault, the Main Himalayan Thrust (MHT), and that this system may continue to the north under the Tibetan Plateau either as a discrete slip interface or as a distributed shear zone [e.g. Avouac 2003, 2008]. It might in particular be expected that elevated temperatures in the Tibetan crust [e.g. England et al 1992, Royden 1993] would favor the development of a shear zone due to the strong Arrhenius-type dependence of strain rate on temperature [Cattin and Avouac 2000]. The postseismic deformation following the Gorkha earthquake provides an opportunity to build on these studies and in particular address the latter subject – as discrete slip and bulk shear often produce different signals in postseismic surface deformation [e.g. Bruhat et al 2011] – with implications for the way this deep strain accommodation feeds stress onto the seismic section of the Main Himalayan Thrust. In this study, we use GPS position timeseries following the Gorkha earthquake to place constraints on the deformation mechanisms at depth and find that the data are best explained by bulk flow in a low-viscosity shear zone in the Tibetan upper crust.

5.2. Mainshock

The 2015 Gorkha earthquake ruptured a ~150x75 km section of the MHT just north of the section that underlies the Kathmandu basin [e.g. Avouac et al 2015, Galetzka et al 2015, Kang and Fialko 2015] (Figures 5.1 and 5.S1), at the lower edge of the region that is inferred as being locked and accruing strain in the interseismic period [Ader et al 2012]. The details of the geometry of the MHT are debated [e.g. Hubbard et al 2016, Wang et al 2017]; here we use the geometry of Elliott et al [2016], which is based on geodetic observations during the earthquake and has a ramp-flat-ramp-flat structure (Figure 5.2). We use this fault geometry and the accompanying coseismic slip model (Figure 5.S1, red dashed lines and gray patches), in which the earthquake was found to have ruptured the back of the upper flat and part of the ramp just below it. A Mw=7.3 aftershock occurred east of the mainshock on May 12, 2015 (Figure 5.S1, blue patches), and we use the Elliott et al [2015] model for it as well. A narrow section of the MHT between the mainshock

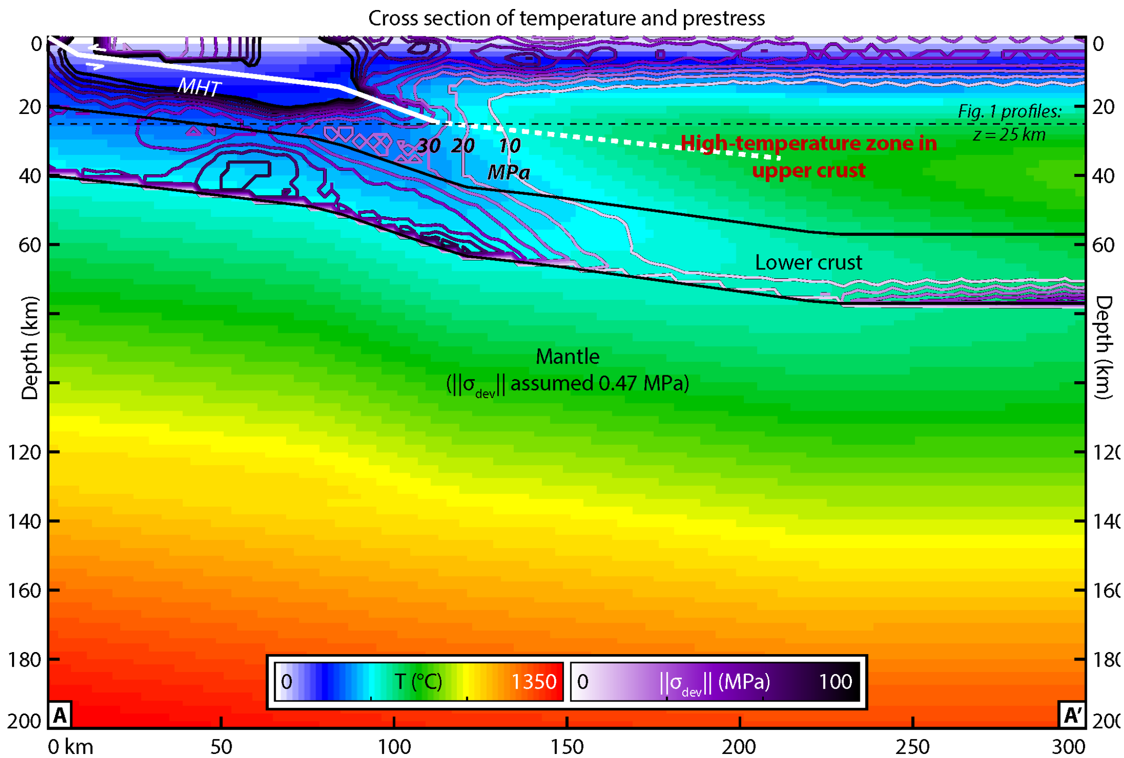

Figure 5.2. Cross section of MHT fault geometry from Elliott et al [2016] (white line), temperature (color shading) and prestress (colored contours) along profile A-A'. Temperature is from Henry et al [1997] (V. Godard, pers. comm.). Temperatures below the base of the Henry et al model (~100 km depth) are linearly extrapolated downwards then capped at 1350 C (Appendix 5.1). Prestress distribution (norm of deviatoric stress tensor) is derived from Godard et al [2004] (Figure 5.S4).

and aftershock likely did not rupture in either and has been interpreted as having rheological properties that may favor steady sliding [e.g. Galetzka et al 2015, Lindsey et al, 2015, Gualandi et al 2016]; we also incorporate this feature into the modeling here.

5.3. Data constraining postseismic deformation

The University of Nevada Reno Geodesy Lab produces daily position timeseries for continuously operated GPS stations in Nepal, as well as some in northern and northeastern Tibet, and we use their data for 53 stations in the area surrounding the Gorkha earthquake. We also use data from 13 continuous GPS stations in southern Tibet that were provided by the Chinese Earthquake Administration (CEA) in the months following the Gorkha earthquake. In addition to the signal of postseismic displacement, all of these GPS timeseries also contain a linear velocity (due to plates' steady motion with respect to the reference frame used), seasonal oscillations due to hydrological, thermoelastic and possibly other processes [e.g. Bettinelli et al 2008, Tsai 2011, Fu and Freymueller 2012], and rapid offsets due to earthquakes, station maintenance and other causes. If a station has been deployed for a sufficiently long time that these signals are clearly distinguishable (ideally >2 years), the signal of postseismic deformation can be extracted using traditional least squares one timeseries at a time (as in Chapter 2) or by network-based methods such as Independent Component Analysis [Gualandi et al, 2016]. The timeseries from several of the CEA stations in Tibet, however, begin only a few months after the earthquake and are ~1 year long. We therefore estimate the linear and seasonal terms at these stations by first estimating them at the sites of stations with longer timeseries and then extrapolating these terms spatially to the sites of the CEA stations using a kriging method. We also remove visually evident spurious and coseismic offsets from all timeseries. Finally, we wish to estimate the cumulative postseismic displacement at all stations even though several of the CEA stations do not cover the first 1-2 postseismic months. To do this, we use the Independent Component Analysis inversion method [Gualandi et al, 2016], which is adapted from the PCA inversion method of Kositsky and Avouac [2010] and accounts for data uncertainties and missing data. This method derives a network-scale estimation of the postseismic displacement signal from the detrended timeseries decomposed into a number of independent components, each associated with a spatial pattern and a temporal function [e.g. Gualandi et al, 2016]. We use this method on the first 1.12 years of data following the mainshock. We find that only one independent component is needed to describe the postseismic motion well, as found by Gualandi et al [2016] for the first 6 months of postseismic data from Nepal. This means that the spatial behavior of postseismic deformation has been relatively stationary over the first postseismic year. We use the first independent component (which is scaled in each component of each station as per its contribution) as the "data" timeseries to compare with our models. The timeseries of uncertainty in position that we use are those from the original UNR and CEA data; for periods in which a station has no data, we assign an uncertainty in position equal to the maximum value of the uncertainty in the timespan that is covered by the timeseries (component by component).

The cumulative postseismic displacements reconstructed from the first independent component at 1.12 years after the mainshock (Figure 5.1, filled circles and black arrows) show several characteristics that are meaningful ahead of any modeling. First, there is no significant deformation updip (south-southwest) or east or west of the mainshock, suggesting that those sections of the MHT remain locked [e.g. Galetzka et al 2015, Gualandi et al 2016]. Second, deformation extends far into Tibet, suggesting that the causative process did so as well. Third, all horizontal motion is to the south-southwest. Fourth, stations in Tibet show negligible postseismic uplift or subsidence, and there is more horizontal than vertical motion at most stations except for those very close to the rupture. These characteristics will be important in distinguishing possible causative mechanisms.

5.4. Kinematic inversion for afterslip

We first want to determine whether the observed postseismic displacements can be explained as having resulted from afterslip on and/or around the rupture, and if so, whether the distribution of afterslip that would be invoked to explain them is physically plausible. To do so, we invert the cumulative 1.12-year three-component GPS displacements for afterslip on an extended version of the Elliott et al [2016] ramp-flat-ramp-flat structure (Figure 5.3). We extend the lower flat ~200 km NNE from the base of the lower ramp to allow afterslip to the north beneath Tibet if the model invokes it. The Elliott et al geometry is 220 km long along strike, centered on the rupture; we extend it 110 km further to the east and west for a total length of ~440 km, and exclude stations that do not overlie this mesh. (We also exclude the Tibetan station REQU as its detrended timeseries contain an unexplained acceleration to the west in late 2015 and this throws off the reconstruction of the first independent component there; we also exclude this station from calculations of model misfit in subsequent forward models.) We invert the displacements for slip on this extended fault surface in a least-squares formulation with spatial smoothing, positivity and boundary conditions,

$$\mathbf{m}_{est} = \mathrm{argmin}(\|(\mathbf{d} - \mathbf{Gm})/\boldsymbol{\sigma}\|_2 + \lambda\|\mathbf{S}^{-1/2}\Delta^2\mathbf{m}\|_2), \quad [5.1.1]$$

$$\mathbf{m} \geq 0, \quad [5.1.2]$$

$$\mathbf{m}_{edges} = 0, \quad [5.1.3]$$

where **d** contains the three-component cumulative 1.12-year postseismic displacements and **σ** contains the three-component position uncertainties at 1.12 years (estimated as described previously). The matrix **G** consists of the Green's functions from reverse slip on each patch of the fault mesh computed within an elastic halfspace. Similarly to Chapter 3, we modulate the degree of spatial smoothing by the sensitivity operator [Ortega, 2013] and choose the overall weight of smoothing from the point of maximum positive curvature of an L-curve (here not in log-log space as that formulation did not work well here). We also

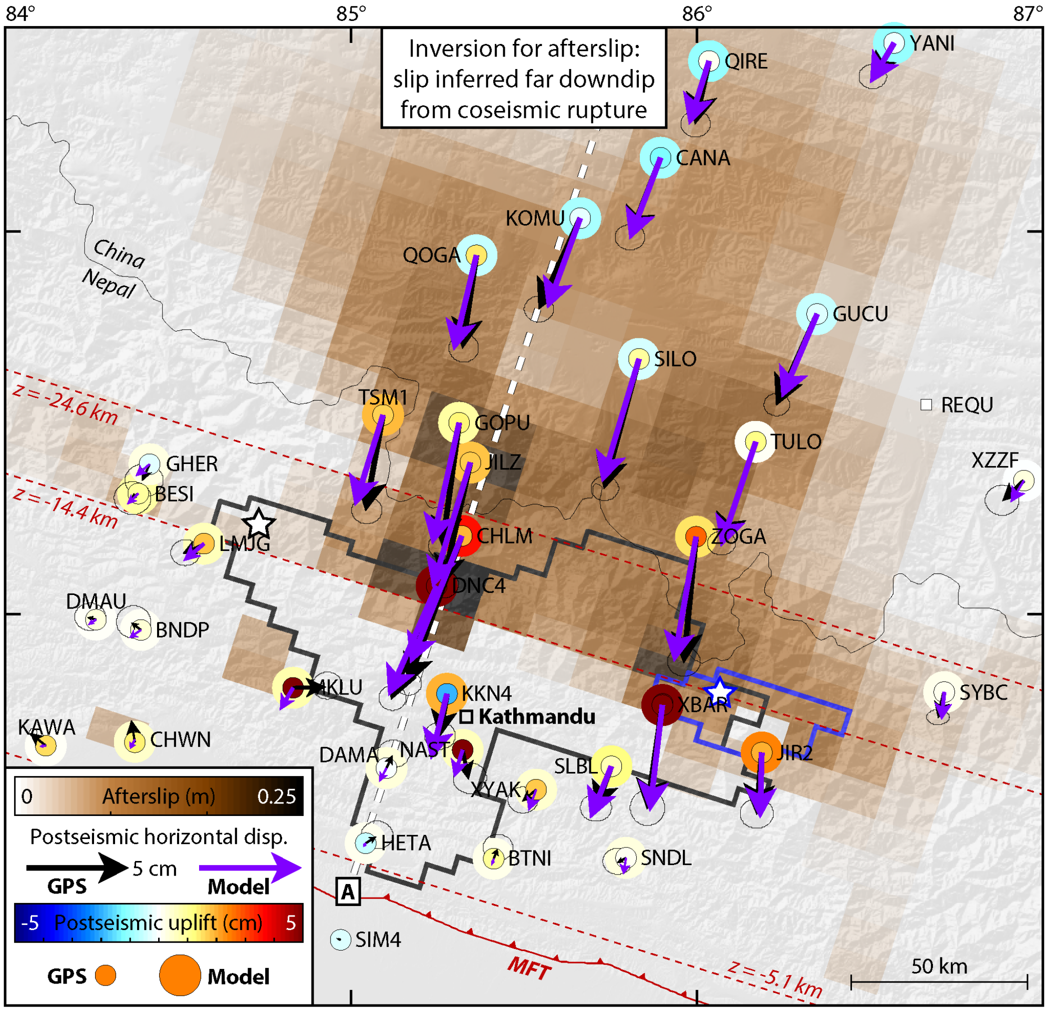

Figure 5.3. Kinematic inversion of cumulative 1.12-year postseismic displacements (filled circles and black arrows) for afterslip on the MHT. Large filled circles and purple arrows are model-predicted 1.12-year vertical and horizontal displacements.

enforce that slip is zero on the extreme western, eastern and downdip edges of the mesh to prevent erroneous slip there. As in Chapter 3, we evaluate the model misfit using the weighted root-mean square error,

$$X^2/N = ((\mathbf{d} - \mathbf{Gm})/\boldsymbol{\sigma})^2/N, \quad [5.2]$$

in which we do not incorporate the number of free parameters into the denominator. We also evaluate the variance reduction,

$$VR = (1 - (((\mathbf{d} - \mathbf{Gm})^T(\mathbf{d} - \mathbf{Gm}))/\mathbf{d}^T\mathbf{d}))*100\ (\%), \quad [5.3]$$

which quantifies how much of the postseismic signal is reproduced by the model.

The inversion yields a model (Figure 5.3) that fits the cumulative displacements adequately, with $X^2/N = 0.93$ and a variance reduction of 83.5%. The cumulative seismic moment released by the afterslip, 9.8×10^{19} Nm, is equivalent to a Mw=7.26 earthquake, 16% of the moment released by the Gorkha mainshock. This is similar to the results of previous kinematic inversions [e.g. Gualandi et al 2016; Zhao and Burgmann 2017] and is two orders of magnitude larger than the total moment released by aftershocks [Gualandi et al 2016], implying that post-Gorkha deformation was predominantly aseismic. However, whether postseismic deformation involved only afterslip is questionable, as the model invokes slip extending >100 km downdip from the mainshock into a region where temperatures at the depth of the fault hypothesized here likely exceed 600° C [Royden, 1993] (Figure 5.1, color shading). Aseismic creep is generally invoked to explain afterslip in the brittle regime [Marone et al 1991, Perfettini and Avouac 2004], which corresponds to temperatures of <350° C in continental crust [Blanpied et al 1991], and it may be questionable that long-term strain could localize into a throughgoing fault at temperatures >250° C higher than this. The inferred magnitude of slip is also nearly constant down dip, and the likelihood of wholesale stress-driven slip extending so far from the mainshock and being so uniform is also questionable. We note that relatively large afterslip is inferred beneath stations DNC4, on the northwest lower edge of the rupture, and XBAR, which overlies the narrow section of fault that Lindsey et al [2015] inferred as having neither ruptured during the mainshock nor the May 12 Mw=7.3 aftershock. To evaluate whether afterslip >100 km downdip from the mainshock is physically plausible, we turn to forward modeling of afterslip driven by coseismic shear stress changes.

5.5. Forward modeling of stress-driven afterslip

As in Chapter 2, we use RELAX [Barbot and Fialko 2010a, b] to model afterslip driven by coseismic shear stress changes. We simulate afterslip on the downdip extension of the coseismic rupture using the previous fault geometry (with the lower flat extended ~200 km NNE). The forward model includes the Mw=7.3 aftershock, which adds to the stress change and thus the deformation on the east side of the rupture. Motivated by the inversion's inference of high inferred afterslip on the narrow area between the mainshock and aftershock, we also allow afterslip in that zone (Figure 5.S1, purple shaded region) by setting the slip in the mainshock and aftershock to be zero there (as nonzero slip would impart a strong stress drop to this region and inhibit afterslip there, as it ultimately does over all but the edges of the coseismic rupture). This zone has low inferred slip in both the mainshock and aftershock and so setting the slip there to zero has a negligible effect on the overall moment release.

Afterslip in RELAX obeys a rate-strengthening constitutive law (2.2), with the parameters v_0 (a constant out front) and $(a-b)\sigma$ governing its behavior. Here we set $(a-b)\sigma$ = 1 MPa, as in Chapter 2 and consistent with results from previous similar studies [Perfettini and Avouac 2004, 2007]. v_0 is a "reference slip rate" of which the afterslip is a perturbation [Perfettini and Avouac 2007, Barbot et al 2009], and a perhaps sensible choice for it is the long-term creep rate on the fault in question; we first set it to 20 mm/yr, the convergence rate across the Nepal Himalaya [Ader et al 2012], which would then be the creep rate on the downdip extension of the MHT if it were completely creeping in the interseismic period. As with the forward models in Chapter 2, we evaluate the model misfit using the weighted root-mean square error,

$$X^2/N = ((\mathbf{d} - \mathbf{Gm})/\boldsymbol{\sigma})^2/N, \qquad [5.4]$$

and the variance reduction,

$$VR = (1 - (((\mathbf{d} - \mathbf{Gm})^T(\mathbf{d} - \mathbf{Gm}))/\mathbf{d}^T\mathbf{d}))*100\ (\%), \qquad [5.5]$$

where d, m and σ are respectively the concatenated vectors of observed displacement timeseries, model-predicted displacement timeseries and location uncertainty timeseries in all components of all stations (again excluding REQU).

Figure 5.4 shows the cumulative 1.12-year afterslip at depth in this stress-driven model and compares the cumulative model-predicted surface displacements to those from the first independent component of the data. Although the azimuth of predicted horizontal motion is to the south-southwest, consistent with the data, two limitations of afterslip as a candidate mechanism to explain the postseismic displacements are visible. First, afterslip is concentrated near the downdip edge of the mainshock (as might be expected for a slip process driven by coseismic stress changes) and does not propagate anywhere near 100 km downdip from the mainshock; the model therefore does not reproduce the broad-scale displacements observed in Tibet. Second, the ratio of uplift to horizontal motion in the model is larger than that in the data: predicted uplift at stations DNC4, CHLM and XBAR is similar to that in the data, but predicted horizontal displacements at those stations are only a fraction of those observed. This model has a X^2/N of 17.32 and a variance reduction

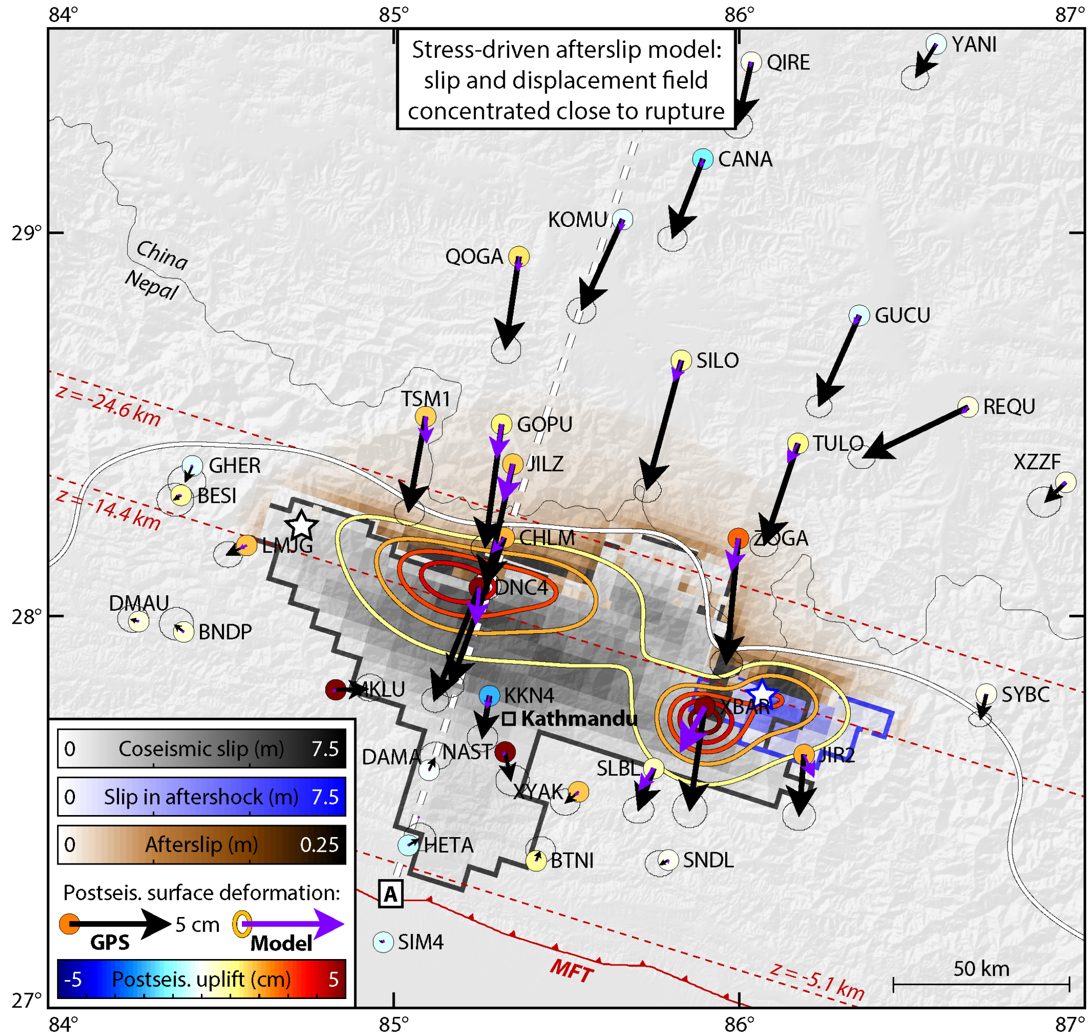

Figure 5.4. Forward model of afterslip downdip of the mainshock driven by coseismic stress changes (v_0 = 20 mm/yr, (a-b)σ = 1 MPa). Brown patches are the magnitude of afterslip at 1.12 years; colored contours are model-predicted uplift and subsidence.

of 32%, far worse than the kinematic inversion. For reference, we run two alternative afterslip models, one in which v_0 is set to 100 mm/yr (perhaps not inconceivable as Perfettini and Avouac [2007] suggested that v_0 may in fact far exceed the long-term slip rate on the fault due to acceleration of creep induced by coseismic dynamic stress changes) and one in which (a-b)σ is set to 10 MPa. The model-predicted horizontal motions in Nepal are larger in these models (Figure 5.S2, 5.S3), but there is visibly far more uplift predicted in the back of the rupture than observed there (as well as 1-2 cm of subsidence predicted in southernmost Tibet where the data indicate gentle uplift), and these models still do not come close to reproducing the displacements further north into Tibet, with cumulative X^2/N

= 8.16 and VR = 52% for the first and X^2/N = 10.81 and VR = 52% for the second, respectively. We conclude that although kinematic inversion can fit the data to an afterslip model, it is unlikely that afterslip was the dominant process responsible for postseismic deformation (particularly in southern Tibet), and we thus turn to considering viscoelastic relaxation, which can produce more distributed displacement fields [e.g. Freed et al 2007]. We note that the first stress-driven afterslip model (Figure 5.4) does successfully reproduce the observed uplift at DNC4 and XBAR as well as some horizontal motion there, with afterslip on the narrow section in between the mainshock and aftershock in particular producing the signal at XBAR. We keep this observation on hand for later use.

5.6. Forward modeling of viscoelastic relaxation

We then use RELAX to compute models of crustal and mantle viscoelastic relaxation induced by coseismic stress changes. Ductile flow generally follows a variant of the constitutive law

$$d\varepsilon/dt = A\sigma^n \exp(-Q/RT), \qquad [5.6]$$

where $d\varepsilon/dt$ is the strain rate, A is a pre-exponential factor, σ is the deviatoric stress, n dictates the power-law dependence of the strain rate on the stress, Q is the activation energy, R is the universal gas constant, and T is absolute temperature, the last three within an Arrhenius-type dependence on temperature [e.g. Freed and Burgmann, 2004]. The long-term effective viscosity, $\sigma (d\varepsilon/dt)^{-1}$, is then controlled by both stress and temperature,

$$\eta_{long} = A^{-1}\sigma^{(1-n)}\exp(Q/RT). \qquad [5.7]$$

The long-term effective viscosity structure can be assumed a priori in the setting of the Gorkha earthquake from existing 2D models of temperature, steady-state stress and rheology. Henry et al [1997] used a 2D finite element scheme to compute a detailed 2D thermal model for the Himalayan collision zone, and Godard et al [2004] used this thermal model along with considerations of subsurface rheology, long-term deformation and topography to build a realistic 2D model of steady-state stress and deformation that was found to correctly predict the topography and interseismic strain. The rheological structure used by Godard et al features a downgoing Indian plate consisting of a 20-km-thick upper crust with the rheology of dry Simpson quartzite, a 20-km-thick diabase lower crust, and a dry olivine mantle; the overriding Tibetan crust also obeys a dry Simpson quartzite

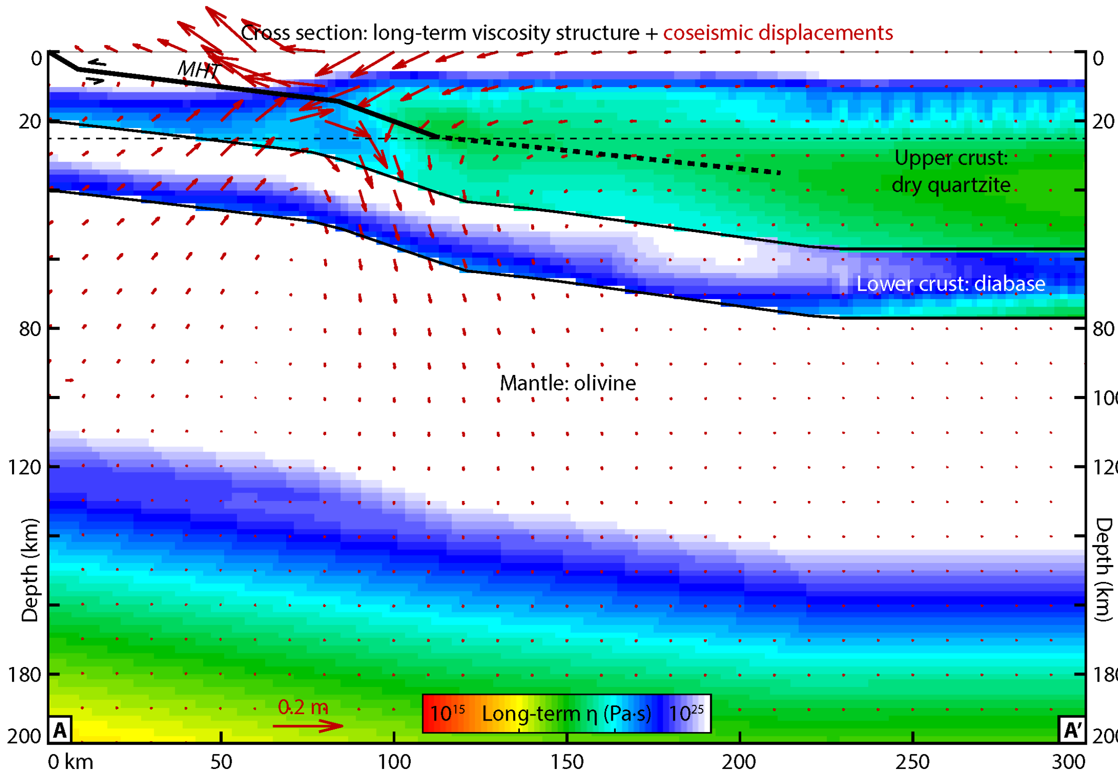

5.5. Long-term effective viscosity structure in profile A-A' as estimated from temperature and prestress (Figure 5.4) and the rheological structure of Godard et al [2004] (labeled). Red arrows are coseismic displacements in the same profile.

rheology [parameters A, n and Q originally from Carter and Tsenn 1987]. We use the Henry et al [1997] thermal structure [V. Godard, pers. comm.] (Figure 5.2, color shading) and the Godard et al [2004] steady-state stress distribution (Figure 5.2, contours, and Figure 5.S4) and rheological structure to build a self-consistent 2D model of the long-term effective viscosity structure (Figure 5.5). This requires some modifications to the temperature and stress models that are described in Appendix 5.1. The long-term effective viscosities are on the order of 10^{19}-10^{20} Pa-s in the high-temperature Tibetan upper crust, higher in the downgoing lower crust due to the stronger diabase rheology, and potentially lower at ~200 km depth in the mantle.

An earthquake perturbs the long-term strain rate by perturbing the stress field,

$$d\varepsilon/dt + \Delta(d\varepsilon/dt) = A(\sigma + \Delta\sigma)^n \exp(-Q/RT). \qquad [5.8]$$

If the prestress σ is far larger than the coseismic stress change $\Delta\sigma$, the latter can be expressed as a perturbation and a binomial approximation can be used to separate the preseismic and coseismic contributions to the stress and strain rate,

$$d\varepsilon/dt + \Delta(d\varepsilon/dt) \approx A\sigma^{n} \exp(-Q/RT) + An\sigma^{n-1}\Delta\sigma \exp(-Q/RT), \qquad [5.9]$$

and the postseismic ductile flow alone is then

$$\Delta(d\varepsilon/dt) \approx An\sigma^{n-1}\Delta\sigma \exp(-Q/RT), \qquad [5.10]$$

which is a Newtonian flow law where the coseismic stress change $\Delta\sigma$ is modulated by a power 1; the other parameters only affect how quickly this Newtonian viscoelastic relaxation occurs at a given location. The effective viscosity is

$$\eta_{short} = (An)^{-1}\sigma^{(1-n)}\exp(Q/RT), \qquad [5.11]$$

which is a factor of n lower than the effective long-term viscosity. As described in Appendix 5.1, we estimate that the minimum prestress in the high-temperature zone in the Tibetan crust is ~1.25 MPa; the magnitude of the coseismic deviatoric stress change in this region is an order of magnitude lower than this or more (Figure 5.S5), suggesting that it is appropriate to model the viscoelastic relaxation following the Gorkha earthquake as a small perturbation to the long-term viscosity structure.

We first use RELAX to model Newtonian viscoelastic relaxation in the upper and lower crust using this viscosity structure (note that the effective short-term viscosity η_{short} used is a factor of n lower than the effective long-term viscosity shown in Figure 5.5), as driven by stress changes in the mainshock and Mw=7.3 aftershock. We find that this produces essentially no postseismic surface displacement (Figure 5.6), with $X^2/N = 24.3$ and a variance reduction of 3%. The effective viscosities involved are orders of magnitude too large for this to be a candidate mechanism to explain the observed displacements.

We then model viscoelastic relaxation in the mantle in this viscosity structure. Assuming an olivine rheology, we find that viscoelastic relaxation in the mantle would induce north-northeast motion and subsidence at the surface, both opposite to the observations (Figure 5.7), with $X^2/N = 31.0$ and variance reduction -35%. The subsidence appears to occur because the region below the earthquake was driven downward during the earthquake (Figure 5.S6, red arrows), and viscoelastic relaxation could have accommodated

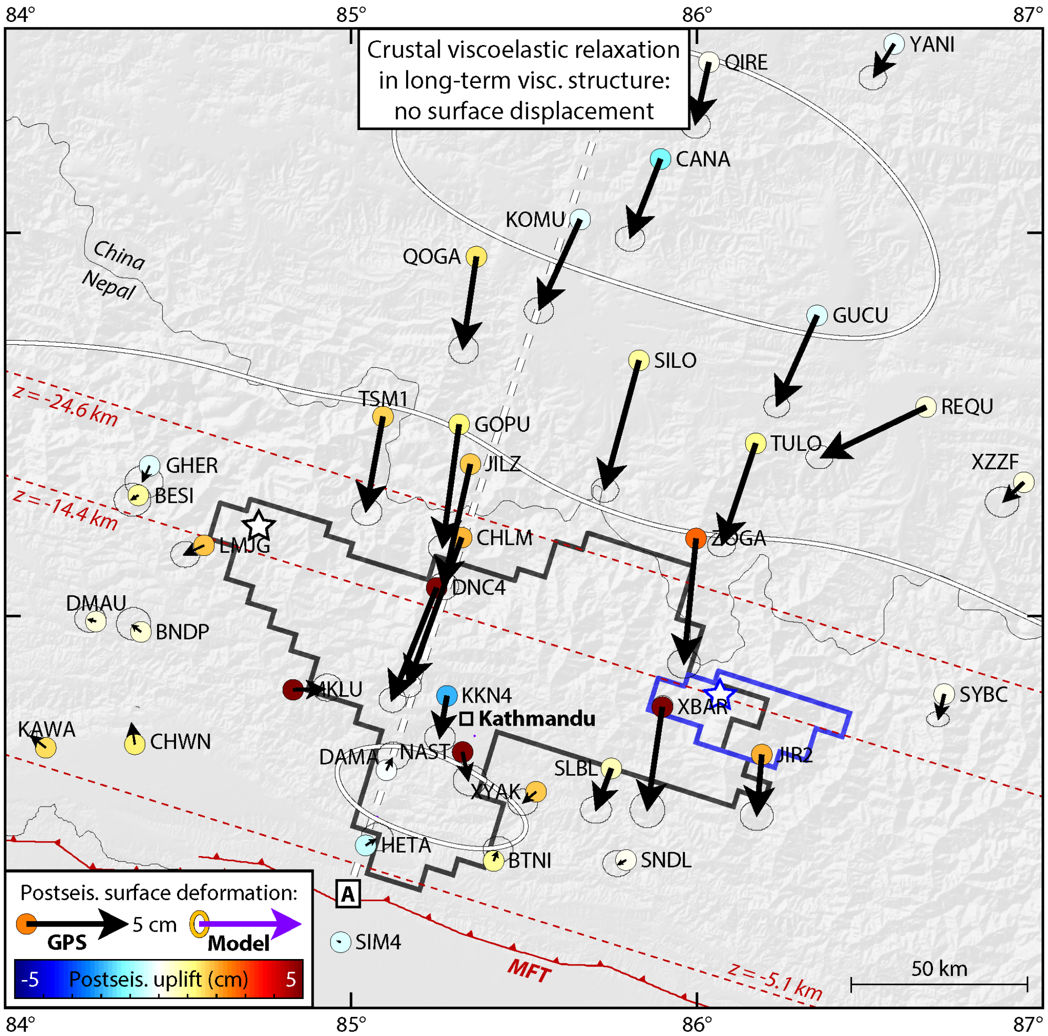

Figure 5.6. (Negligible) cumulative postseismic surface displacements (1.12 years after mainshock) predicted by postseismic viscoelastic relaxation in the upper and lower crust assuming the long-term rheological structure (Figure 5.5).

this by allowing material to flow towards of lesser coseismic displacement. A stronger mantle rheology such as wet dunite, as advocated by Hetenyi et al [2006] in light of considerations of surface topography, produces effective mantle viscosities orders of magnitude higher than the dry olivine rheology (Figure 5.S6, bottom) and would produce negligible deformation at the surface. We conclude that neither crustal nor mantle viscoelastic relaxation could have produced the observed postseismic displacement field if the short-term and long effective viscosity structures are comparable.

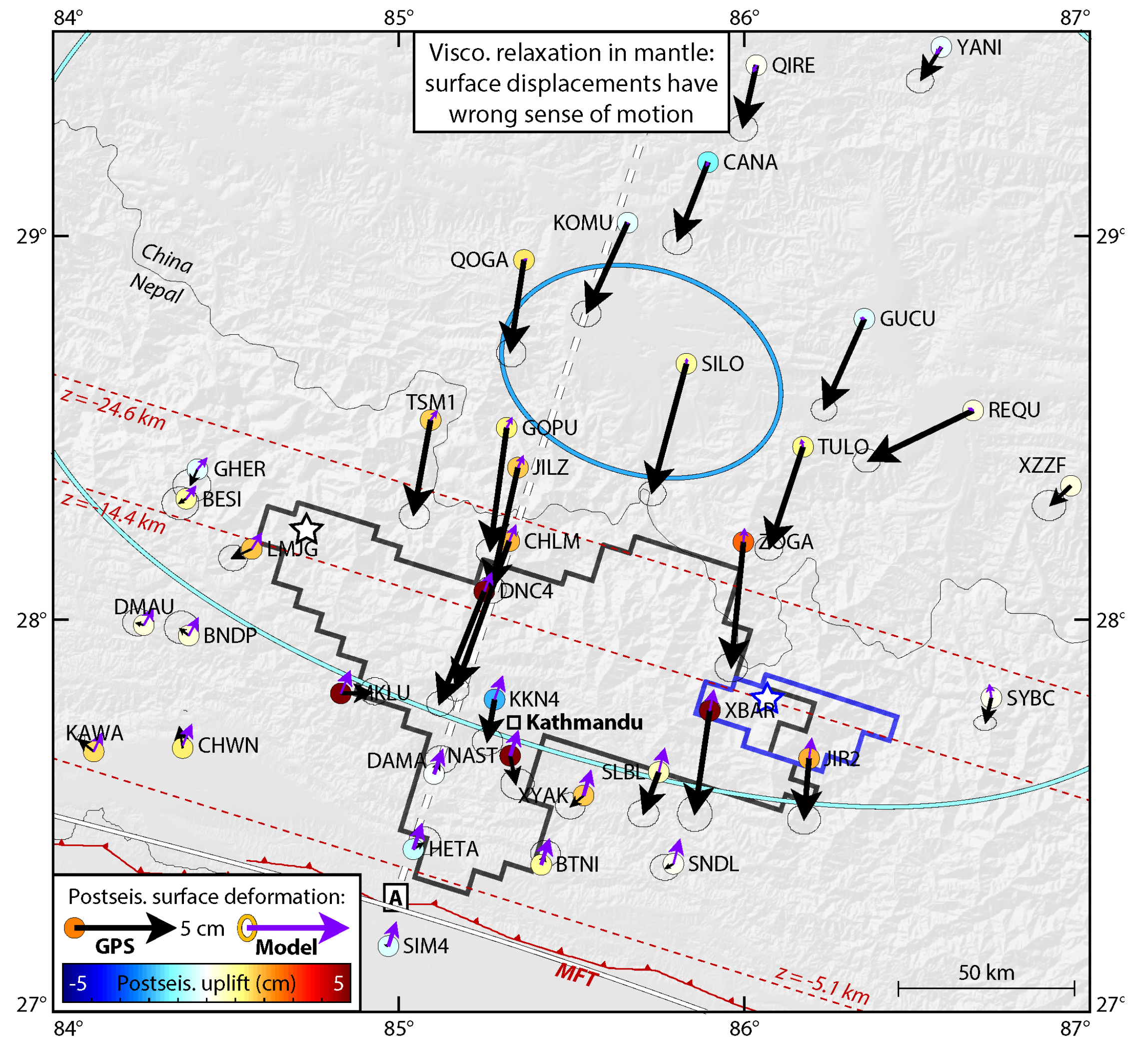

Figure 5.7. Cumulative postseismic surface displacements (1.12 years after mainshock) predicted by viscoelastic relaxation in the mantle assuming an olivine rheology (Figure 5.5, bottom; Figure 5.S6, top). Note that a dunite rheology (Figure 5.S6, bottom) would produce a much higher-viscosity mantle and predict negligible surface deformation; that rheology may be more plausible from considerations of the topography [Hetenyi et al 2006].

5.7. Transient viscoelastic relaxation in the upper crust

The high-temperature zone in the Tibetan upper crust underlies the broad postseismic displacement field observed north of the mainshock. The difficulties afterslip models encounter in reproducing this broad displacement field have been outlined previously, and Zhao et al [2017] found that poroelastic rebound in the crust was also unlikely to reproduce the postseismic deformation as it is a localized, upper-crustal process that produces a relatively short-wavelength displacement field. Viscoelastic relaxation thus seems the best candidate mechanism to explain this broad deformation pattern; the dilemma is that an effective viscosity structure consistent with the long-term deformation of the Himalaya (Figure 5.5) predicts minimal postseismic deformation (Figure 5.6), and conversely, any viscosity structure that fits the postseismic deformation would far overpredict the long-term deformation if it were assumed to apply at steady state. The only remaining possibility is seemingly that the postseismic deformation resulted from a bulk flow process that does not take place at steady-state – transient viscoelastic relaxation. This mechanism has been invoked to explain postseismic deformation in a number of cases where models featuring a single, time-independent bulk rheology have failed to explain observed postseismic deformation [e.g. Pollitz et al 2003; Freed et al 2010, 2012]. Following Masuti et al [2016], this transient rheology can be modeled as a Kelvin solid,

$$d\varepsilon_K/dt = A(\sigma_K - G_K\varepsilon_K)^n \exp(-Q/RT), \qquad [5.12]$$

in which the stress' driving power behind the strain rate is increasingly counteracted by a cumulative strain ε_K, modulated by a constant G_K, until the two are equivalent and the strain rate goes to zero. At steady state $\sigma_K - G_K\varepsilon_K = 0$ and the Kelvin solid does not contribute to deformation; therefore the coseismic stress change, rather than being effectively a perturbation as before, is the entire stress driving the Kelvin solid:

$$d\varepsilon_K/dt = A(\Delta\sigma_K - G_K\varepsilon_K)^n \exp(-Q/RT). \qquad [5.13]$$

We hypothesize that the postseismic deformation following the Gorkha earthquake, and in particular the broad deformation observed in southern Tibet, might be the product of transient viscoelastic relaxation in the high-temperature Tibetan upper crust. Godard et al [2004] employed a dry Simpson quartzite rheology for the upper crust; we assume for simplicity's sake that the transient rheology has the same sensitivity to temperature (value of Q) as this dry quartzite. A high power n would focus the deformation closer to the rupture (e.g. Chapter 2); the broad nature of the observed displacement field (Figure 5.1) instead suggests a low power may be appropriate, and so we assume $n = 1$, consistent with the linear Burgers formulation [e.g. Pollitz et al 2003]. The temporal behavior of the first independent component in the data suggests that an appropriate value for G_K is half the shear modulus, $\mu/2$, here 1.6e10 Pa (Figure 5.9, inset). Under these parameters, much of the postseismic deformation can be relatively well fit ($X^2/N = 5.10$, VR = 66%) by transient viscoelastic relaxation in a Kelvin solid with $A = 5 \times 10^{10}$ Pa^{-n} s^{-1} (Figures 5.8, 5.9).

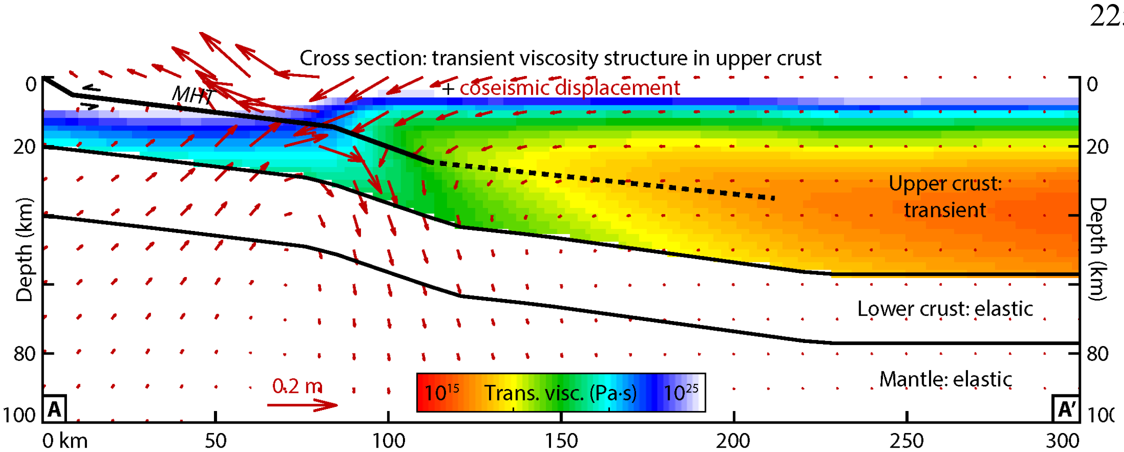

Figure 5.8. Cross section of hypothesized transient (non-steady-state) viscosity structure in the upper crust. Red arrows are coseismic displacements.

Although the effective viscosity in this model is as low as ~7 x 10^{15} Pa-s in the highest-temperature part of the upper crust (Figure 5.8, right), tests show that the postseismic deformation is not sensitive to this part of the model: artifically bounding the effective viscosity to be no lower than 7 x 10^{16} Pa-s produces displacement timeseries that (integrated over time) are only 0.3% different from the unbounded model (Figure 5.S7, yellow arrows), and bounding the effective viscosity to be no lower than 7 x 10^{17} Pa-s produces displacement timeseries only 7.6% different (Figure 5.S7, red arrows). The viscoelastic relaxation, even assuming n = 1, appears to be more sensitive to the part of the effective viscosity structure that is somewhat higher-viscosity but closer to the rupture (Figure 5.8, center). We find also that superimposing the original long-term effective crustal viscosity structure (Figure 5.5) on this Kelvin solid model, which technically completes the full linear Burgers rheology (with a Kelvin solid and Maxwell fluid in series), has a negligible effect on the surface deformation, producing surface displacements that are <0.001% different from the Kelvin-only model (integrated over time).

As an experiment, we then model transient viscoelastic relaxation in the lower crust under the same rapid flow law and temperature structure (Figure 5.S8), momentarily ignoring the diabase rheology used in the lower crust by Godard et al [2004]. We find that even this rheological structure, which is perhaps unrealistically low-viscosity, produces very little surface deformation (Figure 5.S9), with $X^2/N = 23.34$ and VR = 0.06%. Thus even if transient viscoelastic relaxation occurred in the lower crust, its contribution to the surface displacement was likely minimal, and nothing can be gleamed about its nature from the data. Noting this and recalling that viscoelastic relaxation in the mantle would likely have produced surface deformation opposite to that observed (Figure 5.7), we conclude that

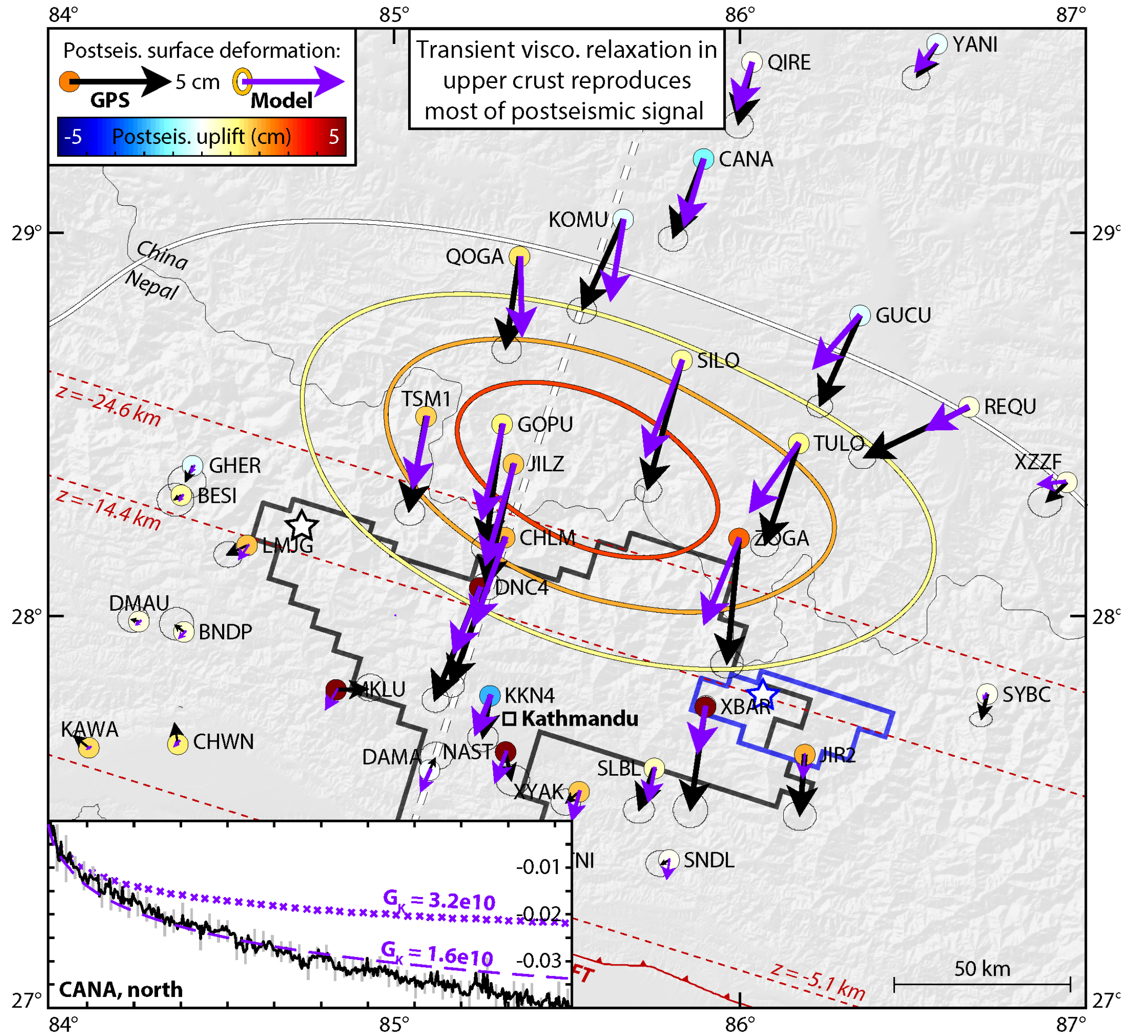

Figure 5.9. Cumulative 1.12-year postseismic surface displacements from transient viscoelastic relaxation in the upper crust (viscosity structure in Figure 5.8). Inset: comparison of displacement timeseries in models where the work-hardening coefficient G_K is equal to the shear modulus (3.2e10 Pa) or equal to half of it.

transient viscoelastic relaxation in the upper crust is a far better candidate to explain the postseismic deformation, and our subsequent models exclude any other form of viscoelastic relaxation.

5.8. Preferred hypothesis: coupled afterslip and transient viscoelastic relaxation

The model of transient viscoelastic relaxation in the upper crust undershoots the observed displacement at stations on the edge of the rupture such as XBAR and DNC4 (Figure 5.9) where the previous forward model of stress-driven afterslip produced the most displacement (Figure 5.4). We hypothesize that transient viscoelastic relaxation in the upper crust drove postseismic displacements in southern Tibet and localized afterslip drove postseismic displacements closer to the rupture. To test this, we subtract the cumulative 1.12-year postseismic displacements from the transient upper crustal relaxation model from the cumulative 1.12-year displacements in the data and then run a kinematic inversion of the residuals for afterslip on the MHT using the same method and weight of smoothing as the inversion in Figure 5.3. The largest afterslip in the resulting model (Figure 5.S10) is concentrated near stations DNC4 and XBAR, where afterslip was concentrated in the stress-driven afterslip model (Figure 5.4).

Motivated by this, we construct a forward model of afterslip (with v_0 = 20 mm/yr and (a-b)σ = 1 MPa as in Figure 5.4) and transient viscoelastic relaxation in the upper crust obeying the previous temperature-dependent Kelvin solid rheology (Figure 5.9), with both driven by stress changes in the mainshock and Mw=7.3 aftershock and each process dynamically feeding back on the other as they operate on a common stress field. This model reproduces both the near-field and far-field aspects of the observations well (X^2/N = 3.60, VR = 77.8%) and it constitutes our preferred model (Figure 5.10). As in the model of stress-driven afterslip alone, afterslip is concentrated near the downdip edge of the rupture and in the narrow zone between the mainshock and aftershock (Figure 5.10, brown patches) and in profile, it makes its largest contribution to the postseismic displacement in the near field (Figure 5.11a, brown line). To assess where viscoelastic relaxation makes the greatest contribution to the postseismic signal, we plot the cumulative 1.12-year viscous strain at 35 km depth (Figure 5.10, blue-green color shading) and in profile A-A' (Figure 5.11b) and integrate the latter into cumulative displacement (Figure 5.11a, blue line). The viscous contribution is at a maximum 0-50 km north of the Nepal/Tibet border and decreases away in both directions, consistent with the previous finding that the model is not sensitive to the very low-viscosity part of the effective viscosity structure as that is located >100 km further to the north (Figure 5.8).

The cumulative 1.12-year surface displacement field (Figure 5.10 and 5.S11) features distributed motion to the south-southwest along with strong localized uplift at DNC4 and XBAR, comparatively moderate uplift near the Nepal/Tibet border as inferred at GPS stations there, and mild subsidence further to the north as also potentially inferred in the GPS (Figure 5.S10). Displacement east, west and south of the mainshock is minimal, consistent with observations. The coupled model also successfully reproduces the reconstructed time evolution of displacement at GPS stations (Figure 5.12), with afterslip and viscoelastic relaxation trading off in the contribution they make as per stations'

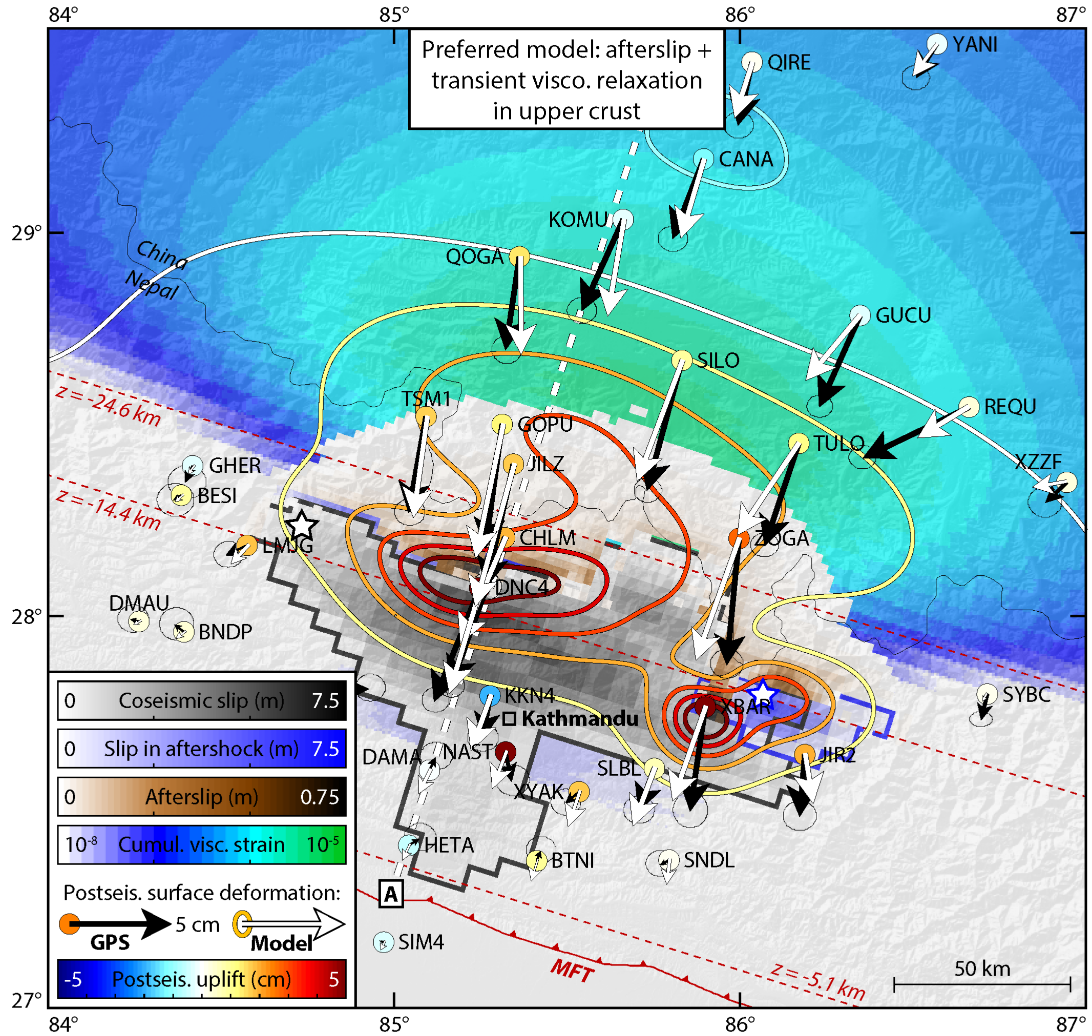

Figure 5.10. Preferred model of postseismic deformation, consisting of transient viscoelastic relaxation in the upper crust (Figures 5.8-5.9) dynamically coupled with localized afterslip (Figure 5.4). Black and white arrows are cumulative observed and model-predicted 1.12-year postseismic horizontal displacements, respectively; filled circles and colored contours are cumulative observed and model-predicted 1.12-year vertical displacements. Brown patches and blue/green-shaded region are cumulative afterslip and viscous strain at 1.12 years, respectively, the latter at 35 km depth.

locations. The displacement timeseries are almost identical to those obtained by summing the displacement timeseries from the individual afterslip and viscoelastic relaxation models (Figure 5.12, Xs), suggesting a low degree of dynamic feedback between the mechanisms.

As characterized here, postseismic deformation should have somewhat re-increased the shear stress on the portion of the MHT that ruptured in the mainshock, as it took place just downdip of the mainshock and had a similar sense of shear (sort of a partially

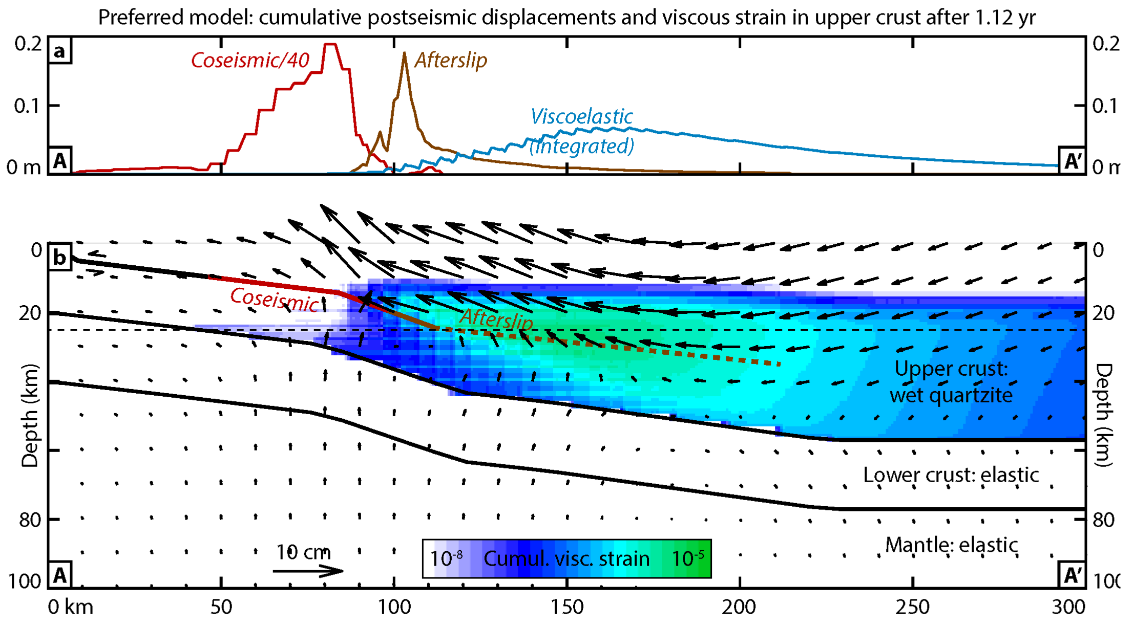

Figure 5.11. a) Comparison of coseismic slip (red, here divided by 40 for ease of plotting) with cumulative 1.12-year afterslip (brown) and cumulative vertically integrated viscous strain (blue) in the preferred model in profile A-A'. **b)** 1.12-year cumulative postseismic displacements (black arrows) and viscous strain (color shading) in profile A-A'.

distributed version of the static stress triggering "domino effect" [Stein et al 1997]). Our model implies that over the first 1.12 years following the mainshock, postseismic deformation re-increased the shear stress by ≥0.05 MPa (0.5 bar) over 38% of the coseismic rupture and by ≥0.02 MPa (0.2 bar) over 56% of it. The stress change west, east and updip of the mainshock was comparatively small (Figure 5.13).

The cumulative seismic moment released by afterslip over the first 1.12 postseismic years in our preferred model is 1.4 x 10^{19} Nm, equivalent to a Mw=6.7 earthquake. This is only 2.3% of the seismic moment released in the mainshock and only 15% of the cumulative postseismic moment release as inferred from the kinematic inversion (9.8 x 10^{19} Nm, equivalent to a Mw=7.26 earthquake), suggesting that viscoelastic relaxation contributed to the bulk of the postseismic signal. Despite this, the shape of the coseismic shear stress change distribution tracks the afterslip distribution (Figure 5.13), likely because afterslip is simply a much nearer-field process. This disparity, with one process seemingly dominating the accommodation of strain and the other seemingly dominating the reloading of the seismogenic zone, may be applicable to other fault systems as well.

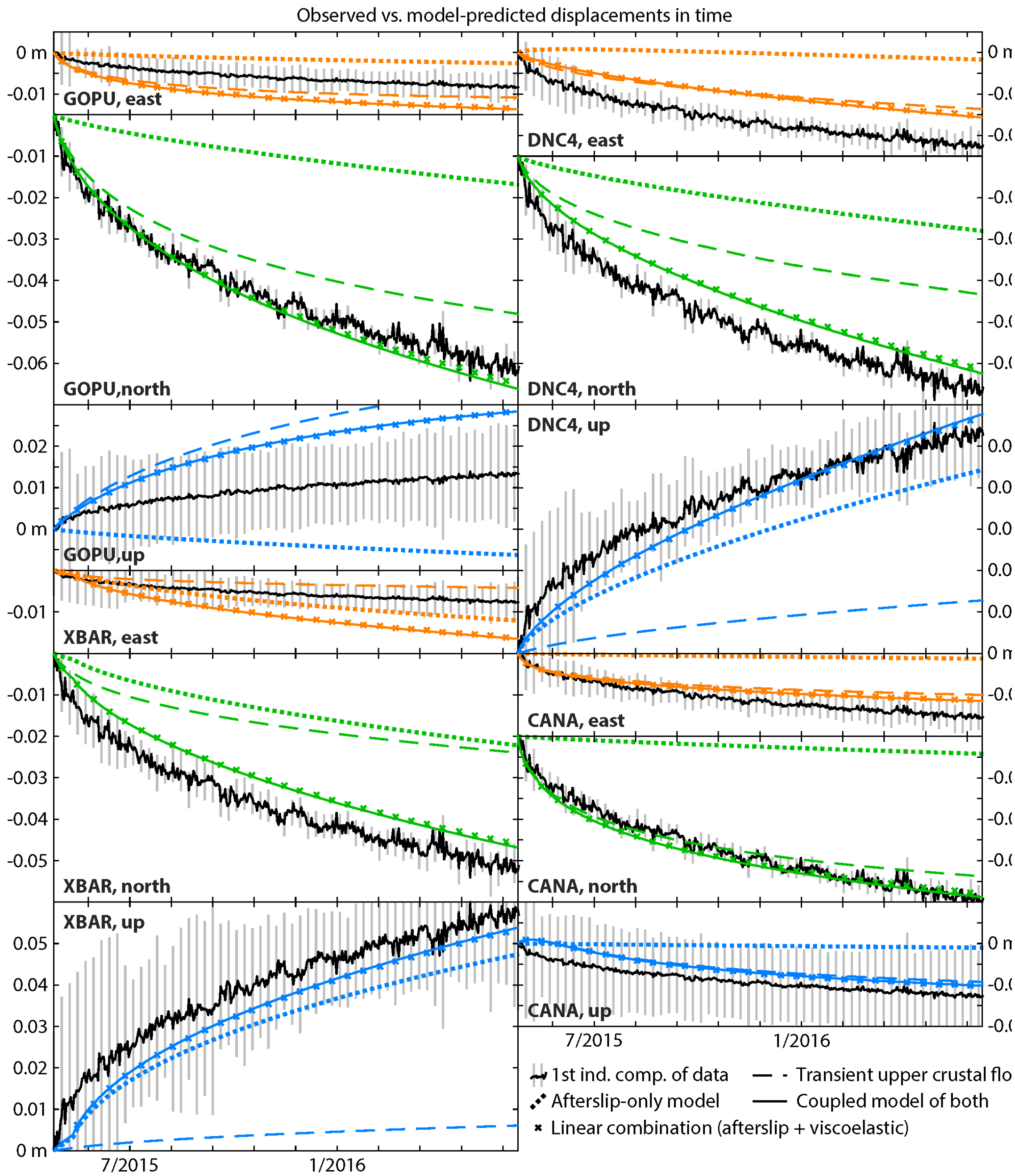

Figure 5.12. Comparison of displacement timeseries predicted by forward models with those predicted from the first independent component of the network's motion. Black timeseries and gray bars are predictions of first independent component of the data and the data uncertainties, respectively. Dotted timeseries are from afterslip-only model (Figure 5.4); dashed timeseries are from model of transient viscoelastic relaxation in the upper crust (Figure 5.9); solid colored timeseries are from preferred model of coupled afterslip and viscoelastic relaxation (Figure 5.10, 5.11).

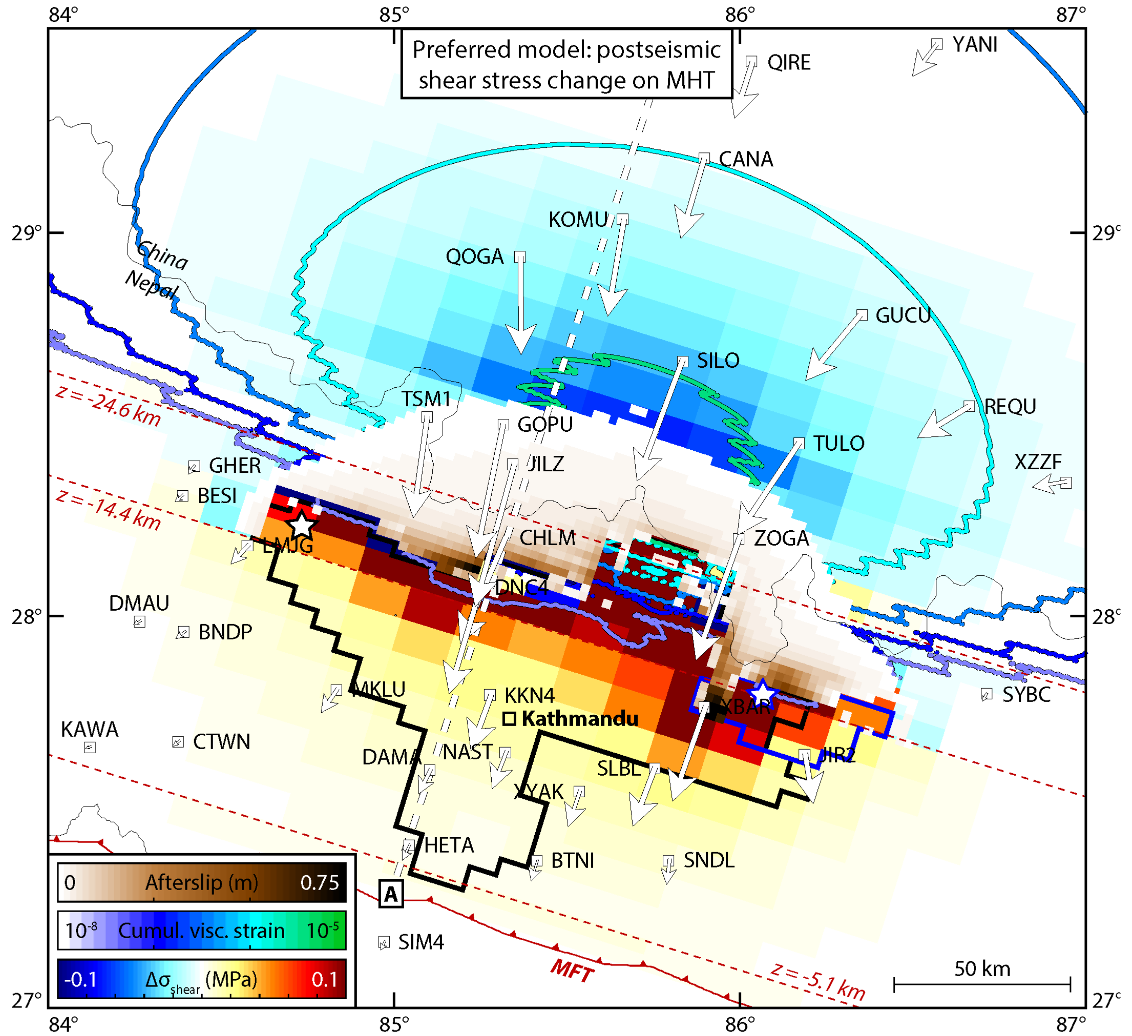

Figure 5.13. Distribution of cumulative 1.12-year shear stress change on the MHT induced by the deformation processes in the preferred model.

postseismic deformation can be well fit to a model of afterslip on the fault plane that ruptured in the mainshock; 2) the afterslip model invoked, however, features slip extending far further from the rupture than stress-driven models suggest is likely; 3) elevated temperatures downdip of the rupture also suggest that deformation there is more likely accommodated by distributed ductile shear than brittle creep; and 4) we find that a model of postseismic viscoelastic relaxation that is geometrically based on external constraints (here temperature, rheology and stress rather than seismic constraints as in Chapter 2) does indeed reproduce characteristics of the observed postseismic deformation better than afterslip models do, in particular the observation that the postseismic displacement pattern is spatially broad (here extending far into southern Tibet, there extending out to the California coast).

The afterslip distribution invoked in the kinematic inversion here (Figure 5.3) has a cumulative seismic moment equivalent to a Mw=7.26 earthquake, and it therefore cannot be dismissed as implausible on the grounds of having a moment release larger than the mainshock, as was the case in Chapter 2. And although the afterslip distributions invoked by kinematic inversions in Gualandi et al [2016] and Zhao et al [2017] have the characteristic that they increase in magnitude of slip away from the rupture before reaching a maximum and then decreasing from there (a feature that would be impossible to reproduce in stress-driven models without invoking some sort of runaway deformation process at depth), our inverted afterslip distribution does not feature any major downdip increase in slip and perhaps is more plausible on those grounds. (We note that Zhao et al disallowed afterslip on the coseismic rupture in their kinematic inversion and simultaneously imposed spatial smoothing, which would have forced slip patches on the edge of the rupture to also have near-zero slip and would likely cause the inferred slip distribution to increase away from the rupture.) Nevertheless, two other considerations make it implausible that afterslip dominated post-Gorkha deformation despite the success of the kinematic inversion in fitting the cumulative 1.12-year GPS displacements. First, as in chapter 2, stress-driven models indicate that afterslip should decrease sharply in magnitude downdip from the rupture (Figure 5.4), as the coseismic stress change that drives it does so (Figure 5.S5). A stress-driven model could conceivably reproduce the afterslip distribution inferred in the inversion if (a-b)σ were to decrease downdip like the stress change Δτ. However, the transition from locking to interseismic creep north of the Gorkha earthquake (Figure 5.1) should correspond to a downdip increase in (a-b)σ from negative (rate-weakening) to positive (rate-strengthening) values, not a decrease. The afterslip distribution inferred in the inversion therefore seems unlikely. Second, the inversion requires afterslip extending down into a region where temperatures at the depth of the prescribed fault plane (~25-35 km) exceed 600° C [e.g. Royden et al 1993, Henry et al 1997, Herman et al 2010] (Figure 5.1, 5.2), far above the temperature range at which brittle creep on localized fault zones is expected to occur [Marone et al 1991, Blanpied et al 1991]. This consideration makes it more plausible that deformation in this region occurs in a distributed shear zone, motivating our models of stress-driven viscoelastic relaxation. As in Chapter 2, we find through these models that a broad postseismic deformation pattern featuring significant motion in both the near- and far-field can more plausibly be explained by a combination of one deformation mechanism that decreases in influence downdip (afterslip) and one that increases in influence downdip (viscoelastic relaxation) rather than by a single process with near-uniform downdip behavior (of which we are unaware of any).

The kinematic inversion nevertheless provides a useful estimate of the equivalent magnitude of the 1.12-year postseismic deformation as compared to other processes. The estimated cumulative seismic moment release is equivalent to a Mw=7.26 earthquake, 16% of that released in the mainshock and two orders of magnitude larger than that released by aftershocks over the same period [Gualandi et al 2016]. In the preferred model, afterslip releases only 15% of the moment from the kinematic inversion but appears to have a control on the shear stress reloading of the coseismic rupture zone by virtue of being much closer to it than the viscoelastic relaxation (Figure 5.13). This suggests that if the Gorkha earthquake and its postseismic deformation are representative of the long-term seismic and aseismic behavior of the MHT, future models of the long-term deformation of the Himalaya could be improved by incorporating viscoelastic relaxation and afterslip, but may not need to incorporate the contribution of aftershocks (perhaps except for especially large ones such as the Mw=7.3 aftershock here).

In parallel, we find that the effective viscosity structure consistent with models of the long-term deformation of the Himalaya predicts negligible postseismic deformation if only the crust is considered (Figure 5.6) and that the effective viscosities suggested by post-Gorkha deformation are at least an order of magnitude lower than those consistent with the long-term deformation (Figure 5.8). If correct, this suggests that transient viscoelastic relaxation may be an important feature of the deformation of the Himalaya. If transient deformation was added to a long-term deformation model [Godard et al, 2004; Herman et al, 2010], the cumulative time-averaged strain rate would presumably increase; therefore, in order to fit the same ~20 mm/yr overall convergence rate, the steady-state rheology would necessarily require a stronger crustal material such as granite or diabase rather than the quartzite rheology used by Godard et al [2004]. This would have implications for the support of the topography of Tibet.

Our finding that a transient viscoelastic rheology is needed to explain post-Gorkha deformation is reminiscent of other studies of postseismic deformation that have invoked time-dependent rheologies [e.g. Pollitz et al, 2003; Freed et al 2010, 2012; Ryder et al, 2011; Huang et al, 2014; Masuti et al 2016]. One difference, however, is that many of those studies inferred a transient rheology because postseismic displacement timeseries featured a "double signal" of rapid early deformation followed by sustained later deformation that rheologies with a single time dependence could not reproduce, even though the latter could reproduce the cumulative magnitudes of postseismic deformation [Freed et al 2010, 2012]; here, by contrast we infer a transient rheology because the best-guess long-term rheology structure (Figure 5.5) produces almost no postseismic deformation at all (Figure 5.6). Our introduction of a transient rheology here therefore has stronger implications for the long-term accommodation of strain (as discussed above) than it would if we were simply modifying a steady-state flow law that nearly fit the data except for its time evolution. However, the transient viscosity structure we infer may not be implausible: tests suggest that the postseismic deformation could be fit adequately with effective viscosities no lower than ~7 x 10^{17} Pa-s (Figure 5.S7), close to the transient viscosities of 9 x 10^{17} Pa-s and 4.4 x 10^{17} Pa-s invoked in Burgers rheologies by Ryder et al [2011] and Huang et al [2014] to respectively explain deformation beneath the Tibetan Plateau following the 2001 Kokoxili, Tibet and 2008 Wenchuan earthquakes.

We note that afterslip and viscoelastic relaxation are strongly segregated in our preferred postseismic model, as the dynamic coupling between them has almost no effect on the total deformation (Figure 5.12) and their contributions to the postseismic deformation have maxima that are separated in profile (Figure 5.11a, brown and blue lines). A more realistic deformation model may feature a more gradual transition between these mechanisms (as otherwise there would presumably be an unresolved strain buildup in the zone in between them). This could be achieved, for example, by simply choosing a higher value of Q in the flow law for viscoelasticity so that the effective viscosity was less dependent on temperature and thus decreased less sharply into the high-temperature zone. As this would add an extra degree of freedom, we retain the value of Q for dry quartzite used by Godard et al [2004].

We infer that viscoelastic relaxation in the mantle would produce horizontal and vertical displacements opposite to those observed (Figure 5.7). It is plausible that the mantle could have made no contribution to post-Gorkha deformation as the Indian plate may be effectively elastic over a thickness of ~180 or >200 km [Jimenez-Munt et al 2008, Tunini et al 2016]. This contrasts with settings such as the Salton Trough, where it was seen in Chapter 2 that the lithosphere-asthenosphere boundary may be as shallow as 45 km and postseismic deformation may be dominated by mantle flow; it also contrasts with findings in studies of postseismic deformation following earthquakes in other continental settings such as the Mojave Desert [e.g. Pollitz et al 2003, Freed et al 2007] and Alaska [e.g. Freed et al 2006]. Postseismic deformation in the India-Asia collision zone may therefore be dominated by crustal rather than mantle processes by virtue of the relatively extreme depth to the asthenosphere and the proportional weakening of the crust due to the thickness of the radiogenic layer [Royden 1993]. This is consistent with the findings that postseismic deformation in the Tibetan Plateau following the Kokoxili and Wenchuan earthquakes was dominated by viscoelastic relaxation in the lower crust [Ryder et al 2011, Huang et al 2014] and that deformation following the 2005 Kashmir earthquake was dominated by afterslip [Jouanne et al 2011, Wang and Fialko 2014].

Our finding that afterslip alone cannot explain post-Gorkha deformation contrasts with that of Wang and Fialko [2017, in prep.], who successfully reproduced the postseismic deformation field inferred from InSAR with a stress-driven afterslip model with the same formulation and using $(a-b)\sigma = 6.5$ MPa. One of our key pieces of evidence disfavoring afterslip alone as a causative mechanism is that it does not reproduce the magnitude of deformation at GPS stations in southern Tibet (Figure 5.3), whose data were not available to Kang and Fialko [2017]. Data from these stations may be of continuing importance in future geodetic studies in particular because the topography and climate of the Himalaya may make InSAR-based analyses difficult there. Nonetheless, we do infer that afterslip downdip of the rupture contributed to postseismic deformation, in agreement with Wang and Fialko [2017]. Our findings are most similar to those of Zhao and Burgmann [2017], who did use GPS data from Tibet (although far further north than the CEA stations) and found that postseismic displacements at stations there did indeed suggest viscoelastic relaxation in the Tibetan crust (also obeying a Burgers rheology as in our preferred model). They also used a stress-driven model of afterslip to show that the afterslip distribution inferred in kinematic inversions was physically implausible, but retained some stress-driven afterslip downdip of the rupture as a second causative process as we do in our preferred model. Our forward models are arguably more sophisticated as they feature afterslip and viscoelastic relaxation dynamically feeding back on one another (although the level of feedback appears to be small) and the viscosity structures are directly derived from models of the thermal structure and prestress conditions through flow laws. Nevertheless, the fact that our preferred interpretation is similar to that of Zhao et al despite the different methods and assumptions used suggests that both interpretations may be on the right track.

We find that post-Gorkha deformation may have re-increased the shear stress by ≥ 0.02 MPa over 56% of the portion of the Main Himalayan Thrust that ruptured in the Gorkha earthquake, and by ≥ 0.05 MPa over ~38% of it, in the first postseismic year. (These alternate stress change values have been found sufficient to trigger earthquakes in alternate settings [King et al 1994, Rydelek and Sacks 1999]). This increases the seismic hazard associated with this section. In contrast, postseismic deformation imparted only minimal stress changes to the sections of the MHT west, east and updip of the rupture, suggesting that simple stress transfer models featuring the mainshock may be adequate to characterize the changes in hazard along those sections.

5.10. Conclusions

We characterize postseismic deformation following the 2015 Gorkha earthquake using GPS data from stations in Nepal and Tibet; we find the latter to be particularly important in constraining the causative processes. Although the cumulative 1.12-year displacements can be fit by a hypothetical afterslip distribution on the downdip extension of the Main Himalayan Thrust, stress-driven models suggest that this distribution of afterslip is physically implausible and temperature considerations point towards viscoelastic relaxation as a more likely candidate mechanism. Our preferred hypothesis is that post-Gorkha deformation dominantly resulted from viscoelastic relaxation obeying a transient rheology in the high-temperature upper crust of Tibet as well as localized afterslip around the downdip edge of the rupture. This deformation would have re-increased the shear stress on the coseismic rupture but not on the neighboring sections of the Main Himalayan Thrust. These findings may be useful in studies of long-term deformation across the Himalaya and the continuing seismic hazard in this region.

5.A. Supporting Information

Appendix 5.1. Preparation of the temperature and stress models (Figures 5.4, 5.S4, 5.5)

The temperature and steady-state stress distributions we use are respectively those from Henry et al [1997] and Godard et al [2004] [V. Godard, pers. comm.]; both models are 2D and extend to ~130 km depth. Both contain topography, which is not supported in RELAX or in the Okada et al [1985] Green's functions used in the kinematic inversions. The GPS stations also sit atop this topography and must also be set as being at 0 km depth in these methods. The Green's functions mapping subsurface deformation to surface displacement should not be much changed as long as the distance from the deformation to the surface does not change; put another way, it matters more in our modeling whether a high-temperature zone sits 25 or 30 km below an observation point than whether it sits 20 or 25 km below sea level. Therefore, as all GPS stations are assumed to sit at 0 km depth, we "flatten" the temperature and prestress models by enforcing that their surfaces are everywhere at 0 km depth and their bases are at 130 km depth and compacting their vertical dimension in between. This is only a ~4% compaction even for the ~5-km topography of the Himalaya and its effect on our models should therefore be small. This flattening is also self-consistent with the Elliott et al [2016] fault geometry, as that model was obtained assuming an elastic halfspace Earth.

Although the Henry et al [1997] thermal model provides spatially uniform numerical values in the crust and mantle, the original Godard et al [2004] model of the distribution of deviatoric stress is lost, and we work from a visual contour plot of the deviatoric stress distribution [V. Godard, pers. comm.], which we digitize. This provides 10-MPa contours of deviatoric stress, and we linearly interpolate between contours to approximate the full distribution. This works except in the high-temperature zone in the Tibetan upper crust, which is sandwiched between 10-MPa contours on the top and botttom (Figures 5.4, 5.S4). (Linear interpolation between these contours would thus produce a uniform prestress of 10 MPa in this zone). We instead log-linearly extrapolate downward from the interpolated values on the top side of the high-temperature zone, and upward from the interpolated values on the bottom side, and then smooth between the extrapolations. This would cause the prestress to be very close to 0 MPa in the center of the high-heat flow zone, which may be unrealistic as the zone participates in accommodating steady long-term shear between the India and Eurasia plates. A ballpark value for the minimum prestress can be estimated from the consideration that this shear zone should over the long term accommodate ~20 mm/yr of shear over its ~45-km width, translating to a strain rate of ~1.6 x 10^{-14}. This should be equal to $A\sigma^{n}$ exp(-Q/RT), where σ is the prestress distribution and A, n, Q and T are already known from the thermal model and the Godard et al [2004] rheological structure, and so we can back out a value for the minimum prestress. Our preferred value is 1.25 MPa, consistent with estimates of the prestress in the high-temperature lower crust of Taiwan [e.g. Hsu et al 2009].

Although the temperature and prestress models extend down to ~130 km depth, we are also interested in possible viscoelastic relaxation at greater depths. We thus linearly extrapolate the Henry et al thermal model downward to ~250 km depth (the base of our models) and cap the temperature (which increases linearly downward) at 1350° C. The effective thermal thickness of the Indian plate as defined by the 1350° C isotherm is ~180 km, similar to estimates of the depth to the lithosphere-asthenosphere boundary from seismic methods [Jimenez-Munt et al 2008; Tunini et al 2016]. Lateral heterogeneities in the deeper part of the prestress model make downward extrapolation impractical, so we instead assume that the Indian mantle has a uniform deviatoric stress of 0.47 MPa after Copley et al [2010]. As in Chapter 2, the Green's functions mapping mantle flow to surface displacement may be biased because RELAX and the Okada formulation assume an elastic halfspace Earth, and so the results of our mantle flow models are best viewed qualitatively. The models of crustal viscoelastic relaxation should be less biased by material inhomogeneity, and in fact Godard et al [2004] assumed a uniform Young's modulus and Poisson's ratio for the crust of 80 GPa and 0.25, respectively, so it is self-consistent to use an elastic halfspace Earth to model viscoelastic relaxation in the crust here. We use the values from Godard et al [2004] for the Young's modulus and Poisson's ratio.

Supplementary Figures

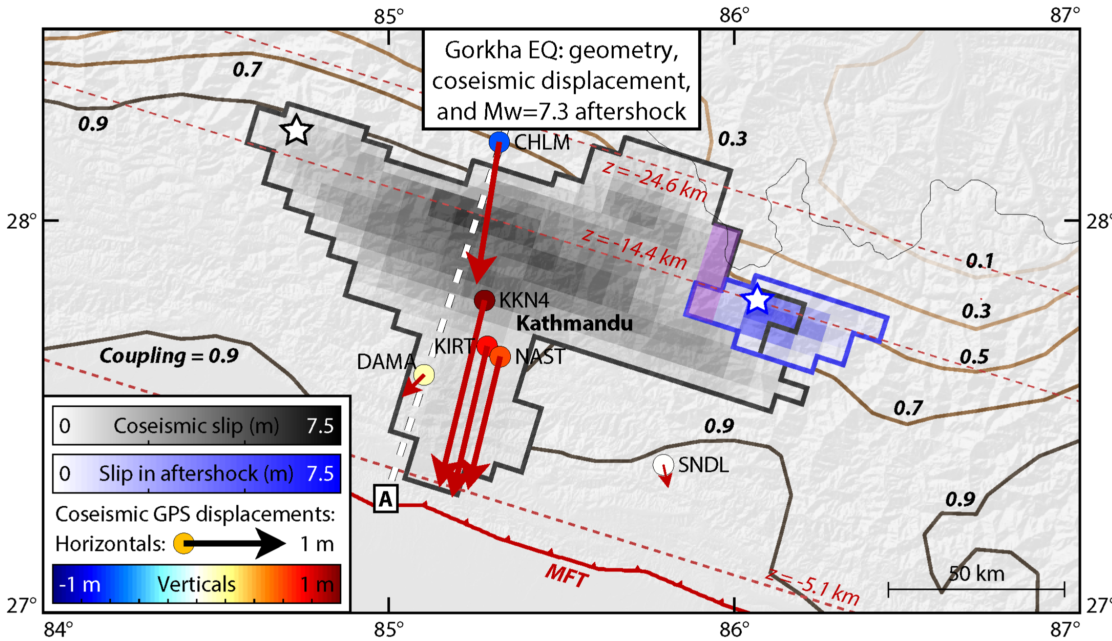

Figure 5.S1. Tectonic setting of the Gorkha earthquake and slip in mainshock and 5/12/2015 aftershock from Elliott et al [2016] models. Brown contours are interseismic coupling from Stevens and Avouac [2015]. Purple shaded region is narrow zone in between mainshock and aftershock that Lindsey et al [2015] inferred did not rupture in either event and where we set the slip in both to zero to allow afterslip.

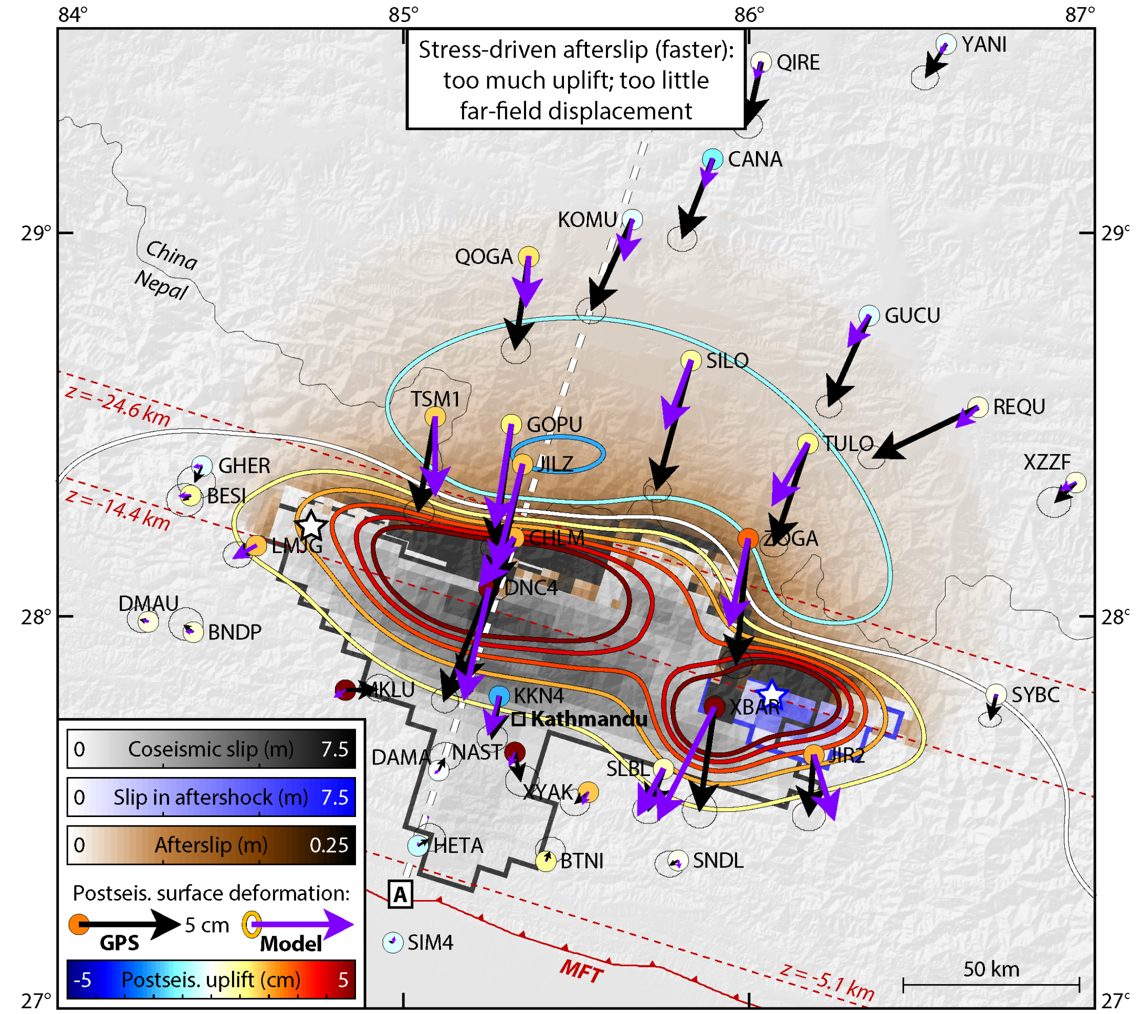

Figure 5.S2. Forward model of afterslip that is modeled as being five times faster than the afterslip in Figure 5.3 (v_0 = 100 mm/yr, (a-b)σ = 1 MPa). Brown patches are the magnitude of afterslip at 1.12 years; colored contours are model-predicted uplift and subsidence.

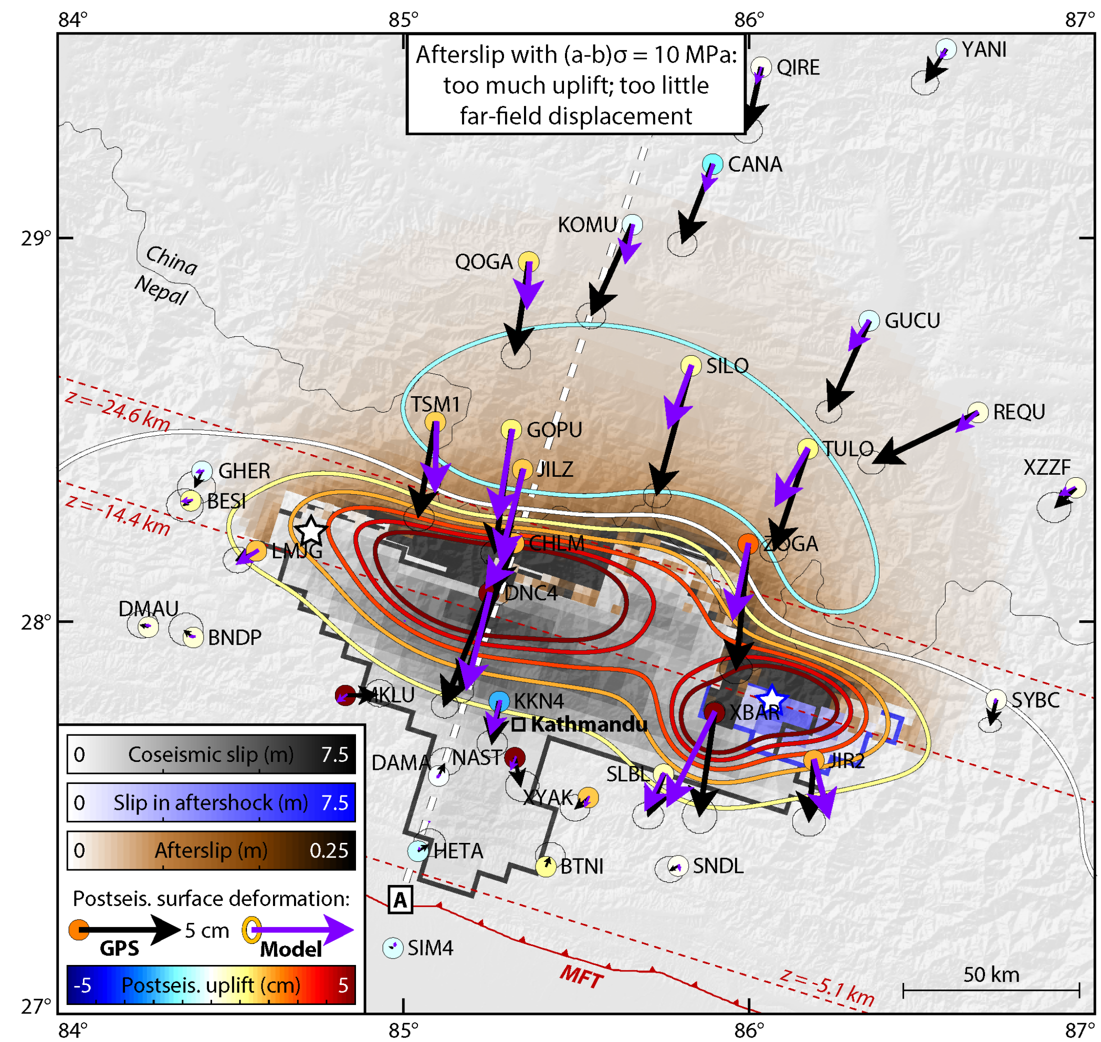

Figure 5.S3. Forward model of afterslip with (a-b)σ = 10 MPa and v_0 = 20 mm/yr. Brown patches are the magnitude of afterslip at 1.12 years; colored contours are model-predicted uplift and subsidence.

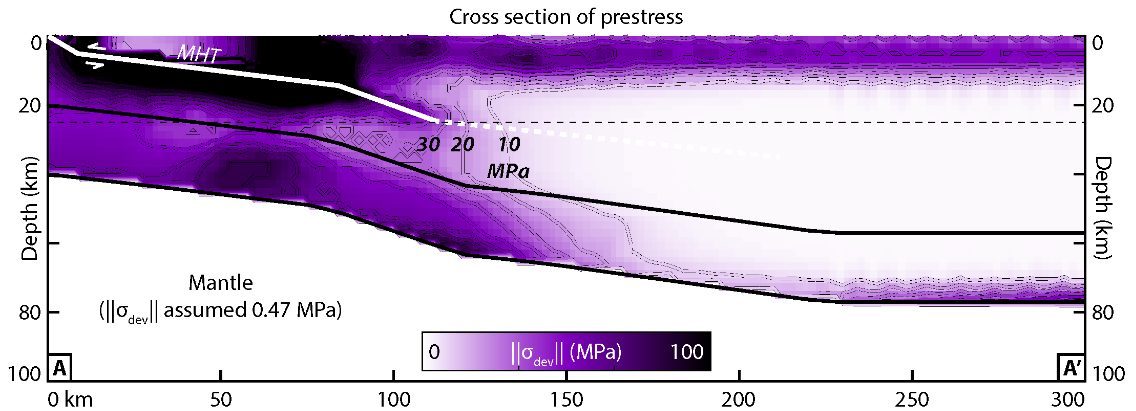

Figure 5.S4. Prestress distribution (norm of deviatoric stress tensor) based on Godard et al [2004] model. Model preparation is described in Appendix 5.1.

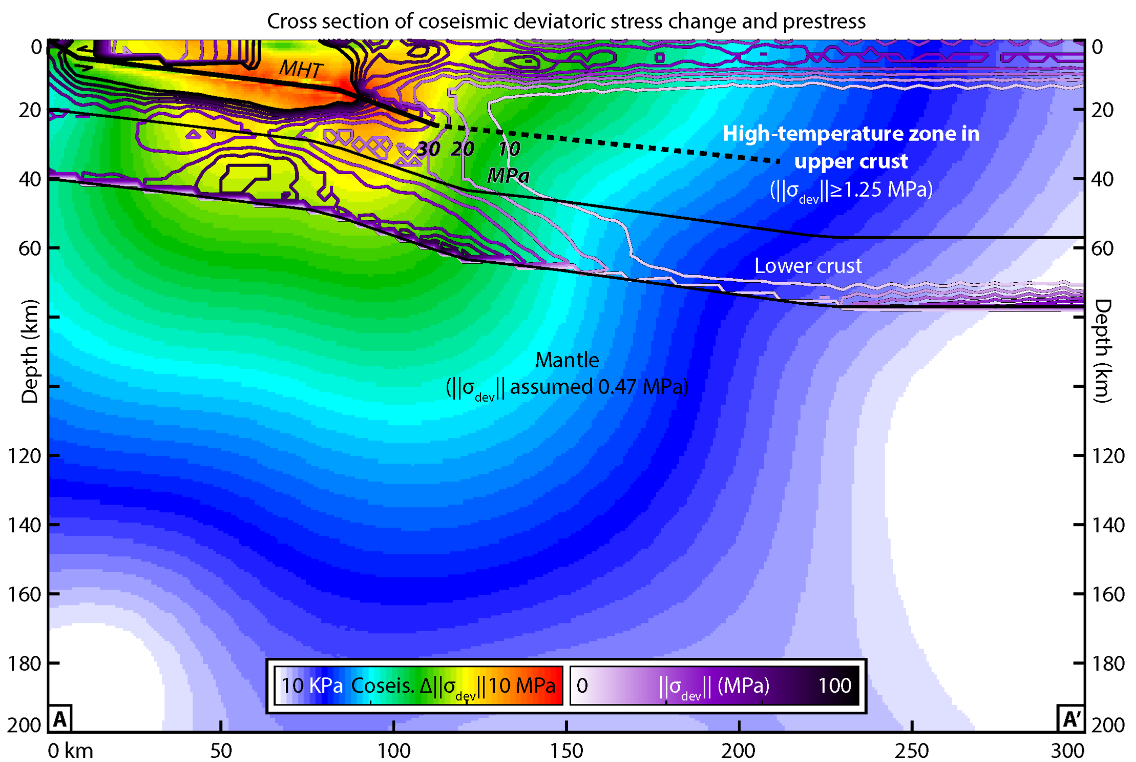

Figure 5.S5. Comparison of the prestress (purple contours) with the magnitude of the coseismic deviatoric stress change (color shading) in profile A-A'.

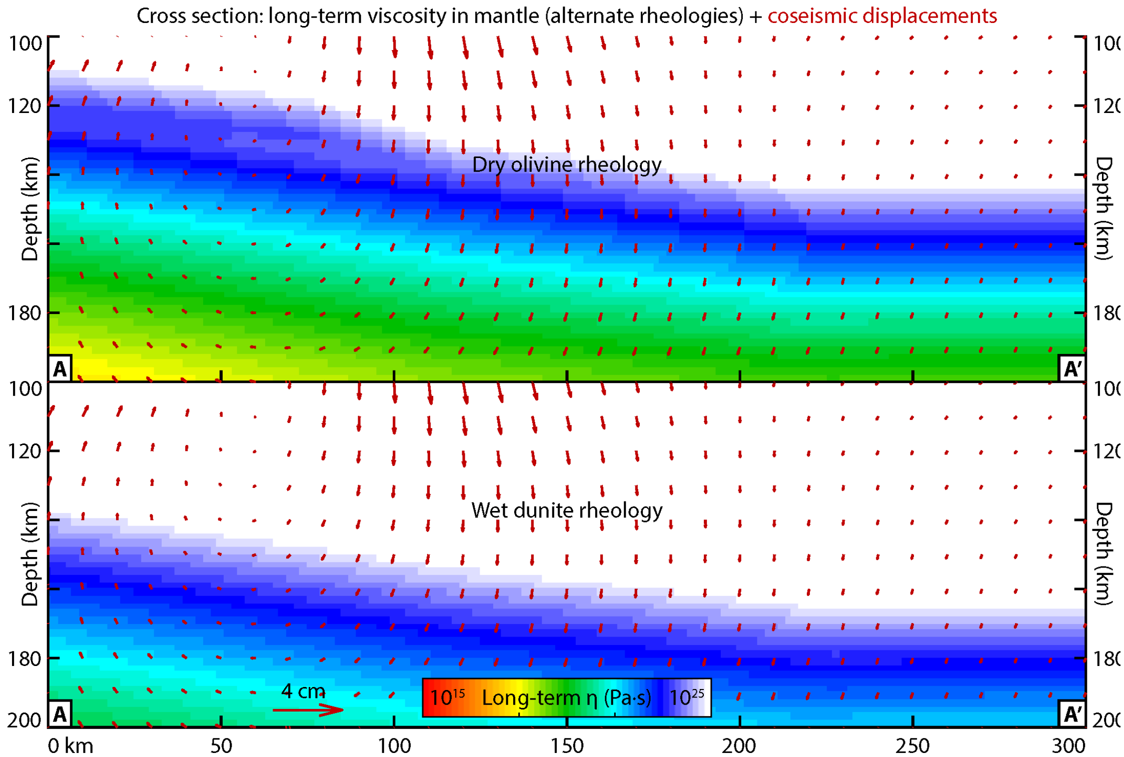

Figure 5.S6. Alternative long-term effective viscosity structures in the mantle in profile A-A’ considering either (top) the Godard et al [2004] dry olivine rheology (Figure 5.5) or (bottom) a wet dunite rheology [Hetenyi et al 2006]. Red arrows are coseismic displacements in the same profile, magnified from Figure 5.5 (note ubiquitous downward motion).

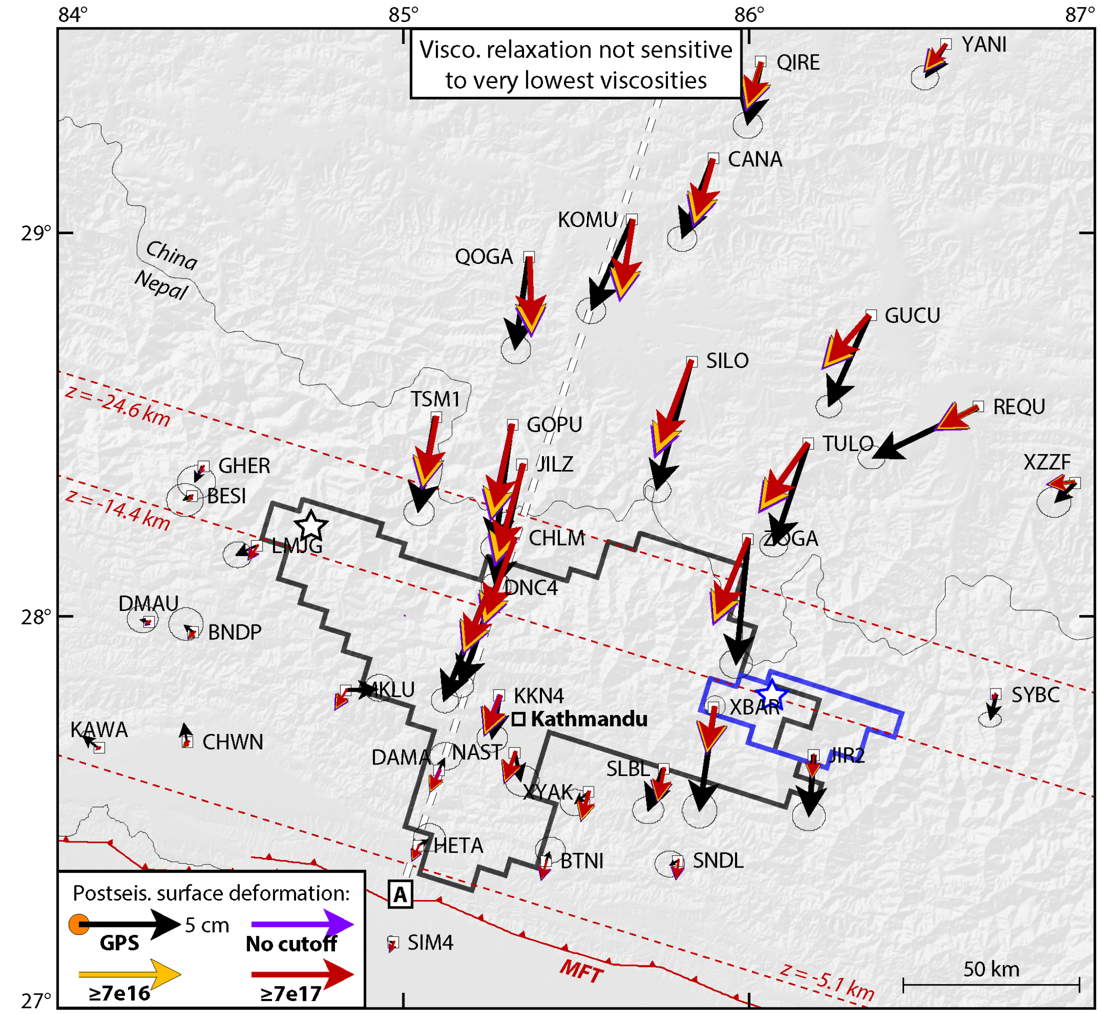

Figure 5.S7. The surface displacements from transient viscoelastic relaxation in the upper crust (purple arrows) change negligibly (0.3% difference) if the effective viscosity is bounded to be >7 x 10^{16} Pa-s (yellow arrows) and only slightly (7.6% difference) if the effective viscosity is bounded to be >7 x 10^{17} Pa-s (red arrows).

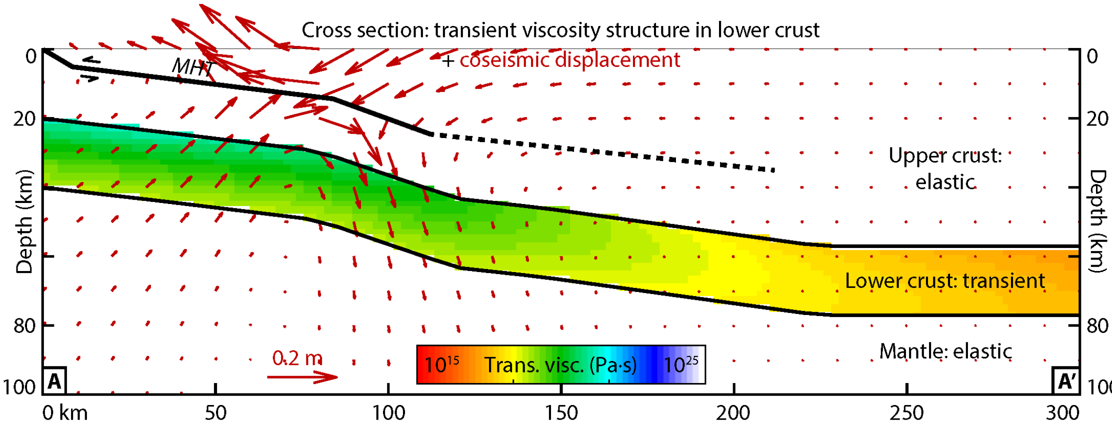

Figure 5.S8. Cross section of hypothesized transient (non-steady-state) viscosity structure in the lower crust. Red arrows are coseismic displacements.

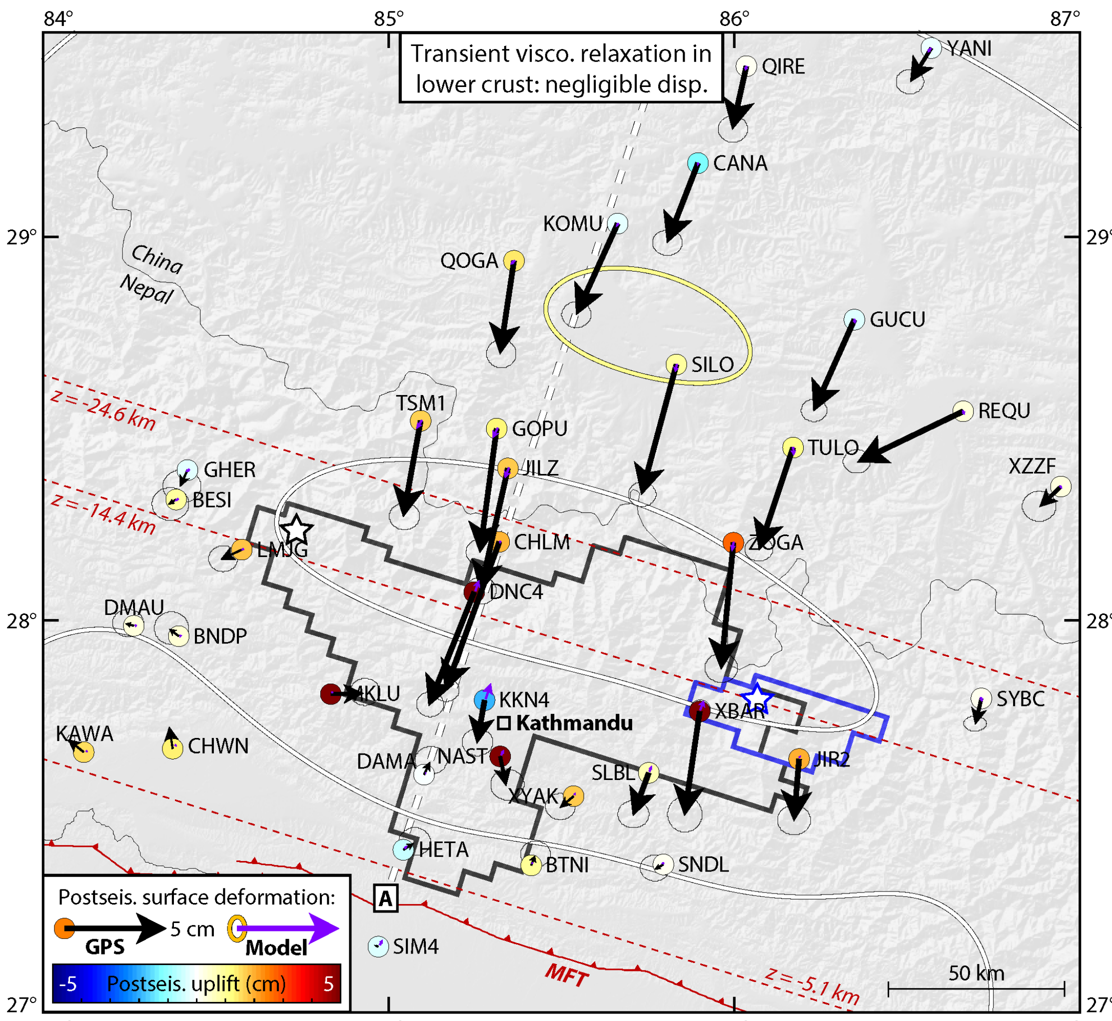

Figure 5.S9. Cumulative 1.12-year postseismic surface displacements from transient viscoelastic relaxation in the lower crust (viscosity structure in Figure 5.S8).

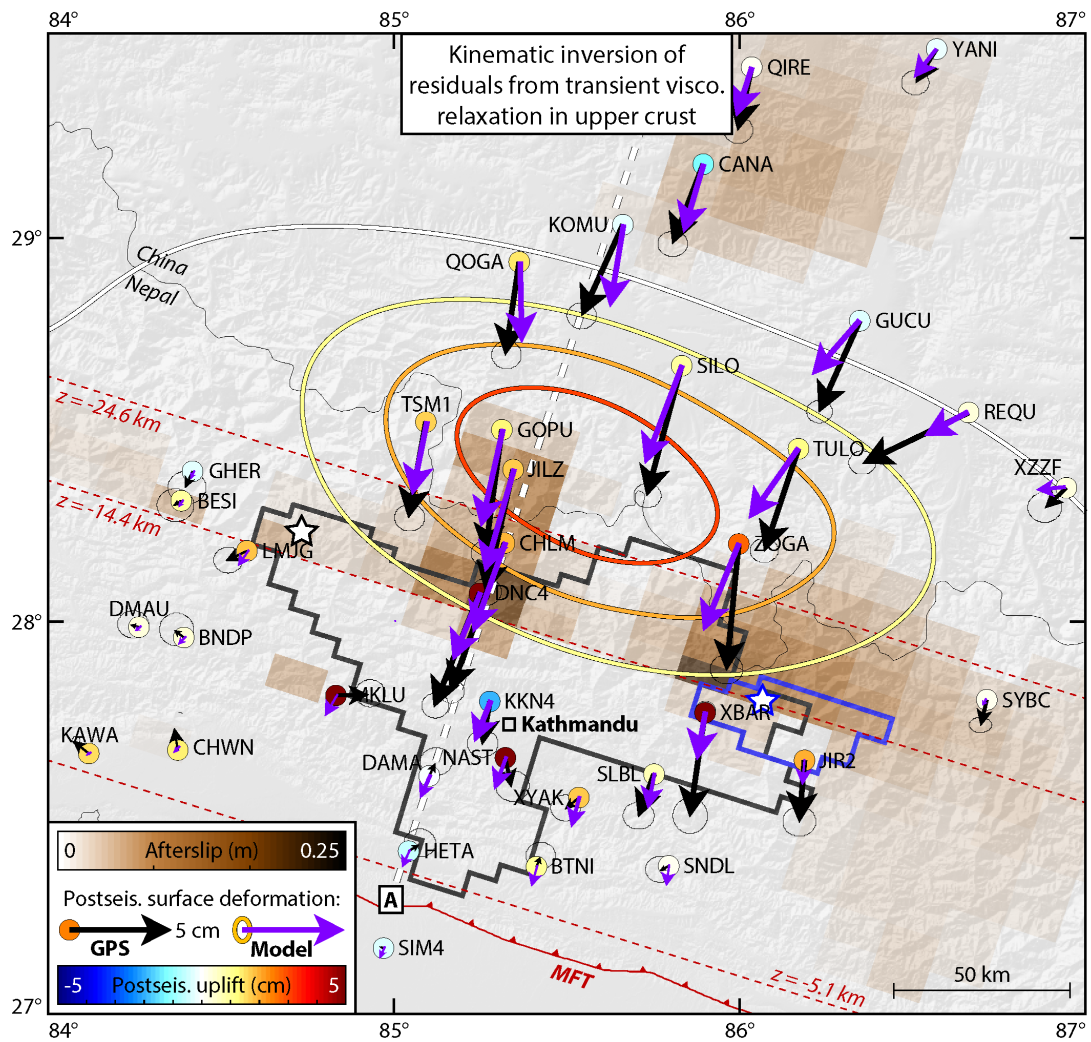

Figure 5.S10. Kinematic inversion (for slip on the MHT) of the residuals from subtracting the model of transient viscoelastic relaxation in the upper crust (Figure 5.9) from the cumulative 1.12-year surface displacements in the data (the difference between the black and purple arrows and between the filled circles and contours).

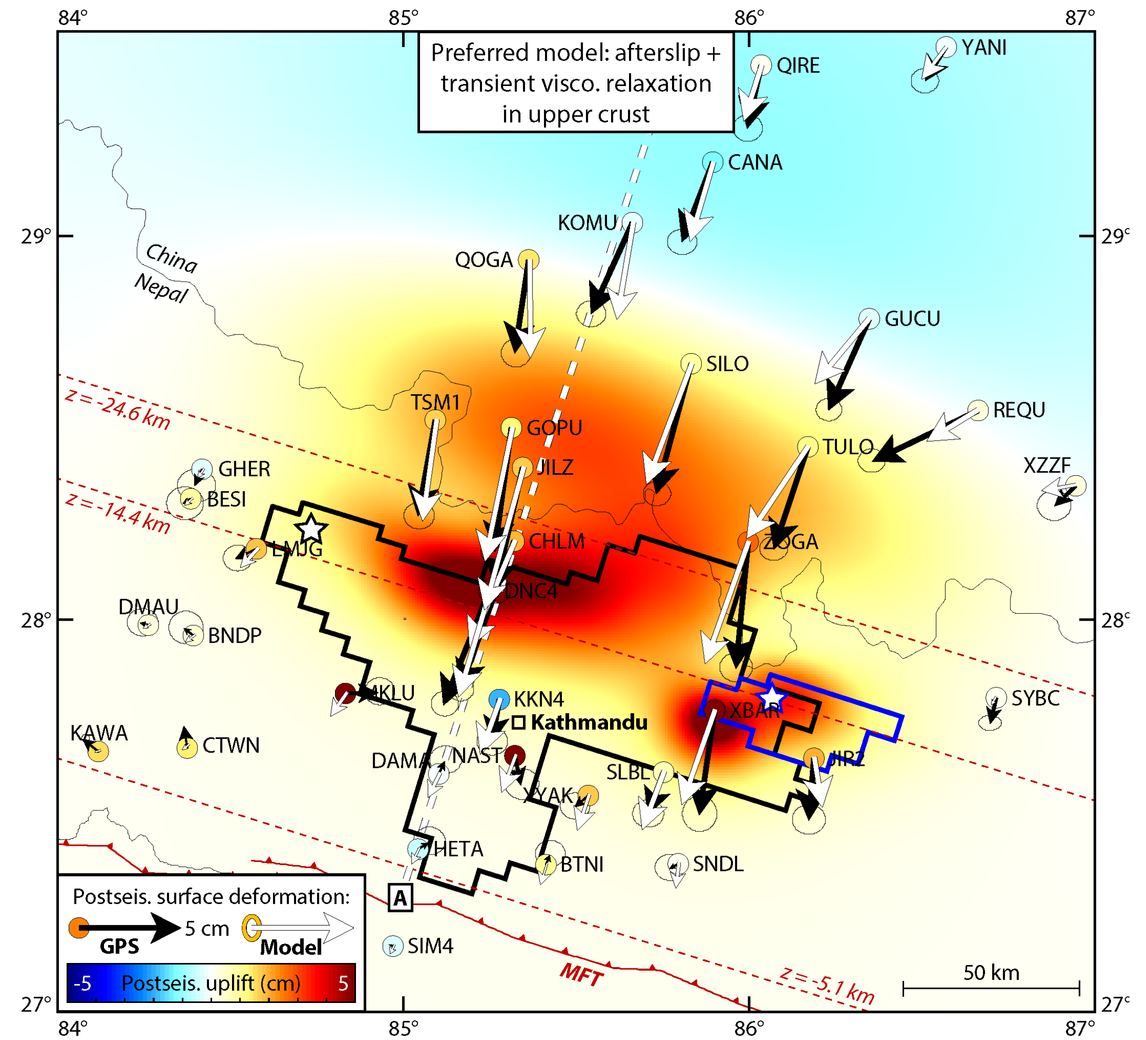

Figure 5.S11. Comparison of cumulative 1.12-year horizontal and vertical surface displacements predicted by the preferred model (white arrows and color shading) with those inferred in GPS (black arrows and filled circles).

BIBLIOGRAPHY

Ader, T., J. P. Avouac, J. Liu-Zeng, H. Lyon-Caen, L. Bollinger, J. Galetzka, J. Genrich, M. Thomas, K. Chanard and S. N. Sapkota (2012). "Convergence rate across the Nepal Himalaya and interseismic coupling on the Main Himalayan Thrust: Implications for seismic hazard." Journal of Geophysical Research: Solid Earth 117(B4).

Aki, K. (1965). "17. Maximum likelihood estimate of b in the formula logN= a-bM and its confidence limits." Bulletin of the Earthquake Research Institute 43: 237-239.

Argus, D., P. Agram, C. Rollins, J. Avouac and S. Barbot (2015). Interseismic Strain Accumulation in Metropolitan Los Angeles Distinguished from Oil and Water management using InSAR and GPS. AGU Fall Meeting Abstracts.

Argus, D. F., M. B. Heflin, A. Donnellan, F. H. Webb, D. Dong, K. J. Hurst, D. C. Jefferson, G. A. Lyzenga, M. M. Watkins and J. F. Zumberge (1999). "Shortening and thickening of metropolitan Los Angeles measured and inferred by using geodesy." Geology 27(8): 703-706.

Argus, D. F., M. B. Heflin, G. Peltzer, F. Crampé and F. H. Webb (2005). "Interseismic strain accumulation and anthropogenic motion in metropolitan Los Angeles." Journal of Geophysical Research: Solid Earth 110(B4).

Arnadottir, T., P. Segall and M. Matthews (1992). "Resolving the discrepancy between geodetic and seismic fault models for the 1989 Loma Prieta, California, earthquake." Bulletin of the Seismological Society of America 82: 2248-2248.

Aster, R., B. Borchers and C. Thurber (2012). "Parameter Estimation and Inverse Problems." Elsevier Academic.

Avouac, J.-P. (2003). "Mountain building, erosion, and the seismic cycle in the Nepal Himalaya." Advances In Geophysics 46: 1-80.

Avouac, J.-P. (2008). "Dynamic processes in extensional and compressional settings-mountain building: from earthquakes to geological deformation." Treatise on Geophysics 6: 377-439.

Avouac, J.-P. (2015). "From geodetic imaging of seismic and aseismic fault slip to dynamic modeling of the seismic cycle." Annual Review of Earth and Planetary Sciences 43: 233-271.

Avouac, J.-P., L. Meng, S. Wei, T. Wang and J.-P. Ampuero (2015). "Lower edge of locked Main Himalayan Thrust unzipped by the 2015 Gorkha earthquake." Nature Geoscience 8(9): 708-711.

Barbot, S., P. Agram and M. De Michele (2013). "Change of apparent segmentation of the San Andreas fault around Parkfield from space geodetic observations across multiple periods." Journal of Geophysical Research: Solid Earth 118(12): 6311-6327.

Barbot, S. and Y. Fialko (2010). "A unified continuum representation of post-seismic relaxation mechanisms: semi-analytic models of afterslip, poroelastic rebound and viscoelastic flow." Geophysical Journal International 182(3): 1124-1140.

Barbot, S. and Y. Fialko (2010). "Fourier-domain Green's function for an elastic semi-infinite solid under gravity, with applications to earthquake and volcano deformation." Geophysical Journal International 182(2): 568-582.

Barbot, S., Y. Fialko and Y. Bock (2009). "Postseismic deformation due to the Mw 6.0 2004 Parkfield earthquake: Stress-driven creep on a fault with spatially variable rate-and-state friction parameters." Journal of Geophysical Research: Solid Earth 114(B7).

Barbot, S., N. Lapusta and J.-P. Avouac (2012). "Under the hood of the earthquake machine: Toward predictive modeling of the seismic cycle." Science 336(6082): 707-710.

Båth, M. (1965). "Lateral inhomogeneities of the upper mantle." Tectonophysics 2(6): 483-514.

Bawden, G. W., W. Thatcher, R. S. Stein, K. W. Hudnut and G. Peltzer (2001). "Tectonic contraction across Los Angeles after removal of groundwater pumping effects." Nature 412(6849): 812-815.

Ben-Zion, Y. and A. Allam (2013). "Seasonal thermoelastic strain and postseismic effects in Parkfield borehole dilatometers." Earth and Planetary Science Letters 379: 120-126.

Ben-Zion, Y. and V. Lyakhovsky (2006). "Analysis of aftershocks in a lithospheric model with seismogenic zone governed by damage rheology." Geophysical Journal International 165(1): 197-210.

Benedetti, L., I. Manighetti, Y. Gaudemer, R. Finkel, J. Malavieille, K. Pou, M. Arnold, G. Aumaître, D. Bourlès and K. Keddadouche (2013). "Earthquake synchrony and clustering on Fucino faults (Central Italy) as revealed from in situ 36Cl exposure dating." Journal of Geophysical Research: Solid Earth 118(9): 4948-4974.

Bergen, K. J., J. H. Shaw, L. A. Leon, J. F. Dolan, T. L. Pratt, D. J. Ponti, E. Morrow, W. Barrera, E. J. Rhodes and M. K. Murari (2017). "Accelerating slip rates on the Puente Hills blind thrust fault system beneath metropolitan Los Angeles, California, USA." Geology 45(3): 227-230.

Bernard, P., P. Briole, B. Meyer, H. Lyon-Caen, J.-M. Gomez, C. Tiberi, C. Berge, R. Cattin, D. Hatzfeld and C. Lachet (1997). "The M s= 6.2, June 15, 1995 Aigion earthquake (Greece): evidence for low angle normal faulting in the Corinth rift." Journal of Seismology 1(2): 131-150.

Bettinelli, P., J.-P. Avouac, M. Flouzat, L. Bollinger, G. Ramillien, S. Rajaure and S. Sapkota (2008). "Seasonal variations of seismicity and geodetic strain in the Himalaya induced by surface hydrology." Earth and Planetary Science Letters 266(3): 332-344.

Bills, B. G., K. D. Adams and S. G. Wesnousky (2007). "Viscosity structure of the crust and upper mantle in western Nevada from isostatic rebound patterns of the late Pleistocene Lake Lahontan high shoreline." Journal of Geophysical Research: Solid Earth 112(B6).

Bird, P., D.D. Jackson, Y. Y. Kagan, C. Kreemer and R. S. Stein (2015). "GEAR1: A Global Earthquake Activity Rate Model Constructed from Geodetic Strain Rates and Smoothed Seismicity." Bulletin of the Seismological Society of America 105(5): 2538-2554.

Blanpied, M., D. Lockner and J. Byerlee (1991). "Fault stability inferred from granite sliding experiments at hydrothermal conditions." Geophysical Research Letters 18(4): 609-612.

Blythe, A., D. Burbank, K. Farley and E. Fielding (2000). "Structural and topographic evolution of the central Transverse Ranges, California, from apatite fissiontrack,(U–Th)/He and digital elevation model analyses." Basin Research 12(2): 97-114.

Bock, Y., and J. Haase, SOPAC Seismogeodetic Network, Scripps Orbit and Permanent Array Center. Other/Seismic Network. doi:10.7914/SN/SO, 2016.

Bowden, D. C. and V. C. Tsai (2017). "Earthquake ground motion amplification for surface waves." Geophysical Research Letters 44(1): 121-127.

Broderick, K. G., (2006), Giant blind thrust faults beneath the Palos Verdes Hills and western Los Angeles Basin, California: Mapping with seismic reflection and deep drilling data, M.S. Thesis, Dept. of Earth Sci., Univ. of California, Santa Barbara, Santa Barbara, CA.

Bruhat, L., S. Barbot and J. P. Avouac (2011). "Evidence for postseismic deformation of the lower crust following the 2004 Mw6. 0 Parkfield earthquake." Journal of Geophysical Research: Solid Earth 116(B8).

Brune, J. N. (1968). "Seismic moment, seismicity, and rate of slip along major fault zones." Journal of Geophysical Research 73(2): 777-784.

Bürgmann, R. and G. Dresen (2008). "Rheology of the lower crust and upper mantle: Evidence from rock mechanics, geodesy, and field observations." Annual Review of Earth and Planetary Sciences 36.

Bürgmann, R., M. G. Kogan, G. M. Steblov, G. Hilley, V. E. Levin and E. Apel (2005). "Interseismic coupling and asperity distribution along the Kamchatka subduction zone." Journal of Geophysical Research: Solid Earth 110(B7).

Burov, E. (2009). "Plate rheology and mechanics." Treatise On Geophysics 6: 99-151.

Carter, N. L. and M. C. Tsenn (1987). "Flow properties of continental lithosphere." Tectonophysics 136(1-2): 27-63.

Cattin, R. and J. Avouac (2000). "Modeling mountain building and the seismic cycle in the Himalaya of Nepal." Journal of Geophysical Research: Solid Earth 105(B6): 13389-13407.

Cattin, R., P. Briole, H. Lyon-Caen, P. Bernard and P. Pinettes (1999). "Effects of superficial layers on coseismic displacements for a dip-slip fault and geophysical implications." Geophysical Journal International 137(1): 149-158.

Chlieh, M., J.-P. Avouac, K. Sieh, D. H. Natawidjaja and J. Galetzka (2008). "Heterogeneous coupling of the Sumatran megathrust constrained by geodetic and paleogeodetic measurements." Journal of Geophysical Research: Solid Earth 113(B5).

Chlieh, M., J. De Chabalier, J. Ruegg, R. Armijo, R. Dmowska, J. Campos and K. Feigl (2004). "Crustal deformation and fault slip during the seismic cycle in the North Chile subduction zone, from GPS and InSAR observations." Geophysical Journal International 158(2): 695-711.

Chlieh, M., H. Perfettini, H. Tavera, J. P. Avouac, D. Remy, J. M. Nocquet, F. Rolandone, F. Bondoux, G. Gabalda and S. Bonvalot (2011). "Interseismic coupling and seismic potential along the Central Andes subduction zone." Journal of Geophysical Research: Solid Earth 116(B12).

Cooke, M. L. and S. T. Marshall (2006). "Fault slip rates from three-dimensional models of the Los Angeles metropolitan area, California." Geophysical research letters 33(21).

Copley, A., J. P. Avouac and J. Y. Royer (2010). "India-Asia collision and the Cenozoic slowdown of the Indian plate: Implications for the forces driving plate motions." Journal of Geophysical Research: Solid Earth 115(B3).

Crook Jr, R., C. R. Allen, B. Kamb, C. M. Payne and R. J. Proctor (1987). "Quaternary geology and seismic hazard of the Sierra Madre and associated faults, western San Gabriel Mountains."

Crowell, B. W., Y. Bock, D. T. Sandwell and Y. Fialko (2013). "Geodetic investigation into the deformation of the Salton Trough." Journal of Geophysical Research: Solid Earth 118(9): 5030-5039.

Daout, S., S. Barbot, G. Peltzer, M. P. Doin, Z. Liu and R. Jolivet (2016). "Constraining the kinematics of metropolitan Los Angeles faults with a slip-partitioning model." Geophysical Research Letters.

Davis, T. L., and J. Namson (1994). "A balanced cross section of the 1994 Northridge earthquake." Nature 372: 167.

Davis, T. L., J. Namson and R. F. Yerkes (1989). "A cross section of the Los Angeles area: Seismically active fold and thrust belt, the 1987 Whittier Narrows earthquake, and earthquake hazard." Journal of Geophysical Research: Solid Earth 94(B7): 9644-9664.

DeMets, C., R. G. Gordon and D. F. Argus (2010). "Geologically current plate motions." Geophysical Journal International 181(1): 1-80.

Deng, J., M. Gurnis, H. Kanamori and E. Hauksson (1998). "Viscoelastic flow in the lower crust after the 1992 Landers, California, earthquake." Science 282(5394): 1689-1692.

Dieterich, J. (1994). "A constitutive law for rate of earthquake production and its application to earthquake clustering." Journal of Geophysical Research: Solid Earth 99(B2): 2601-2618.

Doin, M. P., C. Twardzik, G. Ducret, C. Lasserre, S. Guillaso and S. Jianbao (2015). "InSAR measurement of the deformation around Siling Co Lake: Inferences on the lower crust viscosity in central Tibet." Journal of Geophysical Research: Solid Earth 120(7): 5290-5310.

Dolan, J. F., D. D. Bowman and C. G. Sammis (2007). "Long-range and long-term fault interactions in Southern California." Geology 35(9): 855-858.

Dolan, J. F., S. A. Christofferson and J. H. Shaw (2003). "Recognition of paleoearthquakes on the Puente Hills blind thrust fault, California." Science 300(5616): 115-118.

Dolan, J. F., K. Sieh and T. K. Rockwell (2000). "Late Quaternary activity and seismic potential of the Santa Monica fault system, Los Angeles, California." Geological Society of America Bulletin 112(10): 1559-1581.

Dolan, J. F., K. Sieh, T. K. Rockwell, R. S. Yeats, J. Shaw, J. Suppe, G. J. Huftile and E. M. Gath (1995). "Prospects for larger or more frequent earthquakes in the Los Angeles metropolitan region." Science 267(5195), 199-205.

Dong, D., P. Fang, Y. Bock, M. Cheng and S. i. Miyazaki (2002). "Anatomy of apparent seasonal variations from GPS-derived site position time series." Journal of Geophysical Research: Solid Earth 107(B4).

Donnellan, A., A. Blythe, L. Kellogg and M. Glasscoe (2001). Strain Partitioning Across Metropolitan Los Angeles. ACES Cooperation for Earthquake Simulation, 2nd ACES Workshop Proceedings.

Donnellan, A., B. H. Hager, R. W. King and T. A. Herring (1993). "Geodetic measurement of deformation in the Ventura Basin region, southern California." Journal of Geophysical Research: Solid Earth 98(B12): 21727-21739.

Donnellan, A. and G. A. Lyzenga (1998). "GPS observations of fault afterslip and upper crustal deformation following the Northridge earthquake." Journal of Geophysical Research: Solid Earth 103(B9): 21285-21297.

Duebendorfer, E. M., J. Vermilye, P. A. Geiser and T. L. Davis (1998). "Evidence for aseismic deformation in the western Transverse Ranges, southern California: Implications for seismic risk assessment." Geology 26(3): 271-274.

Elliott, J., R. Jolivet, P. González, J.-P. Avouac, J. Hollingsworth, M. Searle and V. Stevens (2016). "Himalayan megathrust geometry and relation to topography revealed by the Gorkha earthquake." Nature Geoscience 9(2): 174-180.

Ellsworth, W. L. (1990). "The San Andreas Fault System, California." US Geol. Surv. Prof. Pap 1515: 153-185.

England, P., P. Le Fort, P. Molnar and A. Pêcher (1992). "Heat sources for Tertiary metamorphism and anatexis in the Annapurna-Manaslu Region central Nepal." Journal of Geophysical Research: Solid Earth 97(B2): 2107-2128.

England, P. C., R. T. Walker, B. Fu and M. A. Floyd (2013). "A bound on the viscosity of the Tibetan crust from the horizontality of palaeolake shorelines." Earth and Planetary Science Letters 375: 44-56.

Ester, M., H.-P. Kriegel, J. Sander and X. Xu (1996). A density-based algorithm for discovering clusters in large spatial databases with noise. Kdd.

Fay, N., R. Bennett, J. Spinler and E. Humphreys (2008). "Small-scale upper mantle convection and crustal dynamics in Southern California." Geochemistry, Geophysics, Geosystems 9(8).

Fay, N. P. and E. D. Humphreys (2005). "Fault slip rates, effects of elastic heterogeneity on geodetic data, and the strength of the lower crust in the Salton Trough region, southern California." Journal of Geophysical Research: Solid Earth 110(B9).

Feigl, K. L., D. C. Agnew, Y. Bock, D. Dong, A. Donnellan, B. H. Hager, T. A. Herring, D. D. Jackson, T. H. Jordan and R. W. King (1993). "Space geodetic measurement of crustal deformation in central and southern California, 1984–1992." Journal of Geophysical Research: Solid Earth 98(B12): 21677-21712.

Felzer, K. R. and E. E. Brodsky (2006). "Decay of aftershock density with distance indicates triggering by dynamic stress." Nature 441(7094): 735-738.

Fialko, Y. (2004). "Evidence of fluid-filled upper crust from observations of postseismic deformation due to the 1992 Mw7.3 Landers earthquake." Journal of Geophysical Research: Solid Earth 109(B8).

Field, E. H., R. J. Arrowsmith, G. P. Biasi, P. Bird, T. E. Dawson, K. R. Felzer, D. D. Jackson, K. M. Johnson, T. H. Jordan and C. Madden (2014). "Uniform California earthquake rupture forecast, version 3 (UCERF3)—The time-independent model." Bulletin of the Seismological Society of America 104(3): 1122-1180.

Field, E. H., H. A. Seligson, N. Gupta, V. Gupta, T. H. Jordan and K. W. Campbell (2005). "Loss estimates for a Puente Hills blind-thrust earthquake in Los Angeles, California." Earthquake Spectra 21(2): 329-338.

Fletcher, J. M., O. J. Teran, T. K. Rockwell, M. E. Oskin, K. W. Hudnut, K. J. Mueller, R. M. Spelz, S. O. Akciz, E. Masana and G. Faneros (2014). "Assembly of a large earthquake from a complex fault system: Surface rupture kinematics of the 4 April 2010 El Mayor–Cucapah (Mexico) Mw 7.2 earthquake." Geosphere 10(4): 797-827.

Freed, A. M. (2007). "Afterslip (and only afterslip) following the 2004 Parkfield, California, earthquake." Geophysical Research Letters 34(6).

Freed, A. M. and R. Bürgmann (2004). "Evidence of power-law flow in the Mojave desert mantle." Nature 430(6999): 548-551.

Freed, A. M., R. Bürgmann, E. Calais and J. Freymueller (2006). "Stress-dependent power-law flow in the upper mantle following the 2002 Denali, Alaska, earthquake." Earth and Planetary Science Letters 252(3): 481-489.

Freed, A. M., R. Bürgmann, E. Calais, J. Freymueller and S. Hreinsdóttir (2006). "Implications of deformation following the 2002 Denali, Alaska, earthquake for postseismic relaxation processes and lithospheric rheology." Journal of Geophysical Research: Solid Earth 111(B1).

Freed, A. M., R. Bürgmann and T. Herring (2007). "Far-reaching transient motions after Mojave earthquakes require broad mantle flow beneath a strong crust." Geophysical Research Letters 34(19).

Freed, A. M., T. Herring and R. Bürgmann (2010). "Steady-state laboratory flow laws alone fail to explain postseismic observations." Earth and Planetary Science Letters 300(1): 1-10.

Freed, A. M., G. Hirth and M. D. Behn (2012). "Using short-term postseismic displacements to infer the ambient deformation conditions of the upper mantle." Journal of Geophysical Research: Solid Earth 117(B1).

Fu, Y. and J. T. Freymueller (2012). "Seasonal and long-term vertical deformation in the Nepal Himalaya constrained by GPS and GRACE measurements." Journal of Geophysical Research: Solid Earth 117(B3).

Fuis, G., T. Ryberg, N. Godfrey, D. Okaya and J. Murphy (2001). "Crustal structure and tectonics from the Los Angeles basin to the Mojave Desert, southern California." Geology 29(1): 15-18.

Fuis, G. S., D. S. Scheirer, V. E. Langenheim and M. D. Kohler (2012). "A new perspective on the geometry of the San Andreas fault in southern California and its relationship to lithospheric structure." Bulletin of the Seismological Society of America 102(1): 236-251.

Galetzka, J., D. Melgar, J. F. Genrich, J. Geng, S. Owen, E. O. Lindsey, X. Xu, Y. Bock, J.-P. Avouac and L. B. Adhikari (2015). "Slip pulse and resonance of the Kathmandu basin during the 2015 Gorkha earthquake, Nepal." Science 349(6252): 1091-1095.

Gath, E., T. Gonzalez and T. Rockwell (1992). Slip rate of the Whittier fault based on 3-D trenching at Brea, southern California. Geological Society of America Abstracts with Programs.

Glasscoe, M. T., A. Donnellan, L. H. Kellogg and G. A. Lyzenga (2004). "Evidence of strain partitioning between the Sierra Madre fault and the Los Angeles Basin, southern California from numerical models." pure and applied geophysics 161(11-12): 2343-2357.

Godard, V., R. Cattin and J. Lavé (2004). "Numerical modeling of mountain building: Interplay between erosion law and crustal rheology." Geophysical Research Letters 31(23).

Godfrey, N. J., G. S. Fuis, V. Langenheim, D. A. Okaya and T. M. Brocher (2002). "Lower crustal deformation beneath the central Transverse Ranges, Southern California: results from the Los Angeles region seismic experiment." Journal of Geophysical Research: Solid Earth 107(B7).

Gonzalez‐Ortega, A., Y. Fialko, D. Sandwell, F. Alejandro Nava‐Pichardo, J. Fletcher, J. Gonzalez‐Garcia, B. Lipovsky, M. Floyd and G. Funning (2014). "El Mayor‐Cucapah (Mw 7.2) earthquake: Early near‐field postseismic deformation from InSAR and GPS observations." Journal of Geophysical Research: Solid Earth 119(2): 1482-1497.

Grant, L. B., L. J. Ballenger and E. E. Runnerstrom (2002). "Coastal uplift of the San Joaquin Hills, southern Los Angeles Basin, California, by a large earthquake since AD 1635." Bulletin of the Seismological Society of America 92(2): 590-599.

Griffith, W. and M. Cooke (2004). "Mechanical validation of the three-dimensional intersection geometry between the Puente Hills blind-thrust system and the Whittier fault, Los Angeles, California." Bulletin of the Seismological Society of America 94(2): 493-505.

Gualandi, A., J.-P. Avouac, J. Galetzka, J. F. Genrich, G. Blewitt, L. B. Adhikari, B. P. Koirala, R. Gupta, B. N. Upreti and B. Pratt-Sitaula (2016). "Pre-and post-seismic deformation related to the 2015, Mw7. 8 Gorkha earthquake, Nepal." Tectonophysics.

Gualandi, A., E. Serpelloni and M. Belardinelli (2016). "Blind source separation problem in GPS time series." Journal of Geodesy 90(4): 323-341.

Hadley, D. and H. Kanamori (1978). "Recent seismicity in the San Fernando region and tectonics in the west-central Transverse Ranges, California." Bulletin of the Seismological Society of America 68(5): 1449-1457.

Hager, B. H., G. A. Lyzenga, A. Donnellan and D. Dong (1999). "Reconciling rapid strain accumulation with deep seismogenic fault planes in the Ventura basin, California." Journal of Geophysical Research: Solid Earth 104(B11): 25207-25219.

Hamiel, Y., V. Lyakhovsky and A. Agnon (2004). "Coupled evolution of damage and porosity in poroelastic media: theory and applications to deformation of porous rocks." Geophysical Journal International 156(3): 701-713.

Harris, R. A. and P. Segall (1987). "Detection of a locked zone at depth on the Parkfield, California, segment of the San Andreas fault." Journal of Geophysical Research: Solid Earth 92(B8): 7945-7962.

Hauck, M., K. Nelson, L. Brown, W. Zhao and A. Ross (1998). "Crustal structure of the Himalayan orogen at~ 90 east longitude from Project INDEPTH deep reflection profiles." Tectonics 17(4): 481-500.

Hauksson, E. (1987). "Seismotectonics of the Newport-Inglewood fault zone in the Los Angeles basin, southern California." Bulletin of the Seismological Society of America 77(2): 539-561.

Hauksson, E. (1990). "Earthquakes, faulting, and stress in the Los Angeles basin." Journal of Geophysical Research: Solid Earth 95(B10): 15365-15394.

Hauksson, E. (1994). "The 1991 Sierra Madre earthquake sequence in southern California: Seismological and tectonic analysis." Bulletin of the Seismological Society of America 84(4): 1058-1074.

Hauksson, E., M. A. Meier, Z. E. Ross and L. M. Jones (2017). "Evolution of seismicity near the southernmost terminus of the San Andreas Fault: Implications of recent earthquake clusters for earthquake risk in southern California." Geophysical Research Letters 44(3): 1293-1301.

Hauksson, E., J. Stock, K. Hutton, W. Yang, J. A. Vidal-Villegas and H. Kanamori (2011). "The 2010 Mw 7.2 el mayor-Cucapah earthquake sequence, Baja California, Mexico and southernmost California, USA: active seismotectonics along the Mexican Pacific margin." Pure and Applied Geophysics 168(8-9): 1255-1277.

Hauksson, E., W. Yang and P. M. Shearer (2012). "Waveform relocated earthquake catalog for southern California (1981 to June 2011)." Bulletin of the Seismological Society of America 102(5): 2239-2244.

Hearn, E., F. Pollitz, W. Thatcher and C. Onishi (2013). "How do “ghost transients” from past earthquakes affect GPS slip rate estimates on southern California faults?" Geochemistry, Geophysics, Geosystems 14(4): 828-838.

Hearn, E. H. and R. Bürgmann (2005). "The effect of elastic layering on inversions of GPS data for coseismic slip and resulting stress changes: Strike-slip earthquakes." Bulletin of the Seismological Society of America 95(5): 1637-1653.

Hearn, E. H., R. Bürgmann and R. E. Reilinger (2002). "Dynamics of Izmit earthquake postseismic deformation and loading of the Düzce earthquake hypocenter." Bulletin of the Seismological Society of America 92(1): 172-193.

Heaton, T. H. (1982). "The 1971 San Fernando earthquake: A double event?" Bulletin of the Seismological Society of America 72(6A): 2037-2062.

Henry, P., X. Le Pichon and B. Goffé (1997). "Kinematic, thermal and petrological model of the Himalayas: constraints related to metamorphism within the underthrust Indian crust and topographic elevation." Tectonophysics 273(1-2): 31-56.

Herman, F., P. Copeland, J. P. Avouac, L. Bollinger, G. Mahéo, P. Le Fort, S. Rai, D. Foster, A. Pêcher and K. Stüwe (2010). "Exhumation, crustal deformation, and thermal structure of the Nepal Himalaya derived from the inversion of thermochronological and thermobarometric data and modeling of the topography." Journal of Geophysical Research: Solid Earth 115(B6).

Hetényi, G., R. Cattin, J. Vergne and J. L. Nábělek (2006). "The effective elastic thickness of the India Plate from receiver function imaging, gravity anomalies and thermomechanical modelling." Geophysical Journal International 167(3): 1106-1118.

Hill, D. P. (1977). "A model for earthquake swarms." Journal of Geophysical Research 82(8): 1347-1352.

Hill, D. P., Pollitz, F., & Newhall, C. (2002). Earthquake-volcano interactions. *Physics Today*, *55*(11), 41-47.

Hilley, G., R. Bürgmann, P. Z. Zhang and P. Molnar (2005). "Bayesian inference of plastosphere viscosities near the Kunlun Fault, northern Tibet." Geophysical Research Letters 32(1).

Hirth, G. and D. Kohlstedt (2003). "Rheology of the upper mantle and the mantle wedge: A view from the experimentalists." Inside the subduction Factory: 83-105.

Holtkamp, S. and M. R. Brudzinski (2014). "Megathrust earthquake swarms indicate frictional changes which delimit large earthquake ruptures." Earth and Planetary Science Letters 390: 234-243.

Hsu, Y.-J., S.-B. Yu, J. P. Loveless, T. Bacolcol, R. Solidum, A. Luis Jr., A. Pelicano, and J. Woessner (2016). "Interseismic deformation and moment deficit along the Manila subduction zone and the Philippine Fault system." Journal of Geophysical Research: Solid Earth 121(10): 7639-7665.

Hu, J., X. Ding, Z. Li, L. Zhang, J. Zhu, Q. Sun and G. Gao (2016). "Vertical and horizontal displacements of Los Angeles from InSAR and GPS time series analysis: Resolving tectonic and anthropogenic motions." Journal of Geodynamics 99: 27-38.

Huang, H., W. Xu, L. Meng, R. Bürgmann and J. C. Baez (2017). "Early aftershocks and afterslip surrounding the 2015 Mw 8.4 Illapel rupture." Earth and Planetary Science Letters 457: 282-291.

Huang, M.-H., R. Bürgmann and A. M. Freed (2014). "Probing the lithospheric rheology across the eastern margin of the Tibetan Plateau." Earth and Planetary Science Letters 396: 88-96.

Huang, M. H., E. J. Fielding, H. Dickinson, J. Sun, J. A. Gonzalez-Ortega, A. M. Freed and R. Bürgmann (2017). "Fault geometry inversion and slip distribution of the 2010 Mw 7.2 El Mayor-Cucapah earthquake from geodetic data." Journal of Geophysical Research: Solid Earth 122(1): 607-621.

Hubbard, J., R. Almeida, A. Foster, S. N. Sapkota, P. Bürgi and P. Tapponnier (2016). "Structural segmentation controlled the 2015 Mw 7.8 Gorkha earthquake rupture in Nepal." Geology 44(8): 639-642.

Humphreys, E. D. and B. H. Hager (1990). "A kinematic model for the late Cenozoic development of southern California crust and upper mantle." Journal of Geophysical Research: Solid Earth 95(B12): 19747-19762.

Hutton, K., J. Woessner and E. Hauksson (2010). "Earthquake monitoring in southern California for seventy-seven years (1932–2008)." Bulletin of the Seismological Society of America 100(2): 423-446.

Inbal, A., J. P. Ampuero and R. W. Clayton (2016). "Localized seismic deformation in the upper mantle revealed by dense seismic arrays." Science 354(6308): 88-92.

Isaac, S. (1987). Geology and structure of the Yuha Desert between Ocotillo, California, USA and Laguna Salada, Baja California, Mexico, San Diego State University, Department of Geological Sciences.

Jiménez-Munt, I., M. Fernàndez, J. Vergés and J. P. Platt (2008). "Lithosphere structure underneath the Tibetan Plateau inferred from elevation, gravity and geoid anomalies." Earth and Planetary Science Letters 267(1): 276-289.

Johnson, K. M., R. Bürgmann and J. T. Freymueller (2009). "Coupled afterslip and viscoelastic flow following the 2002 Denali Fault, Alaska earthquake." Geophysical Journal International 176(3): 670-682.

Jolivet, R., M. Simons, P. Agram, Z. Duputel and Z. K. Shen (2015). "Aseismic slip and seismogenic coupling along the central San Andreas Fault." Geophysical Research Letters 42(2): 297-306.

Jonsson, S., P. Segall, R. Pedersen and G. Björnsson (2003). "Post-earthquake ground movements correlated to pore-pressure transients." Nature 424(6945): 179-183.

Jouanne, F., A. Awan, A. Madji, A. Pêcher, M. Latif, A. Kausar, J.-L. Mugnier, I. Khan and N. Khan (2011). "Postseismic deformation in Pakistan after the 8 October 2005 earthquake: evidence of afterslip along a flat north of the Balakot-Bagh thrust." Journal of Geophysical Research: Solid Earth 116(B7).

Kanda, R. V. and M. Simons (2010). "An elastic plate model for interseismic deformation in subduction zones." Journal of Geophysical Research: Solid Earth 115(B3).

Kaneko, Y., J.-P. Avouac and N. Lapusta (2010). "Towards inferring earthquake patterns from geodetic observations of interseismic coupling." Nature Geoscience 3(5): 363-369.
Karato, S.-i. (2012). Deformation of earth materials: an introduction to the rheology of solid earth, Cambridge University Press.

Kato, A., J. i. Fukuda, S. Nakagawa and K. Obara (2016). "Foreshock migration preceding the 2016 Mw 7.0 Kumamoto earthquake, Japan." Geophysical Research Letters 43(17): 8945-8953.

Kaufmann, G. and F. Amelung (2000). "Reservoir-induced deformation and continental rheology in vicinity of Lake Mead, Nevada." Journal of Geophysical Research: Solid Earth 105(B7): 16341-16358.

King, G. C., R. S. Stein and J. Lin (1994). "Static stress changes and the triggering of earthquakes." Bulletin of the Seismological Society of America 84(3): 935-953.

Kirby, S. H. (1983). "Rheology of the lithosphere." Reviews of Geophysics 21(6): 1458-1487.

Kohler, M. D. (1999). "Lithospheric deformation beneath the San Gabriel Mountains in the southern California Transverse Ranges." Journal of Geophysical Research: Solid Earth 104(B7): 15025-15041.

Kositsky, A. and J. P. Avouac (2010). "Inverting geodetic time series with a principal component analysis-based inversion method." Journal of Geophysical Research: Solid Earth 115(B3).

Kostrov, V. (1974). "Seismic moment and energy of earthquakes, and seismic flow of rock." Physics of the Solid Earth 1: 13-21.

Kreemer, C., G. Blewitt and E. C. Klein (2014). "A geodetic plate motion and Global Strain Rate Model. Geochemistry, Geophysics, Geosystems 15(10): 3849-3889.

Kroll, K. A., E. S. Cochran, K. B. Richards-Dinger and D. F. Sumy (2013). "Aftershocks of the 2010 Mw 7.2 El Mayor-Cucapah earthquake reveal complex faulting in the Yuha Desert, California." Journal of Geophysical Research: Solid Earth 118(12): 6146-6164.

Kyriakopoulos, C., T. Masterlark, S. Stramondo, M. Chini and C. Bignami (2013). "Coseismic slip distribution for the Mw 9 2011 Tohoku-Oki earthquake derived from 3-D FE modeling." Journal of Geophysical Research: Solid Earth 118(7): 3837-3847.

Lachenbruch, A. H., J. Sass and S. Galanis (1985). "Heat flow in southernmost California and the origin of the Salton Trough." Journal of Geophysical Research: Solid Earth 90(B8): 6709-6736.

Landry, W. and S. Barbot (2016). "Gamra: Simple meshing for complex earthquakes." Computers & Geosciences 90: 49-63.

Lavé, J. and J.-P. Avouac (2000). "Active folding of fluvial terraces across the Siwaliks Hills, Himalayas of central Nepal." Journal of Geophysical Research: Solid Earth 105(B3): 5735-5770.

Leeper, R., B. Rhodes, M. Kirby, K. Scharer, J. Carlin, E. Hemphill-Haley, S. Avnaim-Katav, G. MacDonald, S. Starratt and A. Aranda (2017). "Evidence for coseismic subsidence events in a southern California coastal saltmarsh." Scientific Reports 7.

Lekic, V., S. W. French and K. M. Fischer (2011). "Lithospheric thinning beneath rifted regions of Southern California." Science 334(6057): 783-787.

Leon, L. A., S. A. Christofferson, J. F. Dolan, J. H. Shaw and T. L. Pratt (2007). "Earthquake-by-earthquake fold growth above the Puente Hills blind thrust fault, Los Angeles, California: Implications for fold kinematics and seismic hazard." Journal of Geophysical Research: Solid Earth 112(B3).

Leon, L. A., J. F. Dolan, J. H. Shaw and T. L. Pratt (2009). "Evidence for large Holocene earthquakes on the Compton thrust fault, Los Angeles, California." Journal of Geophysical Research: Solid Earth 114(B12).

Li, Y. G. (1996). "Shear wave splitting observations and implications on stress regimes in the Los Angeles basin, California." Journal of Geophysical Research: Solid Earth 101(B6): 13947-13961.

Lin, J. and R. S. Stein (2004). "Stress triggering in thrust and subduction earthquakes and stress interaction between the southern San Andreas and nearby thrust and strike-slip faults." Journal of Geophysical Research: Solid Earth 109(B2).

Lindsey, E. O., R. Natsuaki, X. Xu, M. Shimada, M. Hashimoto, D. Melgar and D. T. Sandwell (2015). "Line-of-sight displacement from ALOS-2 interferometry: Mw 7.8 Gorkha Earthquake and Mw 7.3 aftershock." Geophysical Research Letters 42(16): 6655-6661.

Lindsey, E. O., R. V. Almeida, K. E. Bradley, J. Hubbard, S. Sathiakumar, R. Mallick, S. Barbot and E. Hill (2017). “Stress shadow prohibits low interseismic coupling on shallow megathrusts, even where they are frictionally unlocked.” AGU Fall Meeting Abstracts.

Lisowski, M., J. Savage and W. Prescott (1991). "The velocity field along the San Andreas fault in central and southern California." Journal of Geophysical Research: Solid Earth 96(B5): 8369-8389.

Liu, Z., S. Owen, D. Dong, P. Lundgren, F. Webb, E. Hetland and M. Simons (2010). "Estimation of interplate coupling in the Nankai trough, Japan using GPS data from 1996 to 2006." Geophysical Journal International 181(3): 1313-1328.

Lutter, W. J., G. S. Fuis, C. H. Thurber and J. Murphy (1999). "Tomographic images of the upper crust from the Los Angeles basin to the Mojave Desert, California: Results from the Los Angeles Region Seismic Experiment." Journal of Geophysical Research: Solid Earth 104(B11): 25543-25565.

Luttrell, K., D. Sandwell, B. Smith‐Konter, B. Bills and Y. Bock (2007). "Modulation of the earthquake cycle at the southern San Andreas fault by lake loading." Journal of Geophysical Research: Solid Earth 112(B8).

Malservisi, R., C. Plattner, M. Hackl and F. Suarez Vidal (2012). Implication of the Central Gulf of California (MX) Earthquake cycle in understanding continental plate boundary rheology. AGU Fall Meeting Abstracts.

Marone, C. (1998). "Laboratory-derived friction laws and their application to seismic faulting." Annual Review of Earth and Planetary Sciences 26(1): 643-696.

Marone, C. J., C. Scholtz and R. Bilham (1991). "On the mechanics of earthquake afterslip." Journal of Geophysical Research: Solid Earth 96(B5): 8441-8452.

Marshall, S. T., M. L. Cooke and S. E. Owen (2009). "Interseismic deformation associated with three‐dimensional faults in the greater Los Angeles region, California." Journal of Geophysical Research: Solid Earth 114(B12).

Marshall, S. T., G. J. Funning and S. E. Owen (2013). "Fault slip rates and interseismic deformation in the western Transverse Ranges, California." Journal of Geophysical Research: Solid Earth 118(8): 4511-4534.

Marshall, S. T. and A. C. Morris (2012). "Mechanics, slip behavior, and seismic potential of corrugated dip‐slip faults." Journal of Geophysical Research: Solid Earth 117(B3).

Masterlark, T. (2003). "Finite element model predictions of static deformation from dislocation sources in a subduction zone: sensitivities to homogeneous, isotropic, Poisson-solid, and half-space assumptions." Journal of Geophysical Research: Solid Earth 108(B11).

Masuti, S., S. D. Barbot, S.-i. Karato, L. Feng and P. Banerjee (2016). "Upper-mantle water stratification inferred from observations of the 2012 Indian Ocean earthquake." Nature 538(7625): 373-377.

Matsu'ura, M., D. D. Jackson and A. Cheng (1986). "Dislocation model for aseismic crustal deformation at Hollister, California." Journal of Geophysical Research: Solid Earth 91(B12): 12661-12674.

McCalpin, J. and S. Nishenko (1996). "Holocene paleoseismicity, temporal clustering, and probabilities of future large (M> 7) earthquakes on the Wasatch fault zone, Utah." Journal of Geophysical Research: Solid Earth 101(B3): 6233-6253.

McNeilan, T. W., T. K. Rockwell and G. S. Resnick (1996). "Style and rate of Holocene slip, Palos Verdes fault, southern California." Journal of Geophysical Research: Solid Earth 101(B4): 8317-8334.

Meade, B. J. and B. H. Hager (2005). "Spatial localization of moment deficits in southern California." Journal of Geophysical Research: Solid Earth 110(B4).

Meade, B. J. and B. H. Hager (2005). "Block models of crustal motion in southern California constrained by GPS measurements." Journal of Geophysical Research: Solid Earth 110(B3).

Meade, B. J., Y. Klinger and E. A. Hetland (2013). "Inference of multiple earthquake-cycle relaxation timescales from irregular geodetic sampling of interseismic deformation." Bulletin of the Seismological Society of America 103(5): 2824-2835.

Meigs, A., D. Yule, A. Blythe and D. Burbank (2003). "Implications of distributed crustal deformation for exhumation in a portion of a transpressional plate boundary, western Transverse ranges, southern California." Quaternary International 101: 169-177.

Meigs, A. J., M. L. Cooke and S. T. Marshall (2008). "Using vertical rock uplift patterns to constrain the three-dimensional fault configuration in the Los Angeles Basin." Bulletin of the Seismological Society of America 98(1): 106-123.

Michel, S., J.-P. Avouac, R. Jolivet an L. Wang (2017). "Seismic and Aseismic Moment Budget and Implication for the Seismic Potential of the Parkfield Segment of the San Andreas Fault." Bulletin of the Seismological Society of America, in press.

Miller, S. A., C. Collettini, L. Chiaraluce, M. Cocco, M. Barchi and B. J. Kaus (2004). "Aftershocks driven by a high-pressure CO2 source at depth." Nature 427(6976): 724-727.

Minson, S., M. Simons and J. Beck (2013). "Bayesian inversion for finite fault earthquake source models I—Theory and algorithm." Geophysical Journal International 194(3): 1701-1726.

Miyazaki, S.-i., P. Segall, J. Fukuda and T. Kato (2004). "Space time distribution of afterslip following the 2003 Tokachi-oki earthquake: Implications for variations in fault zone frictional properties." Geophysical Research Letters 31(6).

Molnar, P. (1979). "Earthquake recurrence intervals and plate tectonics." Bulletin of the Seismological Society of America 69(1): 115-133.

Montési, L. G. and G. Hirth (2003). "Grain size evolution and the rheology of ductile shear zones: from laboratory experiments to postseismic creep." Earth and Planetary Science Letters 211(1): 97-110.

Moreno, M., C. Haberland, O. Oncken, A. Rietbrock, S. Angiboust and O. Heidbach (2014). "Locking of the Chile subduction zone controlled by fluid pressure before the 2010 earthquake." Nature Geoscience 7(4): 292-296.

Morton, D. and R. Yerkes (1987). "Recent reverse faulting in the Transverse Ranges, California." US Geol. Surv. Profess. Pap 1339: 1-5.

Mulargia, F. and A. Bizzarri (2015). "Fluid pressure waves trigger earthquakes." Geophysical Journal International 200(3): 1279-1283.

Myers, D. J., J. L. Nabelek and R. S. Yeats (2003). "Dislocation modeling of blind thrusts in the eastern Los Angeles basin, California." Journal of Geophysical Research: Solid Earth 108(B9).

Nábělek, J., G. Hetényi, J. Vergne, S. Sapkota, B. Kafle, M. Jiang, H. Su, J. Chen and B.-S. Huang (2009). "Underplating in the Himalaya-Tibet collision zone revealed by the Hi-CLIMB experiment." Science 325(5946): 1371-1374.

Neal, R. M. (2003). "Slice sampling." Annals of statistics: 705-741.

Nur, A. and J. R. Booker (1972). "Aftershocks caused by pore fluid flow?" Science 175(4024): 885-887.

Nur, A. and G. Mavko (1974). "Postseismic viscoelastic rebound." Science 183(4121): 204-206.

Okada, Y. (1985). "Surface deformation due to shear and tensile faults in a half-space." Bulletin of the seismological society of America 75(4): 1135-1154.

Okada, Y. (1992). "Internal deformation due to shear and tensile faults in a half-space." Bulletin of the Seismological Society of America 82(2): 1018-1040.

Ortega, F., Aseismic Deformation in Subduction Megathrusts: Central Andes and North-East Japan, Ph.D. thesis, California Institute of Technology, 2013.

Oskin, M., K. Sieh, T. Rockwell, G. Miller, P. Guptill, M. Curtis, S. McArdle and P. Elliot (2000). "Active parasitic folds on the Elysian Park anticline: Implications for seismic hazard in central Los Angeles, California." Geological Society of America Bulletin 112(5): 693-707.

Pandey, M., R. Tandukar, J. Avouac, J. Lave and J. Massot (1995). "Interseismic strain accumulation on the Himalayan crustal ramp (Nepal)." Geophysical Research Letters 22(7): 751-754.

Peltzer, G., P. Rosen, F. Rogez and K. Hudnut (1998). "Poroelastic rebound along the Landers 1992 earthquake surface rupture." Journal of Geophysical Research: Solid Earth 103(B12): 30131-30145.

Peng, Z. and P. Zhao (2009). "Migration of early aftershocks following the 2004 Parkfield earthquake." Nature Geoscience 2(12): 877-881.

Perfettini, H. and J. P. Avouac (2004). "Postseismic relaxation driven by brittle creep: A possible mechanism to reconcile geodetic measurements and the decay rate of aftershocks, application to the Chi-Chi earthquake, Taiwan." Journal of Geophysical Research: Solid Earth 109(B2).

Perfettini, H. and J. P. Avouac (2007). "Modeling afterslip and aftershocks following the 1992 Landers earthquake." Journal of Geophysical Research: Solid Earth 112(B7).

Plattner, C., R. Malservisi, T. H. Dixon, P. LaFemina, G. Sella, J. Fletcher and F. Suarez-Vidal (2007). "New constraints on relative motion between the Pacific plate and Baja California microplate (Mexico) from GPS measurements." Geophysical Journal International 170(3): 1373-1380.

Plesch, A., J. H. Shaw, C. Benson, W. A. Bryant, S. Carena, M. Cooke, J. Dolan, G. Fuis, E. Gath and L. Grant (2007). "Community fault model (CFM) for southern California." Bulletin of the Seismological Society of America 97(6): 1793-1802.

Pollitz, F. F. (2003). "Transient rheology of the uppermost mantle beneath the Mojave Desert, California." Earth and Planetary Science Letters 215(1): 89-104.

Pollitz, F. F. (2003). "Post-seismic relaxation theory on a laterally heterogeneous viscoelastic model." Geophysical Journal International 155(1): 57-78.

Pollitz, F. F. (2015). "Postearthquake relaxation evidence for laterally variable viscoelastic structure and water content in the Southern California mantle." Journal of Geophysical Research: Solid Earth 120(4): 2672-2696.

Pollitz, F. F., R. Bürgmann and W. Thatcher (2012). "Illumination of rheological mantle heterogeneity by the M7. 2 2010 El Mayor-Cucapah earthquake." Geochemistry, Geophysics, Geosystems 13(6).

Pollitz, F. F., G. Peltzer and R. Bürgmann (2000). "Mobility of continental mantle: Evidence from postseismic geodetic observations following the 1992 Landers earthquake." Journal of Geophysical Research: Solid Earth 105(B4): 8035-8054.

Powell, R. E. (1993). "Balanced palinspastic reconstruction of pre-late Cenozoic paleogeology, southern California: Geologic and kinematic constraints on evolution of the San Andreas fault system." Geological Society of America Memoirs 178: 1-106.

Rockwell, T., S. Lindvall, M. Herzberg, D. Murbach, T. Dawson and G. Berger (2000). "Paleoseismology of the Johnson Valley, Kickapoo, and Homestead Valley faults: Clustering of earthquakes in the eastern California shear zone." Bulletin of the Seismological Society of America 90(5): 1200-1236.

Roland, E. and J. J. McGuire (2009). "Earthquake swarms on transform faults." Geophysical Journal International 178(3): 1677-1690.

Rong, Y., D. D. Jackson, H. Magistrale and C. Goldfinger (2014). “Magnitude Limits of Subduction Zone Earthquakes.” Bulletin of the Seismological Society of America 104(5): 2359-2377.

Ross, Z. E., E. Hauksson and Y. Ben-Zion (2017). "Abundant off-fault seismicity and orthogonal structures in the San Jacinto fault zone." Science Advances 3(3): e1601946.

Royden, L. H. (1993). "The steady state thermal structure of eroding orogenic belts and accretionary prisms." Journal of Geophysical Research: Solid Earth 98(B3): 4487-4507.

Rubin, C. M., S. C. Lindvall and T. K. Rockwell (1998). "Evidence for large earthquakes in metropolitan Los Angeles." Science 281(5375): 398-402.

Ryberg, T. and G. S. Fuis (1998). "The San Gabriel Mountains bright reflective zone: Possible evidence of young mid-crustal thrust faulting in southern California." Tectonophysics 286(1): 31-46.

Rydelek, P. A. and I. S. Sacks (1999). "Large earthquake occurrence affected by small stress changes." Bulletin of the Seismological Society of America 89(3): 822-828.

Ryder, I., R. Bürgmann and F. Pollitz (2011). "Lower crustal relaxation beneath the Tibetan Plateau and Qaidam Basin following the 2001 Kokoxili earthquake." Geophysical Journal International 187(2): 613-630.

Rymer, M. J., J. A. Treiman, K. J. Kendrick, J. J. Lienkaemper, R. J. Weldon, R. Bilham, M. Wei, E. J. Fielding, J. L. Hernandez and B. P. Olson (2011). Triggered surface slips in southern California associated with the 2010 El Mayor-Cucapah, Baja California, Mexico, earthquake, US Geological Survey.

Sammis, C. G. and S. W. Smith (2013). "Triggered tremor, phase locking, and the global clustering of great earthquakes." Tectonophysics 589: 167-171.

Savage, J. (1983). "A dislocation model of strain accumulation and release at a subduction zone." Journal of Geophysical Research: Solid Earth 88(B6): 4984-4996.

Savage, J. and R. Burford (1973). "Geodetic determination of relative plate motion in central California." Journal of Geophysical Research 78(5): 832-845.

SCEDC, Southern California Earthquake Data Center, *California Institute of Technology, Dataset*, doi:10.7909/C3WD3xH1, 2013.

Schulte-Pelkum, V., G. Monsalve, A. Sheehan, M. Pandey, S. Sapkota, R. Bilham and F. Wu (2005). "Imaging the Indian subcontinent beneath the Himalaya." Nature 435(7046): 1222-1225.

Segall, P. (2010). "Earthquake and volcano deformation." Princeton University Press.

Segall, P. and R. Harris (1986). "Slip deficit on the San Andreas fault at Parkfield, California, as revealed by inversion of geodetic data." Science 233(4771): 1409-1413.

Shapiro, S. A., E. Huenges and G. Borm (1997). "Estimating the crust permeability from fluid-injection-induced seismic emission at the KTB site." Geophysical Journal International 131(2).

Shaw, J. H., A. Plesch, J. F. Dolan, T. L. Pratt and P. Fiore (2002). "Puente Hills blind-thrust system, Los Angeles, California." Bulletin of the Seismological Society of America 92(8): 2946-2960.

Shaw, J. H., A. Plesch, C. Tape, M. P. Suess, T. H. Jordan, G. Ely, E. Hauksson, J. Tromp, T. Tanimoto and R. Graves (2015). "Unified structural representation of the southern California crust and upper mantle." Earth and Planetary Science Letters 415: 1-15.

Shaw, J. H. and P. M. Shearer (1999). "An elusive blind-thrust fault beneath metropolitan Los Angeles." Science 283(5407): 1516-1518.

Shaw, J. H. and J. Suppe (1996). "Earthquake hazards of active blind-thrust faults under the central Los Angeles basin, California." Journal of Geophysical Research: Solid Earth 101(B4): 8623-8642.

Shelly, D. R., W. L. Ellsworth and D. P. Hill (2016). "Fluid-faulting evolution in high definition: Connecting fault structure and frequency-magnitude variations during the 2014 Long Valley Caldera, California, earthquake swarm." Journal of Geophysical Research: Solid Earth 121(3): 1776-1795.

Shen, Z. K., D. D. Jackson and B. X. Ge (1996). "Crustal deformation across and beyond the Los Angeles basin from geodetic measurements." Journal of Geophysical Research: Solid Earth 101(B12): 27957-27980.

Shen, Z. K., D. D. Jackson and Y. Y. Kagan (2007). “Implications of Geodetic Strain Rate for Future Earthquakes, with a Five-Year Forecast of M5 Earthquakes in Southern California.” Seismological Research Letters 78(1).

Sibson, R. H. (1996). "Structural permeability of fluid-driven fault-fracture meshes." Journal of Structural Geology 18(8): 1031-1042.

Sorlien, C. C., L. Seeber, K. G. Broderick, B. P. Luyendyk, M. A. Fisher, R. W. Sliter and W. R. Normark (2013). "The Palos Verdes anticlinorium along the Los Angeles, California coast: Implications for underlying thrust faulting." Geochemistry, Geophysics, Geosystems 14(6): 1866-1890.

Stein, R. S. (1999). "The role of stress transfer in earthquake occurrence." Nature 402(6762): 605-609.

Stein, R. S., A. A. Barka and J. H. Dieterich (1997). "Progressive failure on the North Anatolian fault since 1939 by earthquake stress triggering." Geophysical Journal International 128(3): 594-604.

Stein, S. and M. Wysession (2009). An introduction to seismology, earthquakes, and earth structure, John Wiley & Sons.

Stevens, V. and J. Avouac (2015). "Interseismic coupling on the main Himalayan thrust." Geophysical Research Letters 42(14): 5828-5837.

Stevens, V. and J. P. Avouac (2017). "Determination of Mmax from Background Seismicity and Moment ConservationDetermination of Mmax from Background Seismicity and Moment Conservation." Bulletin of the Seismological Society of America: 1-19.

Stevens, V. and J. P. Avouac (2016). "Millenary Mw> 9.0 earthquakes required by geodetic strain in the Himalaya." Geophysical Research Letters 43(3): 1118-1123.
Takeuchi, C. S. and Y. Fialko (2013). "On the effects of thermally weakened ductile shear zones on postseismic deformation." Journal of Geophysical Research: Solid Earth 118(12): 6295-6310.

Tanaka, A. and Y. Ishikawa (2002). "Temperature distribution and focal depth in the crust of the northeastern Japan." Earth, planets and space 54(11): 1109-1113.

Tape, C., P. Musé, M. Simons, D. Dong and F. Webb (2009). "Multiscale estimation of GPS velocity fields." Geophysical Journal International 179(2): 945-971.

Tape, C., A. Plesch, J. H. Shaw and H. Gilbert (2012). "Estimating a continuous Moho surface for the California unified velocity model." Seismological Research Letters 83(4): 728-735.

Thatcher, W. and D. P. Hill (1991). "Fault orientations in extensional and conjugate strike-slip environments and their implications." Geology 19(11): 1116-1120.

Tichelaar, B. W. and L. J. Ruff (1989). "How good are our best models? Jackknifing, bootstrapping, and earthquake depth." Eos, Transactions American Geophysical Union 70(20): 593-606.

Toda, S., R. S. Stein, K. Richards‐Dinger and S. B. Bozkurt (2005). "Forecasting the evolution of seismicity in southern California: Animations built on earthquake stress transfer." Journal of Geophysical Research: Solid Earth 110(B5).

Toppozada, T. R., & Branum, D. M. (2002). California M 1 5.5 earthquakes, history and areas damaged. *International Handbook of Earthquake and Engineering Seismology*.

Trugman, D. T. and P. M. Shearer (2017). "GrowClust: A hierarchical clustering algorithm for relative earthquake relocation, with application to the Spanish Springs and Sheldon, Nevada, earthquake sequences." Seismological Research Letters 88(2A): 379-391.

Tsai, V. C. (2011). "A model for seasonal changes in GPS positions and seismic wave speeds due to thermoelastic and hydrologic variations." Journal of Geophysical Research: Solid Earth 116(B4).

Tucker, A. Z. and J. F. Dolan (2001). "Paleoseismologic evidence for a> 8 ka age of the most recent surface rupture on the eastern Sierra Madre fault, northern Los Angeles metropolitan region, California." Bulletin of the Seismological Society of America 91(2): 232-249.

Tunini, L., I. Jiménez-Munt, M. Fernandez, J. Vergés, A. Villaseñor, M. Melchiorre and J. C. Afonso (2016). "Geophysical-petrological model of the crust and upper mantle in the India-Eurasia collision zone." Tectonics 35(7): 1642-1669.

Unsworth, M., A. G. Jones, W. Wei, G. Marquis, S. Gokarn, J. Spratt, P. Bedrosian, J. Booker, C. Leshou and G. Clarke (2005). "Crustal rheology of the Himalaya and Southern Tibet inferred from magnetotelluric data." Nature 438(7064): 78-81.

Utsu, T. (2002). "Statistical features of seismicity." International Geophysics Series 81(A): 719-732.

Vidale, J. E. and P. M. Shearer (2006). "A survey of 71 earthquake bursts across southern California: Exploring the role of pore fluid pressure fluctuations and aseismic slip as drivers." Journal of Geophysical Research: Solid Earth 111(B5).

Villegas-Lanza, J., J.-M. Nocquet, F. Rolandone, M. Vallée, H. Tavera, F. Bondoux, T. Tran, X. Martin and M. Chlieh (2016). "A mixed seismic-aseismic stress release episode in the Andean subduction zone." Nature Geoscience 9(2): 150-154.

Walls, C., T. Rockwell, K. Mueller, Y. Bock, S. Williams, J. Pfanner, J. Dolan and P. Fang (1998). "Escape tectonics in the Los Angeles metropolitan region and implications for seismic risk." Nature 394(6691): 356-360.

Wang, K. and Y. Fialko (2014). "Space geodetic observations and models of postseismic deformation due to the 2005 M7. 6 Kashmir (Pakistan) earthquake." Journal of Geophysical Research: Solid Earth 119(9): 7306-7318.

Wang, K. and Y. Fialko (2015). "Slip model of the 2015 Mw 7.8 Gorkha (Nepal) earthquake from inversions of ALOS-2 and GPS data." Geophysical Research Letters 42(18): 7452-7458.

Weaver, K. D. and J. F. Dolan (2000). "Paleoseismology and geomorphology of the Raymond fault, Los Angeles County, California." Bulletin of the Seismological Society of America 90(6): 1409-1429.

Wei, S., E. Fielding, S. Leprince, A. Sladen, J.-P. Avouac, D. Helmberger, E. Hauksson, R. Chu, M. Simons and K. Hudnut (2011). "Superficial simplicity of the 2010 El Mayor-Cucapah earthquake of Baja California in Mexico." Nature Geoscience 4(9): 615-618.

Wells, D. L. and K. J. Coppersmith (1994). "New empirical relationships among magnitude, rupture length, rupture width, rupture area, and surface displacement." Bulletin of the seismological Society of America 84(4): 974-1002.

Williams, C. F., J. DeAngelo, and J. H. Sass, Heat Flow in the Salton Trough Revisited and Implications for Regional Tectonics, Eos Trans. AGU, 93(51), 2012.

Wright, T. L. (1991). "Structural geology and tectonic evolution of the Los Angeles basin, California." Active Margin Basins 52: 35-134.
Yang, W. and E. Hauksson (2011). "Evidence for vertical partitioning of strike-slip and compressional tectonics from seismicity, focal mechanisms, and stress drops in the east Los Angeles basin area, California." Bulletin of the Seismological Society of America 101(3): 964-974.

Yang, W. and E. Hauksson (2013). "The tectonic crustal stress field and style of faulting along the Pacific North America Plate boundary in Southern California." Geophysical Journal International 194(1): 100-117.

Yang, W., E. Hauksson and P. M. Shearer (2012). "Computing a large refined catalog of focal mechanisms for southern California (1981–2010): Temporal stability of the style of faulting." Bulletin of the Seismological Society of America 102(3): 1179-1194.

Yeats, R. S. (2004). "Tectonics of the San Gabriel Basin and surroundings, southern California." Geological Society of America Bulletin 116(9-10): 1158-1182.

Zaliapin, I. and Y. Ben-Zion (2013). "Earthquake clusters in southern California II: Classification and relation to physical properties of the crust." Journal of Geophysical Research: Solid Earth 118(6): 2865-2877.

Zhao, B., R. Bürgmann, D. Wang, K. Tan, R. Du and R. Zhang "Dominant Controls of Downdip Afterslip and Viscous Relaxation on the Postseismic Displacements Following the Mw7. 9 Gorkha, Nepal, Earthquake." Journal of Geophysical Research: Solid Earth.

Zhao, S., R. Müller, Y. Takahashi and Y. Kaneda (2004). "3-D finite-element modelling of deformation and stress associated with faulting: effect of inhomogeneous crustal structures." Geophysical Journal International 157(2): 629-644.

Zoback, M., M. Zoback, J. Eaton, V. Mount and J. Suppe (1987). "New evidence on the state of stress of the San Andreas fault system." Science 238(4830): 1105-1111.

Appendix

AFTERSHOCKS DRIVEN BY AFTERSLIP AND FLUID PRESSURE SWEEPING THROUGH A FAULT-FRACTURE MESH

(Published as "Aftershocks Driven by Afterslip and Fluid Pressure Sweeping Through a Fault-Fracture Mesh" by Z.E Ross, C. Rollins, and E.S. Cochran, E. Hauksson, J.-P. Avouac, and Y. Ben-Zion, Geophysical Research Letters, 2017)

(In this study I carried out the analysis of the geodetic data, carried out the kinematic modeling of the afterslip source based on this data in Figures A.1 and A.3a, and contributed to the interpretation and the writing and organization of the paper.)

ABSTRACT

A variety of physical mechanisms are thought to be responsible for the triggering and spatiotemporal evolution of aftershocks. Here we analyze a vigorous aftershock sequence and postseismic geodetic strain that occurred in the Yuha Desert following the 2010 M_w 7.2 El Mayor-Cucapah earthquake. About 155,000 detected aftershocks occurred in a network of orthogonal faults and exhibit features of two distinct mechanisms for aftershock triggering. The earliest aftershocks were likely driven by afterslip that spread away from the mainshock with the logarithm of time. A later pulse of aftershocks swept again across the Yuha Desert with square-root time dependence and swarm-like behavior; together with local geological evidence for hydrothermalism, these features suggest the events were driven by fluid diffusion. The observations illustrate how multiple driving mechanisms and the underlying fault structure jointly control the evolution of an aftershock sequence.

A.1. Introduction

The M_w 7.2 El Mayor-Cucapah (EMC) earthquake occurred on 2010-04-04 in Baja California on a set of northwest trending faults, rupturing in bilateral fashion [*Fletcher et al.*, 2014; *Hauksson et al.*, 2011; *Wei et al.*, 2011]. In the northwest, the rupture terminated about 60 km from the hypocenter, at the geologic boundary between the Sierra Cucapah range and the Yuha Desert, and close to the international border (Fig. A.1). In this area, an intense aftershock sequence followed—including 40 events with magnitude greater than 4—and culminated 72 days later in the 2010-06-15 M_w 5.7 Ocotillo earthquake, 20 km from the rupture terminus. There is also evidence that significant postseismic deformation occurred in the Yuha Desert [*M H Huang et al.*, 2016; *Pollitz et al.*, 2012; *Rollins et al.*, 2015; *Rymer et al.*, 2011], which suggests some relationship with the seismicity.

Various physical mechanisms have been proposed to explain the triggering of aftershocks and their spatiotemporal evolution. Aftershocks may reflect time-dependent failure in response to coseismic static [*Ben-Zion and Lyakhovsky*, 2006; *Dieterich*, 1994; *Stein*, 1999] or dynamic [*Felzer and Brodsky*, 2006] stress changes. They may also be driven by coseismic fluid pressurization [*Miller et al.*, 2004; *Mulargia and Bizzarri*, 2015; *Nur and Booker*, 1972] or aseismic afterslip [*Perfettini and Avouac*, 2004]. We used a matched-filter technique to produce a detailed catalog of more than 155,000 aftershocks with M>-2 (Fig. A.1). We show hereafter that the seismicity and geodetic observations of postseismic deformation illuminate multiple concurrent—but distinct—physical processes governing the evolution of the EMC sequence.

A.2. Data

We used continuous seismic data recorded between 2010-04-04 and 2010-06-26 by 112 stations of the Southern California Seismic Network [*SCEDC*, 2013], which includes a temporary deployment of 8 stations in the Yuha Desert following EMC [*Kroll et al.*, 2013]. Only short-period and broadband seismometers were used. All phase data used were produced by SCSN. The waveform-relocated SCSN catalog [*Hauksson et al.*, 2012] contains 22,350 earthquakes in the study region during the period 2000-2016, and these were used as template events to search for additional earthquakes. Focal mechanisms used in the study were taken from the catalog of [*Yang et al.*, 2012]. The seismicity catalog produced in this study is available as Dataset S1. The GPS data used are the filtered, non-detrended time series published by the Scripps Orbit and Permanent Array Center [*Bock and Haase*, 2016].

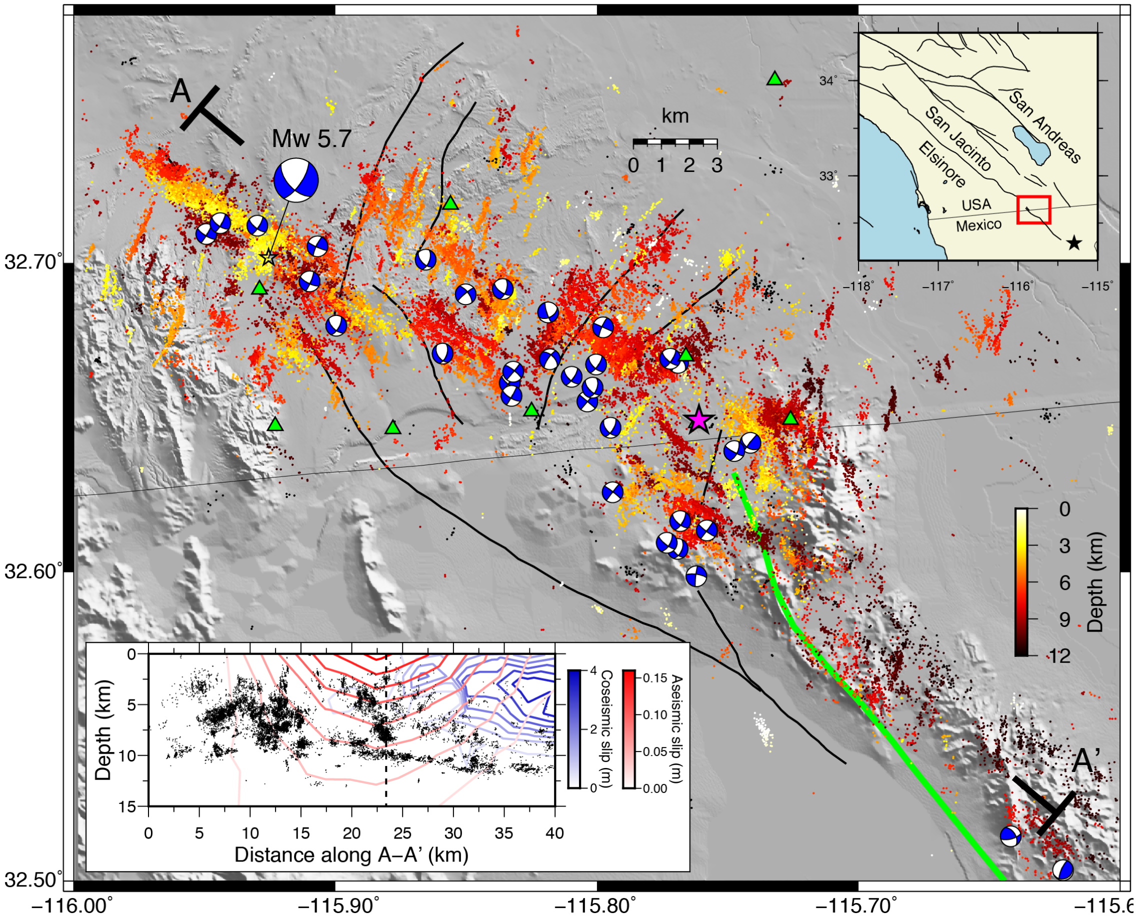

Figure A.1. Map of Yuha Desert and El Mayor-Cucapah aftershocks. Upper right inset shows tectonic setting of study area. Focal mechanisms [*Yang et al.*, 2012] correspond to events with M > 4. Lower left inset shows seismicity within 2 km of A-A', coseismic [*Wei et al.*, 2011], and aseismic slip (see methods). The green line indicates the coseismic surface rupture from optical data [*Wei et al.*, 2011], and black lines indicate faults [*Fletcher et al.*, 2014]. The pink star denotes inferred origin of fluid migration.

A.3. Methods

A.3.1. Matched filter earthquake detection

We used a matched filter algorithm [*Ross et al.*, 2017; *Shelly et al.*, 2016] to detect previously unidentified aftershocks in the EMC sequence. The matched-filter technique uses the records of P- and S-waves from previously identified events to scan continuous records and search for similar waveforms across the network [*A Kato et al.*, 2016]. P- and S-waves templates were constructed using 2.5 s and 4.0 s windows, respectively, starting 0.25 s before the pick. If no S-pick was available at a given station, a v_p/v_s ratio of 1.73 was used. P-wave templates were taken from only the vertical component, while S-wave templates used both horizontals. Template events selected had at least 12 phases with a signal-to-noise ratio greater than 5.0. Each template was then correlated against the continuous data in 24-hour periods on the same stations and channels as the template record. For a given template event and time period, correlation functions were shifted back in time by an amount equal to the observed travel time of the template, and stacked across all stations, channels, and phases. Preliminary detections were then made using a correlation trigger threshold of 8 times the median absolute deviation of the stack for the day, with the time of each trigger defining the origin time of the detected event. Then, returning to the individual phase correlation functions, differential times were measured using a threshold of 7 times the median absolute deviation. At least four differential times were required for subsequent processing of a detected event, ensuring that the stacked correlation function was not dominated by just a single station. Detected events at this stage were assigned a location equal to that of the best-matching template event based on average correlation coefficient. These steps resulted in a total of 155,795 aftershocks detected (including template events).

Magnitudes were then calculated by taking the median peak amplitude ratio between the template and detected event and adding the logarithm of this value to the magnitude of the template event [*Peng and Zhao*, 2009]. Amplitude ratios were only calculated for phases with valid differential times. For the smallest events with low signal-to-noise ratios, individual magnitude values have considerable uncertainty. For a more thorough description of the detection procedure, see [*Ross et al.*, 2017].

Each detected event was then correlated with the 200 nearest template events (in spatial distance) to add in additional differential times, using P- and S-waves on all three components. For this procedure, windows for P- and S-waves were 1.0 and 1.5 s long, respectively. For each station, we saved at most one differential time for each phase, choosing the value with the largest positive cross-correlation coefficient. For a given pair of events, a minimum of eight differential times with correlation coefficients larger than 0.6 was further required. This process resulted in 24.7 million differential times total for the data set, which were used to relocate the catalog with the GrowClust algorithm [*Trugman and Shearer*, 2017]. The relocation parameters used were a minimum correlation coefficient of 0.6, and a minimum of eight differential times, which resulted in 66,337 events being relocated successfully (Fig. A.1).

A.3.2. GPS data processing and inversion

To better understand the postseismic deformation in the Yuha Desert, we used GPS data from six nearby stations in an aseismic slip inversion. First, we detrended the data by estimating the secular velocities due to interseismic deformation and annual and semi-annual oscillations due to tidal, hydrological, thermoelastic and/or other effects [e.g. Dong et al, 2002; Tsai, 2011; Ben-Zion and Allam, 2013] using a least-squares fit to the pre-EMC time series, and then subtracted these signals from the entire time series. (To ensure that the representation of the preseismic signal was robust, we only used stations that had at least two years of data preceding EMC.) A seven-day median filter was applied to the detrended time series, and the position on the first postseismic day was set as the zero-reference value. This is generally indistinguishable from the unfiltered value. To then isolate the localized postseismic deformation in the Yuha Desert, we computed synthetic time series from a model of regional-scale postseismic processes [*Rollins et al.*, 2015], and subtracted the synthetic time series from the detrended postseismic GPS time series. The regional-scale model also included a generic afterslip source in the Yuha Desert, but we excluded this when subtracting the model.

Then, the residual time series were used in a slip inversion on a single right-lateral fault plane aligned with cross section A-A' (Fig. A.1). The fault plane was extended 40 km laterally in both directions and downward to 50 km depth to prevent against boundary effects. Weights were determined from the variance of the first principal component as in the PCAIM method [*Kositsky and Avouac*, 2010]. The inversion was regularized using sensitivity-modulated Laplacian smoothing [*Ortega*, 2013], which enforces stronger penalization of the Laplacian in poorly resolved areas. The absolute weight was chosen using the L-curve approach of second-order Tikhonov regularization [*Aster et al.*, 2012]. To calculate the total moment released, the afterslip distribution was integrated over space and multiplied by an assumed shear modulus of 30 GPa.

A.3.3 Cluster Analysis

The highly-segmented nature of the seismicity structures in the Yuha Desert promotes the possibility of identifying spatially distinct clusters for detailed examination. We used the DBSCAN algorithm [*Ester et al.*, 1996] to perform the cluster analysis in three dimensions. The algorithm has two parameters, a spherical radius, set to 0.4 km, and a minimum number of events, set to 50. Varying the DBSCAN parameters over the ranges 0.3-0.6 km radius and 50-200 minimum events had a negligible influence on the results.

Applying the procedure to all earthquakes in the catalog resulted in 276 clusters (Figure A.S1). For each cluster, we then only kept events with M > 0.5, which was determined to be the magnitude of catalog completeness over the first 70 days. A total of 56 clusters had at least 100 events and are used in the skewness and duration analysis described below.

Then two different metrics were calculated for each cluster. The first was the statistical skewness of the origin times within each cluster [*Roland and McGuire*, 2009],

$$s = \frac{\frac{1}{n}\sum_{i=1}^{n}(t_i-\bar{t})^3}{\left[\frac{1}{n-1}\sum_{i=1}^{n}(t_i-\bar{t})^2\right]^{3/2}}, \tag{A.1}$$

where t_i is the ith origin time, $\bar{t}$ is the mean origin time, and n is the number of events in the cluster.

The second metric used was the effective duration, defined here as,

$$IQR = t_{90} - t_{10}, \tag{A.2}$$

where t_{90} and t_{10} are the 90th and 10th percentiles of the origin times within a cluster. Error estimates were determined by bootstrap resampling of the events within each cluster, calculating each metric for the new sample, and repeating the process 1000 times.

A.4. Results

In the southeastern area beneath the Sierra Cucapah, a long horizontal lineament of aftershocks delineates the lower edge of the EMC rupture area [*Wei et al.*, 2011], which is itself relatively devoid of aftershocks (Fig. A.1, lower left inset). The northern terminus of the rupture edge coincides with a transition from crystalline and volcanic rocks in the south to unconsolidated sedimentary rocks in the north [*Fletcher et al.*, 2014]. Farther north, in the Yuha Desert, the seismicity delineates a complex network of segmented orthogonal faults [*Kroll et al.*, 2013] (Fig. A.1). Individual lineations have typical lengths of 2-3 km, are non-planar, and predominantly dip to the northeast. Focal mechanisms in the region are a mixture of strike-slip and normal faulting [*Yang et al.*, 2012]. Such cross-cutting fault patterns are common in the extensional-transtensional environment of southern California [*Ross et al.*, 2017; *Thatcher and Hill*, 1991] and might be interpreted as fault-fracture meshes formed in the presence of fluids [*Hill*, 1977; *Sibson*, 1996]. In addition, there is extensive geological evidence of hydrothermal activity in the Yuha Desert, including an abundance of mineralization signatures and metals [*Isaac*, 1987].

We first observe that the zone of aftershocks expanded away from the northern EMC rupture terminus with the logarithm of time, over a distance of 30 km in a ~10-day period

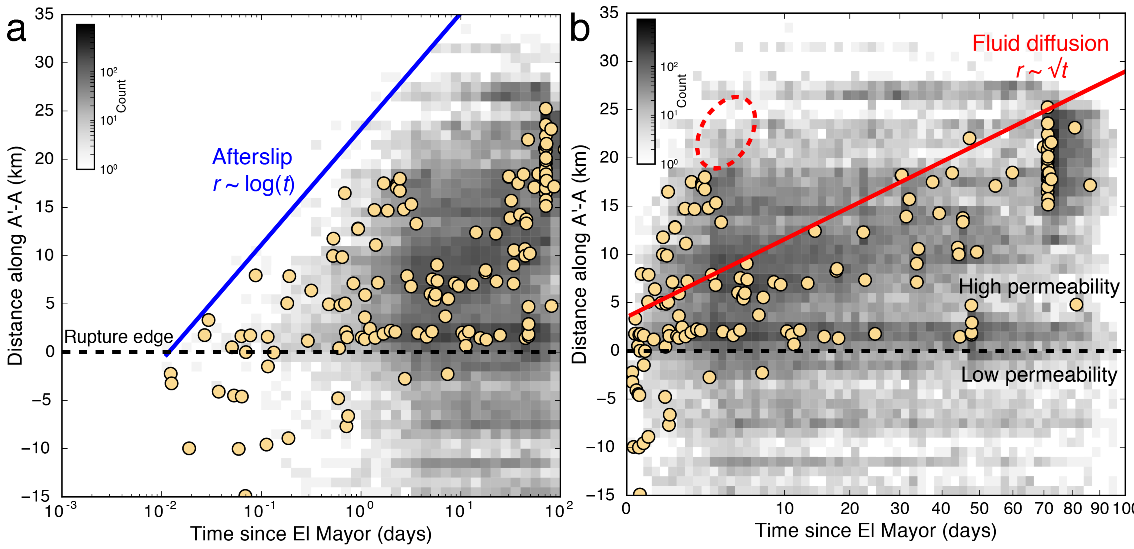

Figure A.2. Spatiotemporal evolution of aftershocks. **a**, Events are shown as binned counts, while events with M > 3.5 are shown as circles. Aftershock zone expands away from the rupture edge with the logarithm of time, suggestive of afterslip. **b**, Same as **a**, but with a square-root time scale. Later events migrate away from the rupture edge with the square-root of time, suggestive of fluid diffusion. Gap of large events (ellipse) is filled in 72 days later during the Ocotillo sequence, which may have been triggered by fluids.

(Fig. A.2a). Afterslip following large earthquakes is also believed to expand spatially with the logarithm of time [*N Kato*, 2007; *Perfettini and Avouac*, 2007], and a similar aftershock migration pattern following the 2004 Parkfield earthquake was inferred to be driven by afterslip [*Peng and Zhao*, 2009]. Figure A.1 shows the inferred afterslip distribution in the bottom left inset, with the peak being nearly coincident with the rupture terminus, and therefore the origin of aftershock migration. The GPS vectors and best-fitting model are shown in Figure A.3a. Over the first 60 days following EMC, the geodetic data require that postseismic deformation released a moment of ~$1.44 \cdot 10^{18}$ N-m (equivalent to a M_w 6.04 earthquake). This is well in excess of the $9.8 \cdot 10^{16}$ N-m moment released by all detected aftershocks over the same period of time. If afterslip was the driving process behind the early aftershocks, it should also have produced geodetic displacements that evolved in time like the cumulative number of aftershocks [*H Huang et al.*, 2017; *Perfettini and Avouac*, 2004; *Villegas-lanza et al.*, 2016]. Notably, we find a close correlation between these quantities at the closest GPS station to the Yuha Desert (Fig. A.3c). Thus, there is ample evidence that the aftershocks were initially triggered by a pulse of aseismic afterslip that swept through the Yuha Desert.

Following this episode, a sequence of intensified seismicity punctuated by M>3.5

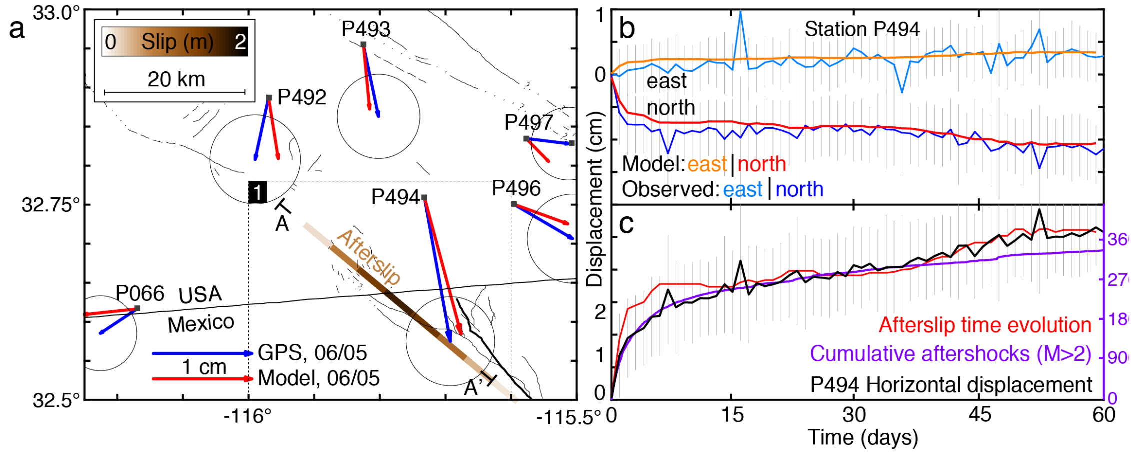

Figure A.3. GPS postseismic displacement, afterslip model and cumulative number of aftershocks. **a**, Map of Yuha Desert region and nearby GPS stations. Blue arrows denote 'residual' postseismic displacements after 60 days, corrected for the contribution of viscoelastic relaxation and afterslip using the model of [*Rollins et al.*, 2015]. Red arrows show the cumulative displacements predicted from the source model derived from the inversion of the residual time series. **b**, Residual postseismic times series and model prediction. Vertical lines denote error bars **c**, Comparison of the cumulative number of aftershocks, afterslip (shown with 7-day median filter), and total horizontal displacement at P494.

events (Fig. A.2b) initiated near the northern tip of the EMC rupture and migrated more than 15 km to the northwest with square-root time dependence. These events migrated slower than the afterslip front initially, but expanded more rapidly over the remaining 70 days of the sequence, culminating in the M_w 5.7 Ocotillo earthquake. As Fig. A.4 shows, the overall pattern is well explained by a diffusion process originating from a single point at a depth of 8km, near the rupture edge at the northern tip of the Sierra Cucapah (pink star in Fig. A.1). The space-time evolution of the aftershocks follows $r = \sqrt{4\pi Dt}$, where r, D, and t are distance, diffusivity, and time, respectively [*Shapiro et al.*, 1997]. A diffusivity of 6 m^2s^{-1} best matches the migration along A-A' (Fig. A.4). These values, along with the history of hydrothermalism in the region, suggest a fluid diffusion process. The migration appears much slower in the fault-normal direction (Fig. A.4; Movie S1), suggesting anisotropic permeability likely controlled by fault zone structure. Brittle damage generated by the mainshock and aftershocks is expected to further increase the permeability in the fault zone [*Hamiel et al.*, 2004]. The lack of migration across the coseismic rupture edge may reflect a permeability barrier related to the change from sedimentary to crystalline rocks.

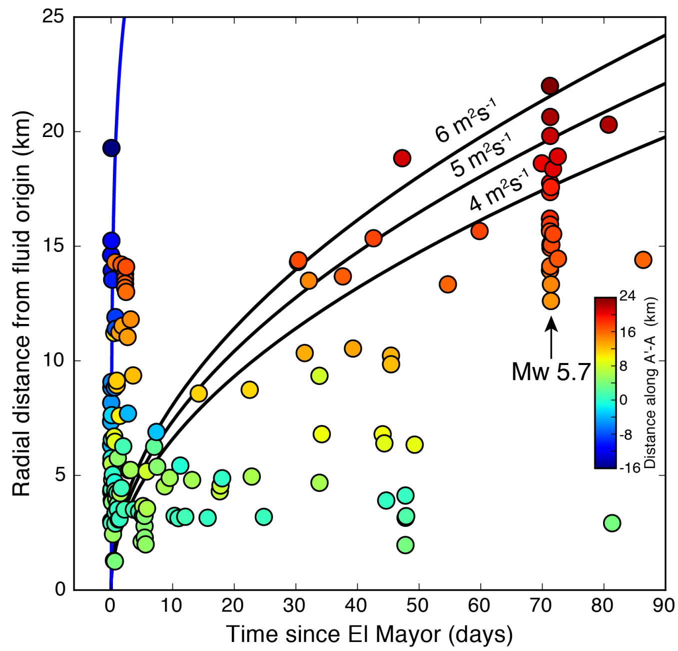

Figure A.4. Spatiotemporal evolution of events with M > 3.5, relative to pink star in Fig. A.1. Black lines correspond to predictions from a diffusion model [*Shapiro et al.*, 1997]. Blue line shows the logarithmic initial expansion of the seismicity.

Over the ~10 day period following EMC, numerous small earthquakes occurred at the eventual site of the Ocotillo earthquake (red ellipse, Fig. A.2), but most of the area was devoid of large events (M > 3.5). However, 72 days after EMC the Ocotillo earthquake was triggered, which may have resulted from the effect of fluid migration. If true, this suggests that the pore pressure changes had a stronger effect at that time than the afterslip stress transfer early in the sequence. Movies S1-S2 illustrate the migration of aftershocks across the Yuha Desert region leading to the Ocotillo earthquake.

The evolving behavior is also reflected in the characteristics of individual aftershock clusters that occur as part of the broader sequence. A variety of empirical relationships have been developed to characterize the spatial, temporal, and magnitude progression of clusters [*Utsu*, 2002], and the parameters which govern these relationships are often used to classify clusters into end-member categories of bursts and swarms [*Zaliapin and Ben-Zion*, 2013]. Bursts are primarily composed of a single large mainshock and aftershocks dominated by one generation with a power law decay rate, and are associated with brittle processes in relatively cold regions [*Ben-Zion and Lyakhovsky*, 2006]. Swarms tend to have complex spatiotemporal histories, no identifiable mainshock,

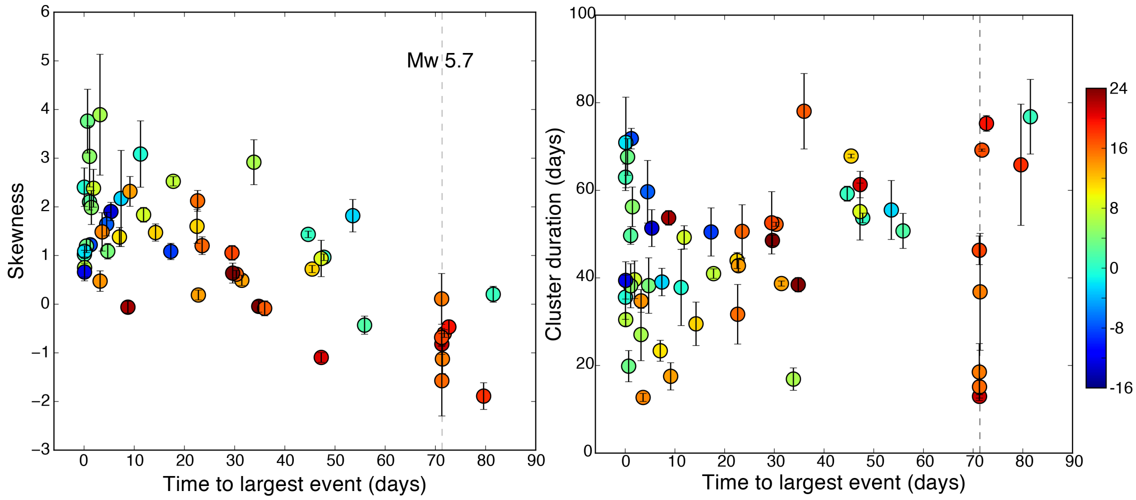

Figure A.5. Cluster evolution metrics. Points represent clusters with at least 100 events. Clusters trend from large positive skewness and short duration, to near-zero skewness and long duration, with increasing time to the largest event. These patterns suggest that clusters become swarm-like over the course of the sequence.

and are associated with ductile processes in relatively hot areas and possibly fluid migration or aseismic slip [*Hauksson et al.*, 2017; *Shelly et al.*, 2016; *Vidale and Shearer*, 2006]. We identified clusters as groupings of events that are spatially compact (Fig. A.S1). The clusters trend from large positive skewness to nearly zero skewness (symmetric) with increasing time after the EMC mainshock (Fig. 5). Bursts are associated with strongly positive skewness, while swarms are associated with near-zero skewness. We next examine cluster duration, defined as the time range spanned by the middle eighty percent of events. For clusters that had their largest event within the first few days after EMC, there are a wide range of cluster durations. From days 10-70, the cluster duration increases moderately with the time to the largest event in the cluster. Together these complementary metrics suggest that the behavior of the EMC aftershocks evolved from burst-like to swarm-like with time.

A.5. Discussion

To summarize, the Yuha Desert aftershocks of EMC exhibit the following features: (1) they delineate an orthogonal mesh of fault segments, (2) they expanded along-strike away from the northern edge of the EMC rupture with a logarithmic time dependence, (3) they correlate spatially with and follow the same logarithmic time evolution as postseismic deformation, (4) seismicity accounts for only 6.8% of the postseismic deformation, (5) another sequence migrated away from the edge of the EMC rupture with the square-root of time, and (6) aftershocks evolved from burst-like to swarm-like with time. The combination of afterslip and fluid migration together with the underlying volumetric fault structure provides the most likely explanation for all these observations. We propose that the EMC rupture arrested at the onset of the Sierra Cucapah, where it encountered a zone dominated by rate-strengthening frictional behavior [*Kaneko et al.*, 2010]. From there, a pulse of afterslip initiated, expanding rapidly across the Yuha Desert and triggering aftershocks throughout. Fluids percolated throughout the deformation zone, starting from a point near the tip of the EMC rupture, and resulted in renewed seismic activity in the form of swarms and larger magnitude events. This second phase ultimately led to the M_w 5.7 Ocotillo earthquake 72 days after EMC. A similar association of creep, swarm-like seismicity, fluids, and barrier effects has been suggested from studies of subduction megathrusts [*Holtkamp and Brudzinski*, 2014; *Moreno et al.*, 2014].

For most earthquake sequences, it is difficult to uniquely identify whether a fluid source triggered the early events in a sequence, or whether early earthquakes started the fluid migration. This sequence is a rare exception with no such ambiguity, as the EMC hypocenter is located 60 km to the southeast of the inferred origin of fluid migration. This study demonstrates that diverse patterns in aftershock sequences can result from several cooperating mechanisms under typical seismotectonic conditions for transtensional regimes. In fluid-saturated areas within or near a rupture, there is likely to be elevated aftershock rates, swarm-like activity, volumetric migration, and/or delayed triggering of large aftershocks. The spatiotemporal evolution of aftershocks in such regions is strongly affected by fault zone permeability, which is controlled by the dominant fault structures, and reactivated at the time of large events.

A.A. Supporting Information

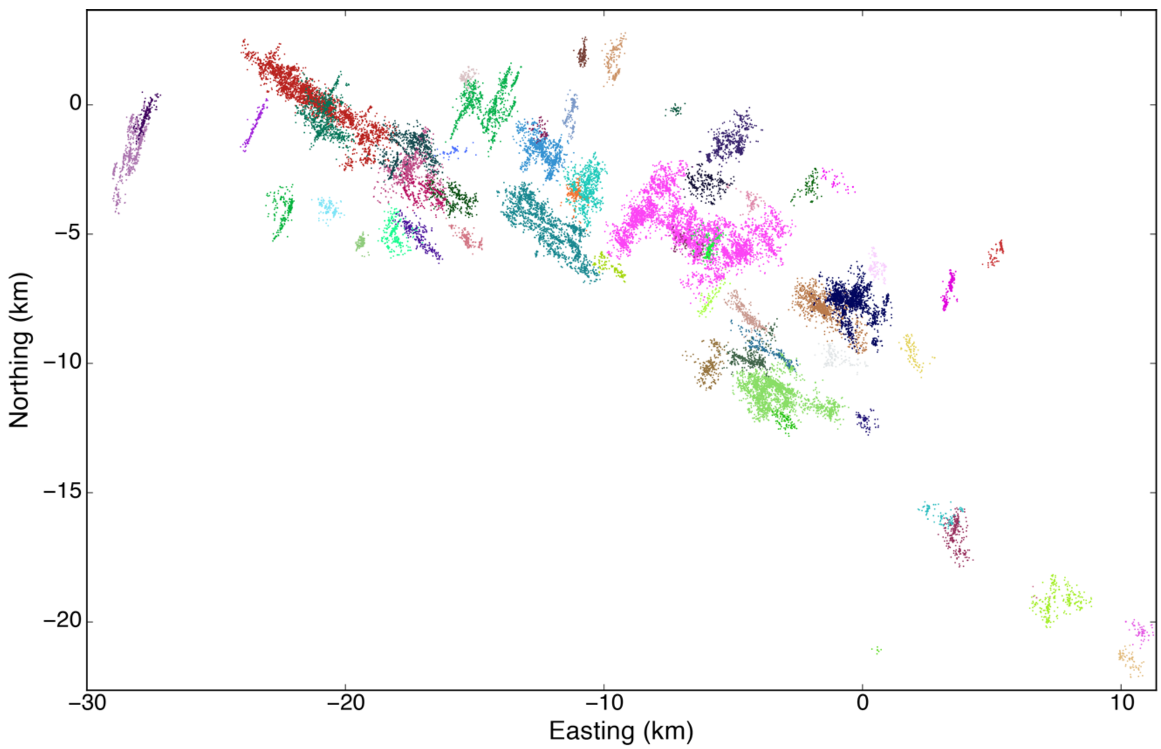

Figure A.S1. Cluster definitions. Each cluster produced by the DBSCAN algorithm is color-coded for visibility. Clusters are spatially-compact and have at least 100 events. Many of the clusters overlap because they are fully separated in depth.

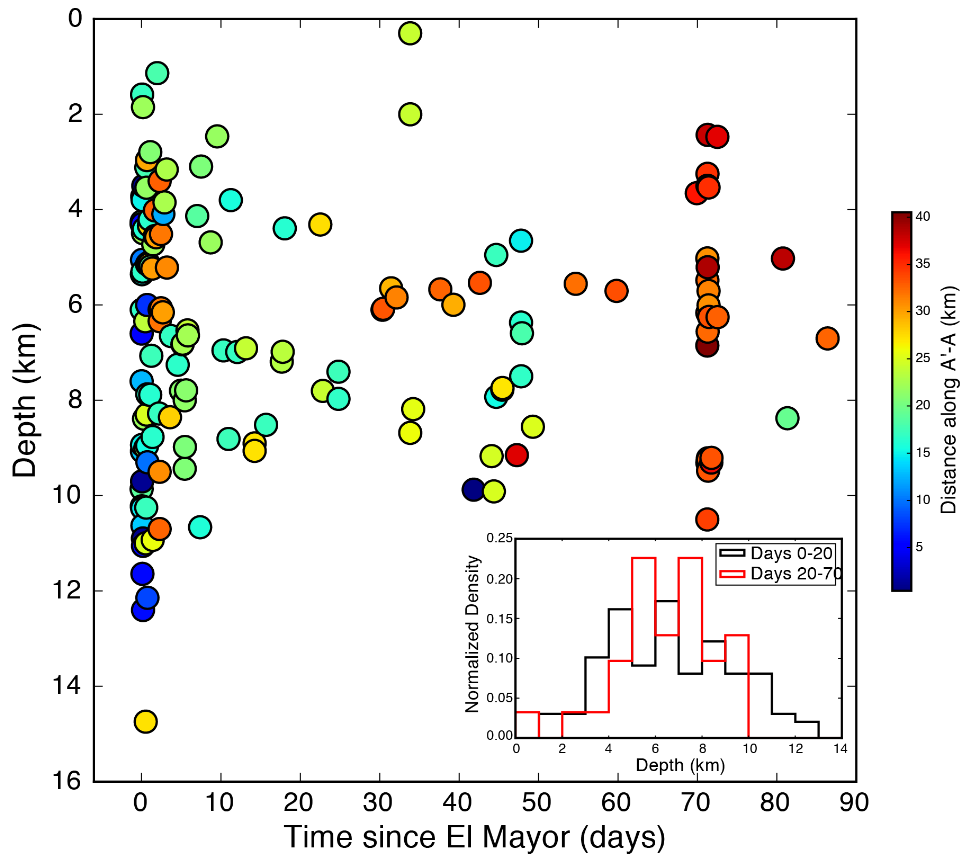

Figure A.S2. Depth evolution for El Mayor-Cucapah aftershocks with M > 3.5. Over the first few days following EMC, events occur over the entire depth range of 0-12 km. Afterward, events occupy a narrower depth range.

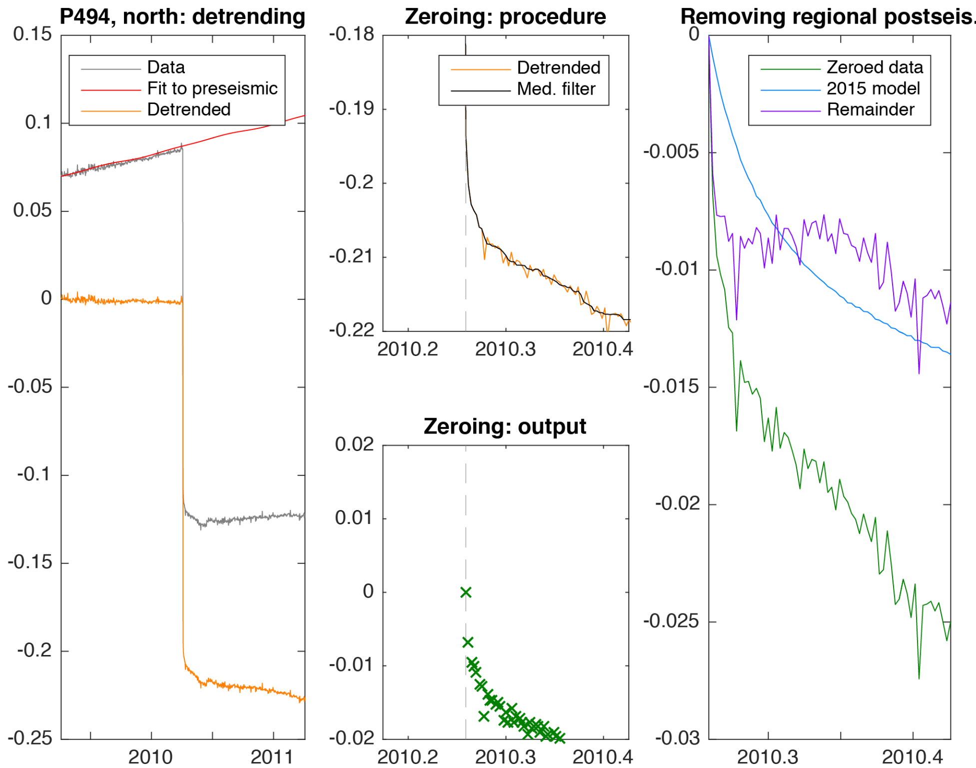

Figure A.S3. Procedure for extraction of the signal of local postseismic deformation from SOPAC GPS timeseries. (left) To detrend the timeseries, we fit the pre-EMC timeseries to a combination of a linear trend, annual and semiannual oscillations, and visually identified offsets, then subtract the prediction of this model in the postseismic period from the timeseries in the postseismic period. (center, top) To ensure that the postseismic timeseries begin at zero, we run a seven-day median filter on the detrended timeseries, then subtract the filtered location on the first postseismic day from the detrended timeseries, yielding a "zeroed" timeseries (center, bottom). (right). To isolate the local postseismic deformation, we remove a published model of larger-scale postseismic deformation [Rollins et al, 2015] from the zeroed timeseries. The published model included an afterslip source in the Yuha Desert that did not fully fit the local postseismic timeseries but helped reduce the regional misfit; we remove the timeseries generated by this afterslip source alone from the timeseries generated by the published postseismic model, and then remove the timeseries of the modified forward model from the zeroed data, yielding the local timeseries we use here.